SYNTHESIS AND PROPERTIES OF NICKEL-CARBOXAMIDE/THIOLATE COMPLEXES FOR MODELING NiSOD AND Ni(II) SENSING

by

ELLEN PATRICIA BROERING

(Under the Direction of Todd C. Harrop)

ABSTRACT

Nickel superoxide dismutase (NiSOD) is a metalloenzyme that disproportionates superoxide ($O_2^{\bullet-}$) to O_2 and H_2O_2 by alternating between reduced and oxidized Ni states. NiSOD's coordination sphere also varies depending on oxidation states. In the reduced form, Ni(II) is coordinated in square-planar geometry by the primary amine of His1, carboxamide-N of Cys2, and two thiolate-S from Cys2 and Cys6. In the oxidized form, the imidazole-N of His1 binds axially in square pyramidal geometry that has proven crucial to accessing Ni(III) and maintaining the diffusion-controlled rate of disproportionation. Given the unusual coordination environment, Ni(II/III) redox, and O_2 tolerance of the Cys-S ligands, we have turned to a synthetic approach to create low molecular weight mimics of the active site and gain insight into NiSOD. Using a metallosynthon precursor, we developed NiN_2S_2 complexes that model reduced NiSOD and vary at one coordination site to tune the electronic environment of the system. As a result of synthetic modifications in two systems, the S character in the redox active molecular orbital was sufficiently suppressed so as to allow access to a high valent Ni state. This is the first observation of a stable Ni(III) species in NiSOD synthetic analogues with structural and electronic donors that match the enzyme. Spectroscopic and computational evidence reveal that

the high valent state is a resonance species of Ni(II)-thiyl radical and Ni(III)-thiolate character. Due to this resonance, the Ni complex exhibits unique reactivity with nitric oxide (NO), resulting in reductive nitrosylation and a dimeric $\{NiNO\}^{10}$ species bridged by thiolates and N-nitrosamines. Turning to oxidized NiSOD models, a peptide-based His-Cysteamine ligand platform was developed, which contains His-N_{Im} poised to bind to Ni in the apical position. However, this system coordinated Ni in an unidentified manner that did not involve the carboxamido-N, as evidenced by spectroscopic characterization. Taken together, these results highlight the reactivity of the amine/carboxamide/thiolate ligand environment of NiSOD. Ni is also found in other metalloenzymes and regulatory systems, and to better understand pathways of Ni trafficking, we have developed a novel N_2S_2 fluorescent sensor based upon the primary coordination sphere of reduced NiSOD to detect Ni(II) in solution.

INDEX WORDS: Nickel, superoxide dismutase, metalloenzyme, sulfur, sensor

SYNTHESIS AND PROPERTIES OF NICKEL-CARBOXAMIDE/THIOLATE COMPLEXES FOR MODELING NiSOD AND Ni(II) SENSING

by

ELLEN PATRICIA BROERING

B.S., Spring Hill College, 2010

A Dissertation Submitted to the Graduate Faculty of The University of Georgia in Partial Fulfillment of the Requirements for the Degree

DOCTOR OF PHILOSOPHY

ATHENS, GEORGIA

2017

SYNTHESIS AND PROPERTIES OF NICKEL-CARBOXAMIDE/THIOLATE COMPLEXES FOR MODELING NiSOD AND Ni(II) SENSING

by

ELLEN PATRICIA BROERING

Major Professor: Todd C. Harrop
Committee: Michael K. Johnson
Jeffrey L. Urbauer

Electronic Version Approved:

Suzanne Barbour
Dean of the Graduate School
The University of Georgia
May 2017

DEDICATION

To my mother, Claire H. Broering

ACKNOWLEDGEMENTS

I would like to thank my advisor, Dr. Todd Harrop, for giving me a place for me in his lab and for the years of mentorship he has provided. Todd, thank you for making me into the best writer, presenter, and chemist I could be. I would also like to thank Dr. Michael Johnson and Dr. Jeffrey Urbauer for serving on my graduate committee and for the support you have shown me over the years. I am fortunate to have such committee members who challenge me, provide letters of reference, and promote my success in so many ways. To Dr. Urbauer and Ramona Urbauer, especially, thank you for your guidance with respect to my graduate school career and my continued studies at UGA. I appreciate the assistance I have received from the research professionals of UGA: thank you Dr. Dennis Phillips, Dr. Dongtao Cui, and Dr. Pingrong Wei for your expertise with mass spectrometry, NMR, and X-ray crystallography, respectively. I am also appreciative to Dr. Charles Kutal for his mentorship over the years and for encouraging my interest in undergraduate education.

To the Harrop group alumni, Dr. Eric Gale, Dr. Vivian Ezeh, Dr. Brian Sanders, and Dr. Melody Walter, thank you for welcoming me into the fold and establishing a lab environment of encouragement, collaboration, and learning. I am especially thankful to Ramsey Steiner and Phan Truong for the skills they have taught me and the never-ending teamwork (team NiSOD). You both make days in lab more fun and more rewarding. Ramsey, I cannot express how grateful I am that graduate school has given me your friendship, in addition to a degree.

Thank you, Mom, for always being my champion, having absolute faith in my abilities, and for always taking my phone calls. My success would not be possible, nor would it mean

anything, without you. Thank you to Greg, for blazing the Broering trail—for better or worse—into post-graduate work, for your perspective, and for reminding me to lean in. I am grateful to my other relatives, especially my late father, my late grandfathers, Aunt Carol, Uncle Paul, and the many other scientists and engineers scattered throughout my family tree who have laid this path for me. To my Georgia guardians, the Newells: thank you, Mrs. Roxanne, for your kindness and boundless generosity; you are my biggest cheerleader! Mr. Bob, I am grateful I have been able to receive and rely on your wisdom in so many aspects of my life, from carpentry to careers. To Linda, thank you for the friendship and the countless 5:30 AM miles we have shared over the past five years. To Sean, thank you for making the last three years of graduate school more meaningful than I ever expected.

TABLE OF CONTENTS

Page

CHAPTER

CHAPTER 1

INTRODUCTION

1.1 An overview: Ni in mammalian physiology

Nickel (Ni) is naturally found in the earth's core, and humans have utilized this transition metal in numerous industrial processes. Ni is mined from ore and is typically used as an alloy with other metals to produce protective coatings, electronic components, pigments, and provide strength in engineered coatings.[1] Because of its widespread use, especially in stainless steel alloys, Ni's role in the environment and biological processes deserve special attention. The use of Ni in mining and manufacturing processes leads to environmental concerns surrounding water pollution, toxicity, and human health hazards.

Humans may take in Ni through the ambient air, food and water sources, and through cigarette usage. Excluding those who work in Ni industries, ingesting Ni in food is the most common form of Ni exposure. The Environmental Protection Agency (EPA) has defined the Maximum Contaminant Level (MCL) for Ni, the legal limit for Ni allowed in public water systems, and the goal for the maximum concentration of Ni which has been determined to have no known adverse health effects in humans, as 0.1 ppm.[2,3] This level of Ni contamination is not common. Indeed, the EPA remanded the Ni MCL in 1995: public water sources are still required to monitor Ni concentrations but are not required to regularly report the value.[2] Data from the Agency for Toxic Substances and Disease Registry (ATSDR) in 2015 estimate that humans consume ~170 μg of Ni per day, which varies depending on growing sources, preparation and

handling, and exposure of food sources to soluble Ni compounds in soils.[4] Despite the nearly unavoidable intake of this metal, there are no enzymes or cofactors that utilize Ni in higher organisms.[1] Bacteria, however, maintain a vital homeostasis of labile Ni(II) and transport the metal throughout their cell for the assembly of nine Ni-containing metalloenzymes such as [NiFe]-hydrogenase, urease, CO-dehydrogenase, methyl coenzyme M reductase, and Ni superoxide dismutase (NiSOD).

At high doses, soluble forms of Ni such as $Ni(OAc)_2$ and $NiCl_2$ are toxic to rats at LD_{50} values of 350 mg/kg and 23 mg/kg, respectively.[5] In humans, Ni poisoning can also occur, manifesting as respiratory illness (possibly due to inhaled $Ni(CO)_4$ from mining sources)[6], skin allergy or contact dermatitis, and kidney diseases.[3,7-10] The National Research Council reports that miners and welders are the population most afflicted with impaired lung function due to inhalation of Ni and suffer ailments such as emphysema, bronchitis, pulmonary fibrosis, and lung and nasal cancers.[4]

In 2009, metallic Ni and Ni compounds were reevaluated by the International Agency for Research on Cancer (IARC) and confirmed respectively as Group 2B, possibly carcinogenic, and Group 1, carcinogenic for humans and animals. In vivo, insoluble Ni particles are taken up by mammalian cells by phagocytosis and maintained within cytoplasmic vacuoles (Figure 1.1).[11] Once within vacuoles inside the cell, compounds can undergo dissolution and release the Ni(II) ion, which is capable of entering the nucleus and interacting with DNA or binding to other cellular macromolecules.[12,13] Ni species that do not easily dissolve in a vacuole or cytoplasm, such as NiO, have a lower toxicity value as compared to other Ni species that can dissociate into a Ni(II) and counter anion. In contrast, soluble Ni forms depend upon and compete with other endogenous metal transmembrane mechanisms, such as ion transporters or Mg(II) or Ca(II)

channels, to cross the cellular-and subsequent nuclear-barriers; therefore, Ni(II) from soluble compounds is less likely to reach the nucleus as compared to those particles taken in wholly by phagocytes (Figure 1.1).[14-16] Insolubles such as NiS and Ni_3S_2 are thus more carcinogenic than $Ni(OAc)_2$, $NiCl_2$, or $NiSO_4$.[1] In fact, cell and animal studies suggest that soluble Ni(II) forms do not lead to cancer unless administered directly or dosed in the presence of other known carcinogens.[4,9]

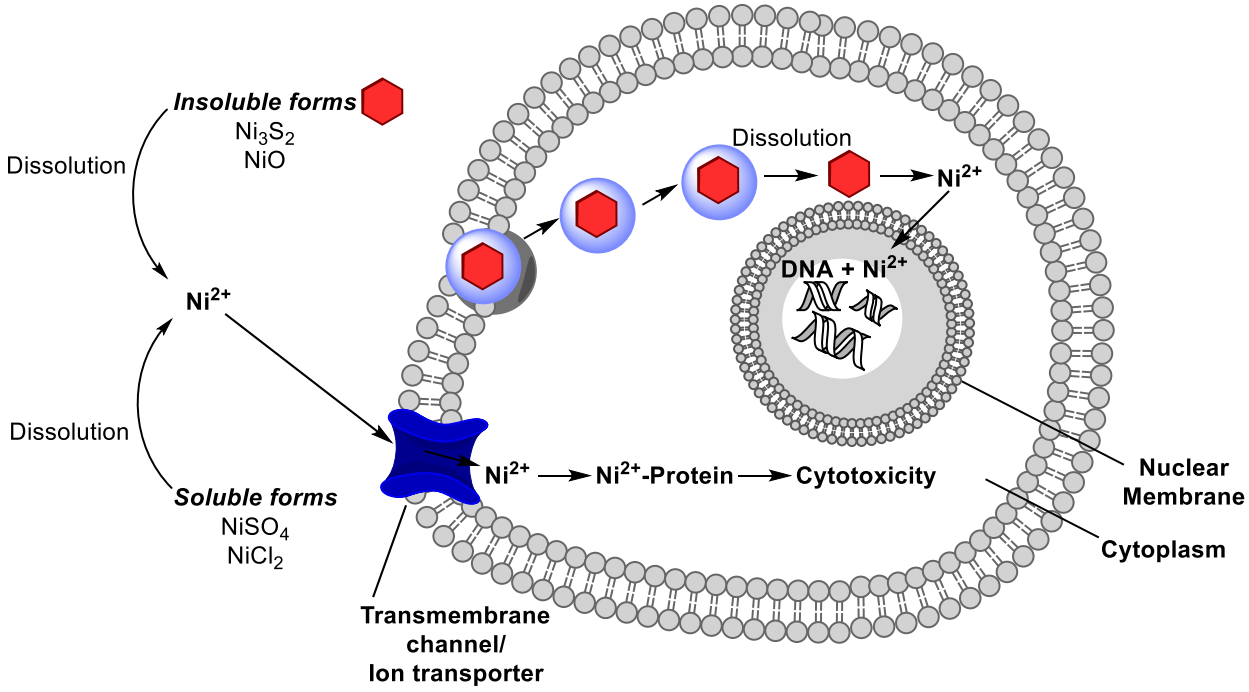

Figure 1.1. Methods in which a cell may uptake Ni depends upon solubility.[9] Insoluble forms of Ni(II) will likely enter the cell through phagocytosis, and once inside the cell can undergo dissolution and release the Ni(II) ion to interact with DNA within the nucleus. Soluble forms of Ni(II) rely upon and compete with ion channels and other transmembrane mechanisms to enter the cytoplasm, after which Ni(II) can react with biological molecules.

The mechanisms of Ni(II) carcinogenicity are not well-defined. Experiments with Chinese hamsters have revealed that injections of Ni result in sister chromatid exchange and chromosomal damage.[17,18] In addition, DNA-protein cross-links and inhibition of DNA repair via methylation or acylation have been observed in vitro following treatment with Ni compounds.[19-22] Cell studies suggest that Ni(II) binds to histone proteins in heterochromatin, the tightly packed form of DNA, to alter histone structure and function.[5,9] Oxidative DNA damage has also been observed as redox active species like Ni_3S_2 and $Ni(CO)_4$, as well as Ni(II) bound to protein residues, are capable of producing reactive oxygen species (ROS).[16,23-25] As there is no evidence to date of Ni binding directly to DNA, the likely path of insoluble Ni carcinogenesis involves binding, damage, and inhibition of other molecules in the cell.[16] The resulting chromosomal aberrations and oxidative damage often prove fatal for mammalian cells with no trafficking system in place to target and export labile Ni. Therefore, further study is needed to better understand the methods in which exposure to elevated Ni concentrations impact human health.

1.2 An overview: Ni trafficking

As Ni toxicity has also been observed in microorganisms, a Ni defense mechanism has evolved to combat high or imbalanced concentrations of labile Ni(II).[26] Ni trafficking machinery has been isolated from classes of bacteria found naturally occurring in various environments, e.g., extremophiles and Ni-resistant organisms found in areas of high Ni contamination, as well as in non-extremophiles, such as *E. coli* and *H. pylori*.[27] Microbiologists have since come to the conclusion that machinery to regulate and traffic Ni pools is common and vital to many bacteria. RcnA (or RcnAB), first observed in *E. coli*, is an efflux pump, which operates to remove both Ni(II) and Co(II) from the cytoplasm by a mechanism that is not well-defined.[26,28] Other Ni

efflux and detoxification proteins exist, although very little is known about their method of recognition, specificity for Ni versus other transition metal ions, or the mechanism for metal export. Examples include CznABC (cadmium, zinc, and nickel resistance) of *H. pylori*[29] and the proton-driven NreB (Ni resistance, member of major facilitator superfamily) of *A. xylosoxidans* and *C. metallidurans*, two nickel-resistant strains found in polluted sites.[30-32]

However, Ni resistance is but one side of the coin of cellular Ni trafficking. Ni is also essential for numerous bacterial processes and is involved in the assembly of nine metalloenzymes. Bacteria that require Ni for life have evolved systems to regulate and distribute the metal throughout the cell and facilitate the incorporation of Ni into metalloenzyme scaffolds (Figure 1.2). Maroney and coworkers draw a comparison between the Ni trafficking pathways for Ni and those for other common transition metal ions, such as Zn, noting that the "traffic pattern for Ni is relatively simple because bacteria that utilize Ni usually feature only one or two target enzymes."[33] Although the majority of the transport pathways for Ni are not yet well understood, in general, the field classifies the various players in Ni trafficking according to occupation: export or efflux, import, metallochaperones and accessory proteins, and metalloregulators.[27,33,34]

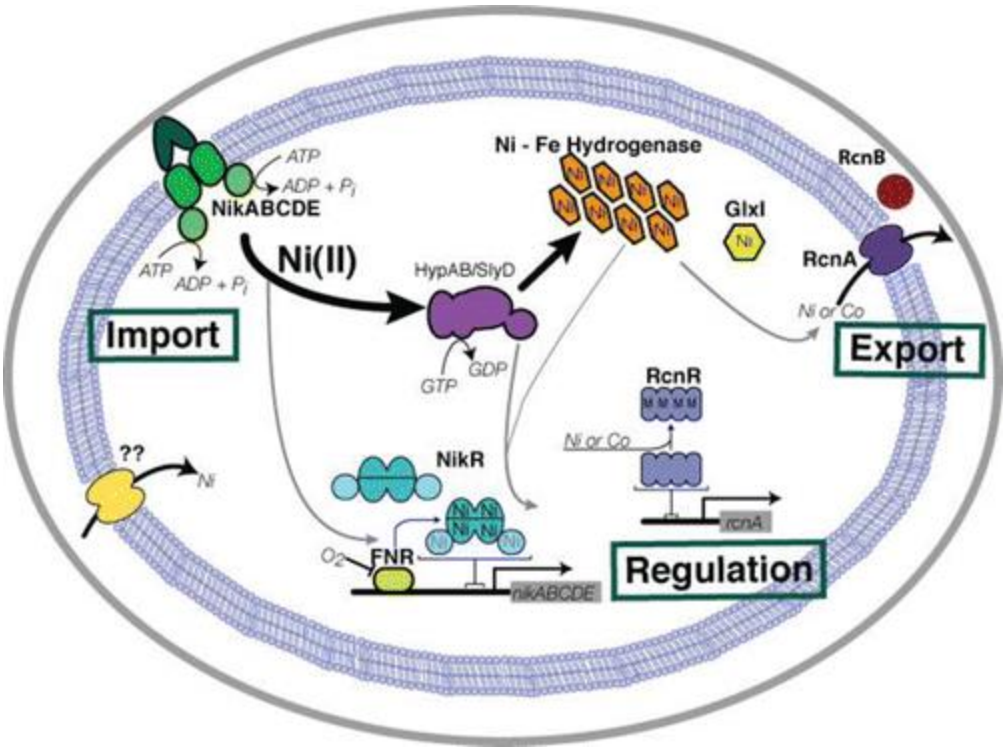

Figure 1.2. A sample representation of Ni trafficking processes in *E. coli*, illustrating the import of Ni by NikABCDE, Ni export by RcnAB proteins, assembly of metalloenzymes by chaperones HypA, HypB, and SlyD, and metalloregulation of NikR and RcnR expression.[33] Figure reprinted with permission from Higgins, K. A.; Carr, C. E.; Maroney, M. J. *Biochemistry* **2012**, *51*, 7816. Copyright 2012 American Chemical Society.

Bacteria must select, uptake, and import Ni from their environment for the assembly of enzymes. Indeed, it was observed by Bartha and Ordal in 1965 that Ni was necessary for growth of two *Hydrogenomonas* strains (hydrogen-oxidizing bacteria), and Ni was later identified as a key component of [NiFe]-hydrogenase.[35] Broadly, there are two methods for the import of Ni by bacteria: (i) intake driven by the hydrolysis of adenosine triphosphate (ATP) by NikABCDE, and

(ii) passive intake through the protein NiCoT (Ni or Co transporter), which lacks ATPase activity.

In *E. coli*, eubacteria, and archaea, the Ni importer NikABCDE features ATP-binding cassette system and is thus a member of ABC-type transporter subfamily, which binds and hydrolyzes ATP to power the exchange of substrates across the cellular membrane.[36-38] NikABCDE is composed of two transmembrane proteins, NikB and NikC, which form a cavity for the Ni; two ATPases to hydrolyze ATP (NikD and NikE); and the periplasmic binding protein (NikA). NikA has been crystalized with Ni(II) in varying coordination numbers (CNs) and geometries, and recent evidence suggests that Ni is held within the binding pocket of NikA via H-bonds and is transported as a Ni(II) complex with stereospecific L-His residues.[39,40] A-ray absorption spectroscopy (XAS) and mutagenesis studies support the claim that recognition of Ni by NikA is dependent on binding to His416.[41]

In prokaryotes and fungi, the NiCoT family import Ni(II) and/or Co(II) into the cell with a K_m of 10-20 nM.[27,42] NiCoTs are one class of permeases, proteins that allow for passive diffusion of ions through the cellular membrane. Several members of the NiCoT family have been isolated from different organisms, such as NixA from *H. pylori*[43] and HoxN from *A. eutrophus*,[42,44] both of which are vital to urease and hydrogenase function. The Ni binding site is likely the His-X_4-Asp-His sequence conserved among many NiCoTs and also found in NikC.[45,46] Beyond these two broad families of Ni importers, evidence suggests that Ni may also be taken into the cell by other indiscriminate metal ion membrane permeases, as in the case of bacterial need or in an environment of elevated Ni concentrations.

The identities of metallochaperones or accessory proteins, which aid in the delivery of Ni for incorporation into metalloenzymes, vary depending on bacterial strain. For this work, it

would be more fitting to discuss the accessory proteins required for Ni insertion into [NiFe] hydrogenase and urease enzymes. HypB and HypA are two maturation proteins required for insertion of Ni(II) to the apo-hydrogenase scaffold, and recent work (2016) has revealed insights into their structures and cooperative relationship.[47,48] HypB exhibits GTPase activity necessary for its Ni chaperone function, meaning that HypB binds and hydrolyzes guanosine triphosphate (GTP) in a conserved G-domain.[49] The HypB found in *E. coli* binds two Ni ions: the "high affinity" (dissociation constant, $K_d \approx 1.3 \pm 0.2 \times 10^{-13}$ M) site is located near the N-terminus and binds Ni(II) in a four-coordinate (4C), S_3N/O planar geometry.[50,51] A second "low affinity" binding site is located in the C-terminus GTPase domain (G-domain) and binds Ni(II) with mM affinity ($K_{d(\text{app})} \approx 1.2 \pm 0.2 \times 10^{-5}$ M) or Zn(II) with ($K_{d(\text{app})} \approx 1$ μM), i.e., the HypB low affinity site does not exhibit a binding preference for Ni.[51] XAS results have demonstrated that M–L bond distances shift with subsequent binding of a metal ion to each HypB site, perhaps as a form of communication for the metallochaperone.[47] Further evidence suggests that Ni or Zn binding in the G-domain site of HypB serves as a regulatory mechanism, as GTPase activity is diminished upon metal binding. The higher affinity and G-domain binding sites of HypB exhibit variations among other organisms.

HypA is a homodimer with Ni and Zn binding domains. *E. coli* and *H. pylori* structures agree that the Ni domain binds two Ni(II) ions per dimer with micromolar affinity by the N-terminal residues but in an unknown coordination geometry.[52,53] Recent work (2017) reveals the terminal amine is a Ni-ligand in HypA (vide infra).[54] The Zn binding domain is better understood, as studies confirm Zn(II) is held in a tetracysteinato, tetrahedral geometry; however, low pH or Cys→Ala/Asp mutations result in a new $Zn(Cys)_2(His)_2$ coordination and a loss of Ni binding and pH sensitivity.[53] Further Cys and His mutations in HypA suggest that the ligands

involved in the Zn binding site control protein conformational changes and, in turn, adjust Ni transport in response to changes in pH.[53]

HypB and HypA together form a complex to deliver Ni to the apo hydrogenase in *E. coli*.[52] Within minutes of combining, a Ni(II) ion moves from the G-domain site of HypB to HypA. Zamble has determined that the rate of Ni transfer from HypB to HypA is affected by the relative abundance of GTP, or its dephosphorylated product, guanosine diphosphate (GDP).[47] Not only does Ni or Zn binding to the HypB G-domain inhibit GTPase activity, but the presence of GDP affects the binding affinity and CN of Ni(II) in the HypB G-domain. As illustrated in Figure 1.3, when the cell initiates GTPase activity, a change in the HypB protein structure occurs, and the Ni-site in the G-domain weakens in its Ni(II) affinity to allow for Ni release.[47] This conformational change promotes the complexation of HypB and HypA followed by the rapid transfer of Ni to the HypA and subsequent release of GDP. Only after the transfer of Ni to an empty metal site on HypA do the two proteins dissociate from each other, and Ni may be subsequently transferred to the hydrogenase enzyme. The final step of Ni insertion involves an undetermined interaction between HypA and the large subunit of the apo-hydrogenase. The complicated interplay among distinct metal binding sites, GTPase activity, and protein conformational changes, in addition to other hydrogenase accessory proteins SlyD and HypF, illustrates the intricate machinery and regulation that bacteria have evolved to direct the delivery of Ni to the enzyme active site.

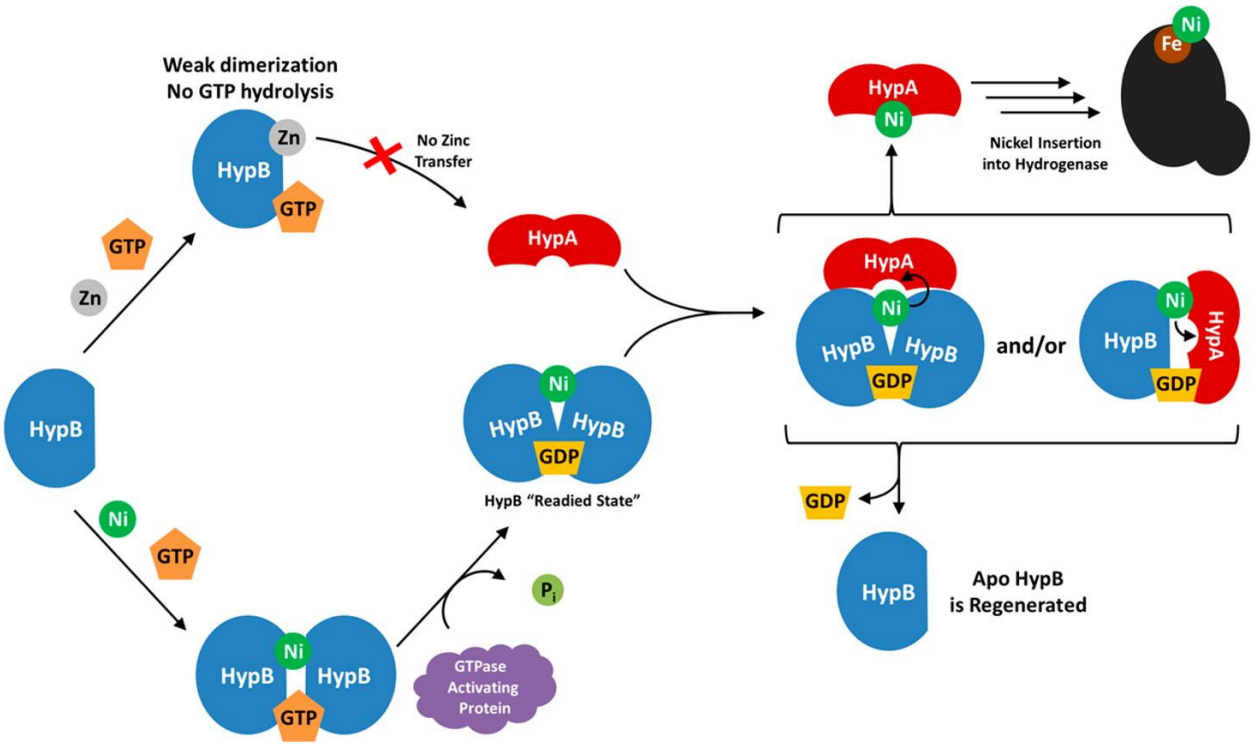

Figure 1.3. The transfer of Ni(II) between HypA and HypB. HypB binds GTP and may bind Ni(II). When GTPase hydrolysis occurs, the affinity for Ni weakens, and complex formation with HypA is initiated. Rapid transfer of the Ni(II) from HypB to HypA occurs, and the HypA protein separates and inserts Ni into hydrogenase. This chaperone pathway does not proceed if Zn(II) binds instead to HypB. Figure reprinted with permission from Lacasse, M. J.; Douglas, C. D.; Zamble, D. B. *Biochemistry* **2016**, *55*, 6821. Copyright 2016 American Chemical Society.

Another Ni metalloenzyme, urease, is assembled via numerous accessory proteins, such as UreD, UreE, UreF, and UreG. The ultimate insertion step of Ni into the apo-urease active site is carried out by UreE. Each UreE accessory protein binds six Ni in likely 6C N/O, His-heavy, pseudo-octahedral geometry (K_d is in the μM range and varies among bacterial strains).[55] UreE from the *K. aerogenes* strain has also been shown through mutagenesis, size exclusion

purification, and UV-vis studies to bind other divalent transition metals, i.e., Cd(II), Co(II), Zn(II), and Cu(II), but with unique coordination environments and affinities.[56,57] This evidence suggests that UreE may utilize specific ligands as a recognition mechanism for Ni(II). XAS results and crystallography of UreE vary depending on organism, but crystal structures reveal that Ni(II) binding spans across separate subunits, utilizing His152, Glu4, and His102 residues from separate monomers.[58] Contrastingly, crystal structures of Zn-UreE reveal Zn(II) tetrahedrally-bound by His residues of a single monomer, again reinforcing that each transition metal elicits a distinct coordination environment and protein conformations.[56,58] The His residues unique to Ni(II) binding by UreE are thought to play a role in the transfer of Ni to the urease active site.

Once thought to only play a role in hydrogenase assembly, HypA and HypB are also needed in the delivery of Ni to urease in the *H. pylori* pathogen; mutation and removal of *hypa* and *hypb* genes from *H. pylori* also silences urease expression.[54,59] Furthermore, Maier et al. has demonstrated interactions among HypA, UreE, and HypB in the urease maturation pathway.[60,61] Insights into the binding motif of Ni(II)-HypA have been published in 2017 by Maroney and have confirmed a 6C Ni(II) environment involving both the N-terminal amine of methionine (Met1) and the imidazole-N of His2 as ligands.[54] Insertion of a Leu residue into the terminal MHE (Met-His-Glu) motif of HypA prevented Ni-binding by Met1 and resulted in decreased urease function; however, the L2 insertion did not prevent HypA-Zn binding or HypA-UreE protein-protein interactions.[54] The depletion of urease function in *H. pylori* resulting from this mutation, despite having other UreEFGH chaperones still available, suggests that the acidic cellular environment unique to the *H. pylori* pathogen necessitate the use of an alternative HypAB pathway.[54,62]

Among metalloregulators, which are so named as they regulate the expression of Ni transport proteins, NikR and RcnR are the most studied. NikR is a DNA-binding protein that controls the expression of the NikABCDE importer in response to cellular Ni homeostasis.[63,64] When Ni concentrations are elevated, NikR represses transcription of the operon for *nikABCDE* genes. Structural studies reveal that *E. coli* NikR is a tetrameric member of the ribbon-helix-helix DNA-binding protein family. Each monomer binds one Ni(II) ion with a $K_d \approx 2$ pM.[34,65,66] This picomolar affinity is controlled by the "high affinity" site on NikR, located at the C-terminal domain, and holds Ni(II) in square-planar, 4C geometry likely composed of residues His87, His89, and Cys95, in addition to His76 from another monomer (Figure 1.4).[67] There are other proposed "low affinity" sites, most notably one near the boundary of the C-terminus and DNA-binding domain revealed by mutagenesis and mass spectrometry studies. This location may explain observations that elevated concentrations of Ni and increased Ni binding at both the high and low affinity sites in NikR increase the protein's affinity for DNA.[66] Likewise, the C-terminal domain of NikR was observed to uptake Ni with a $K_{d(\text{app})}$ two-to-three fold greater in the presence of DNA operators.[66,68] The exact nature of the relay mechanism that controls NikR's responses to DNA, fluctuations in the C-terminal domain, and changing Ni(II) concentrations is not known. NikR from different organisms also exhibits variations in their DNA-bound conformational structures, ranging from *trans* (as seen for *H. pylori* and *P. horikoshii* in which the DNA domains are on opposite faces)[69,70] to *cis* (in *E. coli* with DNA domains close together on one side)[67] conformations.[33]

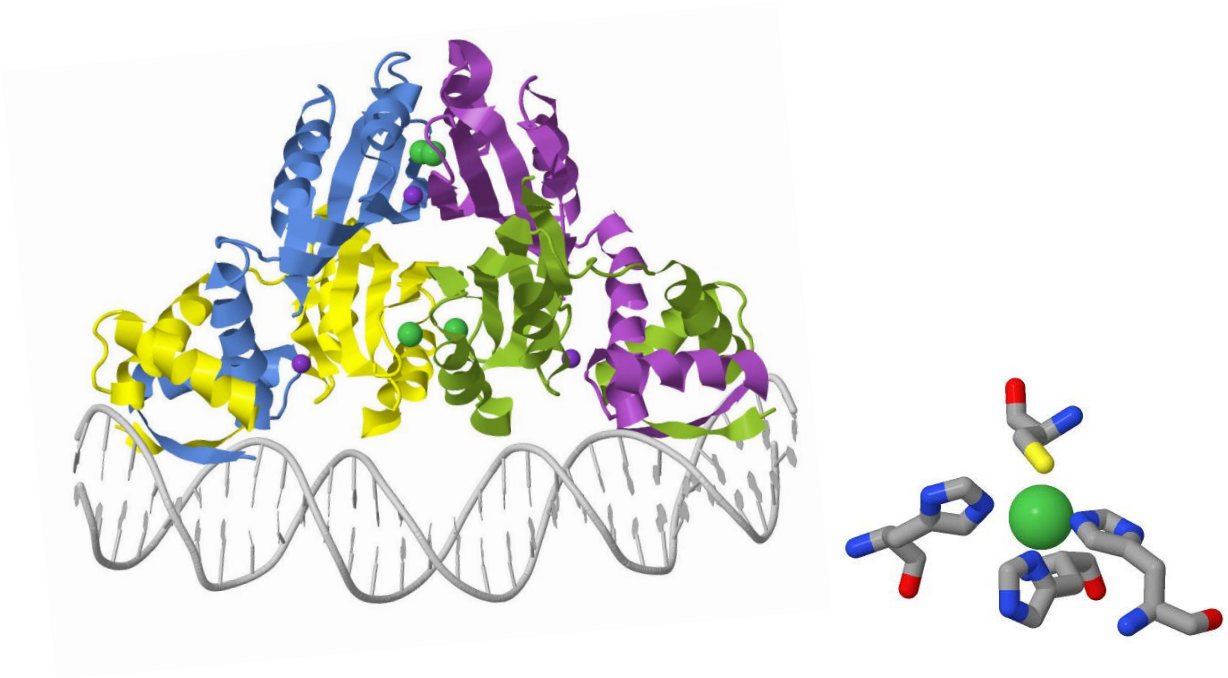

Figure 1.4. X-ray crystal structure of the NikR-DNA complex with the high affinity Ni(II) sites shown with Ni as green spheres, and low affinity sites shown with K(I) as purple spheres from *E. coli* (3.1 Å resolution, Protein Data Bank entry 2HZV). The coordination environment of one high affinity Ni(II) binding site is shown (right). These images were generated with Jmol.

NikR will also bind other endogenous transition metals such as Co(II), Cu(I), Cu(II), and Zn(II) at low affinity sites.[65] Just as certain metal binding preferences were observed in UreE (vide supra), XAS reveals that NikR also changes the ligands involved, geometry, and protein conformation depending on the metal ion. For example, Maroney has found that NikR likely binds Co(II) in a 6C mixed N/O environment that contains His residues but not Cys95.[71] Metallosensing by NikR, and therefore repression of *nikABCDE*, is likely a sophisticated system depending upon Ni(II) selection, ligand and geometry preferences, DNA operator binding affinity, and protein conformational changes.

RcnR is a metalloregulator that controls the expression of the Ni and Co exporters RcnA and RcnB (RcnAB).[72] The tetrameric, helical RcnR binds DNA via two different protein regions, but it will release DNA upon binding Ni(II) and Co(II), likely as a triggering response; Rodrigue et al. suggests that metal binding results in a conformational change unfavorable to DNA binding and will trigger the expression of RcnAB.[26] Unlike the metalloregulators that repress transporter transcription and have two Ni(II) binding sites, i.e., NikR and Nur (vide infra), the upregulator RcnR possesses only one metal binding site.[33] XAS, mutagenesis studies, and β-galactosidase reporter assays (via the lacZ gene) conducted by Maroney have revealed many details about the Ni(II) and Co(II) binding properties of RcnR. RcnR binds Ni(II) or Co(II) in a 6C, mixed $(N/O)_5S$ environment with the sole cysteine residue in RcnR, Cys65, serving as one ligand (Ni–S: 2.62(2) Å; Co–S: 2.31(2) Å).[72,73] Investigating the identity of the other ligands, it was determined that Co(II) is also coordinated by three His ligands, one of which is His3 (Co(II)-RcnR K_d = 5 nM); Ni(II) ligation involves two His ligands, but not His3 (Ni(II)-RcnR K_d = 25 nM).[72] Mutations and lacZ assays also point to the terminal amine-N, His33, His60, and His67 as possible ligands vital for RcnR activity, with His60 not affecting Ni(II) response.[72] Although RcnR has been shown to bind other metal ions, it does so in 4C or 3C environments comprised of alternate protein residues, underlining that protein conformations and ligand environments are determinants in metal recognition.[73]

The final metalloregulator to be discussed here is Nur, a Ni(II) sensor isolated from *S. coelicolor* that regulates the *sodF* gene in response to Ni concentrations and oxidative stress.[74] Nur is a homologue of the Fur (ferric uptake regulator) family of metal-responsive transcription regulators. In conditions of elevated Ni concentrations, Nur binds to the *sodF* and *nikABCDE* genes, to suppress expression of Fe superoxide dismutase (FeSOD) and NikABCDE,

respectively. Ni(II) is required for Nur–*sodF* binding, and no other transition metal triggers this activity.[74] Nur of *S. coelicolor* may also regulate expression of the *sodN* gene that encodes NiSOD, as Ahn et al observed that an inactivating mutation of Nur silenced the expression of NiSOD.[74,75] The crystal structure of Nur reveals it to be a homodimer with a DNA-binding domain and two metal binding sites per monomer. Structural data from Roe and Cha suggest that the Ni-binding site is 6C with mixed N/O ligands, likely including His residues, although solvent molecules from the growth media are also bound to Ni.[76]

As illustrated in this discussion, there is still much to be learned about the mechanisms of Ni trafficking at work in bacteria. Only some of the Ni exporters, importers, chaperones, and regulators have been definitively, structurally characterized. The selected proteins discussed above, such as NikA, HypA, and UreE, seemingly exhibit Ni specificity and recognition based on changing ligands, geometries, and preferred CN, and in the cases of RcnR and NikR, the proteins themselves also reveal distinct conformational changes upon Ni(II) binding.[27,33] Bacteria have evolved trafficking systems to maintain Ni(II) homeostasis that is necessary for assembly of metalloenzymes and for sustaining life. To better understand the role of Ni in biology, the proteins involved in metal trafficking, and the mechanisms of Ni(II) insertion into metalloenzyme scaffolds, it is important to develop sensors capable of selecting and distinguishing Ni from other biologically relevant ions.

1.3 An overview: Ni sensing

Ni(II) homeostasis and the balance between protein-bound and labile pools of the metal ion are fluxional and inherently difficult to study. As illustrated above, there is still much to be discovered about the role of Ni and the transport of the ion in bacteria and mammalian

physiology. The EPA has approved instrumental methods such as inductively-coupled plasma mass spectrometry (ICP-MS) or electrothermal atomic absorption (AA) spectroscopy to quantify levels of Ni as low as 0.005 μg/mL in drinking water or biological samples; however, these techniques require relatively immobile instrumentation, access to ionizing gases or acetylene, co-solvents, and high temperatures.[77-79] The EPA recommends that ICP-MS be used for compliance monitoring for samples containing multiple elements of interest, although ICP-MS procedures also warn that high levels of Fe, Mn, Cr, Cu, Co, and Zn may depress signal intensity of Ni in a sample.[78] Further EPA guidelines suggest colorimetric tests for volatile $Ni(CO)_4$, in which the Ni species is absorbed in a solvent (such as chloramine or iodine in carbon tetrachloride) and then colored with dimethylglyoxime to measure Ni colorimetrically.[78] Although these tests and other sampling train methods provide sensitivity (> 0.1 ppm) and selectivity for Ni, it is more ideal to use an environmental sample directly, without needing harsh vaporizing conditions of ICP-MS or AA, nor relying on the extraction of the Ni species into organic solvents for colorimetric techniques. Fluorescence spectroscopy represents a new, advantageous route for the detection of Ni with, i) relatively little treatment required to prepare an aqueous samples as compared to colorimetric methods, and ii) more compact and portable instrumentation requirements as compared to ICP-MS.

Given nature's many uses for Ni, as well as the potential dangers of Ni in human health, a number of research groups have published fluorescent probes in efforts to selectively detect Ni(II). These include protein- and polymer-based probes, in addition to small molecule sensors, which will be the focus of this discussion. Metal ion sensors typically contain a binding site, fluorescent reporter group, and linker between these moieties (Figure 1.5).[80] For turn-on fluorescent sensors, the mode of operation often depends upon photoinduced electron transfer

(PET). In the example PET mechanism depicted in Figure 1.6a, the sensor features a receptor orbital of energy higher than the fluorophore's highest occupied molecular orbital (HOMO) that quenches fluorescence of the molecule.[80,81] Excitation of the sensor in Figure 1.6a promotes an electron to the excited state and creates a hole in the HOMO, which can be filled by electron transferring from the lone pair of the free receptor. This pairing-up prevents the excited electron of the fluorophore from returning to the ground state via a radiative process and thus prevents fluorescence. Upon chelation of a metal (or in some cases protonation of the receptor), the energy of the receptor orbital is sufficiently stabilized and lowered to a level below that of the fluorophore HOMO (Figure 1.6b). After excitation of an electron, the receptor is incapable of transferring an electron to the fluorophore's orbital; therefore, fluorescence may occur. Taken together, this illustrates that, for recognition-based sensors that rely upon chelation of a metal for enhanced turn-on, careful attention must be paid to the design of the receptor and the energies of the ground and excited state of the chromophore.

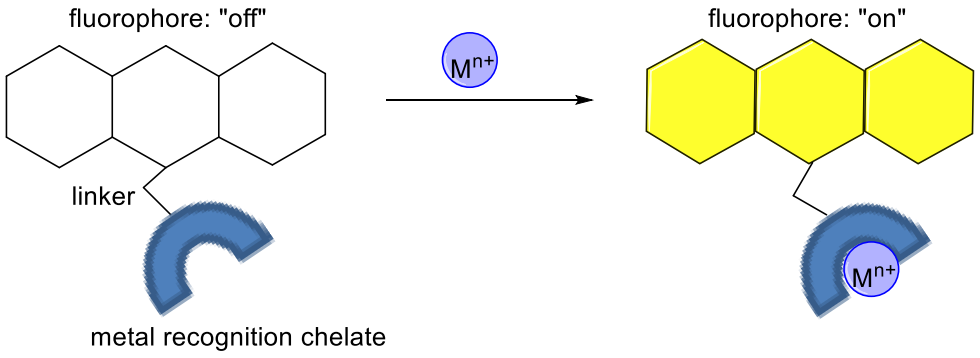

Figure 1.5. General cartoon depiction of the turn-on response of a recognition-based probe upon binding a metal ion M^{n+} to a metal recognition chelate site.[82]

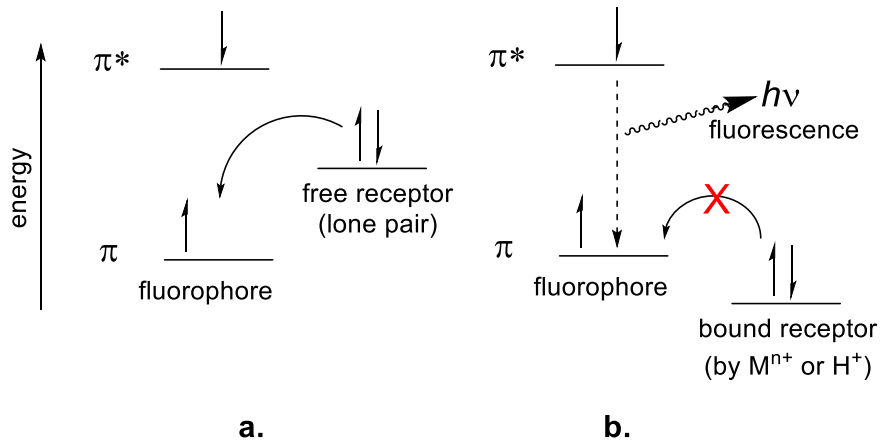

Figure 1.6. Example mechanism of a turn-on fluorescent sensor designed for chelation enhanced fluorescence.[81] (a) In the excited state, fluorescence is quenched by electron transfer from the lone pair on the free receptor. (b) In the excited state, chelation of a metal (or protonation) lowers the energy of the receptor and restores fluorescence.

Transition metal sensing, as opposed to sensing redox-inactive metals, poses challenges to researches to design sensors for the multiple oxidation states of the metal of interest. These challenges may explain why, in general, redox-active metal sensing and trafficking are less well studied as compared to Ca(II), Na(I), and Zn(II) trafficking, for example. An ideal Ni sensor should exhibit specificity for Ni(II) above all other biologically relevant metals, and it should be non-toxic, water soluble, and operate at physiological pH for the spatial and temporal mapping of Ni in biological samples.[80,82] The ideal sensor should also bind Ni(II) with a dissociation constant that can compete with ligands or proteins in vivo. In terms of fluorescent properties, the sensor should produce a significant turn-on response upon binding Ni(II) with a sufficient quantum yield (Φ); this is especially important in light of the low probe concentrations required

for biological samples.[82] The sensor's excitation (λ_{ex}) and emission (λ_{em}) wavelengths should also occur within the visible spectrum.

In polymer-based sensors for transition metals, the metal recognition site or fluorescent reporter group is typically bound to a polymer backbone or substrate.[83-87] For example, Su and coworkers have published coumarin-bound *N*-vinylpyrrolidone[84] or acryloyl chloride[83] systems, in which a piperazine ring acts as an M^{n+} receptor and on-switch for the PET fluorescence mechanism. Su's sensors exhibit activity over a wide pH range and display enhanced, but not selective, turn-on for Ni(II) as compared to the polymer's response to protons and Zn(II), Cu(II), and Co(II). Furthermore, an immobile or substrate-bound sensor is not ideal for intracellular sensing applications.

In 2002, Salins et al. published a modified nickel binding protein from *E. coli* labeled with a fluorescent-tagged Cys residue near the Ni(II) binding site.[88] This protein-based sensor has a detection limit of 10^{-6} M and demonstrates increased quenching upon Ni(II) binding, with a more modest quenching response recorded for Co(II). Taking further inspiration from nature, but without the need for a lengthy protein expression process, Imperiali[89,90] and others[91] have taken advantage of the Amino Terminal Cu(II) and Ni(II) (ATCUN) binding motif from serum albumin to design metal ion fluorescent probes. The distorted square-planar, N_4 ATCUN binding motif is composed of a Gly-Gly-His tripeptide and binds Cu(II) and Ni(II) with high affinity (~10^{-11} M for Cu(II)-ATCUN).[92,93] One sensor features the ATCUN site as part of a pentapeptide sequence tethered to a dansyl (Dns) fluorophore via an amino acid linker (Figure 1.7a).[90] Upon titration with Ni(II) or Cu(II) into buffered solutions (pH 7.0) of the sensor, fluorescent quenching was observed at ~65-85% or ~93%, respectively. More complete quenching response depended on the linker distance between the metal binding site and Dns, indicating an

intramolecular distance-dependent quenching mechanism. Addition of other biologically relevant metal ions did not replicate this quenching effect.[90] The sensor's peptide backbone was adhered to a resin and further modified to replace the second Gly with a β-alanine residue, a replacement that resulted in a quenching response specific for Cu(II) that is reversible upon addition of ethylenediaminetetraacetic acid (EDTA).[90] In conclusion, a turn-off sensor was synthesized that demonstrated varying binding preferences for Ni(II) and Cu(II) that depended on coordination of deprotonated N^- ligands of the peptide backbone, i.e., Gly vs Ala. The sensor's preference for Ni(II) and Cu(II) highlighting nature's intended use of the ATCUN motif to bind both of these ions.

In efforts to synthesize a Ni(II) specific turn-on sensor, Imperiali published a second ATCUN-based peptide operating by a fluorescent resonance energy transfer (FRET) mechanism.[89] A family of hexapeptides was synthesized with a coumarin (DE, donor) or rhodamine (LR, acceptor) derivatized fluorophore on each end. Upon binding Ni(II), the peptide folds in such a way as to bring the fluorophores together, allowing energy transfer from the donor to accepter molecule. Addition of Ni(II) to a buffered solution of each sensor results in a turn-on FRET response for only one, P7 ($K_d \approx 100$ nM; $\lambda_{em} = 588$ nm, pH 7.0, 50 mM HEPES, 150 mM NaCl) (Figure 1.7b).[89] However, addition of Cu(II), and to some extent Fe(II), quenches the fluorescence intensity of the P7 sensor by ~25% and ~10% respectively, making quantitative detection of Ni(II) by P7 difficult. The modifications Imperiali and coworkers make to the ATCUN-derived sensor represent a step towards achieving Ni(II) specificity, although modest quenching from Cu(II) and Fe(II) limit the sensor's application in biological samples.

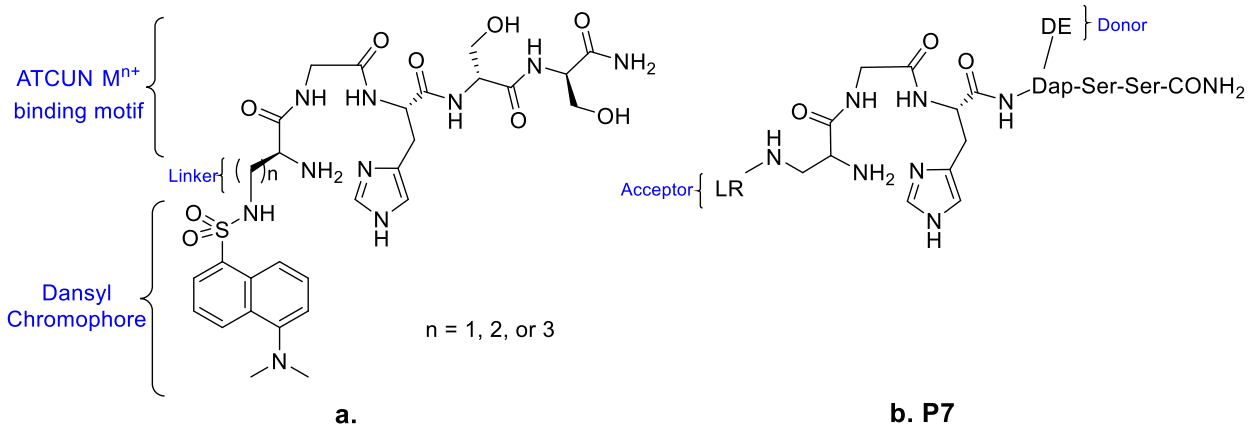

Figure 1.7. (a) the pentapetide Ni(II)-ATCUN binding-motif based sensor with a linker chain, abbreviated as the number of carbons n = 1, 2, or 3, to a dansyl chromophore.[90] (b) P7, the hexapeptide ATCUN-binding motif sensor that operates by a FRET mechanism. DE = 7-diethylaminocoumarin-3-carboxylic acid; LR = lissamine rhodamine B sulfonyl chloride; Dap = (*S*)-2,3-diaminopropanoic acid.[89]

Turning to low-molecular-weight synthetic probes, Fabbrizzi and colleagues report a series of small molecule fluorescent probes for Ni.[94-100] The majority of these sensors feature a N_4 macrocyclic metal binding motif tethered directly to a fluorophore[95,97,98,100] or employ a scorpionate design (scorpionate donors are capable of binding over the plane composed of metal and ligands).[96,99] Earlier generations of a dioxocyclam ligand bound to anthracene were observed to bind both Cu(II) and Ni(II) in water/MeCN mixtures, resulting in a quenching response via a PET mechanism (Figure 1.8a).[98] However, the extent of quenching was most complete with Cu(II) and observed over a narrow pH range: emission is quenched by Ni(II) and Cu(II) at pH = 5 and pH = 3.5 respectively, making these systems incompatible with biological samples. In addition, tetraaza macrocyclic ligands linked with naphthalene, dansyl, 1,3-benzoodioxole, or 1,2,3-trimethoxybenzene fluorophores have also been used to report on oxidation states of

Ni(I)/(II)/(III).[95,97,100] For example, aqueous 0.1 M $HClO_4$ solutions of 1,3-benzoodioxole and 1,2,3-trimethoxybenzene appended cyclams (Figure 1.8b) were electrochemically oxidized to Ni(III) (held at a potential 0.25 V more positive than the Ni(II)/Ni(III) redox couple vs SCE), resulting in a quenching of the fluorescence emission (Ni(III) Φ = 0.08; Ni(II) Φ = 0.20).[97] Electrochemical reduction of the metal yielded restored fluorescence intensity, and this redox cycle was repeated five times without significant loss of signal intensity. The authors note that the redox-dependent off-on fluorescence cycling was observed only in MeCN or acidic solutions (0.1 $HClO_4$); buffered conditions were not feasible due to the instability of the Ni(III) complexes. Although this probe design is novel, the biological application of it is limited: labile pools of Ni in the cytoplasm and most Ni species bound to proteins would not experience such a range in redox potentials or oxidation states.

The scorpionate family of sensors employs a similar cyclic binding motif with a flexible arm connecting the fluorophore.[96,99] The deprotonation and binding of N belonging to the pendant arm, which in turn produces a fluorescent quenching response, are shown to have a pH dependence. The studies were carried out in 4:1 EtOH:H_2O spanning a pH range of 3-11. For the dansyl-appended macrocycle (Figure 1.8c), the maximum fluorescence intensity (λ_{ex}: 332 nm; λ_{em} = 510 nm) is observed at pH < 3.5 when the Dns is unbound and the 6C Ni(II) ion is coordinated by two water molecules and the N_4 ligand frame.[96] At pH < 3.5, the sulfonamide-N of Dns is protonated and exhibits a strong fluorescent signal at λ_{em} = 510 nm and Dans absorption at λ_{max} = 334 nm. As the pH of the EtOH:H_2O mixture increases to 6, the sulfonamide-N is deprotonated and replaces water as a Ni–ligand, which quenches Dns fluorescence. The pH 6 species was crystallized as a 5C Ni(II) in distorted trigonal bipyramidal geometry, a structural change that is also reflected in the redshifted Dns λ_{max} to 312 nm.[96] The

authors propose that electron transfer (eT) or electronic energy transfer process is occurring between the sulfonamide and Ni to quench fluorescence. From pH 7.5-11.5, approximately half of the original emission response returns, possibly due to the additional binding of a water/OH^- resulting in a 6C, octahedral geometry that partially reduces the eT effect between the metal and Dns. The scorpionate arm's movement and pH-dependent coordination of this "molecular machine" provide many insights into the effect of pH on the emission and protonation of the Dns-sulfonamide; however, due to the relatively subtle differences in fluorescence response from pH 6-11.5, this design is perhaps best suited for monitoring Ni in acidic solutions.

Other sensors designed by Fabbrizzi feature open-chain tetraamine ligands linked to an anthracene or $Ru(II)(bipy)_x$ chromophores, where bipy = 2,2′-bipyridine.[94,98] The most promising of which for aqueous biological sensing contains a $[Ru^{II}(bipy)_3]^{2+}$ chromophore that quenches fluorescence by ~95% upon deprotonation of two carboxamide-N and binding of Ni(II) or Cu(II) (Figure 1.8d).[94] In aqueous buffered solutions, a pH-dependent complexation was observed with 1:1 solutions of the sensor and Cu(II) or Ni(II) to result in a neutral complex. The authors hypothesize the deprotonation of the carboxamide-N ligands may only occur in the presence of 3*d* transition metal ions that benefit from a ligand field stabilization: Cu(II) and Ni(II).[94] The addition of other divalent metals such as Mn(II), Fe(II), Co(II), and Zn(II) did not result in a complex that quenched fluorescence intensity to an extent lower than the apo $[Ru^{II}(bipy)_3]^{2+}$ chromophore (Φ = 0.028). A reduced Ru(I) species was not observed nor detected through photolysis experiments, leading the authors to propose an energy transfer quenching mechanism for the probe (Figure 1.8d).[94] Titration studies revealed that the binding of Cu(II) and Ni(II) to the sensor occurs over a very narrow pH range between pH 5-6.8 and pH 7.5-8.5, respectively, and Cu(II) concentrations as low as 10^{-7} M can be detected through quenching.[94] However, the

$[Ru^{II}(bipy)_3]^{2+}$ probe cannot sense Ni(II) at similarly low detection limits; moreover, the narrow conditions for Ni(II) specificity make this probe unsuitable for sensing Ni(II) at physiological pH.

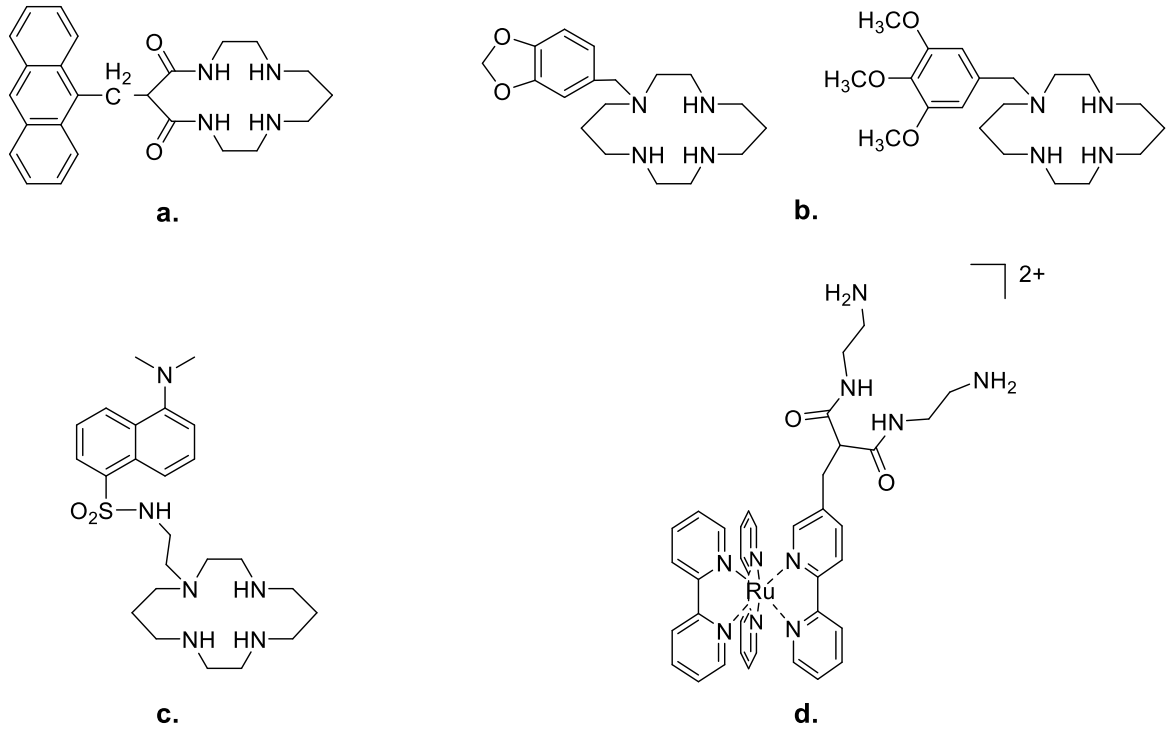

Figure 1.8. Tetraaza-based sensors for the detection of Ni(II). (a) A dioxocyclam ligand linked to an anthracene fluorophore for Cu(II) and Ni(II) detection at low pH.[98] (b) 1,3-benzoodioxole (left) and 1,2,3-trimethoxybenzene (right) appended cyclam ligand for the detection of Ni redox states.[97] (c) Scorpionate-based sensor with a Dns receptor with pH-dependent ligand coordination and geometry.[96] (d) A $[Ru^{II}(bipy)_3]^{2+}$ appended sensor for detection of Cu(II) (pH ~ 7) or Ni(II) (pH ~ 9).[94]

To date (2017), other published fluorescent sensors for Ni(II) feature varying metal binding sites, reporter groups, and operate by different emission mechanisms. Examples include an eT-quenching dioxotetraamine-fluorenyl complex;[101] eximer formation from naphthalene-based probes;[102] two-photon naphthalene-based probes;[103] and 2:1 M:ligand binding probes with a perylene tetracarboxyclic diimide (PDI) fluorophore and two di-(2-picolyl)-amine (DPA) moieties.[104] Analogous to molecules described previously, many probes designed for Ni have difficulties distinguishing Ni(II) from other biologically relevant metals and doing so in physiological conditions.

Unlike the small molecule probes discussed in detail above that only feature N-coordinating ligands, an N/O/S receptor Ni(II) probe was published by Chang in 2009 (Figure 1.9).[105] Chang reports the synthesis of NS1, a boron-dipyrromethene (BODIPY) sensor capable of producing a turn-on response in pH 7.1 HEPES buffer and in A549 (human lung carcinoma) cell cultures. Addition of 50 equiv Ni and excitation at λ_{ex} = 488 nm produced a 25-fold increase in fluorescence intensity at λ_{em} = 507 nm (Φ = 0.055; Φ = 0.002 for the apo-sensor). In metal ion competition studies, Cu(II) does bind to the NS1 sensor; however, the paramagnetic nature of Cu quenches, rather than enhances, the signal intensity from BODIPY, which provides a method for distinguishing between Ni(II) and Cu(II). The proposal is that the turn-on response from Ni is due to the diamagnetic d^8 state resulting from square-planar Ni(II) coordination.[105] To achieve maximum emission, excess Ni(II) is needed, likely due to the relatively weak binding (K_d = 193 ± 5 μM) of the N/O/S chelate. Furthermore, confocal microscopy reveals that NS1 can visualize Ni(II) in A549 cell cultures incubated with the NS1 probe and 100 eq of Ni(II). However, high Ni(II) concentrations with respect to the probe, such as these, are unlikely to be found in nature unless perhaps in polluted environmental sites or bacteria with high levels of Ni contamination.

Unlike other probes that utilize only N-ligands, the NS1 probe attains greater specificity for Ni(II) at physiological pH by employing a mixed N/O/S chelate. Despite the weak binding affinity of NS1 for Ni(II), this work represents the potential for in vivo application of Ni(II) specific sensors to gain understanding about metal trafficking systems and Ni's role in biology.

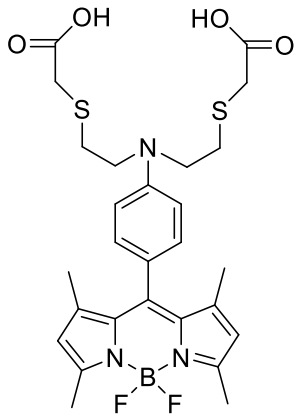

NS1

Figure 1.9. Structure of the NS1 sensor, which is proposed to bind Ni(II) with a N/O/S chelate.[105]

1.4 An overview: Ni metalloenzymes

To date, there are nine known Ni-containing metalloenzymes, with lacate racemase (LarA) as the most recently discovered in 2014.[106,107] Although only nine Ni-dependent enzymes exist, they are responsible for a wide variety of biological processes and utilize the metal cofactor to do redox and non-redox reactions (Table 1.1). For example, in a 2009 review, Ragsdale highlights that seven Ni enzymes are vital to the catalysis or production of molecules

belonging to the global carbon, oxygen, and nitrogen cycles.[108] Of the nine Ni-containing metalloenzymes, four function as a Lewis acid to carry out their respective chemistry; five are redox enzymes and cycle among Ni(I), Ni(II), or Ni(III) oxidation states (see Table 1.1). The five Ni redox enzymes utilize S, often a ligand, to modulate the redox potential of the metal, reactions that span redox potentials over 1.5 V, as each enzyme's active site coordinates Ni in a distinct ligand environment.[108] Herein is presented an overview of the nine known Ni metalloenzymes, their functions, and metal coordination environments.

Table 1.1. Ni-containing metalloenzymes, abbreviations, Ni role, and summary of the enzyme's function.

Enzyme name	**Ni role**	**Enzyme function**
Glyoxalase I (GlxI)	Lewis acid	Detoxification of methylgloxyl
Aci-reductone dioxygenase (ARD)	Lewis acid	Methionine salvage
Urease	Lewis acid	Urea hydrolysis
Lactate racemase (LarA)	Lewis acid	Racemization of D- and L-lactic acid
[NiFe]-hydrogenase	Redox	Reversible reduction of protons to H_2
CO dehydrogenase (CODH)	Redox	Reversible oxidation of CO to CO_2
Acetyl-CoA synthase (ACS)	Redox	Synthesis of acetyl-CoA
Methyl-CoM reductase (MRS)	Redox	Synthesis of methane
Ni superoxide dismutase (NiSOD)	Redox	Disproportionation of superoxide ($O_2^{\bullet-}$)

1.4.1. Glyoxalase I

In the ten-step production of pyruvate from glucose, termed the glycolysis pathway, two intermediates dihyroxyacteone phosphate (DHAP) and gyleraldehyde-3-phosphate (GADP) may react to produce toxic methylglyoxal through off-pathway reaction mechanisms.[109] Ni-containing Glyoxalase I (GlxI) and glyoxalase II detoxify methylglyoxal, which, if left unchecked, can target and modify arginine resides of biomolecules and nucleic acids of DNA.[106] GlxI is responsible for the reaction of glutathione (GSH)-bound methylglyoxal to an *S*-D-lactoylglutathione (Scheme 1.1).[45,108] GlxII converts this species to D-lactate and recovers the GSH molecule, thereby mitigating the potential toxic effect of methylglyoxal.

In humans and some bacterial species, an octahedral Zn(II) occupies the active site of GlxI. In other strains, including *E. coli*, an octahedral Ni(II) is the active form.[110] Ni(II) is coordinated by two His residues, two Glu, and two water molecules (Figure 1.10).[110] The metal functions as a Lewis acid during catalysis, possibly serving to facilitate proton transfer reactions in conjunction with the metal-bound H_2O molecules.[110,111] The likely mechanism of GlxI proceeds by Ni binding the hemithioacetal (the GSH-bound methylglyoxal) through the carbonyl and hydroxyl, thereby displacing Glu122 and one or possibly both H_2O ligands.[110-113] The Glu122 abstracts a proton from the hemithioacetal substrate and reprotonates the adjacent C2 atom resulting in the *S*-D-lactoylglutathione intermediate (Scheme 1.1).[106,111] The intermediate is hydrolyzed back to GSH and lactate by another enzyme in this pathway, Glyoxylase II (GlxII). In *E. coli*, the presence of octahedral Ni(II) is essential for GlxI to carry out this off-pathway glycolysis chemistry.[110]

Scheme 1.1. GlxI catalyzes the reaction of the hemithioacetal of GSH-bound methylglyoxal to produce *S*-D-lactoylglutathione. This reaction proceeds through an enediolate intermediate. GlxII hydrolyses *S*-D-lactoylglutathione by a mechanism not shown to produce D-lactate.

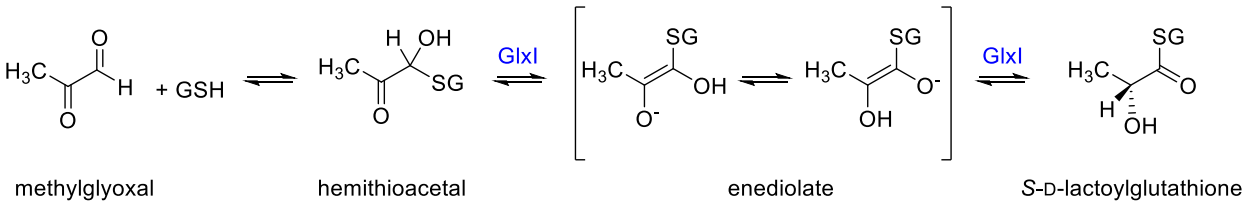

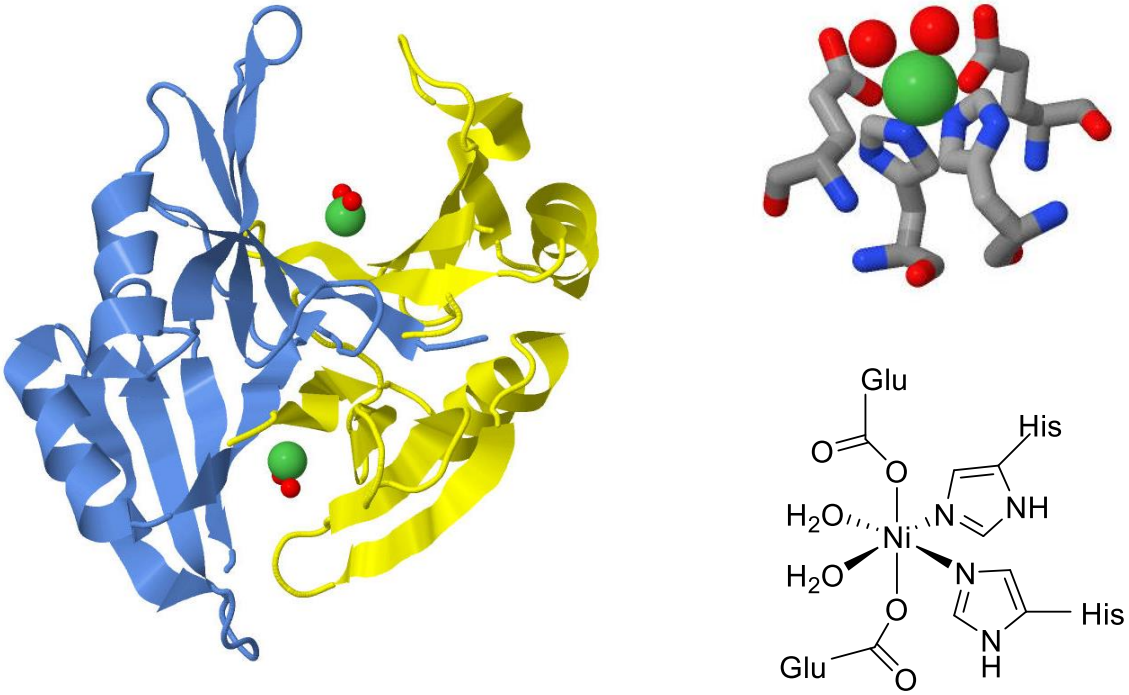

Figure 1.10. X-ray crystal structure of homodimeric GlxI (left) and one active site (upper right) from *M. musculus* (2.5 Å resolution, Protein Data Bank entry 1F9Z). Ni ions are modeled as green spheres; Ni-bound water is modeled as red spheres. These images were generated with Jmol. ChemDraw depiction of the Ni(II) non-redox active site of GlxI (bottom right). [111]

1.4.2. Acireductone dioxygenase

The Ni-containing acireductone dioxygenase (ARD) enzyme belongs to the methionine salvage pathway, which produces the sulfur-containing amino acid methionine from 5′-methylthioadenosine in a series of six steps.[114] Ni-ARD is found in the next-to-last step of the production of methionine. There are two forms of ARD occurring in nature: Fe(II)-ARD is found in mammals, plants and bacteria; Ni(II)-ARD has been discovered in *Klebsiella* and *Bacillus* organisms.[114] Both Fe- and Ni-ARD are oxygen-dependent, and both use the 1,2-dihydrozy-3-keto-5-methylthiopentene (acireductone) substrate to carry out two distinct reactions. In the Fe(II) form, the enzyme reacts with oxygen and acireductone to produce 2-keto-4-methylthiobutanoate and formate ($HCOO^-$) or formic acid[114,115] in the penultimate step before synthesis of methionine (Scheme 1.2, left).[115] In an off-pathway mechanism, Ni(II)-ARD uses the same two substrates to yield 3-methylthiopropionate, formic acid, and an equivalent of CO (Scheme 1.2, right).

Scheme 1.2. The two reactions catalyzed of ARD depending on the active site metal. Ni(II)-ARD catalyzes the off-methionine-pathway formation of CO, formic acid, and 3-methylpropionate (right).[114,115]

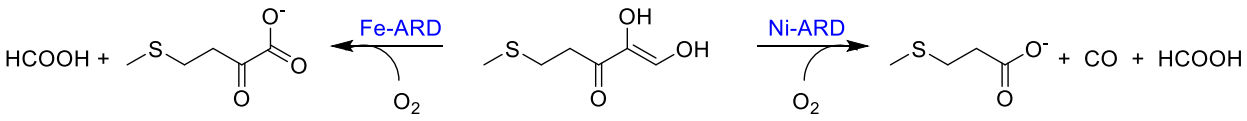

2-keto-4-methylthiobutanoate | 1,2-dihydroxy-3-keto-5-methylthiopentene | 3-methylthiopropionate

The Fe and Ni-bound forms of ARD share identical sequence homology, although the choice of metal does determine which reaction proceeds in vitro.[115] ARD is classified as a member of the cupin superfamily, characterized by a conserved barrel or jelly roll (Figure 1.11, PDD file 1ZRR). Lacking a crystal structure, solution NMR, XAS, spectroscopic and mutagenesis studies reveal the Ni active site to be 6C bound by two His, two Glu, and two water ligands.[116-119] The exact mechanism and role of Ni(II) in ARD are unknown. Acting as a Lewis acid, Ni(II) may promote electron transfer from the acireductone to O_2, resulting in a cyclic metal-peroxo intermediate species that can undergo rearrangement to yield the reaction products (Scheme 1.3).[106,108,120]

Scheme 1.3. Possible formation of a peroxo intermediate and rearrangement for the Ni-catalyzed reaction of ARD.

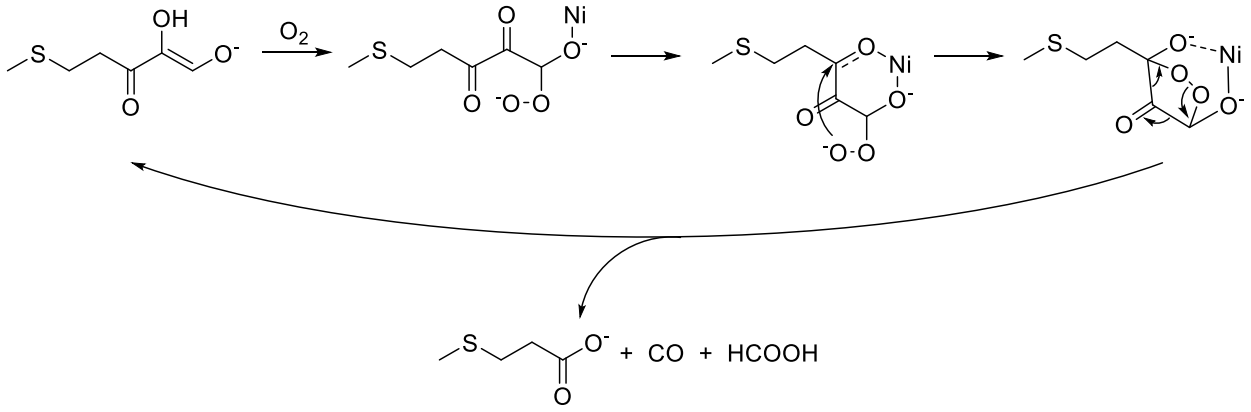

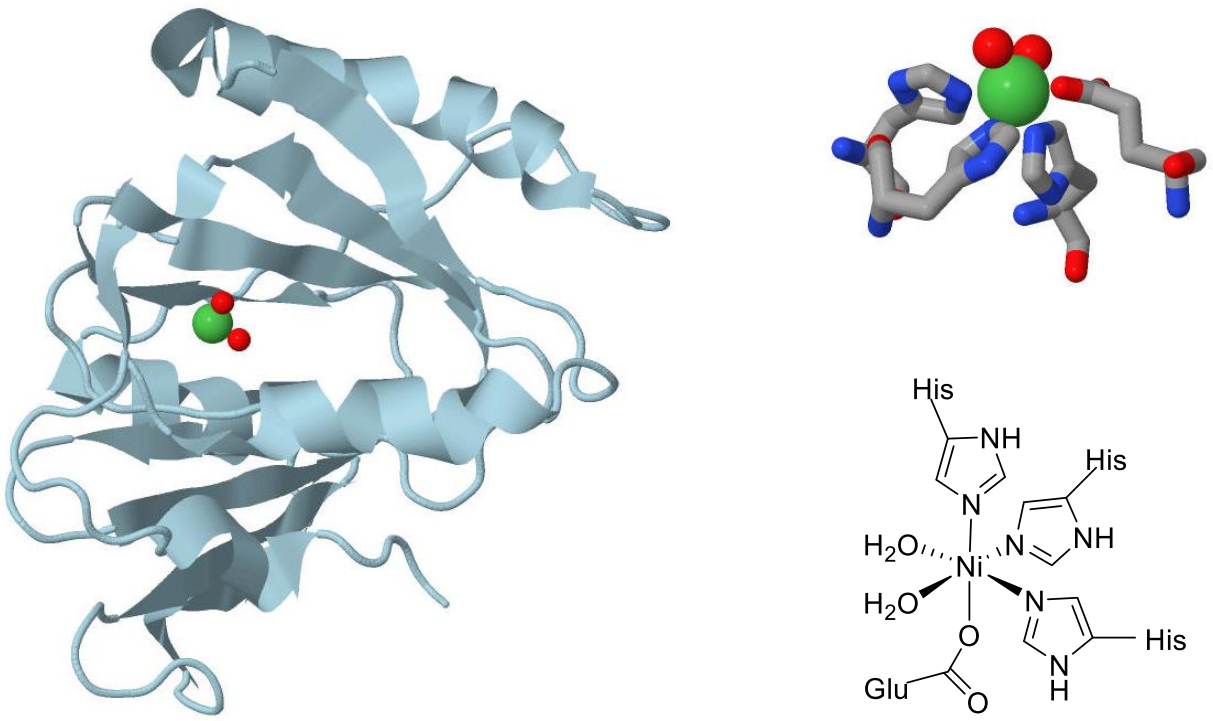

Figure 1.11. Structure of ARD (left) and active site (upper right) from *K. oxytoca* (Protein Data Bank entry 1ZRR).[119] Ni is modeled as a green sphere; Ni-bound water molecules are modeled as red spheres. These images were generated with Jmol. ChemDraw depiction of the Ni(II) non-redox active site of ARD (bottom right).[118]

1.4.3. Urease

Urease was the first Ni metalloenzyme to be discovered, published in 1975,[121] and is vital to the global nitrogen cycle, as it catalyzes the hydrolysis of urea into ammonia and bicarbonate (Scheme 1.4).[108] Due to its ubiquity in plants, fungi, and microorganisms, urease is an important enzyme in medicine and agriculture. Some bacteria use urease, and the products of the urease reaction (ammonia and bicarbonate) as a system of defense against a host.[106] For example, as discussed previously for *H. Pylori*, this pathogen relies on the function of urease and

the bicarbonate byproduct to survive acidic conditions of the human stomach.[62] In agricultural processes, urease is a necessary catalyst for urea-derived fertilizers and in the generation of ammonia.

Scheme 1.4. The hydrolysis of urea catalyzed by the Ni-containing urease enzyme.[106]

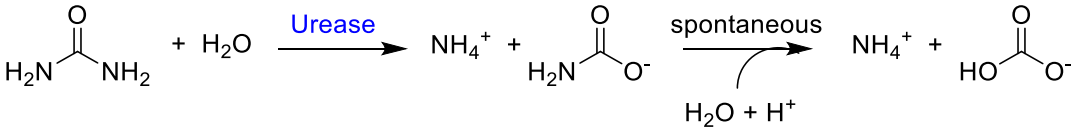

The structure of urease has been isolated from bacterial strains and reveals an overall trimeric structure composed of three subunits, UreA, UreB, and UreC, and one dinuclear active site.[122,123] In *H. pylori*, urease has a supramolecular assembly of fused subunits.[124] The placement of the active site, buried in the subunit UreC, highlights the importance of chaperone proteins that facilitate Ni insertion and enzyme assembly. The urease active site houses two Ni(II) ions with different coordination environments (N_2O_3 and N_2O_4) but are bridged by a water molecule (or hydroxyl) and modified lysine residue (Figure 1.12). One Ni(II) ion is ligated by water and two His; the second Ni(II) has a similar ligand environment with the addition of an Asp residue.[122] The dinuclear center does not change oxidation states but instead acts as a Lewis acid to direct urea binding and hydrolysis. The binding mechanism of urea to one of both Ni ions is not yet definitely determined, although the carbonyl oxygen of urea likely binds to Ni1. There are a few proposals for the mechanism of urease; in most, the bridging water or hydroxide is the base that attacks the carbonyl carbon of the urea, allowing for the release of ammonia following

abstraction of a proton from a nearby source (possibly water, His, or unknown proton source.)[106,123,125-127]

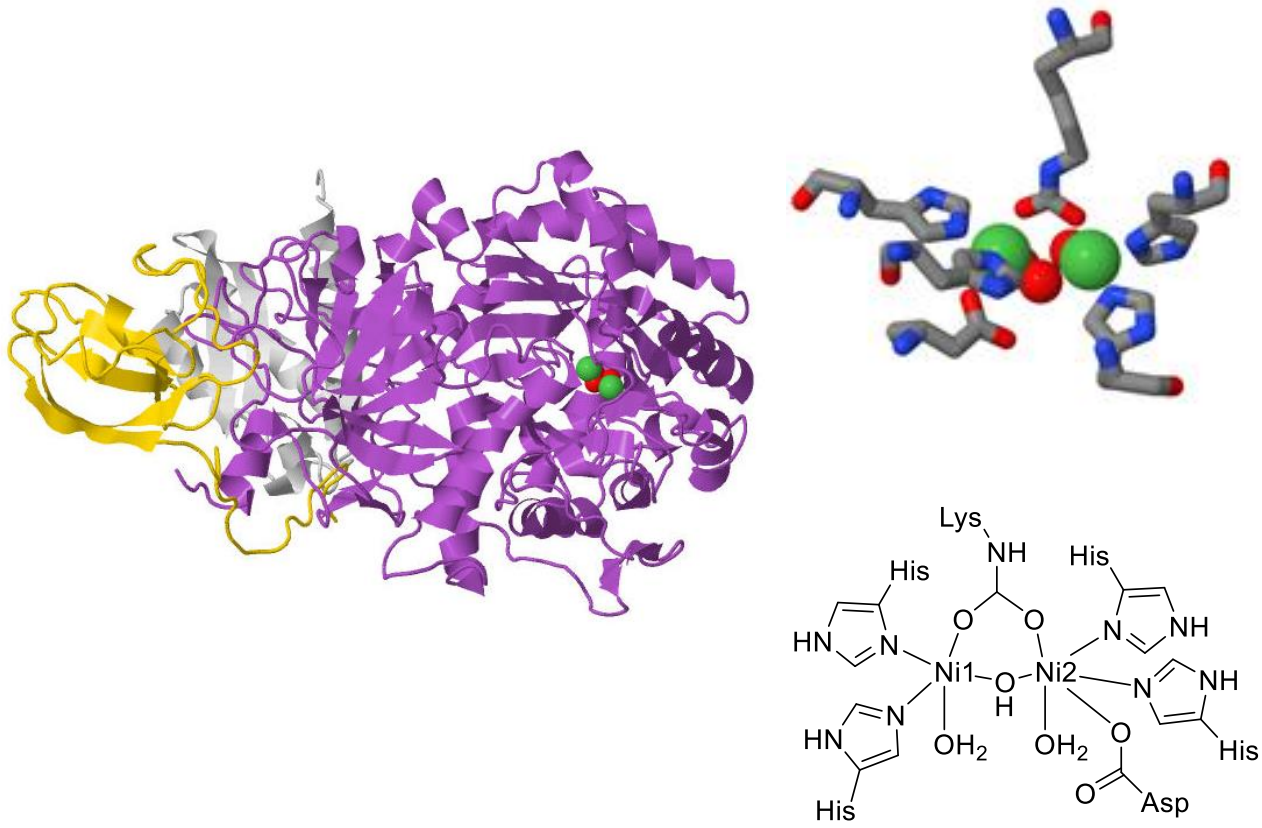

Figure 1.12. X-ray crystal structure of one monomer of the trimeric *K. aerogenes* urease (left), composed of UreA (white), UreB (gold), and UreC subunits (purple). The dinuclear active site (upper right) is located in the UreC subunit (2.2 Å resolution, Protein Data Bank entry 1FWJ). The Ni site is located in UreC. Ni ions are modeled as green spheres; water molecules are modeled as red spheres.[122] These images were generated with Jmol. ChemDraw depiction of the dinculear active site of urease (bottom right).

1.4.4. Lactate racemase

Lactate racemase (LarA) is the most recently discovered Ni-dependent enzyme, first revealed in 2014.[106] LarA is responsible for lactic acid racemization, the interconversion of D- and L-isomers of lactic acid. Isolated from *L. plantarum*, LarA features a Ni housed in an unusual SCS-pincer cofactor derived from nicotinic acid (nicotinamide or niacin) (Figure 1.13).[107,128-130] Nicotinic acid is a necessary factor in the expression and activity of LarA. Although there is still much to be learned about LarA, preliminary characterization and a crystal structure have revealed a unique Ni active site to add to this family of Ni-dependent enzymes. The Ni(II) is held in a distorted square-planar geometry involving (i) His residue and three ligands from a nicotinic moiety: (ii) a Ni-C bond at the C4 position of the pyridine ring, (iii) a thioamide from the C3 of pyridine, and (iv) a thiocarboxylic acid from the pyridine C5 (Scheme 1.5). ESI-MS and crystal structures highlight the sensitivity of this active site to oxygen, as the Ni is lost from the pincer complex under aerobic conditions or in the absence of sulfite, suggesting that the S-ligands of LarA are vulnerable to oxidation by O_2.[129] Biochemical and small molecule studies suggest that the racemization of lactic acid may proceed via a hydride transfer from the lactate substrate to the pyridine-C of the pincer, aided by nearby His108 and/or His174 residues (Scheme 1.5).[129-131] However, recent computational results propose a proton coupled electron transfer (PCET) mechanism and oxidation of the Ni(II).[132] In light of the recent discovery of this enzyme and the questions surrounding this novel Ni-cofactor, it is expected LarA will be the focus of many future studies.

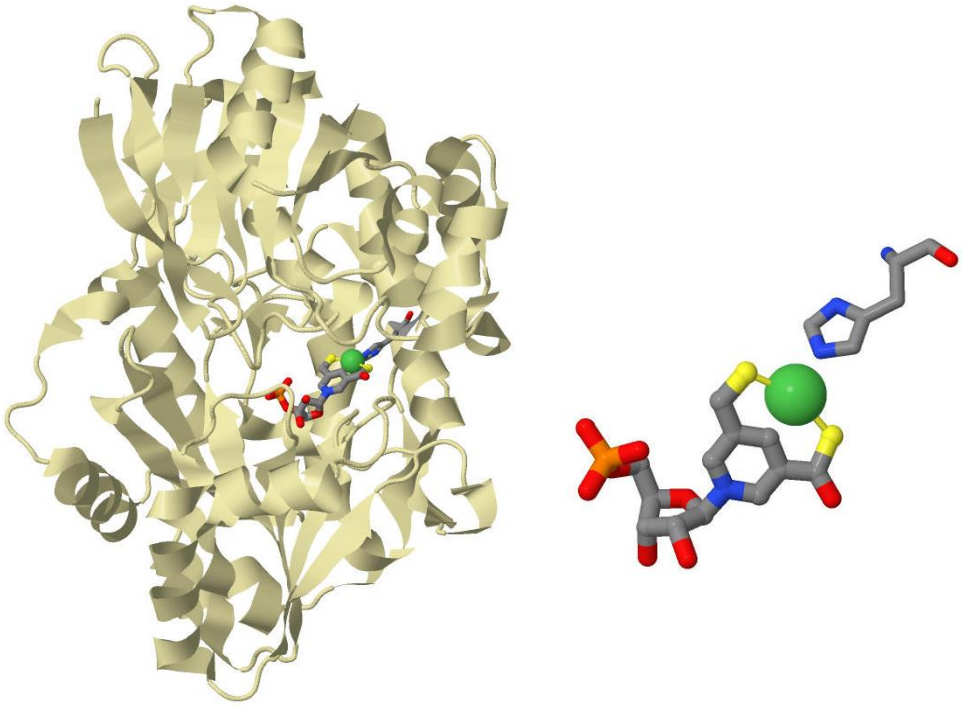

Figure 1.13. X-ray crystal structure of LarA (left) and active site (right) from *L. plantarum* (3.0 Å resolution, Protein Data Bank entry 5HUQ).[129] Ni is modeled as a green sphere. These images were generated with Jmol.

Scheme 1.5. Proposed mechanism for the racemization reaction of lactate by LarA, which may proceed via a hydride transfer.[129]

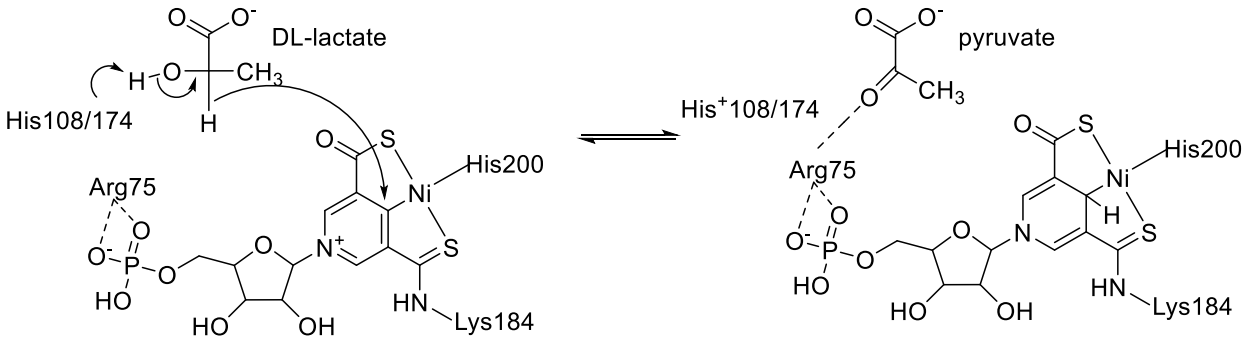

1.4.5. [NiFe]-hydrogenase

Hydrogenases play a crucial role in some bacteria and eukaryotes in the reversible two electron reduction of protons to H_2 and can achieve catalytic turnover of 9000 s^{-1} at 30 °C.[108] Hydrogenases are classified according to the metal(s) that catalyze this transformation: mononuclear [Fe]-hydrogenases or dinuclear [FeFe]- and [NiFe]-hydrogenases that both utilize FeS clusters for electron transfer, where the number of FeS clusters varies depending on microorganism.[133,134] [NiFe]-hydrogenase is composed of a buried active site in which Ni is ligated by four Cys-S. Two of these Cys-S thiolates bridge a low-spin Fe bound to a CO and two CN^- ligands (Figure 1.14). As discussed previously, the assembly of the [NiFe] active site involves complicated coordination of accessory proteins and chaperones.[33,34] Furthermore, the location of the active site ~30 Å beneath the protein surface highlights the need for iron-sulfur cluster electron relays and protein channels to transport substrates and products.[135,136] Purification and study of [NiFe]-hydrogenase has led to characterization of numerous active and inactive intermediate forms of the NiFe site, in which Ni is found in the +1, +2, and +3 redox states.[134,137,138]

Previously thought to be universally inactivated by O_2, a subset of membrane bound [NiFe]-hydrogenases have exhibited O_2-tolerance owing to two additional Cys residues near the proximal FeS; one Cys-thiolate replaces sulfide as a Fe ligand resulting in a unique [4Fe-3S] cluster.[139,140] Mutagenesis and biochemical studies have demonstrated that the Cys residues and the formation of a [4Fe-3S] cluster allow for O_2 tolerance of membrane bound hydrogenases.[141,142] Indeed, mutation of Cys19 to Gly halted the function of *E. coli* [NiFe]-hydrogenase in an atmosphere of less than 1% O_2.[142] Together, Cys19 and the relay system of

iron-sulfur clusters act to facilitate the rapid transfer of electrons to the active site when attacked by O_2.

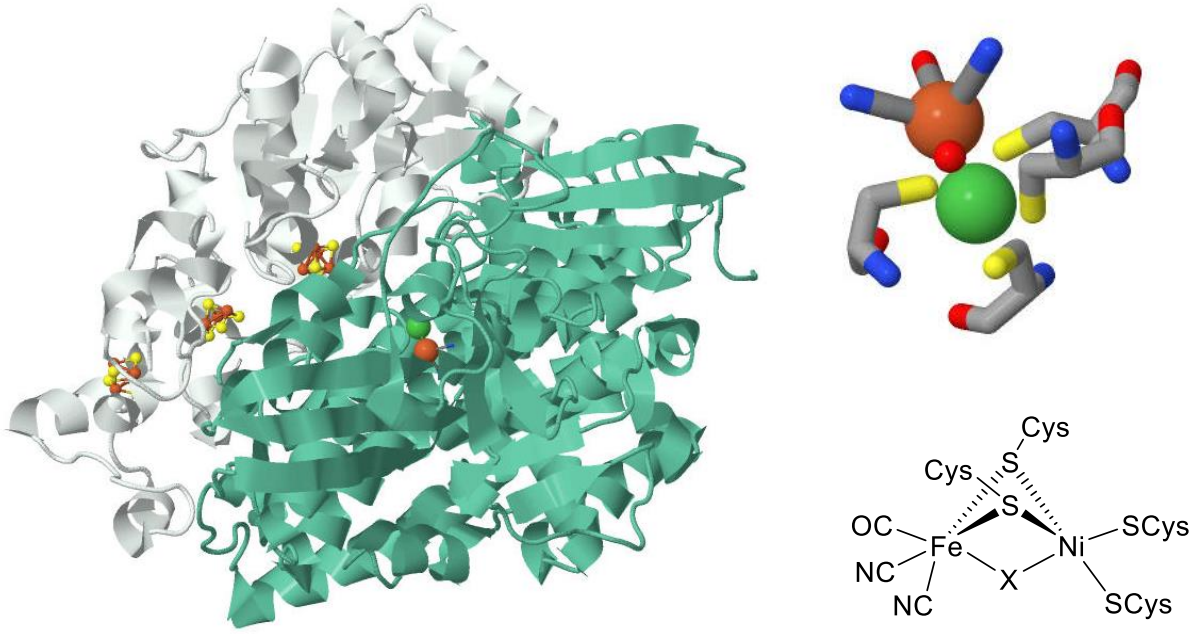

Figure 1.14. X-ray crystal structure of [NiFe]-hydrogenase (left) and active site (upper right) from *D. fructosivorans* (2.1 Å resolution, Protein Data Bank entry 1YRQ). A series of iron sulfur clusters are found in one subunit (white), and the [Ni-Fe] active site is located in the other subunit (teal). Ni is modeled as a green sphere; Fe is modeled as an orange sphere. These images were generated with Jmol. ChemDraw depiction of the oxidized form of [NiFe]-hydrogenase where X is modeled as bridging water, here (bottom right).

1.4.6. Carbon monoxide dehydrogenase

Ni-containing carbon monoxide dehydrogenase (CODH) plays a part in the global carbon cycle by catalyzing the reversible oxidation of carbon monoxide to carbon dioxide via clusters of

Ni and Fe ions at the enzyme active site. Ni-CODH has been isolated as a standalone enzyme with 10 Fe and 1 Ni per monomer, or as a complex with actyl-coenzyme A (CoA-SH) synthase (vide infra).[34,106,108] The overall protein structure of CODH/ACS varies depending on bacterial strain but typically includes a [1Ni-4Fe-4S] C-cluster, [4Fe-4S] B-cluster, and [4Fe-4S] D-cluster (Figure 1.15).[143] The Ni-containing C-cluster is the site of CO oxidation and the B- and D-clusters play a role in electron transfer.[144] The reaction may proceed via CO binding to the Ni of the C-cluster, followed by attack from a Fe-bound hydroxide to produce a bridged Ni-carboxylate intermediate that decomposes to CO_2 (Scheme 1.6).[145] The transient Ni-H produced in this pathway may be released following the transfer of 2 e^-, forming a Ni(0).[144,146,147] However, the mechanism is still debated as some evidence suggests Ni retains a +2 oxidation state throughout.[148]

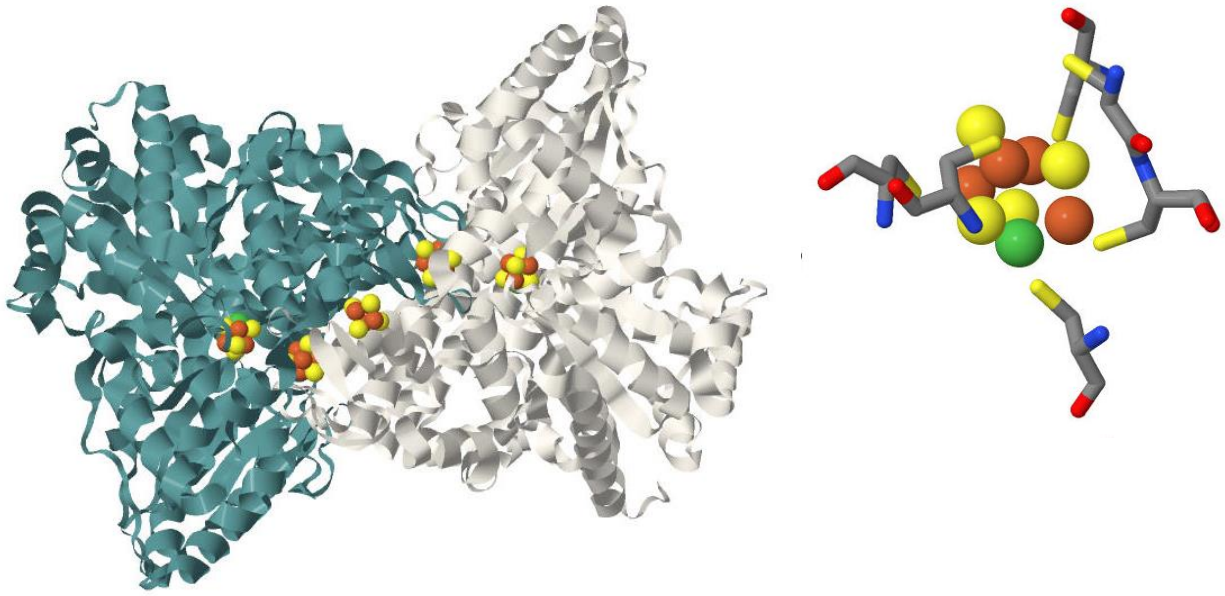

Figure 1.15. X-ray crystal structure of dimeric CODH (left) and active site (upper right) from *C. hydrogenoformans* (1.5 Å resolution, Protein Data Bank entry 3B53).[147] Iron-sulfur clusters and Ni ions are modeled as orange, yellow, and green spheres, respectively. These images were generated with Jmol.

Scheme 1.6. One proposed mechanism of CODH where Ni may pass through a Ni(0) intermediate following release of CO.[106]

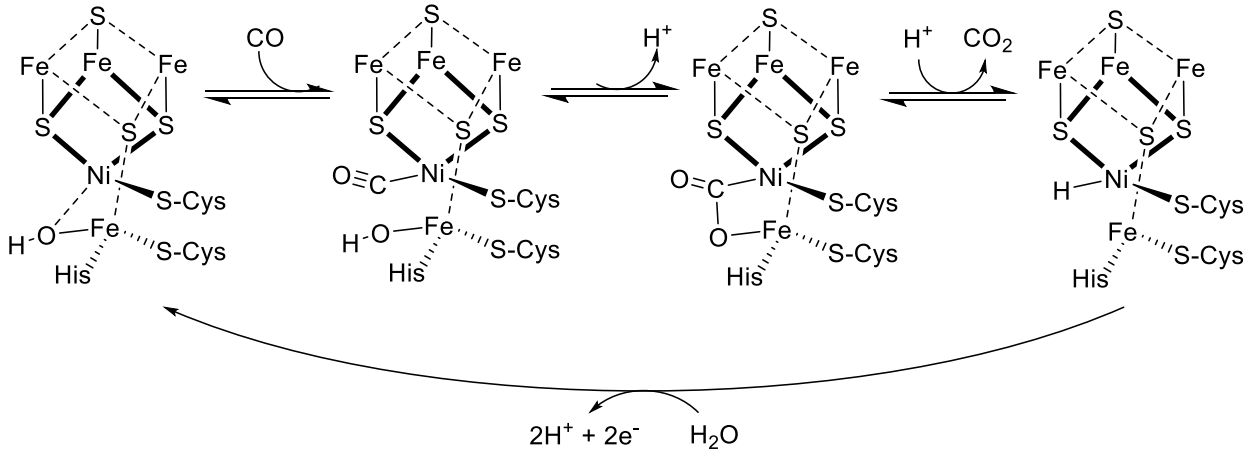

1.4.7. Acetyl-CoA synthase

Acetyl-CoA synthase (ACS) works in conjunction with CODH and a methyl group from a corrinoid Fe-S protein (Co-FeSP) to produce acetyl-S-CoA (Scheme 1.7). Bacteria rely on ACS for the carbon dioxide chemistry described above, as well as for the production of methane. Found within the A cluster of ACS, there are two Ni sites in ACS that are bridged by two cysteine-S: the proximal Ni (Ni_p) is bound via another cysteine residue to an [4Fe-4S] cluster, and the distal Ni (Ni_d) is ligated by two Cys-S and two deprotonated caboxamides of the peptide backbone (Figure 1.16).[149-151] This $Ni_dN_2S_2$ is structurally similar to the reduced site in NiSOD (vide infra); however, there is no known function of the Ni_d site in ACS as it is neither the site of CO binding nor electron transfer. Evidence suggests that the Ni_d ion remains in the +2 state throughout catalysis. Further discussion of the NiN_2S_2 coordination environment, with respect to spectroscopy and NiSOD similarities, follows in Ch. 2. The Ni_p site is more accessible from the protein surface as compared to Ni_d, and crystal structures have shown that Cu(II) and Zn(II) can occupy the proximal site and may complete with Ni for occupancy in vivo, often resulting in inactivation of ACS.[152] Thus, nature requires Ni in a unique [4Fe-4S]-Ni_p-Ni_d conformation to produce acetyl-S-CoA. In contrast to the Ni(II) Ni_d site, during catalysis Ni_p is reduced to the Ni(I) state and binds CO in what is termed the "closed" conformation based on protein dynamics.[153,154] When ACS is in a structurally "open" conformation, Ni_p is the site of proposed methylation by the Co-FeSP protein, followed by oxidation back to Ni(II). Together, the methyl and CO make up the acetyl that is attacked by CoA-SH to yield acetyl-S-CoA.

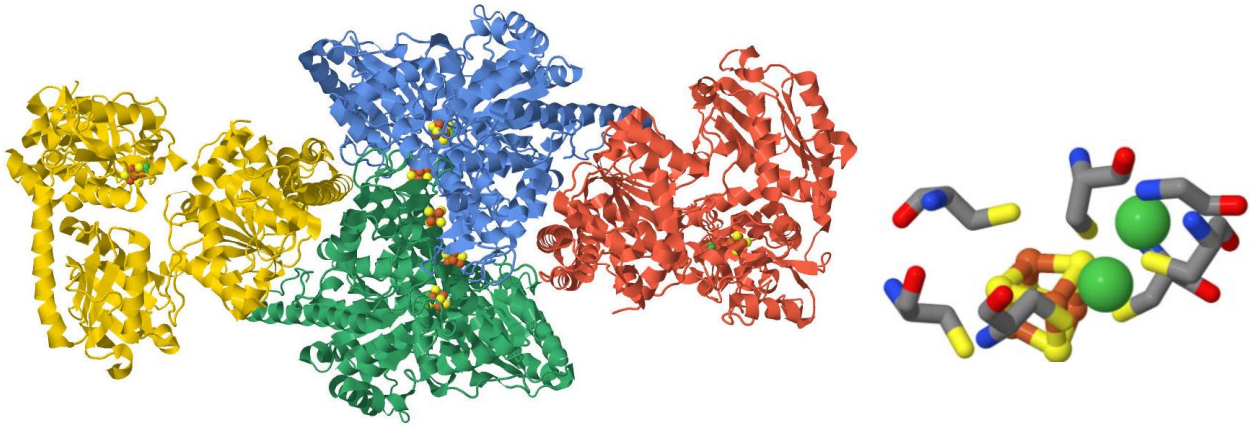

Figure 1.16. X-ray crystal structure of ACS/CODH from *M. thermoacetica* (1.9 Å resolution, Protein Data Bank entry 1OAO) (left).[149] Here, ACS, shown in gold and light red, adheres to a CODH homodimer, shown as blue and green subunits. The ACS active site (right) was crystallized with an iron-sulfur cluster, modeled in orange and yellow, and distal and proximal Ni ions, modeled as a green spheres. These images were generated with Jmol.

Scheme 1.7. A proposed mechanism of ACS in which the Ni_d site remains Ni(II) throughout, and the Ni_p site fluctuates between Ni(II) and Ni(I) as shown.

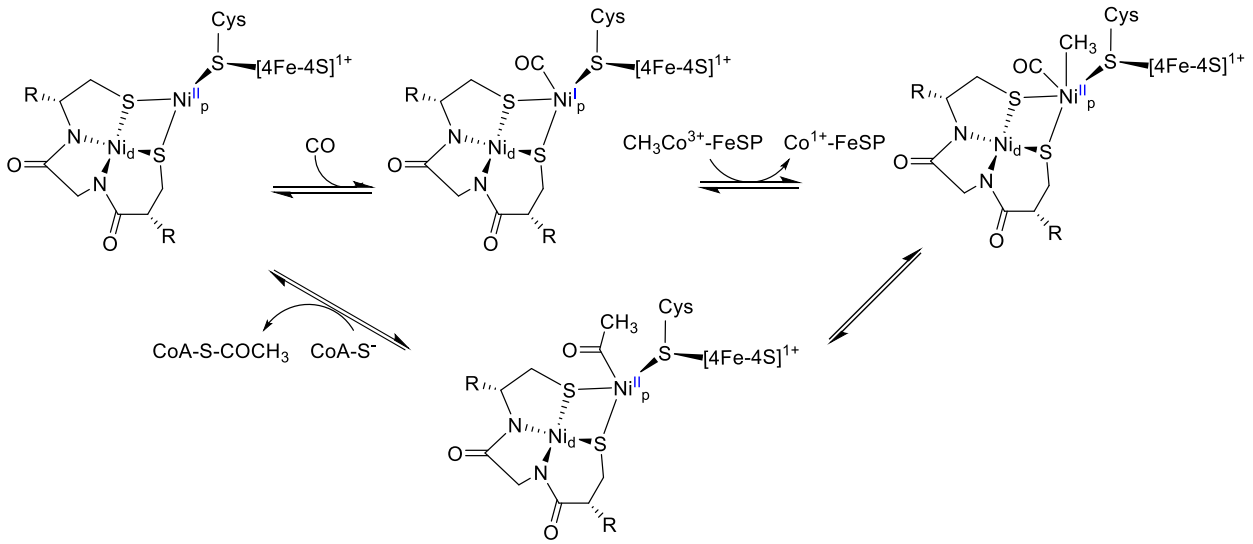

1.4.8. Methyl-coenzyme M reductase

Methane is produced by methanogenic bacteria using the enzyme methyl-coenzyme M reductase (MCR). The overall protein structure of MCR is a helical hexamer (Figure 1.17). The enzyme catalytically uses *N*-7-meraptoheptanoylthreonine phosphate (coenzyme B, CoB-SH) and methyl-*S*-thioethanesulfonate (methyl coenzyme M) to yield methane and the heterodisulfide product CoB-S-S-CoM (Scheme 1.8).[108,155] This transformation occurs in the α-subunit of MCR at the Ni-containing F430 cofactor (Figure 1.17). F430 houses a Ni(I) in a 4C N-coordination tetrapyrrole, the most reduced tetrapyrrole in nature, which recent work has shown is assembled by a 6 e^- reduction and subsequent formation of the ring.[156] An additional Gln side chain coordinates in one axial position, leaving the second axial position available for substrate binding. The production of methane may proceed via attack by the Ni(I) on the methyl of methyl-CoM, resulting in formation of a methyl-Ni(III) species and thiolate of coenzyme-M ($^-$S-CoM in Scheme 1.8), which can be reprotonated by CoB-SH. The Ni(III) is then reduced by electron transfer from CoM-SH to yield methane, Ni(II), and the thiyl radial, CoM-$S^{\bullet-}$.[157,158] Reaction of the CoB-S^- with CoM-$S^{\bullet-}$, followed by electron transfer to the Ni(II), generates the disulfide CoB-S-S-CoM and the Ni(I) cofactor. The methyl can then abstract hydrogen from CoB-SH, producing methane and CoB-thiyl, respectively. Alternative mechanisms have been proposed that suggest the CoM-SH is homolytically cleaved to yield a Ni(II)–SH species and methyl radical, which may abstract a proton from CoB-SH to produce methane and the disulfide as described before.[108,159,160]

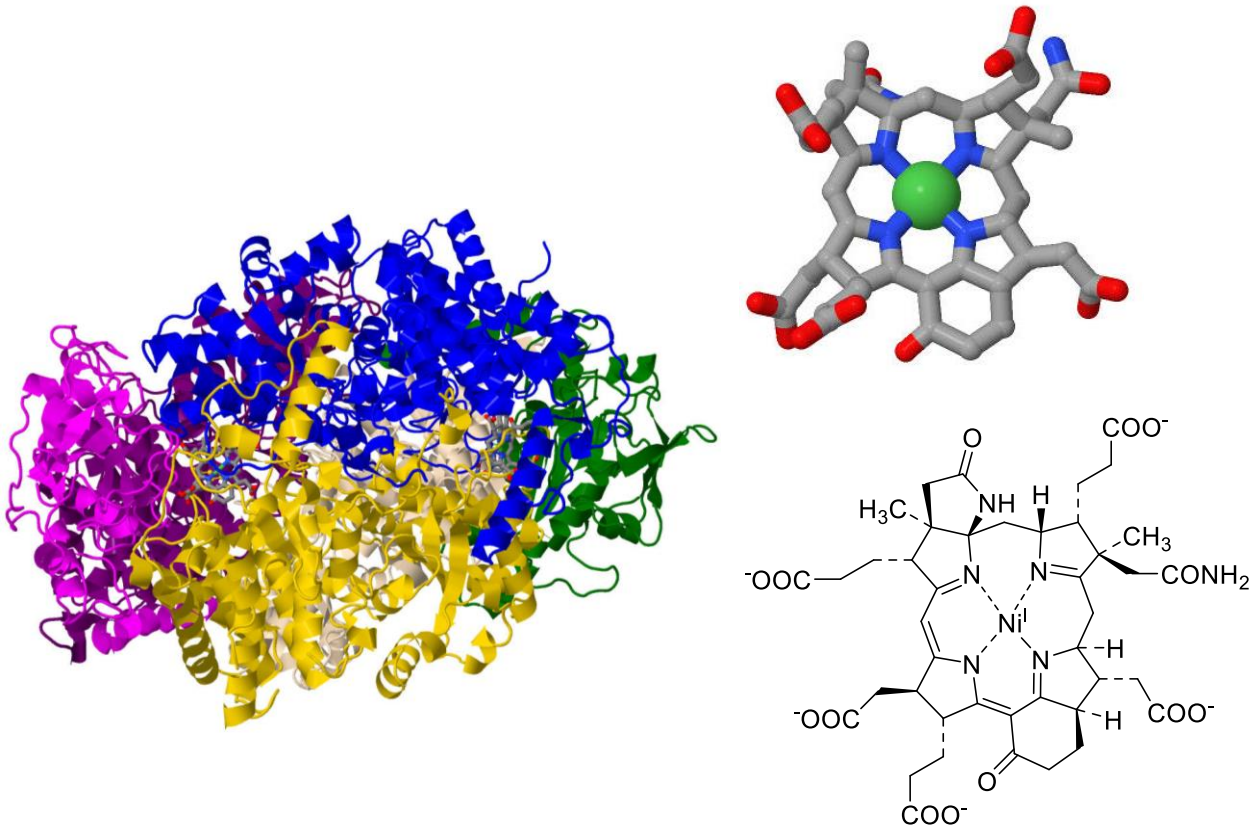

Figure 1.17. X-ray crystal structure of MCR (left) and an F430 cofactor (upper right) from *M. marburgensis* (1.16 Å resolution, Protein Data Bank entry MR1O). Ni is modeled as a green sphere. These images were generated with Jmol. ChemDraw depiction of the F430 structure (bottom right).

Scheme 1.8. One proposed pathway for the production of methane and the disulfide product of CoB-SH and CoM-CH_3 from MCR.[106]

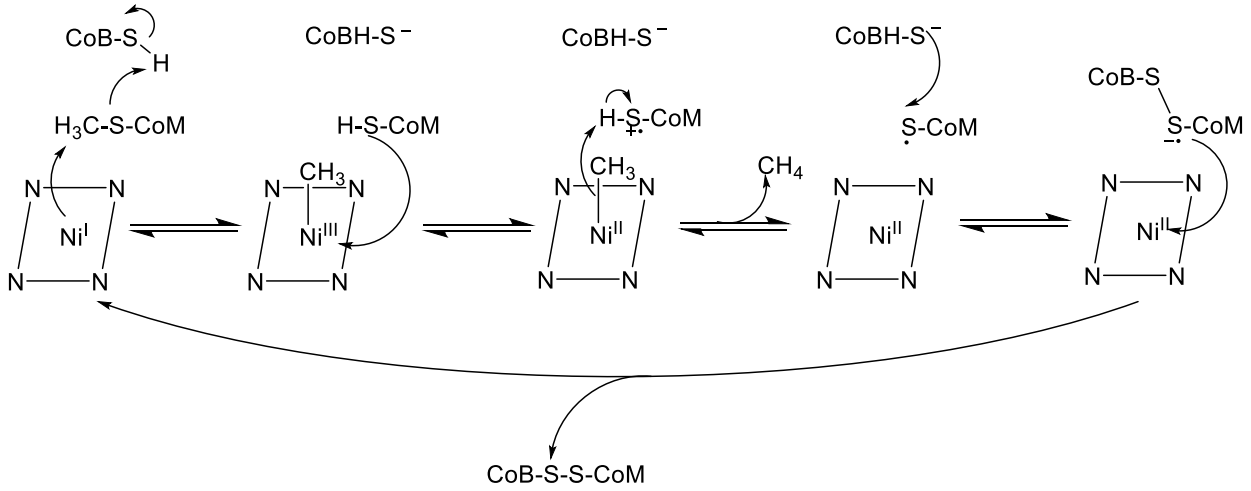

1.4.9. Nickel superoxide dismutase

Nickel superoxide dismutase (NiSOD) is the final Ni enzyme to be discussed and is the focus of this dissertation work. First crystalized in 1996 from *Streptomyces* soil bacteria,[161,162] and found in the genome of cyanobacteria,[163] NiSOD is the newest addition to the class of enzymes known as superoxide dismutases, so named as they serve as a defense mechanism against the superoxide anion ($O_2^{\bullet-}$) in aerobic metabolism. NiSOD is a redox active enzyme, and isolated crystal structures reveal two distinct coordination spheres depending on metal oxidation state: Ni(II)N_2S_2 and Ni(III)N_3S_2 upon binding of His1.[164,165] NiSOD is an enzyme worthy of study for its unique coordination sphere, mechanism of disproportionation chemistry, and its aerobic environment in spite of utilizing S-thiolates ligands. Mutagenesis, computational, spectroscopic, and kinetic studies show that the N-terminal His1 residue,[166-169] as well as an outer sphere amino acid H-bonding network,[170] are vital for the enzyme to maintain its diffusion-

controlled rate of disproportionation. More detailed discussion of native NiSOD and the field's efforts to produce low molecular weight (MW), small molecule analogues of the NiSOD active site follow in Ch. 2's literature review.[171]

1.4.10. Ni metalloenzyme summary

Taken together, nature has employed Ni to carry out very different chemical reactions and serve in both redox and non-redox roles. As in the complex trafficking and defense systems bacteria have evolved for shuttling Ni, the nine Ni-containing metalloenzymes are all found in bacterial species. Although structural homologues of some Ni metalloenzymes have been found in plants and higher order animals (such as Zn-GlxI, Fe-ARD, or Cu/ZnSOD, for example), in most cases the bacterial enzyme's structural and ligand environment have been tuned to bind Ni and carry out reactions at high efficiency. For GlxI, ARD, urease, and LarA, Ni is coordinated by N, O, and water ligands and acts a Lewis acid to promote proton or electron transfer between the substrates and neighboring amino acids. These active site are typically His-rich and octahedral in geometry. With the exception of NiSOD, redox-active Ni enzymes operate in anaerobic environments and exhibit sensitivity to O_2, and yet even NiSOD has evolved in some way as to protect its thiolate ligands from oxidative damage (see Ch. 2). Vulnerability to O_2 is not surprising due to the use of Cys-S in many of the redox-active Ni sites and the propensity of thiolates to undergo irreversible S-oxidation or S-oxygenation upon reaction with O_2. This may speak to why MCR, NiSOD, [NiFe]-hydrogenase, and ACS, for instance, have active sites buried deep within the overall protein structure. Indeed, [NiFe]-hydrogenase and ACS/CODH rely upon solvent channels and iron-sulfur clusters for transport of substrates and products, or shuttle of electrons, respectively, to the active site. There is still many questions to be answered about the

structures and mechanisms of Ni metalloenzymes, especially in light of more recently discovered Ni-containing species such as NiSOD and LarA. Ni enzymes play an important role in the global carbon, nitrogen, and oxygen cycles, and they have far-reaching implications in the areas of greenhouse gas remediation, alternative fuels, and environmentally-sustainable production of commodity chemicals such as acetyl- and methyl-derivatives. Although much can be learned by studying the native enzymes, there is a considerable amount of insight than can be gained by studying the structure, spectroscopy, and reactivity of low MW biomimetic models.

1.5 Research objectives and purpose

The overall objective of this research is to gain greater insight into the role of Ni in biology through the synthesis, characterization, and reactivity properties of low MW molecules of mixed N/S chelates and their Ni complexes. We have accomplished this objective through the synthesis and study of electronically and structurally accurate small molecule biomimetics of the NiSOD enzyme active site and through the development and photophysical characterization of a 4C fluorescent sensor for the detection of Ni.

We design these NiSOD model complexes to (i) replicate the N/S ligand geometry, (ii) achieve a measurable Ni(III/II) redox couple, and (iii) functionally mimic the enzyme's $O_2^{\bullet-}$ disproportionation to hydrogen peroxide (H_2O_2) and oxygen (O_2). We hypothesized that by decreasing the sulfur character in the HOMO of a NiSOD reduced ($NiSOD_{red}$) synthetic analogue, S-based oxidation could be avoided in favor of Ni-based redox and a reversible Ni(III/II) couple. To this end, we synthesized a family of models, building upon previously published Ni(nmp) designs, where nmp^{2-} is the dianion of *N*-(2-mercaptoethyl)picolinamide.[172,173] These complexes feature a benezenethiolate S-donor with an,

i) electron-withdrawing substituent (para-CF_3), or, ii) potential amine-N ligand to model axial His1 seen in native $NiSOD_{ox}$ (ortho-NH_2), iii) or a combination of these two moieties. Characterization and reactivity studies of complexes that possess NH_2 and CF_3 substituents reveal the first structurally accurate model of $NiSOD_{red}$ to achieve a stable high valent Ni state for up to 24 h. Computational and spectroscopic analyses point to the oxidized complex as being a resonance species with Ni(III)-thiolate and Ni(II)-thiyl radical character; this resonance is only made possible through the addition of a fifth N-ligand to the NiN_2S_2 model. Through this work, we have gained insight into the necessary ligand modifications and redox active molecular orbital (RAMO) contributions needed to achieve a Ni(III) state, as observed in NiSOD. Although this species did not exhibit catalytic reactivity with ROS, this work represents an achievement in the field of small molecule NiSOD mimetics, and may point to a Ni(II)-thiyl transition state being employed in the His-on-His-off Ni(III/II) fluctuations in the enzyme.

Other unique reactivity has arisen with nitric oxide (NO) and the Ni(nmp) complex containing the electron-withdrawing CF_3 moiety. To explore the chemistry of this complex with reactive nitrogen species (RNS), a purge of NO(g) was introduced to a solution of the Ni complex and resulted in dissociation of the ligand, nitrosylation of Ni, nitrosylation of the ortho-N species, and formation of a dimer *S,S*-bridged green complex. Moreover, this experiment has been repeated with isotopically labeled $^{15}NO(g)$ to confirm this reactivity, and DFT of the optimized structure of the Ni dimer agrees with the crystal structure. We have assigned this species as $\{NiNO\}^{10}$ with a Ni(I) core.[174] Intramolecular reductive nitrosylation has been observed previously in copper systems, although nitrosylation of the ligand in the case of Cu resulted in displacement of the metal.[175,176] In our system, an N-nitrosamine forms a new chelate to a nitrosylated Ni. This finding represents new chemistry in the formation of Ni-nitrosyls and

N-nitrosamines, and to our knowledge, introduces a new, previously uncharacterized binding mode of nitrosamines to metals. The $\{NiNO\}^{10}$ dimer was only observed for the Ni(nmp) complex that is capable of achieving the Ni(II)-thiyl ↔ Ni(III) species; thus, radical character is the key to this NO(g) reactivity.

As an improvement upon the Ni(nmp) complexes and in efforts to model the oxidized form of NiSOD with an axial N-donor poised to bind Ni, we have turned our attention to peptide-based low MW models. In addition to modeling the $NiSOD_{ox}$ coordination, peptide-derived complexes would afford aqueous solubility that was lacking with Ni(nmp) and allow for reactivity assays and experiments under physiologically-relevant conditions. The synthesis and characterization of a novel His^{Bz}-CSH ligand was carried out, Bz = benzyl and where CSH = cysteamine. This ligand is a near replica of the His1 and Cys2 donors found in NiSOD. However, metalation experiments with Ni resulted in undetermined binding modes and possibly oligomeric peptide structures; FTIR evidence revealed that the carboxamide-N was not engaged in Ni binding under any attempted conditions. In the native enzyme, the ligand environment is arranged in such a way to chelate Ni through three anionic ligands (two S^-, one N^-), a terminal amine-N, and His-N. Although the His^{Bz}-CSH design replicates these donors, it cannot replicate the enzyme's secondary structure that aid in assembly, and the dipeptide ligand cannot replicate with rigidity of the ligand framework that is found in the enzyme. This work has provided future direction for the study of peptide-based analogues, and it has provided further insight into the unique binding environment and assembly of the NiSOD active site.

With respect to the field of Ni(II) fluorescent sensing, we have designed, synthesized, and characterized a unique, N_2S_2 sensing platform inspired from the square-planar framework of $NiSOD_{red}$. When the N_2S_2 chelate is linked to a dansyl chromophore, this molecule is capable of

detecting Ni(II) and producing a fluorescence quenching response (~50%). We hypothesized that the N_2S_2 frame will provide greater specificity for Ni(II), as compared to other solely N-based probes published previously, and produce a sensor with nM affinity for Ni(II). This tetradentate chelate offers more ligand donors than the His^{Bz}-CSH model and is expected to bind Ni(II) in a square-planar coordination environment. However, the quenching response was not specific to Ni; addition of Co(II) and Cu(II) to the sensor also resulted in a decrease in fluorescence intensity to the same magnitude, suggesting that these transition metals can also bind or interact with the sulfonamide-N of the dansyl. The Ni quenching is likely a result of paramagnetism arising from Ni binding in a coordination geometry, namely tetrahedral or in a bidentate octahedral fashion, that renders it high spin. Although the system did not exhibit specificity for Ni(II), this work represents a significant step toward the development of chemical tools to study and map Ni(II) in biology.

Taken together, these complexes will offer the bioinorganic community greater understanding of the coordination environment of NiSOD, the requirements for promoting Ni-character in the RAMO of small molecule complexes in efforts to achieve Ni-based redox, and establish trends for Ni binding in N/S complexes. Herein we present the synthesis, characterization and analyses of four studies of Ni-N/S chemistry: a Ni(II)-thiyl ↔ Ni(III) resonance species in a family of Ni(nmp) complexes (Ch. 3); a $\{NiNO\}^{10}$ complex bound through bridging thiolates and N-nitrosamines (Ch. 4); an N_2S_2 fluorescent sensor designed for the detection of Ni(II) (Ch. 5), and a peptide based $NiSOD_{ox}$ model, His^{Bz}-CSH (Appendix A).

1.6 References

(1) Denkhaus, E.; Salnikow, K. Nickel essentiality, toxicity, and carcinogenicity. *Crit. Rev. Oncol. Hematol.* **2002**, *42*, 35-56.

(2) Drinking Water Requirements for States and Public Water Systems: Chemical Contaminant Rules. Phase V, July 1992. 57 FR 31776, 2016. Environmental Protection Agency.

(3) National Primary Drinking Water Regulations: Nickel. EPA 81.1-F-95-002m-T., 1995. National Service Center for Environmental Publications (NSCEP). Office of Water. Environmental Protection Agency.

(4) Razavet, M.; Artero, V.; Fontecave, M. Proton Electroreduction Catalyzed by Cobaloximes: Functional Models for Hydrogenases. *Inorg. Chem.* **2005**, *44*, 4786-4795.

(5) National Research Council. Medical and biological effects of environmental pollutants: Nickel, 1975. Washington D. C., Committee on Medical and Biological Effects of Environmental Pollutants. National Academy of Sciences.

(6) *Nickel and human health: current perspectives*; Wiley: New York, 1992.

(7) Malo, J. L.; Cartier, A.; Doepner, M.; Nieboer, E.; Evans, S.; Dolovich, J. Occupational asthma caused by nickel sulfate. *J. Allergy Clin. Immunol.* **1982**, *69*, 55-59.

(8) Sunderman, F. W.; Kincaid, J. F. Nickel poisoning. II. Studies on patients suffering from acute exposure to vapors of nickel carbonyl. *J. Am. Med. Assoc.* **1954**, *155*, 889-894.

(9) Goodman, J. E.; Prueitt, R. L.; Dodge, D. G.; Thakali, S. Carcinogenicity assessment of water-soluble nickel compounds. *Crit. Rev. Toxicol.* **2009**, *39*, 365-417.

(10) Dieter, M. P.; Jameson, C. W.; Tucker, A. N.; Luster, M. I.; French, J. E.; Hong, H. L.; Boorman, G. A. Evaluation of tissue disposition, myelopoietic, and immunologic responses in mice after long-term exposure to nickel sulfate in the drinking water. *J. Toxicol. Environ. Health* **1988**, *24*, 357-372.

(11) Evans, R. M.; Davies, P. J. A.; Costa, M. Video Time-Lapse Microscopy of Phagocytosis and Intracellular Fate of Crystalline Nickel Sulfide Particles in Cultured Mammalian-Cells. *Cancer Res.* **1982**, *42*, 2729-2735.

(12) Abbracchio, M. P.; Simmons-Hansen, J.; Costa, M. Cytoplasmic dissolution of phagocytized crystalline nickel sulfide particles: a prerequisite for nuclear uptake of nickel. *J. Toxicol. Environ. Health* **1982**, *9*, 663-676.

(13) Costa, M.; Heck, J. D. Specific Nickel Compounds as Carcinogens. *Trends Pharmacol. Sci.* **1982**, *3*, 408-410.

(14) Costa, M.; Abbracchio, M. P.; Simmonshansen, J. Factors Influencing the Phagocytosis, Neoplastic Transformation, and Cyto-Toxicity of Particulate Nickel Compounds in Tissue-Culture Systems. *Toxicol. Appl. Pharmacol.* **1981**, *60*, 313-323.

(15) Fletcher, G. G.; Rossetto, F. E.; Turnbull, J. D.; Nieboer, E. Toxicity, Uptake, and Mutagenicity of Particulate and Soluble Nickel Compounds. *Environ. Health Perspect.* **1994**, *102*, 69-79.

(16) Kasprzak, K. S.; Sunderman, F. W., Jr.; Salnikow, K. Nickel carcinogenesis. *Mutat. Res.* **2003**, *533*, 67-97.

(17) Sen, P.; Conway, K.; Costa, M. Comparison of the Localization of Chromosome-Damage Induced by Calcium Chromate and Nickel Compounds. *Cancer Res.* **1987**, *47*, 2142-2147.

(18) Conway, K.; Costa, M. Nonrandom Chromosomal Alterations in Nickel-Transformed Chinese-Hamster Embryo Cells. *Cancer Res.* **1989**, *49*, 6032-6038.

(19) Patierno, S. R.; Sugiyama, M.; Basilion, J. P.; Costa, M. Preferential DNA-Protein Cross-Linking by $NiCl_2$ in Magnesium-Insoluble Regions of Fractionated Chinese-Hamster Ovary Cell Chromatin. *Cancer Res.* **1985**, *45*, 5787-5794.

(20) Dally, H.; Hartwig, A. Induction and repair inhibition of oxidative DNA damage by nickel(II) and cadmium(II) in mammalian cells. *Carcinogenesis* **1997**, *18*, 1021-1026.

(21) Hartwig, A.; Kruger, I.; Beyersmann, D. Mechanisms in Nickel Genotoxicity - the Significance of Interactions with DNA-Repair. *Toxicol. Lett.* **1994**, *72*, 353-358.

(22) Hartwig, A.; Mullenders, L. H. F.; Schlepegrell, R.; Kasten, U.; Beyersmann, D. Nickel(II) Interferes with the Incision Step in Nucleotide Excision-Repair in Mammalian-Cells. *Cancer Res.* **1994**, *54*, 4045-4051.

(23) Huang, X.; Frenkel, K.; Klein, C. B.; Costa, M. Nickel induces increased oxidants in intact cultured mammalian cells as detected by dichlorofluorescein fluorescence. *Toxicol. Appl. Pharmacol.* **1993**, *120*, 29-36.

(24) Salnikow, K.; Su, W.; Blagosklonny, M. V.; Costa, M. Carcinogenic metals induce hypoxia-inducible factor-stimulated transcription by reactive oxygen species-independent mechanism. *Cancer Res.* **2000**, *60*, 3375-3378.

(25) Chen, C. Y.; Wang, Y. F.; Huang, W. R.; Huang, Y. T. Nickel induces oxidative stress and genotoxicity in human lymphocytes. *Toxicol. Appl. Pharmacol.* **2003**, *189*, 153-159.

(26) Rodrigue, A.; Effantin, G.; Mandrand-Berthelot, M. A. Identification of rcnA (yohM), a nickel and cobalt resistance gene in *Escherichia coli*. *J. Bacteriol.* **2005**, *187*, 2912-2916.

(27) Macomber, L.; Hausinger, R. P. Mechanisms of nickel toxicity in microorganisms. *Metallomics* **2011**, *3*, 1153-1162.

(28) Bleriot, C.; Effantin, G.; Lagarde, F.; Mandrand-Berthelot, M. A.; Rodrigue, A. RcnB is a periplasmic protein essential for maintaining intracellular Ni and Co concentrations in *Escherichia coli*. *J. Bacteriol.* **2011**, *193*, 3785-3793.

(29) Stahler, F. N.; Odenbreit, S.; Haas, R.; Wilrich, J.; Van Vliet, A. H.; Kusters, J. G.; Kist, M.; Bereswill, S. The novel *Helicobacter pylori* CznABC metal efflux pump is required for cadmium, zinc, and nickel resistance, urease modulation, and gastric colonization. *Infect. Immun.* **2006**, *74*, 3845-3852.

(30) Grass, G.; Fan, B.; Rosen, B. P.; Lemke, K.; Schlegel, H. G.; Rensing, C. NreB from *Achromobacter xylosoxidans* 31A is a nickel-induced transporter conferring nickel resistance. *J. Bacteriol.* **2001**, *183*, 2803-2807.

(31) Park, J. E.; Schlegel, H. G.; Rhie, H. G.; Lee, H. S. Nucleotide sequence and expression of the ncr nickel and cobalt resistance in *Hafnia alvei* 5-5. *Int. Microbiol.* **2004**, *7*, 27-34.

(32) Schmidt, T.; Schlegel, H. G. Nickel and Cobalt Resistance of Various Bacteria Isolated from Soil and Highly Polluted Domestic and Industrial-Wastes. *FEMS Microbiol. Ecol.* **1989**, *62*, 315-328.

(33) Higgins, K. A.; Carr, C. E.; Maroney, M. J. Specific metal recognition in nickel trafficking. *Biochemistry* **2012**, *51*, 7816-7832.

(34) Mulrooney, S. B.; Hausinger, R. P. Nickel uptake and utilization by microorganisms. *FEMS Microbiol. Rev.* **2003**, *27*, 239-261.

(35) Bartha, R.; Ordal, E. J. Nickel-Dependent Chemolithotrophic Growth of Two *Hydrogenomonas* Strains. *J. Bacteriol.* **1965**, *89*, 1015-1019.

(36) Cherrier, M. V.; Cavazza, C.; Bochot, C.; Lemaire, D.; Fontecilla-Camps, J. C. Structural characterization of a putative endogenous metal chelator in the periplasmic nickel transporter NikA. *Biochemistry* **2008**, *47*, 9937-9943.

(37) De Pina, K.; Navarro, C.; Mcwalter, L.; Boxer, D. H.; Price, N. C.; Kelly, S. M.; Mandrand-Berthelot, M.-A.; Wu, L. F. Purification and Characterization of the Periplasmic Nickel-Binding Protein NikA of *Escherichia coli* K12. *Eur. J. Biochem.* **1995**, *227*, 857-865.

(38) Heddle, J.; Scott, D. J.; Unzai, S.; Park, S. Y.; Tame, J. R. H. Crystal structures of the liganded and unliganded nickel-binding protein NikA from *Escherichia coli*. *J. Biol. Chem.* **2003**, *278*, 50322-50329.

(39) Allan, C. B.; Wu, L. F.; Gu, Z. J.; Choudhury, S. B.; Al-Mjeni, F.; Sharma, M. L.; Mandrand-Berthelot, M. A.; Maroney, M. J. An X-ray Absorption Spectroscopic Structural Investigation of the Nickel Site in *Escherichia coli* NikA Protein. *Inorg. Chem.* **1998**, *37*, 5952-5955.

(40) Chivers, P. T.; Benanti, E. L.; Heil-Chapdelaine, V.; Iwig, J. S.; Rowe, J. L. Identification of Ni-(L-His)$_2$ as a substrate for NikABCDE-dependent nickel uptake in *Escherichia coli*. *Metallomics* **2012**, *4*, 1043-1050.

(41) Cavazza, C.; Martin, L.; Laffly, E.; Lebrette, H.; Cherrier, M. V.; Zeppieri, L.; Richaud, P.; Carriere, M.; Fontecilla-Camps, J. C. Histidine 416 of the periplasmic binding protein NikA is essential for nickel uptake in Escherichia coli. *FEBS Lett.* **2011**, *585*, 711-715.

(42) Eitinger, T.; Friedrich, B. A Topological Model for the High-Affinity Nickel Transporter of *Alcaligenes eutrophus*. *Mol. Microbiol.* **1994**, *12*, 1025-1032.

(43) Mobley, H. L. T.; Garner, R. M.; Bauerfeind, P. *Helicobacter pylori* Nickel-Transport Gene *NixA*: Synthesis of Catalytically Active Urease in *Escherichia coli* Independent of Growth Conditions. *Mol. Microbiol.* **1995**, *16*, 97-109.

(44) Eitinger, T.; Friedrich, B. Cloning, Nucleotide-Sequence, and Heterologous Expression of a High-Affinity Nickel Transport Gene from *Alcaligenes eutrophus*. *J. Biol. Chem.* **1991**, *266*, 3222-3227.

(45) Maroney, M. J. Structure/function relationships in nickel metallobiochemistry. *Curr. Opin. Chem. Biol.* **1999**, *3*, 188-199.

(46) Degen, O.; Eitinger, T. Substrate specificity of nickel/cobalt permeases: Insights from mutants altered in transmembrane domains I and II. *J. Bacteriol.* **2002**, *184*, 3569-3577.

(47) Lacasse, M. J.; Douglas, C. D.; Zamble, D. B. Mechanism of Selective Nickel Transfer from HypB to HypA, Escherichia coli [NiFe]-Hydrogenase Accessory Proteins. *Biochemistry* **2016**, *55*, 6821-6831.

(48) Lacasse, M. J.; Zamble, D. B. [NiFe]-Hydrogenase Maturation. *Biochemistry* **2016**, *55*, 1689-1701.

(49) Maier, T.; Lottspeich, F.; Bock, A. GTP Hydrolysis by HypB Is Essential for Nickel Insertion into Hydrogenases of *Escherichia coli*. *Eur. J. Biochem.* **1995**, *230*, 133-138.

(50) Chung, K. C. C.; Cao, L.; Dias, A. V.; Pickering, I. J.; George, G. N.; Zamble, D. B. A High Affinity Metal Binding Peptide from *Escherichia coli* HypB. *J. Am. Chem. Soc.* **2008**, *130*, 14056-14057.

(51) Leach, M. R.; Sandal, S.; Sun, H. W.; Zamble, D. B. Metal binding activity of the *Escherichia coli* hydrogenase maturation factor HypB. *Biochemistry* **2005**, *44*, 12229-12238.

(52) Atanassova, A.; Zamble, D. B. *Escherichia coli* HypA is a zinc metalloprotein with a weak affinity for nickel. *J. Bacteriol.* **2005**, *187*, 4689-4697.

(53) Herbst, R. W.; Perovic, I.; Martin-Diaconescu, V.; O'Brien, K.; Chivers, P. T.; Pochapsky, S. S.; Pochapsky, T. C.; Maroney, M. J. Communication between the Zinc and Nickel Sites in Dimeric HypA: Metal Recognition and pH Sensing. *J. Am. Chem. Soc.* **2010**, *132*, 10338-10351.

(54) Hu, H. Q.; Johnson, R. C.; Merrell, D. S.; Maroney, M. J. Nickel Ligation of the N-Terminal Amine of HypA Is Required for Urease Maturation in *Helicobacter pylori*. *Biochemistry* **2017**, *56*, 1105-1116.

(55) Lee, M. H.; Pankratz, H. S.; Wang, S.; Scott, R. A.; Finnegan, M. G.; Johnson, M. K.; Ippolito, J. A.; Christianson, D. W.; Hausinger, R. P. Purification and Characterization of *Klebsiella aerogenes* UreE Protein: A Nickel-Binding Protein That Functions in Urease Metallocenter Assembly. *Protein Sci.* **1993**, *2*, 1042-1052.

(56) Brayman, T. G.; Hausinger, R. P. Purification, characterization, and functional analysis of a truncated *Klebsiella aerogenes* UreE urease accessory protein lacking the histidine-rich carboxyl terminus. *J. Bacteriol.* **1996**, *178*, 5410-5416.

(57) Colpas, G. J.; Brayman, T. G.; McCracken, J.; Pressler, M. A.; Babcock, G. T.; Ming, L. J.; Colangelo, C. M.; Scott, R. A.; Hausinger, R. P. Spectroscopic characterization of metal binding by Klebsiella aerogenes UreE urease accessory protein. *J. Biol. Inorg. Chem.* **1998**, *3*, 150-160.

(58) Banaszak, K.; Martin-Diaconescu, V.; Bellucci, M.; Zambelli, B.; Rypniewski, W.; Maroney, M. J.; Ciurli, S. Crystallographic and X-ray absorption spectroscopic characterization of *Helicobacter pylori* UreE bound to Ni^{2+} and Zn^{2+} reveals a role for the disordered C-terminal arm in metal trafficking. *Biochem. J.* **2012**, *441*, 1017-1026.

(59) Farrugia, M. A.; Macomber, L.; Hausinger, R. P. Biosynthesis of the urease metallocenter. *J. Biol. Chem.* **2013**, *288*, 13178-13185.

(60) Benoit, S. L.; Mehta, N.; Weinberg, M. V.; Maier, C.; Maier, R. J. Interaction between the *Helicobacter pylori* accessory proteins HypA and UreE is needed for urease maturation. *Microbiology* **2007**, *153*, 1474-1482.

(61) Mehta, N.; Olson, J. W.; Maier, R. J. Characterization of *Helicobacter pylori* nickel metabolism accessory proteins needed for maturation of both urease and hydrogenase. *J. Bacteriol.* **2003**, *185*, 726-734.

(62) Kusters, J. G.; van Vliet, A. H. M.; Kuipers, E. J. Pathogenesis of *Helicobacter pylori* infection. *Clin. Microbiol. Rev.* **2006**, *19*, 449-490.

(63) De Pina, K.; Desjardin, V.; Mandrand-Berthelot, M. A.; Giordano, G.; Wu, L. F. Isolation and characterization of the NikR gene encoding a nickel-responsive regulator in *Escherichia coli*. *J. Bacteriol.* **1999**, *181*, 670-674.

(64) Chivers, P. T.; Sauer, R. T. NikR is a ribbon-helix-helix DNA-binding protein. *Protein Sci.* **1999**, *8*, 2494-2500.

(65) Wang, S. C.; Dias, A. V.; Bloom, S. L.; Zamble, D. B. Selectivity of metal binding and metal-induced stability of *Escherichia coli* NikR. *Biochemistry* **2004**, *43*, 10018-10028.

(66) Chivers, P. T.; Sauer, R. T. NikR repressor: High-affinity nickel binding to the C-terminal domain regulates binding to operator DNA. *Chem. Biol.* **2002**, *9*, 1141-1148.

(67) Schreiter, E. R.; Wang, S. C.; Zamble, D. B.; Drennan, C. L. NikR operator complex structure and the mechanism of repressor activation by metal ions. *Proc. Natl. Acad. Sci. U.S.A.* **2006**, *103*, 13676-13681.

(68) Bloom, S. L.; Zamble, D. B. Metal-selective DNA-binding response of *Escherichia coli* NikR. *Biochemistry* **2004**, *43*, 10029-10038.

(69) Dian, C.; Schauer, K.; Kapp, U.; McSweeney, S. M.; Labigne, A.; Terradot, L. Structural basis of the nickel response in *Helicobacter pylori*: Crystal structures of HpNikR in apo and nickel-bound states. *J. Mol. Biol.* **2006**, *361*, 715-730.

(70) Chivers, P. T.; Tahirov, T. H. Structure of *Pyrococcus horikoshii* NikR: Nickel sensing and implications for the regulation of DNA recognition. *J. Mol. Biol.* **2005**, *348*, 597-607.

(71) Leitch, S.; Bradley, M. J.; Rowe, J. L.; Chivers, P. T.; Maroney, M. J. Nickel-specific response in the transcriptional regulator, *Escherichia coli* NikR. *J. Am. Chem. Soc.* **2007**, *129*, 5085-5095.

(72) Iwig, J. S.; Leitch, S.; Herbst, R. W.; Maroney, M. J.; Chivers, P. T. Ni(II) and Co(II) sensing by *Escherichia coli* RcnR. *J. Am. Chem. Soc.* **2008**, *130*, 7592-7606.

(73) Higgins, K. A.; Chivers, P. T.; Maroney, M. J. Role of the N-terminus in Determining Metal-Specific Responses in the *E. coli* Ni- and Co-Responsive Metalloregulator, RcnR. *J. Am. Chem. Soc.* **2012**, *134*, 7081-7093.

(74) Ahn, B. E.; Cha, J.; Lee, E. J.; Han, A. R.; Thompson, C. J.; Roe, J. H. Nur, a nickel-responsive regulator of the Fur family, regulates superoxide dismutases and nickel transport in *Streptomyces coelicolor*. *Mol. Microbiol.* **2006**, *59*, 1848-1858.

(75) Musiani, F.; Zambelli, B.; Bazzani, M.; Mazzei, L.; Ciurli, S. Nickel-responsive transcriptional regulators. *Metallomics* **2015**, *7*, 1305-1318.

(76) An, Y. J.; Ahn, B. E.; Han, A. R.; Kim, H. M.; Chung, K. M.; Shin, J. H.; Cho, Y. B.; Roe, J. H.; Cha, S. S. Structural basis for the specialization of Nur, a nickel-specific Fur homolog, in metal sensing and DNA recognition. *Nucleic Acids Res.* **2009**, *37*, 3442-3451.

(77) Olmedo, P.; Pla, A.; Hernandez, A. F.; Lopez-Guarnido, O.; Rodrigo, L.; Gil, F. Validation of a method to quantify chromium, cadmium, manganese, nickel and lead in human whole blood, urine, saliva and hair samples by electrothermal atomic absorption spectrometry. *Anal. Chim. Acta* **2010**, *659*, 60-67.

(78) Locating and Estimating Air Emissions from Sources of Nickel. EPA-450/4-84-007f, 1984. Research Triangle Park, NC, U.S. Environmental Protection Agency.

(79) Determination of Trace Elements in Waters and Wastes by Inductively Coupled Plasma-Mass Spectrometry. Method 200.8. Revision 5.4, 1994. Cincinatti, OH, Office of Research and Development. U.S. Environmental Protection Agency.

(80) Li, X.; Gao, X.; Shi, W.; Ma, H. Design strategies for water-soluble small molecular chromogenic and fluorogenic probes. *Chem. Rev.* **2014**, *114*, 590-659.

(81) Hancock, R. D. The pyridyl group in ligand design for selective metal ion complexation and sensing. *Chem. Soc. Rev.* **2013**, *42*, 1500-1524.

(82) Aron, A. T.; Ramos-Torres, K. M.; Cotruvo, J. A.; Chang, C. J. Recognition- and Reactivity-Based Fluorescent Probes for Studying Transition Metal Signaling in Living Systems. *Acc. Chem. Res.* **2015**, *48*, 2434-2442.

(83) Wang, B. Y.; Hu, Y. L.; Su, Z. X. Synthesis and photophysical behaviors of a blue fluorescent copolymer as chemosensor for protons and Ni^{2+} ion in aqueous solution. *React. Funct . Polym.* **2008**, *68*, 1137-1143.

(84) Wang, B. Y.; Liu, X. Y.; Hu, Y. L.; Su, Z. X. Synthesis and photophysical behavior of a water-soluble coumarin-bearing polymer for proton and Ni^{2+} ion sensing. *Polym. Int.* **2009**, *58*, 703-709.

(85) Lei, Y. X.; Li, H.; Gao, W. X.; Liu, M. C.; Chen, J. X.; Ding, J. C.; Huang, X. B.; Wu, H. Y. Highly sensitive conjugated polymer fluorescent sensors based on benzochalcogendiazole for nickel ions in real-time detection. *J. Mater. Chem. C* **2014**, *2*, 7402-7410.

(86) Allzadeh, K.; Rad, N. A. A New Optical Sensor for Selective Monitoring of Nickel Ion Based on A Hydrazone Derivative Immobilized on the Triacetyl Cellulose Membrane. *J. Anal. Bioanal. Tech.* **2016**, *7*, 322-323.

(87) Aksuner, N.; Henden, E.; Yilmaz, I.; Cukurovali, A. A novel optical chemical sensor for the determination of nickel(II) based on fluorescence quenching of newly synthesized thiazolo-triazol derivative and application to real samples. *Sens. Actuators B Chem.* **2012**, *166*, 269-274.

(88) Salins, L. L.; Goldsmith, E. S.; Ensor, C. M.; Daunert, S. A fluorescence-based sensing system for the environmental monitoring of nickel using the nickel binding protein from *Escherichia coli*. *Anal. Bioanal. Chem.* **2002**, *372*, 174-180.

(89) Pearce, D. A.; Walkup, G. K.; Imperiali, B. Peptidyl chemosensors incorporating a FRET mechanism for detection of Ni(II). *Bioorg. Med. Chem. Lett.* **1998**, *8*, 1963-1968.

(90) Torrado, A.; Walkup, G. K.; Imperiali, B. Exploiting polypeptide motifs for the design of selective Cu(II) ion chemosensors. *J. Am. Chem. Soc.* **1998**, *120*, 609-610.

(91) Zheng, Y. J.; Gattas-Asfura, K. M.; Konka, V.; Leblanc, R. M. A dansylated peptide for the selective detection of copper ions. *Chem. Commun.* **2002**, 2350-2351.

(92) Masuoka, J.; Hegenauer, J.; Van Dyke, B. R.; Saltman, P. Intrinsic stoichiometric equilibrium constants for the binding of zinc(II) and copper(II) to the high affinity site of serum albumin. *J. Biol. Chem.* **1993**, *268*, 21533-21537.

(93) Harford, C.; Sarkar, B. Amino terminal Cu(II)- and Ni(II)-binding (ATCUN) motif of proteins and peptides: Metal binding, DNA cleavage, and other properties. *Acc. Chem. Res.* **1997**, *30*, 123-130.

(94) Bolletta, F.; Costa, I.; Fabbrizzi, L.; Licchelli, M.; Montalti, M.; Pallavicini, P.; Prodi, L.; Zaccheroni, N. A $[Ru^{II}(bipy)_3]$-[1,9-diamino-3,7-diazanonane-4,6-dione] two-component system, as an efficient ON-OFF luminescent chemosensor for Ni^{2+} and Cu^{2+} in water, based on an ET (energy transfer) mechanism. *J. Chem. Soc., Dalton Trans.* **1999**, 1381-1385.

(95) Di Casa, M.; Fabbrizzi, L.; Licchelli, M.; Poggi, A.; Sacchi, D.; Zema, M. A novel fluorescence redox switch based on the formal Ni^{II}/Ni^{I} couple. *J. Chem. Soc., Dalton Trans.* **2001**, 1671-1675.

(96) Fabbrizzi, L.; Foti, F.; Licchelli, M.; Maccarini, P. M.; Sacchi, D.; Zema, M. Light-emitting molecular machines: pH-induced intramolecular motions in a fluorescent nickel(II) scorpionate complex. *Chem. Eur. J* **2002**, *8*, 4965-4972.

(97) Fabbrizzi, L.; Licchelli, M.; Mascheroni, S.; Poggi, A.; Sacchi, D.; Zema, M. Water soluble molecular switches of fluorescence based on the Ni(III)/Ni(II) redox change. *Inorg. Chem.* **2002**, *41*, 6129-6136.

(98) Fabbrizzi, L.; Licchelli, M.; Pallavicini, P.; Perotti, A.; Taglietti, A.; Sacchi, D. Fluorescent sensors for transition metals based on electron-transfer and energy-transfer mechanisms. *Chemistry-a European Journal* **1996**, *2*, 75-82.

(99) Fabbrizzi, L.; Licchelli, M.; Poggi, A.; Sacchi, D.; Zampa, C. A chromogenic penta-aza scorpionand for nickel(II) and copper(II) ions. *Polyhedron* **2004**, *23*, 373-378.

(100) Engeser, M.; Fabbrizzi, L.; Licchelli, M.; Sacchi, D. A fluorescent molecular thermometer based on the nickel(II) high-spin/low-spin interconversion. *Chem. Commun.* **1999**, 1191-1192.

(101) Jiang, L. J.; Luo, Q. H.; Wang, Z. L.; Liu, D. J.; Zhang, Z.; Hu, H. W. A dioxotetraamine fluorenyl ligand and its nickel(II) complex - crystal structure and fluorescent sensing properties in aqueous solution. *Polyhedron* **2001**, *20*, 2807-2812.

(102) Banerjee, A.; Sahana, A.; Guha, S.; Lohar, S.; Hauli, I.; Mukhopadhyay, S. K.; Matalobos, J. S.; Das, D. Nickel(II)-Induced Excimer Formation of a Naphthalene-Based Fluorescent Probe for Living Cell Imaging. *Inorg. Chem.* **2012**, *51*, 5699-5704.

(103) Kang, M. Y.; Lim, C. S.; Kim, H. S.; Seo, E. W.; Kim, H. M.; Kwon, O.; Cho, B. R. Detection of Nickel in Fish Organs with a Two-Photon Fluorescent Probe. *Chem. Eur. J* **2012**, *18*, 1953-1960.

(104) Wang, H. X.; Wang, D. L.; Wang, Q.; Li, X. Y.; Schalley, C. A. Nickel(II) and iron(III) selective off-on-type fluorescence probes based on perylene tetracarboxylic diimide. *Org. Biomol. Chem.* **2010**, *8*, 1017-1026.

(105) Dodani, S. C.; He, Q. W.; Chang, C. J. A Turn-On Fluorescent Sensor for Detecting Nickel in Living Cells. *J. Am. Chem. Soc.* **2009**, *131*, 18020-18021.

(106) Boer, J. L.; Mulrooney, S. B.; Hausinger, R. P. Nickel-dependent metalloenzymes. *Arch. Biochem. Biophys.* **2014**, *544*, 142-152.

(107) Zamble, D. It costs more than a nickel. *Science* **2015**, *349*, 35-36.

(108) Ragsdale, S. W. Nickel-based Enzyme Systems. *J. Biol. Chem.* **2009**, *284*, 18571-18575.

(109) Phillips, S. A.; Thornalley, P. J. The Formation of Methylglyoxal from Triose Phosphates - Investigation Using a Specific Assay for Methylglyoxal. *Eur. J. Biochem.* **1993**, *212*, 101-105.

(110) He, M. M.; Clugston, S. L.; Honek, J. F.; Matthews, B. W. Determination of the structure of Escherichia coli glyoxalase I suggests a structural basis for differential metal activation. *Biochemistry* **2000**, *39*, 8719-8727.

(111) Davidson, G.; Clugston, S. L.; Honek, J. F.; Maroney, M. J. An XAS investigation of product and inhibitor complexes of Ni-containing GlxI from *Escherichia coli*: mechanistic implications. *Biochemistry* **2001**, *40*, 4569-4582.

(112) Ly, H. D.; Clugston, S. L.; Sampson, P. B.; Honek, J. F. Syntheses and kinetic evaluation of hydroxamate-based peptide inhibitors of glyoxalase I. *Bioorg. Med. Chem. Lett.* **1998**, *8*, 705-710.

(113) Hall, S. S.; Doweyko, A. M.; Jordan, F. Glyoxalase I enzyme studies. 2. Nuclear magnetic resonance evidence for an enediol-proton transfer mechanism. *J. Am. Chem. Soc.* **1976**, *98*, 7460-7461.

(114) Albers, E. Metabolic characteristics and importance of the universal methionine salvage pathway recycling methionine from 5'-methylthioadenosine. *IUBMB life* **2009**, *61*, 1132-1142.

(115) Dai, Y.; Wensink, P. C.; Abeles, R. H. One protein, two enzymes. *J. Biol. Chem.* **1999**, *274*, 1193-1195.

(116) Al-Mjeni, F.; Ju, T.; Pochapsky, T. C.; Maroney, M. J. XAS investigation of the structure and function of Ni in acireductone dioxygenase. *Biochemistry* **2002**, *41*, 6761-6769.

(117) Pochapsky, T. C.; Pochapsky, S. S.; Ju, T. T.; Mo, H. P.; Al-Mjeni, F.; Maroney, M. J. Modeling and experiment yields the structure of acireductone dioxygenase from *Klebsiella pneumoniae*. *Nat. Struct. Biol.* **2002**, *9*, 966-972.

(118) Chai, S. C.; Ju, T. T.; Dang, M.; Goldsmith, R. B.; Maroney, M. J.; Pochapsky, T. C. Characterization of metal binding in the active sites of acireductone dioxygenase isoforms from *Klebsiella* ATCC 8724. *Biochemistry* **2008**, *47*, 2428-2438.

(119) Pochapsky, T. C.; Pochapsky, S. S.; Ju, T. T.; Hoefler, C.; Liang, J. A refined model for the structure of acireductone dioxygenase from *Klebsiella* ATCC 8724 incorporating residual dipolar couplings. *J. Biomol. NMR* **2006**, *34*, 117-127.

(120) Allpress, C. J.; Grubel, K.; Szajna-Fuller, E.; Arif, A. M.; Berreau, L. M. Regioselective Aliphatic Carbon-Carbon Bond Cleavage by a Model System of Relevance to Iron-Containing Acireductone Dioxygenase. *J. Am. Chem. Soc.* **2013**, *135*, 659-668.

(121) Dixon, N. E.; Gazzola, C.; Watters, J. J.; Blakely, R. L.; Zerner, B. Inhibition of Jack Bean urease (EC 3.5.1.5) by acetohydroxamic acid and by phosphoramidate. An equivalent weight for urease. *J. Am. Chem. Soc.* **1975**, *97*, 4130-4131.

(122) Jabri, E.; Carr, M. B.; Hausinger, R. P.; Karplus, P. A. The Crystal-Structure of Urease from *Klebsiella aerogenes*. *Science* **1995**, *268*, 998-1004.

(123) Benini, S.; Rypniewski, W. R.; Wilson, K. S.; Miletti, S.; Ciurli, S.; Mangani, S. A new proposal for urease mechanism based on the crystal structures of the native and inhibited enzyme from *Bacillus pasteurii*: why urea hydrolysis costs two nickels. *Structure* **1999**, *7*, 205-216.

(124) Ha, N. C.; Oh, S. T.; Sung, J. Y.; Cha, K. A.; Lee, M. H.; Oh, B. H. Supramolecular assembly and acid resistance of *Helicobacter pylori* urease. *Nat. Struct. Biol.* **2001**, *8*, 505-509.

(125) Dixon, N. E.; Riddles, P. W.; Gazzola, C.; Blakeley, R. L.; Zerner, B. Jack Bean Urease (EC 3.5.1.5.) V. On the Mechanism of Action of Urease on Urea, Formamide, Acetamide, N-Methylurea, and Related-Compounds. *Can. J. Biochem.* **1980**, *58*, 1335-1344.

(126) Barrios, A. M.; Lippard, S. J. Interaction of urea with a hydroxide-bridged dinuclear nickel center: An alternative model for the mechanism of urease. *J. Am. Chem. Soc.* **2000**, *122*, 9172-9177.

(127) Pearson, M. A.; Park, I. S.; Schaller, R. A.; Michel, L. O.; Karplus, P. A.; Hausinger, R. P. Kinetic and structural characterization of urease active site variants. *Biochemistry* **2000**, *39*, 8575-8584.

(128) Desguin, B.; Soumillion, P.; Hols, P.; Hausinger, R. P. Nickel-pincer cofactor biosynthesis involves LarB-catalyzed pyridinium carboxylation and LarE-dependent sacrificial sulfur insertion. *Proc. Natl. Acad. Sci. U.S.A.* **2016**, *113*, 5598-5603.

(129) Desguin, B.; Zhang, T.; Soumillion, P.; Hols, P.; Hu, J.; Hausinger, R. P. A tethered niacin-derived pincer complex with a nickel-carbon bond in lactate racemase. *Science* **2015**, *349*, 66-69.

(130) Xu, T.; Bauer, G.; Hu, X. A Novel Nickel Pincer Complex in the Active Site of Lactate Racemase. *ChemBioChem* **2016**, *17*, 31-32.

(131) Xu, T.; Wodrich, M. D.; Scopelliti, R.; Corminboeuf, C.; Hu, X. Nickel pincer model of the active site of lactate racemase involves ligand participation in hydride transfer. *Proc. Natl. Acad. Sci. U.S.A.* **2017**, *114*, 1242-1245.

(132) Wang, B.; Shaik, S. The Nickel-Pincer Complex in Lactate Racemase Is an Electron Relay and Sink that acts through Proton-Coupled Electron Transfer. *Angew. Chem. Int. Ed.* **2017**, DOI 10.1002/anie.201612065.

(133) Fontecilla-Camps, J. C.; Volbeda, A.; Cavazza, C.; Nicolet, Y. Structure/function relationships of [NiFe]- and [FeFe]-hydrogenases. *Chem. Rev.* **2007**, *107*, 4273-4303.

(134) Lubitz, W.; Ogata, H.; Rudiger, O.; Reijerse, E. Hydrogenases. *Chem. Rev.* **2014**, *114*, 4081-4148.

(135) Montet, Y.; Amara, P.; Volbeda, A.; Vernede, X.; Hatchikian, E. C.; Field, M. J.; Frey, M.; Fontecilla-Camps, J. C. Gas access to the active site of Ni-Fe hydrogenases probed by X-ray crystallography and molecular dynamics. *Nat. Struct. Biol.* **1997**, *4*, 523-526.

(136) Volbeda, A.; Montet, Y.; Vernede, X.; Hatchikian, E. C.; Fontecilla-Camps, J. C. High-resolution crystallographic analysis of *Desulfovibrio fructiosovorans* [NiFe] hydrogenase. *Int. J. Hydrogen Energy* **2002**, *27*, 1449-1461.

(137) Siegbahn, P. E. M.; Tye, J. W.; Hall, M. B. Computational studies of [NiFe] and [FeFe] hydrogenases. *Chem. Rev.* **2007**, *107*, 4414-4435.

(138) Vincent, K. A.; Parkin, A.; Armstrong, F. A. Investigating and Exploiting the Electrocatalytic Properties of Hydrogenases. *Chem. Rev.* **2007**, *107*, 4366-4413.

(139) Shomura, Y.; Higuchi, Y. Structural aspects of [NiFe]-hydrogenases. *Rev. Inorg. Chem.* **2013**, *33*, 173-192.

(140) Shomura, Y.; Yoon, K. S.; Nishihara, H.; Higuchi, Y. Structural basis for a [4Fe-3S] cluster in the oxygen-tolerant membrane-bound [NiFe]-hydrogenase. *Nature* **2011**, *479*, 253-256.

(141) Goris, T.; Wait, A. F.; Saggu, M.; Fritsch, J.; Heidary, N.; Stein, M.; Zebger, I.; Lendzian, F.; Armstrong, F. A.; Friedrich, B.; Lenz, O. A unique iron-sulfur cluster is crucial for oxygen tolerance of a [NiFe]-hydrogenase. *Nat. Chem. Biol.* **2011**, *7*, 310-318.

(142) Lukey, M. J.; Roessler, M. M.; Parkin, A.; Evans, R. M.; Davies, R. A.; Lenz, O.; Friedrich, B.; Sargent, F.; Armstrong, F. A. Oxygen-Tolerant [NiFe]-Hydrogenases: The Individual and Collective Importance of Supernumerary Cysteines at the Proximal Fe-S Cluster. *J. Am. Chem. Soc.* **2011**, *133*, 16881-16892.

(143) Dobbek, H.; Svetlitchnyi, V.; Gremer, L.; Huber, R.; Meyer, O. Crystal structure of a carbon monoxide dehydrogenase reveals a [Ni-4Fe-5S] cluster. *Science* **2001**, *293*, 1281-1285.

(144) Volbeda, A.; Fontecilla-Camps, J. C. Structural bases for the catalytic mechanism of Ni-containing carbon monoxide dehydrogenases. *Dalton Trans* **2005**, 3443-3450.

(145) Ha, S. W.; Korbas, M.; Klepsch, M.; Meyer-Klaucke, W.; Meyer, O.; Svetlitchnyi, V. Interaction of potassium cyanide with the [Ni-4Fe-5S] active site cluster of CO dehydrogenase from *Carboxydothermus hydrogenoformans*. *J. Biol. Chem.* **2007**, *282*, 10639-10646.

(146) Kung, Y.; Drennan, C. L. A role for nickel-iron cofactors in biological carbon monoxide and carbon dioxide utilization. *Curr. Opin. Chem. Biol.* **2011**, *15*, 276-283.

(147) Jeoung, J. H.; Dobbek, H. Carbon dioxide activation at the Ni,Fe-cluster of anaerobic carbon monoxide dehydrogenase. *Science* **2007**, *318*, 1461-1464.

(148) Amara, P.; Mouesca, J. M.; Volbeda, A.; Fontecilla-Camps, J. C. Carbon Monoxide Dehydrogenase Reaction Mechanism: A Likely Case of Abnormal CO_2 Insertion to a Ni-H^- Bond. *Inorg. Chem.* **2011**, *50*, 1868-1878.

(149) Darnault, C.; Volbeda, A.; Kim, E. J.; Legrand, P.; Vernede, X.; Lindahl, P. A.; Fontecilla-Camps, J. C. Ni-Zn-[Fe_4S_4] and Ni-Ni-[Fe_4S_4] clusters in closed and open subunits of acetyl-CoA synthase/carbon monoxide dehydrogenase. *Nat. Struct. Biol.* **2003**, *10*, 271-279.

(150) Drennan, C. L.; Doukov, T. I.; Ragsdale, S. W. The metalloclusters of carbon monoxide dehydrogenase/acetyl-CoA synthase: a story in pictures. *J. Biol. Inorg. Chem.* **2004**, *9*, 511-515.

(151) Doukov, T. I.; Blasiak, L. C.; Seravalli, J.; Ragsdale, S. W.; Drennan, C. L. Xenon in and at the end of the tunnel of bifunctional carbon monoxide dehydrogenase/acetyl-CoA synthase. *Biochemistry* **2008**, *47*, 3474-3483.

(152) Riordan, C. G. Acetyl coenzyme A synthase: new insights into one of Nature's bioorganometallic catalysts. *J. Biol. Inorg. Chem.* **2004**, *9*, 509-510.

(153) Seravalli, J.; Kumar, M.; Ragsdale, S. W. Rapid kinetic studies of acetyl-CoA synthesis: Evidence supporting the catalytic intermediacy of a paramagnetic NiFeC species in the autotrophic Wood-Ljungdahl pathway. *Biochemistry* **2002**, *41*, 1807-1819.

(154) Ragsdale, S. W.; Pierce, E. Acetogenesis and the Wood-Ljungdahl pathway of CO2 fixation. *Biochim. Biophys. Acta, Proteins Proteomics* **2008**, *1784*, 1873-1898.

(155) Ragsdale, S. W. Nickel and the carbon cycle. *J. Inorg. Biochem.* **2007**, *101*, 1657-1666.

(156) Zheng, K. Y.; Ngo, P. D.; Owens, V. L.; Yang, X. P.; Mansoorabadi, S. O. The biosynthetic pathway of coenzyme F430 in methanogenic and methanotrophic archaea. *Science* **2016**, *354*, 339-342.

(157) Sarangi, R.; Dey, M.; Ragsdale, S. W. Geometric and Electronic Structures of the Ni^{I} and Methyl-Ni^{III} Intermediates of Methyl-Coenzyme M Reductase. *Biochemistry* **2009**, *48*, 3146-3156.

(158) Li, X. H.; Telser, J.; Kunz, R. C.; Hoffman, B. M.; Gerfen, G.; Ragsdale, S. W. Observation of Organometallic and Radical Intermediates Formed during the Reaction of Methyl-Coenzyme M Reductase with Bromoethanesulfonate. *Biochemistry* **2010**, *49*, 6866-6876.

(159) Chen, S. L.; Blomberg, M. R. A.; Siegbahn, P. E. M. How Is Methane Formed and Oxidized Reversibly When Catalyzed by Ni-Containing Methyl-Coenzyme M Reductase? *Chem. Eur. J* **2012**, *18*, 6309-6315.

(160) Pelmenschikov, V.; Blomberg, M. R. A.; Siegbahn, P. E. M.; Crabtree, R. H. A mechanism from quantum chemical studies for methane formation in methanogenesis. *J. Am. Chem. Soc.* **2002**, *124*, 4039-4049.

(161) Youn, H. D.; Youn, H.; Lee, J. W.; Yim, Y. I.; Lee, J. K.; Hah, Y. C.; Kang, S. O. Unique isozymes of superoxide dismutase in *Streptomyces griseus*. *Arch. Biochem. Biophys.* **1996**, *334*, 341-348.

(162) Youn, H. D.; Kim, E. J.; Roe, J. H.; Hah, Y. C.; Kang, S. O. A novel nickel-containing superoxide dismutase from *Streptomyces* spp. *Biochem. J.* **1996**, *318*, 889-896.

(163) Palenik, B.; Brahamsha, B.; Larimer, F. W.; Land, M.; Hauser, L.; Chain, P.; Lamerdin, J.; Regala, W.; Allen, E. E.; McCarren, J.; Paulsen, I.; Dufresne, A.; Partensky, F.; Webb, E. A.; Waterbury, J. The genome of a motile marine Synechococcus. *Nature* **2003**, *424*, 1037-1042.

(164) Wuerges, J.; Lee, J. W.; Yim, Y. I.; Yim, H. S.; Kang, S. O.; Carugo, K. D. Crystal structure of nickel-containing superoxide dismutase reveals another type of active site. *Proc. Natl. Acad. Sci. U.S.A.* **2004**, *101*, 8569-8574.

(165) Barondeau, D. P.; Kassmann, C. J.; Bruns, C. K.; Tainer, J. A.; Getzoff, E. D. Nickel superoxide dismutase structure and mechanism. *Biochemistry* **2004**, *43*, 8038-8047.

(166) Szilagyi, R. K.; Bryngelson, P. A.; Maroney, M. J.; Hedman, B.; Hodgson, K. O.; Solomon, E. I. S K-edge X-ray absorption spectroscopic investigation of the Ni-containing superoxide dismutase active site: New structural insight into the mechanism. *J. Am. Chem. Soc.* **2004**, *126*, 3018-3019.

(167) Bryngelson, P. A.; Arobo, S. E.; Pinkham, J. L.; Cabelli, D. E.; Maroney, M. J. Expression, reconstitution, and mutation of recombinant *Streptomyces coelicolor* NiSOD. *J. Am. Chem. Soc.* **2004**, *126*, 460-461.

(168) Fiedler, A. T.; Bryngelson, P. A.; Maroney, M. J.; Brunold, T. C. Spectroscopic and computational studies of Ni superoxide dismutase: Electronic structure contributions to enzymatic function. *J. Am. Chem. Soc.* **2005**, *127*, 5449-5462.

(169) Campeciño, J. O.; Dudycz, L. W.; Tumelty, D.; Berg, V.; Cabelli, D. E.; Maroney, M. J. A Semisynthetic Strategy Leads to Alteration of the Backbone Amidate Ligand in the NiSOD Active Site. *J. Am. Chem. Soc.* **2015**, *137*, 9044-9052.

(170) Ryan, K. C.; Guce, A. I.; Johnson, O. E.; Brunold, T. C.; Cabelli, D. E.; Garman, S. C.; Maroney, M. J. Nickel Superoxide Dismutase: Structural and Functional Roles of His1 and Its H-Bonding Network. *Biochemistry* **2015**, *54*, 1016-1027.

(171) Broering, E. P.; Truong, P. T.; Gale, E. M.; Harrop, T. C. Synthetic Analogues of Nickel Superoxide Dismutase: A New Role for Nickel in Biology. *Biochemistry* **2013**, *52*, 4-18.

(172) Gale, E. M.; Patra, A. K.; Harrop, T. C. Versatile Methodology Toward NiN2S2 Complexes as Nickel Superoxide Dismutase Models: Structure and Proton Affinity. *Inorg. Chem.* **2009**, *48*, 5620-5622.

(173) Gale, E. M.; Narendrapurapu, B. S.; Simmonett, A. C.; Schaefer, H. F.; Harrop, T. C. Exploring the Effects of H-Bonding in Synthetic Analogues of Nickel Superoxide Dismutase (Ni-SOD): Experimental and Theoretical Implications for Protection of the Ni-SCys Bond. *Inorg. Chem.* **2010**, *49*, 7080-7096.

(174) Enemark, J. H.; Feltham, R. D. Principles of Structure, Bonding, and Reactivity for Metal Nitrosyl Complexes. *Coord. Chem. Rev.* **1974**, *13*, 339-406.

(175) Tsuge, K.; DeRosa, F.; Lim, M. D.; Ford, P. C. Intramolecular reductive nitrosylation: Reaction of nitric oxide and a copper(ll) complex of a cyclam derivative with pendant luminescent chromophores. *J. Am. Chem. Soc.* **2004**, *126*, 6564-6565.

(176) Lim, M. H.; Wong, B. A.; Pitcock, W. H., Jr.; Mokshagundam, D.; Baik, M.-H.; Lippard, S. J. Direct Nitric Oxide Detection in Aqueous Solution by Copper(II) Fluorescein Complexes. *J. Am. Chem. Soc.* **2006**, *128*, 14364-14373.

CHAPTER 2

LITERATURE REVIEW

SYNTHETIC ANALOGUES OF NICKEL SUPEROXIDE DISMUTASE (NiSOD): A NEW ROLE FOR NICKEL IN BIOLOGY

Broering, E. P.;* Troung, P. T.;* Gale, E. M.; Harrop, T. C. Synthetic Analogues of Nickel Superoxide Dismutase (NiSOD): A New Role for Nickel in Biology. *Biochemistry* **2013**, 52, 4.

2.1 Abstract

Nickel-containing superoxide dismutases (NiSODs) represent a novel approach to the detoxification of superoxide in biology, and thus contribute to the biodiversity of mechanisms for ROS removal. While Ni ions play critical roles in anaerobic microbial redox (hydrogenases, CO dehydrogenase/acetyl coenzyme A synthase), they have never been associated with oxygen metabolism. Several SODs have been characterized from numerous sources, and are classified by their catalytic metal as Cu/ZnSOD, MnSOD, or FeSOD. Whereas aqueous solutions of Cu(II), Mn(II), and Fe(II) ions are capable of catalyzing the dismutation of superoxide, solutions of Ni(II) are not. Nonetheless, NiSOD catalyzes the reaction at the diffusion-controlled limit (~10^9 M^{-1} s^{-1}). To do this, nature has created a Ni coordination unit with the appropriate Ni(III/II) redox potential (~ 0.090 V vs. Ag/AgCl). This potential is achieved by a unique ligand set comprised of residues from the N-terminus of the protein: Cys2 and Cys6 thiolates, the amino terminus and imidazole side chain of His1, and a peptide N-donor from Cys2. Over the past several years synthetic modeling efforts by several groups have provided insight towards understanding the intrinsic properties of this unusual Ni coordination site. Such analogues have revealed information regarding the (i) electrochemical properties that support Ni-based redox, (ii) oxidative protection/stability of the coordinated CysS ligands, (iii) probable H^+ sources for H_2O_2 formation, and (iv) nature of the Ni coordination geometry throughout catalysis. This review includes the results and implications of such biomimetic work as it pertains to the structure and function of NiSOD.

2.2 Introduction

The anionic superoxide radical ($O_2^{\bullet-}$) is an inevitable byproduct of aerobic respiration formed primarily in the mitochondrial matrix upon O_2 reduction along the electron transport chain.[1] If this reactive oxygen species (ROS) is not eliminated, significant damage to surrounding cells will occur leading to a variety of disease states.[1,2] For example, the formation of ROS such as superoxide has been implicated in diseases such as diabetes,[3] neurological disorders like Parkinson's[4] and Alzheimer's[5] as well as the cell death and tissue damage that occur following stroke or heart attack (post-ischemic tissue injury).[6] In order to combat oxidative stress, all aerobic organisms possess metalloenzyme defense systems known as superoxide dismutases (SODs, EC 1.15.1.1) that catalyze the disproportionation of superoxide to hydrogen peroxide (H_2O_2) and molecular oxygen (O_2) through alternate oxidation and reduction of their respective catalytic metal centers (eqs. 2.1-2.3).[1,7,8] Several distinct types of SODs are known and each is classified by the first-row transition metal utilized to carry out the chemistry.[7] The more widely studied SODs include the dinuclear Cu/ZnSOD[9] and the mononuclear MnSOD[10-12] and FeSOD,[11-14] which have been characterized by numerous biochemical, structural, and theoretical techniques. For instance, point mutations in the gene that encodes the mammalian Cu/ZnSOD have been linked with the progression of the neurodegenerative disease Amyotrophic Lateral Sclerosis (ALS or Lou Gehrig's disease).[15] Several features that relate these SODs include: (i) a positively-charged Lys amino acid channel that guides the anionic substrate towards the active site, (ii) utilization of a metal ion that disproportionates $O_2^{\bullet-}$ even in the free $[M(H_2O)_6]^{n+}$ aquated state, (iii) similarity among the primary coordination spheres of the redox-active metal ion (supported mainly by His-N ligation), and (iv) anion-binding affinity at the M^{ox} center supportive of an inner-sphere electron-transfer (eT) mechanism for one of the two SOD

half-reactions (eq. 2.1, oxidative half-reaction with respect to substrate).[8] Recently, a new and distinct class of SOD has been discovered from *Streptomyces* soil bacteria[16] and found in the genome of cyanobacteria[17] that contain Ni at the active site. These SODs show no sequence homology with other SODs, have different and unusual primary coordination spheres, and utilize an active-site metal ion not normally associated with oxygen binding or activation. NiSOD thus represents a new role for Ni in a biological context.

$$M^{ox} + O_2^{\bullet -} \rightarrow M^{red} + O_2 \qquad (2.1)$$

$$M^{red} + O_2^{\bullet -} + 2H^+ \rightarrow M^{ox} + H_2O_2 \qquad (2.2)$$

$$\textit{Overall}: 2\ O_2^{\bullet -} + 2\ H^+ \rightarrow O_2 + H_2O_2 \qquad (2.3)$$

2.2.1. NiSOD Structural and Spectroscopic Properties

The structure of NiSOD has been determined by independent groups on two separate *Streptomyces* strains at high resolution (1.30 Å for *S. coelicolor*[18] and 1.68 Å for *S. seoulensis*[19]). The separate crystallographic investigations yield nearly identical structures, which is not surprising considering they share ~90% amino acid sequence homology. NiSOD is a homohexamer (total MW = 78 kDa) comprised of six interlocked four-helix bundle subunits arranged in the right-handed turn up-down-up-down topology with each subunit housing one solvent inaccessible Ni(III/II) ion (Figure 2.1).

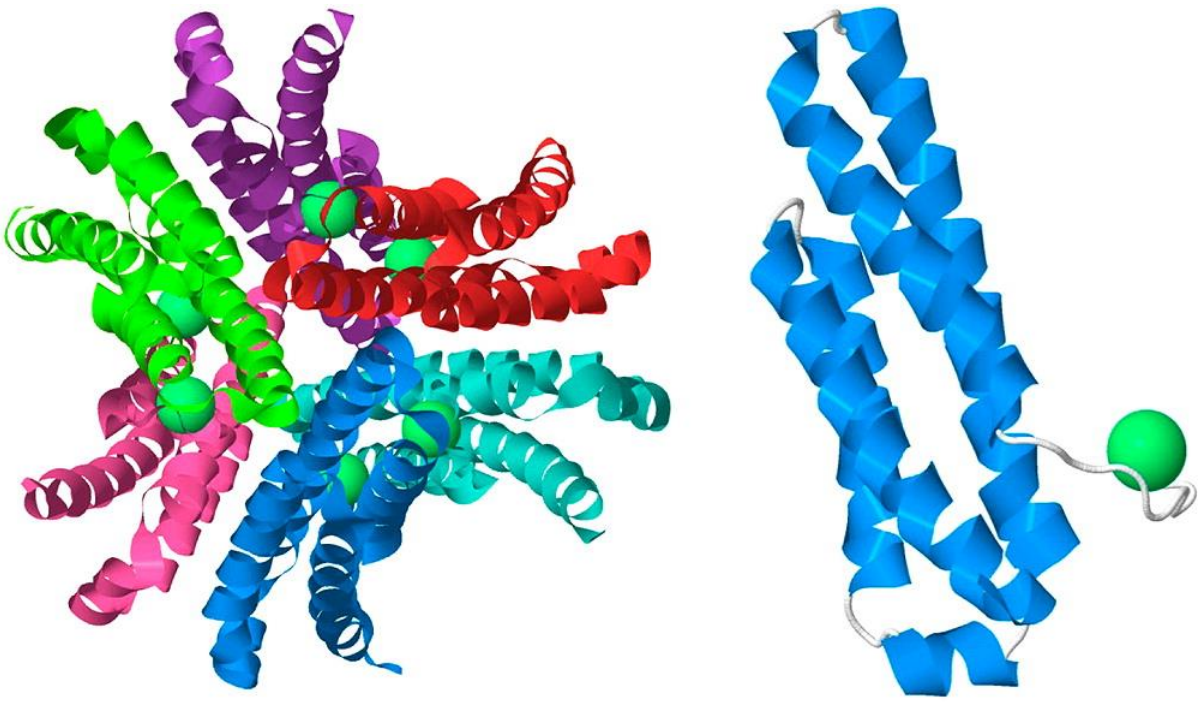

Figure 2.1. X-ray crystal structure of NiSOD from *S. coelicolor* (1.30 Å resolution, Protein Data Bank entry 1T6U). At the left is the NiSOD biological unit as a hexameric assembly of four-helix bundles. Ni centers are shown as green spheres; subunits are shown in different colors. At the right is the NiSOD subunit with nickel binding hook. This image was generated with Jmol.

The overall protein shape is globular with a hollow inner cavity, which is proposed to be a solvent channel. Depending on the strain, the outer diameter spans 60-72 Å with an interior cavity volume of ~ 8800 $Å^3$ that is 20-23 Å in diameter. The global protein structure and solvent-filled interior are somewhat reminiscent of the ferritin cavity for iron storage. Close examination of the subunits reveals that they are mostly stabilized by hydrophobic intersubunit interactions and salt bridges. The residues primarily responsible for chelating Ni comprise the first nine amino acids from the N-terminus with a recognizable Cys-X-X-X-Cys metal binding motif, i.e.,

His-Cys-X-X-Pro-Cys-Gly-X-Tyr. It has been proposed that this sequence may be an identifier for NiSOD, or a means for identifying NiSOD in future protein isolations from other species. These residues form a hook-like shape and have thus been called the "Ni-hook" region of the protein (Figure 2.1). Unlike four-helix bundles in other metalloproteins, the Ni-hook protrudes out of the bundle in NiSOD, a novel mode for metal binding among this structural motif. While arguments exist for a positively-charged substrate guide by a series of Lys residues that line the active site pocket, calculations reveal no significant positively charged surface residues which argue against an electrostatic guide. This result is in agreement with the low ionic strength dependence on the catalytic rate constant (*k*) for NiSOD.[20]

In both crystal structures of NiSOD, the active site Ni is found in two separate coordination geometries that are dependent on the metal oxidation state (Figure 2.2). The mononuclear Ni sites of each subunit appear to operate independently of each other as the closest Ni···Ni separation is ~ 25 Å. Several intersubunit connections, however, could serve as another means of active site communication during catalysis and have been advocated based on mutagenesis studies.[20] As isolated, half of the Ni ions are in the 2+ oxidation state and the other half are in the +3 state highlighting the stability of both states in as-isolated protein. In stark contrast to other known SODs, the reduced form of NiSOD ($NiSOD_{red}$) contains a square-planar Ni(II) ion ligated in an N_2S_2 environment consisting of one deprotonated peptido-N from Cys2, one primary amine-N from the N-terminal His1 residue, and two *cis*-coordinated thiolates from Cys2 and Cys6 (Figure 2.2). During turnover, superoxide oxidizes the Ni(II)-N_2S_2 site, forming a five-coordinate (5C) square-pyramidal Ni(III)-N_3S_2 species ($NiSOD_{ox}$) via coordination of the His1-N_δ (Figure 2.2). The Ni–N (1.9-2.1 Å) and Ni–S distances (2.2-2.3 Å) in the basal coordination plane appear consistent with other known Ni-metalloenzymes with the same donors

as well as small molecule complexes.[21] However, the Ni–HisN distance in $NiSOD_{ox}$ is relatively long (2.3-2.6 Å), which may be explained by the heterogeneity in the crystal structure, i.e., the presence of both Ni(II) and Ni(III) centers. Additionally, long X-ray exposure time appears to reduce the Ni(III) center in $NiSOD_{ox}$ to result in a $NiSOD_{red}$ structure where one can visualize the deligation and C_{β}-C_{γ} rotation of the His1 imidazole plane away from the Ni center by ~ 3-4 Å. Taken together, the structure of NiSOD is very different from its Cu/Zn and Fe, Mn congeners.

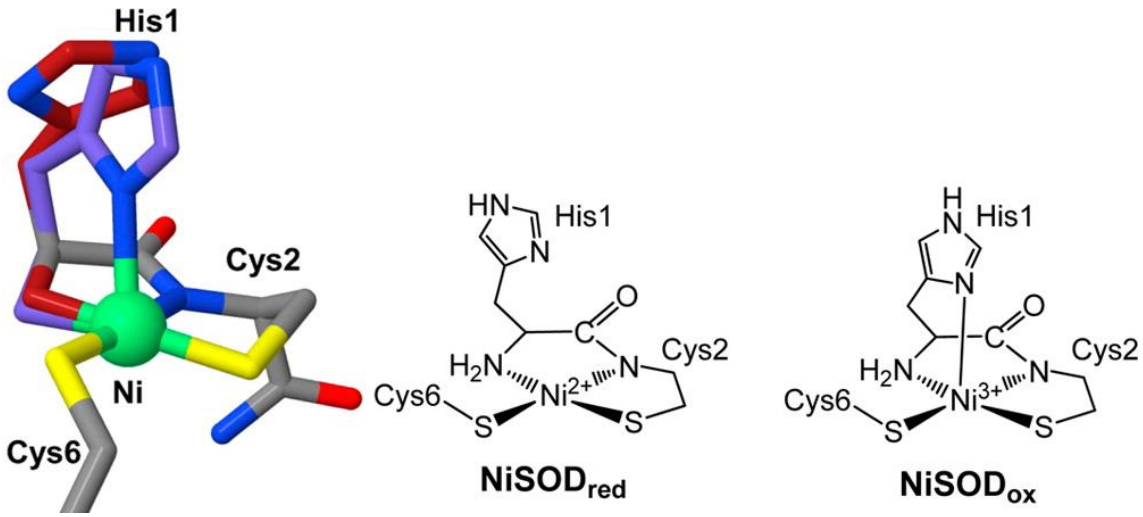

Figure 2.2. Active site of NiSOD from *S. coelicolor* showing the active site residues involved as ligands to the Ni center (left). The violet depiction of His1 represents the $NiSOD_{ox}$ state, whereas the dark red depiction of His1 represents the $NiSOD_{red}$ state where His1 is noncoordinated. This image was generated with Jmol. At the right is a ChemDraw depiction of the Ni(II) and Ni(III) active site geometries in NiSOD.

NiSOD has unique spectroscopic properties that mainly arise from the high valent Ni(III) oxidation state.[20,22,23] The low-spin (S = ½) Ni(III) center in $NiSOD_{ox}$ displays a rhombic EPR spectrum with principal g-values at 2.30, 2.24, and 2.01 with a distinct triplet superhyperfine splitting pattern (A_{zz} = 24.9 G) in the g_z component consistent with axial N-ligation (I = 1) (Figure 2.3).[18,22] As isolated, the enzyme contains an equal distribution of Ni(II) and Ni(III) centers that is reflected in the electronic absorption spectrum of the wild-type (WT) holoenzyme.[23] Because the overall UV-vis represents a mixture of these oxidation states, researchers have attempted to isolate the pure reduced or oxidized enzyme. The fully reduced enzyme was obtained by chemical reduction with dithionite, which resulted in very weak bands in the UV-vis spectrum. The main features in the visible region in the room temperature (RT) spectrum are a shoulder at 362 nm (ε: 880 M^{-1} cm^{-1}) and two peaks at 450 nm (ε: 480 M^{-1} cm^{-1}) and 543 nm (ε: 150 M^{-1} cm^{-1}).[23] These features are hallmarks of square-planar Ni(II)-N_2S_2 coordination complexes,[24] where the λ_{max} peaks have been assigned as ligand-field bands originating from electronic transitions in the d-manifold (d-to-d transitions) of the Ni(II) ion. Subtracting this spectrum from the as-isolated NiSOD spectrum resulted in the UV-vis contributions of $NiSOD_{ox}$. Incidentally, fully oxidized NiSOD could not be obtained even with strong oxidants such as ferricyanide highlighting the instability of six Ni(III) centers in the protein matrix. The high intensity of the main bands at 372 nm (ε: 6800 M^{-1} cm^{-1}) and 502 nm (ε: 1510 M^{-1} cm^{-1}) are due to sulfur-to-nickel charge-transfer (S-to-Ni CT) bands that are σ and π (i.e., S-pπ to Ni-dπ and S-pπ to Ni-dπ) in origin, respectively.[23]

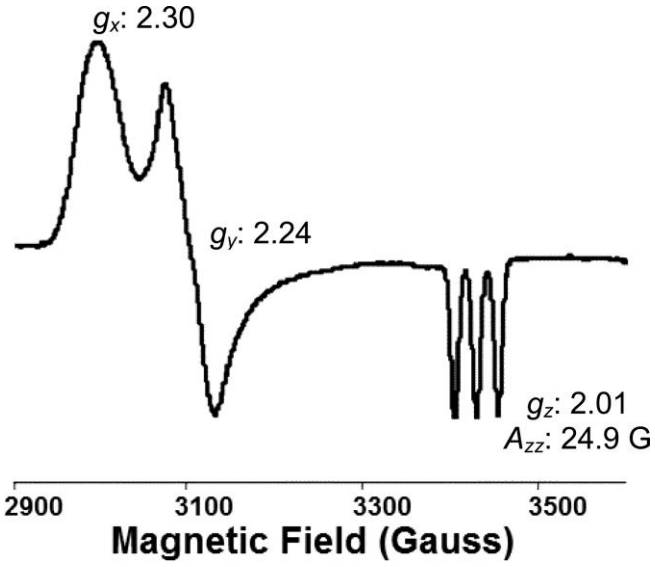

Figure 2.3. EPR spectrum of as-isolated NiSOD from *S. coelicolor* with the selected *g*-values. Sample was prepared in 50 mM HEPES buffer, pH 8.0. EPR collected at 55 K using a microwave frequency of 9.678 GHz, microwave power of 10 mW, and modulation amplitude of 5 G. Adapted from ref. 18.

The presence of the intense CT band in $NiSOD_{ox}$ allowed for a further probe of the nature of this transition from resonance Raman (rR) experiments.[23] Excitation into the S-Ni(III) CT at 413.1 nm resulted in three enhanced vibrational modes at 349, 365, and 391 cm^{-1}. From normal coordinate analysis, the 349 and 365 cm^{-1} peaks are more intense than the third, and were assigned as $\nu_{Ni\text{-}S}$ stretching modes of the coordinated sulfur atoms of Cys2 and Cys6. The peak at 391 cm^{-1} was attributed to either a combined Ni-S stretching and S-C_β-C_α-N bending mode of the Cys2, or perhaps to the $\nu_{Ni\text{-}N(Cys2)}$ stretching mode. Force constants of the Ni-S bonds were also calculated resulting in a value of 1.68-1.79 mdyn $Å^{-1}$ for the Ni-S bonds in $NiSOD_{ox}$.[23,25] This value is characteristic of a high degree of covalency in the Ni-S coordination bond. The covalent

nature of the Ni-S bonds in NiSOD has also been supported by further theoretical studies.[23,25] For comparison, the M-S force constants in NiSOD are on par with other classic electron-transfer metalloproteins such as Fe-S clusters (1.2-1.4 mdyn $Å^{-1}$)[26,27] and blue-copper proteins (~ 1.9 mdyn $Å^{-1}$).[28,29] Hence, metallosulfur systems involved in biological electron transfer and/or redox catalysis contain M-S bonds that exhibit a high degree of metal-sulfur covalency.

Analogous to other SODs, NiSOD catalyzes the dismutation reaction near the diffusion-controlled limit with $k = 1.3 \times 10^9$ M^{-1} s^{-1}.[22] Furthermore, site-directed mutagenesis studies on the protein have revealed that the axial His1-N ligand is crucial for catalysis.[30] This result was further supported by a rigorous DFT study.[23] Other mutagenesis studies have also been performed that reveal the significance of the Cys2 and Cys6 S-ligands[31,32] and secondary-sphere residues vital for catalysis.[20] For example, a combined structural and biochemical study has demonstrated the importance of Tyr9 as a "gatekeeper" residue to allow the $O_2^{\bullet-}$ substrate access to the active site.[20] Similar to other SODs,[33,34] the redox potential of NiSOD is 0.090 V (vs. Ag/AgCl, pH 7.4 phosphate buffer),[20] in between the corresponding oxidation and reduction potentials for superoxide, $E^{o'}$ ($O_2/O_2^{\bullet-}$) = -0.360 V and $E^{o'}$ ($O_2^{\bullet-}/H_2O_2$) = 0.690 V (both vs. Ag/AgCl, pH 7).[35] Thus the novel mixed N/S coordination unit in NiSOD has produced a Ni center that is electrochemically poised to carry out the disproportionation reaction.

2.2.2. NiSOD Questions and Analogue Approach

The atypical coordination sphere and spectroscopy of the redox-active Ni center in NiSOD have generated many questions regarding the structure/function relationship in this enzyme. It is the only SOD that uses a metal whose corresponding aquated species, $[Ni(H_2O)_6]^{2+}$, does not react with $O_2^{\bullet-}$ since its redox potential is > 2 V[36] and well beyond the required

potential for SOD chemistry. It is recognized that the unusual set of donor atoms impart a high degree of covalency in the Ni-L bonds and thus aid in depressing this potential substantially to be within the dismutation window.[12,23,37] Unlike the other SODs, which consist primarily of His-N ligation around the catalytic metal, NiSOD contains two CysS residues which are themselves susceptible to ROS.[38] It has been suggested from DFT studies that the inclusion of the deprotonated peptide, in combination with the CysS donors, all relatively strong-field ligands, aids in promoting primarily Ni-based redox by destabilizing the Ni($d\pi$) set of orbitals via strong Ni–ligand–π–antibonding interactions ($d\pi$-$p\pi$ repulsions).[23,39-41] In this regard, CysS ligation is a logical choice since it appears to promote redox-driven reactions at other biological Ni centers and is a prerequisite for redox-active Ni metalloenzymes; NiFe-hydrogenase, the Ni_pNi_d site of the A-cluster, and the NiFe-cubane of the C-cluster of acetyl-CoA synthase/CO dehydrogenase are relevant examples.[21,42-45] Another distinction from other SODs is the low affinity of the Ni center for anions like azide (N_3^-), a common substitute for $O_2^{\bullet-}$, as other SODs bind this anion in their oxidized form, suggestive of an outer-sphere mechanism for NiSOD. Lastly, the identity of potential H^+-donors for the reductive half-reaction (eq. 2.2) to form H_2O_2 is unknown. Several possible donors have been suggested including a nearby tyrosine residue (Tyr9), the protonated imidazole-N_ε of His1, and Cys2 or Cys6 in the form of a coordinated thiol.[40,46,47]

NiSODs are certainly outliers in the SOD family. They contain a different overall protein fold, metal center, ligand environment/geometry, and spectroscopic properties. The $N_{2/3}S_2$ environment is rather unusual for a metal center that involves interaction with and conversion of ROS since the CysS resides are themselves quite susceptible to form S-oxygenates (SO_x) or disulfides.[38] The unusual chemical nature of the N-ligands should also be noted as N-terminal amine coordination has only been observed in the CO sensor CooA[48] and deprotonated peptido-

N ligation is present in only three metalloenzymes (nitrile hydratase,[49] Ni_d site of acetyl coenzyme A synthase/CO dehydrogenase,[50] and the oxidized P-cluster of nitrogenase[51]).

In sum, the presence of the unique primary coordination sphere in NiSOD has led the bioinorganic community to pose several fundamental questions regarding this enzyme including: (i) What intrinsic properties do the coordinated amino acid ligands, which include two CysS residues, a primary amine-N, and a deprotonated peptido-N impart on the Ni center? (ii) How does such a coordination sphere modulate the redox properties of the Ni center allowing the substrate ($O_2^{\bullet-}$) to preferentially react with Ni to undergo facile one-electron oxidation and reduction and NOT react with the coordinated CysS residues? (iii) How does nature utilize Ni, typically not thought of as an O_2–derivative activator/regulator, to react with and disproportionate $O_2^{\bullet-}$; i.e.; what is the catalytic mechanism? The fundamental biochemistry that governs the dismutation reaction at the Ni site has initiated the construction of low molecular weight (MW) complexes (also termed "synthetic models/analogues" or "biomimetics") that reproduce the primary coordination environment observed in the enzyme. This method has been labeled as the synthetic analogue approach,[52] a paradigm in bioinorganic chemistry that has provided valuable information on the structure and mechanism of numerous metalloenzymes. The objective of such an approach is to gain fundamental insight into the structural and electronic properties of the metal active site germane to catalysis through simpler, low MW constructs. For NiSOD, some of the important criteria for the design and synthesis of suitable models are as follows:

(i) First, the ligand frame must contain a mixed nitrogen/sulfur (N/S) donor set to mimic the primary coordination sphere observed in the enzyme. Indeed, the prerequisite for redox-active Ni in biology is coordination of CysS ligands.

(ii) Second, and beyond a mere stoichiometric replication of the donor atoms, is the electronic nature of the N/S frame and spatial disposition of the donor atoms. The ligand construct must contain one deprotonatable peptide-N (carboxamide-N is the more general terminology), one primary amine-N, and two *cis*-thiolates situated in a planar N_2S_2 arrangement. An additional neutral N-donor ligand (an imidazole-N is preferable) would be required to replicate the low-spin 4C-to-5C Ni(II/III)SOD redox conversion.

(iii) Third, the ligand construct should be amenable to a variety of straightforward modifications much like the environment in the protein matrix of NiSOD. For example, secondary structure, H-bonding or electrostatic interactions should be considered in construction of the model. This important last requirement will allow for electronic and structural "fine tuning" of the biomimetic for its desirable function of superoxide dismutation.

Several groups have employed some or all of these criteria by utilizing (i) small peptides or peptide maquettes typically 3-12 amino acids long that mimic the NiSOD primary sequence,[53-62] (ii) mixed N/S or N/O ligand frames that approximate some aspect of the electronic or structural nature of the NiSOD donors,[63-66] (iii) electronically accurate N_2S_2 or N_3S_2 frames,[67-69] (iv) asymmetric N_2S ligands that approximate the Ni active site with an open coordination site where exogenous N-donors bind (NiN_3S),[70-72] and (v) asymmetric N_2S ligands with NiSOD accurate donors containing an open coordination site where exogenous S-ligands bind to afford NiN_2S_2 species.[73-75] In this review we describe these approaches and their relationship to the active site properties and function in NiSOD. We also propose, at the end, a mechanistic possibility and our current understanding of this unusual metalloenzyme based on the collection

of synthetic modeling work in combination with the protein structural, spectroscopic, and theoretical results.

2.3 Synthetic Analogues of NiSOD

This novel SOD class has provided the bioinorganic community with a new system to test the essential features required for SOD's crucial biological function in ROS regulation. To date (2012), several model systems employing short peptides or longer peptide maquettes (3-12 amino acid residues in length) and low MW (non-maquette) coordination complexes have been constructed. Synthetic endeavors in low MW analogues have been split between complexes which replicate some aspect of the NiSOD structure or function yet are not entirely parallel to the electronic properties of the His1, Cys2, and Cys6 ligands in the enzyme. These latter systems are designated as *approximate models*. Other models which replicate the structural disposition and electronic donor type of that found in NiSOD are labeled as *accurate models*. Research in the maquette area has been especially active as these molecules replicate some aspect of their biological inspiration, taking advantage of secondary/tertiary structural features offered by the biological peptide scaffold. While the construction of low MW models that accurately reproduce the primary coordination sphere of NiSOD are not as widespread, synthetic endeavors towards these model systems are slowly growing. The knowledge gained from both approaches and the structural, electronic, and mechanistic relevance to NiSOD are presented below.

2.3.1. NiSOD Peptide Analogues: Synthetic Models based on Peptide Maquettes

The first NiSOD maquette model was synthesized by Shearer and coworkers which they designated as [Ni(SOD^{M1})] (**1**, where SOD^{M1} = HCDLPCGVYDPA, Figure 2.4).[53] Several

derivatives of **1** were also constructed to electronically modify the His1 ligand, namely [Ni(SOD^{M1}-Im-X)] where X = Me (**1**$^{\mathbf{MeIm}}$), 2,4-dinitrophenyl (**1**$^{\mathbf{DNP}}$), and tosyl (**1**$^{\mathbf{Tos}}$) (Figure 2.4).[55]

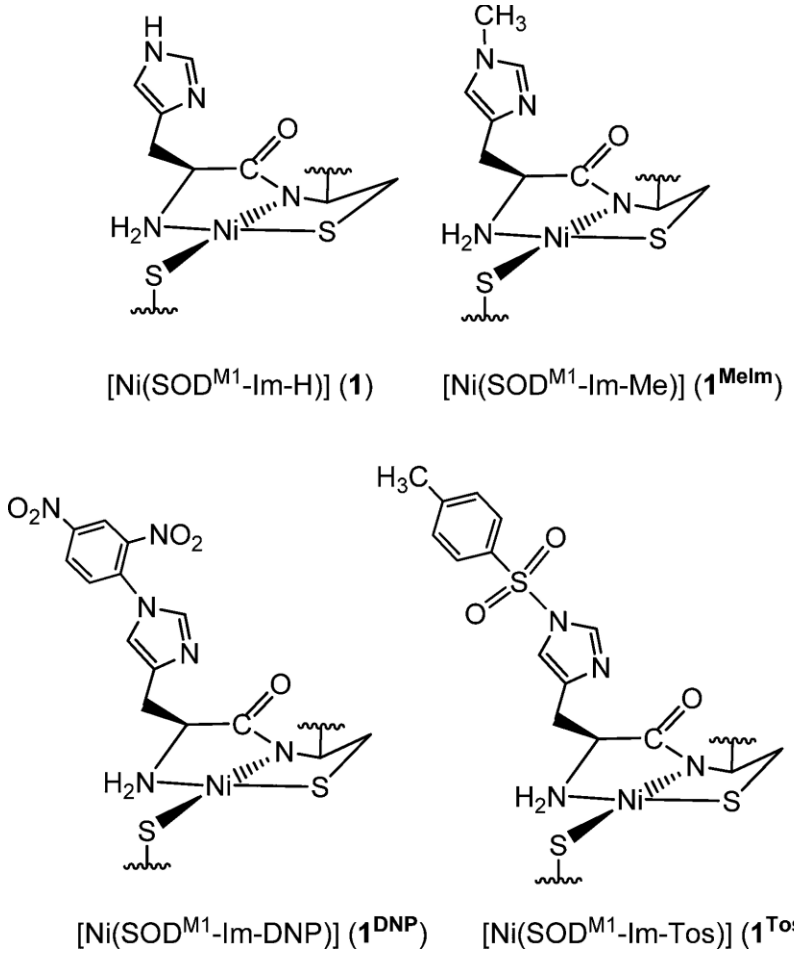

Figure 2.4. Structures of the NiSOD maquette models based on [Ni(SOD^{M1})] (SOD^{M1} = H′CDLPCGVYDPA, H′ = H (**1**), Me (**1**$^{\mathbf{MeIm}}$), 2,4-dinirophenyl (**1**$^{\mathbf{DNP}}$), and tosyl (**1**$^{\mathbf{Tos}}$).

This base maquette is comprised of the first twelve residues from the *S. coelicolor* primary sequence and was shown to coordinate Ni(II) in a 1:1 Ni/peptide ratio under slightly basic conditions. Neutral to slightly acidic conditions did not afford the Ni-coordinated maquettes likely due to protonation of the CysS and peptide-N ligands at these pH values. Additionally, the Ni systems are unstable to air over the course of hours and yield intractable high MW polymeric species upon exposure. Yields for **1** and $\mathbf{1}^{\mathbf{MeIm}}$ were stoichiometric; however, $\mathbf{1}^{\mathbf{DNP}}$ and $\mathbf{1}^{\mathbf{Tos}}$ were low (14-21%) due to the sensitivity of the tosyl and 2,4-dinitrophenyl functional groups to workup conditions. All of the Ni-peptides were characterized by UV-vis, X-ray absorption spectroscopy (XAS), and electrochemistry which are listed in Table 2.1. For example, **1** and its derivatives afforded light beige-pink colored solutions originating from the low-intensity ligand-field band at λ_{avg}: 461 nm (ε_{avg}: 420 M^{-1} cm^{-1}) with a shoulder at λ_{avg}: 553 nm (ε_{avg}: 180 M^{-1} cm^{-1}) in pH 7.4 NEM buffer. These electronic transitions are typical of Ni(II) housed in a planar N_2S_2 coordination sphere.[21,25] XAS further supported the UV-vis with metric parameters (Ni–N_{avg}: 1.90 Å; Ni–S_{avg}: 2.179 Å) and edge transitions consistent with a square-planar Ni(II)-N_2S_2 metal site in all maquettes.[76] The electrochemistry revealed quasi-reversible $E_{½}$ values in the cyclic voltammograms (CVs) with the Ni(III/II) couple ranging from 0.280-0.600 V (vs. Ag/AgCl, pH 7.4 NEM buffer), which trend with the electron-withdrawing ($\mathbf{1}^{\mathbf{DNP}}$, $E_{½}$: 0.470 V; $\mathbf{1}^{\mathbf{Tos}}$, $E_{½}$: 0.598 V) and electron-donating ($\mathbf{1}^{\mathbf{MeIm}}$, $E_{½}$: 0.282 V) nature of the groups attached to the His1-N_{ε} imidazole atom (Table 2.1). All values are within the superoxide disproportionation window suggesting that these NiSOD maquette models can perform SOD redox chemistry (vide infra). Collectively, the structural and spectroscopic features of maquettes based on **1** are nearly identical and resemble those obtained for $NiSOD_{red}$.

Table 2.1. Spectroscopic, Structural, Electrochemical and SOD Activity Kinetic Data for NiSOD and NiSOD Maquette Models.

Complex	λ_{max} [nm] (ε[M^{-1} cm^{-1}])	$E_{1/2}$ (V)[a]	Ni–N, Ni–S (Å)[b]	k (M^{-1} s^{-1})	Refs.
$NiSOD_{red}$ (*S. coelicolor*)	450 (480), 543 (150)[c]	0.090 [d]	1.89, 2.18	7×10^8	18, 20, 23
$NiSOD_{red}$ (*S. seoulensis*)	N/A	N/A	2.01, 2.21	1.3×10^9	19
[Ni(SOD^{M1}-Im-H)] (**1**)	458 (510), 552 (240) [e]	0.434 [e]	1.93, 2.180	$4(3) \times 10^7$	53
[Ni(SOD^{M1}-Im-Me)] ($\mathbf{1}^{\mathbf{MeIm}}$)	461 (360), 554 (160 sh) [e]	0.282 [e]	1.91, 2.182	$6(1) \times 10^6$	55
[Ni(SOD^{M1}-Im-DNP)] ($\mathbf{1}^{\mathbf{DNP}}$)	464 (410 sh), 552 (150 sh) [e]	0.470 [e]	1.89, 2.179	$3(2) \times 10^8$	55
[Ni(SOD^{M1}-Im-Tos)] ($\mathbf{1}^{\mathbf{Tos}}$)	460 (405 sh), 552 (180 sh) [e]	0.598 [e]	1.87, 2.174	$6(2) \times 10^8$	55
[Ni(SOD^{M2})] (**2**)	457 (345), 548 (130 sh) [e]	0.520 [e]	1.875, 2.176	$1(1) \times 10^{-6}$ M (IC_{50})[f]	54
[Ni(mSOD)] (**3**)	454 (432)[g]	N/A	N/A	830 U/μmol [h]	56, 57

[a]Data represents the $E_{1/2}$ value for the Ni(III/II) redox couple normalized to the Ag/AgCl reference electrode based on information found in ref 77-78.[77,78] [b]Ni–S and Ni–N bond distances represent the averages of the two distinct sets of CysS-donors and N-donors from the X-ray crystal structure of NiSOD; metric parameters for the maquette systems were obtained by EXAFS, which cannot distinguish between these sets of atoms. [c]Tris buffer (pH 8.5). [d]Potassium phosphate buffer/pH 7.5. [e]NEM buffer (pH 7.4). [f]Only IC_{50} value measured for **2** where IC_{50} is the concentration of SOD mimic required to effect a 50% reduction in the rate of formazan formation; IC_{50} for Cu/ZnSOD is 4×10^{-8} M. [g]Nonbuffered, deionized H_2O/NaOH mixture measured at pH 7.8. [h]The 1:1 Ni/peptide activity provided (see the text). The activity is defined as the half-limited reduction of NBT by superoxide where 1 unit = 2($Abs_{NBT\text{-}control}$-$Abs_{NBT\text{-}maquette}$)/$Abs_{NBT\text{-}control}$); the activity of NiSOD (*S. coelicolor*) is ~ 45,000 units/□mol per subunit (see ref. 56).

Despite the structural and electronic similarity of the maquettes to $NiSOD_{red}$, accessing Ni(III) was problematic. Achieving this oxidation state (at least transiently) is a requirement to realize functionality in these systems. Indeed, the isolation and characterization of Ni(III) complexes with thiolate ligands is difficult and rare; only one such Ni(III)-thiolate complex has ever been crystallized.[79] Initial attempts to chemically oxidize **1** resulted in decomposition and formation of high-MW polymers. However, utilizing a mild oxidant (I_2) afforded Ni(III) maquettes that could be trapped in situ at low temperature. The resulting X-band EPR spectra of all Ni(III)-peptides are similar (g_{avg} values for g_x: 2.34, g_y: 2.26, g_z: 2.01 at 77 K) and resemble the rhombic S = ½ EPR spectrum of as-isolated NiSOD (see Figure 2.3).[18] The superhyperfine coupling in the g_z component (A_{zz}) is also observed in all Ni(III)-peptides, which ranges from 18.3 to 26.4 G compared to the A_{zz} value of 24.9 G for NiSOD. Interestingly, the A_{zz} values for $\mathbf{1}^{\mathbf{Tos}}$ and $\mathbf{1}^{\mathbf{DNP}}$ are the closest to the enzyme. This value is reflective of the strength of the interaction between the unpaired spin on Ni(III) and the His1-N_δ ligand and the relatively long Ni(III)-NIm bond distance in $NiSOD_{ox}$ defines the extent of this coupling in the enzyme. Thus, the Ni-maquettes with the electron-withdrawing groups on N_ε (i.e., the weaker Lewis base) better resemble A_{zz} in $NiSOD_{ox}$ since they contained the longer Ni-NIm bond. Moreover, this electronic modification should correlate with superoxide reaction kinetics. Indeed, **1** and its derivatives are able to catalytically disproportionate superoxide as monitored by stopped-flow kinetics ($k \sim 10^6$-10^8 M^{-1} s^{-1}, Table 2.1). As expected from EPR, complexes $\mathbf{1}^{\mathbf{DNP}}$ and $\mathbf{1}^{\mathbf{Tos}}$ are the most active NiSOD mimetics with k = 3(2) × 10^8 M^{-1} s^{-1} for $\mathbf{1}^{\mathbf{DNP}}$ and 6(2) × 10^8 M^{-1} s^{-1} for $\mathbf{1}^{\mathbf{Tos}}$. These k values are only one order of magnitude lower than the diffusion-controlled rate observed for all SODs ($k \sim 10^9$ M^{-1} s^{-1}). Accordingly, the nature of the long axial Ni(III)-NIm bond in $NiSOD_{ox}$ is modeled nicely with the SOD^{M1} maquettes with electronic modifications on the His1 residue.

In a second generation system, Shearer reported the synthesis and properties of the Ni maquette complex with the heptapeptide SOD^{M2}, namely [Ni(SOD^{M2})] (**2**, where SOD^{M2} = HCDLPCG, Ni coordination sphere similar to that depicted for **1** in Figure 2.4).[54] Analogous to SOD^{M1}, SOD^{M2} and its derivatives coordinated Ni(II) in a 1:1 ratio under slightly basic conditions affording light beige-pink solutions of **2** with similar UV-vis profiles (Table 2.1). Complex **2** has an appropriate redox potential to act as an SOD [$E_{½}$ = 0.520 V vs. Ag/AgCl, pH 7.4 NEM (see footnote [a] of Table 1 for conversion to NHE)], contains a Ni(II) center in an N_2S_2 environment (XAS), does not bind anions such as N_3^-, and catalytically disproportionates superoxide. Thus, the removal of the last five residues outside of the Ni-hook of native NiSOD does not compromise the Ni affinity or electronic structure with the smaller peptide in **2**. The CV displays quasi-reversible behavior with an E_{ox}-E_{red} peak-to-peak separation (ΔE_p) of 0.240 V, which is suggestive of substantial structural rearrangement taking place about the Ni center during redox. The Ni(III)-peptides cannot be obtained or isolated in pure form upon chemical oxidation or bulk electrolysis suggesting, as with **1**, the relative instability of Ni(III) in this environment. However, the Ni(III)-peptide was obtained *in situ* following sub-stoichiometric addition of KO_2 to afford a rhombic EPR spectrum similar to $NiSOD_{ox}$.[54] Activities were measured using a modified xanthine/xanthine oxidase assay and afforded an IC_{50} value (where IC_{50} = the concentration of SOD mimic to effect a 50% reduction in the rate of formazan formation) of 1×10^{-6} M for **2**, two orders of magnitude lower than the Cu/ZnSOD IC_{50} value (4×10^{-8} M). Replacing His1 in **2** for Ala ($\mathbf{2^{Ala}}$) completely shut off activity comparable to the H1A mutation in NiSOD.[30] Additional insight from DFT and eT rate calculations at overpotential confirmed that the Ni center in **2** remains 5C when cycling through the Ni(III/II) states. Taken

together, maquettes **1**-**2** afford excellent structural and functional models of NiSOD advocating for a 5C Ni center and outer-sphere eT as probable mechanistic features of this enzyme.

At approximately the same time, the groups of Weston and Buntkowsky reported an extensive study on the properties of a Ni(II) nonapeptide maquette that they label as [Ni(mSOD)] (**3**, where mSOD = HCDLPCGVY) (see Figure 2.4 for the analogous Ni coordination structure).[56-59] Similar to the aforementioned NiSOD maquette studies on **1**-**2**, Ni coordinated to mSOD in a mostly 1:1 Ni/peptide ratio in **3** (other ratios were observed based on ESI-MS and UV-vis titrations), affording pink colored solutions.[56,57] Although XAS was not performed to define the Ni coordination sphere in this model, solution NMR, UV-vis, and DFT studies were indicative of an N_2S_2 square-planar environment about the Ni(II) ion. The theoretically estimated Ni–N and Ni–S distances are on-par with those experimentally observed in maquettes **1** and **2**, suggesting similar Ni coordination environments (Table 2.1). In contrast to **1** and **2**, an enhanced stability to ambient lab conditions was noted for **3**. The Ni(III) version of this maquette was not isolated; however, DFT computations predict that the ground state of Ni(III)-mSOD is a triplet and thus high-spin. This result is opposite to what is found with **1**, **2**, and the native enzyme. The $S = 1$ state for Ni(III)-mSOD is supposedly due to the fifth axial ligand arising from the neutral carbonyl-O of the Leu4-Pro5 peptide backbone, rather than axial binding of His1 as seen in **1**, **2,** and $NiSOD_{ox}$. This dissimilar coordination environment is due to a conformational difference with respect to Pro5: in NiSOD, Pro5 is in a *cis* conformation, whereas in **3**, Pro5 is orientated in a *trans* configuration due to H-bonding interactions of the peptide. It was suggested that the Pro5 *trans* arrangement prevents the His1-N_δ from binding, and it was also proposed to prevent the binding of superoxide opposite to His1. The activity of maquette **3** is thus considerably less than native NiSOD (vide infra). As such, a new maquette was constructed to enforce the *cis*

conformation observed in the enzyme.[58] However, this maquette did not affect the reactivity suggesting that this structural perturbation is not responsible for the low activity of these maquettes.

Reactivity studies were conducted with **3** in the presence of KO_2 using the nitroblue tetrazolium (NBT) assay and it was shown to be stable for 60-90 s.[56] In attempts to account for both 1:1 and 2:1 stoichiometries for the Ni/peptide complexes in solution, the xanthine/xanthine oxidase assay was run to establish lower and upper limits of $O_2^{\bullet-}$ activity. The 1:1 complex produced an activity value of 830 U μmol^{-1} (activity defined as the half-limited reduction of NBT by superoxide where 1 unit = 2($Abs_{NBT\text{-}control}$-$Abs_{NBT\text{-}maquette}$)/$Abs_{NBT\text{-}control}$); the 2:1 ratio resulted in activity of 1250 U μmol^{-1}, demonstrating that the nine-residue peptide can serve as a functional NiSOD mimic. Activity studies were repeated with a mutated peptide for which His1 was replaced with Ala to yield a negligible decrease in activity, disputing the essentiality of His1 for catalytic activity. It was proposed instead that Pro5 is responsible for tuning the oxidation state of the biomimetic, as the *trans*-Pro5 residue prevents an axial histidine nitrogen atom from binding to Ni(III) in this maquette.

Further reactivity of **3** was performed using cyanide anion (CN^-) as a substrate analogue.[57] Complexes **1**-**2** show no evidence for binding anions such as azide, and CN^- strips the Ni(II) center from the peptide all pointing towards an outer-sphere mechanism for NiSOD (vide supra). Upon addition of one equivalent of CN^- to **3**, the pink solution turned yellow consistent with a change in the Ni coordination environment. Indeed, MS experiments confirmed the presence of the mono-CN^- adduct of the Ni maquette, [Ni(mSOD)(CN)] (**4**). The UV-vis spectrum of **4** in a pH 7.8 H_2O/NaOH nonbuffered medium revealed mostly UV transitions (λ: 252 nm, ε: 12,000 M^{-1} cm^{-1}; λ_{sh}: 282 nm) and one visible band at 410 nm (ε: 180 M^{-1} cm^{-1}). The

resulting electronic transitions of **4** all blue-shift from the parent Ni(II) square-planar species **3** (see Table 2.1). The formation of **4** was further confirmed by ^{13}C and ^{15}N NMR and FTIR spectroscopy which revealed one strong and single ν_{CN} peak at 2108 cm^{-1} (KBr).

Collectively, the properties and reaction chemistry of the peptide maquettes **1**-**3** provide a somewhat unifying picture of Ni in the SOD coordination sphere. The Ni(II)-N_2S_2 square-planar coordination environment is maintained throughout and affords similar metric parameters and electronic absorption profiles (see Table 2.1). Maquettes **1** and **2** break down and form intractable polymeric species upon air exposure within hours, whereas maquette **3** was stable for days at RT and weeks at 4 °C. The defining feature of the oxidative stability is unknown at present. All of the Ni-maquettes disproportionate $O_2^{\bullet-}$ at rates higher than the spontaneous rate, but significantly lower than in NiSOD. Ni(III) forms of the maquettes are difficult to obtain; however, in situ EPR isolation of Ni(III) maquettes **1** and **2** has been successful, and in one case a Ni(III) species has been confirmed by XAS (**1**$^{\mathbf{MeIm}}$). One defining feature of maquette **3** is the stoichiometric binding of CN^-, a property that supports inner-sphere coordination and eT to $O_2^{\bullet-}$ in NiSOD. Furthermore, replacement of His for Ala does not significantly change the rate in **3**. This result is quite in contrast to the same modification in the enzyme and in maquette **2**. Perhaps the carbonyl-O ligand from Pro5 in **3** supports the SOD reaction albeit through a mechanism different than that in NiSOD. It is difficult to delineate the variances between the systems of Shearer and Weston/Buntkowsky. Perhaps the noted differences lie in the relative instability of some of the maquettes. For example, the nonapeptide Ni-maquette **3** is shown to exist in equilibrium with a 2:1 and 1:1 Ni/peptide species in solution. This observation alone warrants the need for more definitive structural information on **3** or more discrete and crystallizable small molecule analogues. The work on maquette **3** is also controversial as a separate publication from

the same group states that only a 1:1 species exists.[57,59] Additionally, the electronic similarity of $O_2^{\bullet-}$ and CN^- is a bit of a stretch, and one would expect Ni (or any transition metal) to bind the strong-field CN^- ligand. The CN^- binding results are also contradictory to those of anion binding studies performed on the enzyme and in the maquettes of Shearer. Their experiments reveal that CN^-, rather than binding, strips the Ni from the model to form $[Ni(CN)_4]^{2-}$, which may be explained by the use of excess CN^-.[54] In contrast, Buntkowsky proposed that by limiting the stoichiometry to one equivalent, CN^- can bind to the metal center without disrupting the coordination sphere and that this binding capability should translate to the native enzyme. As of 2012, anion binding to the Ni center in NiSOD (ox or red) has yet to be established. Taken together, it appears that the minimal requirement to achieve functionality in these maquettes is the first seven amino acid residues of the Ni-hook as this length appears to bind Ni with high affinity and provides suitable aqueous stability. Additionally, special attention must be given to the positioning of the His1-Im in these maquettes for proper binding to the Ni center so that Ni(III/II) redox cycling is facile and turnover is fast.

2.3.2. NiSOD Low-MW Analogues: NiSOD Approximate Models

The work on approximate models of NiSOD has utilized a variety of different ligand platforms that incorporate some but not all features of the biological coordination unit. The first low MW NiSOD model complex that demonstrated SOD activity was synthesized by Darensbourg and coworkers in 2009.[70] They employed the ligand 1-(2-mercapto-2-methylpropyl)-methyl-1,4-diazacycloheptane (mmp-dachH, where H is a dissociable proton) as an amine-thiol N_2S chelate for Ni (Figure 2.5). Reaction of the deprotonated ligand with Ni(II) salts resulted in a dimeric Ni(II) complex with bridging alkyl thiolates (*S*,*S*-bridged or μ-thiolato

bridge) that approximated the N_2S_2 coordination sphere of $NiSOD_{red}$. Because the active sites of NiSOD function as discrete monomeric species, attempts were made to cleave the μ-thiolato core with biologically-relevant ligands. Although this reaction appears feasible it has not been widely adopted as a successful approach to access monomeric Ni-thiolato complexes. Bridge-splitting of the dimer with imidazole (Im) afforded the monomeric Ni(II) complex [Ni(mmp-mdach)(Im)]Cl (**5**) (Figure 2.5). The geometry about the Ni(II) center in **5** is square-planar arising from the N_2S ligand and the monodentate Im to afford an N_3S chromophore. The Ni–S distance (2.149 Å) is typical for planar Ni-thiolate complexes and similar to NiSOD, but the $Ni–N_{Im}$ is short (1.888 Å) and unlike the enzyme value (~2.3-2.5 Å) due to its location in the equatorial plane. This complex was the first structurally characterized Ni(II) species containing both thiolate and imidazole donors, both of which are key ligands in NiSOD albeit in different positions in the coordination sphere (see Figure 2.5). This orange complex displayed one *d-d* band in the visible region at 467 nm (ε: 500 M^{-1} cm^{-1}), which is different from Ni(II)-N_2S_2 complexes and $NiSOD_{red}$. The CV of **5** exhibited an irreversible oxidation wave (E_{ox}) at 0.43 V in DMF (vs. Ag/AgCl), which has been attributed to thiolate oxidation of the mmp-mdach ligand. This property would suggest that **5** would not be a functional SOD mimic. However, an aqueous solution of **5** (61 μM) provided protection against 100 equiv of $O_2^{\bullet-}$ to NBT (61 μM) preventing formazan formation by ~ 40% in pH 7.4 phosphate buffer. Furthermore, this complex is stable to O_2 and affords S-oxygenated species when reacted with H_2O_2. Thus, this model implicates that the mixed N/S-donors of NiSOD provides O_2-stability to the coordination unit. The exact role of the Ni center in the SOD chemistry was not defined; however, **5** was the first example of a low molecular weight NiSOD functional model.

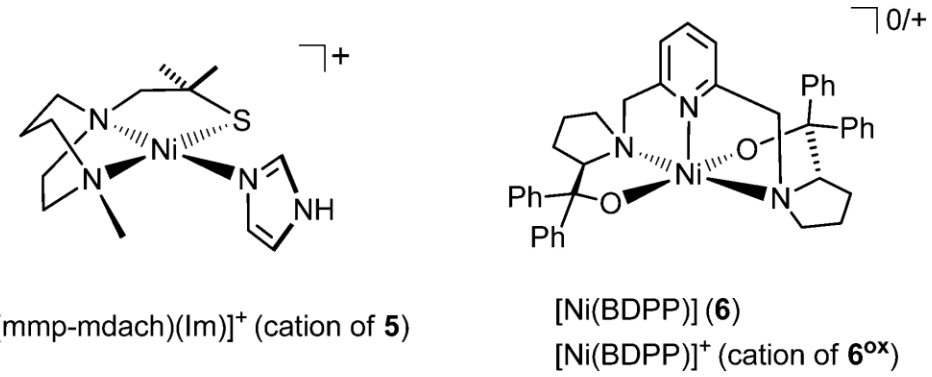

[Ni(mmp-mdach)(Im)]$^+$ (cation of **5**)

[Ni(BDPP)] (**6**)
[Ni(BDPP)]$^+$ (cation of **6^{ox}**)

Figure 2.5. Structures of the NiSOD approximate model complexes [Ni(mmp-mdach)Im]Cl (cation of **5**, left) and [Ni(BDPP)] (**6**, right)/[Ni(BDPP)]PF_6 (cation **6^{ox}**, right) SOD^{M1}). Ph is for phenyl or C_6H_5 for the structures of **6** and **6^{ox}**, respectively.

The first 5C analogue of NiSOD was described in late 2011 by Kuo and coworkers utilizing an N_3O_2 chelate.[65] The pentadentate ligand, 2,6-bis(((*S*)-2-(diphenyl-hydroxymethyl)-1-pyrrolidinyl)methyl)pyridine (H_2BDPP, H represents dissociable protons), employed non-biological donor atoms that included one pyridine-N, two tertiary pyrrolidine-N, and two alcohol-O donors. Due to the steric restrictions imposed by the ligand frame, the pyridine-N would be forced into an axial position upon coordination to Ni regardless of the oxidation state, a clever design strategy to impose a 5C geometry. The resulting Ni(II) complex [Ni(BDPP)] (**6**) contained a Ni(II) center in a distorted square-pyramidal N_3O_2 environment that structurally replicated the 5C geometry of $NiSOD_{ox}$ (Figure 2.5). The X-ray structure of **6** revealed a Ni–N_{py} distance of 1.969 Å with two longer Ni–N_{avg} distances (2.149 Å) from the pyrrolidines and two short Ni–O_{avg} bonds (1.930 Å) from the tertiary-O donors in a *trans* configuration (Figure 2.5). The bond distances in **6** advocate for a diamagnetic low-spin (S = 0) 5C Ni(II) center, although no other evidence was presented to support this electronic configuration. The pale green complex

exhibited a quasi-reversible CV with $E_{½}$ at 0.308 V (vs. Ag/AgCl in CH_2Cl_2) suggesting that the $BDPP^{2-}$ ligand could support Ni(III) with minimal structural rearrangement. Indeed, chemical oxidation of **6** cleanly yielded the Ni(III) complex [Ni(BDPP)](PF_6) (**6^{ox}**) that was structurally characterized by X-ray crystallography. As expected, the Ni-L distances in **6^{ox}** contracted (~ 0.1 Å for equatorial ligands; ~ 0.02 Å for the axial Ni-N_{py}) from the parent Ni(II) complex **6** due to decreased Ni-ligand electron repulsion (Ni–N_{py}: 1.947 Å; N–-$N_{pyrrolidine}$: 2.045 Å; Ni–O: 1.844 Å). In contrast to $NiSOD_{ox}$, the X-band EPR spectrum of **6^{ox}** afforded an axial signal due to the high symmetry and electronic equivalency of the *trans*-N_2O_2 donors in the basal plane ($g_x = g_y$: 2.18, g_z: 2.04 in CH_2Cl_2, 77 K) (see Figure 2.3 for $NiSOD_{ox}$). The hyperfine coupling in the g_z component in **6^{ox}** (A_{zz}: 25.0 G), however, is identical to the coupling in the enzyme. Both of these hyperfine patterns are due to the axial N-ligand. In fact, DFT studies confirm that the majority of the spin-density in **6^{ox}** resides in an MO with significant Ni d_z^2 character much like $NiSOD_{ox}$.[23] Taken together, the data suggested that **6** or **6^{ox}** should be capable of $O_2^{\bullet-}$ disproportionation. Indeed, **6^{ox}** was shown to react with excess KO_2 in MeCN to produce O_2 and Ni(II) complex **6** in stoichiometric yields. Interestingly, the Ni(II) complex **6** did not react with KO_2 to produce H_2O_2. Despite the presence of the RO^- ligands, the spin-state of the Ni center appears to remain low-spin in both Ni oxidation states. This spin-state appears to be a requisite for catalysis as high-spin Ni(III/II) has never been found in enzyme preparations, nor would it be of the appropriate redox potential. Additionally, this model appears to be at odds with data from Cys-to-Ser mutations in the enzyme. This mutation resulted in high-spin Ni(II) centers that could not access the high-valent Ni(III) state.[31,32] Ultimately, this mutation afforded inactive NiSOD. It appears that careful construction of the ligand frame to house 5C and low-spin Ni(II) could be an additional requirement for a functional NiSOD model.

2.3.3. NiSOD Low-MW Analogues: Accurate Models

The first low MW analogue that accurately reproduced the NiSOD primary coordination sphere was the square-planar Ni(II)-N_2S_2 complex, (Me_4N)[Ni(BEAAM)] (**7**, Figure 2.6).[67] This orange-colored complex was structurally characterized by X-ray crystallography and consists of an $N_{amine}N_{carboxamide}S_2$ chromophore with asymmetric Ni–N bonds due to the electronic differences in the N-donors. The spectroscopic and structural properties are summarized in Table 2.2. For example, the Ni–N_{amine} bond distance is notably longer (1.989 Å) than the Ni–$N_{carboxamide}$ distance (1.858 Å). The high resolution of small molecule crystallography has provided the electronic discrepancy in these two Ni–N bonds that is absent in the EXAFS data of the maquette systems **1** and **2**. The variance in Ni-N is due to the good σ-donating ability of the carboxamido-N, which provides for more covalency in this bond. These effects are also manifested in the Ni–S bond it is *trans* to. The Ni–S bond *trans* to the carboxamido-N is significantly elongated (2.177 Å) with respect to the Ni–S bond *trans* to the amine (2.137 Å). A similar difference is observed in the Ni–S distances of $NiSOD_{red}$ (*S. coelicolor*).[18] Analogous to the maquette systems and the enzyme, a double-humped UV-vis spectrum is observed with ligand-field transitions at 461 nm (ε: 290 M^{-1} cm^{-1}) and 556 nm (ε: 70 M^{-1} cm^{-1}) in MeCN underscoring the electronic equivalence of this model and $NiSOD_{red}$. The quasi-reversible Ni(III/II) couple observed for **7** at 0.120 V (vs. Ag/AgCl in MeCN) is also within the potential window for SOD chemistry, but the complex does not react with $O_2^{\bullet-}$. Additionally, bulk oxidation studies at low temperature resulted in the formation of a short-lived purple/blue species that is non-isolable and no other spectroscopic evidence was provided for this oxidized species. The axial N-ligand, which is notably absent from this complex, may be necessary for the stabilization of Ni(III) in these models and in NiSOD.

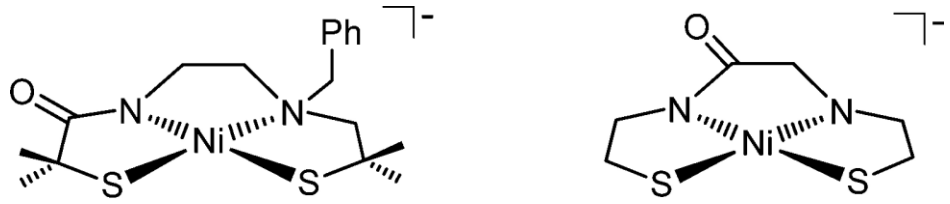

Figure 2.6. Structures of the NiSOD model complexes (Me_4N)[Ni(BEAAM)] (anion of **7,** left) and K[Ni(H2L)] (anion of **8**, right). Ph is phenyl or C_6H_5 for the structure of **7**.

In a follow-up to this communication, Shearer and Hegg reported the NiSOD model, K[Ni(HL2)] (**8**, Figure 2.6), with a similar N_2S_2 ligand frame as in **7** but with the absence of the *gem*-dimethyl groups on the carbon atoms alpha to sulfur.[68] The metric parameters and electronic absorption spectrum are very similar between the two complexes (Table 2.2) suggesting analogous structural/electronic properties. One noted difference, however, is in the CV data, which displayed an irreversible oxidation for **8** at 0.065 V (vs. Ag/AgCl in DMF) indicative of ligand-based redox. Additionally, attempts at chemical oxidation of **8** at low temperatures resulted in an EPR-inactive species that supports S-oxidation to disulfide. The difference in CV data between otherwise structurally (and presumably electronically) equivalent Ni(II) centers was puzzling. The DFT-generated redox-active MOs in **7** and **8** revealed a significant change in the amounts of S-pπ and Ni-dπ character in these complexes. For example, the Ni-character in **8** (32% Ni-dπ; 68% S-pπ) is much lower (and S-character higher) than in **7** (56% Ni-dπ; 32% S-pπ). While the ligand frames are similar, it appears that the methyl substituents on the ligand in **7** clearly aid in stabilizing and supporting Ni-based redox and access to the Ni(III) oxidation state. Even though both complexes do not react with superoxide, the clear differences in the CVs

reveal key factors for obtaining at least Ni(III) in this asymmetric N/S coordination environment by providing steric bulk and enhanced Lewis basicity at the S-donor. Taken together, the results from complexes **7** and **8** propose that well-defined and controlled modifications at or near the S-ligands in Ni-N_2S_2 coordination units can significantly alter the nature of the frontier MOs that ultimately dictate redox behavior in these systems and presumably in the enzyme.

Table 2.2. Spectroscopic, Structural, and Electrochemical Data of NiSOD Low MW Synthetic Analogues.

Complex	λ_{max} [nm] (ε[M^{-1} cm^{-1}])	E_{ox} (V)[a]	Ni–$N_{peptide}$, Ni–N_{amine} (Å)	Ni–$S_{trans\text{-}peptide}$, Ni–$S_{trans\text{-}amine}$ (Å)	Refs.
$NiSOD_{red}$ (*S. coelicolor*)	450 (480), 543 (150)[b]	0.090[c]	1.91, 1.87	2.19, 2.16	18, 20, 23
$NiSOD_{red}$ (*S. seoulensis*)	N/A	N/A	1.94, 2.07	2.18, 2.24	19
(Me_4N)[Ni(BEAAM)] (**7**)	461 (290), 556 (70)[d]	0.120[d]	1.858, 1.989	2.177, 2.137	67
K[Ni(H2L)] (**8**)	449 (340), 570 (70 sh)[e]	0.065[f]	1.862, 1.937	2.1711, 2.1671	68
(Et_4N)[Ni(nmp)(SC_6H_4-*p*-Cl)] (**10**)	450 (5450)[d]	0.236[d]	1.8638, 1.9470	2.2139, 2.1492	73
(Et_4N)[Ni(nmp)(S^tBu)] (**11**)	464 (4540)[d]	0.075[d]	1.882, 1.9635	2.1938, 2.1629	73
(Et_4N)[Ni(nmp)(S-*o*-babt)] (**12**)	450 (3500)[d]	0.276[d]	1.877, 1.947	2.1939, 2.1518	74
(Et_4N)[Ni(nmp)(S-meb)] (**13**)	449 (3900)[d]	0.214[d]	1.863, 1.944	2.172, 2.156	74
K[Ni(GC-OMe)(SC_6H_4-*p*-Cl)] (**15**)	481 (390), 560 (230)[f]	0.220[f]	1.83, 1.99[g]	2.16 (avg.)[g]	75
K[Ni(GC-OMe)(SNAc)] (**17**)	463 (350), 545 (160)[f]	0.310[f]	1.83, 1.99[g]	2.17 (avg.)[g]	75
K[Ni(N_3S_2)] (**19**)	449 (320), 570 (90)[e]	-0.125[f]	1.8575, 1.954	2.1805, 2.1739	69

[a]Data represent the E_{ox} value normalized to the Ag/AgCl reference electrode [E vs NHE = E vs Ag/AgCl(saturated KCl) + 0.199 V] based on information found in ref 77-78; the quasi-reversible $E_{1/2}$ is reported for **7**, and a reversible $E_{1/2}$ is reported for NiSOD, which represent the Ni(III/II) redox couple. [b]Tris buffer (pH 8.5). [c]Potassium phosphate buffer (pH 7.5). [d]MeCN. [e]MeOH. [f]DMF. [g]Metric parameters from EXAFS. The reported Ni–S bond distance represents the average from two separate S scattering atoms.

As a means towards realizing selective S-modifications in NiSOD models, Harrop and coworkers developed a coordinatively unsaturated N_2S ligand that would allow for unconstrained modeling of a second S-ligand (S′) to complete the N_2SS' coordination sphere.[73] Reaction of the deprotonated form of the ligand nmp^{2-} (dianion of *N*-(2-mercaptoethyl)picolinamide) with Ni(II) ultimately led to an intractable *S,S*-bridged dimeric species, $[Ni_2(nmp)_2]$ (**9**). Complex **9** was initially thought to be an unusable precursor due to its poor solubility and the kinetic inertness of *S,S*-bridged square-planar Ni(II) complexes. However, reaction of **9** with different exogenous thiolates afforded the red-colored mononuclear square-planar Ni(II)-N_2S_2 species, (Et_4N)[Ni(nmp)(SR)] (where R represents various alkyl and aromatic thiolate ligands), in very good yields (Figure 2.7). The nmp^{2-} ligand replicates the two five-member chelate rings formed by His1 and Cys2 in NiSOD, while the exogenous thiolate allows for unconstrained modeling of Cys6. Single crystal X-ray analysis in combination with UV-vis, FTIR, ^{1}H NMR, CV and ESI-MS of these complexes revealed a distorted planar coordination sphere with spectroscopic and electrochemical features similar to $NiSOD_{red}$. For example, the metric parameters for **10-13** (Ni–N_{amine}: 1.950 Å; Ni–$N_{carboxamide}$: 1.871 Å; Ni–$S_{\textit{trans}\text{-carboxamide}}$: 2.193 Å; Ni–$S_{\textit{trans}\text{-amine}}$ 2.155 Å, average values)[73,74] are consistent with square-planar Ni(II)-N_2S_2 coordination (see **7** and **8**). In complexes **10-13**, the dominant electronic transition at ~ 450 nm masks the *d-d* bands due to the pyridine-N/Ni(II) CT (see Table 2.2). These complexes also displayed irreversible CVs consistent with ligand-based redox processes. Bulk oxidation studies revealed this to be the case with the oxidation occurring at the monodentate S-ligand to form disulfide and the insoluble *S,S*-bridged dimer **9**. Regardless, the Ni-nmp constructs afforded suitable structural models of $NiSOD_{red}$ that could be modified at one specific coordination position.

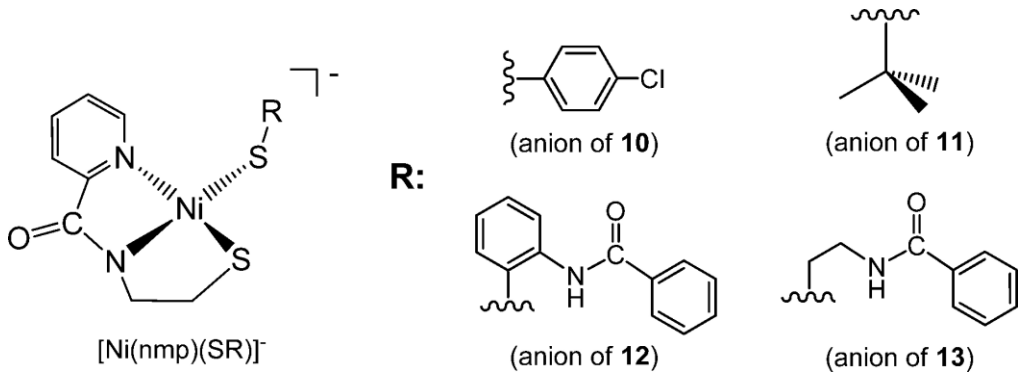

Figure 2.7. Structures of the anionic portion of NiSOD model complexes of general formula (Et_4N)[Ni(nmp)(SR)] [where R = C_6H_4-*p*-Cl in **10**, ^{t}Bu in **11**, *ortho*-benzoylaminobenzene or *o*-babt in **12**, and *N*-(2-mercaptoethyl)benzamide or meb in **13**]. The skewed line represents the point of attachment to the monodentate thiolate ligand.

To demonstrate the utility of this synthetic route, modifications such as appended H-bonding moieties were incorporated into the monodentate S-ligand (see complexes **12** and **13**, Figure 2.7).[74] These modifications are significant since NiSOD contains two key H-bonds to the coordinated cysteine thiolate *trans* to the peptide-N (Cys6).[18,38] The H-bonds in **12** and **13** were shown to be both intra- and intermolecular in nature. In both cases, the H-bond is bifurcated between both S-ligands in the basal plane, but more so with the monodentate thiolate (Figure 2.8). An interesting feature is that H-bonding to sulfur resulted in a decrease in the Ni–S bond distance from the simple alkyl or aryl analogues (compare 2.2139 Å in **10** and 2.1939 Å in **12**, 0.02 Å bond contraction). At first glance, this result is opposite to what one would predict based on a decrease in the Lewis basicity of the H-bonded thiolate ligand. However, examination of the frontier MOs that govern this interaction in **10**-**13**, as well as $NiSOD_{red}$, reveals that the HOMO is anti-bonding in nature with large and nearly equal contributions from *both* Ni-dπ AOs and S-

pπ-ligand orbitals; a so-called dπ-pπ repulsion (filled-filled interaction or four-electron repulsion). The Ni-S contraction in **12** and **13** is the result of stabilization of S-based ligand orbitals upon H-bonding, which result in a decrease in the filled-filled Ni dπ-S pπ antibonding interaction. Theoretical studies on truncated versions of $NiSOD_{red}$ reveal a similar contraction of 0.03 Å when the CysS ligands become fully protonated CysSH thiols.[23] DFT calculations on **10**-**13** also show a decrease in S-character in the HOMO (S-based MOs lowered in energy) and an increase in Ni-character upon incorporation of the H-bond to support more of a metal-based redox-active MO. The H-bonding interaction also resulted in an S-ligand that is less susceptible to reactions with electrophiles/oxidants such as O_2 with an overall stability gain of 15 kcal/mol at the S-atom with the H-bond. Thus, synthetically enforcing H-bond donors in these model complexes (also present at the NiSOD active site) decreases the nucleophilicity of a coordinated S-donor, stabilizes the Ni–S bond via relief of the dπ-pπ interaction, and serves as one potential mechanism that nature has incorporated to protect the CysS donors of NiSOD from oxidative modification/degradation during turnover.

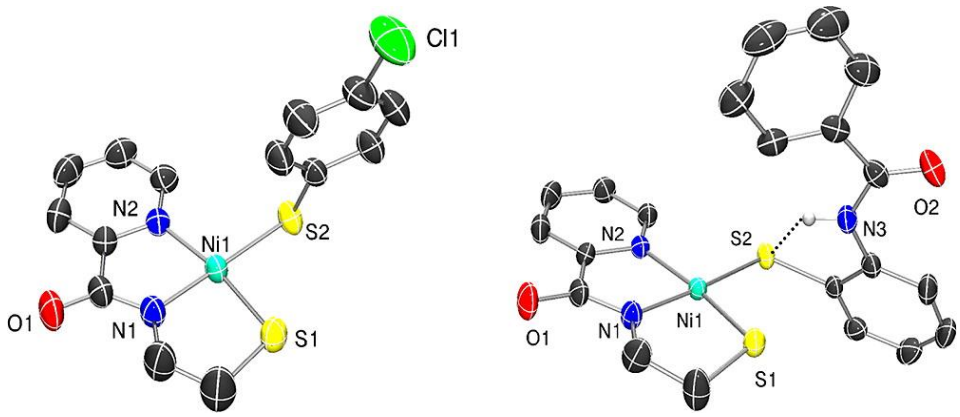

Figure 2.8. X-ray crystal structures of the anions of $NiSOD_{red}$ models $(Et_4N)[Ni(nmp)(SC_6H_4$-*p*-Cl)] (**10**, left) and $(Et_4N)[Ni(nmp)(S$-*o*-babt)] (**12**, right) highlighting intramolecular H-bonding between the carboxamide NH group (N3) and the monodentate thiolate (S2) in complex **12**.

Models **10**-**13** certainly afforded suitable structural analogues of NiSOD with variable synthetic manipulation at one S-coordination position. The tunability of one S-ligand allowed our group to probe secondary sphere interactions with coordinated S-ligands such as H-bonding, which proved to protect the sulfur from oxidation and promote more Ni-based redox. These models suffered, however, from a lack of water stability and solubility thus limiting these studies to organic solvents. To achieve aqueous solubility/stability and ultimately superoxide chemistry, a new N_2S ligand utilizing a peptide backbone consisting of glycine and cysteine (denoted as GC-$OMeH_2$) was synthesized.[75] Analogous to the previous Ni-nmp systems (**10**-**13**), reaction of GC-OMe^{2-} with Ni(II) led to the expected *S*,*S*-bridged dimeric species $[Ni_2(GC\text{-}OMe)_2]$ (**14**) that was used in the construction of monomeric Ni(II) complexes with variability at the fourth coordination position. Reaction of **14** with numerous exogenous thiolates afforded a variety of red/violet-colored mononuclear square-planar Ni(II)-N_2S_2 species of general formula [Ni(GC-

OMe)(SR)] (where R represents various alkyl and aromatic thiolate ligands) in good yields (**15-18**, Figure 2.9). EXAFS, in combination with UV-vis, FTIR, ^{1}H NMR, CV, and ESI-MS, of **15** and **17** revealed a distorted square-planar coordination (Ni–$N_{amine\text{-}avg}$: 1.99 Å; Ni–$N_{peptide\text{-}avg}$: 1.83 Å; Ni–S_{avg}: 2.17 Å) with spectroscopic and electrochemical features similar to $NiSOD_{red}$ and previous models (avg. λ_{max}: 480 nm (ε: 420 M^{-1} cm^{-1}); 560 nm (ε: 200 M^{-1} cm^{-1}) in DMF and irreversible E_{ox} ~ 0.200 V (vs. Ag/AgCl in DMF)) (Table 2.2). Importantly, all of these measurements have been performed in organic solvents such as MeCN and a buffered (pH 7.4) aqueous medium, representing some of the first low MW models to be probed under pseudo-physiological conditions. These structurally characterized peptide-based Ni(II) complexes simulate many of the electronic features of $NiSOD_{red}$; however, they do not afford isolable Ni(III) species or superoxide-reactive systems suggesting again the significance of the fifth HisN-ligand in the enzyme. In fact, saturating these complexes with excess N-methylimidazole does not impart any electrochemical reversibility or other spectroscopic changes. Interestingly, the ^{1}H NMR spectra of **15-18** in D_2O or any protic solvent provide broad, ill-resolved signals which may correspond to variable solution speciation. It was hypothesized that these species could be solvent-bound or S-bridged oligomers due to the lability of the monodentate thiolate ligand. Addition of excess thiolate ligand afforded well-resolved spectra with splitting patterns consistent with a monomeric, diamagnetic square-planar Ni(II) complex. In contrast, dissolution of as-isolated **15-18** (from the synthesis) in aprotic solvents such as CD_3CN afforded neat, readily discernible ^{1}H NMR spectra consistent with one discrete species. These models suggest that the active site fragment of NiSOD may be rather dynamic with a propensity to oligomerize outside of the protein matrix (see the results from the maquette system **3** above). Thus, the surrounding environment and the N_3S_2 chelate may be crucial for maintaining coordinative

integrity. In fact, mutagenesis of just one CysS to SerO (Cys6Ser or Cys2Ser) resulted in inactive enzyme with the addition of two new water ligands.[31,32] The absence of one cysteine thiolate promotes a high-spin (S = 1) aquated Ni(II) center at the NiSOD active site with no evidence of the remaining Ni-SCys bond in the mutants. This finding, coupled with the results on **15-18**, suggests more than redox-modulation/H^+-storage roles for cysteine in NiSOD. It is likely that the presence of both the Cys6 and Cys2 ligands in NiSOD is crucial for proper active site assembly and stabilization.

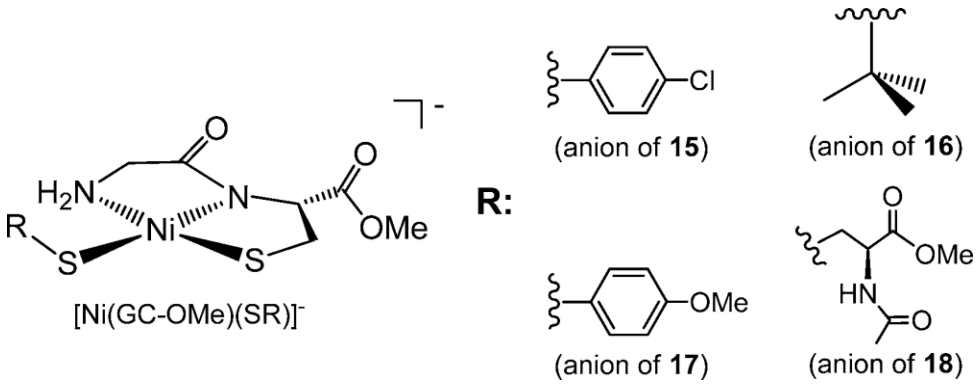

Figure 2.9. Structures of the anionic portion of NiSOD model complexes of general formula K[Ni(GC-OMe)(SR)] (where R = C_6H_4-*p*-Cl in **15**, ^{t}Bu in **16**, C_6H_4-*p*-OMe in **17**, and N-acetyl-L-cysteine or NAc in **18**). The skewed line represents the point of attachment to the monodentate thiolate ligand.

In an effort to obtain functional NiSOD complexes and to assess the role of the axial N-donor, our group designed and synthesized a 5C N_3S_2 ligand frame.[69] This ligand contained the appropriate donor atoms, in an electronic sense, that are situated in a spatial fashion exactly

analogous to the active site of NiSOD. In fact, the presence of the axial N-donor ligand is hypothesized to stabilize, at least to some extent, the high-valent Ni(III) oxidation state (vide supra). If this hypothesis was correct then an appropriately disposed Ni-N_3S_2 complex should be a significant step towards realizing catalytic function in NiSOD small molecule analogues and explains the lack of reactivity of models **7-18**. The corresponding Ni(II) complex with this N_3S_2 ligand, namely K[Ni(N_3S_2)] (**19**, Figure 2.10), was prepared by reacting the ligand with $Ni(OAc)_2 \bullet 4H_2O$ and NaOAc in MeOH to afford **19** in high yield.[69] Complex **19** has been characterized by X-ray crystallography, UV-vis, FTIR, ^{1}H NMR, CV, and ESI-MS. Much like the peptide models **15-18** described above, **19** also demonstrated excellent water solubility. Additionally, **19** is very stable in buffered media; no multiple speciation was observed as monitored by ^{1}H NMR and UV-vis spectroscopies. This stability is likely due to the chelate effect of the N_3S_2 ligand. The UV-vis of **19** in pH 7.5 PIPES buffer resembled the maquette and $NiSOD_{red}$ spectrum with double-humped ligand field bands at 449 nm (ε: 230 M^{-1} cm^{-1}) and 570 nm (ε: 50 M^{-1} cm^{-1}) (Figure 2.10). The structural features are comparable to prior models (see Table 2.2) featuring a 4C Ni(II)-N_2S_2 planar complex with the only exception of the non-coordinated pyridine-N situated ~ 3.2 Å and tilted away from the metal. The Ni–N_{py} distance of this potential fifth ligand as well as the tilt of the pyridine plane is structurally analogous to what is observed for $NiSOD_{red}$. The electrochemistry of **19** displayed the typical irreversible behavior even with a potential N-donor in the ligand frame with E_{ox} = -0.125 V (DMF vs. Ag/AgCl). However, a new reduction wave was found at E_{red} = -1.44 V, which only appeared when the oxidized species is traversed. The large ΔE_p (~ 1.2 V) suggested that a significant structural rearrangement occurred during the redox process. To identify the site of the redox process, bulk oxidation was performed with Fc^+ which resulted in the dinuclear disulfide linked species **20** that

formed from a transient 5C Ni(III) intermediate (Scheme 2.1). Interestingly, the S-atoms in the disulfide linkage of **20** originate from the S-donor *trans* to the carboxamide-N in **19** highlighting the lability of this particular ligand and potentially Cys6 in NiSOD. This conversion mimics the same redox and coordination geometry change as observed in NiSOD. While the results suggested that the axial His1-Im ligand in NiSOD is not entirely responsible for Ni-based redox, it still appears critical for keeping the coordination sphere intact to prevent polymeric RSSR formation. Thus, His1-N binding in combination with the protein structure is primarily responsible for Ni(III/II) cycling in NiSOD. Further support for this hypothesis comes from theoretical studies on the enzyme, which suggest a primarily S-based HOMO in $NiSOD_{red}$[23] along with the long Ni(III)-$N_{imidazole}$ distance (~ 2.5 Å) observed in $NiSOD_{ox}$.[18]

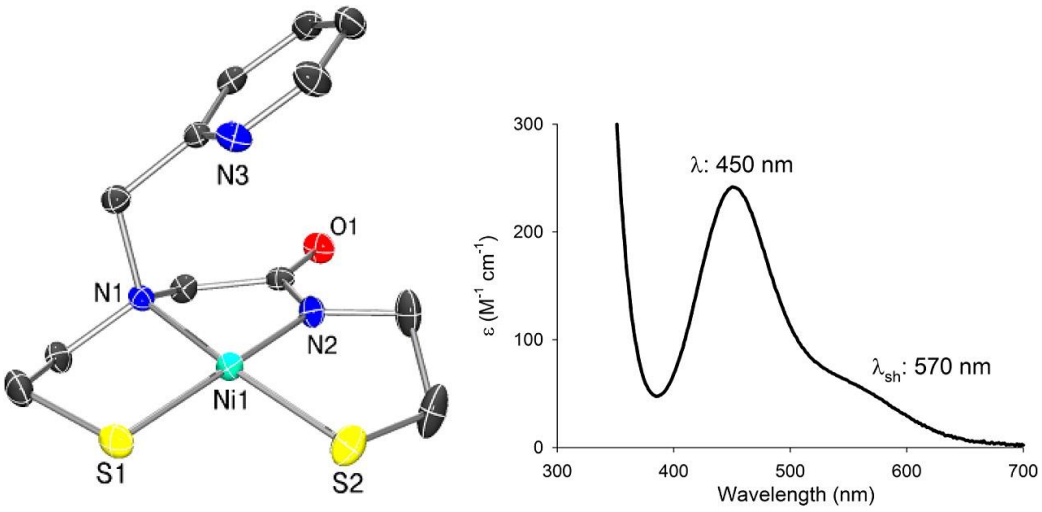

Figure 2.10. X-ray crystal structure of the anion of $K[Ni(N_3S_2)]$ (**19**) (left). The electronic absorption spectrum of **19** in pH 7.5 PIPES buffer at 25 °C (right).

Scheme 2.1. Proposed mechanism of the oxidative conversion of the $NiSOD_{red}$ model complex **19** to the disulfide linked complex **20**.[a]

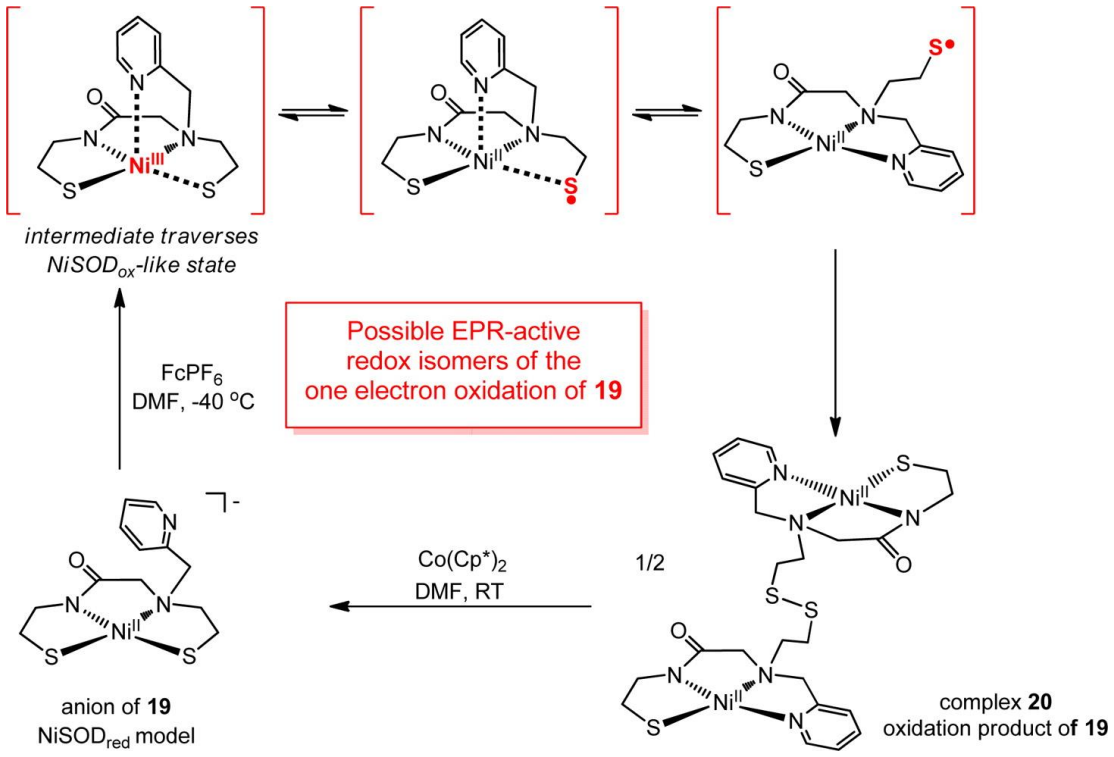

[a]Hypothesized intermediates are shown in red brackets, with paramagnetic atoms shown in bold and colored red. $FcPF_6$ is the chemical oxidant ferrocenium hexafluorophosphate; $CoCp^*_2$ is the chemical reductant decamethylcobaltocene. This scheme was adapted from ref. 69.

2.4 Summary and Outlook

NiSOD presents numerous structural and spectroscopic characteristics that distinguish it from other members of the SOD family; however, it is certainly representative of redox-active Ni metalloenzymes. As such, the results of synthetic modeling work have revealed valuable information regarding the properties of this unique Ni coordination environment. It is evident that the mixed amine/peptide-N ligands assist in the stabilization of high-valent Ni(III) as well as the low-spin electronic configuration of the metal. It is believed that the unique asymmetric N-donor set, in combination with the two CysS donors, sufficiently depress the Ni(III/II) redox

couple so that it is physiologically accessible and within the window of the superoxide redox potentials. All of the models report redox potentials in this range (see Tables 2.1 and 2.2). The $N_{amine}N_{carboxamide}S_2$ coordination environment also provides kinetic stability against O_2 and H_2O_2 (the products of SOD) under turnover conditions as noted in several analogues. Some of the model systems demonstrate SOD functionality albeit at rates significantly lower than the enzyme. Of these functional models, most contain an axial N-ligand. Indeed, NiSOD His1 mutants and certain maquette models that do not have this ligand demonstrate low activity. We suspect that this ligand is crucial in NiSOD. While approximate models such as **5** highlight the potential for functionality even in the absence of a fifth ligand, it appears that the basic requisite for SOD activity is a low-spin Ni center with the correct redox potential (see complex **7** that contains biologically-irrelevant alkoxy ligands). To underscore the importance of His1 in terms of NiSOD function, the Ni(III) state is only achieved, at least transiently, in low MW accurate models that contain this or a similar type of ligand (e.g. py-N).

In regards to the NiSOD catalytic mechanism, the synthetic analogue, biochemical, and theoretical data have led to the following postulates. The 4C square-planar $NiSOD_{red}$ site observed in the crystal structure is likely a resting state of the enzyme that is not catalytically active. Indeed, models such as **7**-**18** that accurately reproduce the structure and electronic spectrum of $NiSOD_{red}$ but lacking a fifth axial N-ligand exhibit mostly irreversible redox potentials (ligand-based redox processes; disulfide formation) and no SOD activity. The one system that displays quasireversible redox behavior (**7**) has never been isolated or proven to be Ni(III). This result can be explained by the electronic structure that defines the nature of the frontier MO involved in this redox process. This MO has significant contributions of both S-pπ and Ni-dπ character, which is symptomatic of a highly covalent Ni–S bond (Figure 2.11). In

theoretical studies on NiSOD, this MO exhibits predominantly S-pπ character as well (HOMO: 26% Ni-dπ, 66% S-pπ; HOMO-1: 36% Ni-dπ, 45% S-pπ).[23]

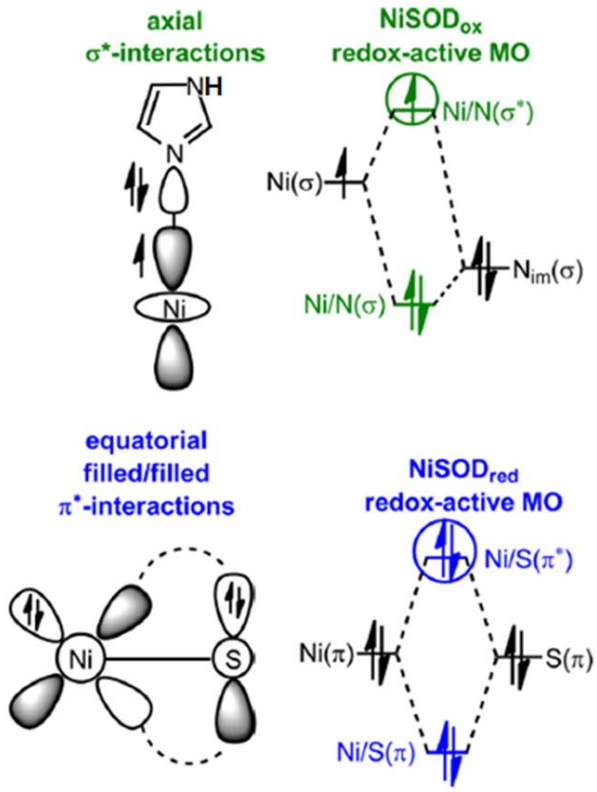

Figure 2.11. Frontier MOs and illustration of the dominant bonding interactions in $NiSOD_{ox}$ (top) and $NiSOD_{red}$ (bottom). This figure was adapted from ref 23.

This result is not at all unique to $NiSOD_{red}$ and has been demonstrated in all accurate Ni(II)-N_2S_2 models (**7**-**19**), which display significant contributions from both Ni and S in this redox-active MO. This begs the question as to what prevents S-oxidation in the enzyme. One possibility is that NiSOD has evolved to prevent S-oxidation by destabilizing the Ni-based AOs

or by stabilizing the S-based ligand group orbitals by some mechanism that cannot be modeled accurately by DFT. Either change will yield a redox-active MO with more Ni character. Stabilization of S-based orbitals has been demonstrated through H-bonding interactions both computationally[39,40,46] and experimentally[74] to increase Ni-character and decrease the nucleophilicity (viz. oxygen reactivity) of the H-bonded sulfur. In addition to S-protection from ROS, full protonation of the coordinated cysteinates to cysteine thiols could serve as a reservoir for H^+ in the formation of H_2O_2 (eq. 2.2). This proposal has been advocated by separate DFT studies.[40,46] Another postulate is that the Ni center remains 5C throughout catalysis.[40,54] Examination of the electronic structure of $NiSOD_{ox}$ reveals a redox-active MO with predominantly Ni-dπ character that is antibonding with respect to the Ni-d_z^2(dσ) AO and N-pσ orbital of the axial His ligand (Figure 2.11).[23] This electronic structure explains the hyperfine in the EPR as well as the relatively long Ni–HisN bond distance in the NiSOD structures. If this orbital was the redox-active MO during catalysis then one would expect the Ni–HisN distance to vary during turnover, which would result in the atypical Ni–Im distance. This analysis excludes the effects imparted by the H-bonding network, His1-Glu17-Arg47. A 5C active species would also minimize the reorganizational energy (λ) that occurs during eT, which has been suggested for the functional maquette system **2**.[54] This explanation makes intuitive sense as eT rates are inherently faster than bond forming/breaking processes. Additionally, all model systems that have been isolated in the Ni(III) form contain the Im axial ligand. We thus propose the mechanism as highlighted in Scheme 2.2.

Scheme 2.2. Proposed Active Forms of NiSOD during Outer-Sphere Turnover (black) and Potential Inner-Sphere Intermediates (gray, I and II)[a]

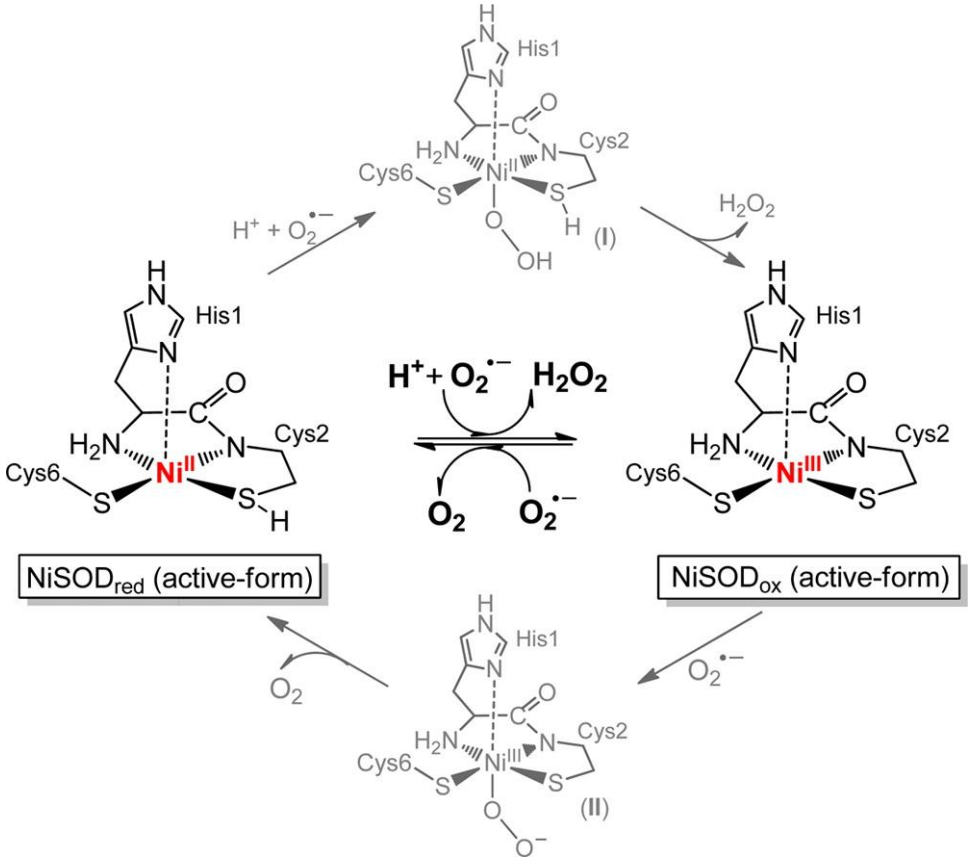

[a]Intermediate I may also be viewed as a Ni(III)−hydroperoxo species after internal transfer of an electron from Ni(II) to the coordinated hydrosuperoxo. The dashed line from HisN to Ni implies a relatively long bond as observed in the X-ray crystal structures of NiSOD (see refs 18 and 19). The protonation of both cysteinates has not been widely established; however, either cysteine is a likely candidate, and we have chosen Cys2 in this depiction for the sake of clarity. If only one CysSH is present, a protonated hydrosuperoxo radical (HOO•) has been proposed to enter the active site (see ref 40) despite the known superoxide pK_a of 4.8.

The debate over outer-sphere versus inner-sphere redox still remains and we will not attempt to elect one in the present account. Most of the biochemical evidence points towards an outer-sphere mechanism including (i) the lack of rate dependence on the ionic strength of the medium; (ii) no evidence of small anions such as N_3^-, even in large excess, to bind to Ni; and (iii) the presence of a non-coordinated Cl^- ligand in the X-ray structure of the NiSOD Tyr9Phe mutant positioned ~ 3.5 Å away from the Ni center (a suggested superoxide binding site). An

outer-sphere mechanism would also keep ROS away from and protect the CysS ligands from S-oxidation/oxygenation. To date (2012), most of the model work is supportive of this proposal. However, evidence for CN^- binding in some maquette models and theoretical studies of substrate coordination suggest otherwise. We anticipate that the bioinorganic synthetic modeling community will have a significant role in addressing these outlying issues in future NiSOD analogue systems.

2.5 References

(1) Valentine, J. S.; Wertz, D. L.; Lyons, T. J.; Liou, L.-L.; Goto, J. J.; Gralla, E. B. The dark side of dioxygen biochemistry. *Curr. Opin. Chem. Biol.* **1998**, *2*, 253-262.

(2) McCord, J. M. In *Critical Reviews of Oxidative Stress and Aging: Advances in Basic Science, Diagnostics, and Intervention*; Rodriguez, H., Cutler, R., Eds.; World Scientific Publishing Co. Pte. Ltd.: Singapore, 2003, p 883-895.

(3) Maritim, A. C.; Sanders, R. A.; Watkins, J. B., III Diabetes, Oxidative Stress, and Antioxidants: A Review. *J. Biochem. Mol. Toxicol.* **2003**, *17*, 24-38.

(4) Kocatürk, P. A.; Akbostanci, M. C.; Tan, F.; Kavas, G. Ö. Superoxide dismutase activity and zinc and copper concentrations in Parkinson's disease. *Pathophysiology* **2000**, *7*, 63-67.

(5) De Leo, M. E.; Borrello, S.; Passantino, M.; Palazzotti, B.; Mordente, A.; Daniele, A.; Filippini, V.; Galeotti, T.; Masullo, C. Oxidative stress and overexpression of manganese superoxide dismutase in patients with Alzheimer's disease. *Neurosci. Lett.* **1998**, *250*, 173-176.

(6) Fortunato, G.; Pastinese, A.; Intrieri, M.; Lofrano, M. M.; Gaeta, G.; Censi, M. B.; Boccalatte, A.; Salvatore, F.; Sacchetti, L. Serum Mn-Superoxide Dismutase in Acute Myocardial Infarction. *Clin. Biochem.* **1997**, *30*, 569-571.

(7) Miller, A.-F. Superoxide dismutases: active sites that save, but a protein that kills. *Curr. Opin. Chem. Biol.* **2004**, *8*, 162-168.

(8) Fridovich, I. In *Encyclopedia of Biological Chemistry*; 1st ed.; Lennarz, W. J., Lane, M. D., Eds.; Elsevier: New York, 2004; Vol. 4, p 135-138.

(9) Tainer, J. A.; Getzoff, E. D.; Richardson, J. S.; Richardson, D. C. Structure and mechanism of copper, zinc superoxide dismutase. *Nature* **1983**, *306*, 284-287.

(10) Borgstahl, G. E. O.; Parge, H. E.; Hickey, M. J.; Beyer, W. F., Jr.; Hallewell, R. A.; Tainer, J. A. The structure of human mitochondrial manganese superoxide dismutase reveals a novel tetrameric interface of two 4-helix bundles. *Cell* **1992**, *71*, 107-118.

(11) Grove, L. E.; Brunold, T. C. Second-Sphere Tuning of the Metal Ion Reduction Potentials in Iron and Manganese Superoxide Dismutases. *Comments Inorg. Chem.* **2008**, *29*, 134-168.

(12) Miller, A.-F. Redox Tuning over Almost 1 V in a Structurally Conserved Active Site: Lessons from Fe-Containing Superoxide Dismutase. *Acc. Chem. Res.* **2008**, *41*, 501-510.

(13) Tierney, D. L.; Fee, J. A.; Ludwig, M. L.; Penner-Hahn, J. E. X-ray Absorption Spectroscopy of the Iron Site in *Escherichia coli* Fe(III) Superoxide Dismutase. *Biochemistry* **1995**, *34*, 1661-1668.

(14) Grove, L. E.; Xie, J.; Yikilmaz, E.; Karapetyan, A.; Miller, A.-F.; Brunold, T. C. Spectroscopic and Computational Insights into Second-Sphere Amino-Acid Tuning of Substrate Analogue/Active-Site Interactions in Iron(III) Superoxide Dismutase. *Inorg. Chem.* **2008**, *47*, 3993-4004.

(15) Brown, R. H., Jr. SOD1 aggregates in ALS: Cause, correlate or consequence? *Nat. Med.* **1998**, *4*, 1362-1364.

(16) Youn, H.-D.; Youn, H.; Lee, J.-W.; Yim, Y.-I.; Lee, J. K.; Hah, Y. C.; Kang, S.-O. Unique Isozymes of Superoxide Dismutase in *Streptomyces griseus*. *Arch. Biochem. Biophys.* **1996**, *334*, 341-348.

(17) Palenik, B.; Brahamsha, B.; Larimer, F. W.; Land, M.; Hauser, L.; Chain, P.; Lamerdin, J.; Regala, W.; Allen, E. E.; McCarren, J.; Paulsen, I.; Dufresne, A.; Partensky, F.; Webb, E. A.; Waterbury, J. The genome of a motile marine *Synechococcus*. *Nature* **2003**, *424*, 1037-1042.

(18) Barondeau, D. P.; Kassmann, C. J.; Bruns, C. K.; Tainer, J. A.; Getzoff, E. D. Nickel Superoxide Dismutase Structure and Mechanism. *Biochemistry* **2004**, *43*, 8038-8047.

(19) Wuerges, J.; Lee, J.-W.; Yim, Y.-I.; Yim, H.-S.; Kang, S.-O.; Carugo, K. D. Crystal structure of nickel-containing superoxide dismutase reveals another type of active site. *Proc. Natl. Acad. Sci. U.S.A.* **2004**, *101*, 8569-8574.

(20) Herbst, R. W.; Guce, A.; Bryngelson, P. A.; Higgins, K. A.; Ryan, K. C.; Cabelli, D. E.; Garman, S. C.; Maroney, M. J. Role of Conserved Tyrosine Residues in NiSOD Catalysis: A Case of Convergent Evolution. *Biochemistry* **2009**, *48*, 3354-3369.

(21) Harrop, T. C.; Mascharak, P. K. In *Concepts and Models in Bioinorganic Chemistry*; Kraatz, H.-B., Metzler-Nolte, N., Eds.; Wiley-VCH: Weinheim, Germany, 2006, p 309-329.

(22) Choudhury, S. B.; Lee, J.-W.; Davidson, G.; Yim, Y.-I.; Bose, K.; Sharma, M. L.; Kang, S.-O.; Cabelli, D. E.; Maroney, M. J. Examination of the Nickel Site Structure and Reaction Mechanism in *Streptomyces seoulensis* Superoxide Dismutase. *Biochemistry* **1999**, *38*, 3744-3752.

(23) Fiedler, A. T.; Bryngelson, P. A.; Maroney, M. J.; Brunold, T. C. Spectroscopic and Computational Studies of Ni Superoxide Dismutase: Electronic Structure Contributions to Enzymatic Function. *J. Am. Chem. Soc.* **2005**, *127*, 5449-5462.

(24) Krüger, H.-J.; Peng, G.; Holm, R. H. Low-Potential Nickel(III,II) Complexes: New Systems Based on Tetradentate Amidate-Thiolate Ligands and the Influence of Ligand Structure on Potentials in Relation to the Nickel Site in [NiFe]-Hydrogenases. *Inorg. Chem.* **1991**, *30*, 734-742.

(25) Fiedler, A. T.; Brunold, T. C. Spectroscopic and Computational Studies of Ni^{3+} Complexes with Mixed S/N Ligation: Implications for the Active Site of Nickel Superoxide Dismutase. *Inorg. Chem.* **2007**, *46*, 8511-8523.

(26) Xiao, Y.; Wang, H.; George, S. J.; Smith, M. C.; Adams, M. W. W.; Jenney, F. E., Jr. ; Sturhahn, W.; Alp, E. E.; Zhao, J.; Yoda, Y.; Dey, A.; Solomon, E. I.; Cramer, S. P. Normal Mode Analysis of *Pyrococcus furiosus* Rubredoxin via Nuclear Resonance Vibrational Spectroscopy (NRVS) and Resonance Raman Spectroscopy. *J. Am. Chem. Soc.* **2005**, *127*, 14596–14606.

(27) Han, S.; Czernuszewicz, R. S.; Kimura, T.; Adams, M. W. W.; Spiro, T. G. Fe_2S_2 Protein Resonance Raman Spectra Revisited: Structural Variations among Adrenodoxin, Ferredoxin, and Red Paramagnetic Protein. *J. Am. Chem. Soc.* **1989**, *111*, 3505-3511.

(28) Qiu, D.; Kilpatrick, L.; Kitajima, N.; Spiro, T. G. Modeling Blue Copper Protein Resonance Raman Spectra with Thiolate-Cu^{II} Complexes of a Sterically Hindered Tris(pyrazolyl)borate. *J. Am. Chem. Soc.* **1994**, *116*, 2585-2590.

(29) Qiu, D.; Dasgupta, S.; Kozlowski, P. M.; Goddard, W. A., III; Spiro, T. G. Chromophore-in-Protein Modeling of the Structures and Resonance Raman Spectra for Type 1 Copper Proteins. *J. Am. Chem. Soc.* **1998**, *120*, 12791-12797.

(30) Bryngelson, P. A.; Arobo, S. E.; Pinkham, J. L.; Cabelli, D. E.; Maroney, M. J. Expression, Reconstitution, and Mutation of Recombinant *Streptomyces coelicolor* NiSOD. *J. Am. Chem. Soc.* **2004**, *126*, 460-461.

(31) Ryan, K. C.; Johnson, O. E.; Cabelli, D. E.; Brunold, T. C.; Maroney, M. J. Nickel superoxide dismutase: structural and functional roles of Cys2 and Cys6. *J. Biol. Inorg. Chem.* **2010**, *15*, 795-807.

(32) Johnson, O. E.; Ryan, K. C.; Maroney, M. J.; Brunold, T. C. Spectroscopic and computational investigation of three Cys-to-Ser mutants of nickel superoxide dismutase: insight into the roles played by the Cys2 and Cys6 active-site residues. *J. Biol. Inorg. Chem.* **2010**, *15*, 777-793.

(33) Lawrence, G. D.; Sawyer, D. T. Potentiometric Titrations and Oxidation-Reduction Potentials of Manganese and Copper-Zinc Superoxide Dismutases. *Biochemistry* **1979**, *18*, 3045-3050.

(34) Barrette, W. C., Jr.; Sawyer, D. T.; Fee, J. A.; Asada, K. Potentiometric Titrations and Oxidation-Reduction Potentials of Several Iron Superoxide Dismutases. *Biochemistry* **1983**, *22*, 624-627.

(35) Sawyer, D. T.; Valentine, J. S. How Super is Superoxide? *Acc. Chem. Res.* **1981**, *14*, 393-400.

(36) Uudsemaa, M.; Tamm, T. Density-Functional Theory Calculations of Aqueous Redox Potentials of Fourth-Period Transition Metals. *J. Phys. Chem. A* **2003**, *107*, 9997-10003.

(37) Shearer, J.; Dehestani, A.; Abanda, F. Probing Variable Amine/Amide Ligation in $Ni^{II}N_2S_2$ Complexes Using Sulfur K-Edge and Nickel L-Edge X-ray Absorption Spectroscopies: Implications for the Active Site of Nickel Superoxide Dismutase. *Inorg. Chem.* **2008**, *47*, 2649-2660.

(38) Grapperhaus, C. A.; Darensbourg, M. Y. Oxygen Capture by Sulfur in Nickel Thiolates. *Acc. Chem. Res.* **1998**, *31*, 451-459.

(39) Mullins, C. S.; Grapperhaus, C. A.; Kozlowski, P. M. Density functional theory investigations of NiN_2S_2 reactivity as a function of nitrogen donor type and N–H···S hydrogen bonding inspired by nickel-containing superoxide dismutase. *J. Biol. Inorg. Chem.* **2006**, *11*, 617-625.

(40) Pelmenschikov, V.; Siegbahn, P. E. M. Nickel Superoxide Dismutase Reaction Mechanism Studied by Hybrid Density Functional Methods. *J. Am. Chem. Soc.* **2006**, *128*, 7466-7475.

(41) Neupane, K. P.; Shearer, J. The Influence of Amine/Amide versus Bisamide Coordination in Nickel Superoxide Dismutase. *Inorg. Chem.* **2006**, *45*, 10552-10566.

(42) Zilbermann, I.; Maimon, E.; Cohen, H.; Meyerstein, D. Redox Chemistry of Nickel Complexes in Aqueous Solutions. *Chem. Rev.* **2005**, *105*, 2609-2625.

(43) Halcrow, M. A.; Christou, G. Biomimetic Chemistry of Nickel. *Chem. Rev.* **1994**, *94*, 2421-2481.

(44) Ragsdale, S. W. Nickel Biochemistry. *Curr. Opin. Chem. Biol.* **1998**, *2*, 208-215.

(45) Ragsdale, S. W. Nickel-based Enzyme Systems. *J. Biol. Chem.* **2009**, *284*, 18571-18575.

(46) Prabhakar, R.; Morokuma, K.; Musaev, D. G. A DFT Study of the Mechanism of Ni Superoxide Dismutase (NiSOD): Role of the Active Site Cysteine-6 Residue in the Oxidative Half-Reaction. *J. Comput. Chem.* **2006**, *27*, 1438-1445.

(47) Szilagyi, R. K.; Bryngelson, P. A.; Maroney, M. J.; Hedman, B.; Hodgson, K. O.; Solomon, E. I. S K-Edge X-ray Absorption Spectroscopic Investigation of the Ni-Containing Superoxide Dismutase Active Site: New Structural Insight into the Mechanism. *J. Am. Chem. Soc.* **2004**, *126*, 3018-3019.

(48) Lanzilotta, W. N.; Schuller, D. J.; Thorsteinsson, M. V.; Kerby, R. L.; Roberts, G. P.; Poulos, T. L. Structure of the CO sensing transcription activator CooA. *Nat. Struct. Mol. Biol.* **2000**, *7*, 876-880.

(49) Nagashima, S.; Nakasako, M.; Dohmae, N.; Tsujimura, M.; Takio, K.; Odaka, M.; Yohda, M.; Kamiya, N.; Endo, I. Novel non-heme iron center of nitrile hydratase with a claw setting of oxygen atoms. *Nat. Struct. Mol. Biol.* **1998**, *5*, 347-351.

(50) Darnault, C.; Volbeda, A.; Kim, E. J.; Legrand, P.; Vernède, X.; Lindahl, P. A.; Fontecilla-Camps, J. C. Ni-Zn-[Fe_4-S_4] and Ni-Ni-[Fe_4-S_4] clusters in closed and open α subunits of acetyl-CoA synthase/carbon monoxide dehydrogenase. *Nat. Struct. Mol. Biol.* **2003**, *10*, 271-279.

(51) Peters, J. W.; Stowell, M. H. B.; Soltis, S. M.; Finnegan, M. G.; Johnson, M. K.; Rees, D. C. Redox-Dependent Structural Changes in the Nitrogenase P-Cluster. *Biochemistry* **1997**, *36*, 1181-1187.

(52) Ibers, J. A.; Holm, R. H. Modeling Coordination Sites in Metallobiomolecules. *Science* **1980**, *209*, 223-235.

(53) Shearer, J.; Long, L. M. A Nickel Superoxide Dismutase Maquette That Reproduces the Spectroscopic and Functional Properties of the Metalloenzyme *Inorg. Chem.* **2006**, *45*, 2358-2360.

(54) Neupane, K. P.; Gearty, K.; Francis, A.; Shearer, J. Probing Variable Axial Ligation in Nickel Superoxide Dismutase Utilizing Metallopeptide-Based Models: Insight into the Superoxide Disproportionation Mechanism. *J. Am. Chem. Soc.* **2007**, *129*, 14605–14618.

(55) Shearer, J.; Neupane, K. P.; Callan, P. E. Metallopeptide Based Mimics with Substituted Histidines Approximate a Key Hydrogen Bonding Network in the Metalloenzyme Nickel Superoxide Dismutase. *Inorg. Chem.* **2009**, *48*, 10560-10571.

(56) Schmidt, M.; Zahn, S.; Carella, M.; Ohlenschläger, O.; Görlach, M.; Kothe, E.; Weston, J. Solution Structure of a Functional Biomimetic and Mechanistic Implications for Nickel Superoxide Dismutases. *ChemBioChem* **2008**, *9*, 2135-2146.

(57) Tietze, D.; Breitzke, H.; Imhof, D.; Kothe, E.; Weston, J.; Buntkowsky, G. New Insight into the Mode of Action of Nickel Superoxide Dismutase by Investigating Metallopeptide Substrate Models. *Chem. Eur. J.* **2009**, *15*, 517-523.

(58) Tietze, D.; Tischler, M.; Voigt, S.; Imhof, D.; Ohlenschläger, O.; Görlach, M.; Buntkowsky, G. Development of a Functional *cis*-Prolyl Bond Biomimetic and Mechanistic Implications for Nickel Superoxide Dismutase. *Chem. Eur. J.* **2010**, *16*, 7572-7578.

(59) Tietze, D.; Voigt, S.; Mollenhauer, D.; Tischler, M.; Imhof, D.; Gutmann, T.; González, L.; Ohlenschläger, O.; Breitzke, H.; Görlach, M.; Buntkowsky, G. Revealing the Position of the Substrate in Nickel Superoxide Dismutase: A Model Study. *Angew. Chem. Int. Ed.* **2011**, *50*, 2946-2950.

(60) Krause, M. E.; Glass, A. M.; Jackson, T. A.; Laurence, J. S. Novel Tripeptide Model of Nickel Superoxide Dismutase. *Inorg. Chem.* **2010**, *49*, 362-364.

(61) Krause, M. E.; Glass, A. M.; Jackson, T. A.; Laurence, J. S. MAPping the Chiral Inversion and Structural Transformation of a Metal-Tripeptide Complex Having Ni-Superoxide Dismutase Activity. *Inorg. Chem.* **2011**, *50*, 2479-2487.

(62) Glass, A. M.; Krause, M. E.; Laurence, J. S.; Jackson, T. A. Controlling the Chiral Inversion Reaction of the Metallopeptide Ni-Asparagine-Cysteine-Cysteine with Dioxygen. *Inorg. Chem.* **2012**, *51*, 10055-10063.

(63) Ma, H.; Chattopadhyay, S.; Petersen, J. L.; Jensen, M. P. Harnessing Scorpionate Ligand Equilibria for Modeling Reduced Nickel Superoxide Dismutase Intermediates. *Inorg. Chem.* **2008**, *47*, 7966-7968.

(64) Ma, H.; Wang, G.; Yee, G. T.; Petersen, J. L.; Jensen, M. P. Scorpionate-supported models of nickel-dependent superoxide dismutase. *Inorg. Chim. Acta* **2009**, *362*, 4563-4569.

(65) Lee, W.-Z.; Chiang, C.-W.; Lin, T.-H.; Kuo, T.-S. A Discrete Five-Coordinate Ni^{III} Complex Resembling the Active Site of the Oxidized Form of Nickel Superoxide Dismutase. *Chem. Eur. J.* **2012**, *18*, 50-53.

(66) Nakane, D.; Funahashi, Y.; Ozawa, T.; Masuda, H. A Square-planar Ni(II) Complex with an Asymmetric N_2S_2 Donor Set as a Model for the Active Site of Nickel-containing SOD: Structural Conversion Driven by Addition of a Strong Donor Ligand in the High Oxidation State. *Chem. Lett.* **2010**, *39*, 344-346.

(67) Shearer, J.; Zhao, N. $[Me_4N](Ni^{II}(BEAAM))$: A Synthetic Model for Nickel Superoxide Dismutase That Contains Ni in a Mixed Amine/Amide Coordination Environment. *Inorg. Chem.* **2006**, *45*, 9637-9639.

(68) Mathrubootham, V.; Thomas, J.; Staples, R.; McCraken, J.; Shearer, J.; Hegg, E. L. Bisamidate and Mixed Amine/Amidate NiN_2S_2 Complexes as Models for Nickel-Containing Acetyl Coenzyme A Synthase and Superoxide Dismutase: An Experimental and Computational Study. *Inorg. Chem.* **2010**, *49*, 5393-5406.

(69) Gale, E. M.; Simmonett, A. C.; Telser, J.; Schaefer, H. F., III; Harrop, T. C. Toward Functional Ni-SOD Biomimetics: Achieving a Structural/Electronic Correlation with Redox Dynamics. *Inorg. Chem.* **2011**, *50*, 9216–9218.

(70) Jenkins, R. M.; Singleton, M. L.; Almaraz, E.; Reibenspies, J. H.; Darensbourg, M. Y. Imidazole-Containing (N_3S)-Ni^{II} Complexes Relating to Nickel Containing Biomolecules. *Inorg. Chem.* **2009**, *48*, 7280-7293.

(71) Mullins, C. S.; Grapperhaus, C. A.; Frye, B. C.; Wood, L. H.; Hay, A. J.; Buchanan, R. M.; Mashuta, M. S. Synthesis and Sulfur Oxygenation of a (N_3S)Ni Complex Related to Nickel-Containing Superoxide Dismutase. *Inorg. Chem.* **2009**, *48*, 9974-9976.

(72) Herdt, D. R.; Grapperhaus, C. A. Kinetic study of nickel-thiolate oxygenation by hydrogen peroxide. Implications for nickel-containing superoxide dismutase. *Dalton Trans.* **2012**, *41*, 364-366.

(73) Gale, E. M.; Patra, A. K.; Harrop, T. C. Versatile Methodology Toward NiN_2S_2 Complexes as Nickel Superoxide Dismutase Models: Structure and Proton Affinity. *Inorg. Chem.* **2009**, *48*, 5620-5622.

(74) Gale, E. M.; Narendrapurapu, B. S.; Simmonett, A. C.; Schaefer, H. F., III; Harrop, T. C. Exploring the Effects of H-Bonding in Synthetic Analogues of Nickel Superoxide Dismutase (Ni-SOD): Experimental and Theoretical Implications for Protection of the Ni−SCys Bond. *Inorg. Chem.* **2010**, *49*, 7080–7096.

(75) Gale, E. M.; Cowart, D. M.; Scott, R. A.; Harrop, T. C. Dipeptide-Based Models of Nickel Superoxide Dismutase: Solvent Effects Highlight a Critical Role to Ni–S Bonding and Active Site Stabilization. *Inorg. Chem.* **2011**, *50*, 10460-10471.

(76) Colpas, G. J.; Maroney, M. J.; Bagyinka, C.; Kumar, M.; Willis, W. S.; Suib, S. L.; Baidya, N.; Mascharak, P. K. X-ray Spectroscopic Studies of Nickel Complexes, with Application to the Structure of Nickel Sites in Hydrogenases. *Inorg. Chem.* **1991**, *30*, 920-928.

(77) Connelly, N. G.; Geiger, W. E. Chemical Redox Agents for Organometallic Chemistry. *Chem. Rev.* **1996**, *96*, 877-910.

(78) Bard, A. J.; Faulkner, L. R. *Electrochemical Methods: Fundamentals and Applications*; 2nd ed.; Wiley and Sons: New York, 2000.

(79) Hanss, J.; Krüger, H.-J. First Isolation and Structural Characterization of a Nickel(III) Complex Containing Aliphatic Thiolate Donors. *Angew. Chem. Int. Ed.* **1998**, *37*, 360-363.

CHAPTER 3

ACCESSING Ni(III)-THIOLATE VERSUS Ni(II)-THIYL BONDING IN A FAMILY OF Ni-N_2S_2 SYNTHETIC MODELS OF NiSOD

Broering, E. P.;* Dillon, S.; Gale, E. M.; Steiner, R. A.; Telser, J.; Brunold, T. C.; Harrop, T. C. Accessing Ni(III)-Thiolate versus Ni(II)-Thiyl Bonding in a Family of Ni-N_2S_2 Synthetic Models of NiSOD. *Inorg. Chem.* **2015**, *54*, 3815-3828.

3.1 Abstract

Superoxide dismutase (SOD) catalyzes the disproportionation of superoxide ($O_2^{\bullet-}$) into H_2O_2 and O_2(g) by toggling through different oxidation states of a first-row transition metal ion at its active site. Ni-containing SODs (NiSODs) are a distinct class of this family of metalloenzymes due to the unusual coordination sphere that is comprised of mixed N/S-ligands from peptide-N and cysteine-S donor atoms. A central goal of our research is to understand the factors that govern reactive oxygen species (ROS) stability of the Ni–S(Cys) bond in NiSOD utilizing a synthetic model approach. In light of the reactivity of metal-coordinated thiolates to ROS, several hypotheses have been proffered and include the coordination of His1-Nδ to the Ni(II) and Ni(III) forms of NiSOD as well as hydrogen bonding or full protonation of a coordinated S(Cys). In this work, we present NiSOD analogues of the general formula $[Ni(N_2S)(SR')]^-$, providing a variable location (SR′ = aryl thiolate) in the N_2S_2 basal plane coordination sphere where we have introduced *o*-amino and/or electron-withdrawing groups to intercept an oxidized Ni species. The synthesis, structure, and properties of the NiSOD model complexes (Et_4N)[Ni(nmp)(SPh-*o*-NH_2)] (**2**), (Et_4N)[Ni(nmp)(SPh-*o*-NH_2-*p*-CF_3)] (**3**), (Et_4N)[Ni(nmp)(SPh-*p*-NH_2)] (**4**), and (Et_4N)[Ni(nmp)(SPh-*p*-CF_3)] (**5**) (nmp^{2-} = dianion of *N*-(2-mercaptoethyl)picolinamide) are reported. NiSOD model complexes with amino groups positioned *ortho* to the aryl-S in SR′ (**2** and **3**) afford oxidized species (**2**^{ox} and **3**^{ox}) that are best described as a resonance hybrid between Ni(III)-SR and Ni(II)-•SR based on UV-vis, magnetic circular dichroism (MCD), and electron paramagnetic resonance (EPR) spectroscopies and on density functional theory (DFT) calculations. The results presented here, demonstrating the high percentage of S(3p) character in the highest occupied molecular orbital (HOMO) of the four-coordinate reduced form of NiSOD ($NiSOD_{red}$), suggest that the transition from $NiSOD_{red}$ to the

five-coordinate oxidized form of NiSOD ($NiSOD_{ox}$) may go through a four-coordinate Ni-•S(Cys) ($NiSOD_{ox}$-His_{off}) that is stabilized by coordination to Ni(II).

3.2 Introduction

Aerobic organisms utilize superoxide dismutase (SOD) metalloenzymes in their defense against the free radical superoxide ($O_2^{\bullet-}$), which if unregulated plays a role in a variety of disease states.[1-8] The most recently discovered class of SODs are the nickel-containing SODs (NiSODs), which utilize Ni in a mixed nitrogen and thiolate coordination environment to catalyze the disproportionation of $O_2^{\bullet-}$ to H_2O_2 and O_2 by cycling through Ni(II/III) redox states (eq. 1 and 2 in Figure 3.1).[9] X-ray crystal structures of NiSOD from two separate *Streptomyces* strains confirm two distinct metal coordination geometries.[10-12] In the reduced form ($NiSOD_{red}$), the low-spin (S = 0) Ni(II) ion lies in a square-planar N_2S_2 environment composed of the N-terminal amine of His1, the deprotonated peptido-N of Cys2, and two thiolato-S from Cys2 and Cys6 (Figure 3.1). The oxidized form ($NiSOD_{ox}$) contains the same ligand set, but the S = ½ Ni(III) ion is five-coordinate and additionally bound to the imidazole-Nδ of His1 resulting in a Ni-N_3S_2 square-pyramidal geometry (Figure 3.1).[10-12]

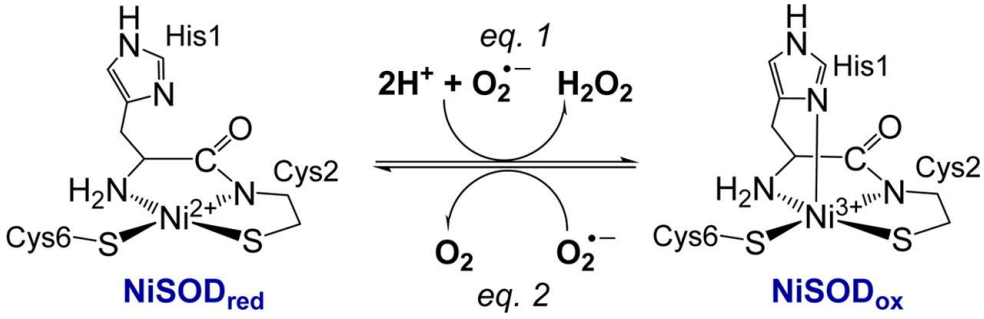

Figure 3.1. Structures of the NiSOD active site and the corresponding SOD half-reactions.

Questions concerning the enzyme's unusual N/S coordination sphere, particularly its stability toward O_2 and reactive oxygen species (ROS) in light of the reactive Ni–S(Cys) bonds[13] and the catalytic mechanism have prompted researchers to develop maquette-based,[14-20] tripeptide,[21-24] and low molecular weight[25-38] analogues that seek to replicate NiSOD's structure and/or function.[39,40] Indeed, several experimental and theoretical efforts have suggested that the mixed peptide-N/amine-N ligation serves as one key factor to promote greater Ni-character in the redox-active molecular orbital of NiSOD, in particular for the Ni(II) or $NiSOD_{red}$ state, thus preventing unwanted S-oxidation/oxygenation.[10,30,41] For example, a direct electronic structure comparison of two planar Ni(II)-N_2S_2 complexes ($NiSOD_{red}$ models) with diamine/dithiolate versus amine/carboxamide/dithiolate donors revealed a significant increase in Ni character of the Ni(dπ)–S(pπ) antibonding highest occupied molecular orbital (HOMO) upon introduction of the carboxamide, i.e. 18% Ni, 74% S for diamine; 33% Ni, 50% S for amine/carboxamide.[30] Direct density functional theory (DFT) computations on truncated versions of $NiSOD_{red}$ clearly demonstrated more S(pπ) character than Ni(dπ) character in the π-antibonding HOMO (25% Ni, 67% S) and HOMO-1 (37% Ni, 44% S).[10] Taken together, these results support a highly covalent Ni–S bond in $NiSOD_{red}$ that nonetheless still has significant S-character in the HOMO even with inclusion of the Ni–$N_{peptide}$ bond. Thus, the enzyme has evolved in such a way to promote Ni-based oxidation via the destabilization of the Ni(dπ) orbitals. This proposal has been verified by examining the electronic structure of the DFT-generated hypothetical four-coordinate (4C) planar version of $NiSOD_{ox}$, namely $NiSOD_{ox}$-His_{off}, that revealed a HOMO composition of 58% Ni(dπ) and 24% S(pπ).[10] On the other hand, the actual $NiSOD_{ox}$ HOMO is predominantly Ni in character with the unpaired electron occupying the Ni d_z^2 orbital, as verified by electron paramagnetic resonance (EPR) spectroscopy. Thus, the electronic structural changes from

$NiSOD_{red}$ → $NiSOD_{ox}$-His_{off} → $NiSOD_{ox}$ gradually move toward more Ni-character in the HOMO. This analysis begs the question as to what prevents $NiSOD_{red}$ from undergoing deleterious S-based redox chemistry upon conversion to $NiSOD_{ox}$. Could a Ni-stabilized S•(Cys) be traversed in such a conversion? To date, few low molecular weight analogues of NiSOD with mixed peptide-N/amine-N/thiolate-S coordination have been shown to achieve catalytic $O_2^{\bullet-}$ disproportionation. Many such complexes are prone to undergo irreversible S-based rather than Ni-based oxidation, although in some cases a transient Ni(III) species has been trapped and observed by EPR spectroscopy.[35,42,43]

The work presented here adopts the methodology developed by our group for synthesizing asymmetric, 4C planar Ni-N_2S_2 models of NiSOD employing the nmp^{2-} ligand (see Chart 3.1; nmp^{2-} = dianion of *N*-(2-mercaptoethyl)picolinamide).[32] Synthesis of such models was achieved through splitting of a proposed *S*,*S*-bridged dimer $[Ni_2(nmp)_2]$ with exogenously added thiolate ions or S_{exo} (where exo refers to the exogenously added monodentate S-ligand) that afforded a variety of Ni(II)-N_2S_2 complexes. We now report this *S*,*S*-bridged species to be the tetramer $[Ni_4(nmp)_4]$ (**1**). The use of S_{exo} to complete the N_2S_2 coordination sphere is synthetically novel in that it provides a specific point of control for modeling Cys6 (see Figure 3.1) at a site-differentiated location in the coordination sphere. In this way, the electronic properties of the complex can be evaluated and tuned by changing S_{exo}. Prior work on Ni(II)-nmp systems focused on synthetic methodology[32] and the electronic influence of second-sphere N–H···S hydrogen-bonds (H-bonds).[33] None of these complexes afforded a stable oxidized species. Instead, oxidation took place at S_{exo} to yield the disulfide of S_{exo} (through a transient thiyl radical) and **1** in quantitative yields. We hypothesized that enforcing a potential N-donor near the Ni center and/or decreasing the basicity of S_{exo} would allow us to intercept a Ni(III) or

Ni(II)-thiyl species. Indeed, the presence of N_{axial} ligands has proven beneficial in spectroscopically observing other Ni(III)-N_2S_2 complexes related to NiSOD.[36,44] Thus, the primary objective of this work is to gauge the impact of electronically deficient S_{exo} and N_{axial}-tethered S_{exo} donors on the redox properties of the corresponding NiSOD model complexes. The synthesis, structure, properties, and reactivity of the following Ni-N_2S_2 complexes will be described: (Et_4N)[Ni(nmp)(SPh-*o*-NH_2)] (**2**), (Et_4N)[Ni(nmp)(SPh-*o*-NH_2-*p*-CF_3)] (**3**), (Et_4N)[Ni(nmp)(SPh-*p*-NH_2)] (**4**), and (Et_4N)[Ni(nmp)(SPh-*p*-CF_3)] (**5**) (Chart 3.1). The NiSOD model complexes with amino groups positioned *ortho* to the aryl-S (**2** and **3**) afforded oxidized species that are best described as a resonance hybrid between Ni(III)-($^-$SR) and Ni(II)-(•SR) and are the first examples of the room temperature (RT) observation of Ni-stabilized thiyl radicals with relatively long (hours) lifetimes.

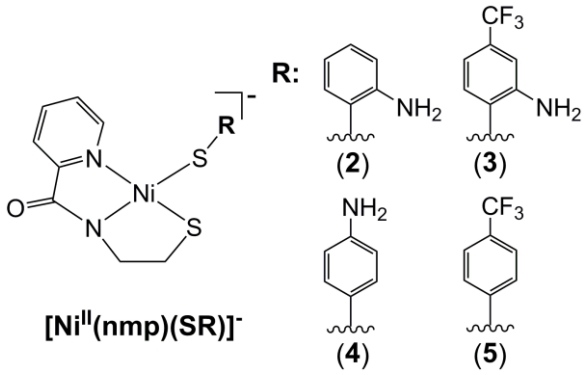

Chart 3.1. General structure of the [Ni(nmp)(SR)]$^-$ complexes reported in this study. R = 2-aminothiophenolate (**2**), 2-amino-4-(trifluoromethyl)benzenethiolate (**3**), 4-aminothiophenolate (**4**), 4-(trifluoromethyl)thiophenolate (**5**).

3.3. Experimental

General Information. All reagents were purchased from commercial sources and used as received unless otherwise noted. Acetonitrile (MeCN), tetrahydrofuran (THF), diethyl ether (Et_2O), and pentane were purified by passage through activated alumina columns of an MBraun MB-SPS solvent purification system and stored under an N_2 atmosphere until use. *N*,*N*-dimethylformamide (DMF) was purified with a VAC solvent purifier containing 4 Å molecular sieves and stored under N_2. The ligand *N*-2-(mercaptoethyl)picolinamide ($nmpH_2$; H represents dissociable protons) and its corresponding Ni(II) complex, $[Ni_4(nmp)_4]$ (**1**), were prepared according to the published procedure.[32] All reactions were performed under an inert atmosphere of N_2 using Schlenk line techniques or under an atmosphere of purified N_2 in an MBraun Unilab glovebox. The syntheses of Et_4N^+ thiolate salts from Et_4NCl and the appropriate sodium thiolate were carried out according to previously published methods.[45,46]

Physical Methods. Fourier transform infrared (FTIR) spectra were collected on a ThermoNicolet 6700 spectrophotometer running the OMNIC software. All samples were run as solid samples prepared as pressed KBr pellets. X-band (9.60 GHz) EPR spectra were obtained using a Bruker ESP 300E EPR spectrometer controlled with a Bruker microwave bridge at 10 K. The EPR was equipped with a continuous-flow liquid He cryostat and a temperature controller (ESR 9) made by Oxford Instruments Inc. EPR spectra were simulated using the program QPOWA, as modified by J. Telser.[47] Electronic absorption spectra were collected at 298 K using a Cary-50 spectrophotometer containing a Quantum Northwest TC 125 temperature control unit. The UV-vis samples were prepared in gastight Teflon-lined screw cap quartz cells with an optical pathlength of 1 cm. Cyclic voltammetry (CV) measurements were performed with a PAR Model 273A potentiostat using a Ag/Ag^+ (0.01 M $AgNO_3$/0.1 M $^nBu_4NPF_6$ electrolyte in MeCN)

reference electrode, Pt counter electrode, and a Glassy Carbon working milli-electrode (diameter = 2 mm). CV measurements were performed at ambient temperature using 3.5 or 8.0 mM analyte in DMF under Ar containing 0.1 M $^{n}Bu_4NPF_6$ as the supporting electrolyte. The "Maximize stability" mode and a low-pass 5.3 Hz filter were used in the PAR PowerCV software. Analyte potentials were referenced against a 0.05-0.1 mM ferrocene standard. ^{1}H NMR spectra were recorded in the listed deuterated solvent on a 400 MHz Bruker BZH 400/52 NMR spectrometer or a Varian Unity Inova 500 MHz NMR spectrometer at RT with chemical shifts internally referenced to tetramethylsilane (TMS = $Si(CH_3)_4$), or the residual protio signal of the deuterated solvent.[48] Low-resolution electrospray ionization mass spectrometry (LR-ESI-MS) data were collected using a Bruker Esquire 3000 plus ion trap mass spectrometer. High resolution electrospray ionization mass spectrometry (HR-ESI-MS) data were collected using an Orbitrap Elite system with precision to the third decimal place. Magnetic circular dichroism (MCD) and low temperature absorption data were collected using a Jasco J-715 spectropolarimeter in conjunction with an Oxford Instrument SM-4000 8T magnetocryostat. The sample for these studies was prepared in a 1:4 (v/v) solvent mixture of MeCN and butyronitrile and sparged with dry O_2(g) for 5 min. Glass strain contributions to the MCD signal were removed by taking the difference between spectra collected with the magnetic field aligned parallel and antiparallel to the light-propagation axis. Elemental analysis for C, H, and N was performed at QTI-Intertek in Whitehouse, NJ and ALS Environmental (formerly Columbia Analytical Services) in Tucson, AZ.

(Et_4N)[Ni(nmp)(SPh-*o*-NH_2)] (2). To a 6 mL DMF slurry of **1** (0.1550 g, 0.1622 mmol) was added a yellow DMF solution (2 mL) of (Et_4N)(SPh-*o*-NH_2) (0.1517 g, 0.5962 mmol) dropwise at RT. The DMF gradually took up a burgundy-red color over time. The mixture was

stirred under N_2 for 20 h in a 40 °C water bath. The resulting dark red, mostly homogeneous solution was filtered through Celite to remove unreacted **1**, and the filtrate was evaporated to dryness via short-path vacuum distillation. The resulting brown-black residue was dissolved in 5 mL of MeCN, cooled to -20 °C, and filtered through a plug of Celite. The dark red MeCN filtrate was removed under vacuum, and the residue stirred in 5 mL of Et_2O overnight to afford 0.2093 g (0.3554 mmol, 60%) of an orange-red powder. ^{1}H NMR (500 MHz, $CDCl_3$ containing 0.05% v/v TMS, δ from TMS): 8.49 (d, 1H, J = 10.0 Hz), 8.13 (d, 1H, J = 10.0 Hz), 7.69 (m, 2H), 7.10 (t, 1H, J = 8.0 Hz), 6.75 (t, 1H, J = 9.3 Hz), 6.48 (m, 2H), 4.81 (s, 2H, NH_2), 3.45 (t, 2H, J = 6.5 Hz, -NCH_2CH$_2$S-), 3.22 (br, 9H integrates high due to presence of excess Et_4N^+), 2.32 (t, 2H, J = 6.5 Hz, -NCH$_2$CH_2S-), 1.25 (br, 20H integrates high due to presence of excess Et_4N^+). FTIR (KBr pellet) ν_{max} (cm^{-1}): 3407 (m, ν_{NH}), 3309 (m, ν_{NH}), 2974 (w), 2915 (w), 2846 (w), 1670 (m, ν_{CO} of residual DMF), 1617 (vs, ν_{CO}), 1593 (vs, ν_{CO}), 1568 (m), 1559 (m), 1475 (m), 1437 (w), 1391 (s), 1293 (w), 1172 (w), 1093 (s), 999 (m), 786 (w), 755 (m), 687 (w), 623 (w), 558 (w), 485 (w). UV-vis (MeCN, 298 K) λ_{max}, nm (ε, M^{-1} cm^{-1}): 453 (7200). LR-ESI-MS (*m/z*): [M-Et$_4$N]$^-$ calcd for $C_{14}H_{14}N_3OS_2Ni$, 362.0 (100.0), 364.0 (49.3), 363.0 (18.1), 365.0 (10.3), 366.0 (10.2); found: 361.9 (100.0), 363.9 (47.4), 362.9 (14.4), 364.9 (8.5), 365.8 (9.4). HR-ESI-MS (*m/z*): [M-Et$_4$N]$^-$ calcd for $C_{14}H_{14}N_3OS_2Ni$, 361.994 (100.0), 363.989 (47.6), 362.996 (15.2), 364.992 (7.2), 365.986 (5.4); found: 361.994 (100.0), 363.990 (48.9), 362.997 (15.0), 364.992 (6.9), 365.986 (8.1). Anal. Calcd for $C_{22}H_{34}N_4OS_2Ni•H_2O•MeCN•0.5DMF$: C, 52.00; H, 7.27; N, 13.08. Found: C, 51.39; H, 6.56; N, 13.21.

(Et$_4$N)[Ni(nmp)(SPh-*o*-NH$_2$-*p*-CF$_3$)] (3). To a 6 mL DMF slurry of **1** (0.2380 g, 0.2490 mmol) was added a bright yellow DMF (3 mL) solution of (Et$_4$N)(SPh-*o*-NH$_2$-*p*-CF$_3$) (0.3012 g, 0.9342 mmol). The solvent gradually took up a reddish-brown color over time. The mixture was

stirred under N_2 for 20 h in a 40 °C water bath. The resulting dark red, mostly homogeneous solution was filtered to remove unreacted **1**, and the filtrate was evaporated to dryness via short-path vacuum distillation. The resulting red-burgundy residue was dissolved in 5 mL of THF, cooled to -20 °C, and filtered through a plug of Celite. The dark red THF filtrate was removed under vacuum to result in a black oily material. This residue was triturated with 5 mL of Et_2O or pentane overnight to afford a burgundy-black powder (0.4150 g, 0.6935 mmol, 74%). ^{1}H NMR (500 MHz, CD_3CN, δ from protio solvent): 8.48 (d, 1H, J = 5.0 Hz), 8.11 (d, 1H, J = 10.0 Hz), 7.83 (t, 1H, J = 8.5 Hz), 7.51 (d, 1H, J = 10.0 Hz), 7.25 (t, 1H, J = 8.5 Hz), 6.69 (s, 1H), 6.60 (d, 1H, J = 10.0 Hz), 5.13 (s, 2H, NH_2), 3.22 (t, 2H, J = 6.5 Hz, -NCH_2CH_2S-), 3.15 (q, 23H, integrates high due to presence of excess Et_4N^+, J = 10.0 Hz), 2.12 (t, 2H, J = 6.5 Hz, -NCH_2CH_2S-), 1.19 (t, 34H, integrates high due to presence of excess Et_4N^+, J = 7.5 Hz). FTIR (KBr pellet) ν_{max} (cm^{-1}): 3407 (w, ν_{NH}), 3286 (w, ν_{NH}), 2980 (w), 2917 (w), 2849 (w), 1765 (w), 1620 (vs, ν_{CO}), 1592 (vs, ν_{CO}), 1483 (m), 1432 (m), 1329 (vs), 1102 (m), 1072 (m), 999 (w), 787 (w). UV-vis (MeCN, 298 K) λ_{max}, nm (ε, M^{-1} cm^{-1}): 448 (3800). LR-ESI-MS (*m/z*): $[M\text{-}Et_4N]^-$ calcd for $C_{15}H_{13}F_3N_3OS_2Ni$, 430.0 (100), 432.0 (49.5), 431.0 (19.1), 433.0 (10.8), 434.0 (10.3); found: 429.8 (100.0), 431.8 (48.0), 430.8 (16.1), 432.8 (9.1), 433.8 (8.8). HR-ESI-MS (*m/z*): $[M\text{-}Et_4N]^-$ calcd for $C_{15}H_{13}F_3N_3OS_2Ni$, 429.981 (100.0), 431.977 (47.6), 430.984 (16.2), 432.979 (6.2), 433.974 (5.3); found: 429.982 (100.0), 431.977 (47.2), 430.985 (16.9), 432.980 (8.1), 433.974 (8.1). Anal. Calcd for $C_{23}H_{33}F_3N_4OS_2Ni \bullet 0.5Et_2O$: C, 50.18; H, 6.40; N, 9.36. Found: C, 50.10; H, 6.07; N, 9.09.

(Et_4N)[Ni(nmp)(SPh-*p*-NH_2)] (4). To a 6 mL DMF slurry of **1** (0.1783 g, 0.1866 mmol) was added a pale yellow DMF solution (2 mL) of (Et_4N)(SPh-*p*-NH_2) (0.1709 g, 0.6717 mmol) dropwise at RT. The DMF solvent gradually took up a burgundy-red color over time. The

mixture was stirred under N_2 for 20 h in a 40 °C water bath. The resulting dark burgundy, mostly homogeneous solution was filtered through Celite to remove unreacted **1**, and the filtrate was evaporated to dryness via short-path vacuum distillation. The resulting brown-black residue was dissolved in 5 mL of MeCN, cooled to -20 °C, and filtered through Celite. The burgundy MeCN filtrate was removed under vacuum and the resulting black residue was stirred in 5 mL of Et_2O overnight to afford 0.1741 g (0.3138 mmol, 47%) of an orange-red powder. ^{1}H NMR (500 MHz, $CDCl_3$ containing 0.05% v/v TMS, δ from TMS): 8.60 (d, 1H, J = 10.0 Hz), 7.69 (m, 4H), 7.12 (t, 1H, J = 10.0 Hz), 6.41 (d, 2H, J = 10.0 Hz), 3.44 (t, 2H, J = 6.5 Hz, -NCH_2CH_2S-), 3.37 (s, 2H, NH_2), 3.31 (q, 10H, integrates high due to presence of excess Et_4N^+, J = 10.0 Hz), 2.31 (t, 2H, J = 6.5, -NCH_2CH_2S-), 1.28 (t, 15H, integrates high due to presence of excess Et_4N^+, J = 7.5 Hz). FTIR (KBr pellet) ν_{max} (cm^{-1}): 3315 (m, ν_{NH}), 3197 (m, ν_{NH}), 2983 (w), 2912 (w), 2841 (w), 1671 (m, ν_{CO} of residual DMF), 1616 (vs, ν_{CO}), 1592 (vs, ν_{CO}), 1486 (s), 1455 (m), 1396 (m), 1268 (w), 1174 (w), 1096 (s), 1002 (w), 817 (w), 794 (w), 766 (w), 718 (w), 704 (w), 688 (w), 631 (w). UV-vis (MeCN, 298 K), λ_{max}, nm (ε, M^{-1} cm^{-1}): 458 (6100). LR-ESI-MS (*m/z*): [M-Et_4N]$^-$ calcd for $C_{14}H_{14}N_3OS_2Ni$, 362.0 (100.0), 364.0 (49.3), 363.0 (18.1), 365.0 (10.3), 366.0 (10.2); found: 361.9 (100.0), 363.9 (43.8), 362.9 (19.1), 364.9 (10.0), 365.9 (7.0). HR-ESI-MS (*m/z*): [M-Et_4N]$^-$ calcd for $C_{14}H_{14}N_3OS_2Ni$, 361.994 (100.0), 363.989 (47.6), 362.996 (15.2), 364.992 (7.2), 365.986 (5.4); found: 361.994 (100.0), 363.989 (47.3), 362.997 (15.5), 364.992 (6.5), 365.986 (8.0). Anal. Calcd for $C_{22}H_{34}N_4OS_2Ni$•H_2O•0.5THF•0.1DMF: C, 52.61; H, 7.40; N, 10.35. Found: C, 52.74; H, 7.91; N, 10.37.

(Et_4N)[Ni(nmp)(SPh-*p*-CF_3)] (5). To a 6 mL DMF slurry of **1** (0.0849 g, 0.0888 mmol) was added a pink DMF solution of (Et_4N)(SPh-*p*-CF_3) (0.1023 g, 0.3328 mmol) dropwise at RT. The solvent gradually took up a burgundy-red color over time. The mixture was stirred under N_2

for 20 h in a 40 °C water bath. The resulting dark red, mostly homogeneous solution was filtered through Celite to remove unreacted **1**, and the filtrate was evaporated to dryness via short-path vacuum distillation. The resulting brown-black residue was dissolved in 5 mL of THF, cooled to -20 °C, and filtered through a plug of Celite. The dark red THF filtrate was removed under vacuum and the resulting dark black residue was stirred in 5 mL of Et_2O overnight to afford 0.0858 g (0.157 mmol, 47%) of a burgundy-black sticky material. ^{1}H NMR (400 MHz, CD_3CN, δ from protio solvent): 8.53 (d, 1H, J = 6.0 Hz), 8.09 (d, 2H, J = 8.4 Hz), 7.83 (t, 1H, J = 8.0 Hz), 7.52 (d, 1H, J = 7.6 Hz), 7.24 (t, 1H, J = 7.0 Hz), 7.17 (d, 2H, J = 8.0 Hz), 3.23 (t, 2H, J = 6.5 Hz, -NCH_2CH$_2$S-), 3.15 (q, 14H, integrates high due to presence of excess Et_4N^+, J = 7.6 Hz), 2.16 (br, 4H, integrates high due to overlap with H_2O, -NCH$_2$CH_2S-), 1.19 (t, 20H, integrates high due to presence of excess Et_4N^+, J = 8.0 Hz). FTIR (KBr pellet) ν_{max} (cm^{-1}): 2981 (w), 2914 (w), 2839 (w), 1670 (s, ν_{CO} of residual DMF), 1623 (vs, ν_{CO}), 1593 (vs, ν_{CO}), 1560 (m), 1486 (m), 1458 (w), 1385 (s), 1323 (s), 1274 (w), 1256 (w), 1183 (w), 1155 (w), 1086 (s), 1058 (m), 1009 (w), 826 (w), 761 (w), 686 (w). UV-vis (MeCN, 298 K), λ_{max}, nm (ε, M^{-1} cm^{-1}): 432 (4600). LR-ESI-MS (*m/z*): [M-Et_4N]$^-$ calcd for $C_{15}H_{12}F_3N_2OS_2Ni$, 415.0 (100.0), 417.0 (49.4), 416.0 (18.7), 418.0 (10.6), 419.0 (10.3); found: 414.8 (100.0), 416.8 (48.0), 415.8 (16.8), 417.8 (8.5), 418.7 (8.9). HR-ESI-MS measured with Na^+ salt (*m/z*): calcd for $C_{15}H_{12}F_3N_2OS_2Ni$, 414.970 (100.0), 416.966 (47.6), 415.973 (16.2), 417.968 (6.2), 418.963 (5.3); found: 414.970 (100.0), 416.965 (47.3), 415.973 (15.8), 417.968 (7.1), 418.962 (8.1). Anal. Calcd for $C_{23}H_{32}F_3N_3OS_2Ni$: C, 50.56; H, 5.90; N, 7.69. Found: C, 49.41; H, 5.99; N, 6.29. A reasonable fit to C, H, N could not be obtained due to the oily nature of the resulting product.

X-ray Crystallographic Data Collection and Structure Solution and Refinement. Red needle-like crystals of **1** were grown by Et_2O layering over a CD_3OD solution of

$Na_3[\{Ni(nmp)\}_3(BTAS)]$ ($BTAS^{3-}$ is the trianion of *N*[1],*N*[3],*N*[5]-tris(2-mercaptoethyl)benzene-1,3,5-tricarboxamide) at RT under aerobic atmosphere. Dark red blade-like crystals of **2** were grown by slow vapor diffusion of Et_2O into a solution of **2** in DMF:C_6H_5Cl (1:1) at RT. Additionally, dark red blade crystals of **4** were grown by slow vapor diffusion of Et_2O into a solution of **4** in THF:DMF (~4:1) at RT. Suitable crystals were mounted on a glass fiber. The X-ray intensity data were measured at 100 K on a Bruker SMART APEX II X-ray diffractometer system with graphite-monochromatic Mo Kα radiation (λ = 0.71073 Å) using ω-scan technique controlled by the SMART software package.[49] The data were corrected for Lorentz and polarization effects[50] and integrated with the manufacturer's SAINT software. Absorption corrections were applied with the program SADABS.[51] Subsequent structure refinement was performed using the SHELXTL 6.1 solution package operating on a Pentium computer. The structure was solved by direct methods using the SHELXTL 6.1 software package.[52,53] All non-hydrogen atoms were refined anisotropically.[54] Non-hydrogen atoms were located from successive difference Fourier map calculations. In the structure of **1**, two carbon atoms (C1 and C2) and one oxygen atom (O1) were found disordered in two sets of each: labeled for the carbon atoms as C1 and C2 (one set) and C1′ and C2′ (other set); and labeled for the oxygen atom as O1 (one set) and O1′ (other set), respectively. The two sets for the atoms (C1 and C2) were divided using the PART commands and proper restraints. The set of C1 and C2 has 46% occupancy while the other (C1′ and C2′) has 54% occupancy. The occupancies for O1 and O1′ are set at 50% each. The structure of **4** has two distinct, but chemically indistinguishable Ni complexes. Selected data and metric parameters for complexes **1**, **2**, and **4** are summarized in Table S3.1 in the Supporting Information and Table 3.1, respectively. Perspective views of the complexes were obtained using ORTEP.[55]

Table 3.1. Selected bond distances (Å) and bond angles (deg) for $[Ni_4(nmp)_4]$ (**1**), $(Et_4N)[Ni(nmp)(SPh\text{-}o\text{-}NH_2)]$ (**2**), and $(Et_4N)[Ni(nmp)(SPh\text{-}p\text{-}NH_2)]$ (**4**).

	1	**2**	**4**[a]
Ni(1)-N(1)	1.866(4)	1.8750(16)	1.8698(14)
Ni(1)-N(2)	1.951(4)	1.9418(16)	1.9450(14)
Ni(1)-S(1)	2.1500(12)	2.1386(6)	2.1474(5)
Ni(1)-S(2)	2.2170(12)	2.2173(6)	2.2160(5)
N(1)-Ni(1)-N(2)	83.47(16)	83.36(7)	83.12(6)
N(1)-Ni(1)-S(1)	87.33(12)	88.62(5)	87.88(4)
N(1)-Ni(1)-S(2)	178.39(14)	178.74(5)	177.51(4)
N(2)-Ni(1)-S(1)	168.73(12)	171.97(5)	168.97(4)
N(2)-Ni(1)-S(2)	95.78(11)	97.60(5)	99.36(4)
S(1)-Ni(1)-S(2)	93.25(5)	90.41(2)	89.621(18)
C(9)-S(2)-Ni(1)	108.44(17)	104.66(6)	107.39(6)

[a]Parameters for one of the two unique, but chemically similar Ni complexes observed in the asymmetric unit of **4**.

Computations. All computations were performed using the ORCA 2.9.0 program developed by Dr. Frank Neese.[56] The crystallographically determined coordinates for **2** provided the initial structures for the computational models **II** and its one-electron oxidized derivative, $\mathbf{II^{ox}}$. Both models were then subjected to unconstrained geometry optimizations within the framework of density functional theory (DFT) using Becke's three-parameter hybrid functional

and the Lee-Yang-Parr correlation functional (B3LYP).[57,58] Ahlrichs' valence triple-ζ basis set, TZV(P) basis set,[59,60] was chosen for the Ni, N, and S atoms, respectively, while Ahlrichs' polarized split valence and auxiliary basis sets,[59] SV(P) and SV/C, were selected for all of the remaining atoms. The spin-restricted formalism was chosen for **II**, while the spin-unrestricted formalism was used for $\mathbf{II^{ox}}$, which was modeled as $S = ½$. Single-point DFT calculations on the geometry-optimized models were performed using the same functional and basis sets as those used in the geometry optimizations. The Pymol program[61] was utilized to generate isosurface plots of MOs and spin densities with isodensity values of 0.05 a.u. and 0.005 a.u., respectively.

The ORCA 2.9.0 program was also employed to compute EPR parameters for the geometry-optimized model $\mathbf{II^{ox}}$ by using the DFT-based coupled-perturbed self-consistent field approach in conjunction with the B3LYP functional. This calculation was performed using the CP(PPP) basis set[62,63] for Ni, Kutzelnigg's NMR/EPR (IGLO-III) basis set[64] for all N and S atoms, and the TZV(P) basis set for the remaining atoms.

Oxidation of 3. To a solution containing 10.9 mg of **3** (0.0194 mmol) stirring in 4 mL of DMF was added ceric ammonium nitrate (CAN) dropwise (1.748 mL of a 10.0 mM DMF solution, 0.0175 mmol) at RT. Upon addition of CAN, the red-brown color associated with the Ni(II)-N_2S_2 complex was replaced by a dark green color. The mixture was stirred for another 15 min at RT and filtered through a 0.2 μm nylon filter to yield a green transparent DMF solution. A red solid of a color consistent with a minor amount of **1** was evident in the filter. The oxidation was monitored by UV-vis and EPR spectroscopy.

Oxidation of 2. Chemical oxidation of **2** was performed in the same manner as with **3** except for using 11.2 mg (0.0227 mmol) of **2** and 2.045 mL of CAN (10.0 mM DMF solution,

0.0205 mmol). The red solution of **2** darkened to green upon addition of CAN. Within minutes the green color paled with the appearance of a red precipitate.

Oxidation of 4. Chemical oxidation of **4** was performed in the same manner as with **3** except for using 9.6 mg (0.020 mmol) of **4** and 1.752 mL of CAN (10.0 mM DMF solution, 0.0175 mmol). The orange-red solution of **4** paled to light orange upon addition of CAN with the appearance of a red precipitate.

Oxidation of 5. Chemical oxidation of **5** was performed in the same manner as with **3** except for using 8.9 mg (0.016 mmol) of **5** and 1.459 mL of CAN (10.0 mM DMF solution, 0.0146 mmol). The orange-red solution of **5** paled to light orange upon addition of CAN with the appearance of a red precipitate.

Reactivity

UV-vis monitoring of 3 and 3^{ox} with NaN_3 and N-methylimidazole. To a 5 mM DMF stock (2.5 mL) of **3**, was added 10 equiv of N-methylimidazole (N-MeIm) or NaN_3, and the UV-vis spectrum was recorded. Solutions were oxidized in the same manner as above in the presence of 10 equiv of N-MeIm or NaN_3 to observe any changes in the electronic absorbance profile to indicate anion binding to the metal center.

Reactivity with KO_2. To 5 mM DMF solutions of **3** or $\mathbf{3^{ox}}$ (generated by adding one equiv of CAN to **3**) was added one equiv of KO_2 in DMF containing 18-crown-6 ether (4.1 equiv).[65] Workup of the reaction is as stated in Chart S3.2 in the SI.

3.4 Results and Discussion

Synthesis. In previous work,[32,33] an *S*,*S*-bridged Ni-nmp unit was used as a metallosynthon to generate 4C planar Ni(II)-N_2S_2 complexes of the general formula

$[Ni(nmp)(SR)]^-$ as active site models of $NiSOD_{red}$. The ligand nmp^{2-} is a tridentate chelate that contains pyridine-N, carboxamide-N, and alkyl thiolate-S donors that replicate the asymmetric ligand environment derived from His1 and Cys2 in the enzyme. In these reports, various ways of changing R on the monodentate thiolate (analogous to Cys6) were explored, and most syntheses were based on splitting a putative $[Ni_2(nmp)_2]$ *S,S*-bridged dimeric complex with various exogenous thiolate ligands. Elemental analysis and FTIR data of the solid were in-line with the proposed formula, but the poor solubility of this complex precluded more detailed spectroscopic and structural analyses. Based on a structure reported herein (vide infra), we describe this complex to be a tetrameric *S,S*-bridged species $[Ni_4(nmp)_4]$ (**1**) (Figure 3.2). While this result alters our prior synthetic schemes, it does not change the ratio of exogenous thiolate-to-Ni(nmp) used, i.e., 1:1 when considering single Ni(nmp) units in the *S,S*-bridged complex. As such, complexes **2-5** were synthesized by reacting a 40 °C DMF slurry of **1** with four equiv of the Et_4N^+ salts of various thiolates to yield the monomeric Ni(II) complexes in modest-to-good yields (50-75%) (Scheme 3.1). All complexes were isolated as analytically-pure (except **5**), dark-red to orange-red solids of moderate stability to air. However, decomposition to the free thiol and **1** occurred when dissolved in protic solvents such as MeOH or H_2O even under anaerobic conditions.

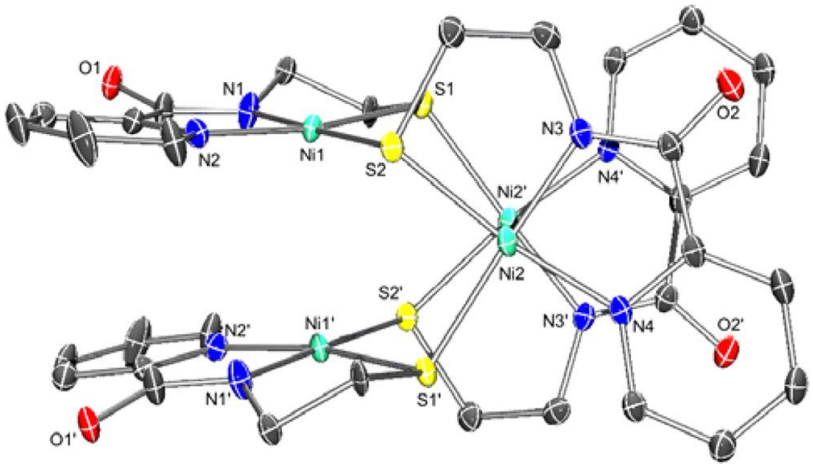

Figure 3.2. ORTEP of $[Ni_4(nmp)_4]$ (**1**) with the atom labeling scheme at 50% thermal probability. H atoms are omitted for clarity.

Scheme 3.1. Synthesis of Ni(II) complexes. R = SPh-*o*-NH_2 (**2**), SPh-*o*-NH_2-*p*-CF_3 (**3**), SPh-*p*-NH_2 (**4**), and SPh-*p*-CF_3 (**5**).

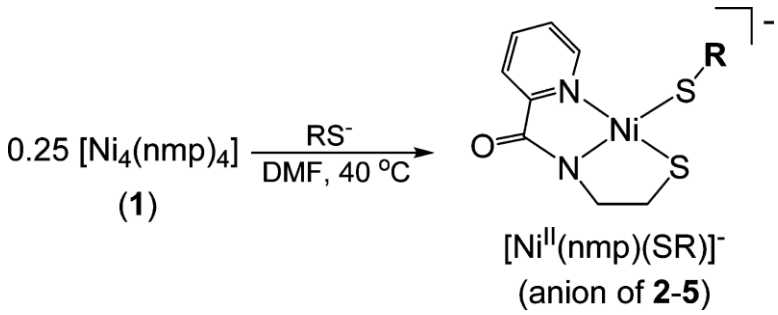

Spectroscopic Properties. Complexes **2-5** are soluble in polar solvents such as DMF and MeCN to form deeply colored red-brown solutions arising from charge-transfer (CT) bands in the 430-460 nm range (ε: 3800-7200 M^{-1} cm^{-1} in MeCN at 298 K). $NiSOD_{red}$ displays an absorption profile with a λ_{max} at 450 nm (ε: 480 M^{-1} cm^{-1}) and a shoulder at 543 nm (ε: 150 M^{-1}

cm^{-1}) arising from *d-d* transitions,[10] a spectroscopic benchmark of 4C planar Ni(II) centers in an N_2S_2 coordination environment.[40] These ligand-field bands are masked in **2-5** by the intense CT features that involve electronic transitions between py-N and Ni(II).[33] Further solution measurements such as ^{1}H NMR revealed that all complexes are diamagnetic, as expected for a 4C planar Ni(II) ion (see Figures S3.5, S3.7, S3.9, and S3.11 in the Supporting Information (SI)). These results do not exclude higher coordination numbers, as low-spin tbp or square-pyramidal Ni(II) would also be $S = 0$, but NMR results of known *o*-aminothiophenolate N,S-coordinated planar Ni(II) complexes exhibit shifts in the NH_2 resonance (δ_{NH2}) by +1.4 ppm upon coordination.[66] Additionally, the symmetric and asymmetric N–H stretches (ν_{NH}) of the NH_2 group red-shift by ~200 cm^{-1} upon coordination.[66] The NH_2 proton resonance is close (+0.15 - 0.28 ppm) to the value obtained for the free thiolate and there are no significant changes in ν_{NH} in **2**-**4**. These minor changes in δ_{NH2} and ν_{NH} confirm that no Ni(II)–NH_2Ph bond exists in **2**-**4** under the conditions used.

Structural Characterization. The tetrameric complex **1** and monomeric complexes **2** and **4** have been characterized by X-ray diffraction, the details of which can be found in the experimental section, Table 3.1, and Table S3.1 of the SI. Complex **1** crystallizes with four separate Ni(nmp) fragments bridged by the alkyl-S of another Ni(nmp) complex (Figure 3.2). A summation of the significant bond lengths and angles is provided in Table 3.1 and a comparison with other monomeric $[Ni(nmp)(SR)]^-$ complexes is provided in Table 3.2. The tetramer is formed through specific Ni–S–Ni linkages (e.g. Ni1–S2–Ni2–S1′), such that each nmp-S bridges a different 4C planar Ni(II) ion. Compared to other reported $[Ni(nmp)(SR)]^-$ structures with NiN_2S_2 coordination,[32,33] the average Ni–$N_{carboxamide}$ distance (1.862 Å) is significantly shorter than that for Ni–N_{py} (1.943 Å), due to strong σ-donation by the carboxamide ligand. This

property, along with the monodentate nature of SR, generally results in a longer Ni–S_{exo} versus Ni–S_{nmp} bond distance. Indeed, this bond is considerably longer in **1** (2.208 Å) than the Ni–S bond originating from the coordinated nmp^{2-} ligand (2.155 Å). In this case, S_{exo} represents a metallothiolate from another Ni(nmp) unit instead of an exogenously added thiolate ligand in prior reports. The average Ni---Ni separation is 3.4 Å, which precludes any direct Ni–Ni interaction.

Table 3.2. Selected bond distances (Å) for $[Ni(nmp)(SR)]^-$ NiSOD model complexes.[a]

R	Ni-$N_{carboxamide}$	Ni-N_{py}	Ni-S_{nmp}	Ni-S_{exo}
SPh-*p*-Cl	1.8638(14)	1.9470(14)	2.1492(5)	2.2139(4)
S^{t}Bu	1.882(2)	1.9635(19)	2.1629(7)	2.1938(7)
S-*o*-babt[b]	1.877(3)	1.947(3)	2.1518(12)	2.1939(14)
S-meb[c]	1.863(7)	1.944(7)	2.156(3)	2.172(3)
SPh-*o*-NH_2	1.8750(16)	1.9418(16)	2.1386(6)	2.2173(6)
SPh-*p*-NH_2	1.8698(14)	1.9450(14)	2.1474(5)	2.2160(5)
Average	1.872 ± 0.008	1.948 ± 0.008	2.151 ± 0.008	2.201 ± 0.018

[a]Bond distances reported for Ni(1), N(1), N(2), S(1), and S(2) of unit cell. [b]S-*o*-babt = anion of *o*-benzoylaminobenzenethiol. [c]S-meb = anion of *N*-(2-mercaptoethyl)benzamide

Analogous to previously published $[Ni(nmp)(SR)]^-$ structures,[32,33] **2** and **4** (Figures 3.3 and 3.4, respectively and Figure S3.1 in the SI) demonstrated distorted 4C planar Ni(II) centers with two N- and two S-ligands in a *cis* disposition resulting in a Ni(II)-N_2S_2 coordination sphere

as in $NiSOD_{red}$. Crystallographic details and selected bond distances and angles are presented in Tables 3.1-3.2. Complex **4** crystallizes with two unique, but chemically equivalent Ni(II)-N_2S_2 complexes. Bond distances are comparable to **1** and other $[Ni(nmp)(SR)]^-$ structures ($Ni–N_{carboxamide}$: 1.8750 Å (**2**), 1.8698 Å (**4**); $Ni–N_{py}$: 1.9418 Å (**2**), 1.9450 Å (**4**); $Ni–S_{nmp}$: 2.1386 Å (**2**), 2.1474 Å (**4**); $Ni–S_{exo}$: 2.2173 Å (**2**), 2.2160 Å (**4**); see Table 3.2 for a comparison with all structurally characterized Ni-nmp complexes) and reflect a trend in the electronic nature or Lewis basicity of the differing donor atoms. To emphasize the strong-field nature of the carboxamide donor, other 4C planar $NiSOD_{red}$ models ($N = 4$)[29,31,35,43] with multidentate chelates exhibit short $Ni–N_{carboxamide}$ bonds (avg: 1.861 Å) and long $Ni–S_{trans\text{-}carboxamide}$ bonds (avg: 2.175 Å) in their crystal structures. Thus, the lengthening of the $Ni–S_{exo}$ bonds in **2** and **4** is not solely due to the monodentate S_{exo} coordination. $NiSOD_{red}$ exhibits similar distances (average from the two reported *Streptomyces* structures): $Ni–NH_2$(His1): 1.97 ± 0.14 Å; $Ni–N_{peptide}$(Cys2): 1.93 ± 0.02 Å; Ni–S(Cys2): 2.20 ± 0.06 Å; Ni–S(Cys6 – *trans* to peptide-N): 2.19 ± 0.01 Å.[11,12] The trends expected for the different Ni–N and Ni–S bonds are presumably muted in the enzyme structures due to poor resolution and the redox heterogeneity in the crystals (equal mix of Ni(II) and Ni(III) ions). In **2** and **4**, the closest $Ni–NH_2$ distance is 4.4 Å, establishing the absence of any five-coordinate species in the solid-state. The $Ni\cdots N_{His}$ distance is also long in $NiSOD_{red}$, 4.26 Å (PDB: 1T6U) and 3.81 Å (PDB: 1Q0D), indicative of the non-bonding nature of this potential N-donor in the enzyme. Due to the *ortho*-positioning of the aniline-NH_2 in **2**, the N and coordinated S_{exo} are separated by 3.024 Å (sum of the van der Waals radii for N and S is 3.55 Å), which would suggest an intramolecular hydrogen bond with the ligated S. However, the N–H–S angle is estimated to be 110° (if H is placed in an ideal position), suggesting relatively poor orbital overlap between the donor-acceptor pair. Strong hydrogen bonds are usually linear in

nature, i.e., ∠N–H···S ≈ 180°.[67] To emphasize the importance of this angle, hydrogen bonding to coordinated S-ligands in other NiSOD model compounds usually results in a decrease by 0.02-0.03 Å in the Ni–S distance due to relief of the Ni(dπ)-S(pπ) anti-bonding interaction, as the S lone pair is engaged in the hydrogen bond.[33,41] No such contraction of the Ni–S bonds was observed when compared to the non-hydrogen-bonded complex **4**. Collectively analyzing the six structurally characterized complexes in this family (Table 3.2) reveal that distances to the nmp^{2-} ligating atoms are largely invariable. The largest variations appear in S_{exo} (Ni–S(avg.): 2.201 ± 0.018 Å), which range from 2.172 to 2.217 Å and generally correlate with the electronic nature of this particular S-donor.

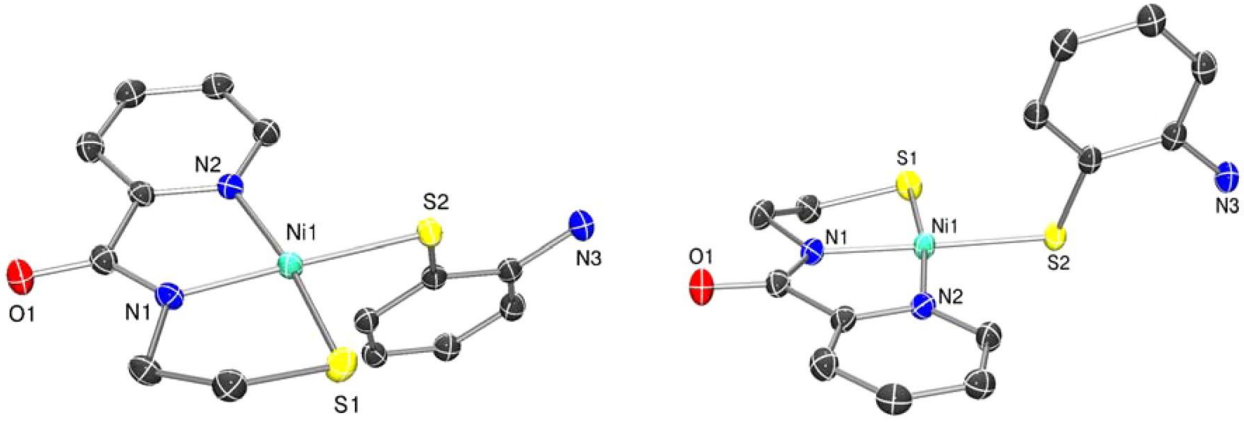

Figure 3.3. Different views of the ORTEP of the anion of $(Et_4N)[Ni(nmp)(SPh\text{-}o\text{-}NH_2)]$ (**2**) with the atom labeling scheme at 50% thermal probability. H atoms are omitted for clarity.

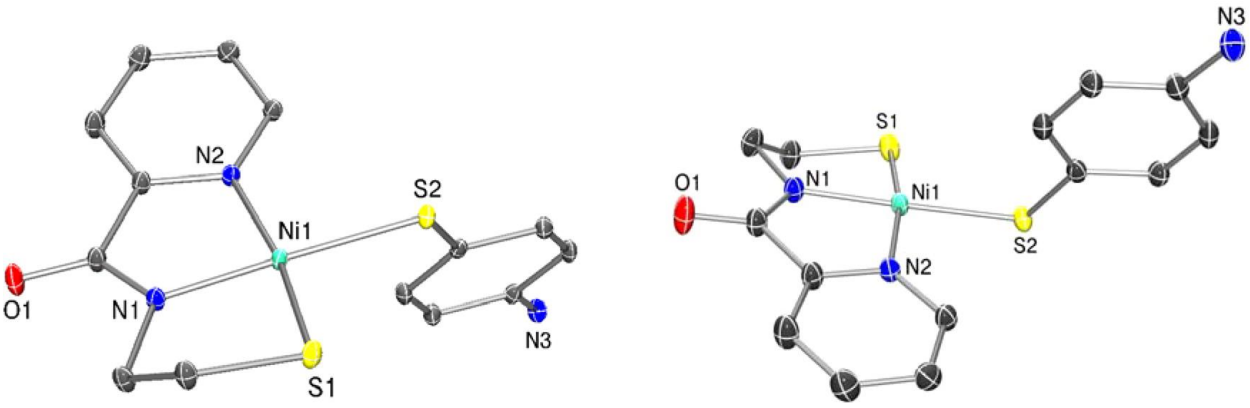

Figure 3.4. Different views of the ORTEP of the anion of $(Et_4N)[Ni(nmp)(SPh\text{-}p\text{-}NH_2)]$ (**4**) with the atom labeling scheme at 50% thermal probability. H atoms are omitted for clarity.

Electrochemistry. To assess the role of the *o*-NH_2 group in the electrochemical activity of the Ni-nmp complexes, we performed cyclic voltammetry (CV) on **2**-**5**. Previously reported $[Ni^{II}(nmp)(SR)]^-$ complexes display irreversible waves in their CVs with cathodic and anodic peaks assigned to redox activity associated with the coordinated RS^- ligand, i.e., $[Ni^{II}(nmp)(SR)]^- \rightarrow 0.25\ [Ni^{II}_4(nmp)_4]$ (**1**) + 0.5 RSSR.[32,33] Similar CVs and redox assignments were observed with the peptide-based $[Ni^{II}(GC\text{-}OMe)(SR)]^-$ (GC-OMe is the dianion of H_2N-Gly-L-Cys-OMe) complexes.[34] In both cases, R represented simple aryl/alkyl thiolates or more complex thiolates with appended hydrogen-bonding moieties. In this study, we anticipated that providing a potential N-donor ligand from the *o*-aminothiophenolate would provide a viable mechanism to capture an oxidized species related to $NiSOD_{ox}$.

Representative CVs are displayed in Figures 3.5-3.6 and Figures S3.2-S3.3 in the SI. All CVs were recorded in DMF at RT and *E* values are reported versus an externally referenced ferrocene/ferrocenium (Fc/Fc^+) couple using a glassy carbon working electrode and 0.1 M $^nBu_4NPF_6$ as the supporting electrolyte. Electrochemical measurements on **4** and **5**, complexes

without an *o*-NH_2 group, revealed irreversible waves (ΔE_p: ~ 1.5 V) in the CV that are due to S_{exo} redox. The CV of **5** (containing the *p*-CF_3 group), for example, displayed two distinct electrochemical events at potentials of -1.64 V (E_{red}) and -0.19 V (E_{ox}) (Figure 3.5) that we assign as the RS• (or 0.5 RSSR) → RS^- and RS^- → RS• (or 0.5 RSSR) electrochemical reactions, respectively. These values are on par with reported potentials for simple organic disulfides such as PhSSPh (E_{ox}: -0.49, E_{red}: -2.12 V vs. Fc/Fc^+ in DMF)[68] and even more structurally complex thiolates that display qualitatively similar CVs.[69] The CV of a related 4C planar Ni(II)-NS_3 complex, $[Ni(pdmt)(SPh)]^-$ (pdmt = pyridine-2,6-dimethanethiolate) that also owes its electrochemical activity to the monodentate thiolate PhS^-, resembles the CV of **5** with values (E_{ox}: -0.47, E_{red}: -1.73 V in DMF) ~ +0.20 V shifted from that of free PhSSPh (above) due to coordination to Ni(II).[70] The comparative positive shift of ~0.40 V in the $E_{red/ox}$ associated with **5** from PhSSPh is in-line with the electron-withdrawing *p*-CF_3 substituted aryl thiolate ligand. Complex **4** with the *p*-NH_2 substitution on SR behaved similarly (E_{ox}: -0.51 V in DMF) with additional low current intensity waves that we have yet to identify (Figure S3.2 in the SI). Again, comparison with *p*-NH_2-PhSSPh-*p*-NH_2 (E_{ox}: -0.88, E_{red}: -2.33 V vs. Fc/Fc^+ in DMF)[68] revealed a slight shift upon coordination of the thiolate to Ni(II). Regardless, the CVs of **4** and **5** only reflect ligand-based electrochemistry with no indication of a Ni(III/II) process. Additional verification of the reactions displayed in Scheme 3.2 (left side) comes from bulk oxidation experiments with CAN or Fc^+, which yielded **1** and the corresponding disulfide in near stoichiometric yield. Collectively, the $[Ni^{II}(nmp)(SR)]^-$ complexes with simple alkyl/aryl R-groups do not go through any observable Ni(III) state, as all oxidation chemistry is associated with S_{exo} (even the electron-deficient S_{exo} in **5**) and is suggestive of the high S-character in the HOMO of these complexes.

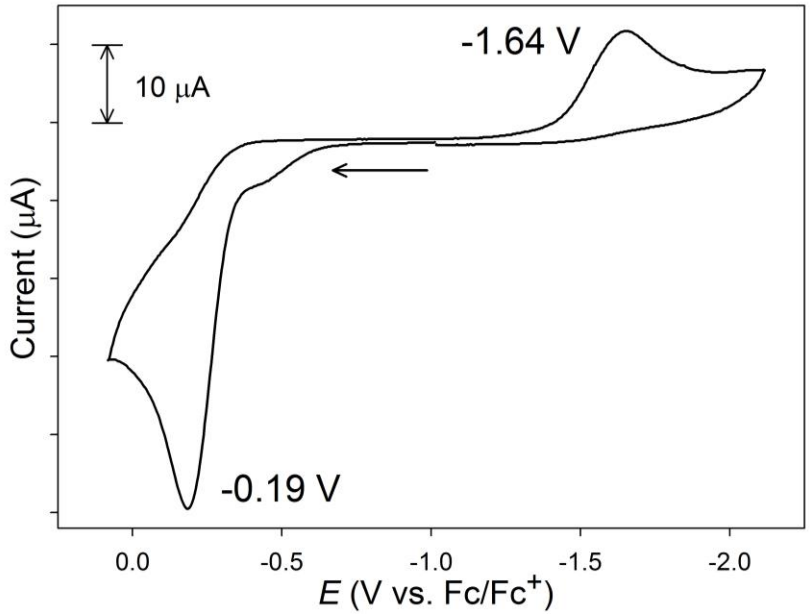

Figure 3.5. CV of an 8 mM solution of **5** in DMF at RT (glassy carbon working electrode, 0.1 M $^{n}Bu_4NPF_6$ as supporting electrolyte, 100 mV/s scan speed). The arrow shows the direction of the scan.

Scheme 3.2. General redox activity of $[Ni(nmp)(SR)]^{-}$ complexes.

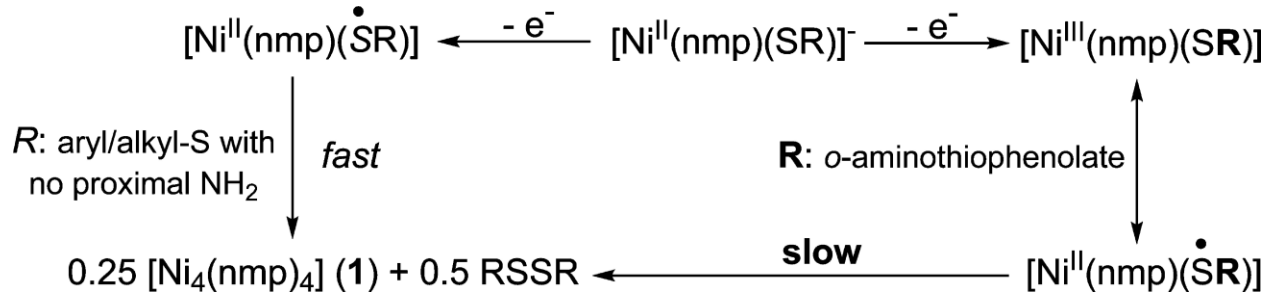

The CVs of **2** and **3** displayed similar irreversible waves with the exception of a quasi-reversible wave observed at $E_{1/2}$ = -0.69 V and -0.43 V for **2** and **3**, respectively (DMF, RT), that

was slightly superimposed on E_{ox}. As expected, the oxidation of **2** is easier than **3** because of the *p*-CF_3 substitution on S_{exo}. Since the free *o*-aminothiophenolate is irreversibly oxidized at more positive potentials, this $E_{1/2}$ may be assigned as a metal-centered Ni(III/II) electron-transfer process. For simplicity, we will limit our discussion to complex **3**, but similar CVs were observed for **2** (see Figure S3.3 in the SI). The possibility of isolating and characterizing an oxidized NiSOD model, as suggested by the electrochemistry, led us to generate this species (termed $\mathbf{3^{ox}}$) by chemical oxidation with CAN and to study its redox properties. Interestingly, the CV of in situ generated $\mathbf{3^{ox}}$ displayed a redox-couple at $E_{1/2}$ = -0.43 V (ΔE_p ~ 0.060 V; and i_{pa}/i_{pac} ≈ 1) that was remarkably similar to the CV of **3** (Figure 3.6 and Figure S3.3 in the SI). Additional metrics such as the linear (r^2 = 0.991, of $\mathbf{3^{ox}}$) i_p vs. $v^{1/2}$ plot support that this couple is a reversible, diffusion-controlled process. Scanning from either side of the isolated $E_{1/2}$ does not result in any changes (Figure 3.6). It is important to reiterate that $[Ni^{II}(nmp)(SR)]^-$ complexes do not exhibit any reversibility in their CVs (see Figure 3.5). The appearance of such a wave in the CV of **3** is thus a new feature in these otherwise isostructural NiSOD model complexes. A unique feature of **3** is the presence of the *o*-NH_2 group that must be the stabilizing feature to allow observation of such an oxidized species on the CV timescale. We propose that this redox event is due to one of the following couples: (i) $[Ni^{II}(nmp)(SR)]^-/[Ni^{III}(nmp)(SR)]$ or (ii) $[Ni^{II}(nmp)(SR)]^-/[Ni^{II}(nmp)(•SR)]$. In case (ii), the *o*-$NH_2$ group supports a coordinated S-radical to prevent formation of RSSR and **1** that would result in the typical irreversible CVs (Scheme 3.2). Of course, a resonance description of $[Ni^{III}(nmp)(SR)] \leftrightarrow [Ni^{II}(nmp)(•SR)]$ is the more realistic possibility (vide infra) (Scheme 3.2, right side).

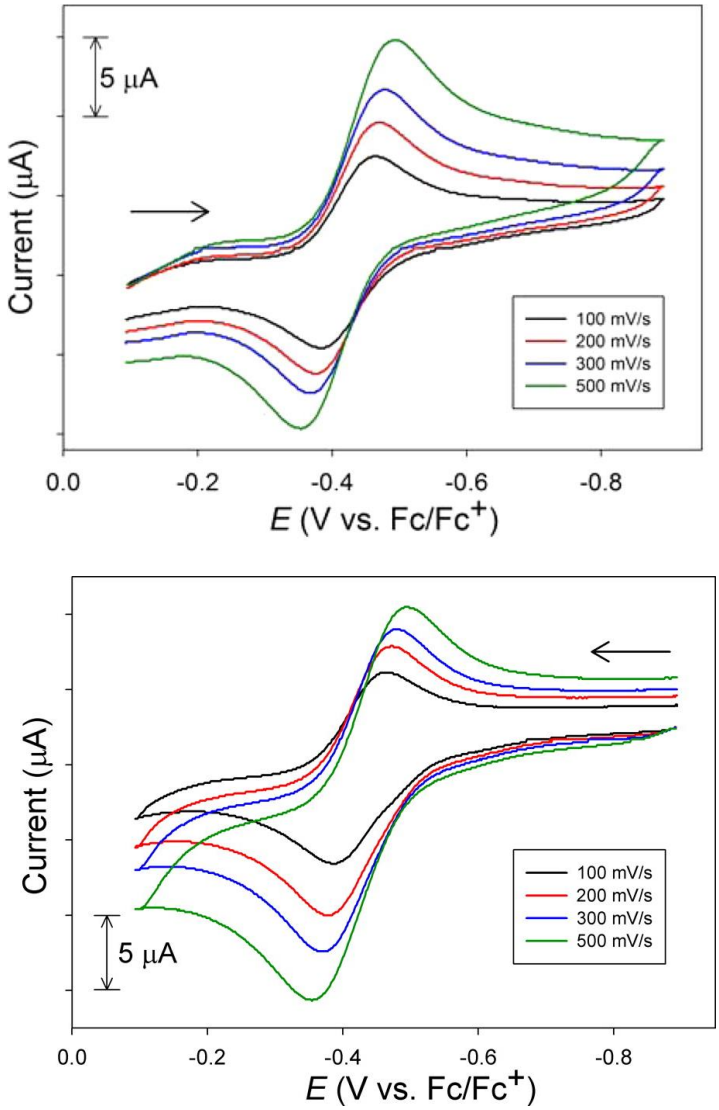

Figure 3.6. CV of a 3.5 mM solution of $\mathbf{3^{ox}}$ in DMF at RT from different scan directions (see arrow, glassy carbon working electrode, 0.1 M $^{n}Bu_4NPF_6$ as supporting electrolyte).

Properties of $\mathbf{3^{ox}}$. Exposure of DMF solutions of **2** or **3** to air or O_2(g) resulted in an immediate color change of the solution from red to green accompanied by the eventual formation of a red precipitate. These solutions afforded a broad, low-energy feature at ~900 nm in the RT electronic absorption spectrum. This transformation occurs on the minute (**2,** full formation of **1**

within minutes) or hour (**3**, ~70% **1** after 24 h) timescale with the red precipitate confirmed to be **1**, suggesting the same ultimate fate as seen with other $[Ni(nmp)(SR)]^-$ complexes (Scheme 3.2). The difference here, however, is that transient oxidized complexes are spectroscopically observable. Furthermore, chemical reduction of in situ generated $\mathbf{3^{ox}}$ with $[Co(Cp)_2]$ resulted in regeneration of the reduced species **3** as verified by UV-vis, ^{1}H NMR, and ESI-MS experiments. Thus, bulk chemical oxidation and reduction mirrored the electrochemical observations and was also a reversible process. Due to the longer lifetime of $\mathbf{3^{ox}}$, we limit our discussion below to this species although similar spectroscopic observations were noted for **2**.

To better identify the oxidized complex, we performed in situ spectroscopic characterization of the reaction mixture after chemically oxidizing **3** with oxidants such as CAN or Fc^+ salts. For example, addition of a stoichiometric amount of CAN to a DMF solution of **3** at RT immediately generated a green solution with a broad and intense absorption band at 910 nm concomitant with disappearance of the CT band associated with **3** at 450 nm (Figure 3.7). Low-energy bands in this region have been observed in 4C planar Ni(III) complexes with N_2S_2 dicarboxamido-dithiolato coordination and were attributed to S-to-Ni(III) CT transitions,[44] a common spectroscopic feature for Ni(III)-N/S coordination complexes. Interestingly, Ni(II)-N_2S_2 complexes containing *o*-aminothiophenolate ligands with radical character also exhibit a low-energy band in a similar range in their UV-vis spectra. However, it must be noted that these bands are observed for the Ni-coordinated *o*-iminosemiquinonato form that would require the loss of two protons and one electron from the original *o*-aminothiophenol (see Chart S3.1 in the SI).[66] A close structural comparison of the C–C (avg: 1.397 ± 0.011 Å), C–S (1.773 Å), and C–N (1.392 Å) distances of S_{exo} in **2**, and by analogy **3**, did not reveal any contraction in the C–N (1.348 Å), C–S (1.724 Å) distances, nor the quinoid structure (avg: 1.405 ± 0.0226 Å) typical of

a *o*-iminosemiquinonate and are more consistent with a coordinated thiophenolate anion[71] (Chart S3.1). It is thus unlikely that an N,S-coordinated *o*-iminosemiquinonate is present in $\mathbf{2^{ox}}$ or $\mathbf{3^{ox}}$. However, spectroscopically characterized metal-thiyl complexes with thiophenolate ligands of Ni(II) (λ = 670-800 nm in CH_2Cl_2),[72] Co(III) (λ = 780 nm in CH_2Cl_2),[73] Ru(III) (λ = 850 nm in acetone),[74] and V(IV) (λ = 910 nm in MeCN)[75] exhibit broad and distinct low-energy bands similar to $\mathbf{3^{ox}}$. These are significantly red-shifted from the broad transition observed for the free phenylthiyl radical (λ = 460-500 nm) generated by pulse radiolysis in pH 11 aqueous solution.[71] Most of these metal-thiyl complexes have been observed at low temperature due to rapid formation of the disulfide, which is not surprising considering the second order decay rate for disulfide formation from free PhS• ($k = 9.6 \times 10^9$ M^{-1} s^{-1}).[71] These facts make the spectroscopic observation of $\mathbf{3^{ox}}$ even more noteworthy in that this species is stable for hours at 298 K. After 24 h in DMF, the green color of $\mathbf{3^{ox}}$ faded and the red precipitate of **1** was isolated in ~70% yield.

An X-band EPR spectrum was collected for in situ generated $\mathbf{3^{ox}}$ at 10 K in a DMF glass and is shown in Figure 3.7 along with a simulated fit. According to the simulation, the three *g*-values observed are g = 2.132 ($\sim g_{\|}$), 2.028, and 2.004 (g_{avg} = 2.055; $g_{\perp} \approx 2.016$) with line widths of 35, 30, 45 MHz, respectively. The typical EPR pattern for Ni(III), as seen in complexes that unambiguously contain Ni(III), such as Ni^{III}F430M,[76] the oxidized cofactor from methyl coenzyme M reductase (MCR), and a wide variety of Ni(III) tetraazamacrocyclic[77,78] and amino acid[79,80] complexes can be described by $g_{\perp} \approx 2.2 - 2.3$ and $g_{\|} = 2.00$, which arise from a low-spin d^7 configuration with the single unpaired electron residing in the Ni d_{z^2} orbital.[80] EPR parameters for relevant, formally Ni(III) complexes are summarized in Table S3.2. This classical Ni(III) EPR pattern is the reverse of that seen here for $\mathbf{3^{ox}}$, so the present complex cannot be an exclusive Ni(III) species with a $d_{z^2}^{\ 1}$ ground state.

EPR spectra previously reported for Ni(III)-N_2S_2 complexes that more closely resemble **3** do not exhibit quite the classical pattern described above, as the symmetry of these complexes is often lower, leading to more rhombic EPR spectra, but most do have $g_{\perp} \approx 2.2 - 2.3$ and $g_{\parallel} \approx 2.00$.[10,36,43,44,81-83] Moreover, their spectra are more anisotropic with *g*-spreads, $g_{max} - g_{min} \approx 0.3$, as opposed to 0.128 for $\mathbf{3^{ox}}$, and with an overall greater deviation from the free electron (radical) *g* value ($g_e = 2.00$) than for $\mathbf{3^{ox}}$ (2.055), namely with $g_{avg} \approx 2.2$.[10,36,44,81,83] The lower *g*-spread in $\mathbf{3^{ox}}$, smaller deviation from g_e, and ambiguous electronic ground state (see computational section below) would be more consistent with a coordinated S-radical with a smaller degree of electron delocalization onto the Ni *d*-orbitals, as observed in Ni-S_4 (bis-dithiolene) complexes,[84,85] than in classical Ni(III) complexes and even in other oxidized Ni(II) complexes with N_2S_2 donor sets. Thus, taken together, the UV-vis and EPR spectra support a Ni(III)-SR ↔ Ni(II)-•SR description for $\mathbf{3^{ox}}$, rather than a genuine Ni(III)-SR species.

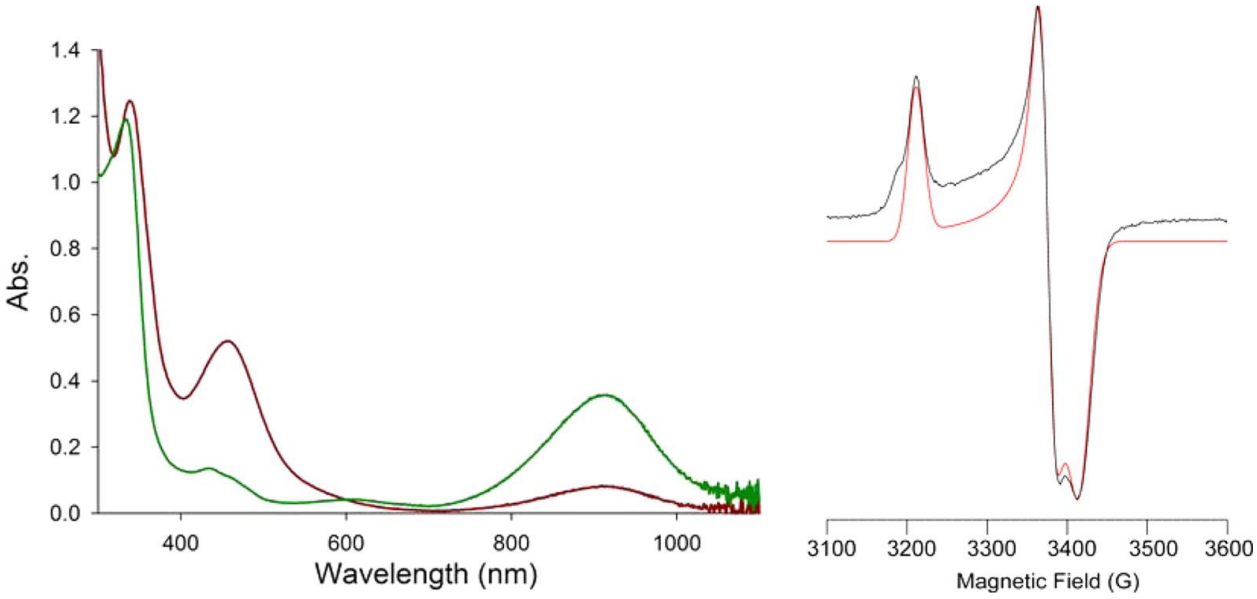

Figure 3.7. (Left) UV-vis spectrum of **3** (red trace) and in situ generated $\mathbf{3^{ox}}$ (green trace) by addition of CAN to **3** in DMF at 298 K. (Right) X-band EPR spectrum (black trace) and simulation (red trace) of in situ generated $\mathbf{3^{ox}}$ in DMF at 10 K. Simulation parameters: g = [2.132, 2.028, 2.004], W = 35, 30, 45 MHz.

Low-temperature absorption and MCD. The low temperature (4.5 K) absorption spectrum of $\mathbf{2^{ox}}$, generated by sparging **2** with O_2(g) for 5 min, exhibited a broad band centered at ~22,000 cm^{-1} (455 nm) and a lower energy feature at ~10,000 cm^{-1} (1,000 nm) (Figure 3.8, top). The MCD spectrum of this sample (Figure 3.8, bottom) exhibited negatively signed features corresponding to the bands observed in the low temperature absorption spectrum, as well as a prominent feature at ~16,000 cm^{-1} (625 nm). All MCD features increase in intensity with decreasing temperature, characteristic of *C*-term behavior and indicative of a paramagnetic species. Note that the three features observed in the MCD spectrum of $\mathbf{2^{ox}}$ coincide with the three absorption bands observed at room temperature of in situ generated $\mathbf{3^{ox}}$ (Figure 3.7), providing

further evidence that $\mathbf{2^{ox}}$ and $\mathbf{3^{ox}}$ have nearly identical electronic structures. Given the relatively high intensities of the MCD features exhibited by $\mathbf{2^{ox}}$, it can be concluded that in this species, and by analogy in $\mathbf{3^{ox}}$, significant unpaired spin density resides on the Ni atom. In support of this conclusion, the large ratio of MCD-to-absorption intensity of the feature at ~16,000 cm^{-1} (625 nm) indicates that the corresponding transition contains significant Ni 3*d* → 3*d* character.

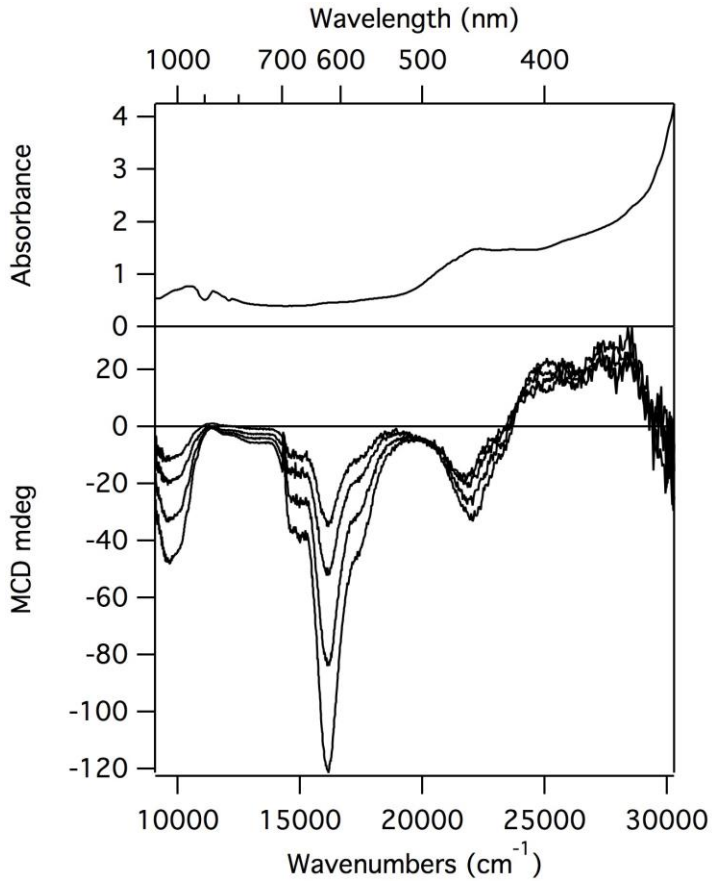

Figure 3.8. Low temperature absorption (4.5 K, top) and MCD (4.5, 8, 15, and 25 K, bottom) spectra of $\mathbf{2^{ox}}$ generated in situ by sparging **2** in a 1:4 (v/v) solvent mixture of MeCN/butyronitrile with O_2(g) for 5 min.

Computations. To obtain further insight into the geometric and electronic structures of $\mathbf{2^{ox}}$, DFT geometry optimization and property calculations were performed for a model of this species (termed $\mathbf{II^{ox}}$). An analogous geometry optimization for a model of the crystallographically-characterized precursor **2** (model **II**) yielded Ni–ligand bond distances that agree reasonably well with the experimental values, thus validating our approach used to generate a model of the structurally ill-defined complex $\mathbf{2^{ox}}$ (Table 3.3). During the geometry optimization of $\mathbf{II^{ox}}$, the Ni atom retained a 4C planar geometry with Ni–ligand bond distances somewhat shorter than those in its one-electron reduced counterpart **II** (Table 3.3). A DFT calculation of the EPR parameters for $\mathbf{II^{ox}}$ yielded *g*-values of 2.16, 2.06, and 2.04, which agree well with the *g*-values determined experimentally for $\mathbf{3^{ox}}$ of 2.132, 2.028, 2.004 (Figure 3.7). Therefore, an analysis of the computed electronic structure description for $\mathbf{II^{ox}}$ is warranted.

Table 3.3. Ni–ligand bond distances in DFT-optimized models of **II** and $\mathbf{II^{ox}}$ compared with X-ray crystallographically determined values for **2**.

	DFT		X-ray Structure of **2**
	II	$\mathbf{II^{ox}}$	$(Et_4N)[Ni(nmp)(SPh\text{-}o\text{-}NH_2)]$
$Ni\text{-}S_{exo}$	2.278	2.211	2.218
$Ni\text{-}S_{nmp}$	2.198	2.169	2.138
$Ni\text{-}N_{carboxamide}$	1.895	1.880	1.875
$Ni\text{-}N_{py}$	1.981	1.990	1.942

A comparison of the spin up (α) and spin down (β) manifolds of MOs obtained from a spin-unrestricted DFT calculation for $\mathbf{II^{ox}}$ (Figure 3.9) revealed that the βLUMO (βMO#93) corresponds to the formally singly occupied MO, as its α-counterpart (αMO#83, not shown) is occupied. To higher energy, the βLUMO+2 (βMO#95) can be identified as the Ni $3d_{x^2-y^2}$ based MO, while the βLUMO+1 (βMO#94) is mainly localized on the aryl-carboxamide moiety of the supporting nmp^{2-} ligand. As expected for a 4C planar complex, the occupied Ni $3d_{z^2}$, $3d_{xy}$, $3d_{xz}$, and $3d_{yz}$ based orbitals (βMO#88, #81, #87, and #84, respectively) are significantly stabilized relative to the unoccupied Ni $3d_{x^2-y^2}$ based βMO#95.

The βLUMO has predominant S 3p (53% total: 26% from S_{exo} and 27% from S_{nmp}) and Ni 3*d* (21%; mainly $3d_{xz}$ and some $3d_{yz}$) orbital character, suggesting that the removal of an electron from **II** results in partial oxidation of both the thiolates and the Ni(II) ion. Consistent with this prediction, a plot of the spin density for $\mathbf{II^{ox}}$ shows that the unpaired electron is delocalized over the two S and the Ni atoms (Figure 3.9, inset). Consequently, our computational results obtained for $\mathbf{II^{ox}}$ indicate that $\mathbf{2^{ox}}$ is best described as a hybrid of Ni(III)/$(SR)_2$ ↔ Ni(II)/$(SR)_2^{\bullet}$ resonance structures. This description is consistent with the intense MCD features and sizeable *g*-spread displayed by $\mathbf{3^{ox}}$ relative to a free thiyl.

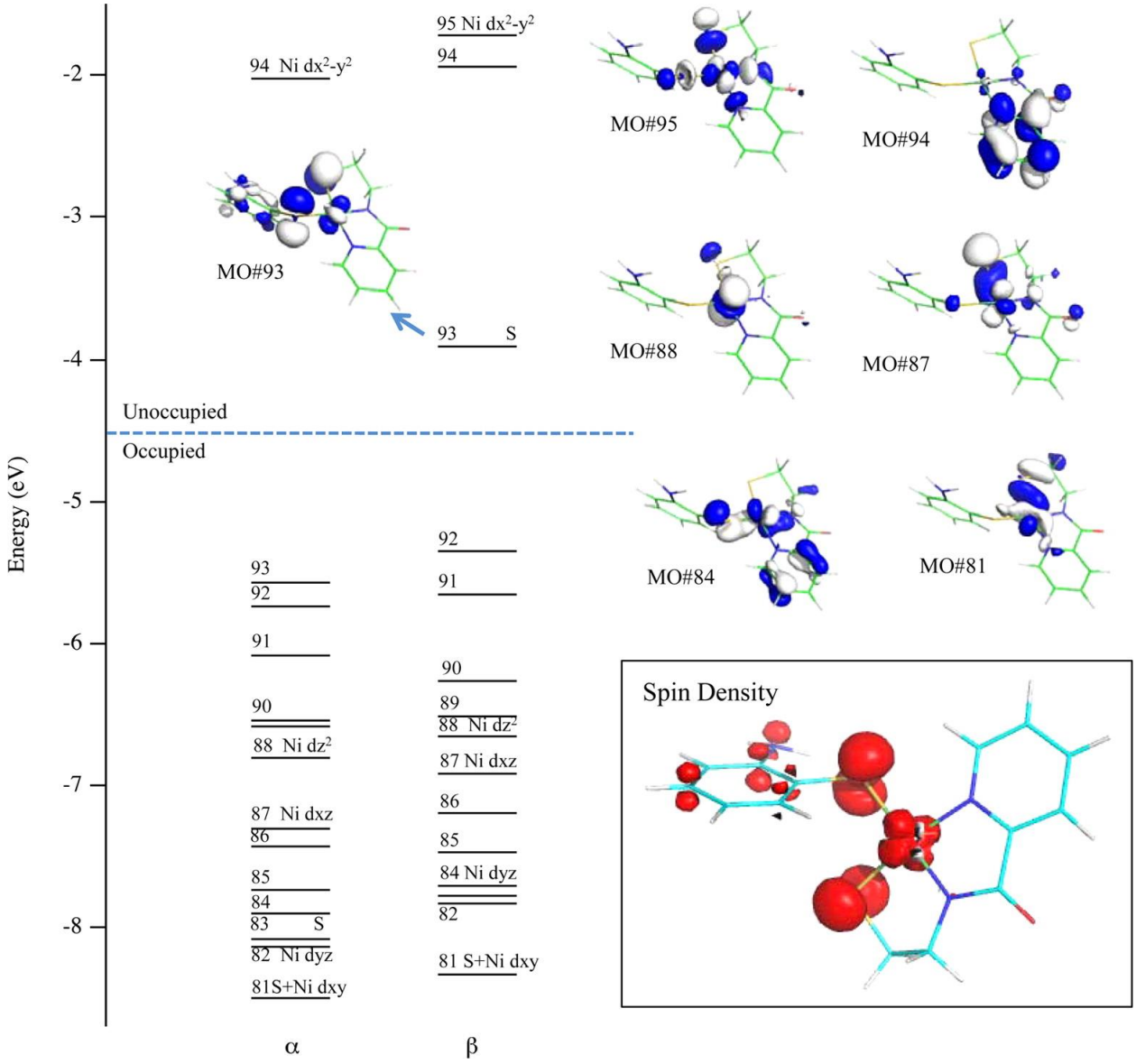

Figure 3.9. Relevant portion of the MO diagram and isosurface plots of select *β*MOs obtained from a spin-unrestricted DFT calculation for **II^{ox}**. Inset: Spin density plot for **II^{ox}** (red = positive spin density; white = negative spin density).

Reactivity of 3^{ox} with Azide and Superoxide. The azide anion (N_3^-) is often employed as a redox-inert analogue of superoxide to obtain information on M–$O_2^{\bullet-}$ interactions. NiSOD

shows no direct Ni-N_3^- interaction based on EPR, UV-vis and resonance Raman (rR) studies.[10,12] To evaluate the anion affinity of the Ni center in **3** and $\mathbf{3}^{ox}$, we added excess (10 equiv) NaN_3 to this NiSOD model and monitored its UV-vis spectrum. As observed for NiSOD, the UV-vis spectrum of **3** or $\mathbf{3}^{ox}$ did not change upon the addition of N_3^- (Figure 3.10) even after 1 h. Despite the presence of the potentially coordinating amine-N from S_{exo}, we tested whether the presence of 10 equiv of N-MeIm impacted any Ni–N_3^- bonding. Indeed, addition of N-MeIm resulted in a ~30 nm blue-shift in λ_{max} of **3** that may imply a Ni···N-MeIm interaction; however, no other direct evidence for a Ni–NMeIm bond was obtained. Analogous to the results in the absence of N-MeIm, no change was observed in the UV-vis spectrum when 10 equiv of N_3^- are added (Figure 3.10); thus, much like NiSOD, the Ni center in **3** and $\mathbf{3}^{ox}$ does not bind N_3^-.

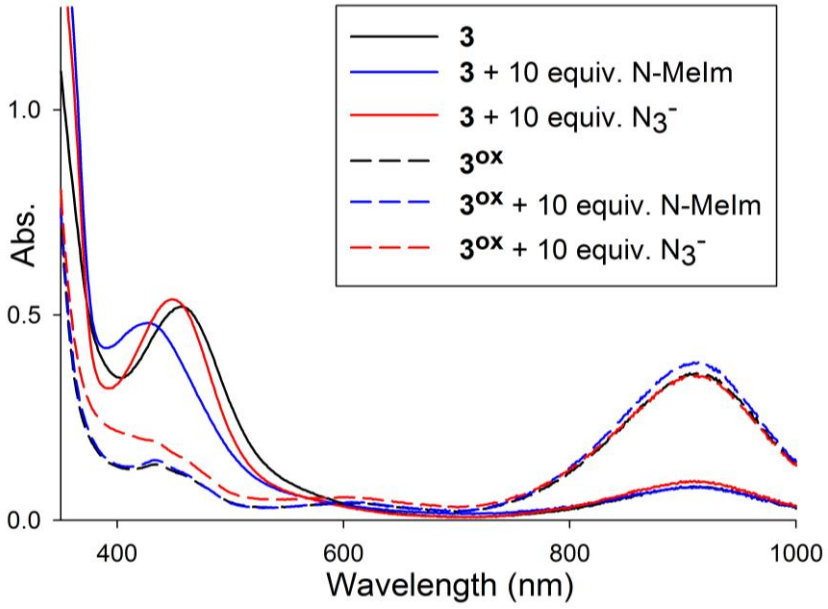

Figure 3.10. UV-vis spectra of **3** (black) and $\mathbf{3}^{ox}$ (black dash); **3** + 10 equiv N-MeIm (blue) and $\mathbf{3}^{ox}$ + 10 equiv N-MeIm (blue dash); **3** + 10 equiv N_3^- (red) and $\mathbf{3}^{ox}$ + 10 equiv N_3^- (red dash). All experiments were performed in DMF at 298 K.

To evaluate the potential of **3** and $\mathbf{3^{ox}}$ as SOD catalysts, experiments were performed with 18-crown-6 ether solubilized KO_2 in DMF at 298 K. Addition of a stoichiometric amount of KO_2 to a DMF solution of **3** resulted in no reaction as monitored by UV-vis. However, the same reaction with in situ generated $\mathbf{3^{ox}}$ produced an immediate solution color change from green to red-brown. To obtain more information as to the products formed in this reaction, fractional precipitation and isolation of components present in the reaction mixture were performed (see Chart S3.2). After vacuum distilling DMF from the reaction mixture, MeCN was added that afforded a red-orange precipitate and a brown MeCN-soluble portion. The MeCN-insoluble component was identified as the tetrameric species **1** based on FTIR data. Two separate reactions of $\mathbf{3^{ox}}$ and $O_2^{\bullet-}$ revealed that the bulk of the Ni-nmp ends up as **1** (avg: 65% yield). Further attempts at separating components in the MeCN-soluble portion by selective precipitation with THF and Et_2O revealed the presence of **3** and the free unbound sulfinate (RSO_2^-) and sulfonate (RSO_3^-) of S_{exo} based on ESI-MS (Figure S3.4 in the SI). Unfortunately, quantitative isolation of species other than **1** was not possible due to similar solubility profiles and the presence of CAN-related species. Additionally, no O_2(g) generation was observed utilizing electrochemical detection methods.[86] One can envision two primary reaction paths of $\mathbf{3^{ox}}$ with superoxide: (i) $O_2^{\bullet-}$ behaves as an outer-sphere reductant to furnish the corresponding Ni(II) complex **3** and O_2 (Scheme 3.3i), or (ii) $O_2^{\bullet-}$ oxygenates the S_{exo} atom of $\mathbf{3^{ox}}$ to generate the resulting sulfinate (RSO_2^-) and tetramer **1** (Scheme 3.3ii). Scheme 3.3i would be more in-line with a Ni(III) assignment for $\mathbf{3^{ox}}$, whereas Scheme 3.3ii is more consistent with a Ni(II)-thiyl. However, one could envision the formation of similar products in both pathways if the product Ni(II) species **3** in Scheme 3.3i reacted with O_2 in a manner other than as an outer-sphere Ni(II) oxidant (i.e., "other products" in Scheme 3.3i). Either scenario explains the lack of any detectable O_2(g) via

electrochemistry, although the path in Scheme 3.3ii is more consistent with the significant amount of isolated **1** in the reaction mixture. Regardless of the path at work, these results advocate for a Ni(II)-thiyl assignment for $\mathbf{3^{ox}}$.

Scheme 3.3. Possible scenarios for the reaction of $\mathbf{3^{ox}}$ with superoxide.

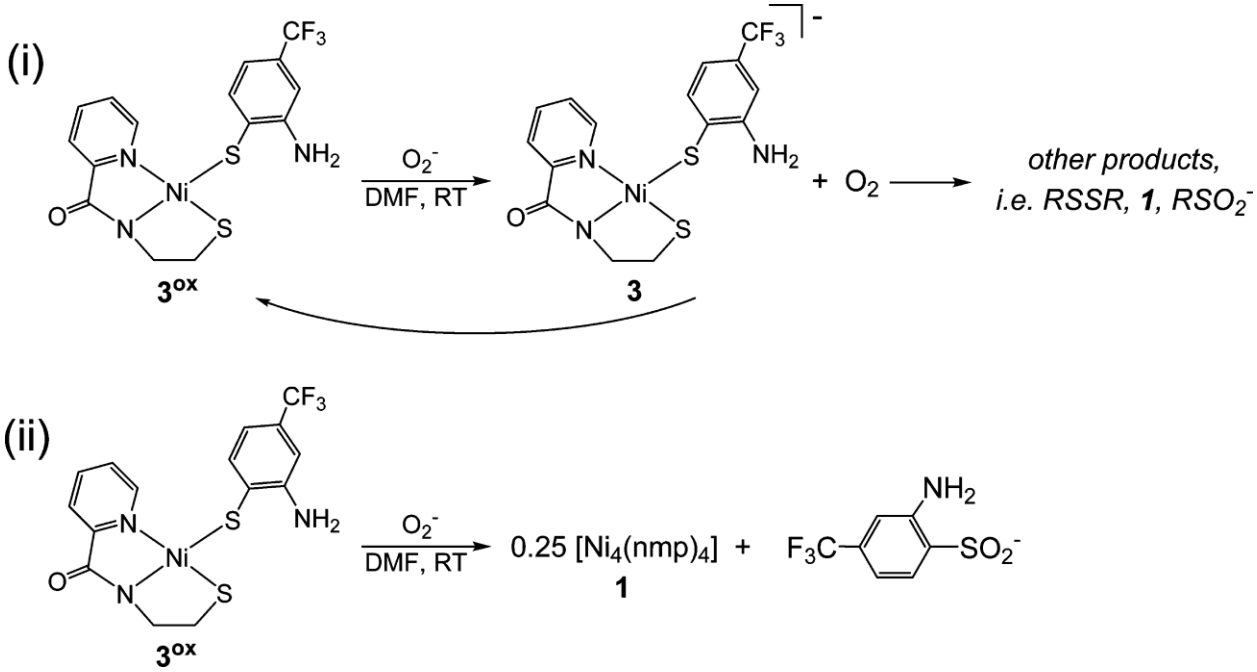

3.5 Conclusions

In summary, we have prepared and characterized four Ni(II)-N/S complexes of the general formula $[Ni(N_2S)(SR')]^-$, where SR′ represents a site-differentiated location of the N_2S_2 coordination sphere as models of NiSOD. The SR′ ligand was functionalized with electron withdrawing substituents and/or a tethered N-donor in efforts to promote formation of an oxidized Ni(III) complex that would be structurally and electronically analogous to the Ni-N_3S_2

coordination sphere of $NiSOD_{ox}$. We hypothesized that incorporation of a weak N_{axial} ligand in SR′ from *o*-aminothiophenolate could mimic the long (2.3-2.6 Å) Ni–NHis bond in NiSOD and would be required to obtain such an oxidized species. Indeed, site-directed variants and DFT calculations revealed that the axial Ni–NHis bond in $NiSOD_{ox}$ is crucial for maintaining the rate ($k \approx 10^9$ M^{-1} s^{-1})[87,88] and appropriate electrochemical potential (0.090 V vs. Ag/AgCl, pH 7.4, phosphate buffer) for turnover.[10,89] In addition, the few low MW NiSOD models that access Ni(III) or that exhibit some SOD activity contain an N_{axial} ligand.[27,35,36] Chemical oxidation of NiSOD models **4** and **5** that lack this potential N-donor resulted in quantitative formation of **1** and the disulfide (R′SSR′) of the monodentate thiolate. This result was not too surprising given the expected high percentage of S-character in the HOMO of such Ni(II)-N_2S_2 complexes, although we had initially anticipated the electron-deficient thiolate in **5** would prevent such chemistry. Chemical oxidation of models **2** and **3** that contain a potential N-donor ligand resulted in the transient formation of an oxidized species (**2^{ox}** and **3^{ox}**) that is best described as a resonance hybrid of a Ni(III)-thiolate and Ni(II)-thiyl species: [Ni(III)-SR] ↔ [Ni(II)-•SR]. This assignment was confirmed through a variety of experimental (X-ray, UV-vis, MCD, EPR, reactivity) and theoretical (DFT) techniques. These results may at first appear incongruent with the actual mechanism of NiSOD. Most experimental work supports an outer-sphere electron transfer mechanism for $O_2^{\bullet-}$ disproportionation with the Ni(III/II) center possibly remaining 5C throughout catalysis.[8,39,40] In the first turnover, conversion of 4C $NiSOD_{red}$ to 5C $NiSOD_{ox}$ likely results in a 4C planar intermediate ($NiSOD_{ox}$-His_{off}) before formation of $NiSOD_{ox}$ due to the kinetics of electron transfer versus Ni-N(His) bond formation. Although this transient species has never been observed experimentally, DFT computations on $NiSOD_{ox}$-His_{off} indicate a predominant Ni-based HOMO and support a Ni(III) oxidation state (vide supra) even before

axial His1 binding. This assignment is in contrast to the Ni(III)-thiolate ↔ Ni(II)-thiyl resonance description for the NiSOD models **2**^{ox} and **3**^{ox}. However, S•(Cys) radicals have been observed in other enzymes,[90] some of which function through such a radical species.[91-97] Based on the EPR spectrum, Ni exists in the 3+ state in $NiSOD_{ox}$ with no indications of a coordinated S•(Cys), but the results presented here suggest that the transition from $NiSOD_{red}$ to $NiSOD_{ox}$-His_{off} may go through a Ni-stabilized/coordinated S•(Cys).

3.6 Supporting Information

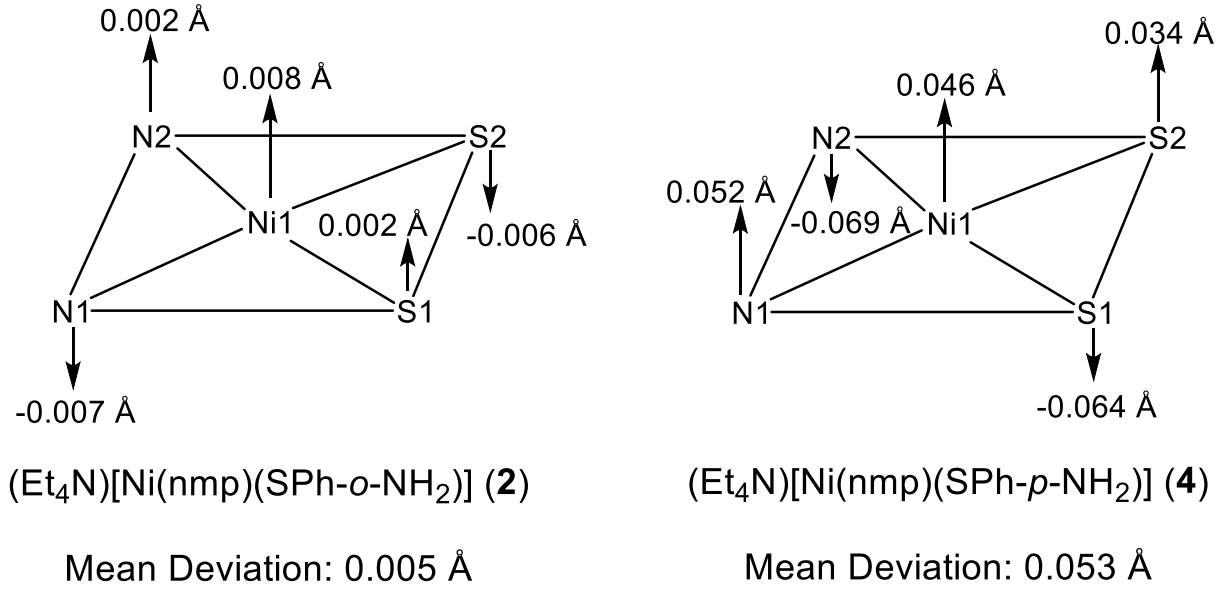

Figure S3.1. Schematic representation of the NiN_2S_2 plane for (Et_4N)[Ni(nmp)(SPh-*o*-NH_2)] (**2**) and (Et_4N)[Ni(nmp)(SPh-*p*-NH_2)] (**4**) and deviations of each atom from the weighted least-square plane. N2, N1, and S1 represent the donor atoms derived from the nmp^{2-} ligand, whereas S2 originates from the exogenous S donor (S_{exo}).

Table S3.1. Summary of crystal data and intensity collection and structure refinement parameters for $[Ni_4(nmp)_4]$ (**1**), $(Et_4N)[Ni(nmp)(SPh\text{-}o\text{-}NH_2)]$ (**2**), and $(Et_4N)[Ni(nmp)(SPh\text{-}p\text{-}NH_2)]$ (**4**).

Parameters	**1**	**2**	**4**
Formula	$C_{32}H_{32}N_8Ni_4O_4S_4$	$C_{22}H_{34}N_4NiOS_2$	$C_{22}H_{34}N_4NiOS_2$
Formula weight	955.70	493.36	493.36
Crystal system	Monoclinic	Monoclinic	Monoclinic
Space group	C2/c	*P*2(1)/n	*P* 21/c
Crystal color, habit	Red	Red, blade	Red, blade
a, Å	19.4038(19)	11.5155(19)	20.0499(11)
b, Å	13.7950(14)	10.0686(16)	11.8010(7)
c, Å	15.5713(16)	20.095(3)	20.4272(13)
α, deg	90	90	90
β, deg	126.8520(10)	92.038(2)	100.585(1)
γ, deg	90	90	90
V, $Å^3$	3335.2(6)	2328.4(7)	4751.0(5)
Z	4	4	8
$\rho_{calcd,}$ g/cm^3	1.903	1.407	1.379
T, K	100(2)	100(2)	100(2)
abs coeff, μ (MoKα), mm^{-1}	2.528	1.034	1.014
θ limits, deg	1.97-25.99	2.01-30.03	2.002-30.519
total no. of data	19261	34465	75036
no. of unique data	3274	6815	14491
no. of parameters	263	271	541
GOF of F^2	1.080	1.023	1.021
R_1,[a] %	0.0393	0.0378	0.0371
wR_2,[b] %	0.1031	0.0873	0.0959
max, min peaks, $e/Å^3$	0.9280, 0.7029	0.420, -0.497	0.696, -0.651

[a] $R_1 = \Sigma| |F_o| - |F_c| | / \Sigma |F_o|$; [b] $wR_2 = \{\Sigma[w(F_o^2 - F_c^2)^2]/\Sigma[w(F_o^2)^2]\}^{1/2}$

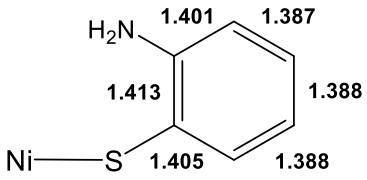

(**2**)

C-S: 1.7730 Å
C-N: 1.392 Å
C-C (avg.): 1.397 ± 0.011 Å

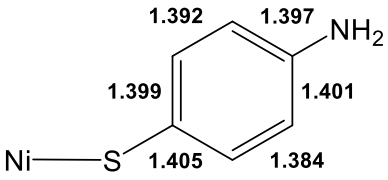

(**4**)

C-S: 1.7722 Å
C-N: 1.406 Å
C-C (avg.): 1.396 ± 0.007 Å

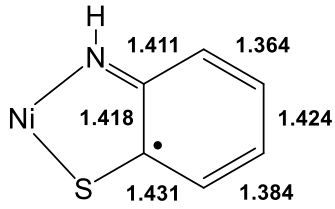

Ni-coordinated o-iminothiosemiquinonate
C-S: 1.724 Å
C-N: 1.348 Å
C-C (avg.): 1.405 ± 0.026 Å

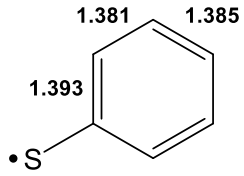

phenylthiyl radical (calc.)
C-S: 1.750 Å
C-C (avg.): 1.386 ± 0.006 Å

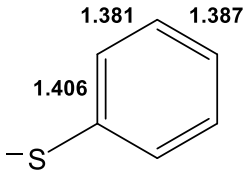

phenylthiolate anion (calc.)
C-S: 1.756 Å
C-C (avg.): 1.391 ± 0.013 Å

Chart S3.1. (Top) Relevant bond distances of the S_{exo} ligand in the anions of **2** and **4**. (Bottom) Same parameters for a structurally-characterized Ni(II)-N,S-coordinated *o*-iminothiosemiquinonate (see *J. Am. Chem. Soc.* **2001**, *123*, 10012) and the calculated bond lengths of the phenylthiyl radical and phenylthiolate anion (ROHF/3-21G*, see *J. Phys. Chem.* **1992**, *96*, 5344).

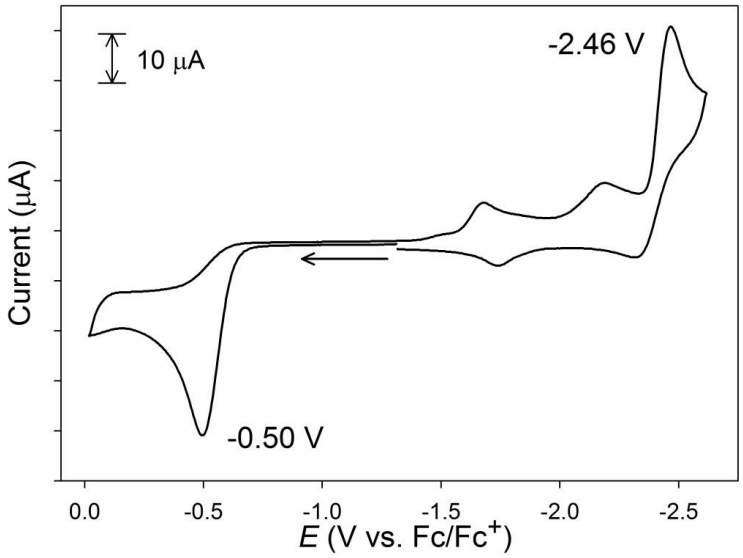

Figure S3.2. CV of an 8 mM solution of **4** in DMF at RT (glassy carbon working electrode, 0.1 M $^{n}Bu_4NPF_6$ as supporting electrolyte, 100 mV/s scan speed). Arrow shows direction of scan.

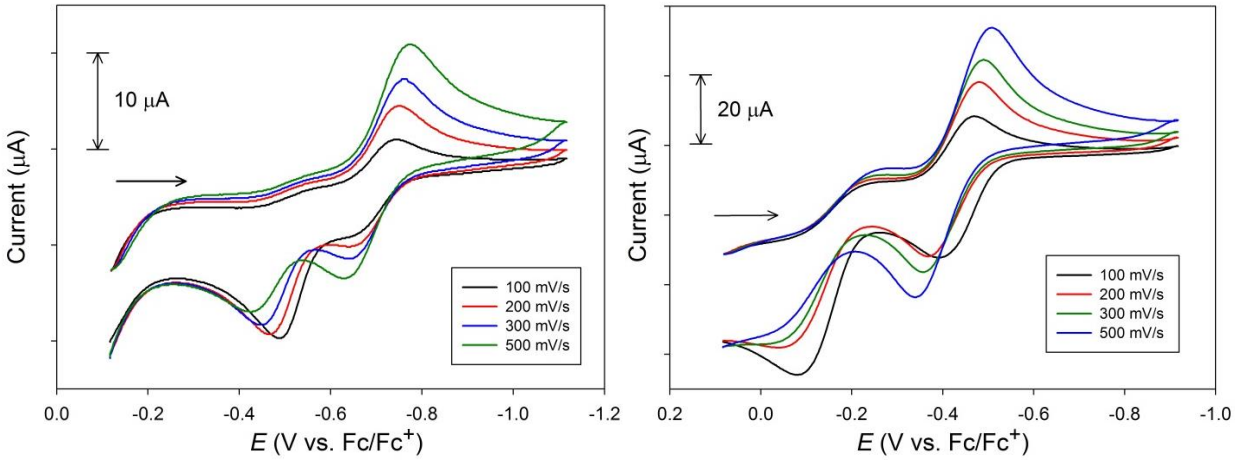

Figure S3.3. CV of 8 mM solutions of **2** (left) and **3** (right) in DMF at RT (glassy carbon working electrode, 0.1 M $^{n}Bu_4NPF_6$ as supporting electrolyte, 100 mV/s scan speed). Arrow shows the direction of the scan.

Table S3.2. EPR parameters for Ni(III) coordination complexes with N_xS_y donor sets relevant to the present study.

Complex	*g* values: [max, mid, min], avg	Ground state assignment [a]	Reference
***cis*-N2S2 donor set, N3S2 donor set [b]**			
[Ni(nmp)(SPh-*o*-NH_2-*p*-CF_3)] (**3^{ox}**)	[2.132, 2.028, 2.004], 2.055	$\left(d_{z^2}^{\ 1}\right)$	this work
$[Ni(emb)]^-$	[2.29, 2.11, 2.04], 2.15	uncertain	*Inorg. Chem.* **1987**, *26*, 3645.
$[Ni(ema)]^-$	[2.23, 2.18, 2.01], 2.14	$d_{z^2}^{\ 1}$	*Inorg. Chem.* **1991**, *30*, 734.
$[Ni(phma)]^-$	[2.20, 2.17, 2.01], 2.13	$d_{z^2}^{\ 1}$	*Inorg. Chem.* **1991**, *30*, 734.
$[Ni(emi)]^-$	[2.44, 2.27, 1.96], 2.22	uncertain	*Inorg. Chem.* **1991**, *30*, 734.
$[Ni(phmi)]^-$ $[Ni(phmi)(py)]^-$	[2.55, 2.14, 2.00], 2.23 [2.313, 2.281, 2.000], 2.198	uncertain $d_{z^2}^{\ 1}$	*Angew. Chem. Intl. Ed.* **1998**, *37*, 260
$[Ni(ema)\cdot(CH_2)_3]^-$	[2.36, 2.23, 2.01], 2.20	$d_{z^2}^{\ 1}$	*Inorg. Chem.* **2007**, *46*, 7536.
$[Ni(L_1)]$	[2.26, 2.19, 2.01], 2.15	$d_{z^2}^{\ 1}$	*Inorg. Chem.* **2014**, *53*, 6512.
$[Ni(L)(im)]^{+\,c}$	[2.315, 2.177, 2.029], 2.174	$d_{z^2}^{\ 1}$	*Inorg. Chem.* **2010**, *49*, 6399.
S4 donor set [d]			
$[Ni(nbdt)_2]^-$	[2.14, 2.05, 2.05], 2.08	uncertain	*J. Am. Chem. Soc.* **1990**, *112*, 3218.
$[Ni(mnt)_2]^-$	[2.14, 2.04, 1.99], 2.06	$\left(d_{xz}^{\ 1}\right)^g$	*Inorg. Chem.* **1998**, *37*, 1361.
$[Ni(S_2C_2Me_2)_2]^-$	[2.118, 2.041, 2.000], 2.053	$\left(d_{xz}^{\ 1}\right)^g$	*Inorg. Chem.* **2001**, *40*, 4257.
$[Ni(S(NH)C_6H_4)_2]^-$	[2.126, 2.028, 2.005], 2.053	uncertain	*Inorg. Chem.* **1967**, *89*, 2866.
***trans*-N2S4 donor set**			
$[Ni(pdtc)_2]^{-\,e}$	[2.137, 2.137, 2.038], 2.104	$d_{z^2}^{\ 1}$	*J. Am. Chem. Soc.* **1990**, *112*, 2955.
N6 donor set [f]			
$[Ni(H\__3G_3a)(NH_3)_2]$	[2.178, 2.178, 2.019], 2.125	$d_{z^2}^{\ 1}$	*Inorg. Chem.* **1978**, *17*, 1630.
$[Ni(Me_2[14]aneN_4)(NCO)_2]^+$	[2.169, 2.169, 2.055], 2.131	$d_{z^2}^{\ 1}$	*Inorg. Chem.* **1973**, *12*, 1.

Ligand abbreviations: ema = *N*,*N*′-ethylenebis-2-mercaptoacetamide; (ema)·$(CH_2)_3$ = *N*,*N*′-ethylenebis(2-propylmercaptoacetamide); emb = *N*,*N*′-ethylenebis(*o*-mercaptobenzamide); emi = *N*,*N*′-ethylenebis-2-mercaptoisobutyramide; $H_{-3}G_3a$ = trianion (i.e., mono-H) of tripeptide glycylglycylglycinamide; im = imidazole; L = dianion of 2,2′-(2,2′-bipyridine-6,6′-diyl)bis(1,1-diphenylethanethiol); L_1 = trianion of *N*-(2-mercapto-2-methylpropanoyl)-*N*'-(2-mercapto-2-methylpropyl)-1,2-diaminoethane; Me_2[14]aneN_4 = 2,3-dimethyl-1,4,8,11-tetraazacyclo-tetradecane; mnt = dianion of maleonitriledithiolate ($S_2C_2(CN)_2^{2-}$); nbdt = dianion of norbornane-2,3-dithiolate; nmp = dianion of *N*-(2-mercaptoethyl)picolinamide); pdtc = dianion of pyridine-2,6-bis(thiocarboxylate); phma = *N*,*N*′-1,2-phenylenebis-2-mercaptoacetamide); phmi = tetraanion of *N*,*N*′-1,2-phenylenebis(2-sulfanyl-2-methylpropionamide); py = pyridine; $S(NH)C_6H_4)_2^-$ = dianion of *o*-amidothiophenolate.

[a] As determined in the original work, parentheses indicates a ground state that is extensively delocalized onto the ligands, as opposed to being largely Ni-3*d*-centered. For a detailed discussion of **3^{ox}**, see the main text.

[b] In a number of cases for these four-coordinate N2S2 donor set complexes, imine N donor base (typically pyridine or imidazole) was added which coordinates on one axial position and gives a characteristic triplet hyperfine splitting (^{14}N, I = 1) at g_{min}, indicating that this corresponds to the molecular *z* direction (i.e., so that this is g_z) and that the ground state is $d_{z^2}^{\ 1}$; however, a shift in the ground state may have occurred with base binding (e.g., for pyridine binding to [Ni(emi)]$^-$). Such EPR results of axial base binding are not included here, except for the case of [Ni(phmi)]$^-$, as a representative example, and the last member of this series, as explained in footnote *c*.

[c] For this complex, no formal Ni(III) species with an N2S2 donor set was observed. Upon oxidation of the four-coordinate Ni(II) parent compound, [Ni(L)] (S2N2 donor set), a diamagnetic di-Ni(III) complex is formed; however, addition of excess imidazole to this complex leads to formation of mononuclear [Ni(L)(im)]$^+$, which has a $d_{z^2}^{\ 1}$ ground state as supported by extensive computational analysis (calculated spin density on Ni alone = 82%; calculated g = [2.252, 2.199, 2.071]).

[d] The electronic structure of such square-planar S4 donor set bis-dithiolato complexes has historically been the source of much controversy (see *Inorg. Chem.* **2011**, *50*, 9741; *Chem.-Eur. J.* **2007**, *13*, 2783). Among many examples, the dimethylthiolene complex listed herein has been thoroughly analyzed (see *Inorg. Chem.* **2001**, *40*, 4257; *Chem.-Eur. J.* **2003**, *125*, 9158). The electronic structure of the nbdt complex has not been so analyzed (and that its reported EPR is axial is unexpected), but may be similar to the mnt complex; the nbdt complex does not coordinate axial bases, in contrast to those with more unambiguous $d_{z^2}^{\ 1}$ ground states (e.g., the (ema)·$(CH_2)_3$, emb, and emi complexes, and the pdtc complex with its "built-in" axial imino N-donors). Its ground state was given as $\left(d_{x^2-y^2}^{\ 1}\right)$, but this seems unreasonable in light of subsequent experimental and theoretical studies on such systems.

[e] This 6-coordinate complex has a *trans*-N2S4 donor set. Hyperfine coupling from two equivalent, axial ^{14}N ligands was well resolved at both $g_\perp$ and $g_\parallel$. A complex enriched in ^{61}Ni (I = 3/2) was also prepared and all evidence support a $d_{z^2}^{\ 1}$ ground state.

[f] These 6-coordinate complexes with non-redox active ligands are classic examples of Ni(III) with $d_{z^2}^{\ 1}$ ground state. The tripeptide complex has equivalent, *trans* ammine ligands which give rise to resolved ^{14}N hyperfine coupling at $g_\parallel$; the tetraaza macrocycle complex has equivalent, *trans N*-cyanato ligands; the EPR data is for powder, hence no hyperfine coupling was resolved.

[g] The coordinate system used by Huyett *et al*. for the mnt complex was defined so that the *z* axis was perpendicular to the molecular plane, and the *y* axis bisected the chelate rings with the *x* axis between the rings; the later model of Lim *et al*., which is used here, defined the *x* axis as bisecting the chelate ring and the *y* axis bisecting the S-Ni-S angle external to the chelates. In the more recent calculations, those for the dimethyldithiolene, the unpaired spin is only partially (25%; with 60% on the S atoms) on Ni (in $3d_{xz}$ AO; $5b_{2g}$ using D_{2h} symmetry) (see *J. Am. Chem. Soc.* **2003**, *125*, 9158). The calculated g values for this complex are: g = [2.115, 2.040, 1.969], in excellent agreement with experiment.

A 3 mL DMF solution of **3** (56.5 mg, 0.101 mmol) was mixed with CAN (55.3 mg, 0.101 mmol) to generate the green-colored **3^{ox}.** To this solution was added a ~2 mL DMF solution of KO_2 (7.8 mg, 0.11 mmol) solubilized with 18C6 (104.1 mg, 0.3938 mmol). Upon addition of KO_2, the green color of **3^{ox}** immediately changed to brown-red. This solution was allowed to mix at RT for ~5 min. DMF was then removed via short-path vacuum distilation and the dark residue was worked-up as follows:

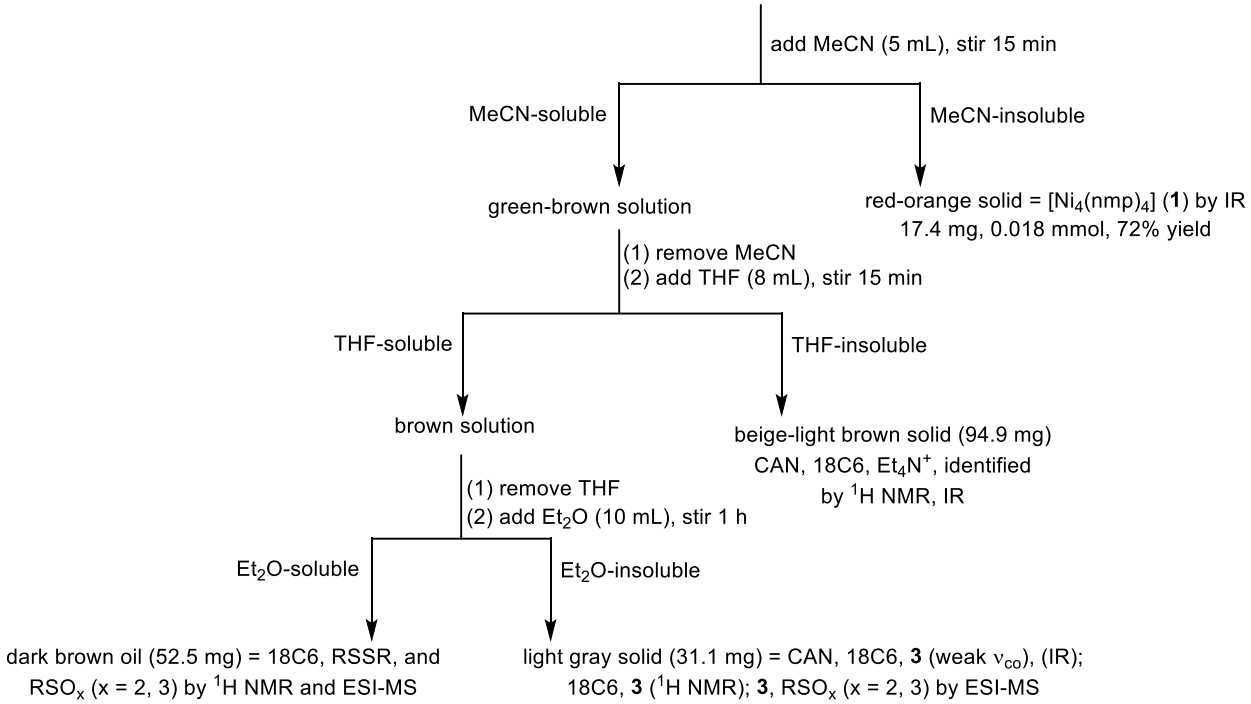

Chart S3.2. Workup flowchart for the reaction of **3^{ox}** with KO_2 in DMF at RT.

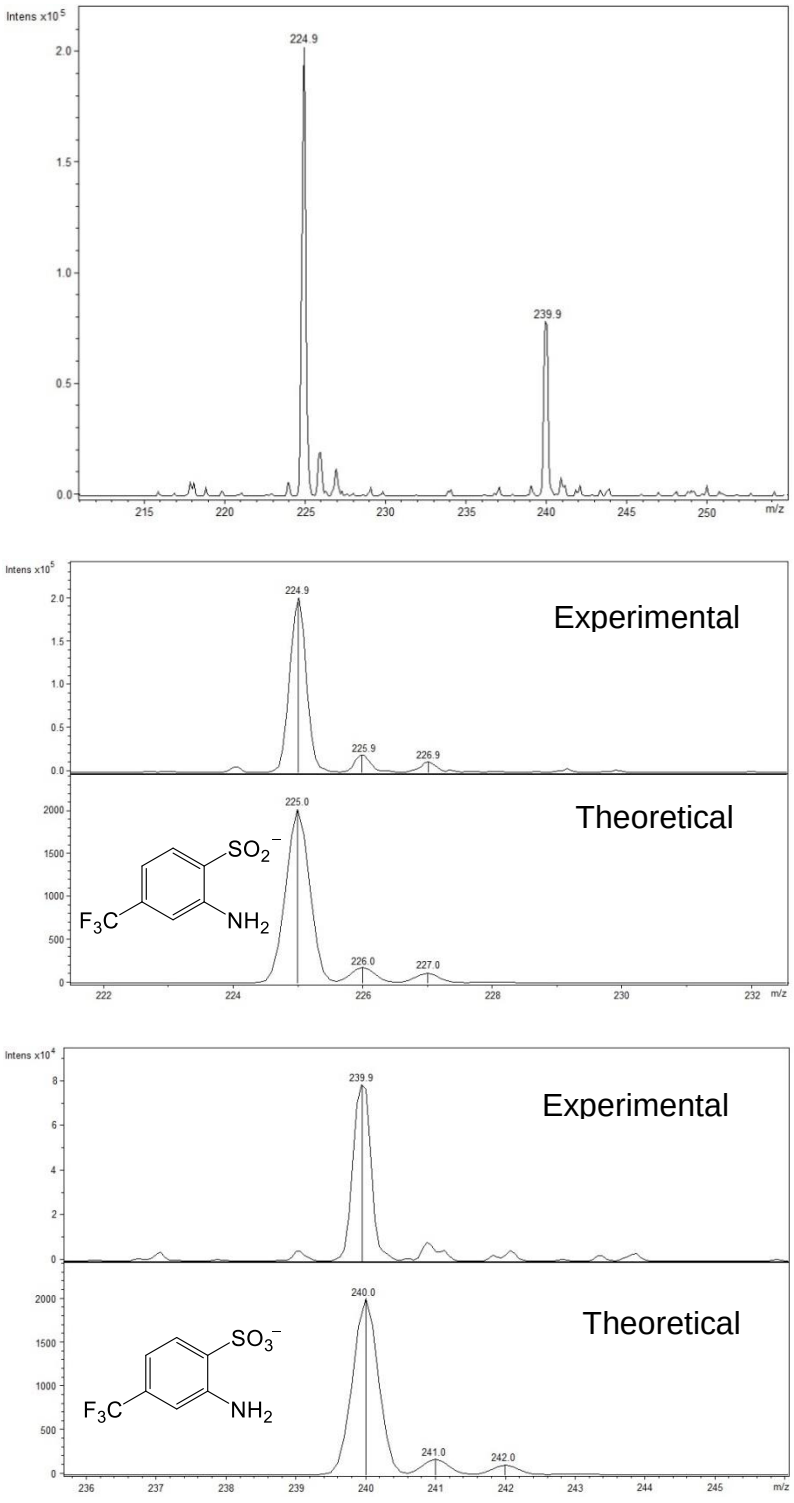

Figure S3.4. Low resolution ESI-MS (negative mode) of the Et_2O-soluble portion from Chart S3.2. Middle and bottom represent a zoom-in of the *m/z* 224.9 and 239.9 peaks. Theoretical fit on the bottom.

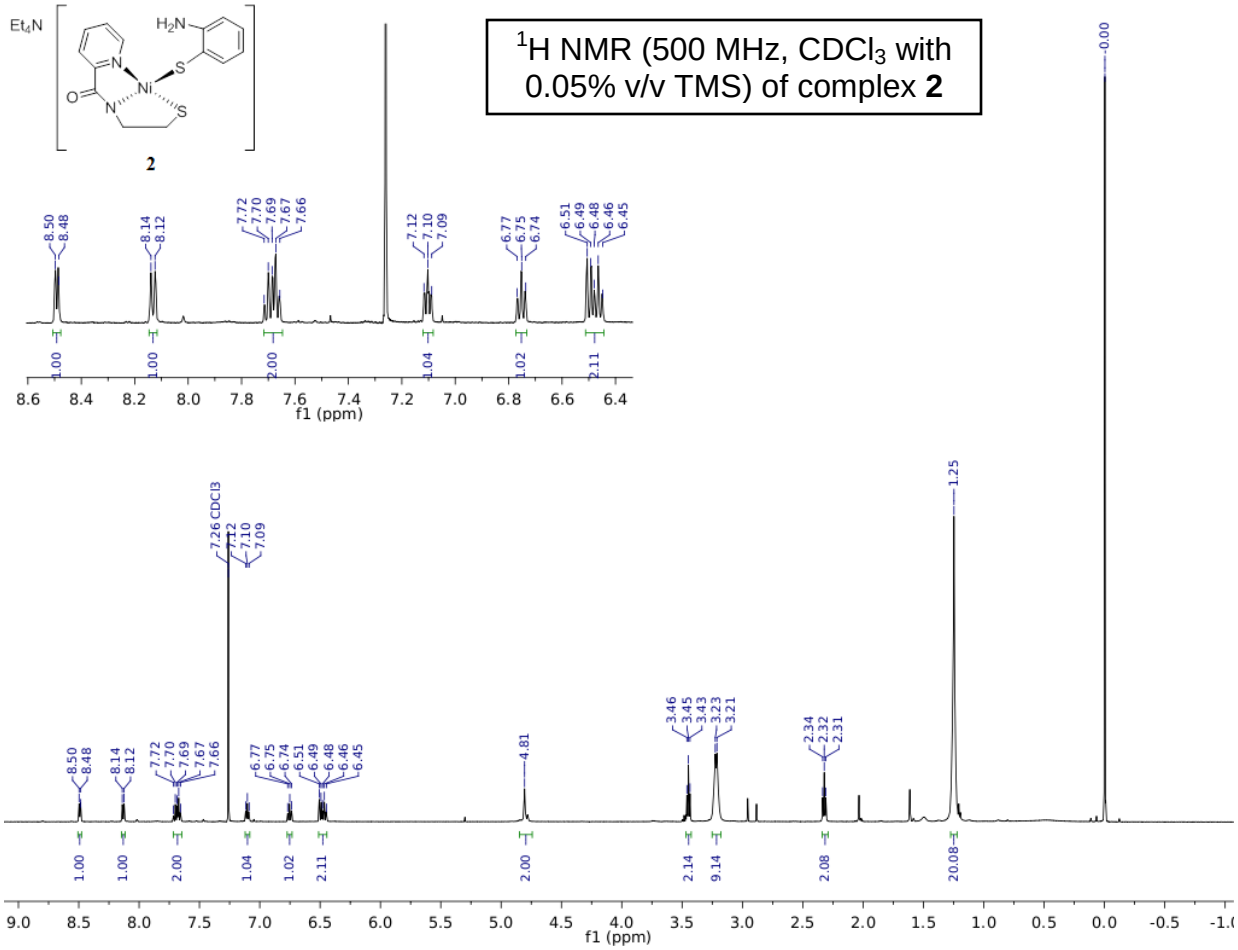

Figure S3.5. ^{1}H NMR spectrum of **2** in $CDCl_3$ containing 0.05% v/v TMS at RT. Inset shows expanded aromatic region. Residual protio solvent (7.26 ppm), H_2O (1.61 ppm), and TMS (0.00 ppm) are present. A minor amount of DMF (8.02, 2.96, 2.88 ppm) and MeCN (2.03 ppm) from workup are also present.

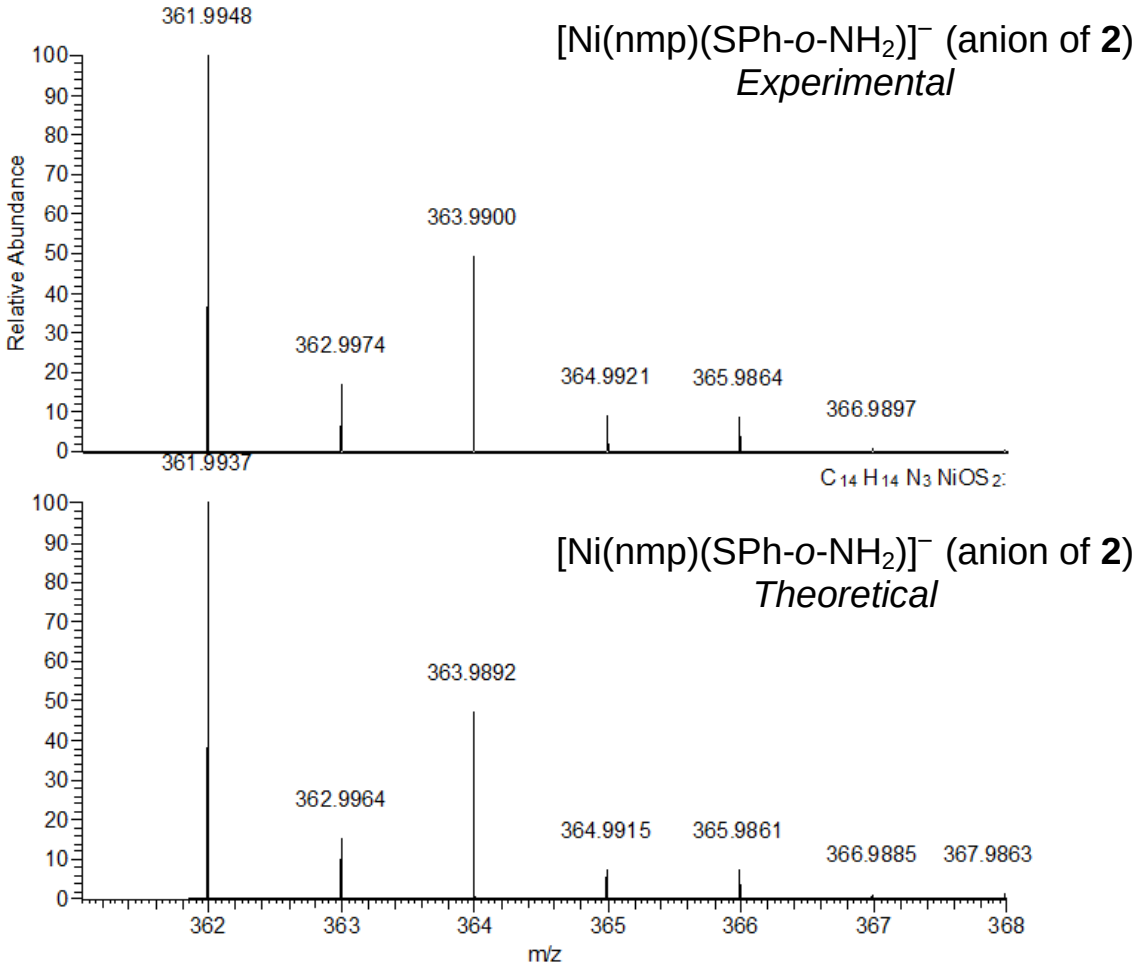

Figure S3.6. (Top) High resolution ESI-MS (negative mode) of the anion of **2** $[M\text{-}Et_4N]^-$ in MeCN at RT. (Bottom) Theoretical MS for the anion of **2**.

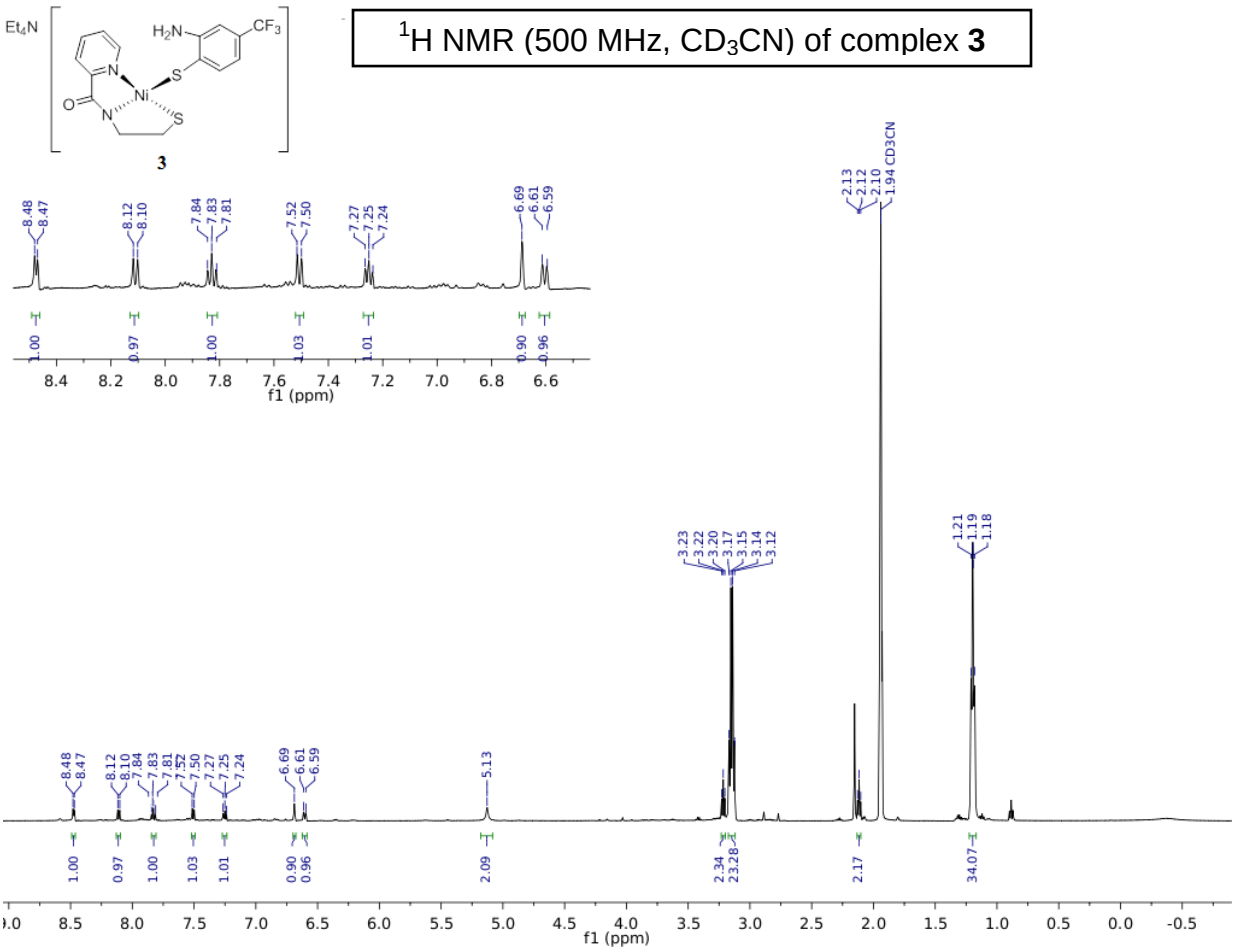

Figure S3.7. ^{1}H NMR spectrum of **3** in CD_3CN at RT. Inset shows expanded aromatic region. Residual protio solvent (1.94 ppm) and H_2O (2.13 ppm) are present. A minor amount of DMF (7.92, 2.89, 2.77 ppm) and pentane (1.28, 0.89 ppm) from workup are also present.

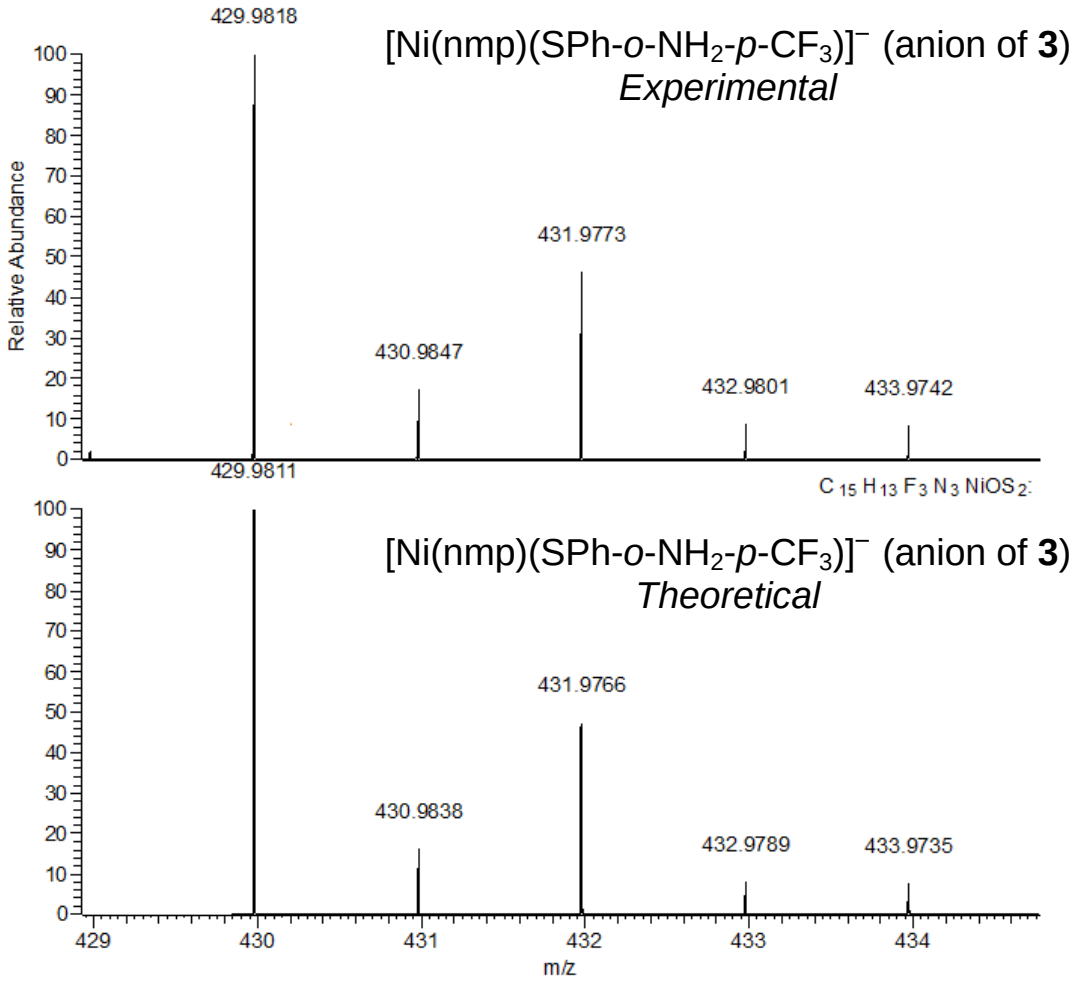

Figure S3.8. (Top) High resolution ESI-MS of the anion of **3** $[M\text{-}Et_4N]^-$ in MeCN at RT. (Bottom) Theoretical MS for the anion of **3**.

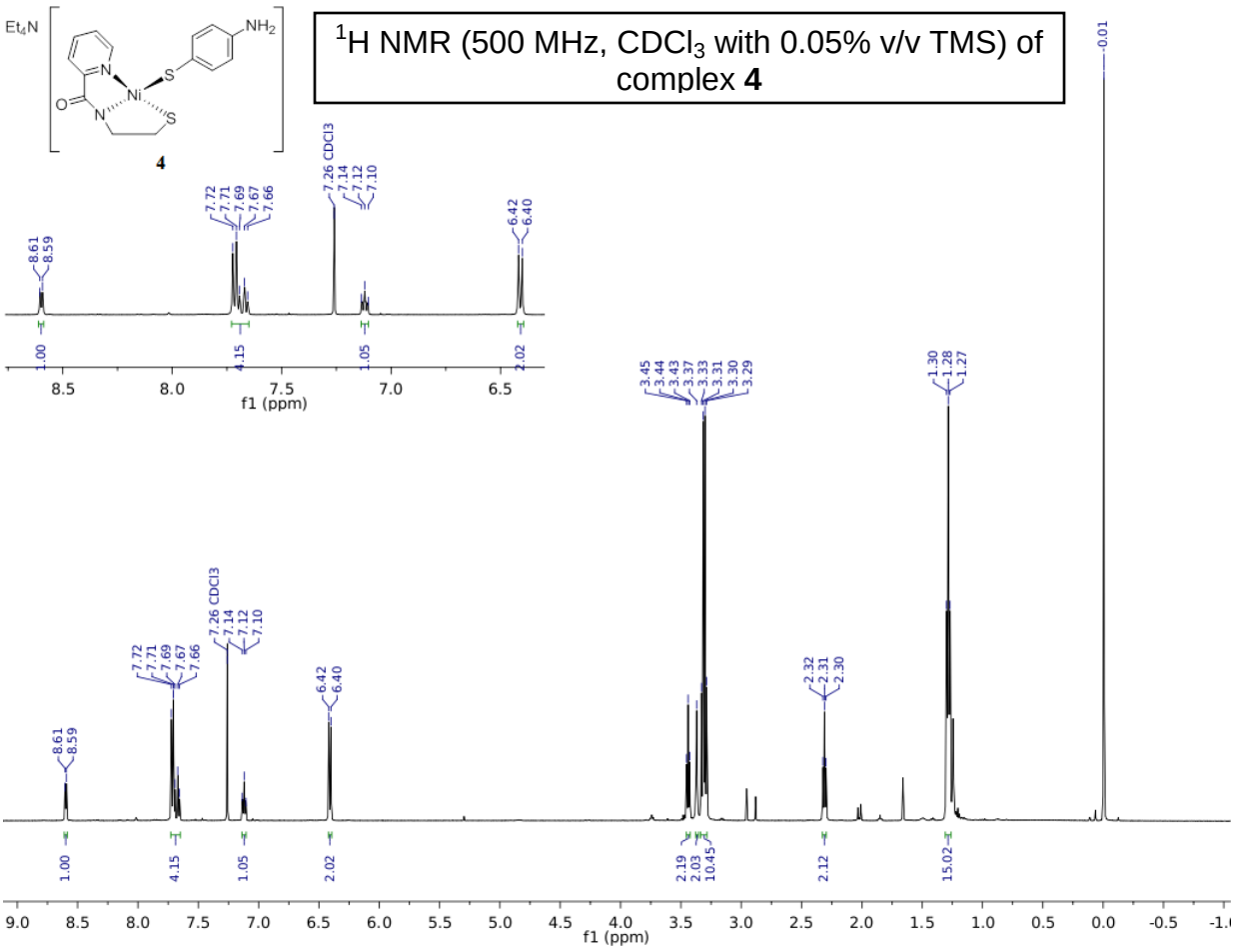

Figure S3.9. ^{1}H NMR spectrum of **4** in $CDCl_3$ containing 0.05% v/v TMS at RT. Inset shows expanded aromatic region. Residual protio solvent (7.26 ppm), H_2O (1.66 ppm), and TMS (0.00 ppm) are present. A minor amount of DMF (8.02, 2.95, 2.88 ppm), THF (3.74, 1.85 ppm), and MeCN (2.03 ppm) from workup are also present.

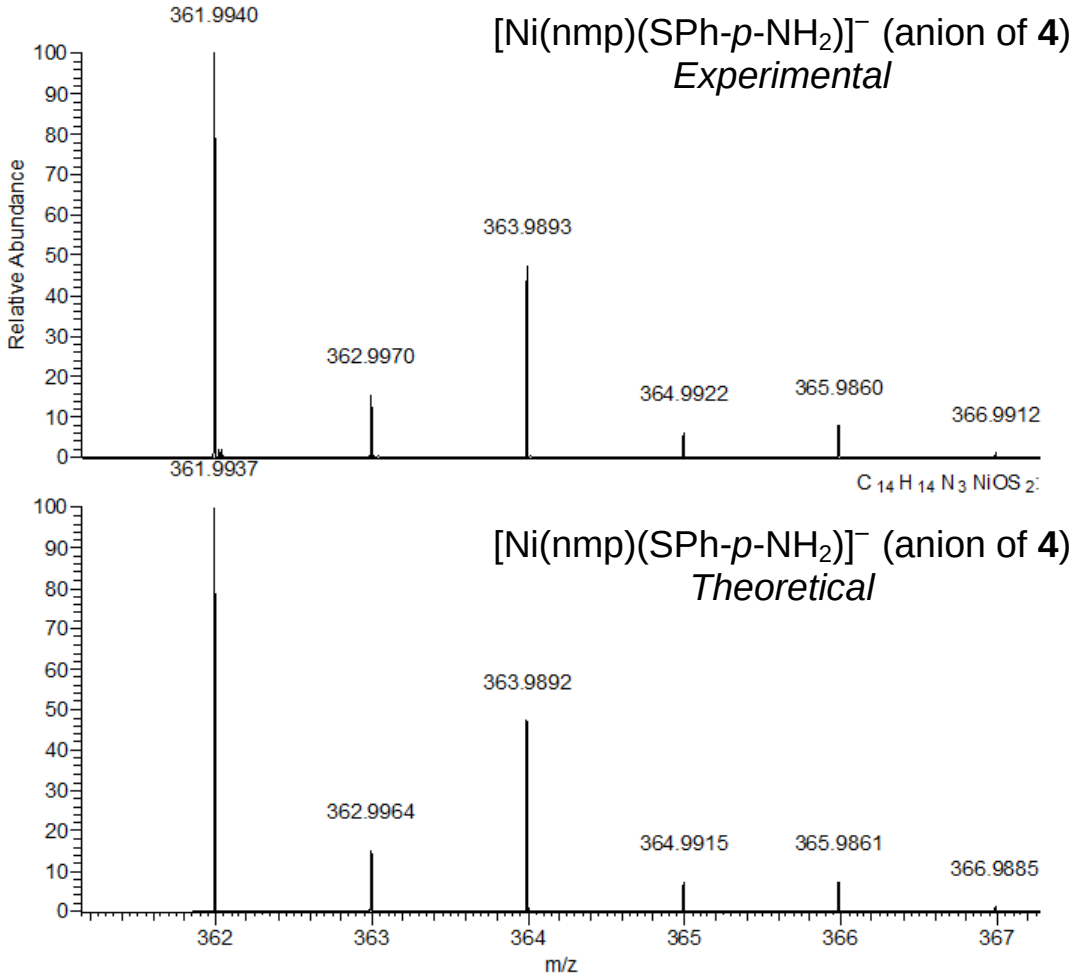

Figure S3.10. (Top) High resolution ESI-MS of the anion of **4** $[M\text{-}Et_4N]^-$ in MeCN at RT. (Bottom) Theoretical MS of the anion of **4**.

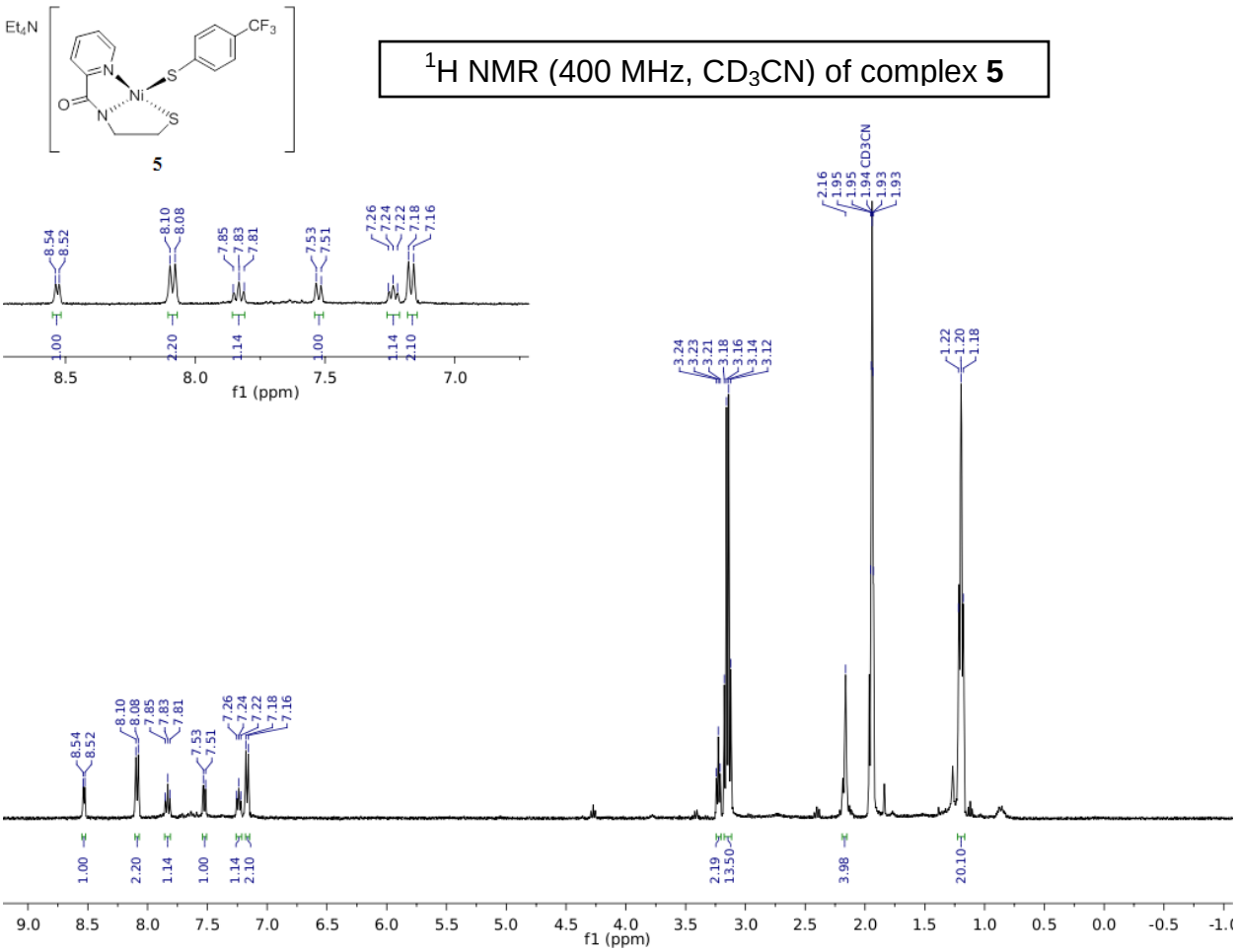

Figure S3.11. ^{1}H NMR spectrum of **5** in CD_3CN at RT. Inset shows expanded aromatic region. Residual protio solvent (1.94 ppm) and H_2O (2.16 ppm) are present. A minor amount of THF (3.64, 1.80 ppm) and Et_2O (3.42, 1.12 ppm) from workup is also present.

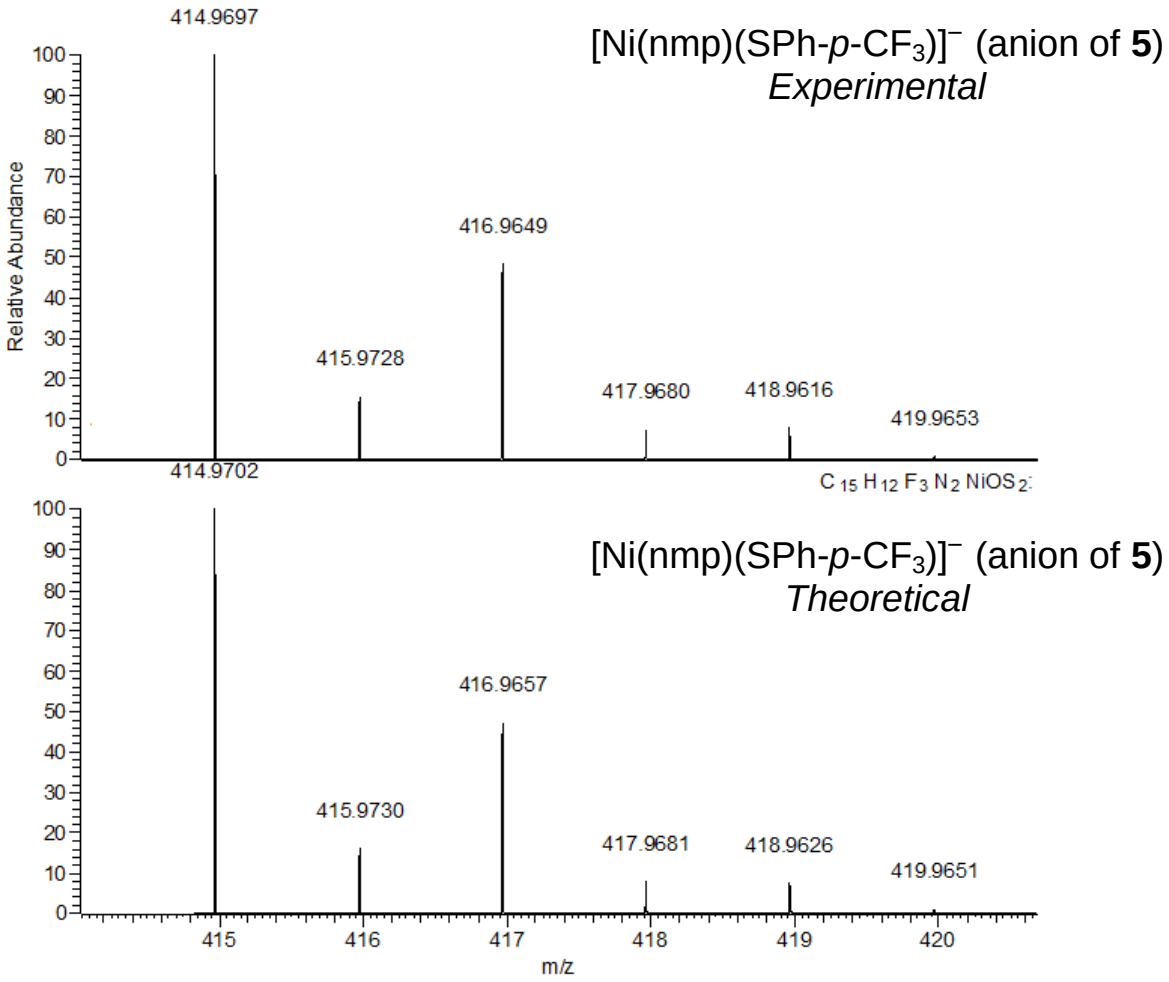

Figure S3.12. (Top) High resolution ESI-MS of the anion of **5** [M-Na]⁻ in MeCN at RT. (Bottom) theoretical MS of the anion of **5**.

3.6 References

(1) Valentine, J. S.; Wertz, D. L.; Lyons, T. J.; Liou, L.-L.; Goto, J. J.; Gralla, E. B. The Dark Side of Dioxygen Biochemistry. *Curr. Opin. Chem. Biol.* **1998**, *2*, 253-262.

(2) Miller, A.-F. Superoxide Dismutases: Active Sites That Save, but a Protein That Kills. *Curr. Opin. Chem. Biol.* **2004**, *8*, 162-168.

(3) McCord, J. M. In *Critical Reviews of Oxidative Stress and Aging: Advances in Basic Science, Diagnostics, and Intervention*; Rodriguez, H., Cutler, R., Eds.; World Scientific Publishing Co. Pte. Ltd.: Singapore, 2003, p 883-895.

(4) De Leo, M. E.; Borrello, S.; Passantino, M.; Palazzotti, B.; Mordente, A.; Daniele, A.; Filippini, V.; Galeotti, T.; Masullo, C. Oxidative Stress and Overexpression of Manganese Superoxide Dismutase in Patients with Alzheimer's Disease. *Neurosci. Lett.* **1998**, *250*, 173-176.

(5) Kocatürk, P. A.; Akbostanci, M. C.; Tan, F.; Kavas, G. Ö. Superoxide Dismutase Activity and Zinc and Copper Concentrations in Parkinson's Disease. *Pathophysiology* **2000**, *7*, 63-67.

(6) Maritim, A. C.; Sanders, R. A.; Watkins, J. B., III Diabetes, Oxidative Stress, and Antioxidants: A Review. *J. Biochem. Mol. Toxic.* **2003**, *17*, 24-38.

(7) Fortunato, G.; Pastinese, A.; Intrieri, M.; Lofrano, M. M.; Gaeta, G.; Censi, M. B.; Boccalatte, A.; Salvatore, F.; Sacchetti, L. Serum Mn-Superoxide Dismutase in Acute Myocardial Infarction. *Clin. Biochem.* **1997**, *30*, 569-571.

(8) Sheng, Y.; Abreu, I. A.; Cabelli, D. E.; Maroney, M. J.; Miller, A.-F.; Teixeira, M.; Valentine, J. S. Superoxide Dismutases and Superoxide Reductases. *Chem. Rev.* **2014**, *114*, 3854–3918.

(9) Miller, A.-F. Superoxide dismutases: Ancient enzymes and new insights. *FEBS Lett.* **2012**, *586*, 585-595.

(10) Fiedler, A. T.; Bryngelson, P. A.; Maroney, M. J.; Brunold, T. C. Spectroscopic and Computational Studies of Ni Superoxide Dismutase: Electronic Structure Contributions to Enzymatic Function. *J. Am. Chem. Soc.* **2005**, *127*, 5449-5462.

(11) Wuerges, J.; Lee, J.-W.; Yim, Y.-I.; Yim, H.-S.; Kang, S.-O.; Carugo, K. D. Crystal Structure of Nickel-Containing Superoxide Dismutase Reveals Another Type of Active Site. *Proc. Natl. Acad. Sci. U.S.A.* **2004**, *101*, 8569-8574.

(12) Barondeau, D. P.; Kassmann, C. J.; Bruns, C. K.; Tainer, J. A.; Getzoff, E. D. Nickel Superoxide Dismutase Structure and Mechanism. *Biochemistry* **2004**, *43*, 8038-8047.

(13) Grapperhaus, C. A.; Darensbourg, M. Y. Oxygen Capture by Sulfur in Nickel Thiolates. *Acc. Chem. Res.* **1998**, *31*, 451-459.

(14) Neupane, K. P.; Shearer, J. The Influence of Amine/Amide versus Bisamide Coordination in Nickel Superoxide Dismutase. *Inorg. Chem.* **2006**, *45*, 10552-10566.

(15) Shearer, J.; Long, L. M. A Nickel Superoxide Dismutase Maquette That Reproduces the Spectroscopic and Functional Properties of the Metalloenzyme *Inorg. Chem.* **2006**, *45*, 2358-2360.

(16) Tietze, D.; Breitzke, H.; Imhof, D.; Kothe, E.; Weston, J.; Buntkowsky, G. New Insight into the Mode of Action of Nickel Superoxide Dismutase by Investigating Metallopeptide Substrate Models. *Chem.-Eur. J.* **2009**, *15*, 517-523.

(17) Tietze, D.; Tischler, M.; Voigt, S.; Imhof, D.; Ohlenschläger, O.; Görlach, M.; Buntkowsky, G. Development of a Functional *cis*-Prolyl Bond Biomimetic and Mechanistic Implications for Nickel Superoxide Dismutase. *Chem.-Eur. J.* **2010**, *16*, 7572-7578.

(18) Tietze, D.; Voigt, S.; Mollenhauer, D.; Tischler, M.; Imhof, D.; Gutmann, T.; González, L.; Ohlenschläger, O.; Breitzke, H.; Görlach, M.; Buntkowsky, G. Revealing the Position of the Substrate in Nickel Superoxide Dismutase: A Model Study. *Angew. Chem., Int. Ed.* **2011**, *50*, 2946-2950.

(19) Shearer, J. Use of a Metallopeptide-Based Mimic Provides Evidence for a Proton-Coupled Electron-Transfer Mechanism for Superoxide Reduction by Nickel-Containing Superoxide Dismutase. *Angew. Chem., Int. Ed.* **2013**, *52*, 2569 –2572.

(20) Shearer, J.; Peck, K. L.; Schmitt, J. C.; Neupane, K. P. Cysteinate Protonation and Water Hydrogen Bonding at the Active-Site of a Nickel Superoxide Dismutase Metallopeptide-Based Mimic: Implications for the Mechanism of Superoxide Reduction. *J. Am. Chem. Soc.* **2014**, *136*, 16009–16022.

(21) Krause, M. E.; Glass, A. M.; Jackson, T. A.; Laurence, J. S. Novel Tripeptide Model of Nickel Superoxide Dismutase. *Inorg. Chem.* **2010**, *49*, 362-364.

(22) Krause, M. E.; Glass, A. M.; Jackson, T. A.; Laurence, J. S. MAPping the Chiral Inversion and Structural Transformation of a Metal-Tripeptide Complex Having Ni-Superoxide Dismutase Activity. *Inorg. Chem.* **2011**, *50*, 2479-2487.

(23) Glass, A. M.; Krause, M. E.; Laurence, J. S.; Jackson, T. A. Controlling the Chiral Inversion Reaction of the Metallopeptide Ni-Asparagine-Cysteine-Cysteine with Dioxygen. *Inorg. Chem.* **2012**, *51*, 10055-10063.

(24) Krause, M. E.; Glass, A. M.; Jackson, T. A.; Laurence, J. S. Embedding the Ni-SOD Mimetic Ni-NCC within a Polypeptide Sequence Alters the Specificity of the Reaction Pathway. *Inorg. Chem.* **2013**, *52*, 77-83.

(25) Ma, H.; Chattopadhyay, S.; Petersen, J. L.; Jensen, M. P. Harnessing Scorpionate Ligand Equilibria for Modeling Reduced Nickel Superoxide Dismutase Intermediates. *Inorg. Chem.* **2008**, *47*, 7966-7968.

(26) Ma, H.; Wang, G.; Yee, G. T.; Petersen, J. L.; Jensen, M. P. Scorpionate-Supported Models of Nickel-Dependent Superoxide Dismutase. *Inorg. Chim. Acta* **2009**, *362*, 4563-4569.

(27) Lee, W.-Z.; Chiang, C.-W.; Lin, T.-H.; Kuo, T.-S. A Discrete Five-Coordinate Ni^{III} Complex Resembling the Active Site of the Oxidized Form of Nickel Superoxide Dismutase. *Chem.-Eur. J.* **2012**, *18*, 50-53.

(28) Nakane, D.; Funahashi, Y.; Ozawa, T.; Masuda, H. A Square-planar Ni(II) Complex with an Asymmetric N_2S_2 Donor Set as a Model for the Active Site of Nickel-containing SOD: Structural Conversion Driven by Addition of a Strong Donor Ligand in the High Oxidation State. *Chem. Lett.* **2010**, *39*, 344-346.

(29) Shearer, J.; Zhao, N. $[Me_4N](Ni^{II}(BEAAM))$: A Synthetic Model for Nickel Superoxide Dismutase That Contains Ni in a Mixed Amine/Amide Coordination Environment. *Inorg. Chem.* **2006**, *45*, 9637-9639.

(30) Shearer, J.; Dehestani, A.; Abanda, F. Probing Variable Amine/Amide Ligation in $Ni^{II}N_2S_2$ Complexes Using Sulfur K-Edge and Nickel L-Edge X-ray Absorption Spectroscopies: Implications for the Active Site of Nickel Superoxide Dismutase. *Inorg. Chem.* **2008**, *47*, 2649-2660.

(31) Mathrubootham, V.; Thomas, J.; Staples, R.; McCraken, J.; Shearer, J.; Hegg, E. L. Bisamidate and Mixed Amine/Amidate NiN_2S_2 Complexes as Models for Nickel-Containing Acetyl Coenzyme A Synthase and Superoxide Dismutase: An Experimental and Computational Study. *Inorg. Chem.* **2010**, *49*, 5393-5406.

(32) Gale, E. M.; Patra, A. K.; Harrop, T. C. Versatile Methodology Toward NiN_2S_2 Complexes as Nickel Superoxide Dismutase Models: Structure and Proton Affinity. *Inorg. Chem.* **2009**, *48*, 5620-5622.

(33) Gale, E. M.; Narendrapurapu, B. S.; Simmonett, A. C.; Schaefer, H. F., III; Harrop, T. C. Exploring the Effects of H-Bonding in Synthetic Analogues of Nickel Superoxide Dismutase (Ni-SOD): Experimental and Theoretical Implications for Protection of the Ni−SCys Bond. *Inorg. Chem.* **2010**, *49*, 7080–7096.

(34) Gale, E. M.; Cowart, D. M.; Scott, R. A.; Harrop, T. C. Dipeptide-Based Models of Nickel Superoxide Dismutase: Solvent Effects Highlight a Critical Role to Ni–S Bonding and Active Site Stabilization. *Inorg. Chem.* **2011**, *50*, 10460-10471.

(35) Gale, E. M.; Simmonett, A. C.; Telser, J.; Schaefer, H. F., III; Harrop, T. C. Toward Functional Ni-SOD Biomimetics: Achieving a Structural/Electronic Correlation with Redox Dynamics. *Inorg. Chem.* **2011**, *50*, 9216–9218.

(36) Gennari, M.; Orio, M.; Pécaut, J.; Neese, F.; Collomb, M.-N.; Duboc, C. Reversible Apical Coordination of Imidazole between the Ni(III) and Ni(II) Oxidation States of a Dithiolate Complex: A Process Related to the Ni Superoxide Dismutase. *Inorg. Chem.* **2010**, *49*, 6399-6401.

(37) Gennari, M.; Retegan, M.; DeBeer, S.; Pécaut, J.; Neese, F.; Collomb, M.-N.; Duboc, C. Experimental and Computational Investigation of Thiolate Alkylation in Ni^{II} and Zn^{II} Complexes: Role of the Metal on the Sulfur Nucleophilicity. *Inorg. Chem.* **2011**, *50*, 10047-10055.

(38) Mullins, C. S.; Grapperhaus, C. A.; Frye, B. C.; Wood, L. H.; Hay, A. J.; Buchanan, R. M.; Mashuta, M. S. Synthesis and Sulfur Oxygenation of a (N_3S)Ni Complex Related to Nickel-Containing Superoxide Dismutase. *Inorg. Chem.* **2009**, *48*, 9974-9976.

(39) Shearer, J. Insight into the Structure and Mechanism of Nickel-Containing Superoxide Dismutase Derived from Peptide-Based Mimics. *Acc. Chem. Res.* **2014**, *47*, 2332−2341.

(40) Broering, E. P.; Truong, P. T.; Gale, E. M.; Harrop, T. C. Synthetic Analogues of Nickel Superoxide Dismutase: A New Role for Nickel in Biology. *Biochemistry* **2013**, *52*, 4-18.

(41) Mullins, C. S.; Grapperhaus, C. A.; Kozlowski, P. M. Density Functional Theory Investigations of NiN_2S_2 Reactivity as a Function of Nitrogen Donor Type and N–H···S Hydrogen Bonding Inspired by Nickel-Containing Superoxide Dismutase. *J. Biol. Inorg. Chem.* **2006**, *11*, 617-625.

(42) Neupane, K. P.; Gearty, K.; Francis, A.; Shearer, J. Probing Variable Axial Ligation in Nickel Superoxide Dismutase Utilizing Metallopeptide-Based Models: Insight into the Superoxide Dismutase Disproportionation Mechanism. *J. Am. Chem. Soc.* **2007**, *129*, 14605-14618.

(43) Nakane, D.; Wasada-Tsutsui, Y.; Funahashi, Y.; Hatanaka, T.; Ozawa, T.; Masuda, H. A Novel Square-Planar Ni(II) Complex with an Amino-Carboxamido-Dithiolato-type Ligand as an Active-Sie model of NiSOD. *Inorg. Chem.* **2014**, *53*, 6512−6523.

(44) Fiedler, A. T.; Brunold, T. C. Spectroscopic and Computational Studies of Ni^{3+} Complexes with Mixed S/N Ligation: Implications for the Active Site of Nickel Superoxide Dismutase. *Inorg. Chem.* **2007**, *46*, 8511-8523.

(45) Rosenfield, S. G.; Armstrong, W. H.; Mascharak, P. K. Convenient synthesis and properties of $(R_4N)_2[Ni(SAr)_4]$ (Ar = C_6H_5, p-C_6H_4Cl, p-$C_6H_4CH_3$, and m-C_6H_4Cl) and the structure of tetraethylammonium tetrakis(p-chlorobenzenethiolato)nickelate(II). *Inorg. Chem.* **1986**, *25*, 3014-3018.

(46) Palermo, R. E.; Power, P. P.; Holm, R. H. Ligand Substitution Properties of the MFe_3S_4 Double-Cubane Cluster Complexes $[Mo_2Fe_6S_8(SR)_9]^{3-}$ and $[M_2Fe_7S_8(SR)_{12}]^{3-}$ (M = Mo, W). *Inorg. Chem.* **1982**, *21*, 173-181.

(47) Belford, R. L.; Belford, G. G. Eigenfield expansion technique for efficient computation of field-swept fixed-frequency spectra from relaxation master equations. *J. Chem. Phys.* **1973**, *59*, 853-854.

(48) Fulmer, G. R.; Miller, A. J. M.; Sherden, N. H.; Gottlieb, H. E.; Nudelman, A.; Stoltz, B. M.; Bercaw, J. E.; Goldberg, K. I. NMR Chemical Shifts of Trace Impurities: Common Laboratory Solvents, Organics, and Gases in Deuterated Solvents Relevant to the Organometallic Chemist. *Organometallics* **2010**, *29*, 2176–2179.

(49) *SMART v5.626: Software for the CCD Detector System*; Bruker AXS: Madison, WI, 2000.

(50) Walker, N.; Stuart, D. An empirical method for correcting diffractometer data for absorption effects. *Acta Crystallogr.* **1983**, *A39*, 158-166.

(51) Sheldrick, G. M. *SADABS, Area Detector Absorption Correction*; University of Göttingen: Göttingen, Germany, 2001.

(52) Sheldrick, G. M. *SHELX-97, Program for Refinement of Crystal Structures*; University of Göttingen: Göttingen, Germany, 1997.

(53) Sheldrick, G. M. A short history of SHELX. *Acta Crystallogr.* **2008**, *A64*, 112-122.

(54) Sheldrick, G. M. *SHELXTL 6.1, Crystallographic Computing System*; Siemens Analytical X-Ray Instruments: Madison, WI, 2000.

(55) Burnett, M. N.; Johnson, C. K. *ORTEP-III, Report ORNL-6895*; Oak Ridge National Laboratory: Oak Ridge, TN, 1996.

(56) Neese, F. The ORCA program system. *Wiley Interdiscip. Rev. Comput. Mol. Sci.* **2012**, *2*, 73-78.

(57) Becke, A. D. Density-Function Thermochemistry .3. The Role of Exact Exchange. *J. Chem. Phys.* **1993**, *98*, 5648-5652.

(58) Lee, C.; Yang, W.; Parr, R. G. Development of the Colle-Salvetti correlation-energy formula into a functional of the electron-density. *Phys. Rev. B: Condens. Matter Mater. Phys.* **1998**, *37*, 785-789.

(59) Schäfer, A.; Horn, H.; Ahlrichs, R. Fully Optimized Contracted Gaussian Basis Sets for Atoms Lithium to Krypton. *J. Chem. Phys.* **1992**, *97*, 2571-2577.

(60) Neese, F. Prediction and interpretation of the ^{57}Fe isomer shift in Mössbauer spectra by density functional theory. *Inorg. Chim. Acta* **2002**, *337*, 181-192.

(61) The PyMOL Molecular Graphics System. The PyMOL Molecular Graphics System, Version 1.5.0.4. Schrödinger, LLC.

(62) Wachters, A. J. H. Gaussian Basis Set for Molecular Wavefunctions Containing Third-Row Atoms. *J. Chem. Phys.* **1970**, *52*, 1033-1036.

(63) The Ahlrichs (2d2fg,3p2df) polarization functions were obtained from the TurboMole basis set library under ftp.chemie.uni-karlsruhe.de/pub/basen Sc-Zn: 2p functions from ref. 60, plus one f-function from the TurboMole library.

(64) Kutzelnigg, W.; Fleischer, U.; Schindler, M. *The IGLO Method: Ab Initio Calculation and Interpretation of NMR Chemical Shifts and Magnetic Susceptibilities*; Springer-Verlag: Heidelberg, 1990; Vol. 23.

(65) Gampp, H.; Lippard, S. J. Reinvestigation of 18-Crown-6 Ether/Potassium Superoxide Solutions in Me_2SO. *J. Am. Chem. Soc.* **1983**, *22*, 357-358.

(66) Herebian, D.; Bothe, E.; Bill, E.; Weyhermüller, T.; Wieghardt, K. Experimental Evidence for the Noninnocence of *o*-Aminothiophenolates: Coordination Chemistry of *o*-Iminothionebenzosemiquinonate(1-) π-Radicals with Ni(II), Pd(II), Pt(II). *J. Am. Chem. Soc.* **2001**, *123*, 10012-10023.

(67) Jeffrey, G. A. *An Introduction to Hydrogen Bonding*; 1 ed.; Oxford University Press, Inc.: New York, 1997.

(68) Antonello, S.; Daasbjerg, K.; Jensen, H.; Taddei, F.; Maran, F. Formation and Cleavage of Aromatic Disulfide Radical Anions. *J. Am. Chem. Soc.* **2003**, *125*, 14905-14916.

(69) Chang, T. M.; Tomat, E. Disulfide/thiol switched in thiosemicarbazone ligands for redox-directed iron chelation. *Dalton Trans.* **2013**, *42*, 7846-7849.

(70) Krüger, H.-J.; Holm, R. H. Chemical and Electrochemical Reactivity of Nickel(II,I) Thiolate Complexes: Examples of Ligand-Based Oxidation and Metal-Centered Oxidative Addition. *Inorg. Chem.* **1989**, *28*, 1148-1155.

(71) Tripathi, G. N. R.; Sun, Q.; Armstrong, D. A.; Chipman, D. M.; Schuler, R. H. Resonance Raman Spectra and Structure of Phenylthiyl Radical. *J. Phys. Chem.* **1992**, *96*, 5344-5350.

(72) Stenson, P. A.; Board, A.; Marin-Becerra, A.; Blake, A. J.; Davies, E. S.; Wilson, C.; McMaster, J.; Schröder, M. Molecular and Electronic Structures of One-Electron Oxidized Ni^{II}–(Dithiosalicylidenediamine) Complexes: Ni^{III}–Thiolate versus Ni^{II}–Thiyl Radical States. *Chem.-Eur. J.* **2008**, *14*, 2564-2576.

(73) Kimura, S.; Bill, E.; Bothe, E.; Weyhermüller, T.; Wieghardt, K. Phenylthiyl Radical Complexes of Gallium(III), Iron(III), and Cobalt(III) and Comparison with Their Phenoxyl Analogues. *J. Am. Chem. Soc.* **2001**, *123*, 6025-6039.

(74) Grapperhaus, C. A.; Poturovic, S. Electrochemical Investigations of the [Tris(2-(diphenylphosphino)thiaphenolato)ruthenate(II)] Monoanion Reveal Metal- and Ligand-Centered Events: Radical, Reactivity, and Rate. *Inorg. Chem.* **2004**, *43*, 3292-3298.

(75) Chang, Y.-H.; Su, C.-L.; Wu, R.-R.; Liao, J.-H.; Liu, Y.-H.; Hsu, H.-F. An Eight-Coordinate Vanadium Thiolate Complex with Charge Delocalization between V(V)-Thiolate and V(IV)-Thiyl Radical Forms. *J. Am. Chem. Soc.* **2011**, *133*, 5708-5711.

(76) Jaun, B. Coenzyme F430 from Methanogenic Bacteria: Oxidation of F430 Pentamethyl Ester to the Ni(III) Form. *Helv. Chim. Acta* **1990**, *73*, 2209-2217.

(77) Wieghardt, K.; Walz, W.; Nuber, B.; Weiss, J.; Ozarowski, A.; Stratemeier, H.; Reinen, D. Crystal structure of bis[bis(1,4,7-triazacyclononane)nickel(III)] dithionate heptahydrate and its single-crystal EPR spectrum. *Inorg. Chem.* **1986**, *25*, 1650-1654.

(78) Gore, E. S.; Busch, D. H. Stable octahedral, low-spin nickel(III) complexes of a tetradentate macrocyclic ligand having saturated nitrogen donors. *Inorg. Chem.* **1973**, *12*, 1-3.

(79) Wang, J.-F.; Kumar, K.; Margerum, D. W. Direct Determination of Self-Exchange Electron-Transfer Rate Constants of Nickel(III,II) Complexes by ^{61}Ni EPR Line Broadening. *Inorg. Chem.* **1989**, *28*, 3481-3484.

(80) Lappin, A. G.; Murray, C. K.; Margerum, D. W. Electron Paramagnetic Resonance Studies of Nickel(III)-Oligopeptide Complexes. *Inorg. Chem.* **1978**, *17*, 1630-1634.

(81) Krüger, H.-J.; Peng, G.; Holm, R. H. Low-Potential Nickel(III,II) Complexes: New Systems Based on Tetradentate Amidate-Thiolate Ligands and the Influence of Ligand Structure on Potentials in Relation to the Nickel Site in [NiFe]-Hydrogenases. *Inorg. Chem.* **1991**, *30*, 734-742.

(82) Green, K. N.; Brothers, S. M.; Jenkins, R. M.; Carson, C. E.; Grapperhaus, C. A.; Darensbourg, M. Y. An Experimental and Computational Study of Sulfur-Modified Nucleophilicity in a Dianionic NiN_2S_2 Complex. *Inorg. Chem.* **2007**, *46*, 7536-7544.

(83) Hanss, J.; Krüger, H.-J. First Isolation and Structural Characterization of a Nickel(III) Complex Containing Aliphatic Thiolate Donors. *Angew. Chem. Int. Ed.* **1998**, *37*, 360-363.

(84) Lim, B. S.; Fomitchev, D. V.; Holm, R. H. Nickel Dithiolenes Revisited: Structures and Electron Distribution from Density Functional Theory for the Three-Member Electron-Transfer Series $[Ni(S_2C_2Me_2)_2]^{0,1-,2-}$. *Inorg. Chem.* **2001**, *40*, 4257–4262.

(85) Szilagyi, R. K.; Lim, B. S.; Glaser, T.; Holm, R. H.; Hedman, B.; Hodgson, K. O.; Solomon, E. I. Description of the Ground State Wave Functions of Ni Dithiolenes Using Sulfur K-edge X-ray Absorption Spectroscopy. *J. Am. Chem. Soc.* **2003**, *125*, 9158–9169.

(86) Carvalho, N. M. F.; Antunes, O. A. C.; Horn Jr., A. Electrochemical behavior of mononuclear Fe(III) complexes as models for oxygenases: reactivity of Fe(II) species electrochemically formed *in situ* toward dioxygen. *Dalton Trans.* **2007**, *2007*, 1023-1027.

(87) Herbst, R. W.; Guce, A.; Bryngelson, P. A.; Higgins, K. A.; Ryan, K. C.; Cabelli, D. E.; Garman, S. C.; Maroney, M. J. Role of Conserved Tyrosine Residues in NiSOD Catalysis: A Case of Convergent Evolution. *Biochemistry* **2009**, *48*, 3354-3369.

(88) Ryan, K. C.; Guce, A. I.; Johnson, O. E.; Brunold, T. C.; Cabelli, D. E.; Garman, S. C.; Maroney, M. J. Nickel Superoxide Dismutase: Structural and Functional Roles of His1 and Its H-Bonding Network. *Biochemistry* **2015**, *54*, 1016-1027.

(89) Bryngelson, P. A.; Arobo, S. E.; Pinkham, J. L.; Cabelli, D. E.; Maroney, M. J. Expression, Reconstitution, and Mutation of Recombinant *Streptomyces coelicolor* NiSOD. *J. Am. Chem. Soc.* **2004**, *126*, 460-461.

(90) Giles, N. M.; Giles, G. I.; Jacob, C. Multiple roles of cysteine in biocatalysis. *Biochem. Biophys. Res. Commun.* **2003**, *300*, 1-4.

(91) Licht, S.; Gerfen, G. J.; Stubbe, J. Thiyl Radicals in Ribonucleotide Reductases. *Science* **1996**, *271*, 477-481.

(92) Fontecave, M.; Ollagnier-de-Choudens, S.; Mulliez, E. Biological Radical Sulfur Insertion Reactions. *Chem. Rev.* **2003**, *103*, 2149-2166.

(93) Cutsail III, G. E.; Telser, J.; Hoffman, B. M. Advanced paramagnetic resonance spectroscopies of iron–sulfur proteins: Electron nuclear double resonance (ENDOR) and electron spin echo envelope modulation (ESEEM). *Biochim. Biophys. Acta* **2015**, *1853*, 1370-1394.

(94) Grove, T. L.; Benner, J. S.; Radle, M. I.; Ahlum, J. H.; Landgraf, B. J.; Krebs, C.; Booker, S. J. A Radically Different Mechanism for *S*-Adenosylmethionine–Dependent Methyltransferases. *Science* **2011**, *332*, 604-607.

(95) Silakov, A.; Grove, T. L.; Radle, M. I.; Bauerle, M. R.; Green, M. T.; Rosenzweig, A. C.; Boal, A. K.; Booker, S. J. Characterization of a Cross-Linked Protein−Nucleic Acid Substrate Radical in the Reaction Catalyzed by RlmN. *J. Am. Chem. Soc.* **2014**, *136*, 8221−8228.

(96) Wang, J.; Woldring, R. P.; Román-Meléndez, G. D.; McClain, A. M.; Alzua, B. R.; Marsh, E. N. G. Recent Advances in Radical SAM Enzymology: New Structures and Mechanisms. *ACS Chem. Biol.* **2014**, *9*, 1929−1938.

(97) Broderick, J. B.; Duffus, B. R.; Duschene, K. S.; Shepard, E. M. Radical *S*-Adenosylmethionine Enzymes. *Chem. Rev.* **2014**, *114*, 4229−4317.

CHAPTER 4

NO REACTIVITY OF A Ni-N_2S_2 SYNTHETIC MODEL OF NiSOD

Broering, E. P.;* Troung, P. T.; Rodrigues, A. V.; Stemmler, T. L.; Harrop, T. C. To be submitted to *Chemical Communications*.

4.1 Abstract

A low molecular-weight synthetic analogue of the reduced nickel superoxide dismutase ($NiSOD_{red}$) active site displays unique reactivity with nitric oxide (NO). The resulting $\{NiNO\}^{10}$ complex is dimeric and contains bridging thiolates and N-nitrosamines coordinated to the Ni through the amine-N.

4.2 Novel NO Reactivity of a Ni(II)N_2S_2 Synthetic Model of NiSOD

The $NiSOD_{red}$ model $(Et_4N)[Ni(nmp)(SPh\text{-}o\text{-}NH_2\text{-}p\text{-}CF_3)]$ (**1**) where nmp^{2-} is the dianion of *N*-(2-mercaptoethyl)picolinamide[1] can be oxidized to a Ni species that is best described as a resonance hybrid between Ni(II)-thiyl and Ni(III)-thiolate as evidenced by UV-vis spectroscopy, electron paramagnetic resonance (EPR) spectroscopy, magnetic circular dichroism (MCD), and computational studies.[2] This oxidized complex is achieved due to modifications on the exogenous thiolate SR′, which distinguish **1** from other $[Ni(nmp)(SR')]^{1-}$ compounds.[1-3] Due to the decreased Lewis basicity on the S-donor, this modification decreases S-character in the highest occupied molecular orbital (HOMO) to promote Ni-based redox behavior. Namely, the electron-withdrawing character of the *p*-CF_3 group, in addition to the presence of an ortho NH_2, allow access to a higher oxidation state. In light of the resonance species with thiyl radical character, the reactivity of **1** was explored with reactive oxygen species (ROS).[2] To assess potential intermediates, the present work employs NO as an ROS analogue. The resulting Ni-NO product is a dinuclear Ni nitrosyl bridged by S-thiolates and N-nitrosamines, as deduced from X-ray diffraction (XRD) (**3**) (Figure 4.1). In addition to the X-ray structure of **3**, the spectroscopic and theoretical description of this $\{NiNO\}^{10}$ species and proposed mechanistic details of its formation are also described.

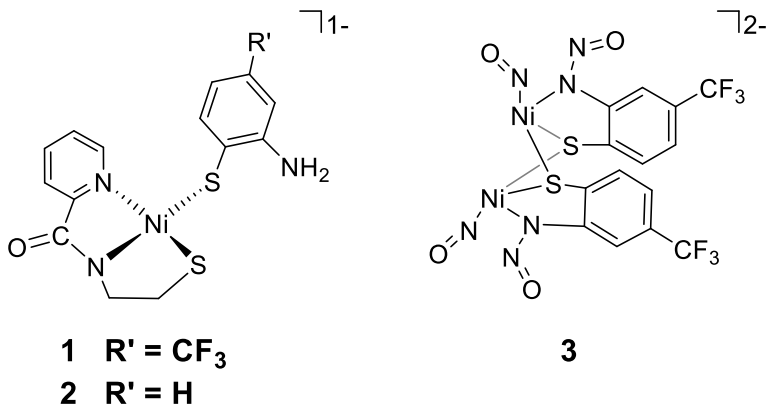

1 **R' = CF_3**
2 **R' = H**

3

Figure 4.1. *(Left)* The anion of (Et_4N)[Ni(nmp)(SR′)] (**1** or **2**). *(Right)* The anion of the dimeric {NiNO}^{10} species (**3**).

The $NiSOD_{red}$ analogue **1** was prepared according to previously published procedures.[2] Due to difficulties in obtaining X-ray quality crystals, structural characterization of **1** was carried out by X-ray absorption spectroscopy (XAS), and is consistent with other $[Ni(nmp)(SR')]^{1-}$ complexes.[1-6] The X-ray absorption near edge spectrum (XANES) of **1** shows a 1s → 4p transition centered at 8336.3 eV corresponding to a four coordinate (4C), square-planar Ni. Edge analysis at the rising edge of 8340 eV confirms the expected Ni(II) oxidation state of **1** (Figure 4S.1).[7] Although the placement of the ortho-NH_2 of SR′ is within the van der Waals radii to engage in an intramolecular hydrogen bond (H-bond) with the thiolate,[2] XAS confirms that it is not close enough to serve as an apical donor to the Ni center. Simulations and fits of the extended X-ray absorption fine structure (EXAFS) region of **1** reveal two S-ligands at an average distance of 2.17 Å and two O/N ligands at an average distance of 1.90 Å (Table 4S.3), comparable to other $S = 0$, Ni(II)N_2S_2 square-planar complexes.[2]

The dimeric nitrosylated complex **3** was synthesized by purging a DMF solution of **1** with NO(g) for 60 s at RT. The red-brown color of **1** changed to green over the course of 30 min, the first indicator of potential nitrosylation. After workup, **3** was isolated as a green solid in 94% yield. Complex **3** is soluble in DMF, and moderately soluble in other organic solvents; however, solutions of **3** (CH_2Cl_2, MeOH, THF, MeCN) are unstable to vacuum, which results in loss of NO(g) as indicated by FTIR and color change from green to brown (Figure 4S.11). Also, solutions of **3** experience a loss of NO upon exposure to O_2 (FTIR, Figure 4S.12). Complex **3** is assigned as a $\{NiNO\}^{10}$ species, according to the Enemark-Feltham notation,[8] formally a d^9 Ni(I) coordinated to $NO^{\bullet}$. The UV-vis spectrum of **3** (DMF, 298K) reveals the disappearance of the charge transfer (CT) band of **1** and appearance of a broad absorbance at λ = 686 nm (ε = 150 $M^{-1}cm^{-1}$) and shoulder at λ = 425 nm (ε = 3000 $M^{-1}cm^{-1}$) (Figure 4S.10). These features are in-line with other Ni-nitrosyls bound to thiolate ligands.[9]

Single crystals of the nitrosylated product were grown by Et_2O diffusion into an MeCN solution of **3** at -20 °C. Data for XRD revealed a novel nitrosylated species formulated as $(Et_4N)_2[Ni_2(\mu\text{-}SR')_2(NO)_4]$, where nmp^{2-} is no longer bound (Figure 4.2). The Ni-NO is held in a distorted tetrahedral geometry (τ_4 = 0.728)[10] via a deprotonated N-nitrosamine and bridging RS^- from two different benzenthiolates. The relevant metric parameters and X-ray data are listed in Table 4.1 and in Tables 4S.1 and 4S.2 of the supporting information. The Ni···Ni distance is 3.068 Å, precluding the possibility for a Ni–Ni bond. The Ni–N(O) distance of **3** (1.659 Å) is in-line with other structurally characterized $\{NiNO\}^{10}$ complexes, which typically exhibit Ni–N(O) bonds of 1.58-1.69 Å.[11-16] The N–N(O) bond distance of 1.299 Å of the amine-N is similar to other reported N-nitrosamines (1.276-1.331 Å).[17-19] Together with the bent N–N–O bond angle (114.2°), this suggests sp^2-hybridization on the amine-N. A notable difference from other

structurally characterized metal-nitrosyl/N-nitrosamine complexes is coordination through th amine-N of the nitrosamine. Among other coordinated N-nitrosamines, the typical binding mode to a metal occurs instead through the N or O of the nitroso moiety.[20,21] To date (2017), there have been no other structures reported for aniline derived N-nitrosamines bound to a metal center via the amine-N.

There are few examples of $\{NiNO\}^{10}$ species supported by bridging thiolates, and these typically exhibit Ni—S bond distances of approximately ~2.3 Å.[9,22,23] Rabinovich has observed that Ni-thiolate bond distances for 4C complexes are longer than those belonging to thiones or thioureas (2.14-2.30 Å), but can be elongated up to 2.48 Å in Ni complexes with higher coordination numbers.[23,24] Upon nitrosylation and ligand rearrangement, the 2.317 and 2.355 Å Ni—S distances in **3** are lengthened as compared to the starting Ni(II) complex **1** (XAS = 2.17 Å avg, vide supra) and are consistent with other tetrahedral Ni-NO species published.[9,22,23]

The reaction described above and in Scheme 4.1 was carried out with isotopically labeled ^{15}NO under identical conditions providing **3-^{15}NO** in 87% yield. Consistent with the crystal structure, the solid-state FTIR spectrum of **3** exhibits ν_{NO} at 1747 cm^{-1} that shifts in **3-^{15}NO** (Figure 4S.3-4S.4). The ν_{15NO} stretch is obscured by other stretching frequencies in the FTIR of **3-^{15}NO**, and we would expect a $\Delta\nu_{NO}$ ~ 31 cm^{-1} to 1716 cm^{-1} based on a simple harmonic oscillator calculation. Indeed, a shoulder is observed in the FTIR of **3-^{15}NO** at ~1719 cm^{-1}, which likely belongs to the ν_{15NO} (Figure 4S.4). Another distinction between the FTIR in **3-^{15}NO** is the shift from 1258 cm^{-1} in **3** to 1250 cm^{-1} in **3-^{15}NO**, which is assigned to the N-nitrosamine. Uncomplexed N-nitrosamines exhibit distinct ν_{NO} and ν_{NN} stretches in the FTIR typically spanning 1420-1550 cm^{-1} and 930-1150 cm^{-1}, respectively.[20,25,26] However, work by Richter-Addo has shown that these two vibrations can overlap in metal complexes (e.g., Fe porphyrin

complexes with N-nitrosamines) and instead appear as one resonant band in the 1200-1300 cm^{-1} region.[20] The shifts and convergence of these bands signify that that metal-bound N-nitrosamine ν_{NO} stretches are weaker and appear at lower energies than free N-nitrosamines, and ν_{NN} stretches are stronger and appear at higher energies in metal complexes than in their free counterparts.[20] Because we only observe one stretch at 1258 cm^{-1} that is sensitive to isotopic labeling, we can assign this feature as an overlap, or resonance mode, belonging to the N-nitrosamine. The shift of $\Delta\nu$ = 8 cm^{-1} in **3** is less than is observed for the Fe systems ($\Delta\nu$ = 19 cm^{-1}), which may speak to the difference in metal and oxidation state, Ni(I) vs Fe(III).[20] Also, the unique N-nitrosamine binding mode to the Ni ion in **3**, as opposed to alkyl-bound N-nitrosamines, is expected to affect the energy of the ν_{NN} stretching frequency.

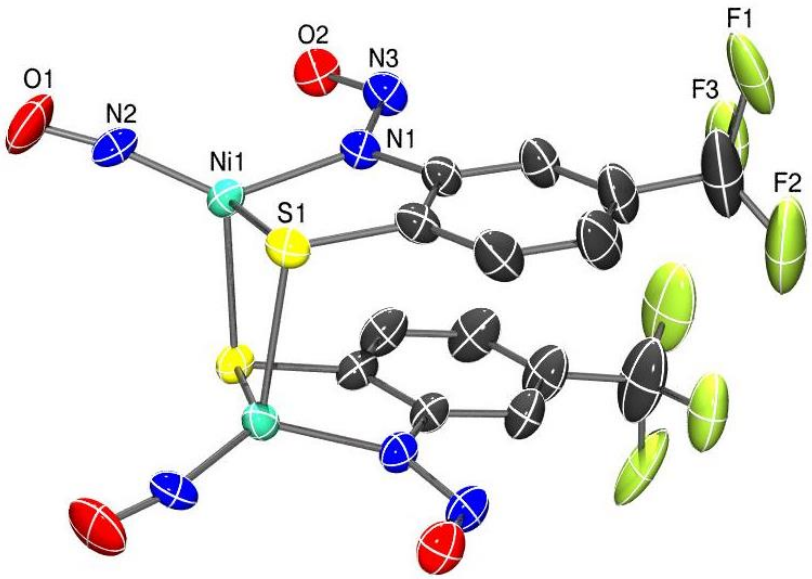

Figure 4.2. ORTEP of the anion of $(Et_4N)_2[Ni_2(SC_6H_3\text{-}o\text{-}N\text{-}p\text{-}CF_3)_2(NO)_4]$ (**3**) with the atom labeling scheme at 50% thermal probability. H atoms are omitted for clarity.

^{1}H NMR (DMSO-d_6) reveals **3** to be a diamagnetic complex, as observed for other {NiNO}^{10} species. Broadened peaks are present corresponding to the original aminobenzenethiolate signals of **1** with the exception of the protons belonging to NH_2, which are lost upon nitrosylation (Figure 4S.5). Low resolution electrospray ionization mass spectrometry (LR-ESI-MS) of **2** shows a peak at *m/z* 307.9 corresponding to $[Ni_2(\mu\text{-}SR')(NO)_2]^-$, i.e., one half of the X-ray crystal structure, indicating that the symmetric dimer may be cleaved under the ionizing conditions of the MS instrument (Figure 4S.7). A peak at *m/z* 309.9 appears in the LR-ESI-MS of **3-^{15}NO**, consistent with isotopic labeling and the increase in mass by two units corresponding to $[Ni_2(\mu\text{-}SR')(^{15}NO)_2]^-$. Upon characterizing the Et_2O-soluble filtrate from the workup of **3**, ^{1}H NMR ($CDCl_3$) and LR-ESI-MS reveal the fate of the nmp^{2-} ligand, which is lost as $nmpH_2$ upon reaction of **1** with NO(g) (Figure 4S.6 and Figure 4S.9), with the protons arising from the original NH_2 of **1**.

The NO chemistry observed with **1** is unique to this particular NiSOD model. An identical reaction with the NiSOD model of the general formula $[Ni(nmp)(SR')]^-$, where SR′ is the analogous aminobenzenethiolate lacking a CF_3 group (**2**), does not result in a nitrosylated species with NO(g) (Scheme 4.1). Although **2** can achieve a transient Ni(III) state, the lifetime of $\mathbf{2^{ox}}$ is much shorter than $\mathbf{1^{ox}}$ (min vs h), owing to the absence of the electron-withdrawing CF_3 group.[2] Reaction with NO(g) results in formation of $[Ni_4(nmp)_4]$, a metallosynthon and precursor to monomeric $[Ni(nmp)(SR')]^{1-}$ species that has been characterized previously as the product of irreversible oxidation at the exogenous thiolate position.[1,2]

Furthermore, in situ generation of $\mathbf{1^{ox}}$, followed by a purge of NO(g) resulted in irreversible S-based oxidation to form the $[Ni_4(nmp)_4]$ tetramer. The addition of nitrosonium (NO^+) to **1** does not result in any Ni-NO species. Indeed, addition of $NOBF_4$ to a DMF solution

of **1** resulted in bleaching of the solution and formation of precipitate assigned as [$Ni_4(nmp)_4$)]. Taken together, these experiments illustrate that the more stable high valent Ni state with radical character found in **1** (as compared to **2**) is necessary to yield nitrosylated complexes such as **3**.

Scheme 4.1. Reactivity of **1** and **2** with NO(g) and NO^+.

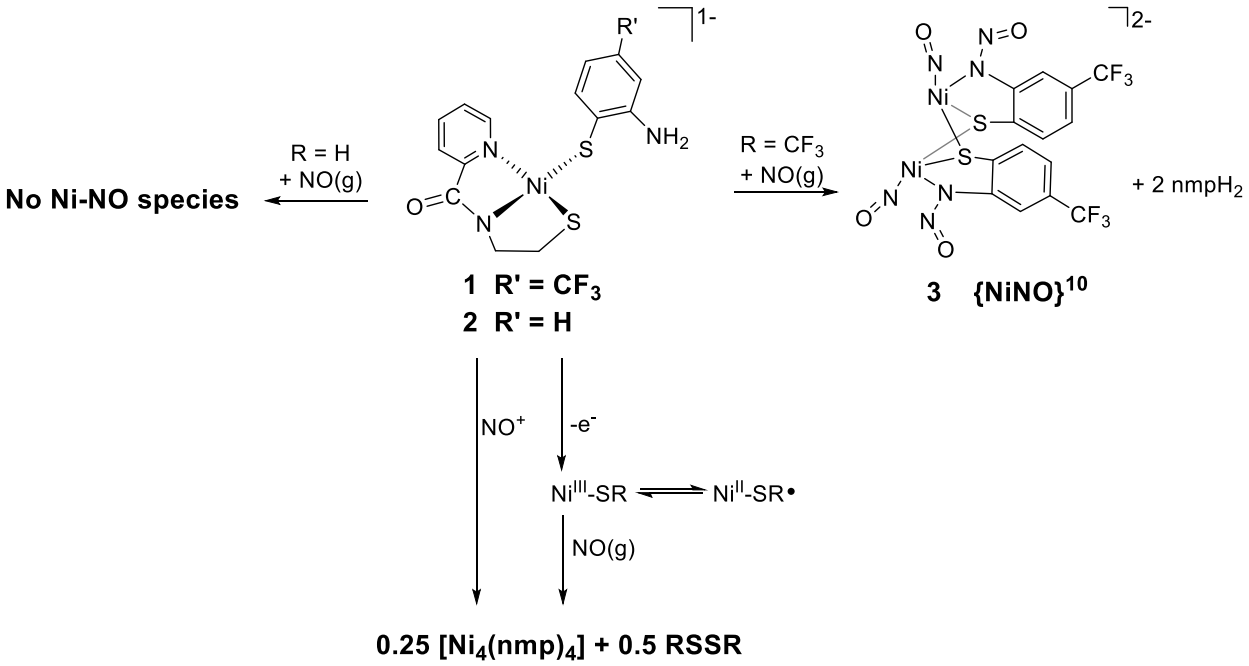

Density functional theory (DFT) calculations have proven to be a powerful tool to better understand the nature of $\{MNO\}^{10}$ complexes.[14,16,27-29] To gain further insight into the electronic structure of **3**, DFT computations at the OLYP/def2-TZVPP level of theory were performed. The DFT optimized model, **3*** was obtained using coordinates from the crystal structure of **3**, and the resulting bond distances and bond angles of **3*** structure are in close agreement with the experimentally determined values (Table 4.1). For example, the DFT determined ν_{NO} of 1730

cm^{-1} of the Ni-NO aligns well with the experimentally determined ν_{NO} of 1747 cm^{-1}. In **3***, the LUMO (MO 155) and LUMO+1 (MO 156) appear nearly degenerate with energies of 3.11 and 3.14 eV, respectively. Similarly, the energies of LUMO+2 (MO157) and LUMO+3 (MO 158) are nearly overlapping at 3.33 and 3.36 eV, respectively. Each is composed of primarily Ni-NO(π*) antibonding character. The largest N-nitrosamine orbital character is observed in the HOMO-2 (MO 152) and HOMO-3 (MO 151), with very little Ni character contributing to the overall energy. The HOMO is composed of Ni d_{z^2} that is antibonding to the π orbitals of the NO unit as well as antibonding to the bridging S ligands. Ni($d\pi$)-S($p\pi$) antibonding interactions are expected for square-planar N_2S_2 Ni complexes[5] and were observed for the parent complex **1** as well.[2]

The relatively short Ni—N(O) bond distances of ~1.65 Å and linear Ni-NO units have been observed in $\{NiNO\}^{10}$ complexes, and computations by Conradie and Ghosh have provided explanations for these trends.[30] In $\{NiNO\}^{10}$ complexes, as in **3**, the HOMO is Ni(d_{z^2}) based, with other contributions arising from Ni s or p character. The mixing of s and p contribution results in a "shrunken top lobe"[30] of the d_{z^2} orbital and a weakened Ni($d\pi$)-NO(π*) antibonding interaction, which results in a more linear Ni-NO bond. The d/s/p orbital mixing are more prevalent in tetrathedral, $\{NiNO\}^{10}$ complexes that lack equatorial ligands or ligands trans to the MNO unit.[30] Indeed, the computations on **3*** confirm that the $\{NiNO\}^{10}$ species adopts a distorted tetrahedral geometry. If the Ni ion were to maintain the square-planar geometry of **1** following nitrosylation, we would instead expect to observe a more bent Ni-NO bond angle to accommodate for a greater degree of Ni/S antibonding character that would arise in the HOMO.

The insights from DFT also explain the deligation of the nmp^{2-} ligand that occurs upon nitrosylation of **1**. Five coordinate $\{NiNO\}^{10}$ complexes are rare, and it is more likely for these

low valent MNO species to have lower coordination numbers and disfavor having strong field ligands trans to the NO. Conradie and Ghosh explain that the absence of trans or equatorial ligands avoids strong antibonding interactions between the Ni(d_σ) orbitals and ligand lone pairs.[30] By this description the {NiNO}^{10} is stabilized by the loss of the nmp^{2-} chelate in favor of coordinating the nearby N-nitrosamine to form the tetrahedral complex.

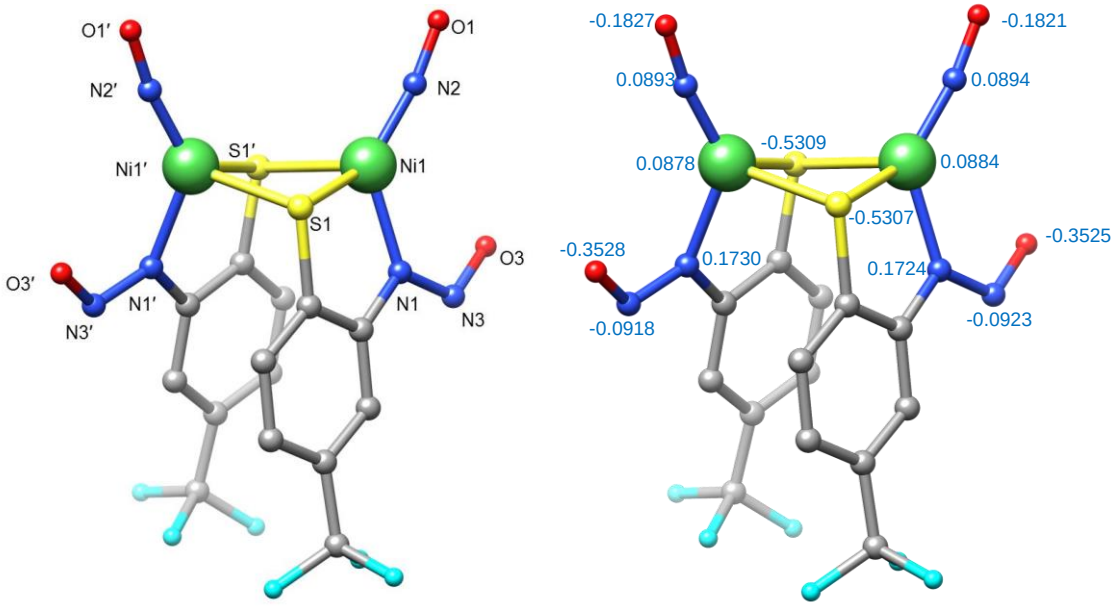

Figure 4.3. Geometry-optimized structure of **3** (**3***) (BP86/D3BJ/def2-TZVPP) with atom labels (left) and Mulliken atomic charges on Ni, S, O, and N atoms (right). Green = nickel; yellow = sulfur; blue = nitrogen; red = oxygen; cyan = fluorine.

Table 4.1. Selected Bond Distances (Å) and Bond Angles (deg) for the X-ray crystallographically determined values for **3**, compared with DFT-optimized model **3***.

	X-ray structure **3**	DFT optimized structure **3***
Ni1-S1	2.3169(7)	2.292
Ni1-S1′	2.3555(6)	2.343
Ni1-N2	1.659(7)	1.648
Ni1-N1	1.971(2)	1.975
N2-O1	1.182(8)	1.19
N1-N3	1.299(3)	1.325
N3-O2	1.269(3)	1.253
S1-Ni-S1′	96.66(2)	90.2
S1-Ni-N1	86.21(6)	86.6
S1′-Ni-N1	99.10(6)	98.7
S1-Ni-N1	123.8(5)	125.7
N2-Ni-S1′	109.8(6)	113.0
N1-Ni-N2	133.6(5)	132.5
Ni1-N2-O1	167.8(12)	170.8
N1-N3-O3	114.2(2)	115.7
τ_4	0.73	0.72

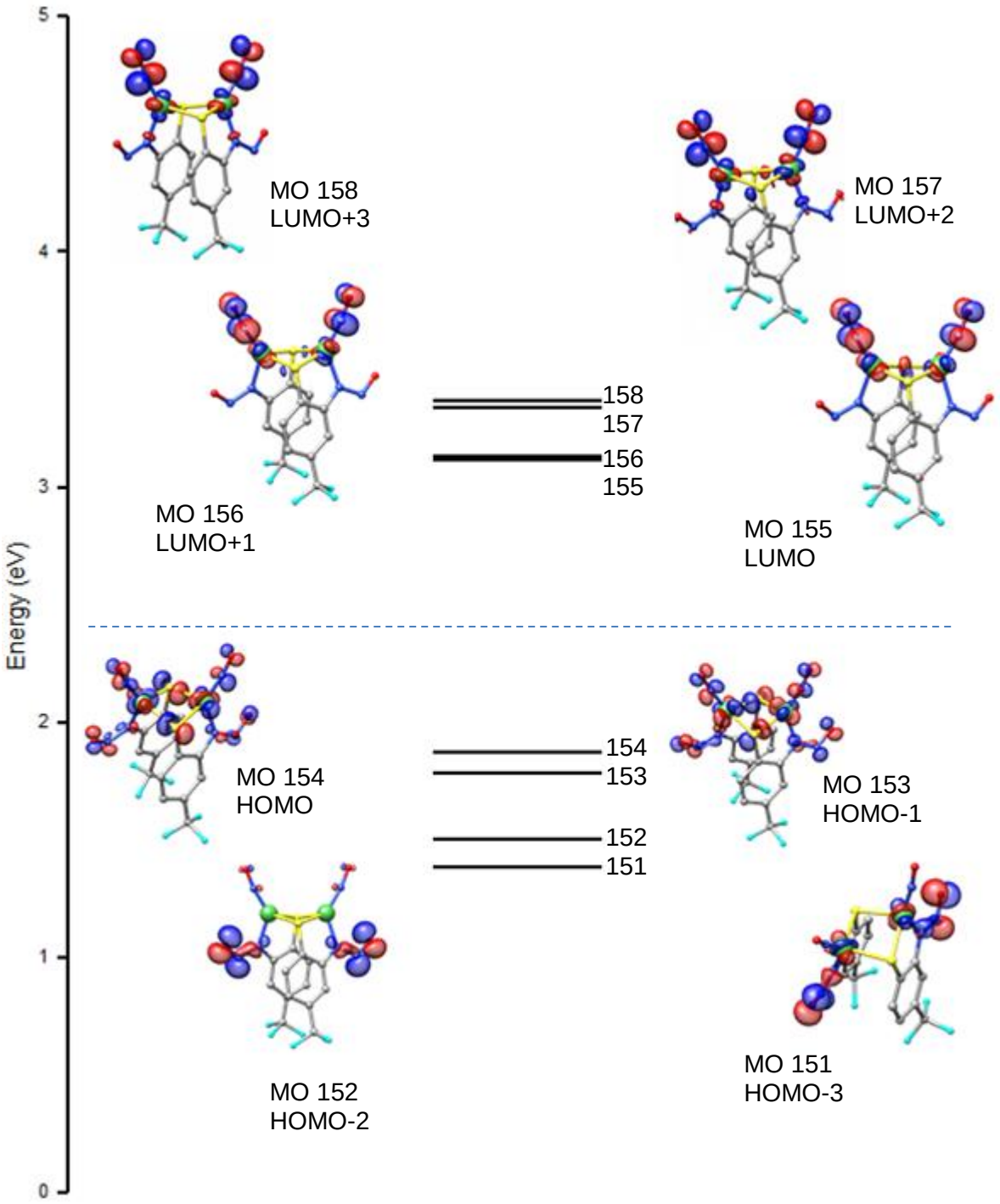

Figure 4.4. Orbital energy diagram of **3*** with HOMO-LUMO gap in blue. The MOs descend in the order LUMO+3, LUMO+2, LUMO+1, LUMO, HOMO, HOMO-1, HOMO-2, and HOMO-3. Dashed line indicates the level below which MOs are occupied.

Having observed lability of the NO in solution, and owing to the highly nitrosylated nature of **3**, we explored if **3** could serve as a suitable NO donor. As a preliminary test, we turned to known NO receptors that mimic heme receptors found in nature. The metalloporphryin [Fe(TPP)Cl], where TPP = tetraphenylporphyrin, was used to monitor the ability of **3** to transfer or donate NO^- to the Fe(III) center.[31-34] To an MeCN solution of [Fe(TPP)Cl] was added 0.5 equiv of **3**. Isolation of the Fe porphyrin and characterization by FTIR revealed product indistinguishable from the starting material, suggesting that **3** is incapable of transferring NO^- to [Fe(TPP)Cl] (Figure 4S.14). This result is not surprising, as our oxidation state assignment of the MNO species in **3** is $\{NiNO\}^{10}$, with the NO moiety having $NO^\bullet$ character rather than NO^- character. $NO^\bullet$ reacts readily with Fe(II) but not Fe(III).[31]

The metalloporphyrin [Co(TPP)(NO)] was first structurally characterized and published by Scheidt in 1973.[35] Since then, the $\{CoNO\}^8$ complex has been used as an analytical tool to monitor the transfer of NO from a donor to the Co porphyrin.[9,36,37] We have employed the methyl ether derivative of [Co(TPP)], namely 5,10,15,20-Tetrakis(4-methoxyphenyl)-21*H*,23*H*-porphine iron(III) chloride ([Co(T(-OMe)PP)]), to explore the $NO^\bullet$ donorability of **3**. The reaction of [Co(T(-OMe)PP)] with 0.5 equiv **3** was carried out in CH_2Cl_2. After stirring for 24 h, isolation of the [Co(T(-OMe)PP)] and characterization by FTIR reveals a ν_{NO} band at 1694 cm^{-1} that which shifts to 1663 cm^{-1} ($\Delta\nu_{NO}$ = 31 cm^{-1}) for the reaction of [Co(T(-OMe)PP)] with **3-^{15}NO** under identical conditions (Figures 4S.15-4S.16). This ν_{NO} value is consistent with previously reported [Co(TPP)(NO)] species[36-38] and is evidence that **3** releases NO. The UV-vis spectrum of the isolated product suggests a mixture of [Co(T(-OMe)PP)(NO)] and unreacted [Co(T(-OMe)PP)]. A decrease in absorbance and broadening of the Soret band is apparent upon coordination of NO, as is a 3 nm red-shift in the Q-band region. However, this red-shift is less

than the 10 nm shift expected for a fully nitrosylated [Co(T(-OMe)PP)] species, indicating that the transfer of NO from **3** is not stoichiometric (Figure 4S.17).[38] Likely, due to the antibonding Ni-NO nature of the HOMO, the NO from the metal is labile than from the N-nitrosamine.

The reduction of a metal with simultaneous nitrosylation of the ligand has been observed before in Cu(II) cyclam systems[39,40] and in Cu(II) fluorescein complexes.[41] In both cases, N-nitrosation of the chelate triggers electron transfer to the metal, deligation, and release of reduced Cu(I). A similar mechanism is occurring for the reaction of **1** with NO to reduce the Ni(II) to Ni(I), with some noticeable differences: (i) an MNO species has been trapped in the reduced state, and (ii) although deligation of the nmp^{2-} occurs, N-nitrosation of the exogenous ligand results in formation of a new coordinated bond to Ni. Compared to the N_2S_2 chelate in **1**, the macrocycle in the Cu(II) cyclam complexes is more stable, yet nitrosation of the amine weakens the M-N binding and facilitates the release of Cu.[39] The propensity for Cu(I) to prefer tetrahedral geometry, rather than the cyclam-enforced square-planar coordination, also contributes to dissociation of the metal.[39] Similar binding preferences are also at play in the Ni system: upon formation of the Ni(I)-NO bond, the covalent bonds that characterize the $Ni(II)N_2S_2$ square-planar system[2] are weakened, which can lead to the loss of nmp^{2-} (Scheme 4.2). Furthermore, the preference for $\{NiNO\}^{10}$ to adopt 4C tetrahedral geometries (discussed above) would also encourage the deligation of the tridentate nmp^{2-} in favor of binding the nearby N-NO.

Scheme 4.2. Proposed mechanism for the formation of **3.**

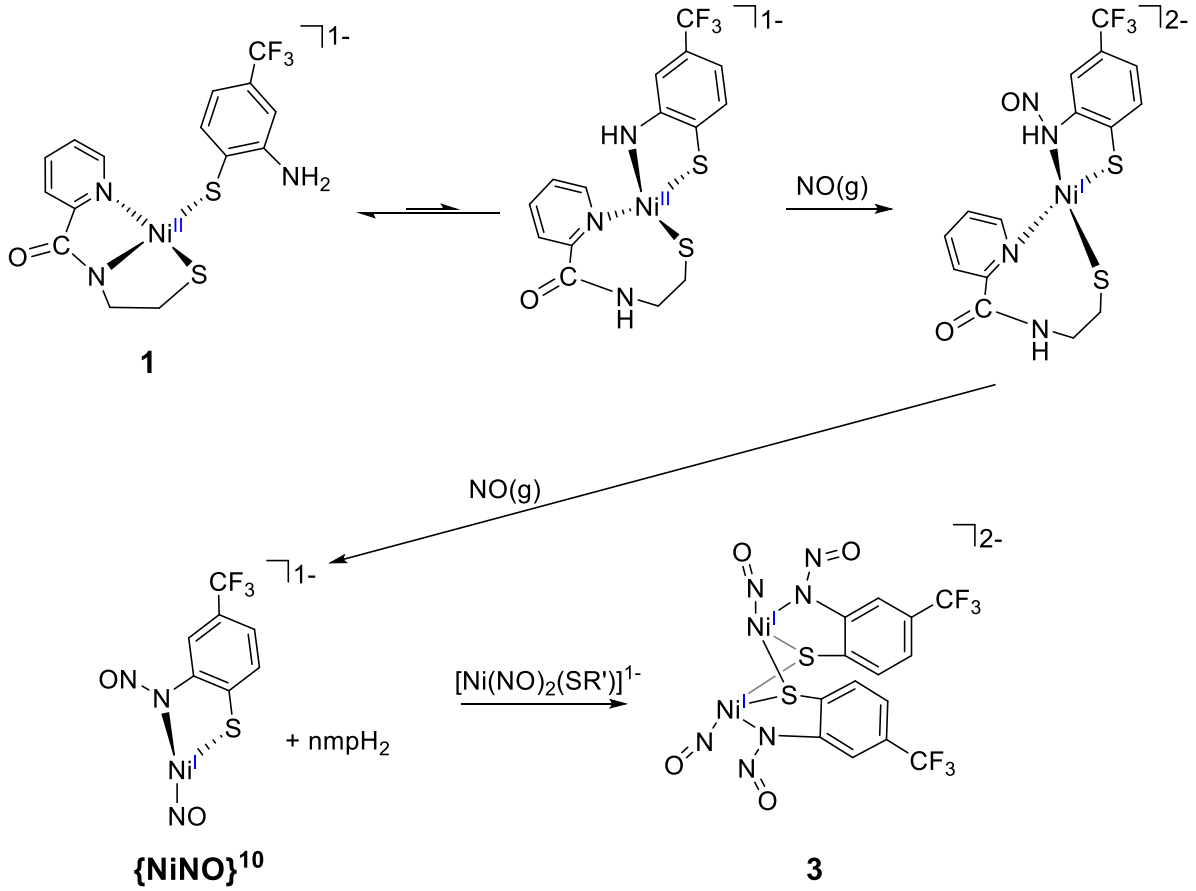

The coordination of an N-nitrosamine bound through the amine-N to a metal has not been structurally characterized before. This binding mode and the overall reactivity of **1** with NO(g) have only been observed with the Ni(II) complex that can achieve an oxidized state with significant thiyl radical character.[2] It is therefore this stabilizing thiyl state that allows for reactivity with the $NO^{\bullet}$ radical to result in reductive nitrosylation and trapping of the $\{NiNO\}^{10}$ species. The dimer **3** is highly nitrosylated, and it can lose NO under ambient conditions, vacuum, and can transfer the NO to a Co porphyrin receptor. This mechanism of reductive

nitrosylation and the novel metal-bound N-nitrosamine coordination represents a new route to capture MNO species and explore the reactivity of NO with metal centers.

4.3 Supporting Information

Experimental

General Information. All reagents were purchased from commercial sources and used as received unless otherwise noted. Research grade nitric oxide gas (NO(g), UHP, 99.5%) was obtained from Matheson Tri-Gas. The NO(g) was purified by passage through an Ascarite II® (sodium hydroxide-coated silica, purchased from Aldrich) column and handled under anaerobic conditions. ^{15}NO(g) (^{15}N ≥ 98%) was procured from Cambridge Isotope Labs and used as received. Acetonitrile (MeCN), dichloromethane (CH_2Cl_2), tetrahydrofuran (THF), and diethyl ether (Et_2O) were purified by passage through activated alumina columns of an MBraun MB-SPS solvent purification system and stored under an N_2 atmosphere until use. *N*,*N*-dimethylformamide (DMF) was purified with a VAC solvent purifier containing 4 Å molecular sieves and stored under N_2. Methanol (MeOH) was stored over 3 Å molecular sieves for at least one week and degassed using the freeze-pump-thaw method before using. The synthesis of (Et_4N)[Ni(nmp)(SPh-*o*-NH_2-*p*-CF_3)] (**1**) was carried out according to the previously published procedure.[2] All reactions were performed under an inert atmosphere of N_2 using Schlenk line techniques or under an atmosphere of purified N_2 in an MBraun Unilab glovebox.

Physical Methods. Fourier transform infrared (FTIR) spectra were collected on a ThermoNicolet 6700 spectrophotometer running the OMNIC software. All FTIR samples were prepared inside a glovebox under an inert atmosphere of purified N_2. Electronic absorption spectra were collected at 298 K using a Cary-50 spectrophotometer containing a Quantum

Northwest TC 125 temperature control unit. All UV-vis samples were prepared in gastight Teflon-lined screw cap quartz cells with an optical pathlength of 1 cm. ^{1}H NMR spectra were recorded in the listed deuterated solvent on a 400 MHz Bruker BZH 400/52 NMR spectrometer or a Varian Unity Inova 500 MHz NMR spectrometer at RT with chemical shifts internally referenced to tetramethylsilane (TMS = $Si(CH_3)_4$), or the residual protio signal of the deuterated solvent as previously reported.[42] Low-resolution electrospray ionization mass spectrometry (LR-ESI-MS) data were collected using a Bruker Esquire 3000 plus ion trap mass spectrometer. Elemental analysis for C, H, and N was performed at ALS in Tucson, AZ.

Reactivity of 1 with NO(g). A red-brown solution of **1** (0.0517 g, 0.0917 mmol) in 3 mL of DMF was purged with NO(g) for 1 min at RT. Upon stirring under an NO(g) atmosphere, the homogenous solution changed in color from red-brown to green-brown within 5 min. Within 30 min, the solution color was primary green. After stirring for 2 h, the DMF was removed by short-path vacuum distillation and the resulting green residue was stirred in 6 mL of Et_2O for 48 h to afford 0.0380 g (0.433 mmol, 94%) of **3** as a green powder. FTIR (KBr pellet) ν_{max} (cm^{-1}): 3436 (w), 3067 (w), 2983 (m), 2948 (w), 1747 (s, ν_{NO}), 1691 (s), 1636 (s), 1591 (vs), 1566 (s), 1478 (m), 14610 (m), 1442 (m), 1395 (m), 1325 (vs), 1258 (s), 1167 (s), 1105 (vs), 1077 (vs), 1021 (m), 1002 (m), 886 (w), 800 (m), 761 (w), 714 (w), 681 (w), 622. (w). ^{1}H NMR (500 MHz, $(CD_3)_2SO$, δ from protio solvent). 3.20 (q, 3H, J =10 Hz), 1.15 (t, 4H, J = *10* Hz). UV-vis (DMF, 298 K) λ_{max}, nm (ε, $M^{-1}cm^{-1}$): 425 nm (3000), 686 nm (150). LR-ESI-MS (m/z): calc. for $[Ni(SPh\text{-}o\text{-}N\text{-}p\text{-}CF_3)(NO)_2]^{1-}$, $C_7H_3F_3N_3NiO_2S$, 307.9 (100.0), 308.9 (8.7), 309.9 (43.0), 310.4 (4.6), 311.9 (7.0); found: 307.9 (100.0), 308.9 (8.9), 309.9 (44.6), 310.9 (6.5), 311.9 (7.4). Anal. cald for $C_{30}H_{46}F_6N_7Ni_2O_3S_2$: C, 42.48; H, 5.47; N, 11.56; Found: C, 44.02; H, 6.07; N, 9.36.

The Et_2O soluble material from trituration and filtration was collected and dried to yield 0.030 g of a beige transparent residue. ^{1}H NMR (500 MHz, $CDCl_3$ with 0.05% v/v TMS, δ from TMS): 8.55 (d, 1H, J = 5 Hz), 8.40 (br s, 1H, N*H*), 8.20 (d, 1H, J = 10 Hz), 7.85 (t, 1H J = 5 Hz), 7.45 (t, J = 5 Hz), 3.75 (t, 2H, OC-HN-C*H*2CH2-S, J = 5 Hz), 2.98 (t, 2H, OC-HN-CH2C*H*2-S, J = 5.0 Hz).

Reactivity of 1 with ^{15}NO(g). The reaction of **1** with ^{15}NO was carried out as described above except for using 0.0515 g (0.0917 mmol) of **1** and ^{15}NO(g) to yield 0.0307 g (0.0399 mmol, 87%) of **3-^{15}NO** as a green powder. FTIR (KBr pellet) ν_{max} (cm^{-1}): 3432 (w), 3064 (w), 2982 (m), 2923 (m), 1691 (s, ν_{NO}), 1674 (m), 1633 (s), 1590 (s), 15645 (m), 1478 (m), 1458 (m), 1441 (m), 1411 (m), 1395 (m), 1325 (vs), 1297 (m), 1250 (m), 1228 (m), 1166 (s), 1105 (vs), 1077 (vs), 1020 (m), 1001 (m), 979 (m), 887 (w), 816 (w), 797 (m), 761 (m), 713 (m), 680 (w), 621 (w). LR-ESI-MS (m/z): calc. for [Ni(SPh-*o*-N-*p*-CF_3)($^{15}NO)_2$]$^{1-}$, $C_7H_3F_3N^{15}N_2NiO_2S$, 309.9 (100.0), 310.9 (8.7), 311.9 (43.0), 312.9 (4.6), 313.9 (7.0); found: 309.9 (100.0), 310.9 (12.5), 311.9 (41.4), 312.9 (5.8), 313.9 (4.1). The Et_2O soluble material from trituration and filtration was collected and dried to yield 0.0140 g of a light green oil.

Reactivity of 1^{ox} with NO(g). To a 4 mL DMF solution of **1** (0.0398 g, 0.0709 mmol) was added one equiv ceric ammonium nitrate (CAN, 0.0385 g, 0.0702 mmol). The dark green solution was purged with a stream of NO(g) for 1 min at RT, and the solution immediately changed color to red-brown. Red insoluble precipitate was observed. The mixture was stirred for 1 h under an NO(g) atmosphere, and the DMF was removed by short-path vacuum distillation. The resulting red-brown residue was stirred in Et_2O overnight and filtered to afford 0.0562 g of a red-brown product. This product is sparingly soluble in all organic solvents attempted. FTIR reveals this product contains $[Ni_4(nmp)]_4$. FTIR (KBr pellet) ν_{max} (cm^{-1}): 3239 (w, br), 3084 (w,

br), 2937 (w), 1748 (w), 1653 (ν_{CO}, vs), 1598 (m), 1438 (s), 1382 (s) 1325 (s), 1132 (m), 1034 (m), 821 (m), 734 (m), 675 (s), 623 (w).

Reactivity of 2 with NO(g). To a red solution of **2** (0.0534 g, 0.108 mmol) in 3 of mL DMF was purged with NO(g) for 1 min at RT. No color change or precipitation was visible over 30 min stirring under an NO(g) atmosphere. The DMF was removed by short-path vacuum distillation and the resulting red oily residue was stirred in 5 mL Et_2O overnight. The residue remained oily, accounting for a higher than expected mass of 0.0601 g. The solid is sparingly soluble in organic solvents. FTIR reveals this product contains $[Ni_4(nmp)]_4$, although strong stretches at 1091 cm^{-1} and 1021 cm^{-1} may point to an S-oxygenated species as well (ν_{SO}). FTIR (KBr pellet) ν_{max} (cm^{-1}): 2982 (w), 2845 (w), 1762 (w), 1692 (s), 1673 (s, DMF), 1628 (ν_{CO}, vs), 1599 ($\nu_{CO,}$ vs), 1565 (m), 1479 (m), 1460 (m), 1385 (m), 1261 (w), 1176 (w), 1091.3 (s), 1020 (s), 797 (vs), 759 (s), 687 (m), 621 (w), 485 (w).

UV-vis monitor of 1 with $NOBF_4$. To a 5 mM DMF stock of **1** was added one equiv of $NOBF_4$, which resulted in bleaching of the solution and an absence of any spectral features in the UV-vis absorbance profile. This bleaching, in addition to formation of a red precipitate, is consistent with formation of $[Ni(nmp)]_4$ and RSSR

Reactivity of 3 with [Fe(TPP)Cl]. To a 2 mL MeCN solution containing 0.0183 g (0.0260 mmol) of [Fe(TPP)Cl] was added 0.5 equiv of **3** (0.0115 g, 0.0131 mmol) in 2 mL MeCN, with no observed color change. The dark red-brown solution was stirred for 2 h in the dark at RT, and the MeCN was removed in vacuo. The brown residue was stirred in 6 mL MeOH and filtered to afford 0.0164 g of a purple solid. FTIR analysis shows that the purple solid is unreacted [Fe(TPP)Cl] that was recovered at 90.3% (0.02346 mmol).

NO Transfer from 3 to [Co(T-(OMe)PP)]. To a 2 mL CH_2Cl_2 solution containing 0.0.158 g (0.0200 mmol) of [Co(T-(OMe)PP)] was added 0.5 equiv of **3** (0.0087 g, 0.0099 mmol) in 1.5 mL CH_2Cl_2 with no observed color change. The red-brown solution was stirred for 24 h in the dark at RT, and the CH_2Cl_2 was removed in vacuo. The brown residue was stirred in 6 mL MeOH and filtered to afford 0.0156 g of a purple solid. FTIR analysis shows that the purple solid contains CoNO compound. The UV-vis spectrum of a 4.1 μM solution indicates a mixture of [Co(T-(OMe)PP)] and [Co(T-(OMe)PP)(NO)] species.

^{15}NO Transfer from 3-^{15}NO to [Co(T-(OMe)PP)]. This reaction was performed under identical conditions as with **3** expect for using 0.0093 g (0.011 mmol) **3-^{15}NO** and 0.0167 g (0.0211 mmol) [Co(T-(OMe)PP)] to afford 0.0161 g of a purple solid.

Computational details. Density functional theory (DFT) calculations were performed with the ORCA electronic structure package, version 3.0.3.[43] Geometry optimization and frequency analysis of all models were performed using the BP86 functional[44,45] along with resolution-of-the-identity (RI) approximation[46] and Grimme's D3(BJ) dispersion correction[47,48] with coordinates from the crystal structures of **1** and **2**. The triple-ζ basis set, def2-TZVPP,[49,50] was used for geometry optimization and frequency analysis with an automatically constructed auxiliary basis set on all atoms. No imaginary frequencies were found.

Single-point energy (SPE) calculations were performed on the optimized structures using the OLYP functional (OPTX exchange functional of Cohen and Handy[51] coupled with Lee, Yang, and Parr's correlation functional[52]) with RI approximation.[46] The triple-ζ basis set, def2-TZVPP,[49,50] was used for all atoms with the matching auxiliary basis set def2-TZVPP/J. UCSF Chimera[53] was used to generate model structures and to visualize isosurface plots of MOs and spin-density plots with isodensity values of 0.05 and 0.002 a.u., respectively.

Structural data

X-ray Crystallographic Data Collection and Structure Solution and Refinement. Green blade crystals of **3** were grown by slow vapor diffusion of Et_2O into an MeCN solution of **3** at -20 °C. A dark green crystal was mounted on the top of a glass fiber. The X-ray intensity data were measured at 100 K temperature on a Bruker SMART APEX II X-ray diffractometer system with graphite- monochromated Mo Kα radiation (λ = 0.71073 Å) using ω-scan technique. The data were collected in 1464 frames with 10 s exposure times. The data were corrected for Lorentz and polarization effects[54] and integrated with the manufacturer's SAINT software. Absorption corrections were applied with the program SADABS.

Subsequent structure refinement was performed using the SHELXTL-2013[55,56] solution package operating on a Pentium computer. The structure was solved by direct methods using the SHELXTL 2013 software package. Non-hydrogen atomic scattering factors were taken from the literature tabulations.[57] Non-hydrogen atoms were located from successive difference Fourier map calculations. The atoms of one of the NO groups and three atoms of fluorine in the molecule were found disordered in the adjacent positions in two sets of each. For NO: N(2), O(1) (one set) (with 65% occupancies) and N(2′), O(1′) (another set) (with 35% occupancies); For fluorine: F(1), F(2), F(3) (one set) (with 51% occupancies) and F(1′), F(2′), F(3′) (another set) (with 49% occupancies). Each of these two sets is divided using the PART commands and proper restraints. In the final cycles of each refinement, all the non-hydrogen atoms were refined in anisotropic displacement parameters. The asymmetric unit contains half a molecule in the form of $C_{15}H_{23}N_4O_2F_3SNi$ with a two-fold axis passing through the middle of Ni(1) and Ni(1A). The total formula is in the form of $C_{30}H_{46}N_8O_4F_6S_2Ni_2$. Selected data and metric parameters for **3** are summarized in Tables 4S.1 and 4S.2 in the Supporting Information. Perspective views of the

complexes were obtained using ORTEP,[58] omitting N(2′), O(1′), F(1′), F(2′), F(3′), and hydrogen atoms for clarity. Using CheckCIF to determine alerts, the highest alerts are at level C that are false alerts.

Table 4S.1. Summary of Crystal Data and Intensity Collection and Structure Refinement Parameters for $(Et_4N)_2[Ni_2(\mu\text{-}SR')_2(NO)_4]$ (**3**)

Parameters	**3**
Formula	$C_{30}H_{46}F_6N_8Ni_2O_4S_2$
Formula weight	878.28
Crystal system	Monoclinic
Space group	*C* 2/c
Crystal color, habit	Green, square
a, Å	23.2608(14)
b, Å	10.7528(6)
c, Å	17.4230(10)
α, deg	90
β, deg	117.9760(10)
γ, deg	90
V, $Å^3$	3848.6(4)
Z	4
ρ_{calcd}, g/cm^3	1.516
T, K	100(2)
abs coeff, μ (Mo Kα), mm^{-1}	1.161
θ limits, deg	1.983-30.500
total no. of data	30284
no. of unique data	5892
no. of parameters	282
GOF of F^2	1.054
R_1, [a] %	0.0468
wR_2, [b] %	0.1463
max, min peaks, $e/Å^3$	1.426, -0.578

[a] $R_1 = \Sigma| |F_o| - |F_c| | / \Sigma |F_o|$; [b] $wR_2 = \{\Sigma[w(F_o^2 - F_c^2)^2]/\Sigma[w(F_o^2)^2]\}^{1/2}$

Table 4S.2. Selected Bond Distances (Å) and Bond Angles (deg) for $(Et_4N)_2[Ni_2(\mu\text{-}SR')_2(NO)_4]$ (**3**)

Ni(1)-N(2')	1.621(11)
Ni(1)-N(2)	1.659(7)
Ni(1)-N(1)	1.971(2)
Ni(1)-S(1)	2.3169(7)
Ni(1)-S(1)#1	2.3555(7)
S(1)-C(1)	1.767(3)
S(1)-Ni(1)#1	2.3555(7)
N(1)-N(3)	1.299(3)
N(1)-C(2)	1.422(3)
N(2)-O(1)	1.182(8)
N(2')-O(1')	1.162(12)
C(1)-C(2)	1.409(3)
C(1)-C(6)	1.401(4)
C(2)-C(3)	1.386(4)
C(3)-C(4)	1.392(4)
C(4)-C(5)	1.387(5)
C(4)-C(7)	1.486(5)
C(5)-C(6)	1.374(4)
C(7)-F(1')	1.307(13)
C(7)-F(2)	1.258(18)
C(7)-F(3)	1.330(8)
C(7)-F(2')	1.405(16)
C(7)-F(3')	1.408(12)
C(7)-F(1)	1.429(15)
N(4)-C(9)	1.499(4)
N(4)-C(11)	1.503(4)
N(4)-C(15)	1.527(4)
N(4)-C(13)	1.551(4)
C(8)-C(9)	1.510(5)
C(10)-C(11)	1.511(5)
C(12)-C(13)	1.503(4)
C(14)-C(15)	1.545(4)
N(3)-O(2)	1.269(3)

N(2')-Ni(1)-N(1)	126.0(12)
N(2)-Ni(1)-N(1)	133.6(5)
N(2')-Ni(1)-S(1)	118.3(10)
N(2)-Ni(1)-S(1)	123.8(5)
N(1)-Ni(1)-S(1)	86.21(6)
N(2')-Ni(1)-S(1)#1	122.0(13)
N(2)-Ni(1)-S(1)#1	109.8(6)
N(1)-Ni(1)-S(1)#1	99.10(6)

S(1)-Ni(1)-S(1)#1	96.66(2)
C(1)-S(1)-Ni(1)	96.14(8)
C(1)-S(1)-Ni(1)#1	102.68(8)
Ni(1)-S(1)-Ni(1)#1	82.07(2)
N(3)-N(1)-C(2)	113.5(2)
N(3)-N(1)-Ni(1)	126.90(17)
C(2)-N(1)-Ni(1)	119.63(15)
O(1)-N(2)-Ni(1)	167.8(12)
O(1')-N(2')-Ni(1)	170(2)
C(2)-C(1)-C(6)	118.5(2)
C(2)-C(1)-S(1)	120.53(19)
C(6)-C(1)-S(1)	120.9(2)
C(3)-C(2)-C(1)	119.9(2)
C(3)-C(2)-N(1)	124.1(2)
C(1)-C(2)-N(1)	116.0(2)
C(2)-C(3)-C(4)	120.3(3)
C(3)-C(4)-C(5)	120.3(3)
C(3)-C(4)-C(7)	119.5(3)
C(5)-C(4)-C(7)	120.1(3)
C(6)-C(5)-C(4)	119.7(3)
C(5)-C(6)-C(1)	121.3(3)
F(2)-C(7)-F(3)	112.9(12)
F(1')-C(7)-F(2')	102.7(10)
F(1')-C(7)-F(3')	110.2(8)
F(2')-C(7)-F(3')	102.9(11)
F(1')-C(7)-C(4)	117.9(10)
F(2)-C(7)-C(4)	115.7(11)
F(3)-C(7)-C(4)	113.8(4)
F(2')-C(7)-C(4)	111.7(10)
F(3')-C(7)-C(4)	110.2(5)
F(2)-C(7)-F(1)	110.8(11)
F(3)-C(7)-F(1)	97.1(8)
C(4)-C(7)-F(1)	104.5(8)
C(9)-N(4)-C(11)	110.4(2)
C(9)-N(4)-C(15)	113.1(2)
C(11)-N(4)-C(15)	109.5(2)
C(9)-N(4)-C(13)	107.6(2)
C(11)-N(4)-C(13)	110.0(2)
C(15)-N(4)-C(13)	106.1(2)
N(4)-C(9)-C(8)	116.6(3)
N(4)-C(11)-C(10)	116.5(3)
C(12)-C(13)-N(4)	114.5(2)
N(4)-C(15)-C(14)	113.3(2)
O(2)-N(3)-N(1)	114.2(2)

X-ray absorption spectroscopy (XAS) of 1

Nickel K-edge XAS data were collected in transmission mode for **1** while the sample was in the solid form. Sample **1** is oxygen-sensitive and was prepared in an anaerobic glovebox immediately prior to data collection. A solid sample of **1** was diluted with inert boron nitride (BN) at a 4:1 BN/sample ratio w/w, the sample was packed anaerobically into a transmission cell holder, the sample was wrapped with Kapton tape, and the sample was immediately flash frozen in liquid nitrogen. XAS data were collected at the Stanford Synchrotron Radiation Lightsource (SSRL) on beamline 7-3 which utilizes a Si[220] double crystal monochromator with an inline mirror for X-ray focusing and for harmonic rejection. During data collection, samples were maintained at 12 K using a liquid He continuous flow cryostat. Transmittance XAS spectra were collected in 5 eV increments in the pre-edge region (8100 to 8320 eV), 0.25 eV increments in the edge region (8325-8385 eV) and 0.05 $Å^{-1}$ increments in the extended X-ray absorption fine structure (EXAFS) region (out to k = 14 $Å^{-1}$), integrating from 1 to 25 s in a k^3 weighted manner for a total scan length of approximately 40 min. X-ray energies were individually calibrated by collecting a Ni-foil absorption spectra simultaneously with the compound spectra; the first inflection point of the Ni-foil spectrum was assigned at 8333 eV. Spectra were closely monitored for photo reduction and for spectral anomalies during data collection and analysis.

XAS spectra were processed using the Macintosh OS X version of the EXAFSPAK program suite[59] integrated with the Feff v8 software[60] for theoretical model generation. Data reduction utilized a Gaussian spline for background removal in the pre-edge region and a three-region cubic spline throughout the EXAFS. Data were converted to k-space using a Ni E_0 value of 8370 eV. The k^3 weighted EXAFS was truncated between 1.0 and 13.0 $Å^{-1}$ for filtering purposes. This k range corresponds to a spectral resolution of ca. 0.12 Å for all Ni-ligand

interactions; therefore only independent scattering environments outside 0.12 Å were considered resolvable in the EXAFS fitting analysis.[61] EXAFS fitting analysis was performed first on filtered data and then verified on the raw unfiltered data. EXAFS data were fit using both single and multiple scattering amplitude and phase functions calculated with the program Feff v8. Single scattering theoretical models were calculated for carbon, nitrogen, and sulfur coordination to simulate Ni nearest-neighbor ligand environments. Scale factor (Sc) and E_0 values, used in a static manner during the simulations, were calibrated by fitting crystallographically characterized Ni models; specific values include a Scale Factor of 0.84 and E_0 values of -12.2 eV for Ni-O/N/C ligands and -10.5 eV for Ni-S scattering. Criteria for judging the best-fit simulation utilized both the lowest mean square deviation between data and fit (F'), corrected for the number of degrees of freedom, and a reasonable Debye-Waller factor.[62,63] Pre-edge analysis was done using EDG_FIT software, which is bundled with EXAFSPAK. A spline function was best-fit between 8328 eV and 8342 eV and a two-peak model was applied to accommodate the 1s → 3d and 1s → 4p pre-edge features. The extrapolated line was then subtracted from raw data to yield baseline corrected spectra. Pre-edge features were modeled using pseudo-Voigt line shapes (simple sums of Lorentzian & Gaussian functions), and the energy position measured; the full width at half-maximum (fwhm) and the peak heights for each transition were varied. A fixed 50:50 ratio of Lorentzian to Gaussian function successfully reproduced the spectral features of the pre-edge transitions. Peak transition areas were determined for all spectra over the energy range of 8330-8340 eV using the program Kaleidagraph.[64] Normalized areas are represented in units of 10^{-2} eV.[7,65]

Table 4S.3. Summary of best-fit simulations to Ni EXAFS[a] for **1.** Sample was best fit with O/N and S-ligation in the nearest neighbor (first shell) ligand coordination environment. **1** also displays long-range scattering arising from multiple carbon atoms.

Nearest Neighbor Ligand Environment[b]				**Long Range Ligand Environment**[b]								
Atom[c]	**R(A)**[d]	**CN**[e]	**σ^{2}**[f]	**Atom**[c]	**R(A)**[d]	**CN**[e]	**σ^{2}**[f]	**Atom**[c]	**R(A)**[d]	**CN**[e]	**σ^{2}**[f]	***F'***[g]
N	1.90	2.0	5.40	C	2.78	1.0	2.03	C	3.82	3.5	4.22	0.34
S	2.17	2.0	2.72	C	3.33	1.5	1.50					

[a] Data were fit over a *k* range of 1 to 14.0 $Å^{-1}$. [b] Independent metal-ligand scattering environment. [c] Scattering atoms: N (nitrogen) C (Carbon) Oxygen (O). [d] Average metal-ligand bond length from two transmission scans. [e] Average metal-ligand coordination number from two transmission scans. [f] Average Debye-Waller factor in $Å^2 \times 10^3$ from two transmission scans. [g] Number of degrees of freedom weighted mean square deviation between data and fit.

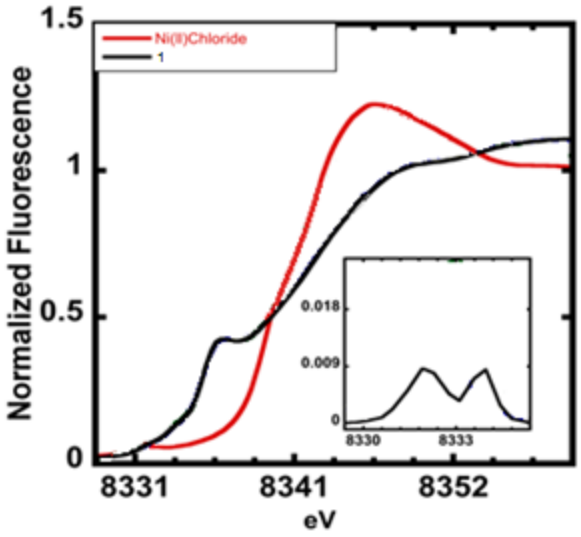

Figure 4.S1. Comparison of X-ray Absorption Near Edge Structure (XANES) data for **1** (black trace) with Ni(II) chloride control (red trace). A prominent 1s → 4p transition is observed for **1** centered at 8336.3 eV, consistent with square-planar geometry.[7] Edge analysis reveals **1** to be in the Ni(II) oxidation state, as indicated by the normalized half height of the rising edge at ~8340 eV. Inset: The baseline subtracted, normalized 1s → 3d pre-edge transition is observed and appears as two peaks centered at 8331.6eV and ~8334 eV. The corresponding 1s → 3d peak area value for **1** is 1.84 x 10^{-2} eV (range: 8330-8334 eV).

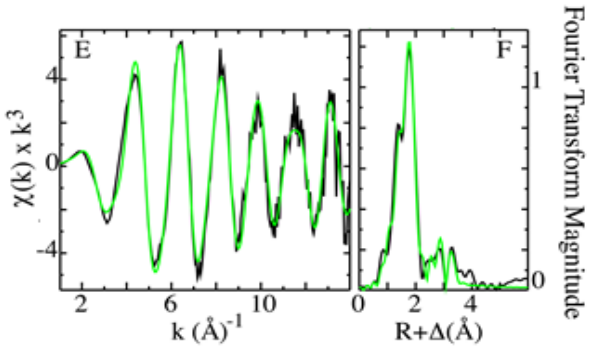

Figure 4.S2. EXAFS spectrum (left) and Fourier transform (right) of **1**. Raw data are plotted in black; best fit simulations are plotted in green.

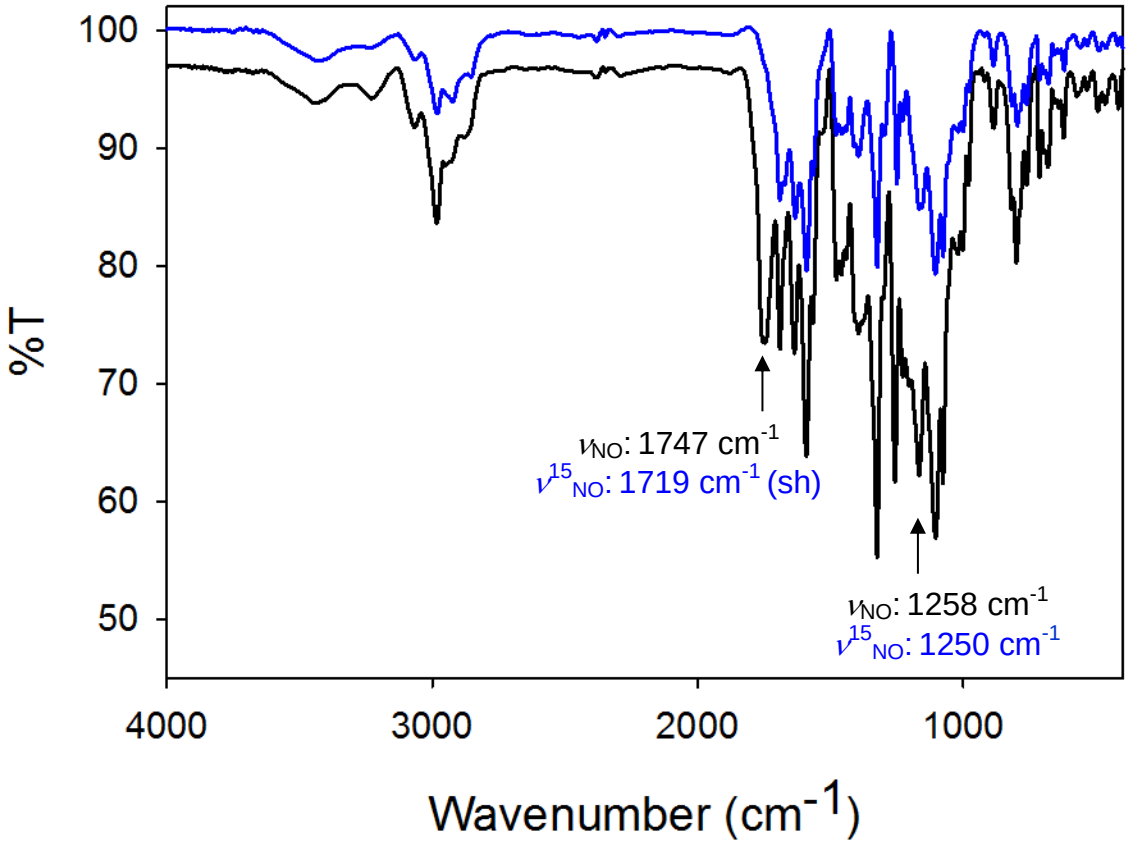

Figure 4S.3. Solid-state (KBr) FTIR spectra (offset) of **3** (black trace) and **3-^{15}NO** (blue trace)

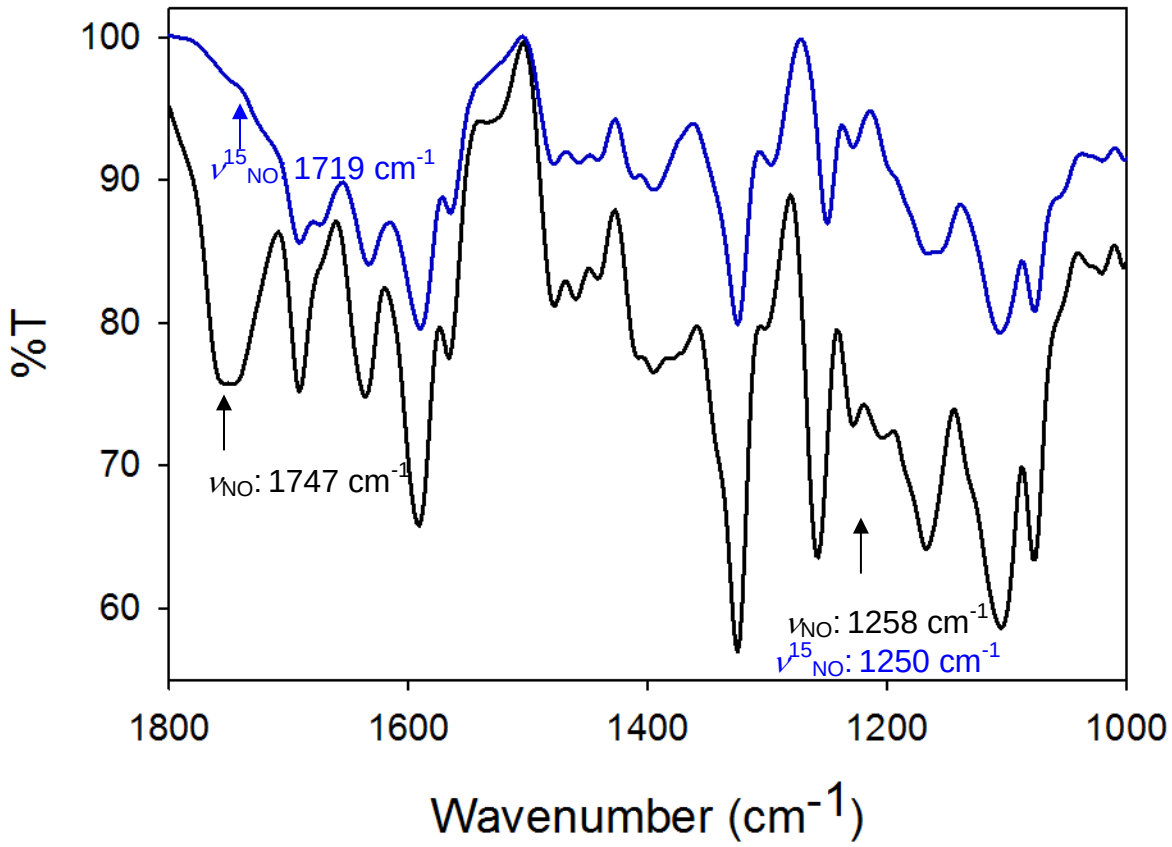

Figure 4S.4. Solid-state (KBr) FTIR spectra (offset) of the region from 1800 to 1000 cm^{-1} of **3** (black trace) and **3-^{15}NO** (blue trace) with a shoulder assigned to ν_{15NO} indicated.

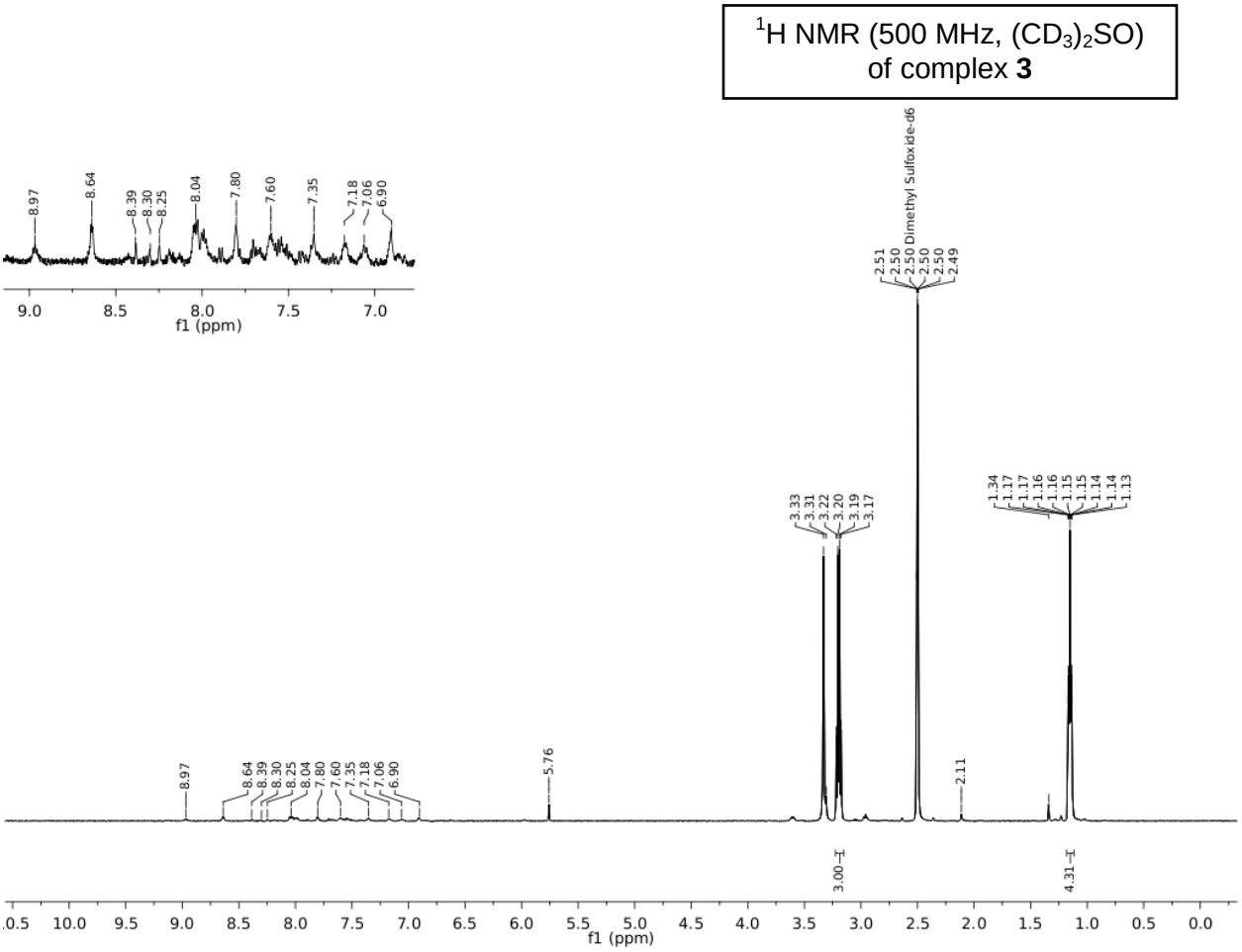

Figure 4S.5. ^{1}H NMR spectrum of **3** (500 MHz, $(CD_3)_2SO$) at RT. Inset shows expanded aromatic region. Residual protio solvent (2.50, 3.20 ppm) and H_2O (3.33 ppm) are present.

^{1}H NMR (500 MHz, $CDCl_3$ containing 0.05% v/v TMS) of Et_2O filtrate from workup of **3**

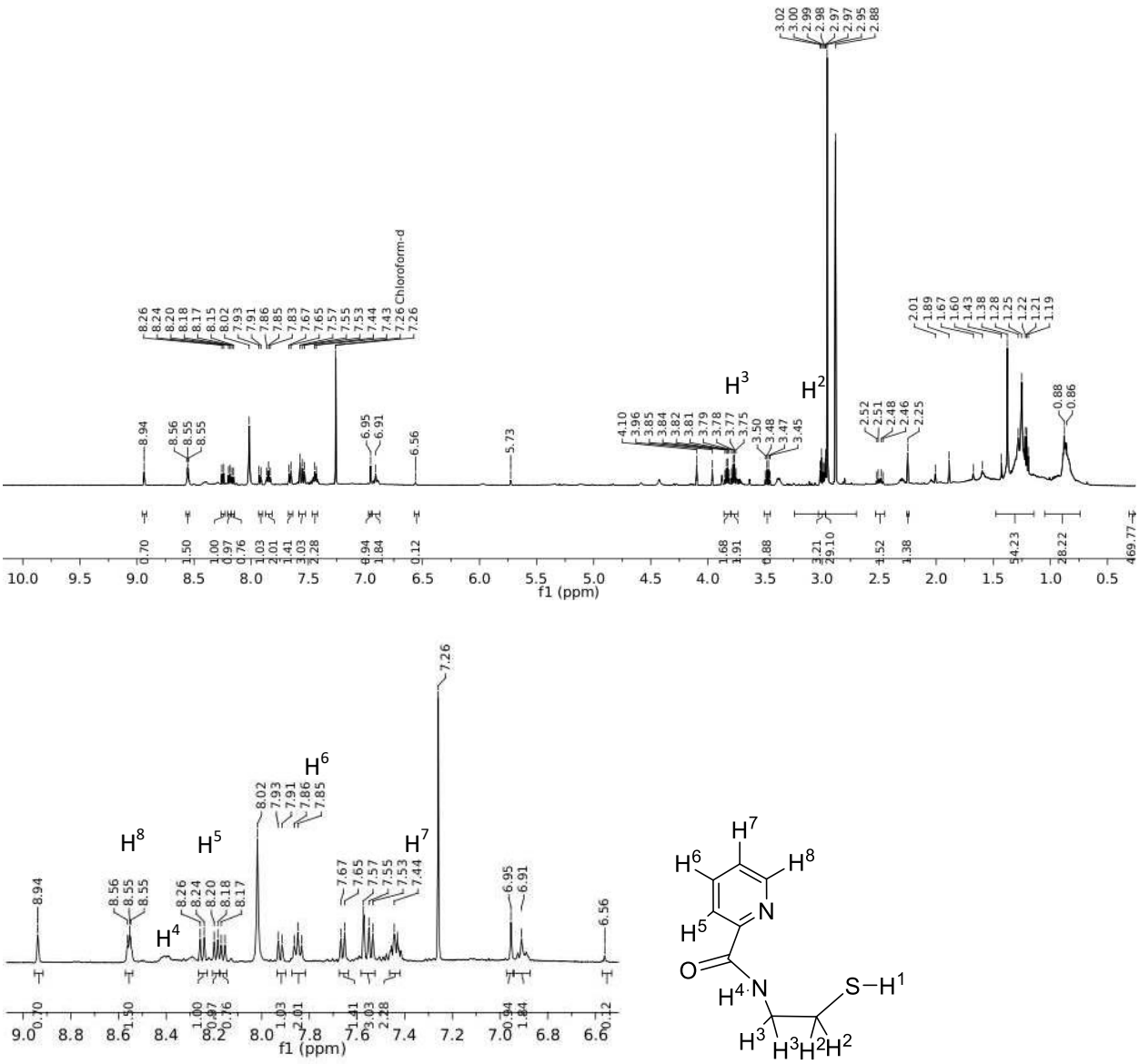

Figure 4S.6. *Top:* ^{1}H NMR spectrum of the Et_2O filtrate from the reaction of **1** and NO(g) (500 MHz, $CDCl_3$ containing 0.05% v/v TMS) at RT . Residual protio solvent (7.26 ppm) and DMF (2.88, 2.95, 8.02 ppm) are present. *Bottom*: Expansion of the aromatic region with $nmpH_2$ peaks assigned in comparison to authentic $nmpH_2$.[1]

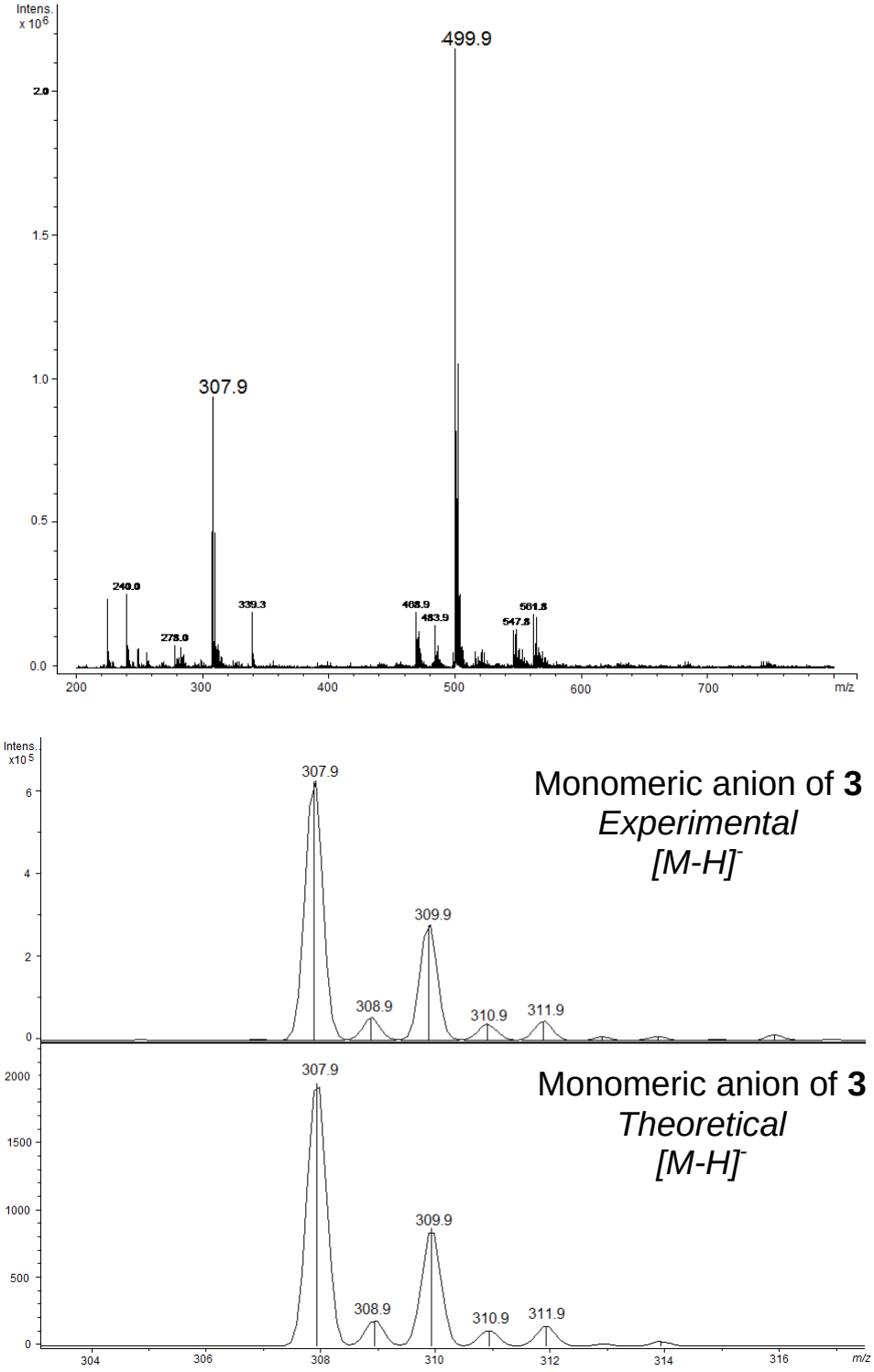

Figure 4.S7. Low resolution ESI-MS (negative mode) of **3** (top). Middle and bottom represent a zoom-in of the *m/z* 307.9 peak. Theoretical fit on the bottom.

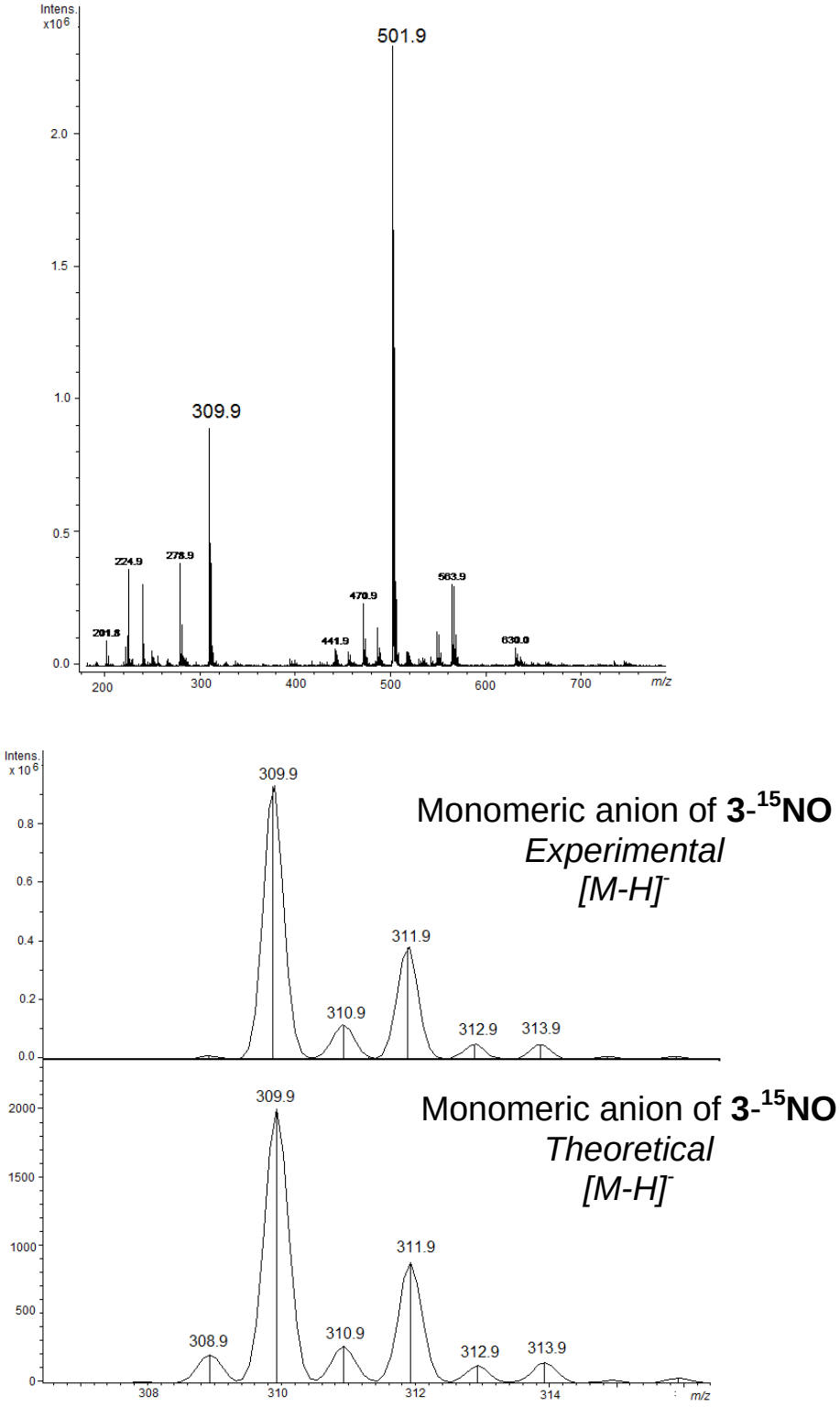

Figure 4.S8. Low resolution ESI-MS (negative mode) of **3-^{15}NO** (top). Middle and bottom represent a zoom-in of the *m/z* 309.9 peak. Theoretical fit on the bottom.

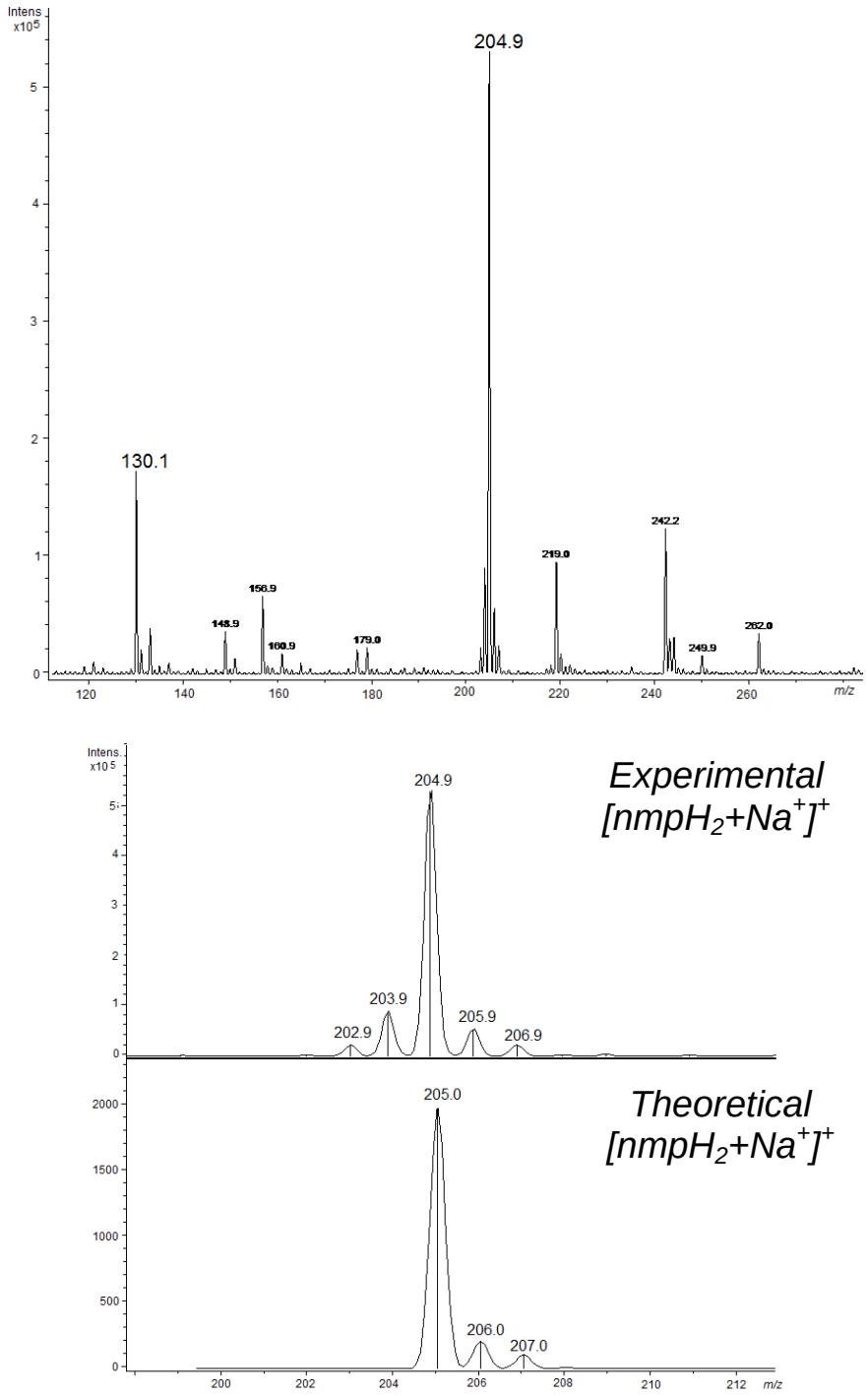

Figure 4.S9. Low resolution ESI-MS (positive mode) of the Et_2O filtrate from the reaction of **1** and NO(g) (top). Middle and bottom represent a zoom-in of the *m/z* 204.9 peak. Theoretical fit on the bottom. The isotopic peaks at 202.9 and 203.9 are an artifact of the high voltages required to obtain this sample.

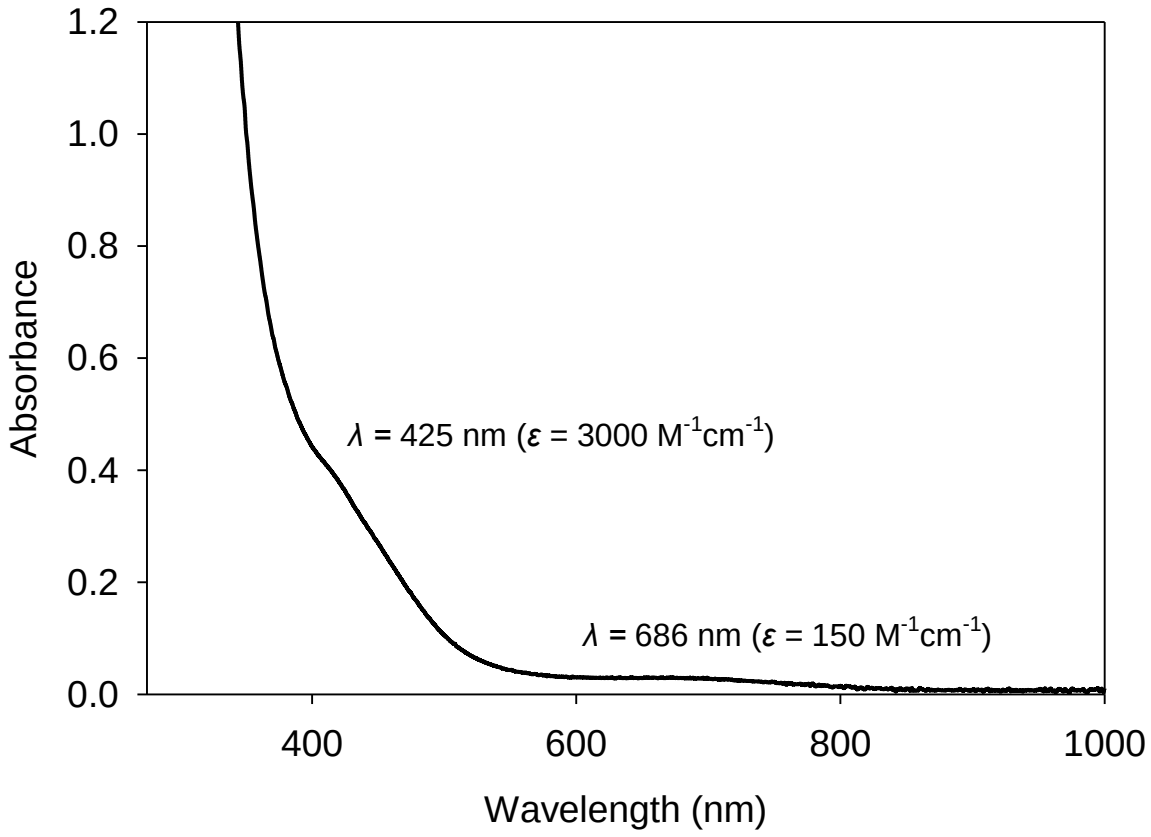

Figure 4S.10. UV-vis spectrum of a 0.13 mM solution of **3** in DMF at 298 K.

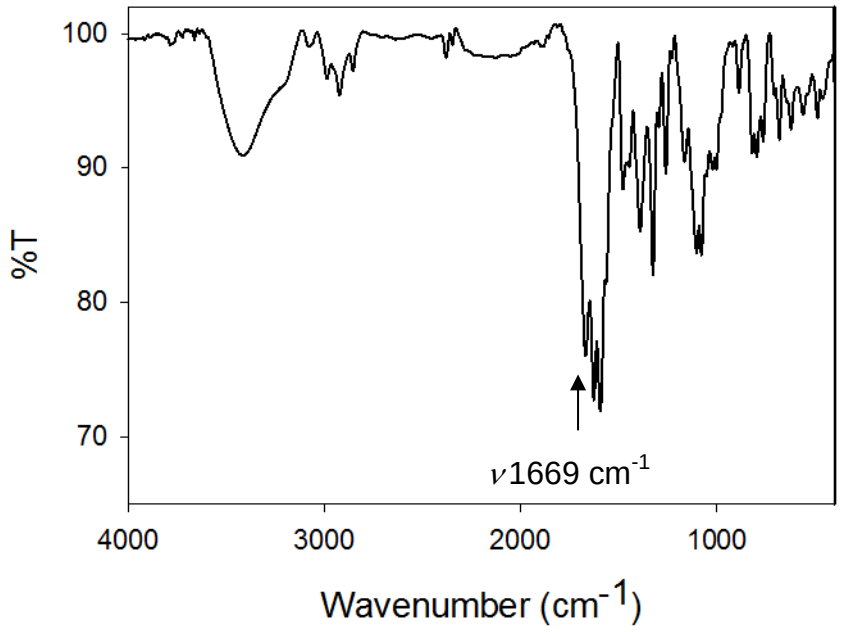

Figure 4S.11. Solid-state (KBr) FTIR spectra with the ν_{NO} absent, demonstrating loss of NO upon pulling vacuum on an MeCN solution of **3**.

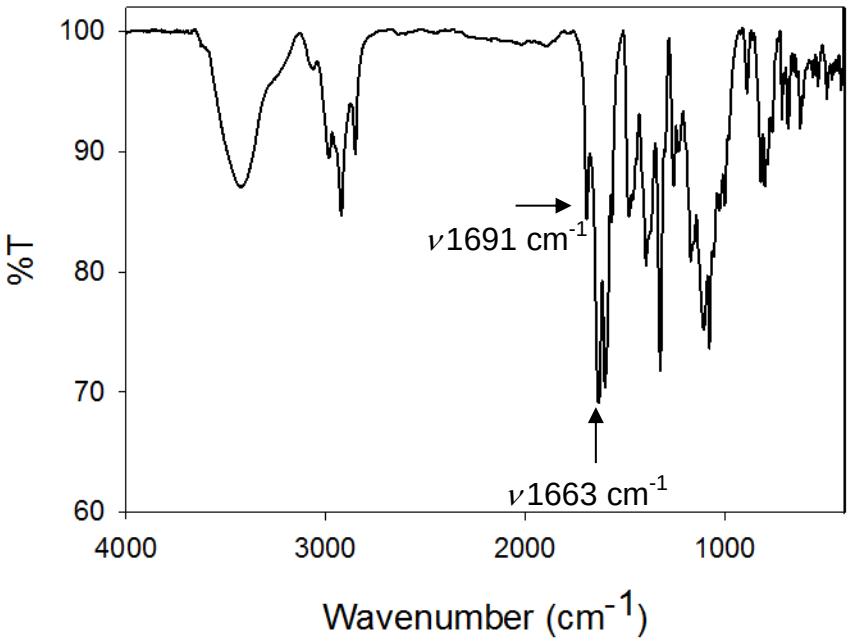

Figure 4S.12. Solid-state (KBr) FTIR spectra with the ν_{NO} absent, demonstrating loss of NO upon exposure to ambient O_2 in a CH_2Cl_2 solution of **3**.

TableS4.4. Löwdin population analysis derived from the DFT calculations for selected MOs of **3*** from OLYP/def2-TZVPP. Only s and p contributions were tabulated for N and S atoms.

	Atom Number					0	1	2	3	4	5	6	7	8	9	10	12	11	13
ORCA MO	**MO Label**	**M O #**	**Energy eV**	**Energy kcal/mol**	**Energy kJ/mol**	**Ni1**	**Ni1'**	**S1**	**S1'**	**N2**	**O1**	**N2'**	**O1'**	**N3**	**O3**	**N1**	**N3'**	**O3'**	**N1'**
149	HOMO-4	150	1.0903	25.14	105.1954	32.4	32.4	5.2	5.3	0.9	0.9	1.0	1.0	0.8	2.8	1.7	0.8	2.6	1.8
150	HOMO-3	151	1.3854	31.95	133.6676	12.4	12.3	1.9	2.0	0.6	0.3	0.6	0.2	7.2	20.6	2.1	7.0	20.3	2.1
151	HOMO-2	152	1.5065	34.74	145.3517	2.5	2.5	0.0	0.1	1.0	0.9	1.0	0.9	11.2	24.3	3.6	11.4	24.7	3.7
152	HOMO-1	153	1.7835	41.13	172.0775	20.6	20.8	7.5	7.4	4.2	3.6	4.1	3.5	3.3	4.3	2.3	3.3	4.3	2.3
153	HOMO	154	1.8759	43.26	180.9925	19.4	19.4	8.2	8.3	3.7	3.0	3.7	3.0	2.0	3.9	1.8	2.1	3.8	1.6
154	LUMO	155	3.1148	71.83	300.5254	14.4	15.5	3.0	2.9	14.4	8.5	15.7	9.3	0.0	0.1	0.1	0.1	0.1	0.1
155	LUMO+1	156	3.1327	72.24	302.2525	13.6	12.7	2.4	2.5	17.5	10.2	16.2	9.5	0.3	0.3	0.1	0.4	0.3	0.1
156	LUMO+2	157	3.3395	77.01	322.2052	16.4	15.7	3.1	3.0	15.4	8.8	14.8	8.3	0.6	0.5	1.4	0.7	0.4	1.4
157	LUMO+3	158	3.3652	77.60	324.6848	14.8	15.4	2.0	2.1	15.7	8.8	16.3	9.1	0.5	0.3	1.1	0.6	0.3	1.2
158	LUMO+4	159	3.7607	86.70	362.8438	1.4	1.3	0.9	0.8	0.1	0.0	0.1	0.0	13.1	9.4	1.3	13.3	9.5	1.3

Table 4S.5. Optimized BP86/def2-TZVPP Cartesian coordinates (Å) for **3***.

Ni	2.31913037140267	1.46065440171494	2.00420848999077
Ni	0.73186076862472	-1.04797552997178	3.14581057251599
S	2.50218238278749	-0.79373438141114	1.63090401427207
S	0.16018008870792	1.15267507405614	2.86214802524778
N	3.28574230526270	2.35288833068148	2.99684919720630
O	3.89918086538132	2.90271782904907	3.85592798416457
N	1.19833342940804	-1.73781080907892	4.56797735499362
O	1.69787511248896	-2.12384362901107	5.57708240180556
N	1.78257725305789	2.74480922304121	-0.60925430802322
O	2.02867260254576	3.79830373749270	0.02346555238509
N	1.85993460938824	1.62190452922002	0.09039844651213
O	-0.68966392205778	-3.61898758475508	2.22804603630930
N	-1.19783333862288	-2.66762923835471	1.58963651523353
N	-0.70407451754138	-1.46700488716498	1.85661982713363
C	0.07896752137157	-0.74178607906058	-3.91344455266538
C	0.59819448899857	-0.75105268981148	-2.51548107603623
C	-3.50723995828373	0.27454016823202	-1.87025855578659
C	0.78396292253209	-1.97388221895279	-1.84980965802760
C	0.95342418656639	0.45408676440014	-1.90485028886382
C	-2.53796187069155	0.48719932600009	-0.75702522361842
C	1.35752402315195	-1.97680663931357	-0.58340937595301
C	1.52691289659577	0.45882155791349	-0.62162626160120
C	-2.13463594835161	1.79034554197509	-0.42264882693461
C	-2.09001486100788	-0.60963495084153	-0.01678605374191
C	1.75463488699034	-0.78131939954546	0.03395992219969
C	-1.30619387076352	1.98315652182332	0.67709105588175
C	-1.24690601745511	-0.42246327147172	1.09193421800531
C	-0.87277968465945	0.89958281458713	1.45550213784475
H	0.46007469766764	-2.90561276288353	-2.31115643802816
H	0.77478924609520	1.40617568372283	-2.39704941830323
H	-2.44805421669299	2.63636755169922	-1.03240043801979
H	-2.36507519492161	-1.62354799935393	-0.29433894361083
H	1.47268468694761	-2.90883757583777	-0.03048378556475
H	-0.94648379995576	2.98022987147567	0.93030932325347
F	1.09752720458251	-0.81848291870692	-4.85780662064319
F	-0.61664080230548	0.38571188134284	-4.23520628552412
F	-0.73876917847320	-1.80277287773499	-4.19735202930602
F	-3.44688257253952	1.24253975112173	-2.83706912110718
F	-3.36203024429860	-0.92280467976864	-2.50571867527386
F	-4.82794655193327	0.29283956348149	-1.43400513832213

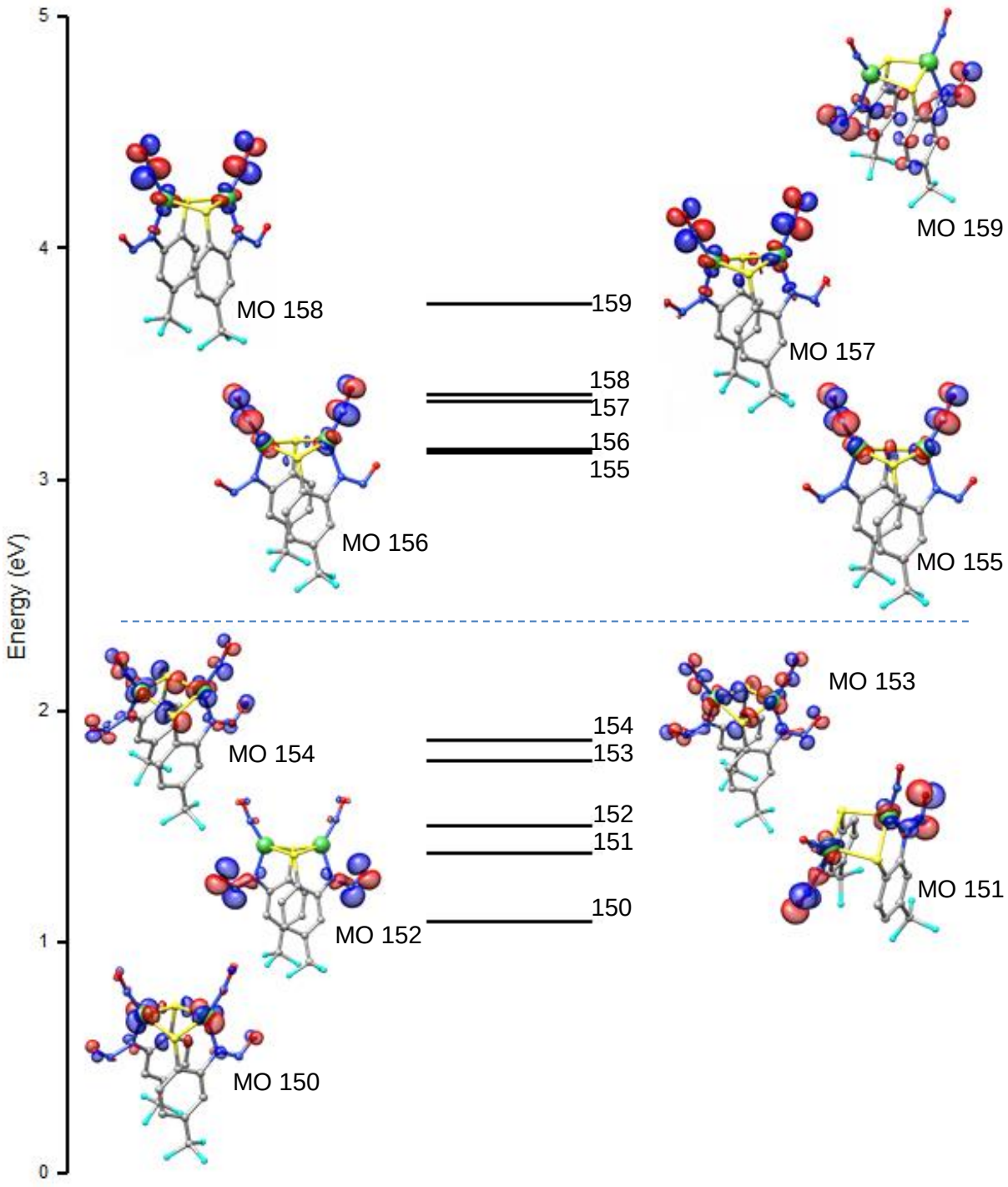

Figure 4S.13. Orbital energy diagram of **3*** with HOMO-LUMO gap in blue. The MOs descend in the order LUMO+4, LUMO+3, LUMO+2, LUMO+1, LUMO, HOMO, HOMO-1, HOMO-2, HOMO-3, HOMO-4. Dashed line indicates the level below which MOs are occupied.

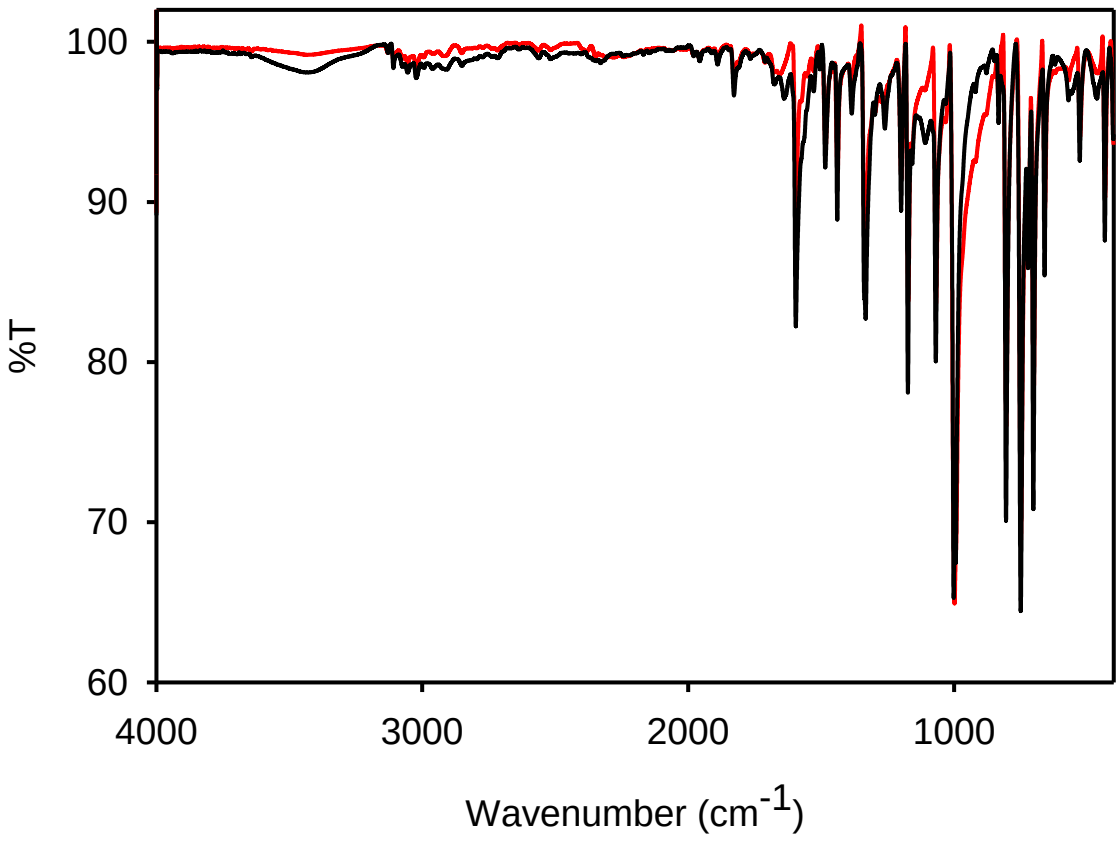

Figure 4S.14. Solid-state (KBr) FTIR spectra of the solid isolated (red trace) from the reaction of [Fe(TPP)Cl] and **3** signifying no transfer of NO occurred. FTIR of [Fe(TPP)Cl] standard is also shown (black trace).

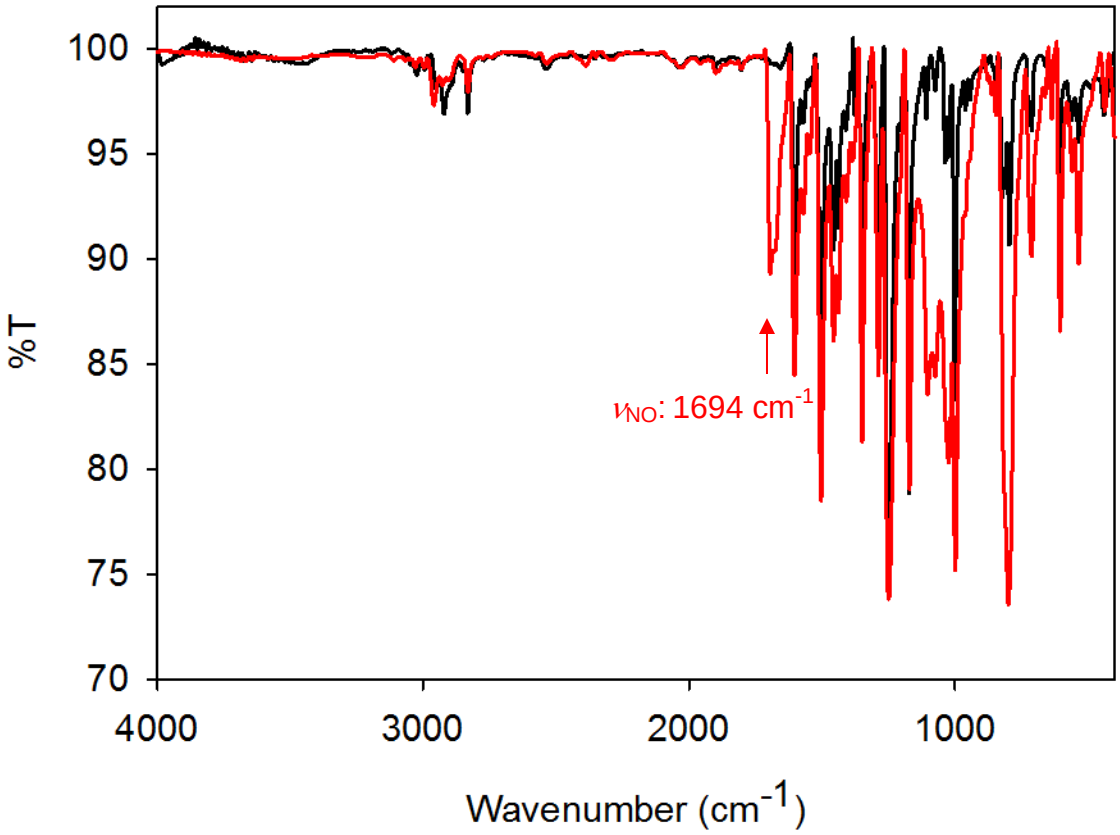

Figure 4S.15. Solid-state (KBr) FTIR spectra demonstrating formation of [Co(T-(OMe)PP)(NO)] (red trace) from the reaction of [Co(T(-OMe)PP)] with 0.5 equiv **3**. FTIR of [Co(T(-OMe)PP)] standard is also shown (black trace).

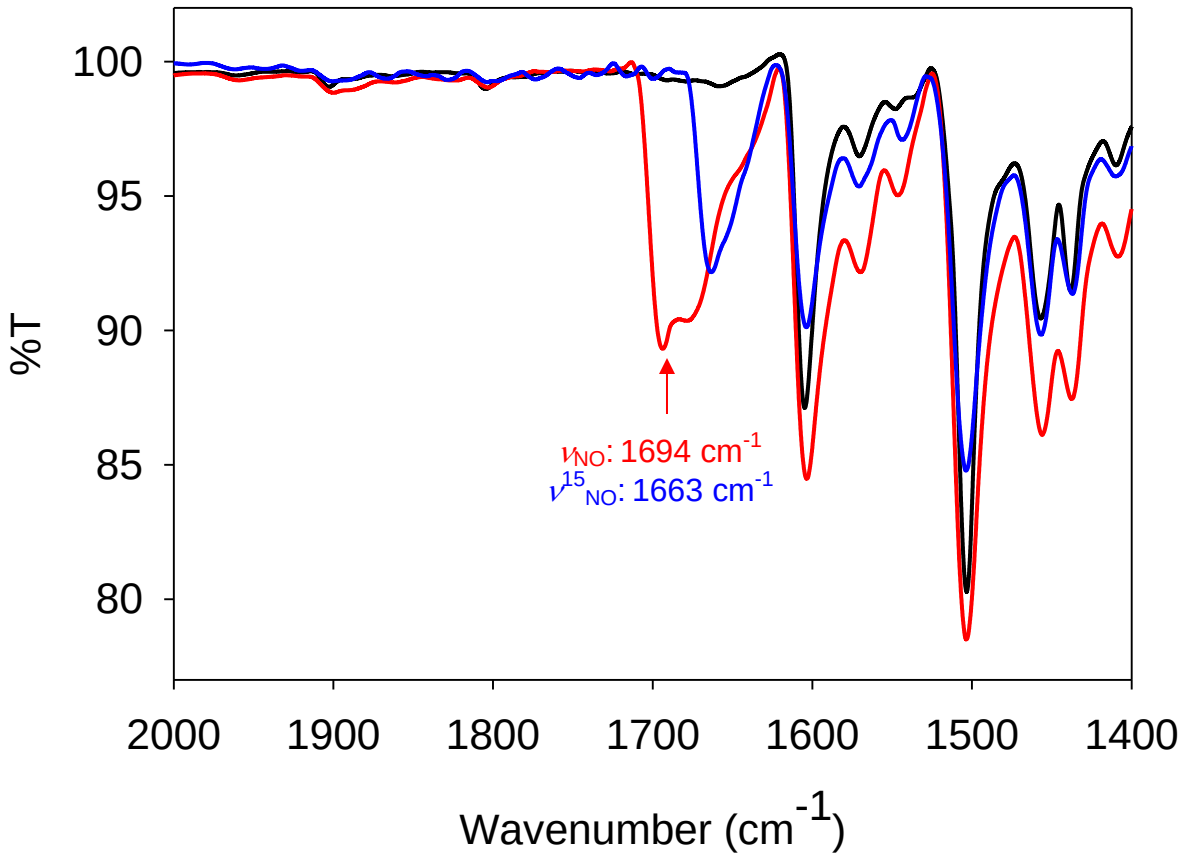

Figure 4S.16. Solid-state (KBr) FTIR spectra from 2000 to 1400 cm^{-1} demonstrating formation of [Co(T(-OMe)PP)(NO)] (red trace) or [Co(T(-OMe)PP)(^{15}NO)] (blue trace) from the reaction of [Co(T(-OMe)PP)] with 0.5 equiv **3** or **3-^{15}NO**. FTIR of [Co(T(-OMe)PP)] standard is also shown (black trace).

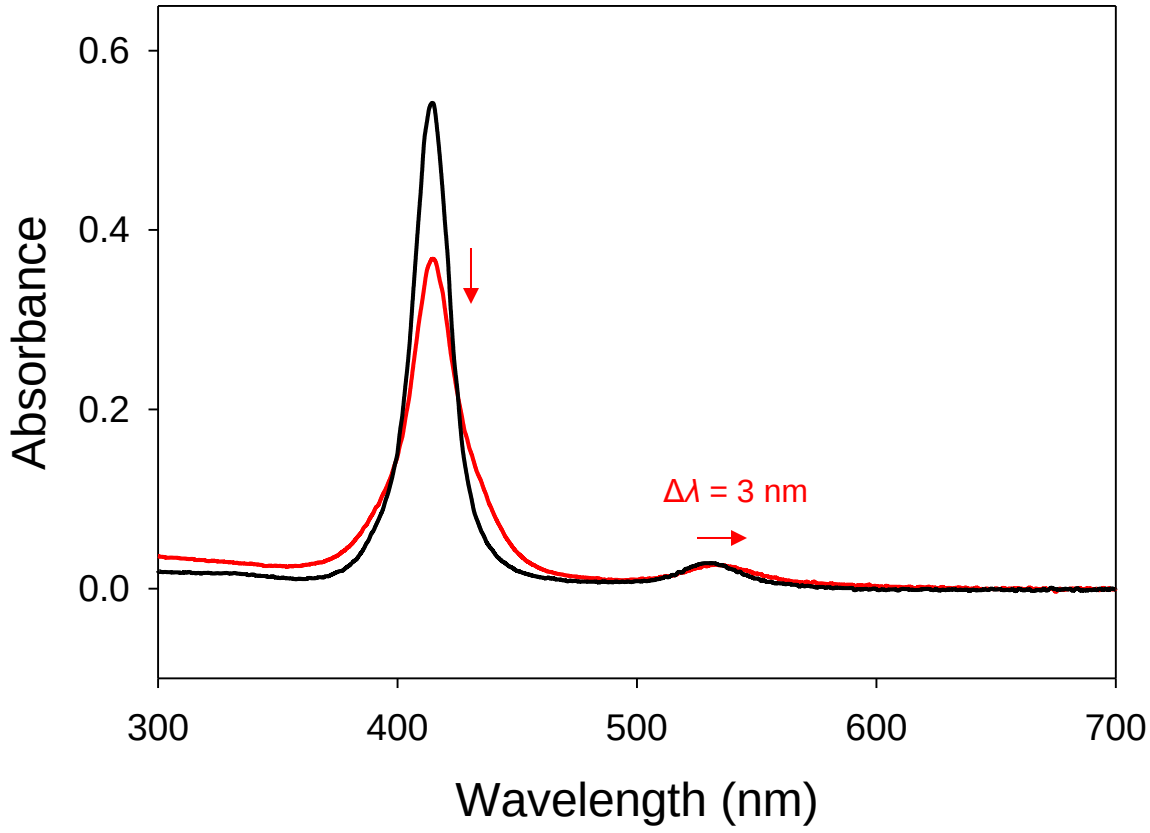

Figure 4S.17. UV-vis of [Co(T(-OMe)PP)] (4.15 μM in CH_2Cl_2, 298 K, black trace) and after reacting with 0.5 equiv **3** to form the $\{CoNO\}^8$ complex [Co(T(-OMe)PP)(NO)] (4.1 μM in CH_2Cl_2) (red trace).

4.4 References

(1) Gale, E. M.; Patra, A. K.; Harrop, T. C. Versatile Methodology Toward NiN_2S_2 Complexes as Nickel Superoxide Dismutase Models: Structure and Proton Affinity. *Inorg. Chem.* **2009**, *48*, 5620-5622.

(2) Broering, E. P.; Dillon, S.; Gale, E. M.; Steiner, R. A.; Telser, J.; Brunold, T. C.; Harrop, T. C. Accessing Ni(III)-Thiolate versus Ni(II)-Thiyl Bonding in a Family of Ni-N_2S_2 Synthetic Models of NiSOD. *Inorg. Chem.* **2015**, *54*, 3815–3828.

(3) Gale, E. M.; Narendrapurapu, B. S.; Simmonett, A. C.; Schaefer, H. F., III; Harrop, T. C. Exploring the Effects of H-Bonding in Synthetic Analogues of Nickel Superoxide Dismutase (Ni-SOD): Experimental and Theoretical Implications for Protection of the Ni−SCys Bond. *Inorg. Chem.* **2010**, *49*, 7080–7096.

(4) Steiner, R. A.; Dzul, S. P.; Stemmler, T. L.; Harrop, T. C. Synthesis and Speciation-Dependent Properties of a Multimetallic Model Complex of NiSOD That Exhibits Unique Hydrogen-Bonding. *Inorg. Chem.* **2017**, *56*, 2849-2862.

(5) Broering, E. P.; Truong, P. T.; Gale, E. M.; Harrop, T. C. Synthetic Analogues of Nickel Superoxide Dismutase: A New Role for Nickel in Biology. *Biochemistry* **2013**, *52*, 4-18.

(6) Mathrubootham, V.; Thomas, J.; Staples, R.; McCraken, J.; Shearer, J.; Hegg, E. L. Bisamidate and Mixed Amine/Amidate NiN_2S_2 Complexes as Models for Nickel-Containing Acetyl Coenzyme A Synthase and Superoxide Dismutase: An Experimental and Computational Study. *Inorg. Chem.* **2010**, *49*, 5393-5406.

(7) Colpas, G. J.; Maroney, M. J.; Bagyinka, C.; Kumar, M.; Willis, W. S.; Suib, S. L.; Baidya, N.; Mascharak, P. K. X-ray Spectroscopic Studies of Nickel Complexes with Application to the Structure of Nickel Sites in Hydrogenases. *Inorg. Chem.* **1991**, *30*, 920-928.

(8) Enemark, J. H.; Feltham, R. D. Principles of Structure, Bonding, and Reactivity for Metal Nitrosyl Complexes. *Coord. Chem. Rev.* **1974**, *13*, 339-406.

(9) Tennyson, A. G.; Dhar, S.; Lippard, S. J. Synthesis and Characterization of $\{Ni(NO)\}^{10}$ and $\{Co(NO)_2\}^{10}$ Complexes Supported by Thiolate Ligands. *J. Am. Chem. Soc.* **2008**, *130*, 15087-15098.

(10) Yang, L.; Powell, D. R.; Houser, R. P. Structural variation in copper(I) complexes with pyridylmethylamide ligands: structural analysis with a new four-coordinate geometry index, t_4. *Dalton Trans.* **2007**, 955-964.

(11) Maffett, L. S.; Gunter, K. L.; Kreisel, K. A.; Yap, G. P. A.; Rabinovich, D. Nickel nitrosyl complexes in a sulfur-rich environment: The first poly(mercaptoimidazolyl)borate derivatives. *Polyhedron* **2007**, *26*, 4758-4764.

(12) Wright, A. M.; Zaman, H. T.; Wu, G.; Hayton, T. W. Nitric Oxide Release from a Nickel Nitrosyl Complex Induced by One-Electron Oxidation. *Inorg. Chem.* **2013**, *52*, 3207-3216.

(13) Wright, A. M.; Wu, G.; Hayton, T. W. Late-Metal Nitrosyl Cations: Synthesis and Reactivity of $[Ni(NO)(MeNO_2)_3][PF_6]$. *Inorg. Chem.* **2011**, *50*, 11746-11753.

(14) Varonka, M. S.; Warren, T. H. Three-Coordinate N-Heterocyclic Carbene Nickel Nitrosyl Complexes. *Organometallics* **2010**, *29*, 717-720.

(15) Wright, A. M.; Wu, G.; Hayton, T. W. Formation of N_2O from a Nickel Nitrosyl: Isolation of the *cis*-$[N_2O_2]^{2-}$ Intermediate. *J. Am. Chem. Soc.* **2012**, *134*, 9930-9933.

(16) Iluc, V. M.; Miller, A. J. M.; Hillhouse, G. L. Synthesis and characterization of side-bound aryldiazo and end-bound nitrosyl complexes of nickel. *Chem. Commun.* **2005**, 5091-5093.

(17) Yi, G. B.; Khan, M. A.; Richter-Addo, G. B. The First Metalloporphyrin Nitrosamine Complex - Bis(Diethylnitrosamine)(Meso-Tetraphenylporphyrinato)Iron(III) Perchlorate. *J. Am. Chem. Soc.* **1995**, *117*, 7850-7851.

(18) Ohwada, T.; Miura, M.; Tanaka, H.; Sakamoto, S.; Yamaguchi, K.; Ikeda, H.; Inagaki, S. Structural features of aliphatic N-nitrosamines of 7-azabicyclo[2.2.1]heptanes that facilitate N-NO bond cleavage. *J. Am. Chem. Soc.* **2001**, *123*, 10164-10172.

(19) Albinati, A.; Affolter, S.; Pregosin, P. S. Reactions of Cyclopalladated N-Nitrosoanilines with Sn(IV) Reagents - Crystal-Structure of the Bis Cyclopalladated Complex Cis-$Pd(Onn(CH_3)(C_6H_4))_2$. *J. Organomet. Chem.* **1990**, *395*, 231-254.

(20) Xu, N.; Goodrich, L. E.; Lehnert, N.; Powell, D. R.; Richter-Addo, G. B. Five- and Six-Coordinate Adducts of Nitrosamines with Ferric Porphyrins: Structural Models for the Type II Interactions of Nitrosamines with Ferric Cytochrome P450. *Inorg. Chem.* **2010**, *49*, 4405-4419.

(21) Lee, J.; Chen, L.; West, A. H.; Richter-Addo, G. B. Interactions of organic nitroso compounds with metals. *Chem. Rev.* **2002**, *102*, 1019-1065.

(22) Schebler, P. J.; Riordan, C. G.; Guzei, I. A.; Rheingold, A. L. Phenyltris((tert-butylthio)methyl)borate: A Second Generation S_3^- Ligand That Enforces Tetrahedral Coordination. *Inorg. Chem.* **1998**, *37*, 4754-4755.

(23) Maffett, L. S.; Gunter, K. L.; Kreisel, K. A.; Yap, G. P. A.; Rabinovich, D. Nickel Nitrosyl Complexes in a Sulfur-Rich Environment: The First Poly(mercaptoimidazolyl)borate Derivatives. *Polyhedron* **2007**, *26*, 4758-4764.

(24) Garner, M.; Lewinski, K.; Pattek-Janczyk, A.; Reglinski, J.; Sieklucka, B.; Spicer, M. D.; Szaleniec, M. Structural and spectroscopic characterisation of bis-ligand complexes of iron(II), nickel(II) and nickel(III) with the hydrotris(methimazolyl)borate anion: soft S_6 donor sets generating a weak ligand field. *Dalton Trans.* **2003**, 1181-1185.

(25) Williams, R. L.; Pace, R. J.; Jeacocke, G. J. Applications of Solvent Effects .1. The Spectra of Secondary Nitrosamines. *Spectrochim. Acta* **1964**, *20*, 225-236.

(26) Di Salvo, F.; Estrin, D. A.; Leitus, G.; Doctorovich, F. Synthesis, structure, and reactivity of aliphatic primary nitrosamines stabilized by coordination to $[IrCl_5]^{2-}$. *Organometallics* **2008**, *27*, 1985-1995.

(27) Puiu, S. C.; Warren, T. H. Three-coordinate beta-diketiminato nickel nitrosyl complexes from nickel(I)-lutidine and nickel(II)-alkyl precursors. *Organometallics* **2003**, *22*, 3974-3976.

(28) Fomitchev, D. V.; Furlani, T. R.; Coppens, P. Combined X-ray diffraction and density functional study of [Ni(NO)(h^5-Cp*)] in the ground and light-induced metastable states. *Inorg. Chem.* **1998**, *37*, 1519-1526.

(29) Heinemann, F. W.; Pritzkow, H.; Zeller, M.; Zenneck, U. 1,2,4-triphospholyl nickel complexes: Evidence for a dimerization equilibrium that includes a sigma-pi rearrangement of the triphospholyl ligand. *Organometallics* **2000**, *19*, 4283-4288.

(30) Conradie, J.; Ghosh, A. Stereochemical Diversity of $\{MNO\}^{10}$ Complexes: Molecular Orbital Analyses of Nickel and Copper Nitrosyls. *Inorg. Chem.* **2014**, *53*, 4847-4855.

(31) Sanders, B. C.; Patra, A. K.; Harrop, T. C. Synthesis, properties, and reactivity of a series of non-heme $\{FeNO\}^{7/8}$ complexes: Implications for Fe-nitroxyl coordination. *J. Inorg. Biochem.* **2013**, *118*, 115-127.

(32) Harrop, T. C.; Song, D. T.; Lippard, S. J. Interaction of nitric oxide with tetrathiolato iron(II) complexes: Relevance to the reaction pathways of iron nitrosyls in sulfur-rich biological coordination environments. *J. Am. Chem. Soc.* **2006**, *128*, 3528-3529.

(33) Chiang, C. Y.; Darensbourg, M. Y. Iron nitrosyl complexes as models for biological nitric oxide transfer reagents. *J. Biol. Inorg. Chem.* **2006**, *11*, 359-370.

(34) Rhine, M. A.; Rodrigues, A. V.; Urbauer, R. J. B.; Urbauer, J. L.; Stemmler, T. L.; Harrop, T. C. Proton-Induced Reactivity of NO- from a $\{CoNO\}^{8}$ Complex. *J. Am. Chem. Soc.* **2014**, *136*, 12560-12563.

(35) Scheidt, W. R.; Hoard, J. L. Stereochemistry of Low-Spin Cobalt Porphyrins .1. Structure and Bonding in a Nitrosylcobalt Porphyrin and Their Bearing on One Rational Model for Oxygenated Protoheme. *J. Am. Chem. Soc.* **1973**, *95*, 8281-8288.

(36) Richter-Addo, G. B.; Hodge, S. J.; Yi, G. B.; Khan, M. A.; Ma, T.; Van Caemelbecke, E.; Guo, N.; Kadish, K. M. Synthesis characterization, and spectrochemistry of cobalt porphyrins containing axially bound nitric oxide. *Inorg. Chem.* **1996**, *35*, 6530-6538.

(37) Kumar, M.; Dixon, N. A.; Merkle, A. C.; Zeller, M.; Lehnert, N.; Papish, E. T. Hydrotris(triazolyl)borate Complexes as Functional Models for Cu Nitrite Reductase: The Electronic Influence of Distal Nitrogens. *Inorg. Chem.* **2012**, *51*, 7004-7006.

(38) Sanders, B. C.; Hassan, S. M.; Harrop, T. C. NO_2^- Activation and Reduction to NO by a Nonheme $Fe(NO_2)_2$ Complex. *J. Am. Chem. Soc.* **2014**, *136*, 10230-10233.

(39) Tsuge, K.; DeRosa, F.; Lim, M. D.; Ford, P. C. Intramolecular reductive nitrosylation: Reaction of nitric oxide and a copper(ll) complex of a cyclam derivative with pendant luminescent chromophores. *J. Am. Chem. Soc.* **2004**, *126*, 6564-6565.

(40) Khin, C.; Lim, M. D.; Tsuge, K.; Iretskii, A.; Wu, G.; Ford, P. C. Amine nitrosation via NO reduction of the polyamine copper(II) complex $Cu(DAC)^{2+}$. *Inorg. Chem.* **2007**, *46*, 9323-9331.

(41) Lim, M. H.; Wong, B. A.; Pitcock, W. H., Jr.; Mokshagundam, D.; Baik, M.-H.; Lippard, S. J. Direct Nitric Oxide Detection in Aqueous Solution by Copper(II) Fluorescein Complexes. *J. Am. Chem. Soc.* **2006**, *128*, 14364-14373.

(42) Fulmer, G. R.; Miller, A. J. M.; Sherden, N. H.; Gottlieb, H. E.; Nudelman, A.; Stoltz, B. M.; Bercaw, J. E.; Goldberg, K. I. NMR Chemical Shifts of Trace Impurities: Common Laboratory Solvents, Organics, and Gases in Deuterated Solvents Relevant to the Organometallic Chemist. *Organometallics* **2010**, *29*, 2176–2179.

(43) Neese, F. The ORCA program system. *WIREs Comput. Mol. Sci.* **2012**, *2*, 73-78.

(44) Becke, A. D. Density functional calculations of molecular bond energies. *J. Chem. Phys.* **1986**, *84*, 4524-4529.

(45) Perdew, J. P. Density-functional approximation for the correlation energy of the inhomogeneous electron gas. *Phys. Rev. B* **1986**, *33*, 8822-8824.

(46) Neese, F. An Improvement of the Resolution of the Identity Approximation for the Formation of the Coulomb Matrix. *J. Comput. Chem.* **2003**, *24*, 1740-1747.

(47) Grimme, S.; Antony, J.; Ehrlich, S.; Krieg, H. A consistent and accurate *ab initio* parametrization of density functional dispersion correction (DFT-D) for the 94 elements H-Pu. *J. Chem. Phys.* **2010**, *132*, 154104.

(48) Grimme, S.; Ehrlich, S.; Goerigk, L. Effect of the Damping Function in Dispersion Corrected Density Functional Theory. *J. Comput. Chem.* **2011**, *32*, 1456-1465.

(49) Weigend, F.; Ahlrichs, R. Balanced basis sets of split valence, triple zeta valence and quadruple zeta valence quality for H to Rn: Design and assessment of accuracy. *Phys. Chem. Chem. Phys.* **2005**, *7*, 3297-3305.

(50) Schäfer, A.; Horn, H.; Ahlrichs, R. Fully optimized contracted Gaussian basis sets for atoms Li to Kr. *J. Chem. Phys.* **1992**, *97*, 2571-2577.

(51) Cohen, A. J.; Handy, N. C. Dynamic correlation. *Mol. Phys.* **2001**, *99*, 607-615.

(52) Lee, C.; Yang, W.; Parr, R. G. Development of the Colle-Salvetti correlation-energy formula into a functional of the electron density. *Phys. Rev. B* **1988**, *37*, 785-789.

(53) Pettersen, E. F.; Goddard, T. D.; Huang, C. C.; Couch, G. S.; Greenblatt, D. M.; Meng, E. C.; Ferrin, T. E. UCSF Chimera—A Visualization System for Exploratory Research and Analysis. *J. Comput. Chem.* **2004**, *25*, 1605-1612.

(54) Walker, N.; Stuart, D. An empirical method for correcting diffractometer data for absorption effects. *Acta Crystallogr.* **1983**, *A39*, 158-166.

(55) Sheldrick, G. M. A short history of SHELX. *Acta Crystallogr.* **2008**, *A64*, 112-122.

(56) Sheldrick, G. M. SHELXTL-2013, Crystallographic Computing System; Siemens Analytical X-Ray Instruments: Madison, WI, 2013.

(57) Cromer, D. T.; Waber, J. T. In *International Tables for X-ray Crystallography*; The Kynoch Press: Birmingham, England, 1974.

(58) Burnett, M. N.; Johnson, C. K. *ORTEP-III, Report ORNL-6895*; Oak Ridge National Laboratory: Oak Ridge, TN, 1996.

(59) George, G. N.; George, S. J.; Pickering, I. J. EXAFSPAK; Stanford Synchotron Radiation Lightsource: Menlo Park, CA, 2001; http://www-ssrl.slac.stanford.edu/~george/exafspak/exafs.htm.

(60) Rehr, J. J.; Ankudinov, A. L. Progress and challenges in the theory and interpretation of X-ray spectra. *J. Synchrotron Radiat.* **2001**, *8*, 61-65.

(61) Riggs-Gelasco, P. J.; Stemmler, T. L.; Penner-Hahn, J. E. XAFS of dinuclear metal sites in proteins and model compounds. *Coord. Chem. Rev.* **1995**, *144*, 245-286.

(62) Cotelesage, J. J. H.; Pushie, M. J.; Grochulski, P.; Pickering, I. J.; George, G. N. Metalloprotein active site structure determination: Synergy between X-ray absorption spectroscopy and X-ray crystallography. *J. Inorg. Biochem.* **2012**, *115*, 127-137.

(63) Bencze, K. Z.; Kondapalli, K. C.; Stemmler, T. L. *X-Ray Absorption Spectroscopy In Applications of Physical Methods in Inorganic and Bioinorganic Chemistry: Handbook, Encyclopedia of Inorganic Chemistry*; John Wiley & Sons, Ltd.: Chichester, UK, 2007.

(64) Synergy Software, KaleidaGraph 4.1.3., 2011, [data analysis-graphing application : for Macintosh and Windows operating systems] http://www.synergy.com.

(65) Randall, C. R.; Shu, L. J.; Chiou, Y. M.; Hagen, K. S.; Ito, M.; Kitajima, N.; Lachicotte, R. J.; Zang, Y.; Que, L. X-Ray-Absorption Pre-Edge Studies of High-Spin Iron(II) Complexes. *Inorg. Chem.* **1995**, *34*, 1036-1039.

CHAPTER 5

A CHEMOSENSOR FOR Ni(II) EMPLOYING N/S-BASED DONORS

Broering, E. P.;* Harrop, T. C. To be submitted to *Inorganic Chemistry*.

5.1 Abstract

In human physiology, nickel (Ni) compounds are classified as carcinogens and have been implicated in respiratory illnesses. In bacteria, however, Ni is an essential element in the production of key metalloenzymes, and as such, bacterial trafficking systems have evolved to control the import, export, and integration of Ni into these vital enzymes. Due to Ni's many functions, it is necessary to have a greater understanding of the transport and role of this metal in biological systems. Reported herein is the design and synthesis of a fluorescent sensor for Ni(II), which was designed to mimic the strong-field nature of the active site found in NiSOD. Here we report the construction of these new sensors for Ni(II) with the general formula [Ni(N_2S_2-Dns)][1], composed of thiolate-S, carboxamide-N, and tertiary amine-N ligands attached to a fluorescent dansyl (Dns) reporter group.

5.2 Introduction

Ni(II) is utilized by bacteria in the structure and function of vital metalloenzymes, such as [Ni-Fe] hydrogenase, methyl coenzyme M reductase, urease, CO dehydrogenase, and Ni superoxide dismutase (NiSOD).[1,2] Bacteria also possess a trafficking system for Ni(II) to closely regulate concentration of the metal ion in the cell, and some species, including *Helicobacter pylori* and *Escherichia coli*, employ Ni(II) as a pathogenic response to external threats.[3,4] However, the Ni(II) tracking machinery that controls influx, efflux, and metalloenzyme assembly is not well understood. Furthermore, questions remain with respect to the role of soluble and insoluble forms of Ni(II), cellular uptake, and toxicity in mammalian health. For humans, the inhalation of insoluble species of Ni(II) arising from mining processes appear to be the greatest

threat,[5,6] although the contamination of water sources with soluble Ni(II) compounds is also an environmental concern.[7]

To gain greater insight into the transport and function of metals in biology, researchers have developed sensors capable of reporting $[M]^{n+}$ via a fluorescent response upon chelating the metal species. Under physiological conditions, the trafficking of transition metals such as Cu(II)[8] and Zn(II)[9] has been the focus of much study;[10-12] however, there is a paucity of cell-compatible probes tailored for Ni(II) recognition. For example, many of the probes published to date (2017) are not specific for Ni(II) and exhibit a fluorescent response in the presence of other biologically relevant ions;[13] others are not functional under aqueous conditions at physiological pH.[14,15] The most promising Ni(II) sensor for biological application was published by Chang and coworkers and utilizes a boron-dipyrromethene (BODIPY) reporter tethered to an N/O/S chelate to produce a turn-on fluorescent response upon binding Ni(II).[16] This report is the first to indicate that incorporating sulfur chelates affords Ni(II) specificity, an improvement over solely nitrogen-based ligands and previously published macrocyclic structures.[14,15,17] This NS1 sensor published by Chang was successfully employed in A549 cell lines to visualize cellular Ni(II). However, the greatest emissive response for NS1 occurs for Ni(II) concentrations greater than 50-fold in excess of sensor, and high Ni concentrations (100 μM) are unlikely to be encountered intracellularly. Moreover, the K_d of this system is relatively weak (193 ± 5 μM) compared to other Ni(II) scaffolds in biology, such as enzymes and chaperone proteins.[4,16] The requirement of excess Ni and weak binding are likely attributed to the low affinity of the methyl ester and thioether ligands.

Taking inspiration from nature, a sensor has been designed, synthesized, and characterized that is composed of an N-carboxamide, N-amine, and two S-thiolates as a probable

square-planar chelate for Ni(II) with the general formula N_2S_2-Dns (**3**) (Figure 5.1). Nature uses these donors to bind Ni(II) in the reduced active site structure of NiSOD and in the distal Ni site of acetyl coenzyme A synthase.[18] A dansyl chloride (Dns) chromophore was tethered to the N_2S_2 platform to serve as a reporter for Ni(II) (Figure 5.1). As has been reported for other Dns-containing sensors, it is expected that the lone pair of the sulfonamide-N will engage in a Ni—N bond and change the electronic nature of the system to allow for a fluorescent response (Figure 5.2). Upon binding Ni(II), the energy of the lone pair should be sufficiently lowered as to allow fluorescence. We predict that the strong-field nature of the square-planar chelate will result in a significant turn-on response upon binding Ni(II), resulting in an $S = 0$ $[Ni(N_2S_2\text{-Dns})]^{1-}$ complex that should be highly fluorescent. The development of a high affinity, tight-binding (nM) Ni(II) sensor is necessary to better understand metalloenzyme assembly involving Ni(II) as a catalytic center, as well as the pathways for Ni(II) transport in other bacterial processes.

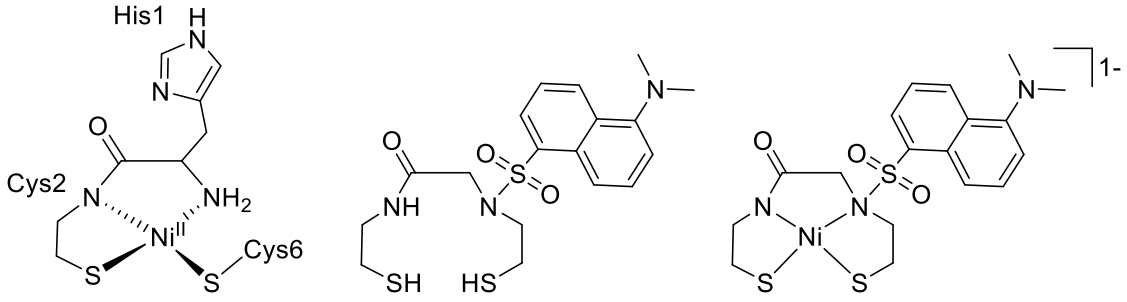

Figure 5.1: Structures of the reduced active site of NiSOD, the apo N_2S_2-Dns tetradentate sensor (**2**), and the anionic form of the proposed $[Ni(N_2S_2\text{-Dns})]^{1-}$ (**3**).

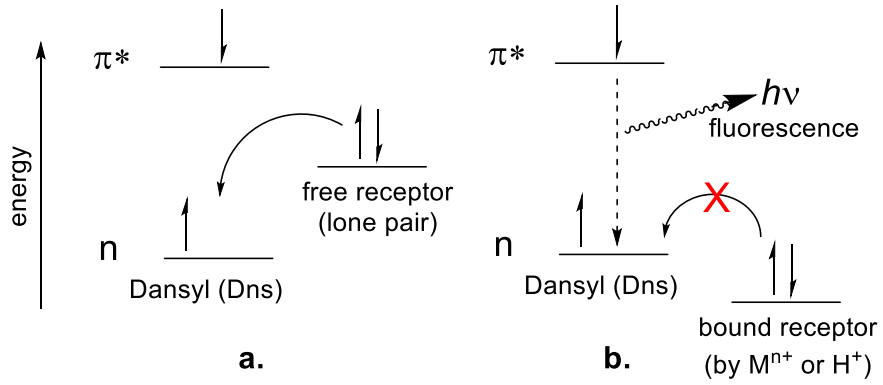

Figure 5.2. Proposed mechanism of the turn-on fluorescent sensor designed for Ni(II) chelation. (a) In the excited state, fluorescence is quenched by electron transfer from the lone pair on the free receptor. (b) In the excited state, chelation of a metal (or protonation) lowers the energy of the receptor and restores fluorescence.

5.3 Experimental

General Information. All reagents were purchased from commercial sources and used as received unless otherwise noted. Acetonitrile (MeCN), dichloromethane (CH_2Cl_2), tetrahydrofuran (THF), diethyl ether (Et_2O), and pentane were purified by passage through activated alumina columns of an MBraun MB-SPS solvent purification system and stored under an N_2 atmosphere until use. *N*,*N*-dimethylformamide (DMF) was purified with a VAC solvent purifier containing 4 Å molecular sieves and stored under N_2. Metalation reactions were carried out in methanol (MeOH) that was stored over 3 Å molecular sieves for at least one week and degassed using the freeze-pump-thaw method before using. *S*-trityl cysteamine (**I**),[19] *N*-(2-bromoacetyl)-*S*-(trihenylmethyl)-2-aminoethanethiol,[20] (**II**), and *N*-[2-((2-triphenylmethyl)thio)ethyl)amino)acetyl]-*S*-(tiphenylmethyl)-2-aminoethanethiol[21] (N_2S_2-$(Tr)_2$, **III**) were prepared and checked according to published procedures. All syntheses were

performed under an inert atmosphere of N_2 using Schlenk line techniques or under an atmosphere of purified N_2 in an MBraun Unilab glovebox. Fluorescence experiments were performed aerobically in MeOH and buffer solutions that were passed through 0.3 μm filters prior to use. Piperazine-*N*,*N*′-bis(2-ethanesulfonic acid) (PIPES) (pH 7.2, 100 mM KCl) and *N*-cyclohexyl-2-aminoethanesulfonic acid (CHES) (pH 9.0, 100 mM KCl) buffers were prepared in 18.2 MΩ cm^{-1} water and treated with Chelex 100 resin to remove trace metals prior to use. The protected and deprotected sensors **2** and **3** were stored in foil or in the dark to prevent photodegradation.

Physical Methods. Fourier transform infrared (FTIR) spectra were collected on a ThermoNicolet 6700 spectrophotometer running the OMNIC software. All samples were run as solid samples prepared as pressed KBr pellets. Electronic absorption spectra were collected at 298 K using a Cary-50 spectrophotometer containing a Quantum Northwest TC 125 temperature control unit. Fluorescence spectra were collected at 298 K using a Varian Eclipse fluorometer containing a Quantum Northwest TC 125 temperature control unit. All UV-vis and fluorescence samples were prepared in gastight Teflon-lined screw cap quartz cells with an optical pathlength of 1 cm. Quartz cells were rinsed with 10% HNO_3 to remove trace metals prior to every experiment. The fluorescence readings were recorded 15-30 min after addition of Ni(II) to allow for complete reaction. Samples were excited at λ_{ex} = 350 nm and scanned for emission from 360-750 nm. Integrated intensities were reported over the range of 450-650 nm for an average of three trials. Emission and excitation slit widths were set at 5 nm. ^{1}H NMR spectra were recorded in the listed deuterated solvent on a 400 MHz Bruker BZH 400/52 NMR spectrometer or a Varian Unity Inova 500 MHz NMR spectrometer at RT with chemical shifts internally referenced to tetramethylsilane (TMS = $Si(CH_3)_4$), or the residual protio signal of the deuterated

solvent as previously reported.[22] Low-resolution electrospray ionization mass spectrometry (LR-ESI-MS) data were collected using a Bruker Esquire 3000 plus ion trap mass spectrometer.

Synthesis of N_2S_2-Tr_2-Dns (1). To a solution of **III** (0.5272 g, 0.7765 mmol) in 20 mL THF/MeCN (1:1) was added 1 equiv dansyl chloride (0.2146 g, 0.7955 mmol), 3.1 equiv K_2CO_3 (0.3318 g, 2.401 mmol), and 1.1 equiv NaI (0.1231 g, 0.8212 mmol). The orange mixture was refluxed under an N_2 atmosphere for 20 h. The solvent was removed by short path vacuum distillation to yield an orange-brown solid. The solid was dissolved in 50 mL CH_2Cl_2 and washed with 50 mL satd. $NaHCO_3$ solution, 50 mL satd. NaCl, and the organic layer was dried over $MgSO_4$ and filtered. The CH_2Cl_2 was removed by rotovap evaporation. The resulting brown oil was purified by silica chromatography with hexane/EtOAc (2:1) to yield 0.3648 g (0.4000 mmol, 49%) of a green-yellow oil. Trituration (4mL × 3) with Et_2O yields a green-yellow glassy foam. ^{1}H NMR (500 MHz, $CDCl_3$ containing 0.05% v/v TMS, δ from TMS): 8.49 (d, 1H, J = 5.0 Hz), 8.06 (t, 2H, J = 10.0 Hz), 7.43 (t, 2H, J = 7.5 Hz), 7.38 (d, 2H, J = 10.0 Hz), 7.09-7.28 (m, 25H, integrates high due to residual protio solvent), 6.14 (t, br, 1H, N*H*, J = 7.5 Hz), 3.44 (s, 2H, integrates high due to overlap with residual Et_2O), 2.93 (t, 2H, J = 10.0 Hz, -NC*H*$_2$CH$_2$S-), 2.83 (s, 6H, N(C*H*$_3$)$_2$), 2.70 (t, 2H, J = 10.0 Hz, -NC*H*$_2$CH$_2$S-), 2.35 (t, 2H, J = 7.5 Hz, -NCH$_2$C*H*$_2$S-), 2.13 (t, 2H, J = 5.0 Hz, -NCH$_2$C*H*$_2$S-). ^{13}C NMR (125 MHz, $CDCl_3$ containing 0.05% v/v TMS, δ from TMS): 167.41 (C=O), 151.96, 144.47, 144.23, 132.87, 131.10, 130.59, 128.81, 129.73, 129.42-129.35, 128.72, 127.80, 126.68, 123.11, 118.36, 115.19, 50.73, 48.82, 45.28, 38.13, 31.16, 29.56. FTIR (KBr pellet) ν_{max} (cm^{-1}): 3393 (w, ν_{NH}), 3059 (w), 2965 (m), 2862 (w), 2781 (w), 1955 (w), 1680 (s, ν_{CO}), 1578 (m), 1525 (m), 1490 (m), 1446 (m), 1404 (w), 1264 (m), 1024 (vs, ν_{SO}), 799 (vs), 744 (m), 695 (s), 619 (m), 569 (w), 487 (w). UV-vis (MeCN, 298 K) λ_{max}, nm: 345. LR-ESI-MS (*m/z*): $[M+Na^+ + 2H_2O + CH_3CN]^+$ calcd for $C_{58}H_{60}N_4NaO_5S_3$: 1013.3 (100),

1014.3 (66.6), 1015.3 (35.4), 1016.3 (12.4); found: 1013.4 (100.0), 1014.4 (70.8), 1015.4 (39.6), 1016.3 (15.1).

Synthesis of N_2S_2-Dns (2). To a solution of **1** (0.5425 g, 0.5947 mmol) in 5 mL CH_2Cl_2 and 3 mL trifluoroacetic acid (TFA) was added 3 equiv Et_3SiH (0.28 mL, 1.8 mmol). The yellow-orange color of the solution bleached upon addition of Et_3SiH, and the resulting pale yellow solution stirred for 1.5 h. The solution was concentrated by short path distillation to remove the CH_2Cl_2, and the remaining TFA solution was filtered to remove Ph_3CH. The remaining TFA was removed, and the beige oil was redissolved in 25 mL CH_2Cl_2. To this solution was added 25 mL deionized H_2O and K_2CO_3 until the organic layer was basic. The organic layer was separated, washed with 25 mL satd. NaCl solution, dried over $MgSO_4$, and filtered. The CH_2Cl_2 was removed by rotary evaporation and the resulting green-yellow oil was triturated with hexane to remove residual Ph_3CH. Triturations with Et_2O (3 × 4 mL) yielded 0.2078 g (0.4860 mmol, 82%) of a bright green-yellow foam. ^{1}H NMR (500 MHz, $CDCl_3$ containing 0.05% v/v TMS, δ from TMS): 8.58 (d, 1H, J = 10.0 Hz), 8.27 (d, 1H, J = 10.0 Hz), 8.22 (d, 1H, J = 10.0 Hz), 7.61 (t, 1H, J = 5.0 Hz), 7.55 (t, 1H, J = 5.0 Hz), 7.22 (d, 1H, J = 5.0 Hz), 6.85 (s, br, 1H, N*H*), 3.85 (s, 2H), 3.56 (t, 2H, J = 7.5 Hz, -NC*H*$_2$CH$_2$S-), 3.29 (t, 2H, J = 5.0 Hz, -NC*H*$_2$CH$_2$S-), 2.89 (s, 6H, N(C*H*$_3$)$_2$), 2.70 (t, 2H, J = 5.0 Hz, -NCH$_2$C*H*$_2$S-), 2.45 (t, 2H, J = 5.0 Hz, -NCH$_2$C*H*$_2$S-), 1.41 (t, 1H, J = 10 Hz , S*H*), 1.30 (t, 1H, J = 10 Hz, S*H*). ^{13}C NMR (125 MHz, $CDCl_3$ containing 0.05% v/v TMS, δ from TMS): 168.27 (C=O), 153.23, 132.82, 131.53, 130.74, 130.16, 129.92, 129.46, 129.01, 128.30, 123.35, 118.40, 115.54, 53.09, 51.97, 45.42, 42.35, 24.13, 22.94. FTIR (KBr pellet) ν_{max} (cm^{-1}): 3375 (m, br ν_{NH}), 3070 (w), 2939 (m), 2868 (w), 2835 (w), 2739 (w), 2562 (w), 2359 (w), 1687 (vs, ν_{CO}), 1574 (m), 1535 (m), 1448 (m), 1406 (m), 1324 (m), 1145 (vs, ν_{SO}), 1087 (m), 917 (m), 795 (s), 731 (m), 623 (m), 568 (m).

UV-vis (MeOH, 298 K) λ_{max}, nm (ε, M^{-1} cm^{-1}): 340 (8700), 253 (28000). LR-ESI-MS (*m/z*): $[M+K^+]^+$ calcd for $KC_{18}H_{25}N_3O_3S_3$, 466.0 (100), 467.0 (23.0), 468.0 (22.6), 469.0 (4.0); found: 466.0 (100.0), 467.0 (22.4), 468.0 (21.6), 469.0 (4.1).

General procedure for the bulk metalation of 2. To a 3 mL MeOH solution of **2** was added 3.5 equiv Na° or KH and the green-yellow color of the solution paled slightly. After stirring for 15 min, 1 equiv Ni(II) was added in the form of $NiCl_2$ or $[Ni(H_2O)_6](BF_4)_2$ resulting in an immediate darkening of the solution and formation of a dark brown or dark brown/green precipitate. The mixture stirred for 1 h, and the precipitate was removed by filtration. Removal of the MeOH from the filtrate in vacuo yielded a light brown residue.

Synthesis of 3 with Na° and $NiCl_2$. To a 3 mL MeOH solution of **2** (0.0512 g, 0.119 mmol) was added 3.4 equiv Na° (0.0089 g, 0.39 mmol) in 2 mL MeOH. The green-yellow solution paled slightly upon stirring for 15 min. 1 mole equiv (0.0152 g, 0.118 mmol) of anhydrous $NiCl_2$ in 1 mL MeOH was added, and an immediate color change to brown and formation of a brown precipitate was observed. Upon stirring for 2 h, 0.0242 g of a dark precipitate was removed by filtration, and FTIR (KBr pellet) analysis reveals this to contain unbound carboxamide-N (ν_{CO} = 1673 cm^{-1}). The solvent was removed from the filtrate to yield the pale brown residue **3** (0.0178, 0.0314 mmol, 26% yield). ^{1}H NMR (400 MHz, CD_3OD, RT, δ from protio solvent signal): 8.36 (d, 1H, *J* = 8.0 Hz), 8.29 (d, 1H, *J* = 12 Hz), 8.01 (d, 1H, *J* = 8.0 Hz), 7.56 (t, 1H, *J* = 8.0 Hz), 7.46 (t, 1H, *J* = 8.0 Hz), 7.00 (d, 1H, *J* = 4.0 Hz), 4.96 (s, 2H), 3.33 (m, 2H, *J* = 4 Hz, integrates high due to overlap with CD_3OD), 2.86 (s, 6H, $N(CH_3)_2$, integrates high due to overlap with CH_2), 2.82 (t, 2H, *J* = 4.0 Hz, overlap with Me), 2.70 (t, 2H, *J* = 8.0 Hz), 2.60 (t, 2H, *J* = 8.0 Hz), FTIR (KBr pellet) ν_{max} (cm^{-1}): 3418 (m, br), 2927 (w), 2835 (w),

2779 (w), 1687 (m), 1627 (vs, ν_{CO}), 1590 (vs, ν_{CO}), 1435 (vs), 1331 (w), 1193 (w), 1145 (w), 1031 (s, ν_{SO}), 976 (m), 787 (m), 612 (w), 448 (w).

Synthesis of 3 with KH and $[Ni(H_2O)_6](BF_4)_2$. To a 2 mL MeOH solution of **2** (0.0891 g, 0.208 mmol) was added 3.6 equiv KH (0.0301 g, 0.753 mmol) in 2 mL MeOH. The green-yellow solution paled slightly upon stirring for 15 min. 1 mole equiv (0.0715 g, 0.210 mmol) of $[Ni(H_2O)_6](BF_4)_2$ in 1 mL MeOH was added metal to ligand and an immediate color change to brown and formation of a red-brown precipitate was observed. Upon stirring for 2 h, 0.1072 g of a dark precipitate was removed by filtration, and FTIR (KBr pellet) analysis reveals this to be unbound carboxamide-N (ν_{CO} = 1674 cm^{-1}) and KBF_4 (ν_{BF} = 1064 cm^{-1}, 1029 cm^{-1}). The solvent was removed from the filtrate to yield the pale brown residue **3** (0.0245, 0.0432 mmol, 21% yield). ^{1}H NMR (400 MHz, CD_3OD, RT, δ from protio solvent signal): 8.35 (d, 1H, J = 8.0 Hz), 8.29 (d, 1H, J = 8.0 Hz), 7.97 (d, 1H, J = 8.0 Hz), 7.55 (t, 1H, J = 8.0 Hz), 7.46 (t, 1H, J = 4.0 Hz), 7.10 (d, 1H, J = 4.0 Hz), 4.97 (s, 2H), 3.33 (m, 2H, J = 4 Hz, integrates high due to overlap with CD_3OD), 2.86 (s, 6H, $N(CH_3)_2$, integrates high due to overlap with CH_2), 2.82 (t, 2H, J = 4.0 Hz, overlap with Me), 2.68 (t, 2H, J = 8.0 Hz), 2.60 (t, 2H, J = 8.0 Hz). FTIR (KBr pellet) ν_{max} (cm^{-1}): 3420 (m, br), 2924 (m), 2833 (m), 2781 (w), 2386 (w), 1634 (s, ν_{CO}), 1571 (s, ν_{CO}), 1437 (s), 1310 (w), 1189 (w), 1136 (m), 1034 (vs, ν_{SO}), 977 (m), 794 (m), 748 (w), 697 (w), 614 (w), 446 (w).

Job's Method of Continuing Variation. The binding stoichiometry of Ni:sensor (**2**) was determined by monitoring the UV-vis spectra at λ = 340 nm and λ = 408 nm in MeOH at 298 K for three trials. In the presence of 1.5% Et_3N, The concentration of $[Ni(H_2O)_6]Cl_2$ was increased from 0-100 μM in direct opposition to decreasing concentrations of **2** from 100-0 μM. The mole

fraction of **2** was plotted vs. the absorbance of **2** to extrapolate the binding stoichiometry for the Ni complex.

Fluorescence Measurements

Competition studies. $[Ni(H_2O)_6](BF_4)_2$ was used to prepare the Ni(II) stock solutions. MeOH solutions of Na(I), K(I), Co(II), Zn(II), and Fe(II) were prepared from their tetrafluoroborate salts. Solutions of Cu(II) and Mn(II) were prepared from their chloride salts. A typical measurement contained 10 μM of **2** and 10 mol-equiv of base (Et_3N, 100 μM). After incubating for 15 min, 1 mol-equiv of metal ions were added and the solution incubated for another 15 min before measuring the fluorescent response. Data were plotted for I/I_0, where bars represent the average integrated fluorescence response (*I*) over the average initial integrated emission (*Io*) for three trials (integrated from 450-650 nm).

Scheme 5.1. Synthesis of the N_2S_2-Dns sensor **2**.

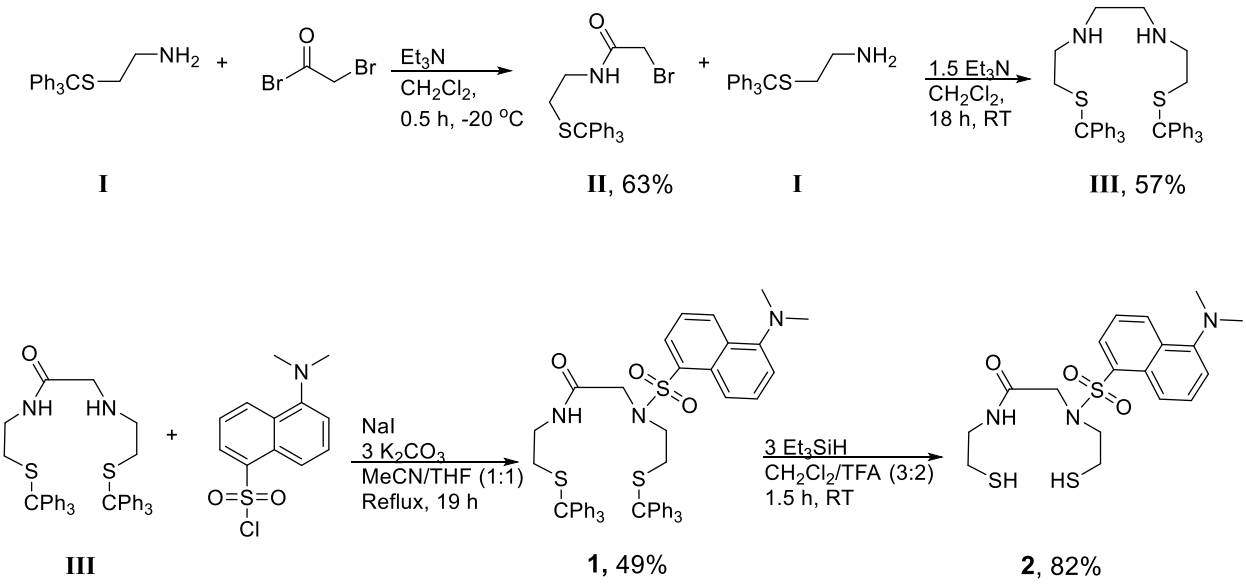

5.4 Results and Discussion

Synthesis. The syntheses of the precursor compounds **I-III** were carried out as reported previously.[19,21,23] The trityl protected apo-sensor **1** was synthesized by reacting **III** with 1 equiv dansyl chloride in the presence of NaI and excess K_2CO_3 under refluxing conditions. Purification on silica afforded **1** in modest yield, and trityl deprotection by TFA and 3 equiv Et_3SiH resulted in N_2S_2-Dns **2** (Scheme 5.1). The sensor **2** is soluble in organic solvents as well as pH 7.2 PIPES and pH 9.0 CHES buffers. Furthermore, UV-vis demonstrates that MeOH solutions of **2** are stable under aerobic conditions for more than 24 h.

Bulk metalation of **2** was carried out with either $NiCl_2$ or $[Ni(H_2O)_6](BF_4)_2$ to study the photophysical characteristics of the Ni(II)-bound sensor (see supporting information). Upon deprotonation of the thiolates and carboxamide-N with 3.5 equiv base (either Na° or KH), 1 equiv Ni(II) was added, which resulted in formation of dark brown precipitate and brown solution. In all metalation trials, the formation of the MeOH precipitate accounts for over half of the total reaction mass. Following removal of the solid, the potassium or sodium complex of **3** is obtained as the pale brown filtrate.

Spectroscopic properties. Ligands **1-2** form bright green-yellow solutions in organic solvents and exhibit λ_{max} = 340 nm (8700 M^{-1} cm^{-1}) with a second λ_{max} at higher energy at 253 nm (27900 $M^{-1}cm^{-1}$) in MeOH that are due to the electronic absorbance of the dansyl chromophore (Figure 5.3). The 340 nm feature is in-line with other Dns-derived sensors, and this is assigned as charge transfer (CT) transitions from the dimethylamino-N to the π-antibonding (π^*) orbital of the naphthalene ring.[24] The transition at higher energy is assigned as a $\pi \rightarrow \pi^*$ transition, arising from the naphthalene.[25] ^{1}H NMR, ^{13}C NMR, FTIR, and ESI-MS are consistent with formation of **1** and **2**.

Deprotonation of **2** with 3.5 equiv base (Na°, KH, or Et_3N) results in minimal change in the electronic absorption spectrum, λ_{max} = 344 nm. The precipitate resulting from metalation accounts for >50% of the reaction mass and is insoluble in all organic solvents, which makes characterization of this product difficult. FTIR (KBr pellet) analysis of the MeOH insoluble material reveals peaks of varying intensities (weak to very strong) corresponding to ν_{CO} = 1673-1677 cm^{-1}, indicating that ligand is present—or rather, the carboxamide-N of **2** in the precipitate is still protonated and unbound to Ni. Attempts to solubilize this precipitate in DMF or MeCN were unsuccessful; a minor amount of solubilized material was characterized by FTIR to reveal a spectrum that matches the original precipitate characterization, i.e., the unreacted ν_{CO} of the starting ligand. This precipitate may be attributed to an *S,S*-bridged species, which typically exhibit insolubility in organic solvents.[19] For example, Hegg and coworkers formed an *S,S*-bridged, trinuclear Ni complex upon reacting **III** with $Ni(OAc)_2$ and Na° in MeOH.[23] Greater solubility in MeOH was afforded by cation exchange with Et_4N^+, and the dark, brown/green complex was isolated from CH_3CN. Similar chemistry may be occurring upon metalation of **2** to result in a multinuclear or oligomeric species with limited solubility and darkness of color.

The pale brown product potassium or sodium complex of **3** is sparingly soluble in organic solvents except for MeOH. The FTIR of **3** (KBr pellet) reveals a shift in the ν_{CO} from 1672 cm^{-1} in the free ligand to 1622-1637 cm^{-1}, consistent with shifts observed for other carboxamide ligands upon binding Ni.[19,20,26,27] The UV-vis of **3** exhibits a λ_{max} at 308 nm (MeOH, 298 K), a blue-shift from the apo sensor, which suggests perturbation of the Dns $n \rightarrow \pi^*$ transition arising from N—Ni binding (Figure 5.3). This result is as expected, as the engagement of the N lone pair in a bond affects the energy of the Dns transition. At higher concentrations (~100 μM) of **3**, broad, low intensity shoulders at λ = 408 nm and λ = 505 nm appear and are attributed to ligand

field bands of the Ni-N_2S_2 chelate (Figure 5S.1). Reduced NiSOD and other N_2S_2 Ni complexes typically exhibit lower intensity bands in their UV-vis profiles at approximately 450 and 550 nm due to formally *d-d* transitions.[28-30] Likewise, the UV-vis of **III** reveals two ligand field transitions at 440 nm (ε = 340 $M^{-1}cm^{-1}$) and 570 nm (sh, ε = 70 $M^{-1}cm^{-1}$).[23] These *d-d* transitions are obscured in **2** and **3** by the high energy CT bands belonging to Dns. The two transitions appearing at 340 nm and 408 nm were monitored to determine 1:1 binding stoichiometry of Ni:sensor by Job's method of continuous variation (Figure 5S.3).

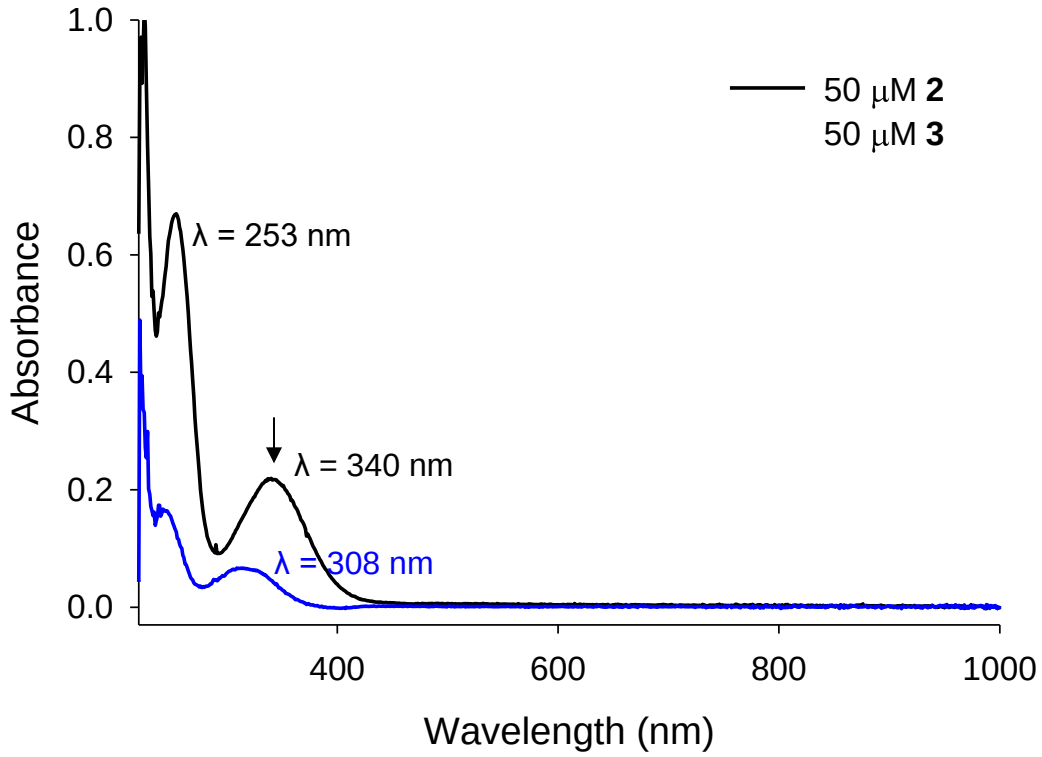

Figure 5.3. UV-vis spectra of a 50 μM solution of the N_2S_2-Dns sensor **2** (black trace) and 50 μM solution of the isolated Ni complex (**3**) (blue trace) resulting from bulk metalation with 3.5 equiv KH and 1 equiv $[Ni(H_2O)_6](BF_4)_2$ in MeOH at 298 K.

The isolated complex **3** is diamagnetic by ^{1}H NMR; however, the aliphatic peaks corresponding to the N_2S_2 ligand framework are of low intensity (obscured by the CD_3OD signal or integrating for fewer protons than expected) (Figure 5S.14, 5S.18). If the N_2S_2 coordination sphere is degrading in some way, possibly from abstraction of a proton adjacent to the tertiary amine of the Dns, the loss of Dns may be observed in the LR-ESI-MS(-). Indeed, the *m/z* 233.9 peak corresponding to Dns does appear as an abundant peak in the MS spectra of metalation reactions. A molecular ion corresponding to $[Ni(N_2S_2\text{-Dns})]^{1-}$ (*m/z* 482) has never been observed in the LR-ESI-MS, possibly due to the ionizing conditions of the instrument. Taken together, the low intensity of the N_2S_2 aliphatic signals in the ^{1}H NMR and the loss of dansyl from **2** as seen in the ESI-MS, in addition to the most abundant peak being a singly-charged fragment of mass less than predicted, may point to degradation of some portion of **2** upon deprotonation and metalation under bulk synthetic conditions.

By fluorescence, **2** has a broad emission profile centered at λ_{em} = 541 nm (λ_{ex} = 350 nm, MeOH, 298 K) that is consistent with other Dns based sensors (Figure 5.4).[24,31] In contrast, the emission of isolated **3** shifts at λ_{em} = 460 nm, and the color of concentrated solutions of **3** appears bright blue under long and short-wave UV light (Figure 5S.2). However, this 81 nm shift was not observed with any in situ metalation experiments (vide infra), nor observed for other Dns sensors in terms of magnitude. Rather, it and may be due to the K^+ cation of **3** interacting with the tertiary amine-N. The blue color and shift has also been observed with an authentically generated tripotassium salt of **2**, $K_3(N_2S_2\text{-Dns})$.

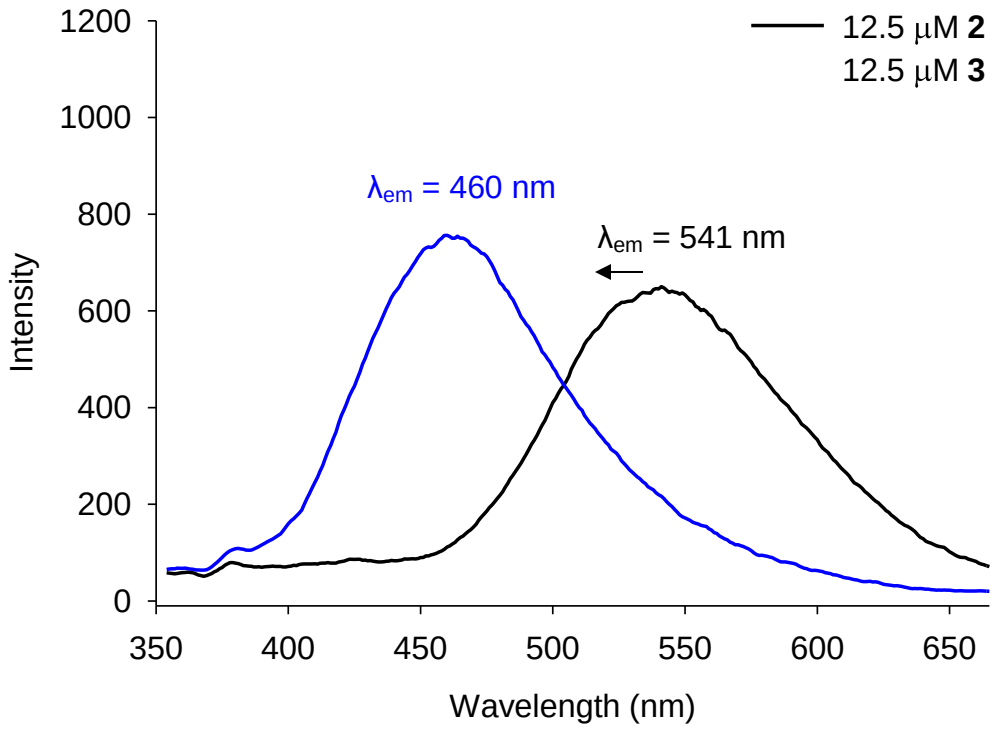

Figure 5.4. Emission spectra of 12.5 μM solutions of the N_2S_2-Dns sensor **2** (black trace) and isolated Ni complex **3** (blue trace) resulting from bulk metalation with 3.5 equiv KH and 1 equiv $[Ni(H_2O)_6](BF_4)_2$ in MeOH at 298 K. λ_{ex}: 350 nm. Slit width: 5 nm.

Fluorescence response. The initial prediction was that Ni-binding through the N-sulfonamide would allow CT to occur between the N and naphthalene ring of Dns to result in a turn-on response. However, addition of 1-10 equiv of Ni(II) to MeOH solutions of **2** in the presence of Et_3N, the tripotassium salt of **2**, or deprotonated **2** resulted in a partial quenching response (approximately 50% quenched) (Figure 5.5). Furthermore, the 81 nm λ_{em} blue-shift to 460 nm observed in the emission spectrum of **3** was not observed in the in situ metalation experiments. Instead, emission was centered at 541 nm, i.e., there was no change in λ_{em} as compared to **2**. Furthermore, adding up to 10 equiv Et_3N to **2** produced no significant change in

the fluorescence intensity. The quenching of the signal intensity from **2** upon addition of Ni may be due to incomplete deprotonation of the thiolate or carboxamide-N, either of which would prevent Ni(II) binding in the expected square-planar fashion.

To aid in deprotonation of **2** and mimic biological conditions, experiments were carried out in PIPES buffer (0.050 mM PIPES, 100 mM KCl, pH = 7.2) and in a MeOH:CHES (1:1) (0.050 M CHES, 100 mM KCl, pH = 9.0) mixture. The relatively pH 9 of CHES has been used previously to encourage metal coordination to dansyl-based fluorophores.[32] Despite the use of buffers, the expected blue-shift in λ_{em} was not observed upon addition of Ni to **2**, and the use of aqueous media resulted in lower emission intensities as compared to organic solvents for both **2** and **3**. This result suggests Ni is engaging the tertiary amine in an unexpected way that significantly dampens the energy of that N- naphthalene electronic transition, likely though an internal charge transfer (ICT) mechanism as seen in previous sensors from our lab.[33,34] The lower intensity of **2** and **3** in CHES may also be due to proton interaction with the N atom on the chromophore, as suggested by Dns studies in aqueous media.[35] In particular, Dns fluorescent behavior in water has been shown to depend on the protonation state of the electron-accepting sulfonamide-N and electron-donating N-methylamino moieties.[31,36,37] The separation of these two substituents, in addition to electron delocalization over the naphthalene ring, is responsible for the fluorescent properties of the chromophore, and thus protonation at either of these positions can disrupt electron transfer. Research on Dns systems has shown fluorescence to be quenched at pH values between 0-4 due to the protonation of the N-methylamino group, which has a pK_a of 3.8 in H_2O.[36] Protonation of the N-methylamine typically results in a blue-shift in the absorbance of Dns due to destabilization of the CT transition between the N and naphthalene ring, which prevents fluorescence.[31] At pH values greater than 4, CT is restored and the

fluorescence is turned on. For secondary sulfonamide-N, the pK_a in water is 9.9, and deprotonation typically results in enhanced fluorescence intensity.[36] Both the UV-vis and the emission profile of the deprotonated sulfonamide usually appear at higher energy as compared to neutral Dns, a blue-shift which is attributed to loss of electron acceptor character in the sulfonyl moiety.[31] Taken together, this evidence demonstrates that Dns fluorescent behavior is sensitive to protonation and pH. To avoid protonation changes based on pH and establish the properties of the sensor in organic solvents, we conducted competition experiments in MeOH.

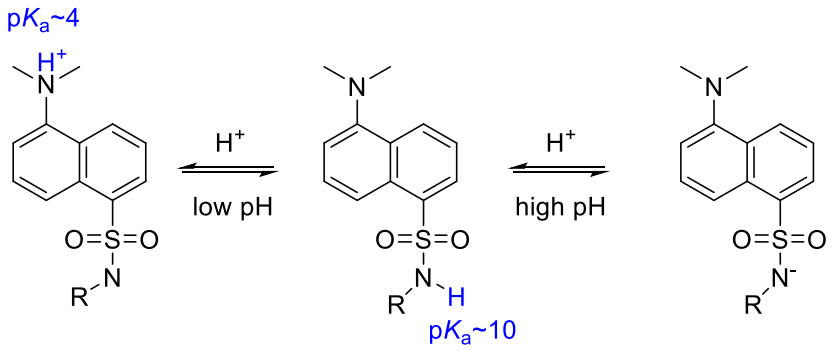

Figure 5.5. Acid-base equilibrium for the Dns chromophore in aqueous media.[31]

Competition studies. Although a turn-on sensor is preferred for metal sensing, we evaluated if the turn-off property exhibited by **2** with Ni(II) salts were unique to Ni. Competition studies with other biologically relevant metals were carried out with 10 μM **2,** 10 equiv Et_3N, and 1 equiv metal as tetrafluoroborate or chloride salts in MeOH (Figure 5.6). The alkali metals, Na(I), K(I) and Mg(II), produced a minimal quenching effect (5%, 2%, and 4% respectively), as did d^5 Mn(II) (5%), as compared to **2**. Addition of Zn(II) resulted in enhanced fluorescent

intensity by 10%. Zn has previously been shown to bind to the deprotonated sulfonamide of Dns, and this binding coordination has been exploited as a sensing strategy.[36] Koike and coworkers developed a N_4 cyclam-based sensor for Zn at physiological pH, which binds to the N^- of the sulfonamide in the apical position to give a distorted pyramidal geometry and turn-on fluorescence.[36] A similar coordination may be occurring in **2**, and interaction of Zn(II) with the lone pair of the sulfonamide-N is promoting enhanced CT.

The intensity of **2** was most quenched by the addition of Co(II), Ni(II), and Cu(II), which dampened the fluorescence intensity by 43%, 44%, and 47%, respectively. Co(II) and Cu(II) have been shown to bind N_2S_2 chelates, although the majority of published, mixed N/S platforms are macrocyclic and involve S-thioether ligands rather than S-thiolates.[38-42] Co(II) and Cu(II) coordination to these N_2S_2 ligands typically require distorted geometries with axial donors, and in the case of Co(II), are high spin.[39,40] For Co(II) and Cu(II) to bind to **2**, it is likely that solvent binding to provide higher coordination numbers or a dramatic change in geometry or ligand stoichiometry would need to occur. Instead, these metal ions may be interacting with the sulfonamide-N in some form of dipole interaction to perturb CT. The initial hypothesis was that Cu(II) would prevent any fluorescence signal from **2** due the paramagnetic nature of the d^9 metal ion. Chang also observed interference from Cu(II) in NS1 at concentrations 50-fold greater than NS1.[16] Adding 1 mole equiv of Cu(II) to NS1 avoided the undesired quenching effect from their sensor. Imperiali and coworkers designed a Dns sensor derived from the Amino Terminal Copper and Nickel (ATCUN) binding motif, which depended on Cu(II) binding to an N_4 peptide chelate and paramagnetically quenching Dns.[17] Interference from the unpaired electron of Cu(II) with the CT of the Dns chromophore may also apply to our system, as Cu(II) produced the greatest decrease in fluorescence signal of any metal.

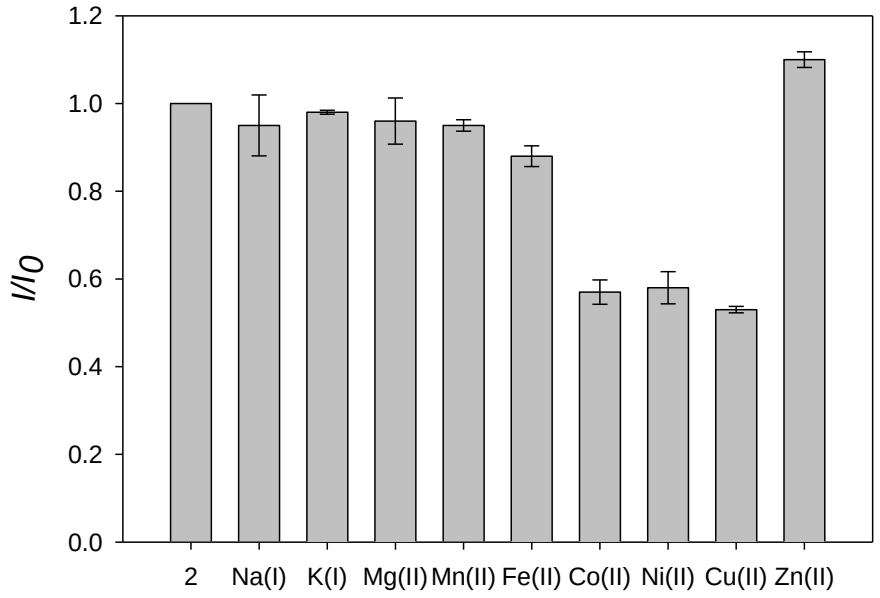

Figure 5.6. Fluorescence response of **2** to various ions (average of three trials) in MeOH at 298 K (λ_{ex} = 350 nm). Bars represent the integrated fluorescence response (I) over the initial integrated emission (I_0).

5.5 Conclusion and Future Directions

In conclusion, a Dns-appended N_2S_2 platform was designed based upon the reduced active site geometry of NiSOD. Although it was initially expected that coordination from the N lone pair to Ni would result in a turn-on fluorescent response, experimental evidence instead suggests that binding of Ni prevents CT from occurring fully, and fluorescence intensity is quenched by ~50% as compared to the free sensor **2**. Cu(II) and Co(II) also produce quenching responses, indicating that the N_2S_2-Dns platform has some affinity for these transition metals as well. Paramagnetic quenching is likely responsible for this observation, indicating that Ni has adopted a geometry that results in a high spin state. Possible structures include bidentate chelation to afford a 1:2 Ni/**2** stoichiometry and tetrahedral Ni(II) (Figure 5.7, left). If the

sulfonamide-N were coordinating to Ni, it is expected that a shift in the UV-vis or emission spectrum would be observed. Tetrahedral geometry can also result in paramagnetic quenching of Dns, with solvent or anion binding in the absence of sulfonamide-N or carboxamide-N → Ni coordination (Figure 5.7, right). Barriers to achieving specificity for Ni(II) include ensuring the complete deprotonation of the N-carboxamide and S-thiolates, to ensure 1:1 Ni/**2** binding as we have seen for other N_2S_2 chelates. By changing the electronic nature of the carboxamide, Ni(II) may more readily bind to the N_2S_2 chelate. Future directions include appending the nearest cysteamine with a methyl ester substituent to provide increased water solubility of the sensor, as well as more facile deprotonation of the amide. As compared to free cysteine, the methyl ester functionality decreases the pK_a of the NH_3 and SH from 10.8 to 8.9 and 8.3 to 6.56, respectively.[43] Utilizing cysteine methyl ester in the synthesis of a sensor will afford a more readily deprotonated carboxamide-N and a strong-field ligand environment poised to bind Ni(II) in a square-planar environment.

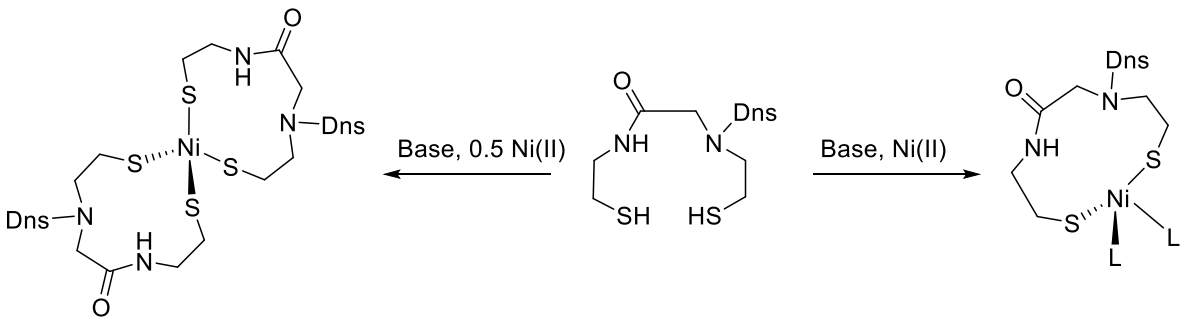

Figure 5.7. Possible coordination of **2** to Ni(II) upon deprotonation of the thiolates and metalation, which would result in high spin Ni and paramagnetic quenching of Dns fluorescence. At left, bidentate coordination could result in 4C, tetrahedral Ni(II). At right, solvent or another ligand, L, can bind to result in a tetrahedral geometry.

5.6 Supporting Information

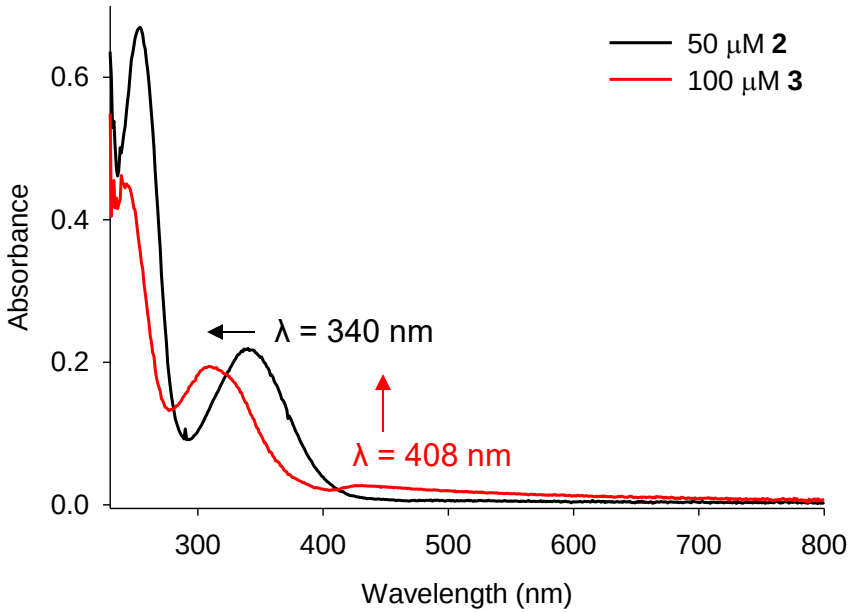

Figure 5S.1. UV-vis spectra of a 50 μM solution of apo N_2S_2-Dns (**2**) (black trace) and 100 μM solution of the isolated Ni complex (**3**) resulting from bulk metalation (red trace) in MeOH at 298 K. A small transition at λ = 408 nm is present at 100 μM or greater concentrations of **3**.

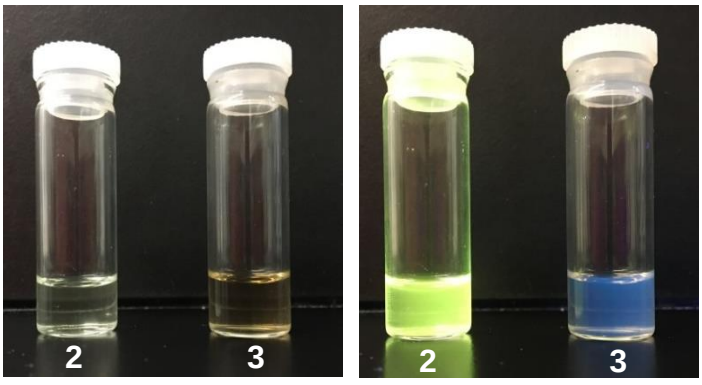

Figure 5S.2. Color change and fluorescent properties observed under long-wave UV light for 2.5 mM MeOH solutions of **2** (left) or **3** (right) isolated from bulk metalation with 3.5 equiv KH and 1 equiv $[Ni(H_2O)_6](BF_4)_2$ in MeOH at RT.

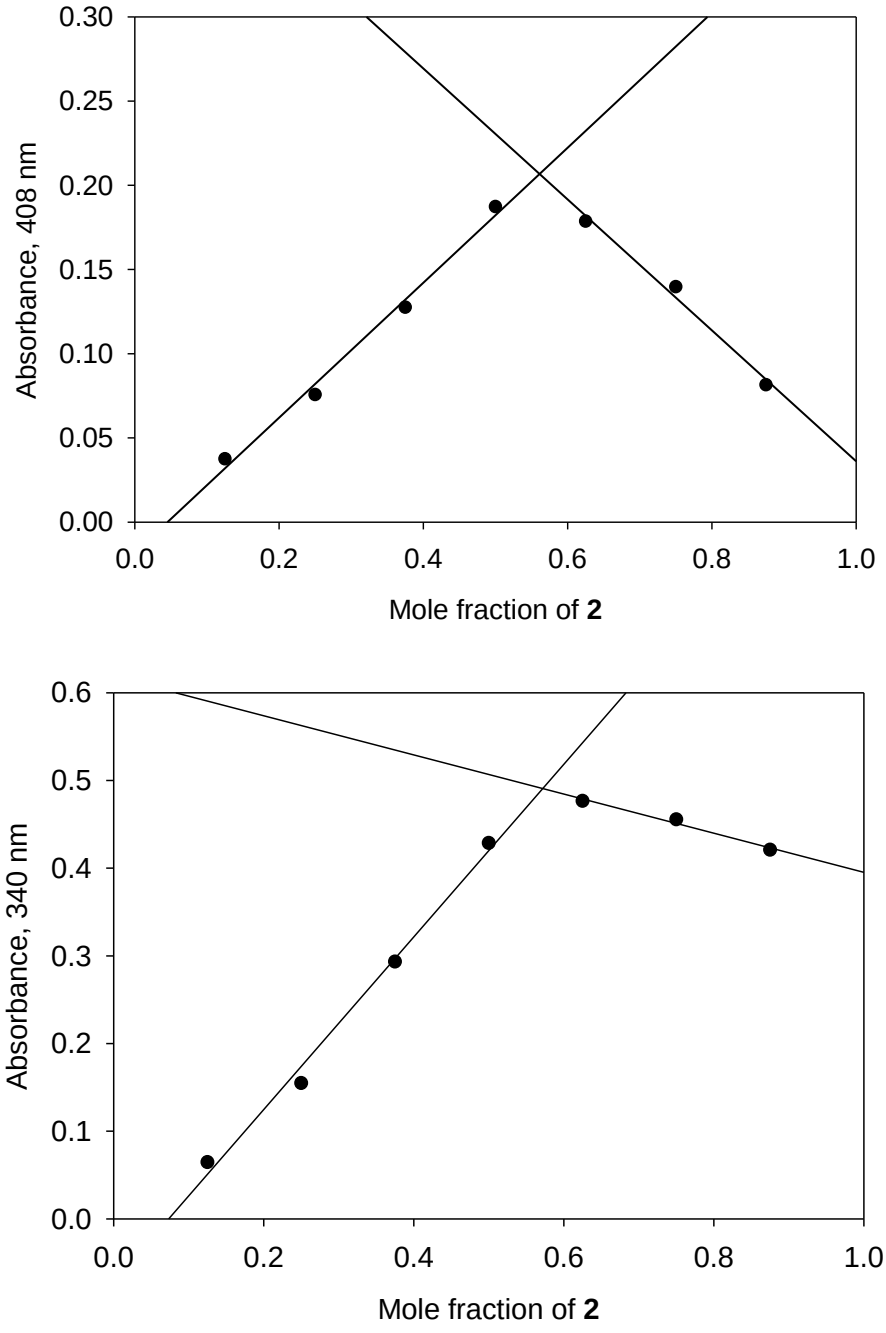

Figure 5S.3. Job's plot to determine binding stoichiometry of Ni(II) to **2**. The intercepts of 0.55 (monitoring λ = 408 nm) (top) and 0.57 (monitoring λ = 340 nm) (bottom) signify an approximately 1:1 metal/sensor stoichiometry.

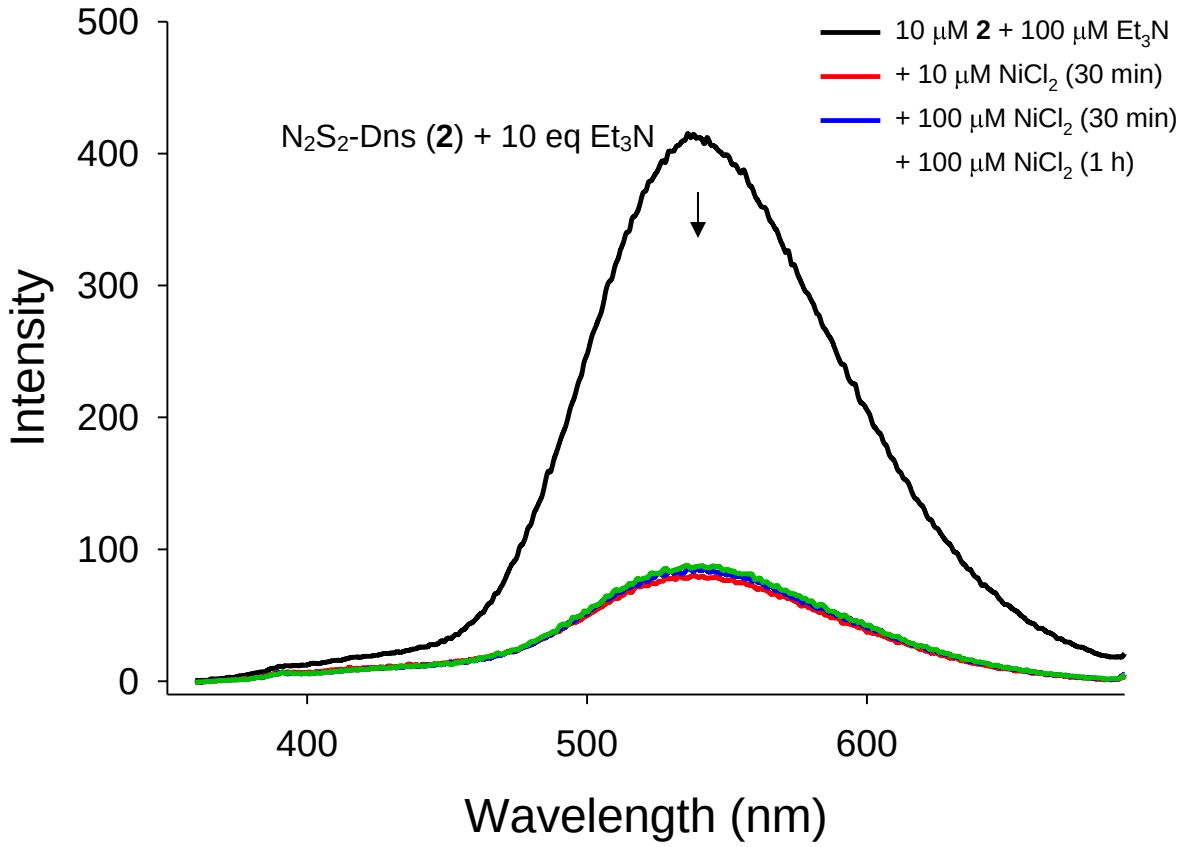

Figure 5S.4. Emission spectrum of a 10 μM MeOH solution of **2** (black trace) containing 10 equiv Et_3N and after adding 10 μM $NiCl_2$ (red trace) or 100 μM $NiCl_2$ (green trace) at 298 K. The blue trace was recorded 1 h after adding 100 μM $NiCl_2$. λ_{ex}: 350 nm. Slit width: 5 nm.

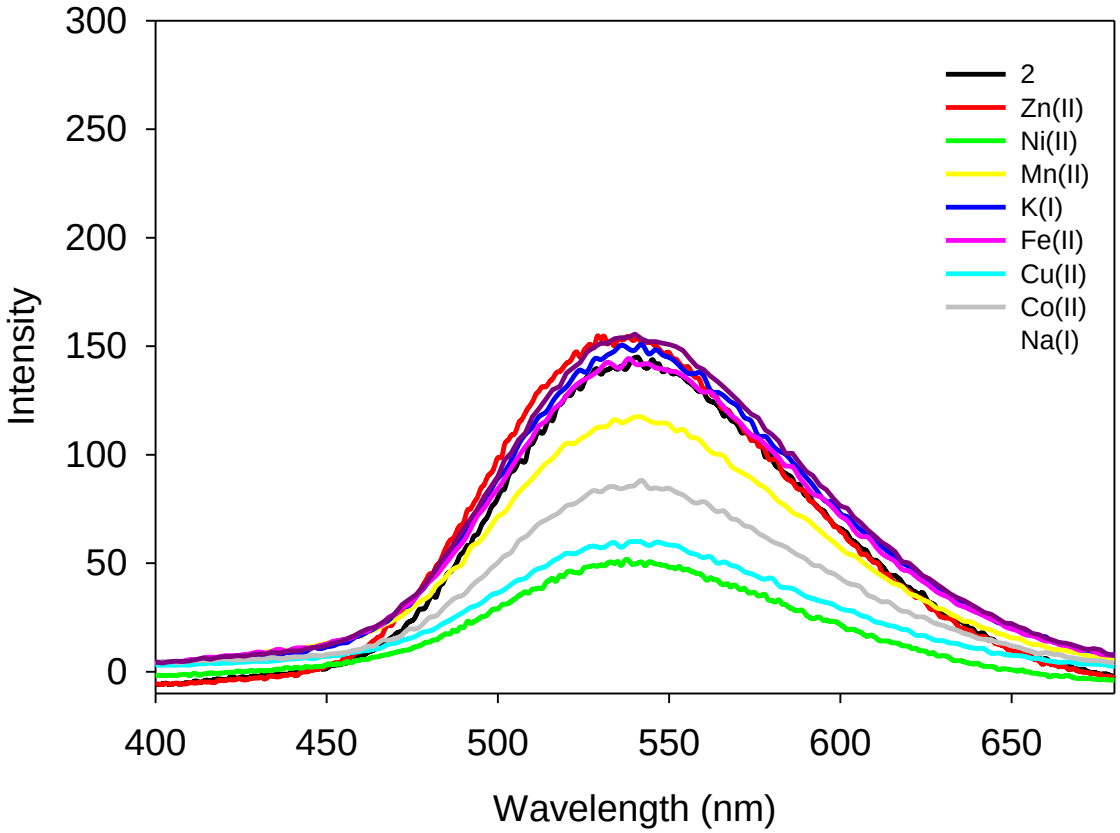

Figure 5S.5. Emission spectrum of a 10 μM MeOH solution of **2** (black trace) containing 10 equiv Et_3N and after adding 10 μM of M^{n+} at 298 K. λ_{ex}: 350 nm. Slit width: 5 nm.

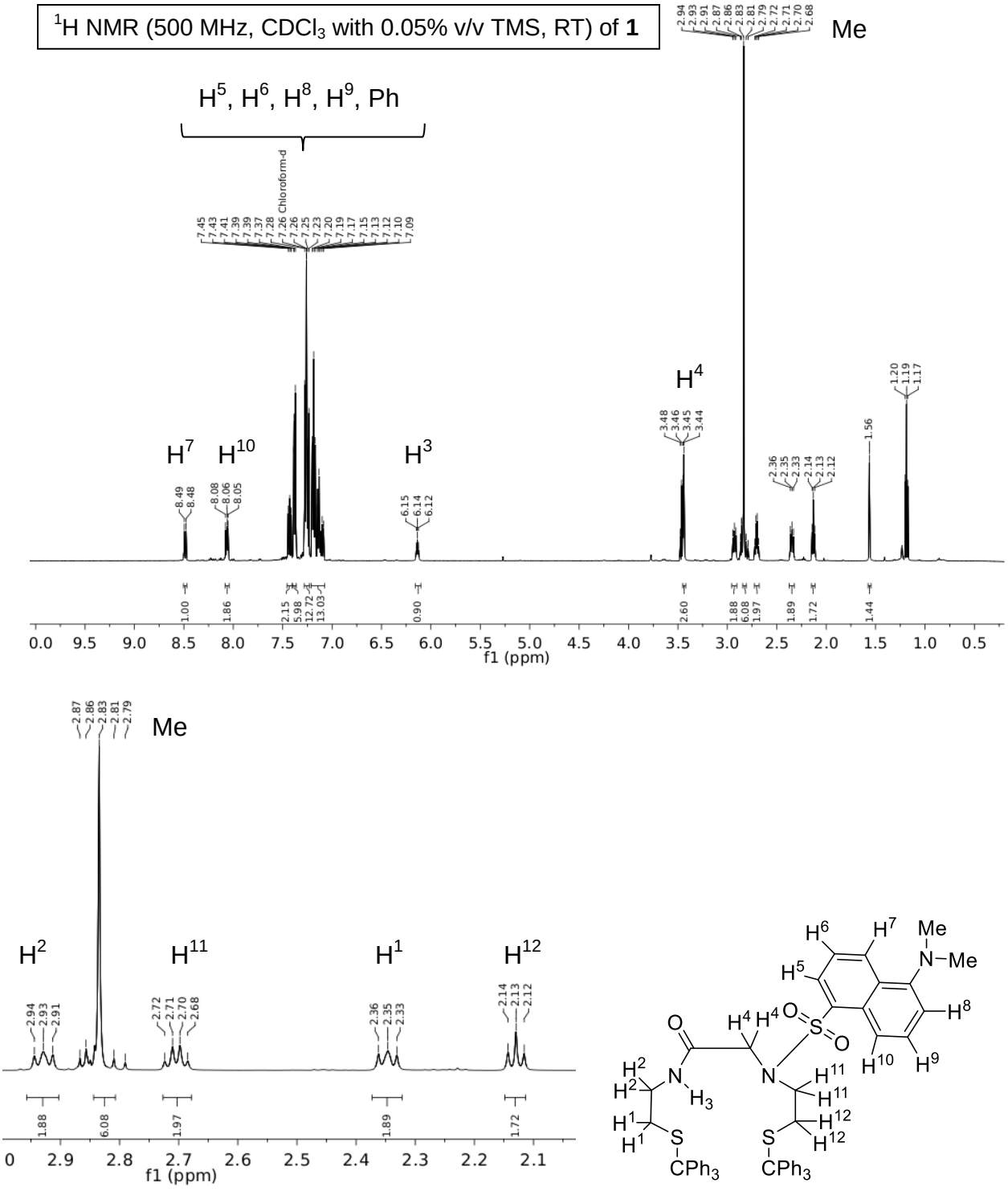

Figure 5S.6. *Top*: ^{1}H NMR spectrum of N_2S_2-$(Tr)_2$-Dns (**1**) in $CDCl_3$ containing 0.05% v/v TMS at RT (δ vs. residual protio solvent signal). The peaks at 7.26, 3.46, 1.19, and 1.56 are from protio solvent, Et_2O, and water, respectively. *Bottom*: expansion of the aliphatic region.

^{13}C NMR (125 MHz, $CDCl_3$ with 0.05% v/v TMS, RT) of **1**

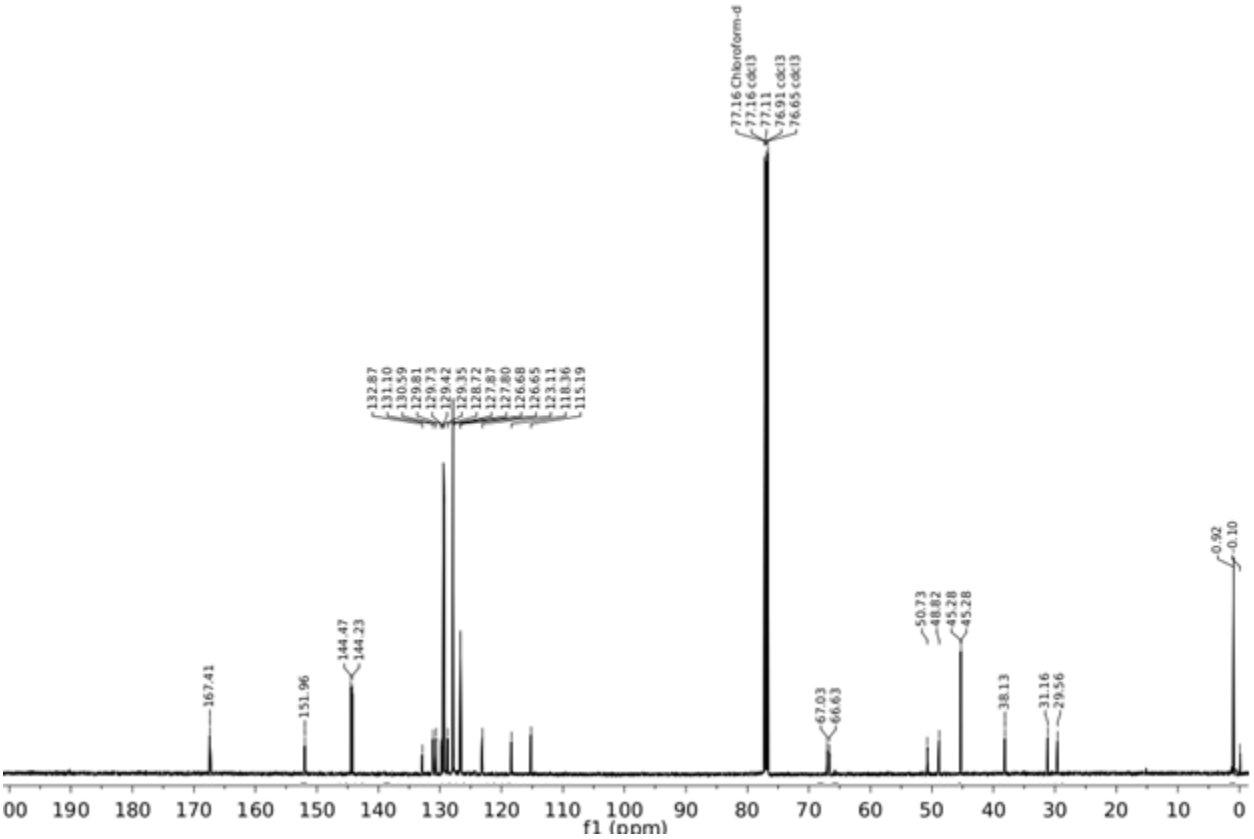

Figure 5S.7. ^{13}C NMR spectrum of N_2S_2-$(Tr)_2$-Dns (**1**) in $CDCl_3$ containing 0.05% v/v TMS at RT (δ vs. residual solvent signal). Solvent signal at 77.16 ppm is indicated.

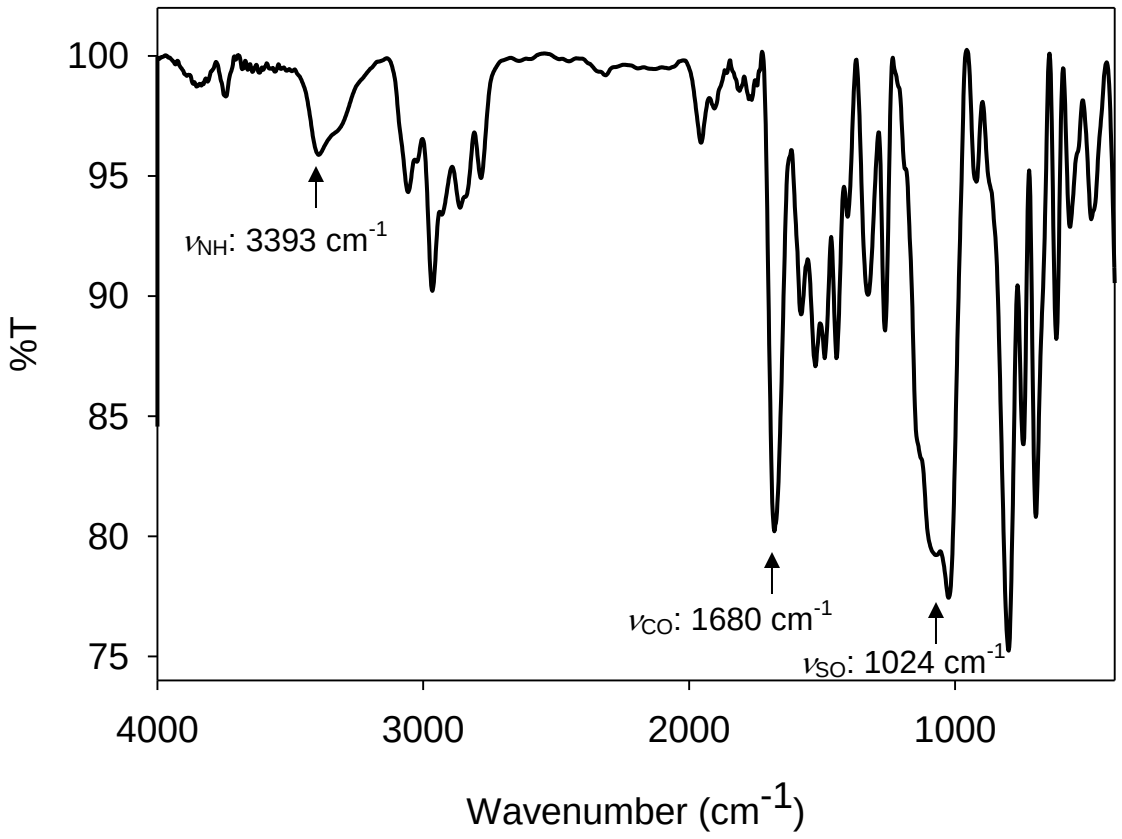

Figure 5S.8. Solid-state FTIR spectrum of N_2S_2-$(Tr)_2$-Dns (**1**) in a KBr matrix at RT.

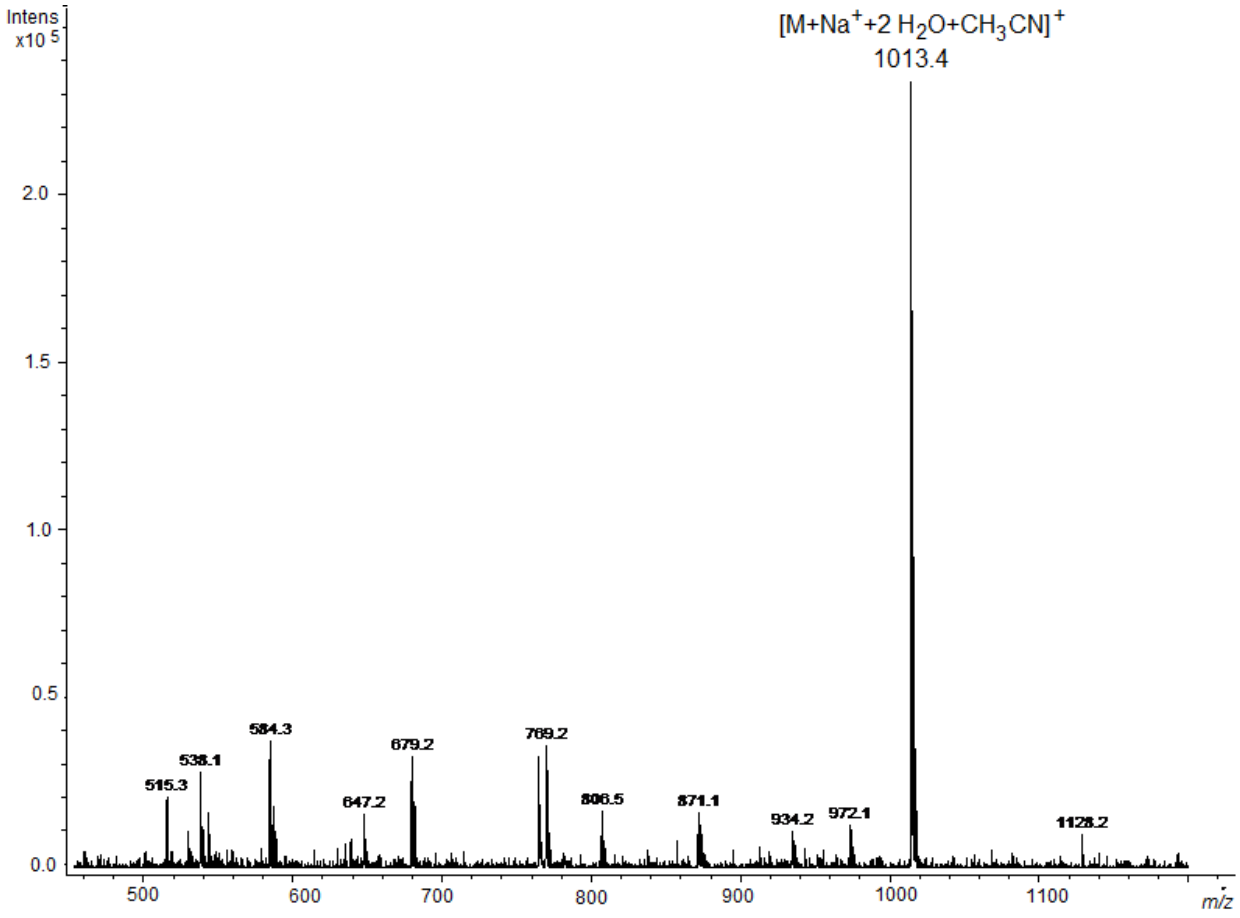

Figure 5S.9. Low resolution ESI-MS (positive mode) of N_2S_2-$(Tr)_2$-Dns (**1**).

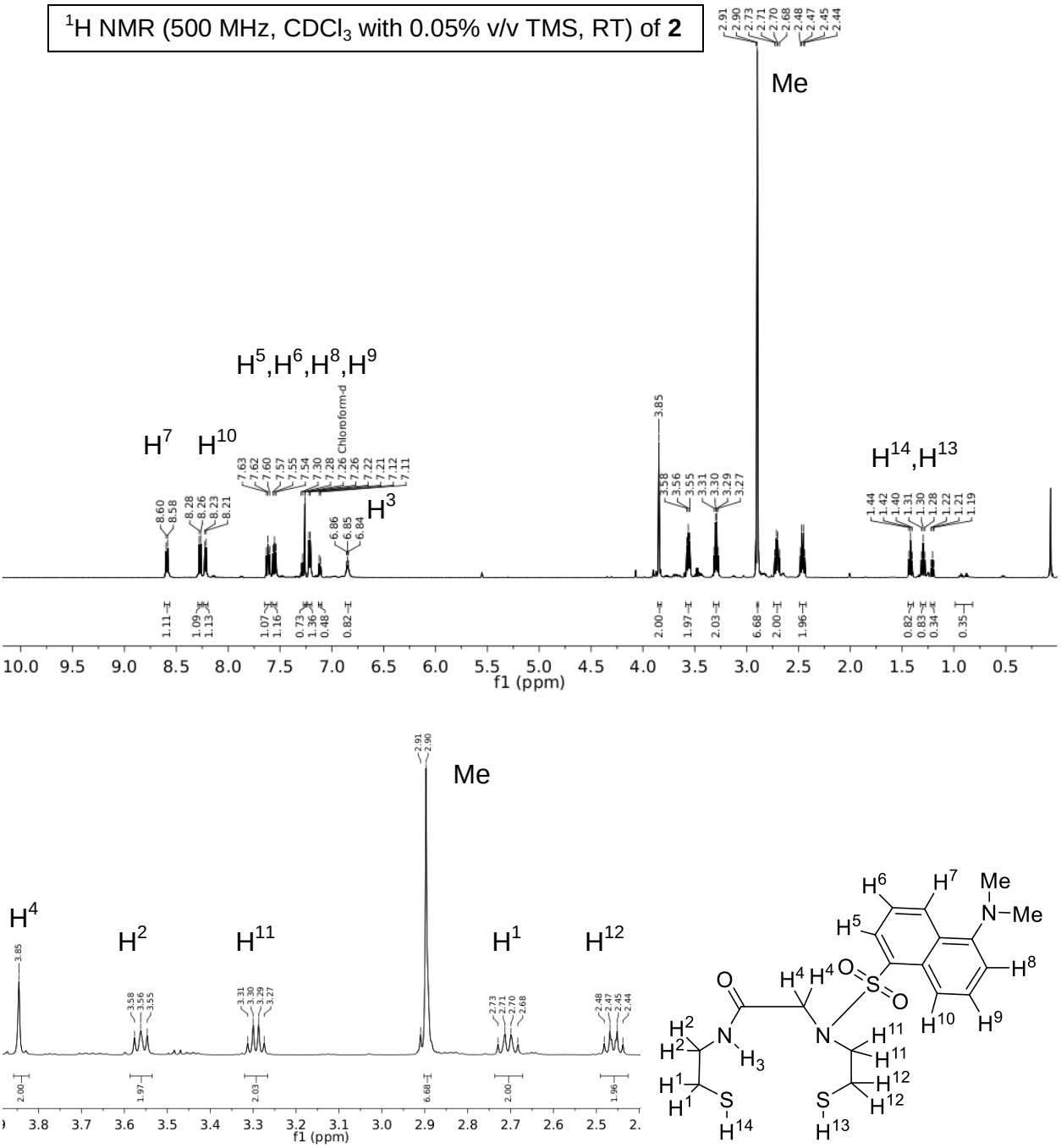

Figure 5S.10. *Top*: ^{1}H NMR spectrum of N_2S_2-Dns (**2**) in $CDCl_3$ containing 0.05% v/v TMS at RT (δ vs. residual protio solvent signal). The peaks at 7.26, 3.46, and 1.19 are from protio solvent and Et_2O respectively. *Bottom*: expansion of the aliphatic region.

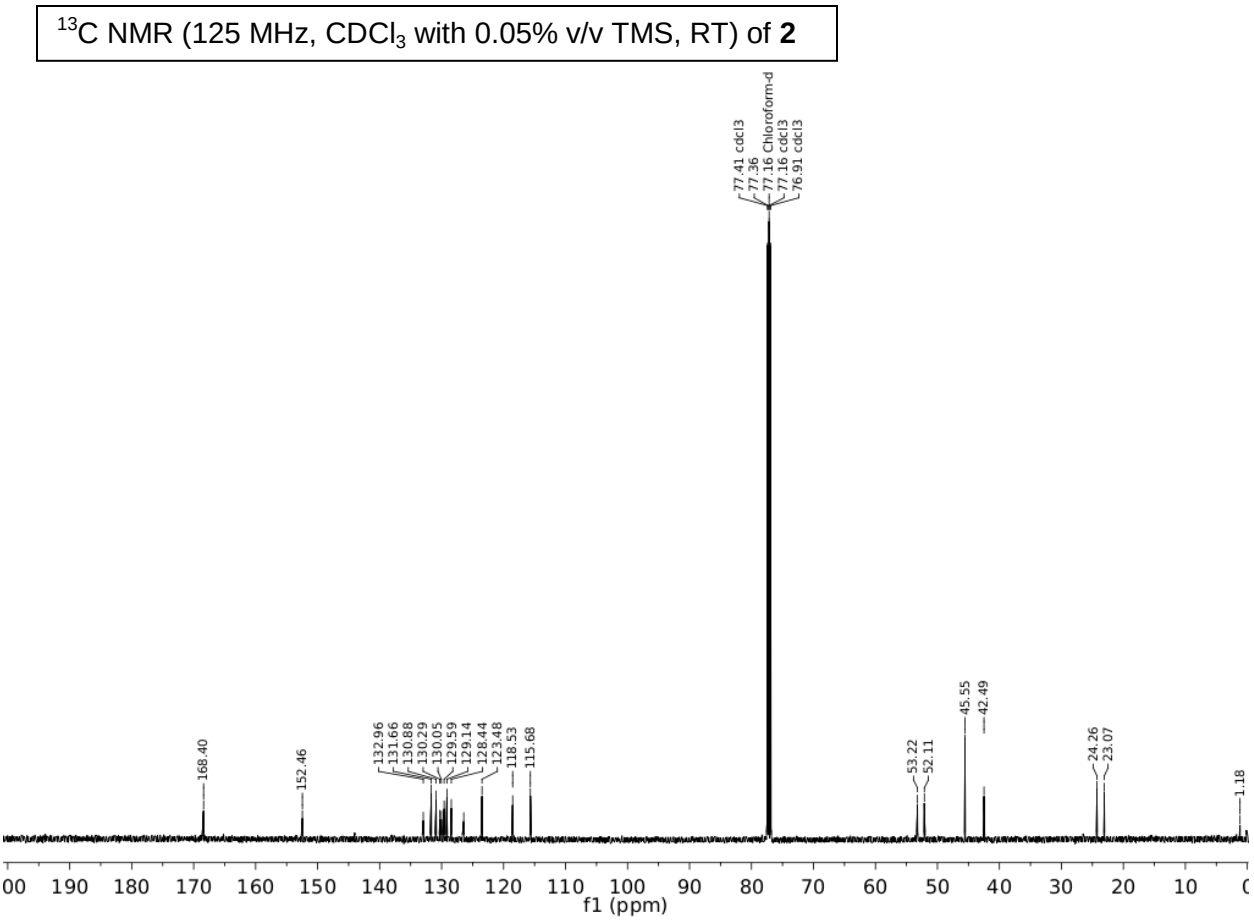

Figure 5S.11. ^{13}C NMR spectrum of N_2S_2-Dns (**2**) in $CDCl_3$ containing 0.05% v/v TMS at RT (δ vs. residual solvent signal). Solvent signal at 77.16 ppm is indicated.

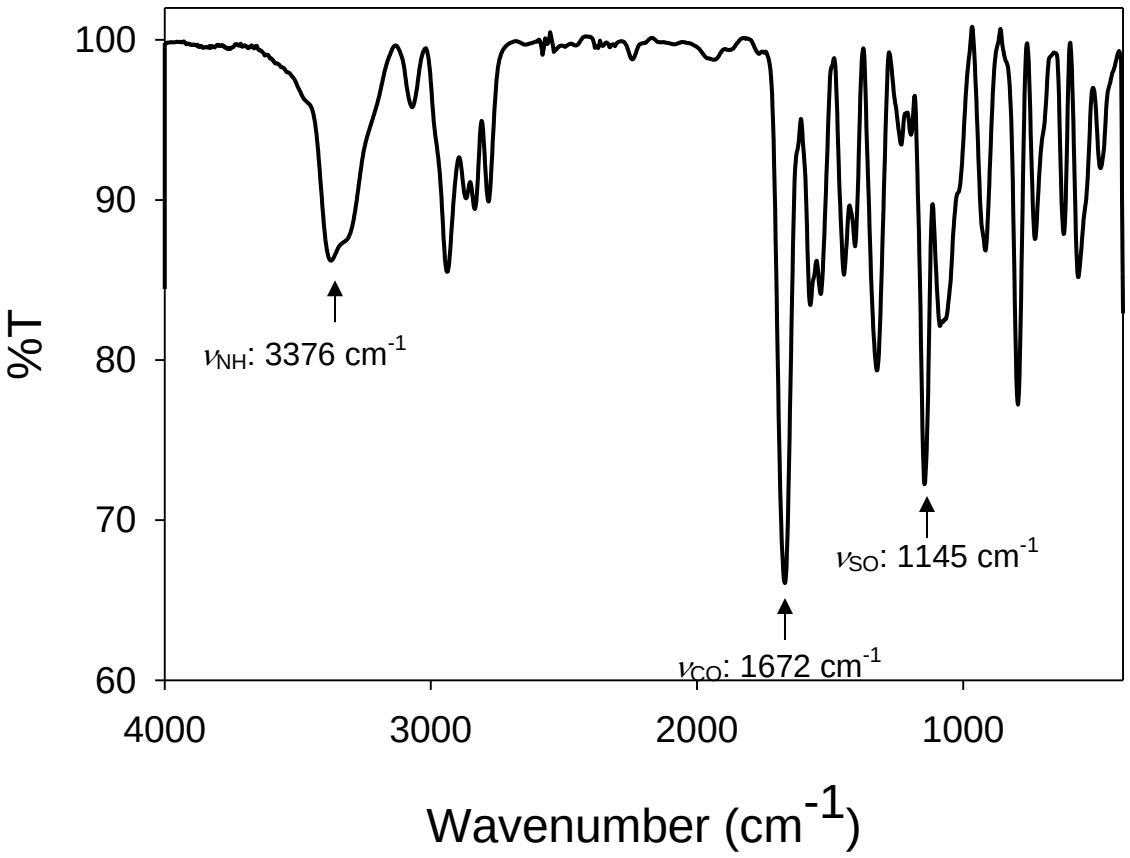

Figure 5S.12. Solid-state FTIR spectrum of N_2S_2-Dns (**2**) in a KBr matrix at RT.

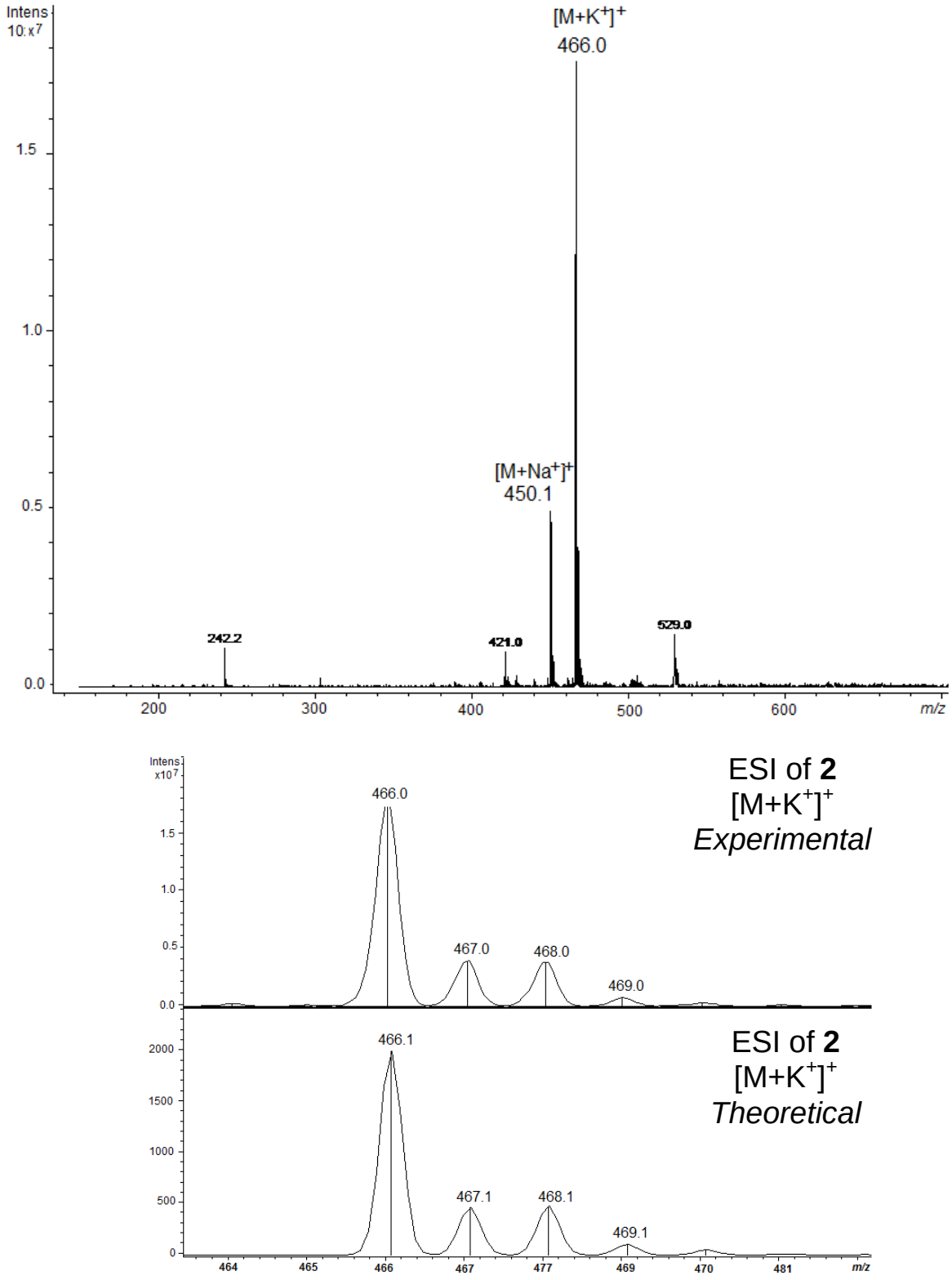

Figure 5S.13. Low resolution ESI-MS (positive mode) of N_2S_2-Dns (**2**) (top). Middle and bottom represent a zoom-in of the *m/z* 466.0 peak. Theoretical fit on the bottom.

^{1}H NMR (400 MHz, CD_3OD, RT) of **3**

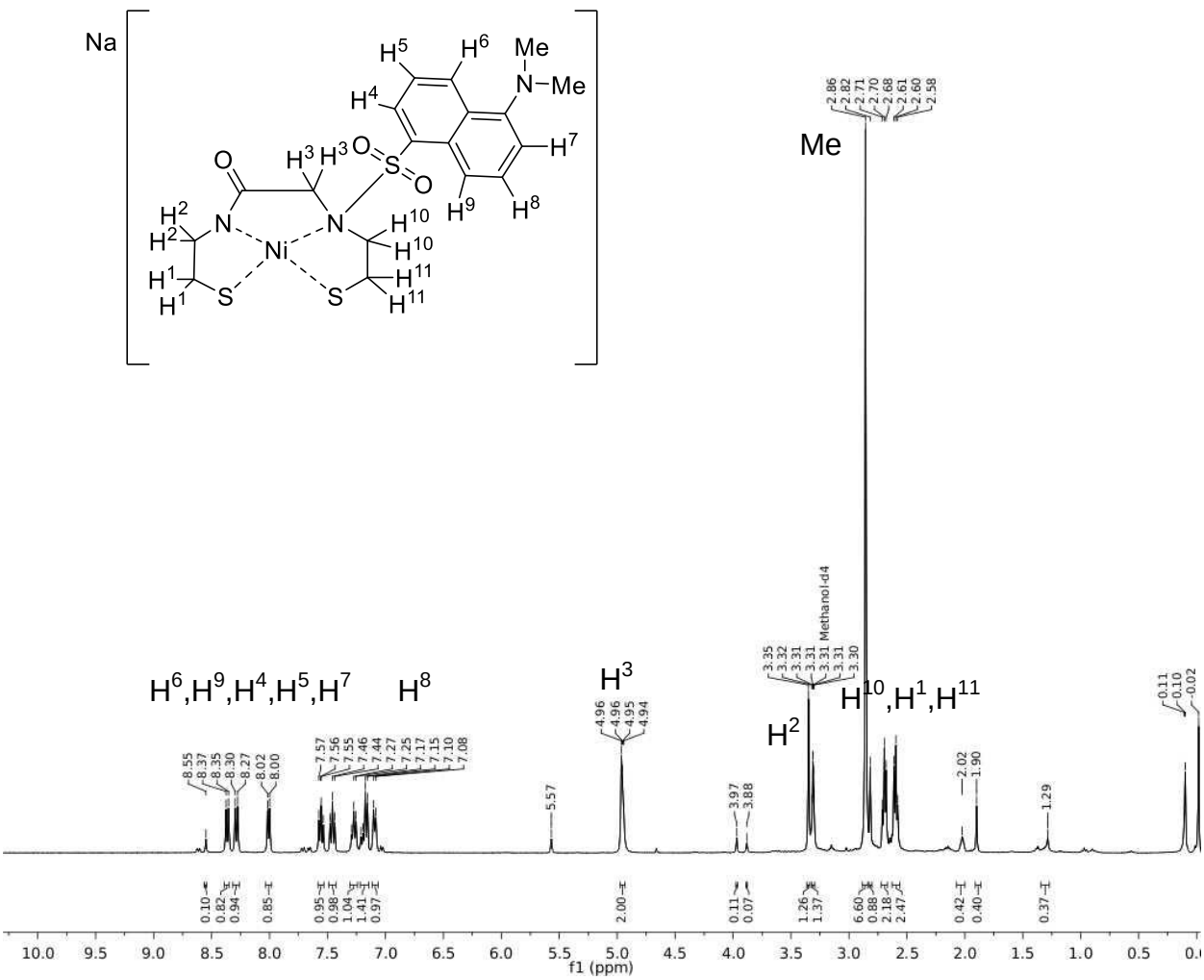

Figure 5S.14. ^{1}H NMR spectrum of (**3**) in CD_3OD (δ vs. residual protio solvent signal). The peaks at 3.31 and 2.00 are from protio solvent and residual CD_3CN respectively. Peaks corresponding to Ph_3CH carried through from deprotection of **1** are also present at 7.27 (m), 7.15 (m), and 5.57 (s).

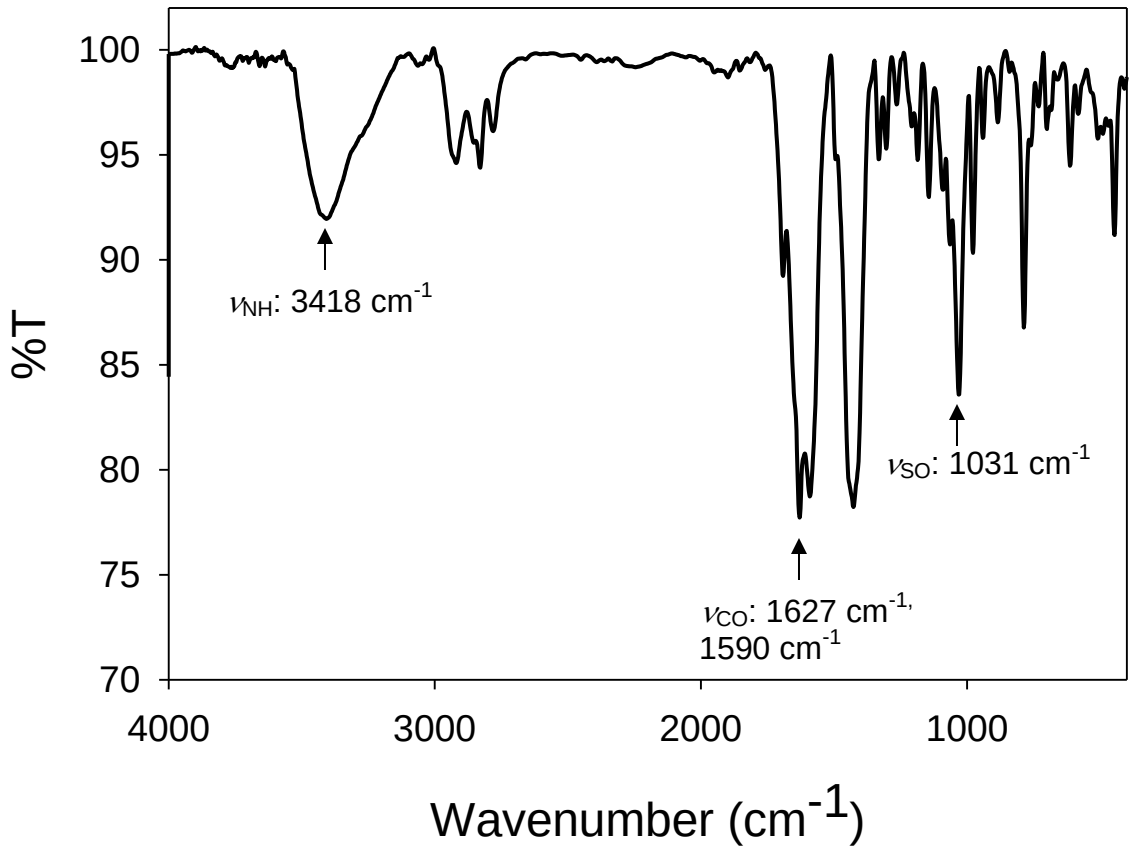

Figure 5S.15. Solid-state FTIR spectrum of filtrate (**3**) resulting from the metalation of **2** with 3.4 equiv Na° and 1 equiv anhydrous $NiCl_2$ in MeOH.

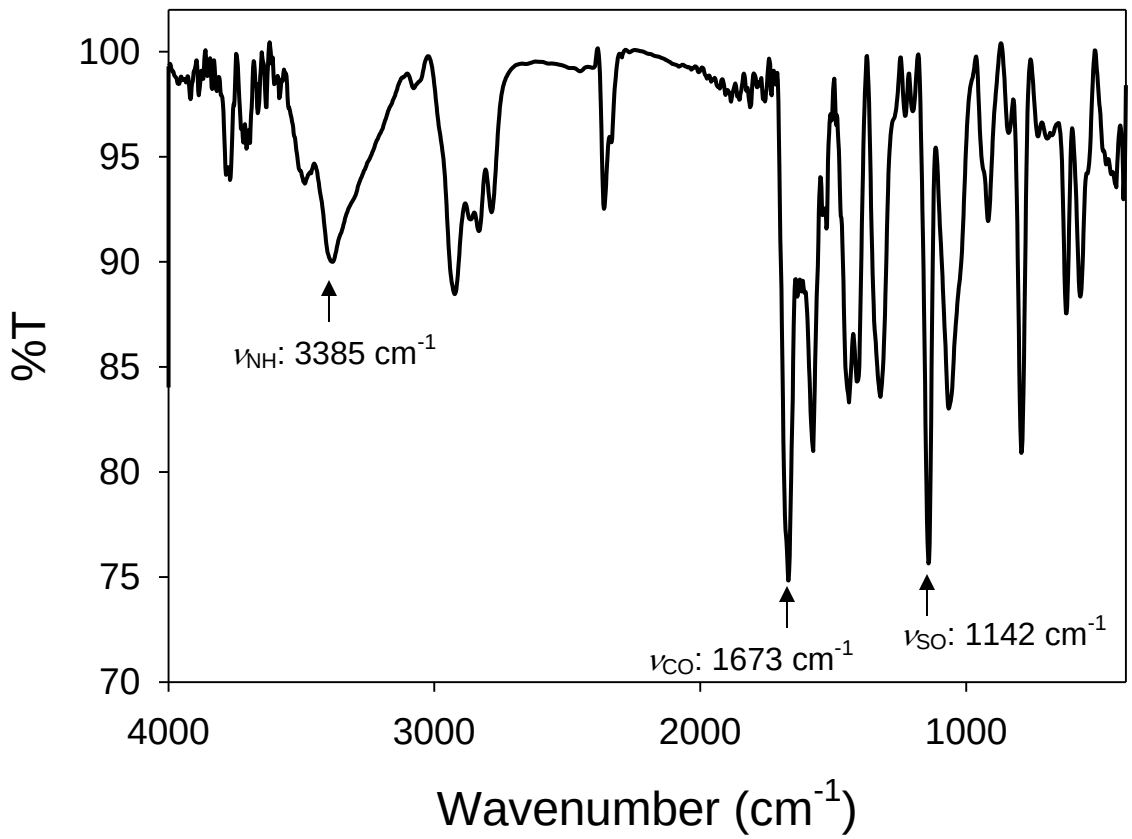

Figure 5S.16. Solid-state FTIR spectrum of precipitate resulting from the metalation of **2** with 3.4 equiv Na° and 1 equiv anhydrous $NiCl_2$ in MeOH.

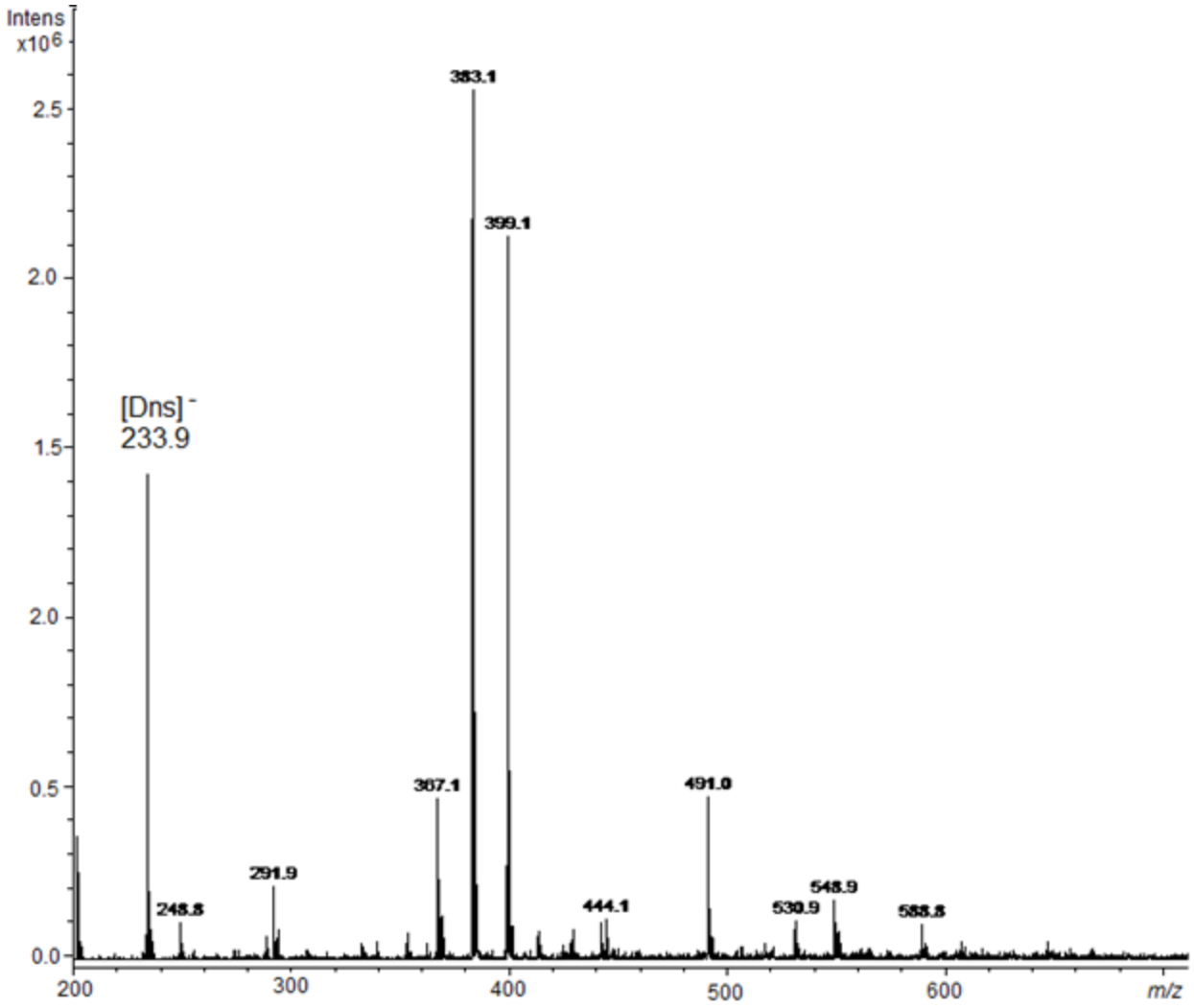

Figure 5S.17. Low resolution ESI-MS (negative mode) of the filtrate resulting from the metalation of **2** with 3.4 equiv Na° and 1 equiv anhydrous $NiCl_2$ in MeOH. The *m/z* = 233.9 corresponds to loss of Dns. The *m/z* = 383.1 and 399.1 peaks have not been identified.

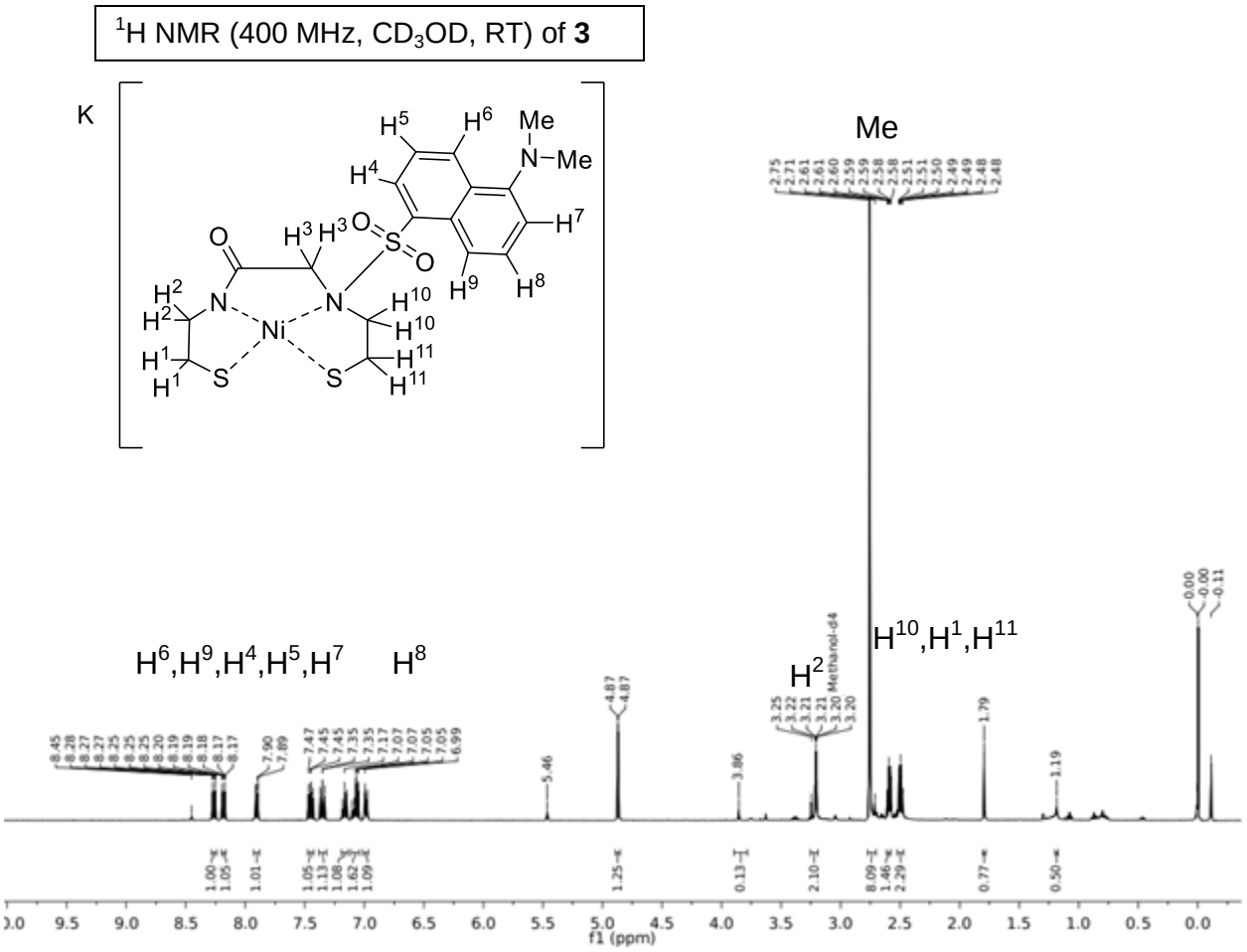

Figure 5S.18. ^{1}H NMR spectrum of (**3**) in CD_3OD (δ vs. residual protio solvent signal). The multiplet peaks at 0.90 and 1.19 ppm are from residual hexane.

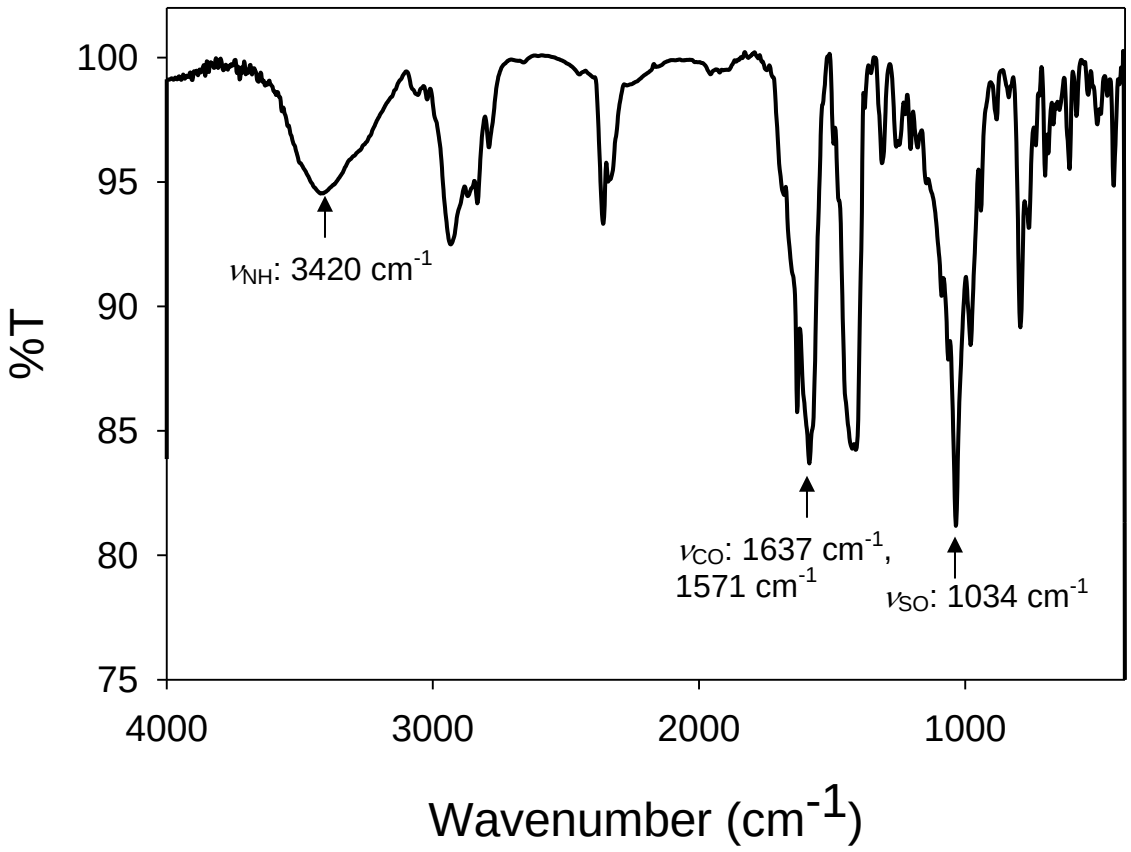

Figure 5S.19. Solid-state FTIR spectrum of filtrate (**3**) resulting from the metalation of **2** with 3.5 equiv KH and 1 equiv $[Ni(H_2O)_6](BF_4)_2$ in MeOH.

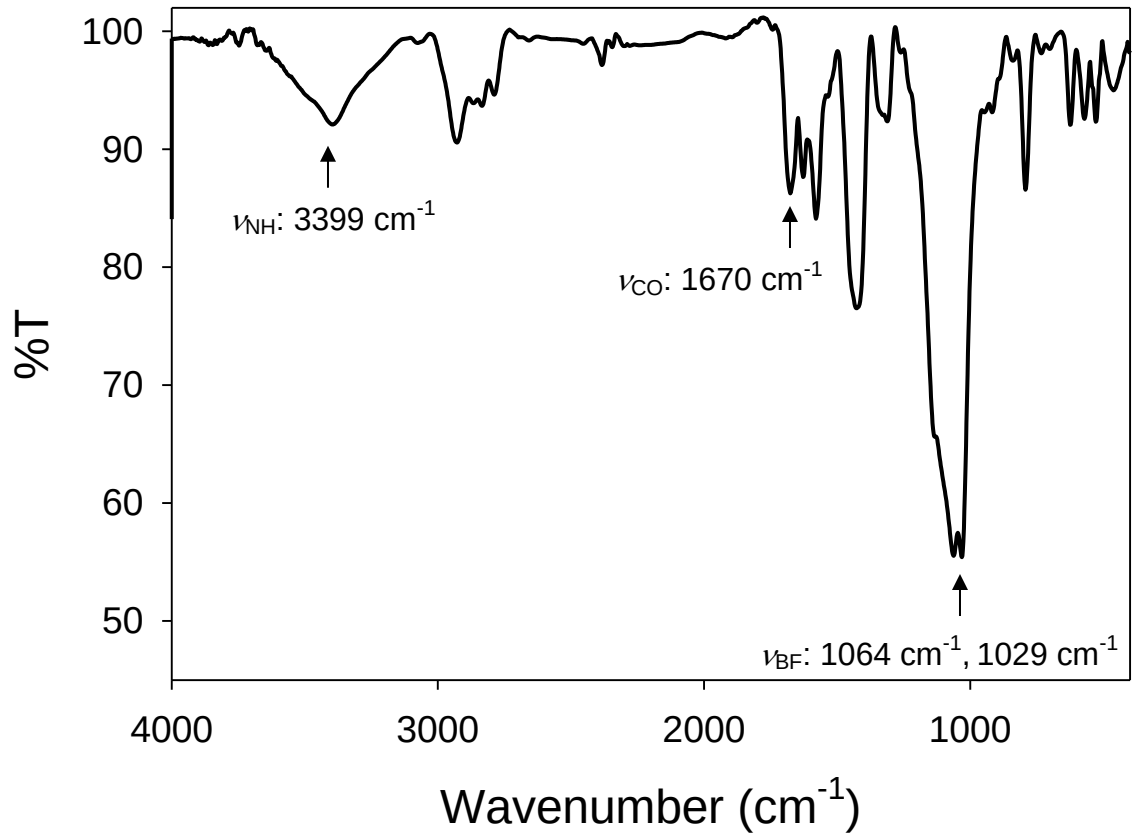

Figure 5S.20. Solid-state FTIR spectrum of precipitate resulting from the metalation of **2** with 3.5 equiv KH and 1 equiv $[Ni(H_2O)_6](BF_4)_2$ in MeOH.

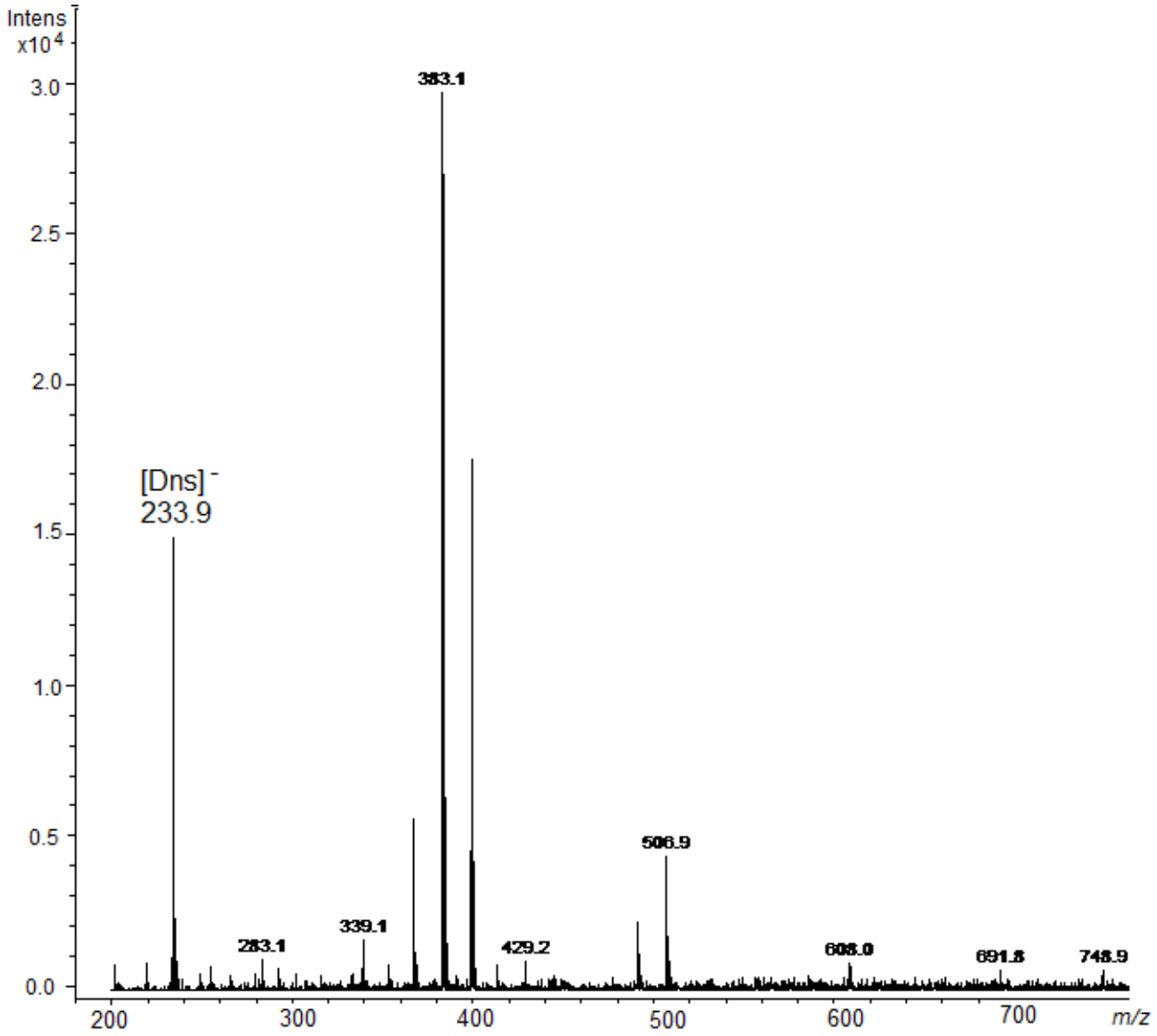

Figure 5S.21. Low resolution ESI-MS (negative mode) of the filtrate resulting from the metalation of **2** 3.5 equiv KH and 1 equiv $[Ni(H_2O)_6](BF_4)_2$ in MeOH. The *m/z* = 233.9 corresponds to loss of Dns. The *m/z* = 383.1 and 399.1 peaks have not been identified.

5.7 References

(1) Ragsdale, S. W. Nickel-based Enzyme Systems. *J. Biol. Chem.* **2009**, *284*, 18571-18575.

(2) Boer, J. L.; Mulrooney, S. B.; Hausinger, R. P. Nickel-dependent metalloenzymes. *Arch. Biochem. Biophys.* **2014**, *544*, 142-152.

(3) Mulrooney, S. B.; Hausinger, R. P. Nickel uptake and utilization by microorganisms. *FEMS Microbiol. Rev.* **2003**, *27*, 239-261.

(4) Higgins, K. A.; Carr, C. E.; Maroney, M. J. Specific metal recognition in nickel trafficking. *Biochemistry* **2012**, *51*, 7816-7832.

(5) Denkhaus, E.; Salnikow, K. Nickel essentiality, toxicity, and carcinogenicity. *Crit. Rev. Oncol. Hematol.* **2002**, *42*, 35-56.

(6) Goodman, J. E.; Prueitt, R. L.; Dodge, D. G.; Thakali, S. Carcinogenicity assessment of water-soluble nickel compounds. *Crit. Rev. Toxicol.* **2009**, *39*, 365-417.

(7) Zambelli, B.; Ciurli, S. Nickel and human health. *Met. Ions Life Sci.* **2013**, *13*, 321-357.

(8) Cotruvo, J. A.; Aron, A. T.; Ramos-Torres, K. M.; Chang, C. J. Synthetic fluorescent probes for studying copper in biological systems. *Chem. Soc. Rev.* **2015**, *44*, 4400-4414.

(9) Nolan, E. M.; Lippard, S. J. Small-Molecule Fluorescent Sensors for Investigating Zinc Metalloneurochemistry. *Acc. Chem. Res.* **2009**, *42*, 193-203.

(10) Carter, K. P.; Young, A. M.; Palmer, A. E. Fluorescent Sensors for Measuring Metal Ions in Living Systems. *Chem. Rev.* **2014**, *114*, 4564-4601.

(11) Domaille, D. W.; Que, E. L.; Chang, C. J. Synthetic fluorescent sensors for studying the cell biology of metals. *Nat. Chem. Biol.* **2008**, *4*, 168-175.

(12) Aron, A. T.; Ramos-Torres, K. M.; Cotruvo, J. A.; Chang, C. J. Recognition- and Reactivity-Based Fluorescent Probes for Studying Transition Metal Signaling in Living Systems. *Acc. Chem. Res.* **2015**, *48*, 2434-2442.

(13) Pearce, D. A.; Walkup, G. K.; Imperiali, B. Peptidyl chemosensors incorporating a FRET mechanism for detection of Ni(II). *Bioorganic & medicinal chemistry letters* **1998**, *8*, 1963-1968.

(14) Fabbrizzi, L.; Licchelli, M.; Pallavicini, P.; Perotti, A.; Taglietti, A.; Sacchi, D. Fluorescent Sensors for Transition Metals Based on Electron-Transfer and Energy-Transfer Mechanisms. *Chem. Eur. J.* **1996**, *2*, 75-82.

(15) Bolletta, F.; Costa, I.; Fabbrizzi, L.; Licchelli, M.; Montalti, M.; Pallavicini, P.; Prodi, L.; Zaccheroni, N. A $[Ru^{II}(bipy)_3]$-[1,9-diamino-3,7-diazanonane-4,6-dione] two component system, as an efficient ON–OFF luminescent chemosensor for Ni^{2+} and Cu^{2+} in water, based on an ET (energy transfer) mechanism. *J. Chem. Soc., Dalton Trans.* **1999**, *1999*, 1381–1385.

(16) Dodani, S. C.; He, Q.; Chang, C. J. A Turn-On Fluorescent Sensor for Detecting Nickel in Living Cells. *J. Am. Chem. Soc.* **2009**, *131*, 18020–18021.

(17) Torrado, A.; Walkup, G. K.; Imperiali, B. Exploiting Polypeptide Motifs for the Design of Selective Cu(II) Ion Chemosensors. *J. Am. Chem. Soc.* **1998**, *120*, 609-610.

(18) Ragsdale, S. W. Nickel-Based Enzyme Systems. *J. Biol. Chem.* **2009**, *284*, 18571-18575.

(19) Gale, E. M.; Patra, A. K.; Harrop, T. C. Versatile Methodology Toward NiN_2S_2 Complexes as Nickel Superoxide Dismutase Models: Structure and Proton Affinity. *Inorg. Chem.* **2009**, *48*, 5620-5622.

(20) Gale, E. M.; Simmonett, A. C.; Telser, J.; Schaefer, H. F., III; Harrop, T. C. Toward Functional Ni-SOD Biomimetics: Achieving a Structural/Electronic Correlation with Redox Dynamics. *Inorg. Chem.* **2011**, *50*, 9216–9218.

(21) O'Neil, J. P.; Wilson, S. R.; Katzenellenbogen, J. A. Preparation and Structural Characterization of Monoamine-Monoamide Bis(thiol) Oxo Complexes of Technetium(V) and Rhenium(V). *Inorg. Chem.* **1994**, *33*, 319-323.

(22) Fulmer, G. R.; Miller, A. J. M.; Sherden, N. H.; Gottlieb, H. E.; Nudelman, A.; Stoltz, B. M.; Bercaw, J. E.; Goldberg, K. I. NMR Chemical Shifts of Trace Impurities: Common Laboratory Solvents, Organics, and Gases in Deuterated Solvents Relevant to the Organometallic Chemist. *Organometallics* **2010**, *29*, 2176–2179.

(23) Mathrubootham, V.; Thomas, J.; Staples, R.; McCraken, J.; Shearer, J.; Hegg, E. L. Bisamidate and Mixed Amine/Amidate NiN_2S_2 Complexes as Models for Nickel-Containing Acetyl Coenzyme A Synthase and Superoxide Dismutase: An Experimental and Computational Study. *Inorg. Chem.* **2010**, *49*, 5393-5406.

(24) Hancock, R. D. The pyridyl group in ligand design for selective metal ion complexation and sensing. *Chem. Soc. Rev.* **2013**, *42*, 1500-1524.

(25) Alam, R.; Mistri, T.; Mondal, P.; Das, D.; Mandal, S. K.; Khuda-Bukhsh, A. R.; Ali, M. A novel copper(II) complex as a nitric oxide turn-on fluorosensor: intracellular applications and DFT calculation. *Dalton Trans.* **2014**, *43*, 2566-2576.

(26) Gale, E. M.; Cowart, D. M.; Scott, R. A.; Harrop, T. C. Dipeptide-Based Models of Nickel Superoxide Dismutase: Solvent Effects Highlight a Critical Role to Ni–S Bonding and Active Site Stabilization. *Inorg. Chem.* **2011**, *50*, 10460-10471.

(27) Broering, E. P.; Dillon, S.; Gale, E. M.; Steiner, R. A.; Telser, J.; Brunold, T. C.; Harrop, T. C. Accessing Ni(III)-Thiolate versus Ni(II)-Thiyl Bonding in a Family of Ni-N_2S_2 Synthetic Models of NiSOD. *Inorg. Chem.* **2015**, *54*, 3815–3828.

(28) Fiedler, A. T.; Bryngelson, P. A.; Maroney, M. J.; Brunold, T. C. Spectroscopic and Computational Studies of Ni Superoxide Dismutase: Electronic Structure Contributions to Enzymatic Function. *J. Am. Chem. Soc.* **2005**, *127*, 5449-5462.

(29) Fiedler, A. T.; Brunold, T. C. Spectroscopic and Computational Studies of Ni^{3+} Complexes with Mixed S/N Ligation: Implications for the Active Site of Nickel Superoxide Dismutase. *Inorg. Chem.* **2007**, *46*, 8511-8523.

(30) Broering, E. P.; Truong, P. T.; Gale, E. M.; Harrop, T. C. Synthetic Analogues of Nickel Superoxide Dismutase: A New Role for Nickel in Biology. *Biochemistry* **2013**, *52*, 4-18.

(31) Metivier, R.; Leray, I.; Valeur, B. Photophysics of calixarenes bearing two or four dansyl fluorophores: charge, proton and energy transfers. *Photochem. Photobiol. Sci.* **2004**, *3*, 374-380.

(32) Lim, M. H.; Lippard, S. J. Copper complexes for fluorescence-based NO detection in aqueous solution. *J. Am. Chem. Soc.* **2005**, *127*, 12170-12171.

(33) Ezeh, V. C.; Harrop, T. C. A sensitive and selective fluorescence sensor for the detection of arsenic(III) in organic media. *Inorg. Chem.* **2012**, *51*, 1213-1215.

(34) Ezeh, V. C.; Patra, A. K.; Harrop, T. C. Four-coordinate As(III)-N,S complexes: synthesis, structure, properties, and biological relevance. *Inorg. Chem.* **2010**, *49*, 2586-2588.

(35) Li, Y. H.; Chan, L. M.; Tyer, L.; Moody, R. T.; Himel, C. M.; Hercules, D. M. Study of Solvent Effects on Fluorescence of 1-(Dimethylamino)-5-Naphthalenesulfonic Acid and Related Compounds. *J. Am. Chem. Soc.* **1975**, *97*, 3118-3126.

(36) Koike, T.; Watanabe, T.; Aoki, S.; Kimura, E.; Shiro, M. A novel biomimetic zinc(II)-fluorophore, dansylamidoethyl-pendant macrocyclic tetraamine 1,4,7,10-tetraazacyclododecane (cyclen). *J. Am. Chem. Soc.* **1996**, *118*, 12696-12703.

(37) Zheng, Y. J.; Gattas-Asfura, K. M.; Konka, V.; Leblanc, R. M. A dansylated peptide for the selective detection of copper ions. *Chem. Commun.* **2002**, 2350-2351.

(38) Denny, J. A.; Foley, W. S.; Todd, A. D.; Darensbourg, M. Y. The ligand unwrapping/rewrapping pathway that exchanges metals in S-acetylated, hexacoordinate $N_2S_2O_2$ complexes. *Chem. Sci.* **2015**, *6*, 7079-7088.

(39) Goodman, D. C.; Reibenspies, J. H.; Goswami, N.; Jurisson, S.; Darensbourg, M. Y. A New Macrocyclic N_3S_2 Ligand and Its Nickel(II), Cobalt(II), Rhodium(III)-103, and Rhodium(III)-105 Complexes. *J. Am. Chem. Soc.* **1997**, *119*, 4955-4963.

(40) Tamayo, A.; Casabo, J.; Escriche, L. S.; Gonzalez, P.; Lodeiro, C.; Rizzi, A. C.; Brondino, C. D.; Passeggi, M. C. G.; Kivekas, R. a.; Sillanpaa, R. Structural and EPR studies on single-crystal and polycrystalline samples of copper(II) and cobalt(II) complexes with N_2S_2-based macrocyclic ligands. *Inorg. Chem.* **2007**, *46*, 5665-5672.

(41) Bruckner, C.; Rettig, S. J.; Dolphin, D. 2-Pyrrolythiones as monoanionic bidentate N,S-chelators: Synthesis and molecular structure of 2-pyrrolylthionato complexes of nickel(II), cobalt(III), and mercury(II). *Inorg. Chem.* **2000**, *39*, 6100-6106.

(42) Contreras, R. R.; Fontal, B.; Bahsas, A.; Suarez, T.; Reyes, M.; Bellandi, F.; Nava, F.; Cancines, P. Synthesis of copper, nickel and cobalt complexes containing a new N_2S_2 ligand: benzyl-*N*,*N*'-alkylbis(2-amino-1-cyclopentencarbodithioate). *Transit. Metal. Chem.* **2004**, *29*, 51-55.

(43) Perrin, D. D. *Dissociation Constants of Organic Bases in Aqueous Solution*; Suppl, 1972 ed.; Butterworths: London, 1972.

CHAPTER 6

CONCLUSIONS

We have successfully developed, synthesized, and characterized Ni complexes with carboxamide and thiolate ligands as low molecular weight synthetic analogues of nickel superoxide dismutase (NiSOD) and platforms for Ni(II) sensing. Additionally, we have also observed unique reactivity and structurally characterized the reaction product of a Ni complex with nitric oxide (NO(g)). For all of this work, we have derived inspiration from the mixed N/S coordination environment of the reduced and oxidized NiSOD active site. Although other groups have sought to model NiSOD through peptide-based or low-molecular weight mimics, few have published complexes that both structurally and electronically match the donors in the native enzyme. Our systems involve a thiolate, carboxamide-N, and amine ligands corresponding to the Cys-S, peptido-N from Cys2, and amine/s of His1.

By incorporating a series of four exogenous thiolates, a family of $[Ni(N_2S)SR']^{1-/0}$ complexes were synthesized, characterized, and evaluated for their reactivity. The exogenous thiolate position, SR′, provided a point of control that could be varied to tune the S character in the redox active molecular orbital and thereby promote Ni-based redox, rather than S-based redox. In two of the complexes in this family, metal based redox was achieved, as evidenced by electron paramagnetic resonance (EPR), UV-vis, and magnetic circular dichroism (MCD) spectroscopies. The Ni(III) state was made possible through the inclusion of a secondary sphere amine at the SR′ position, and it was further stabilized (for ~24 hours) by the addition of an

electron-withdrawing trifluoromethyl group para to the S to decrease basicity at the SR′. MCD and density functional theory (DFT) computational results reveal that the high valent Ni is in fact a resonance species, possessing Ni(II)-thiyl radical character as well. The results from this system suggest that NiSOD may also traverse through a thiyl species in the course of its Ni(II/III) ping-pong mechanism.

With respect to modeling enzyme activity, none of the $[Ni(N_2S)SR']^{1-/0}$ complexes exhibited $O_2^{\bullet-}$ disproportionation activity; however, the species that is capable of Ni-based redox also displays novel reactivity with NO(g). The result of this reactivity is a nitrosylated dimer with Ni and SR′. DFT results from the crystallographically characterized $[Ni_2(\mu\text{-}SR')_2(NO)_4]^{2-}$ confirm this structure represents the energy minimum upon formation of the $\{NiNO\}^{10}$ and N-NO. Due to the weaker basicity at the SR′ position, or possibly due to the NH_2 engaged with the S or metal, the reactive center of the Ni center is poised for nitrosylation. Like Cu(II) complexes which have been characterized previously, the Ni(II) complex undergoes intramolecular nitrosylation, forming an N-nitrosamine and Ni(I) center. However, unlike the Cu(II) systems, Ni is also nitrosylated and trapped by coordinating to a new ligand, the NNO. This conformation is likely stabilized by the distorted tetrahedral geometry of the new chelate and the low coordination number preference exhibited by $\{NiNO\}^{10}$. This reactivity and metal-to-N-nitrosamine binding mode has not been explored in the literature and may represent new reactivity pathways for NO(g) and metals in biology.

Looking toward the oxidized structure of the NiSOD active site, we sought to develop of five coordinate (5C) complex of the formula $[Ni(N_3S)SR']^{1-}$, where again SR′ represents an exogenous thiolate. This model, based upon the His1 and Cys2 donors in the enzyme, provided an N-imidazole ligand, as is observed in the apical coordination site of oxidized NiSOD. The

ligand His^{Bz}-CSH, where Bz is benzyl and CSH is cysteamine, was synthesized and characterized successfully, yet the Ni(II) complex that results from metalation is ill-defined. All FTIR spectra of the Ni(II) complexes that were synthesized lack the expected shift in the carbonyl stretch that indicate metal binding; therefore, the carboxamide-N of His^{Bz}-CSH was not coordinating to Ni. This may be the result of ill-defined protonation, or the formation of an S,S-bridged or oligomeric Ni(His^{Bz}-CSH) species. In order to avoid these complications, the ligand design was modified to replace the secondary amine with an imine, which we predict will position the N lone in the plane and increase the chances of Ni(II) binding. The synthesis of this ligand has been carried out, and future directions include the metalation and characterization of the Ni complex. We expect this model of the NiSOD oxidized active site will be able to access the Ni(III) state due to the position of the axial imidazole-N ligand of His and provide insight into the requirements for achieving Ni-based redox.

Taking inspiration from the N/S basal plane donors of NiSOD, a four coordinate (4C) ligand of the formula N_2S_2-Dns, where Dns is the dansyl chromophore, was synthesized. The objective of this project is the development of a Ni(II) specific sensor that can bind Ni(II) with high affinity and produce a detectable, fluorescent response. The use of metal-specific sensors has provided the biological community with a powerful tool to better understand metal trafficking and signaling processes in cells. Although a quenching response was detected for Ni(II), the intensity also decreased upon additions of Co(II) and Cu(II) to the sensor. Paramagnetic quenching is likely responsible through sensor coordination to high spin Ni(II) in tetrahedral or octahedral geometry. Future directions for this sensor include modification with a methyl ester moiety adjacent to the carboxamide of the N_2S_2 frame. We predict this modification will afford greater aqueous solubility, and it will furthermore change the electronic properties of

the carboxamide, making deprotonation and metal binding at that position more facile. The development of Ni(II) specific fluorescent sensors for cellular imaging is a promising field, as there are many questions remaining about the transport of Ni(II) and the assembly of Ni-containing metalloenzymes in bacteria.

In summary, this work has provided the bioinorganic community with greater insight into the binding of Ni(II) to carboxamide and thiolate ligands. The development of NiSOD models is an impactful strategy to learn more about the mechanism of the enzyme, its structure, O_2 tolerance, and the promotion of metal based redox. The synthetic challenges of creating structurally and electronically accurate models of NiSOD are apparent, yet they are necessary to make the strongest comparisons to the native enzyme. For this reason, future directions of this work include the development of other ligands that contain the amine-N, imidazole-N, and anionic N-carboxamide and S-thiolates for the coordination of Ni and efforts toward producing a catalytically active Ni(III/II) complex that can mimic NiSOD's structure and function.

APPENDIX A

PROGRESS TOWARDS SYNTHETIC MODELS OF NiSOD CONTAINING A MODIFIED HIS^{Bz}-CYS LIGAND PLATFORM

A.1 Introduction

Superoxide dismutases (SODs) are the first line of defense against oxidative stress caused by the reactive oxygen species (ROS) superoxide ($O_2^{\bullet-}$). In *Streptomyces* soil bacteria, nickel containing SODs (NiSODs) catalyze the disproportionation of $O_2^{\bullet-}$ to H_2O_2 and O_2 through alternate metal oxidation and reduction cycles, as observed for the other SOD families.[1-3] Ni superoxide dismutase (NiSOD) has provided the bioinorganic community with a number of questions regarding its structure and function, given the unique Ni-N/S coordination environment and O_2 tolerance of NiSOD despite employing non-innocent CysS-ligands. In the reduced state, the enzyme contains an active site Ni(II) ion in a square-planar N_2S_2 geometry from the two thiolates of Cys2 and Cys6, the peptido-N of Cys2, and the N-terminal -NH_2 group of His1.[2,3] In the oxidized state, the His1-N_{Im} binds to Ni(III) resulting in a five coordinate (5C) square-pyramidal geometry. Insight into the 5C species has revealed that the axial N-donor is vital to achieving a stable Ni(III) state. Upon binding His1-N_{Im}, the frontier molecular orbital (MO) of oxidized NiSOD ($NiSOD_{ox}$) is primarily Ni-d_{z^2} in character.[4] In comparison, the MO of reduced, 4C NiSOD is largely covalent in character and composed of S-pπ (66%) with a lesser

contribution from Ni-dπ (26%).[4] Furthermore, the axial Ni—NHis bond is necessary to maintain the high (~10^9 $M^{-1}s^{-1}$) catalytic rate of $O_2^{\bullet-}$ disproportionation.[4-6]

Utilizing synthetic strategies to promote Ni character in the redox active MO, we have developed several NiSOD model complexes of the general formula $[Ni(N_2S)(SR')]^{1-/0}$, where SR′ represents a variable monodentate thiolate in the basal plane coordination sphere.[7-9] However, these complexes have lacked a fifth N-donor capable of binding to the Ni center, modeling His1-N_{Im} of $NiSOD_{ox}$. To date (2017), the only low molecular weight synthetic NiSOD analogous to achieve a stable Ni(III) state have contained internal or external N-donors.[9-13] We, and others, have recognized the importance of a fifth N-ligand, which promotes Ni character in the redox active MO, allowing for Ni(III/II) redox, and serves to stabilize high valent Ni.

Since our review in 2012, Masuda,[14] Shearer,[15-18] and others[11,19,20] have published NiSOD mimics to gain insight into the metalloenzyme's active site, although replicating catalytic $O_2^{\bullet-}$ turnover remains elusive. Masuda and coworkers investigated the mechanism of NiSOD turnover by synthesizing Ni(II) N_2S_2 square-planar complexes containing amino, carboxamido, and dithioether ligands (Figure A.1).[14] Ni complexes were synthesized from the ligands: *N*-(2-mercapto-2-methylpropanoyl)-*N′*-(2-mercapto-2-methylpropyl)-1,2-diaminoethane (L_1), *N*-(2-methylmercapto-2-methylpropanoyl)-*N′*-(2-methylmercapto-2-methylpropyl)-1,2-diaminoethane (L_2), and *N*-(2-Benzylmercapto-2-methylpropanoyl)-1,2-diaminoethane (L_3). Complexes **$[Ni(L_1)]^-$** and **$[Ni(L_2)]^+$** were characterized by UV-vis spectroscopy and revealed the expected *d*-*d* transitions, λ_{max} = 438-450 nm, consistent with native NiSOD.[4] However, **$[Ni(L_3)]^{2+}$** exhibited transitions more in-line with high spin (S = 1) Ni(II) in acetonitrile (MeCN), dimethylformamide (DMF), and dimethyl sulfolxide (DMSO), indicating formation of a 5C or 6C species in these solvents. Solvent-dependent redox behavior is also observed for **$[Ni(L_1)]^-$** and **$[Ni(L_3)]^{2+}$**: in

protic solvents, the amino-carboxamido-dithiolato complex **[Ni(L$_1$)]$^-$** exhibits an irreversible Ni(III)/(II) couple (e.g., 0.303 V, H_2O, vs NHE), which the authors attribute to solvent binding to the metal center. In contrast, a reversible Ni-based redox couple is observed from -0.114 V (MeCN) to -0.103 V (DMSO) vs NHE depending on solvent. For **[Ni(L$_2$)]$^+$** and **[Ni(L$_3$)]$^{2+}$**, irreversible couples are observed for all solvents except for CH_2Cl_2 and acetone, respectively. Masuda attributes the solvent-dependent behavior and large range in redox potentials for **[Ni(L$_1$)]$^-$** vs. **[Ni(L$_2$)]$^+$** and **[Ni(L$_3$)]$^{2+}$** to the greater negative charge of the ligand **L$_1$** (-3) and impact of the dithiolato vs dithioether donors. The lower redox potential of **[Ni(L$_1$)]$^-$** is more in-line with SOD function and is consistent with nature's use of S-thiolate donors in NiSOD, rather than thioether donors, to carry out $O_2^{\bullet-}$ disproportionation.

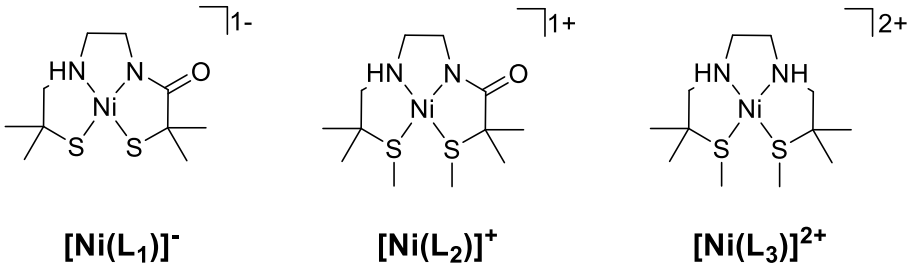

Figure A.1. Structures of the dithiolate anion and dithiother cations of NiSOD model complexes **[Ni(L$_1$)]$^-$**, **[Ni(L$_2$)]$^+$**, and **[Ni(L$_3$)]$^{2+}$**.

Additional coordination dynamics and reactivity were explored with the dithiolate **[Ni(L$_1$)]$^-$**.[14] Oxidation of **[Ni(L$_1$)]$^-$** with ferrocenium hexafluorophosphate at -60 °C resulted in

disappearance of the N_2S_2 electronic absorbance feature at 449 nm and emergence of N/O(σ) → Ni($d_{x^2-y^2}$) and S/N/O(π) → Ni(σ) charge transfer (CT) transitions at 400 nm and ~500 nm, respectively (acetone/DMF, 4;1, v/v, -60 °C).[4,14,21,22] These features shift to 393 nm and 575 nm in the presence of excess (10 equiv) 1-methylimidazole, indicating Ni-N_{Im} binding to this external N-donor. The EPR of oxidized **[Ni(L_1)]** with 10 equiv imidazole is also in-line with a Ni(III) species axially bound to N, given by the triplet hyperfine feature, A_N= 2.5 mT, observed at g_z = 2.01. Hyperfine splitting is also observed for the native NiSOD due to the axial HisN donor in the oxidized state.[4] UV-vis and Raman evidence suggest an end-on superoxo bound to the Ni(II) center of **[Ni(L_1)]**$^-$, and the EPR spectra of free KO_2 shifts from g = 2.10 to 2.21 upon addition of the Ni complex. The $g_{//}$ shifts to lower energy, rather than higher energy. This EPR shift was unexpected by the authors and explored with DFT computational studies, which determined that the energy gap of 0.29 eV between the π_x* and π_y* of $O_2^{\bullet-}$ resulting from Ni(II)–$O_2^{\bullet-}$ binding (vs. 1.07 eV for free $O_2^{\bullet-}$) is responsible. Adding 10 equiv. of 1-methylimidazole to the proposed Ni(II)–$O_2^{\bullet-}$ species resulted in an EPR spectrum resembling Ni(III) bound to an axial N-donor. Conversely, addition of KO_2 to oxidized **[Ni(L_1)]** with 10 equiv 1-methylimidazole reduced the Ni species back to Ni(II). No evidence of Ni(III) bound to $O_2^{\bullet-}$ or N_3^- was observed. Taken together, the reactivity evidence led the authors to propose a mechanism for NiSOD involving superoxide directly binding to the Ni(II) followed by proton transfer. Due to lack of evidence of Ni(III)-bound $O_2^{\bullet-}$ in their systems, NiSOD is proposed to catalyze $O_2^{\bullet-}$ to O_2 via a through-space interaction. Although this mechanism may reflect the reactivity of **[Ni(L_1)]**$^-$, its application to NiSOD is limited: the model does not account for sources of H^+, and there has been no biochemical evidence, as of early 2017, to suggest native NiSOD operates via an inner sphere mechanism. This study is yet another in the NiSOD

modeling field to establish the necessity of S-thiolate and axial-N donors to achieve NiSOD activity.

Shearer has published follow-up studies into the **[Ni(SOD^{M1})]** metallopeptide-based NiSOD mimic and its derivatives, where SOD^{M1} = HCDLPCGVYDPA (see Figure A.2 and Ch. 2).[15-18,23] Modifications to the peptide sequence to yield a bisamidate/bisthiolate Ni(II) coordination were previously shown to render the **[Ni(SOD^{M1})]** maquette catalytically inactive. Closer examination published in 2013 using X-ray absorption spectroscopy (XAS), FTIR, electrospray ionization mass spectrometry (ESI-MS), and stopped flow kinetics demonstrated that the bisamidate modification resulted in rapid S-oxidation of the Cys ligands upon exposure to O_2 or $O_2^{\bullet-}$, as the Cys ligands were more susceptible to oxidation due to activation of filled Ni(dπ)-S(pπ) antibonding orbitals.[17] This result is not unsurprising, as work by Grapperhaus and others on S-oxidation/oxygenation chemistry have demonstrated the vulnerability of S-thiolates upon exposure to O_2.[24-26]

Another SOD^{M1} peptide modification, which replaces the terminal His residue with *N*-methylhistidine (H^{Me}), to yield the **[Ni(SOD^{M1}H^{Me})]** system, was previously shown to result in a catalytically active NiSOD maquette, albeit at a slow rate (k = 6(1) × 10^6 M^{-1} s^{-1}, pH 8.0).[27] A more recent (2013) publication concerning the kinetic properties of **[Ni(SOD^{M1}H^{Me})]** suggest a proton coupled electron transfer (PCET) mechanism is at play.[23] Calculations of the H/D kinetic isotope effect in D_2O (KIE, ~20), in addition to bond dissociation free energies, supported a PCET mechanism with a tunneling component to allow for abstraction of an H atom and reduction of **[Ni(III)(SOD^{M1}H^{Me})]** to **[Ni(II)(SOD^{M1}H^{Me})]** by 1-hydroxy-2,2,6,6-tetramethylpiperidine (TEMPO-H). Coupled with kinetic studies with TEMPO-H/TEMPO$^{\bullet}$ reactivity, S K-edge XAS results suggest that the cysteines of SOD^{M1}H^{Me} are protonated in the

Ni(II) state at physiological pH.[23] However, the author warns that the PCET mechanism observed for the SOD^{M1} metallopeptide may not apply to the native enzyme, and more study of NiSOD in biology is warranted.[16]

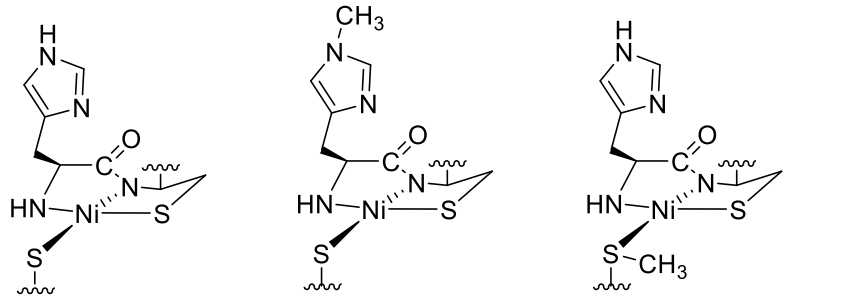

Figure A.2. Structure of the NiSOD maquette base model [Ni(SOD^{M1})] (SOD^{M1} = HCDLPCGVYDPA) (left), the methylhistidine version [Ni($SOD^{M1}H^{Me}$)] (center), and methylcysteine version [Ni($SOD^{M1}C(6)C^{Me}$)] (right).

Shearer also used the **[Ni(SOD^{M1})]** system to probe how NiSOD protects the Cys-S ligands from oxidative damage. Building upon the S K-edge XAS results which supported a protonated Cys in **[Ni($SOD^{M1}H^{Me}$)]**, Shearer utilized S-methylated derivatives of the peptide maquette and DFT computations to identify the likely site of protonation.[15] Ni was unable to bind to the SOD^{M1} peptide backbone containing methylcysteine at the Cys2 position; however, Ni(II) was shown to readily bind when the Cys6 residue was derivatized with methyl ($C(6)C^{Me}$). The **[Ni($SOD^{M1}C(6)C^{Me}$)]** variant was successfully isolated and characterized, and cyclic voltammetry studies revealed different results from the **[Ni(SOD^{M1})]** parent system:

[Ni(SOD^{M1}C(6)C^{Me})] cannot achieve a Ni(III) redox state from -0.2 to 1.0 V (vs NHE) and is thus not SOD active.[15] The methylcysteine is responsible for the change in redox behavior, since binding affinity studies and XAS results confirm that Ni(II) is bound in a 4C N_2S_2 ligand environment as expected, with a K_d of 3 uM at pH 7.4, which is similar to other SOD^{M1} maquettes, indicating that the methylcysteine does not have a significant impact on Ni(II) binding.

DFT computations were performed to model either methylation or protonation at Cys6. As a result of methylation, a -0.027 Å contraction to 2.208 Å (contracted as compared to **[Ni(SOD^{M1})]**) in the Ni—S(Cys6^{Me}) bond trans to the amide was observed, due to relief of the filled/filled Ni(3dπ)-S(3π) antibonding interactions.[7,8,26,28] Protonation at Cys6 also results in contraction of the Ni—S(Cys6) bond by 0.03 Å; and inclusion of a water molecule modeled in a H-bond to the cysteinates in the DFT calculations produces the shortest Ni—S distance of 2.18 Å. The geometric parameters for the [SODCys(6)H$^+$ + H_2O] model most closely resembles the previously published **[Ni(SOD^{M1})]** complex, leading the authors to conclude that at pH 7.4, their **[Ni(SOD^{M1})]** system is protonated at the Cys6 position and is associated to at least one H_2O molecule. The isosurface plots of these mutants reveal that **[Ni(SOD^{M1}C(6)C^{Me})]** and **[Ni(SOD^{M1}C(6)H$^+$)]** are similar with the lowest unoccupied molecular orbital (LUMO) composed of primarily Ni($3d_{x^2-y^2}$) character and the highest occupied molecular orbital by two (HOMO-2) composed of Ni($3d_{z^2}$). However, as compared to the parent **[Ni(SOD^{M1})]**, the LUMO of the variants contains more Ni character resulting in a less colavent Ni-L bond, and the HOMO-2 of the variants contains more amine/amide character with some contribution from the Ni($3d_{xy}$), which was not observed for **[Ni(SOD^{M1})]**. The HOMO, HOMO-1, and HOMO-3 **[Ni(SOD^{M1}C(6)C^{Me})]** and **[Ni(SOD^{M1}C(6)H$^+$)]** are primarily S/N(π)-Ni(3dπ) antibonding

orbitals, and addition of a H_2O molecule increases the covalency and S contribution in the LUMO. Shearer proposes, as have others, that the enzyme uses H bonding to water molecules and cysteine protonation to tune NiSOD catalysis and protect the cysteine ligands from oxidative damage.[15]

Using spectroscopic evidence that protonation of Cys6 is trapped at pH 9.5, as well as the computationally-derived MOs, an H atom transfer mechanism is in-line for the superoxide reduction half reaction, followed by electron transfer (ET).[15] By using a Potential Energy Surfaces technique, a transition state was calculated that showed the singly occupied molecular orbital spin density was shared between the Ni—S and the O-O orbitals of **[Ni(SOD^{M1}C(6)H^{+})]** and $O_2^{\bullet-}$, respectively. The addition of an H_2O molecule in the Potential Energy Surface calculations resulted in, (i) a lower reaction barrier, (ii) lower pK_a by 3 units for the $CysH^+$, and (iii) less negative charge buildup on the $O_2^{\bullet-}$; these results still support an proton transfer (PT) mechanism.[15] However, it is unlikely that a PT/ET mechanism can extend to the native enzyme. The rate of NiSOD catalysis is not affected by changing pH,[29,30] and the $O_2^{\bullet-}$ is incapable of interacting with the NiSOD active site in the same geometry as the computations predict.

Building upon a 2012 mixed N/O complex that could accomplish one half of the NiSOD catalytic cycle,[10] Lee and coworkers turned to an N_3S_2 complex to more accurately model the enzyme (Figure A.3).[11] The synthesis of $[Ni(H_2BA^{R}TPP)]^{2+}$, where R = phenyl (Ph) or isopropryl (*i*Pr), was carried out to yield 2,6-bis((2-(*N*-anilinylthiocarbonyl)pyrrolidini-1-yl)methyl)pyridine ($H_2BA^{Ph}TPP$), or 2,6-bix((2-(*N*-isopropylaminothiocarbonyl)pyrrolidini-1-yl)methyl)pyridine ($H_2BA^{iPr}TPP$), respectively, bound to Ni(II) in 5C, distorted square pyramidal geometries. Oxidation of $[Ni(H_2BA^{R}TPP)]^{2+}$ by cyclic voltammetry (CV) resulted in a quasireversible Ni(III)/(II) couple, attributed to dissociation of thioamide protons; oxidation by

ceric ammonium nitrate (CAN) produced an EPR spectrum consistent with a square pyramidal Ni(III) species for the R = *i*Pr species. Despite this observation, neither complex exhibited NiSOD catalytic activity with KO_2.[11] Instead, reaction with KO_2, or with other bases such as Et_3N or NaH, resulted in the formation of a deprotonated, 5C Ni(II) species with the Ni bound by imido-thiolates. DFT studies on $[Ni(H_2BA^{iPr}TPP)]^{3+}$ revealed that the unpaired electron is primarily located in the d_{z^2} orbital of Ni(III) overlapping with the axial pyridine p_z orbital. The oxidation of $[Ni(H_2BA^{iPr}TPP)]^{2+}$ is allowed due to the strong pyridine-N donor in the axial position as well as the isopropyl thioamide. Conversely, the phenyl groups of $[Ni(H_2BA^{Ph}TPP)]^{2+}$ delocalize the electron density away from the Ni and prevent oxidation to Ni(III).[10] Although the donors are electronically dissimilar from that of native NiSOD, this work underscores the requirements to achieve Ni-based redox activity, namely, (i) a fifth N-donor poised to bind to the metal, and (ii) significant Ni character in the redox-active MO.

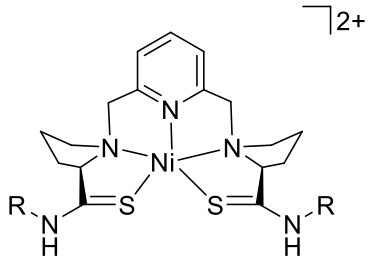

$[Ni(H_2BA^{R}TPP)]^{2+}$

Figure A.3. Structure of the cation of the N_3S_2 NiSOD synthetic model $[Ni(H_2BA^{R}TPP)]^{2+}$, (R = Ph or *i*Pr).

In combination with these recent studies (2013-2016), the justification for the inclusion of S-thiolates, carboxamide-N, and axial-N donors in ligand design has been established in the NiSOD analogue literature. To model NiSOD donors, the use of peptides has also been explored by our group through the Gly-Cys methyl ester (GC-OMe) ligand to gain insight into NiSOD's Ni hook binding motif and active site stabilization.[31] Although the GC-OMe Ni complex exhibited a redox potential within the window for disproportionation chemistry, it was still irreversible, and the GC-OMe Ni complex did not display any NiSOD activity.[31]

The objective of this work is to contruct a ligand with mixed N/S coordination but with an N_{axial} donor. The inclusion of the fifth N-donor in the ligand backbone is a synthetic step forward, as compared to N-donors tethered via exogenous, monodentate ligands of the Ni(nmp) family.[7-9] Presented herein is the synthesis and characterization of a new peptide-based ligand platform composed of a His^{Bz}-CSH peptide (where Bz = benzyl and CSH = cysteamine) that structurally and electronically replicates NiSOD's three donor atoms from His1 and Cys2 (Figure A.4). The proposal is that His^{Bz}-CSH will coordinate Ni with an exogenous thiolate donor (SR′) to provide the Ni(II) complex with the general formula, $[Ni(N_3S)(SR')]^{1-}$. Unlike the previously published Ni(nmp) family, the amino-acid derived His^{Bz}-CSH ligand is expected to provide solubility and stability in protic solvents. Unlike previous models, the His^{Bz}-CSH ligand design incorporates an N_{Im} covalently attached as a member of the tetradentate chelate, which is poised to bind axially to Ni and may potentially stabilize the high valent state for Ni-based catalysis. This work represents progress towards the first low molecular weight peptide-based NiSOD analogue, which accurately mimics the structure and electronic environment of the native enzyme.

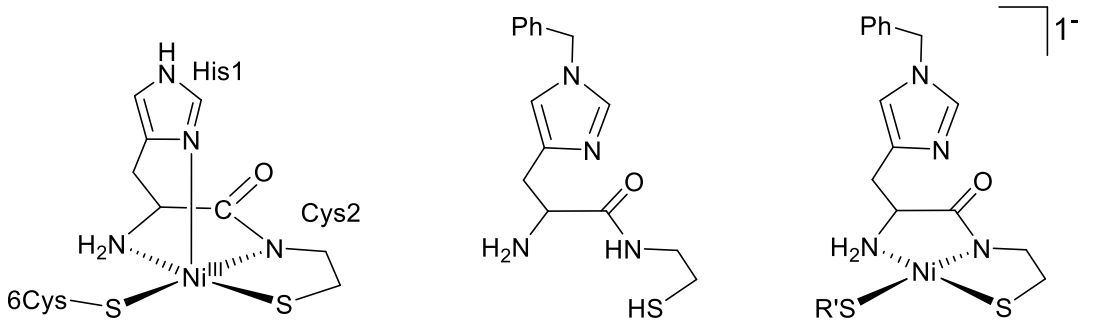

Oxidized NiSOD **2** **[Ni(His^{Bz}-CSH)(SR')]$^{1-/0}$**

Figure A.4. The structure of the oxidized NiSOD active site (left). The N_2S ligand, His^{Bz}-CSH (**2**) where CSH = cysteamine. The proposed structure of the anion of [Ni(His^{Bz}-CSH)(SR′)]$^{1-}$ where SR′ is contributed from an exogenous thiolate donor.

A.2. Results and Discussion

The syntheses of the Boc-His(Bzyl)-CS-trit (**1**) and His^{Bz}-CSH ligand (**2**) as a trifluoroacetic acid (TFA) adduct are depicted in Scheme A.1. Benzyl-protected His was employed in efforts to prevent unwanted side reactivity at the N_{Im} position. The synthesis of *S*-tritylcysteamine has been reported previously.[7,32] The coupling of Boc-His(Bzl)-OH and 1 equiv *S*-tritylcysteamine was carried out in CH_2Cl_2 at 0 °C under a N_2(g) atmosphere utilizing the carbodiimide peptide coupling reagent, 1-ethyl-3-(3-dimethylaminopropyl)carbodiimide hydrochloride (EDC·HCl) in the presence of *N*-hydroxysuccinimide (NHS). After stirring overnight at RT, workup and purification by column chromatography (silica, THF:CH_2Cl_2, 1:1, R_f = 1) afforded **1** in 69% yield as a white solid. Compound **1** has been characterized by ^{1}H NMR, ^{13}C NMR, FTIR, and low resolution (LR) ESI-MS (see supporting information).

The combination of EDC and NHS peptide coupling reagents provides a stable and amine-reactive NHS-ester intermediate at the His-OH with little risk of racemization.[33,34] Furthermore, the byproduct of the EDC/NHS reaction is a water-soluble *O*-acylisourea that can be removed with aqueous workup. This property offers a distinct advantage over previous His^{Bz}-CSH coupling attempts that employ *N,N'*-dicyclohexylcarbodiimide (DCC). DCC was initially utilized instead of EDC to afford **1** in good yield, unreacted DCC, unreacted *S*-tritylcysteamine, and the insoluble urea byproduct of DCC, dicyclohexylurea (DCU) under identical conditions as depicted in Scheme A.1. Although DCU can be removed by filtration with approximately 80-90% recovery, no reaction stoichiometry adjustments or chromatography conditions were found to achieve separation of **1** from unreacted DCC, which appears in the ^{1}H NMR as a multiplet at ~1.5-2.0 ppm ($CDCl_3$). It is possible that the presence of DCC could hinder future metalation reactions, and for this reason, we looked to EDC, its water solubility, and water-soluble isourea byproduct as an alternative synthetic route. EDC proved to be the more effective choice: excess EDC can be used to shift the reaction equilibrium and improve yield, unreacted EDC·HCl can be removed by an aqueous wash in the course of a base workup, and EDC can be removed cleanly to preclude any unwanted Ni binding in subsequent synthesis steps.

Scheme A.1. Synthesis of the His^{Bz}-CSH ligand (**1**), purified on silica (CH_2Cl_2:THF, 1:1, R_f = 1.0), and synthesis of the deprotected His^{Bz}-CSH ligand (**2**) obtained as a trifluoroacetic acid (TFA) adduct.

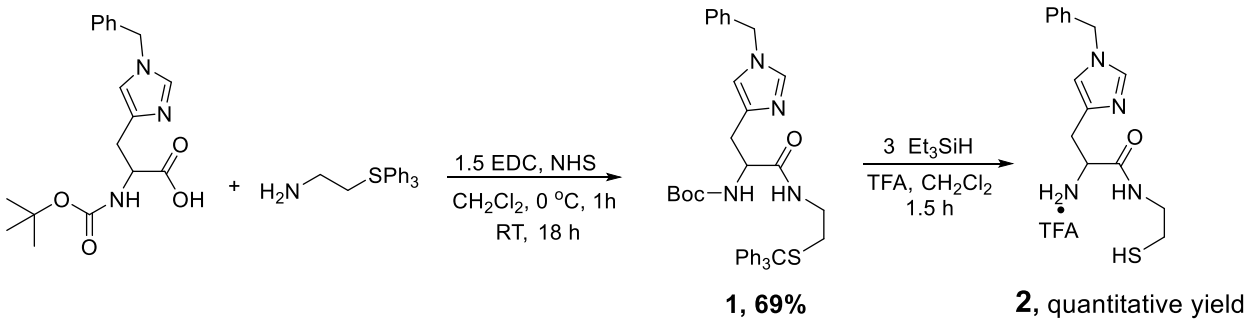

1, 69% **2**, quantitative yield

The trityl and Boc deprotection of **1** to yield **2** was carried out according to Scheme A.1 and as follows: **1** was dissolved CH_2Cl_2/TFA (1:1) v/v, which produces the bright orange color typical of the trityl carbocation. Addition of three equiv Et_3SiH to scavenge the carbocation results in a disappearance of color. The solution was stirred for 1.5 h at RT, after which the CH_2Cl_2 was removed by vacuum distillation and the TFA-insoluble Ph_3CH was filtered off. Removal of the TFA by vacuum distillation yields an opaque white oil. Excess, free TFA is removed by dissolving the white oil in MeCN (**2** has complete solubility in MeCN but not CH_2Cl_2) and adding excess $NaHCO_3$. Visual effervescence is observed, and unreacted $NaHCO_3$ can be removed by filtration and additional washing with MeCN. The remaining Ph_3CH can be removed by triturating with hexane or with Et_2O, which upon removal yields a white foam in quantitative yield. The yields typically exceed 100% due to added mass of TFA; in calculating the species as an adduct of one TFA molecule, the yield is 82%.

Compound **2** has been characterized by ^1H NMR, ^{13}C NMR, FTIR, and ESI-MS (see supporting evidence). Additional evidence of TFA salt formation is observed in ^1H NMR and ^{13}C

NMR spectra: for ^{1}H NMR, (CD_3CN, RT, 400 MHz) a broad feature is present at approximately 6-7 ppm, and the downfield shift of the His_{Im}-N*H* (~8.6 ppm) is indicative of and sensitive to the degree of protonation (Figure AS.8). Other evidence of N_{Im} protonation is seen in the shift of the benzyl CH_2 from 5.9 ppm to 5.3 ppm and splitting of the expected singlet peak into a triplet. ^{13}C NMR (CD_3CN, RT, 125 MHz) provides definitive evidence for a TFA adduct with a quartet at 162.38 ppm (J = 20 Hz, through-bond ^{13}C to ^{19}F coupling) and a quartet at 118.13 ppm (J = 291.2 Hz, ^{13}C to ^{19}F coupling) (Figure AS.10). Attempts to remove TFA by stirring **2** in MeCN with $NaHCO_3$ or K_2CO_3, were moderately successful as seen by ^{1}H NMR characterization (Figure AS.9). The ^{13}C NMR spectrum remains a useful tool to observe low intensity signatures of TFA. LR-ESI-MS (MeOH, positive mode) reveals the expected molecular ion of **2** as a free base at *m/z* 305.2 in addition to smaller peaks corresponding to $[M+Na^+]^+$ and $[M+K^+]^+$. Solid-state FTIR reveals a strong ν_{CO} stretch at 1672-1681 cm^{-1} corresponding to the carbonyl of **2**, which can be broadened by the ν_{CO} of TFA

The metalation of **2** with multiple Ni(II) salts has been carried out under varying conditions, which have been summarized in Table 5.1. Analogous to the $[Ni(nmp)(SR')]^{1-}$ system,[7,9] the proposal is that metalation of **2** would result in the *S-S* bridged dimeric or tetrameric species (See Ch. 3, Scheme 3.1). Combination of the Ni(II) salt, base, and **2** produced a color change to a reddish-brown species that displays moderate solubility in organic solvents. The ^{1}H NMR of the resulting red-brown exhibits displays broad, ill-defined peaks consistent with a paramagnetic complex. Color changes and low intensity *d-d* bands observed in the UV-vis spectrum at λ_{max} ~ 410-450 nm are consistent with a $Ni(II)N_2S_2$ species (Figure AS.14).[4,21,35] However, there is little-to-no shift in the FTIR ν_{CO} of any resulting Ni complex, indicating that deprotonation of the peptide and binding of the carboxamide-N did not occur under any of the

attempted conditions (Figure AS.13; Table 5.1). In general, a shift of ~50 cm^{-1} is typically expected for carboxamide-N → Ni binding.[7-9,31] In light of the TFA that persists, this metalation chemistry may be due to ill-defined deprotonation, i.e., addition of base to **2** deprotonates the peptide and/or the NH_2, in addition to SH deprotonation. Other explanations include His-N_{Im} → Ni binding instead of carboxamide-N → Ni binding, or the formation of oligomeric *S*-bridged species, which may explain moderate solubility of the red species.

Table 5.1: Conditions and results of selected Ni(II) reactions with **2.** All UV-vis are qualitative at RT. All FTIR were taken at RT.

Ni(II) salt	**Conditions**	**UV-vis λ_{max} (nm), Solvent**	**FTIR ν_{co} (cm^{-1}, KBr)**
$Ni(OAc)_2 \cdot 4\ H_2O$[a]	1 equiv Na(OAc), MeOH, 4 h	454 (MeOH)	1678
$Ni(OAc)_2 \cdot 4\ H_2O$[a]	1 equiv Na(OAc), MeOH, 12 h, 40 °C	418 (MeOH)	1686
$Ni(OAc)_2 \cdot 4\ H_2O$[a]	MeOH, 18 h, 40 °C	451 (MeOH)	1685
$NiCl_2$	3 equiv NaH, DMF, 18 h, 40 °C	454 (DMF)	1683
$NiCl_2$	5 equiv Et_3N, MeCN, 16 h, 30 °C	418 (MeCN)	1681
$Ni(acac)_2$[b]	MeOH, stir 1 h	411 (MeOH)	1694
$[Ni(H_2O)_6](BF_4)_2$	2.5 equiv K°, MeOH, 1.5 h	383 (MeOH)	1684
$[Ni(H_2O)_6](BF_4)_2$	2.25 equiv NaH, DMF, 1 h	421 (MeCN)	1685
$[Ni(H_2O)_6](BF_4)_2$	2.25 equiv KH, DMF, 1 h	415 (DMF)	1685

[a]OAc: acetate. [b]acac: acetylacetonate

As shown in Figure A.5, the primary amine of the His^{Bz}-CSH ligand **1** was modified to an imine (affording **4**). The proposal is this modification would, (i) position the imine-N lone pair in the plane of the coordinating Ni ion, and (ii) remove a potential site of deprotonation, namely the NH_2 of **2**. To this end, H_2N-His(Bzl)-CSH-trit **(3)** synthesized by stirring **1** in TFA for 30 min at RT to remove the Boc protecting group followed by a basic workup (Scheme A.2). LR ESI-MS (MeOH, RT) and ^1H NMR ($CDCl_3$, RT) are consistent with formation of the trityl-protected, free amine **3**. The ^1H NMR shift of the peptide-NH (~7.5 ppm) and broadness attributed to the amine-NH_2 (~2.0 ppm) serve as positive indicators for the complete removal of TFA from the ligand. In the course of some syntheses of **3**, impurities which manifest themselves as low-intensity aromatic peaks in the ^1H NMR ($CDCl_3$) between 5-7 ppm are present. The impurities can be successfully separated by precipitation in CH_2Cl_2 with hexane; the filtrate is the pure amine **3**.

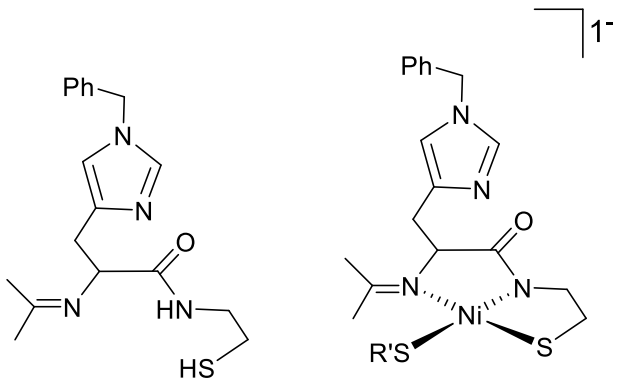

4 **$[Ni(His^{Bz}\text{-}CSH)(SR')]^{1-/0}$**

Figure A.5. The modified $((CH_3)_2)$CN-His^{Bz}-CSH ligand **(4)** and proposed structure of the anion of $[Ni(His^{Bz}\text{-}CSH)(SR')]^{1-}$ resulting from Ni(II) binding of **4.**

Scheme A.2. Synthesis of the imine modified His^{Bz}-CSH ligand **5**.

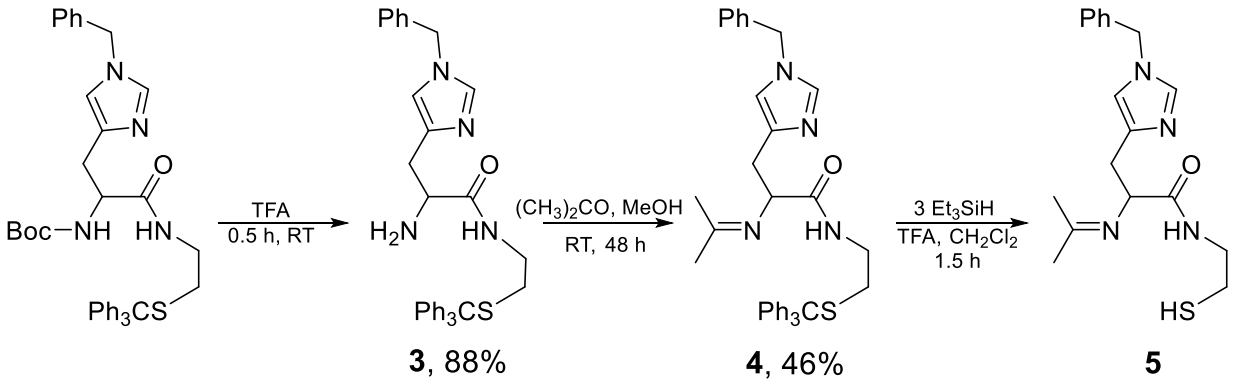

To generate the imine **(4)**, **3** was stirred in 5 mL of dry acetone and 2 mL MeOH with a $CaSO_4$ drying agent for 48 hours at RT. This Schiff base condensation was also carried out successfully in neat acetone at RT and in neat acetone under refluxing conditions yet with no improvement in yield as compared to the acetone/MeOH mixture under dry conditions. Filtration to remove $CaSO_4$, removal of the acetone/MeOH in vacuo, and basic workup yielded the imine in 45-60% yield. ^{1}H NMR ($CDCl_3$, RT) of **4** reveals the disappearance of the broad NH_2 feature and appearance of two CH_3 singlet peaks at 0.89 ppm and 0.95 ppm, attributed to the imine. LR ESI-MS (+) (MeOH, RT) also confirms formation of the product. Trityl deprotection was carried out by stirring **4** in 5 mL CH_2Cl_2 and minimal TFA (~1 mL) for 1.5 h at RT with 3 equivalents Et_3SiH. The TFA and CH_2Cl_2 were removed by vacuum distillation, and the oil was redissolved in 3 mL MeCN and neutralized by stirring with $NaHCO_3$ for ~2 h. Excess $NaHCO_3$ was removed by filtration; Ph_3CH was removed by triturating the concentrate with hexane (**5** has partial solubility in Et_2O). This material is not completely free of impurities, although ^{1}H NMR and LR ESI-MS indicate the presence of the desired product. Further purification is needed before proceeding with metalation of **5**. The design of imine modified His^{Bz}-CSH avoids many of the

complications encountered for the ligand **2** upon addition of Ni(II), namely the persistence of a TFA adduct and potential deprotonation of the primary amine. However, **5** still provides four of the five ligands that are present in NiSOD and can serve as a structural and electronic model for NiSOD.

A.3. Conclusions and future directions

In summary, numerous attempts at coordination of a variety of Ni(II) salts to **2** resulted in ill-defined red-brown Ni complexes that lack the coordination of the peptide-N (FTIR) and appear paramagnetic by ^{1}H NMR (Table 5.1). The partial or incomplete deprotonation of the peptide-NH impedes Ni(II) coordination in the expected manner, and may result in Ni complexes with the His_{Im} bound instead (Figure A.6). Therefore, the synthesis of the His^{Bz}-CSH analogue was modified to afford an imine (**5**), which removes the deprotonatable amine protons (NH_2 in **2**) and forces the N lone pair into the coordination plane. Future directions include metalation of **5** and characterization of the resulting complex, which we hypothesize will serve as a precursor to the development of peptide-based, low molecular weight synthetic analogues of the oxidized, 5C state of NiSOD.

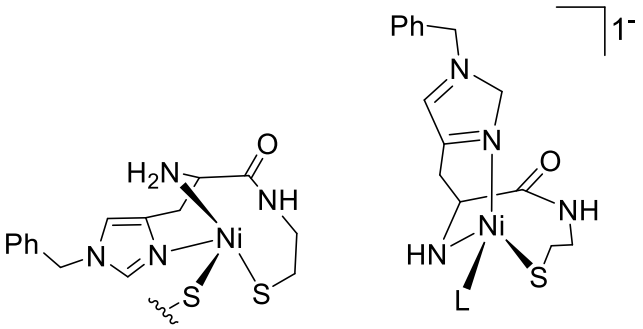

Figure A.6. Two possible structures of Ni complexes resulting from metalation of **2** that are in line with protonated carboxamide-N and paramagnetic ^{1}H NMR.

A.4. Supporting Information

Experimental

General Information. All reagents were purchased from commercial sources and used as received unless otherwise noted. Acetonitrile (MeCN), dichloromethane (CH_2Cl_2), diethyl ether (Et_2O), and pentane were purified by passage through activated alumina columns of an MBraun MB-SPS solvent purification system and stored under an N_2 atmosphere until use. *N*,*N*-dimethylformamide (DMF) was purified with a VAC solvent purifier containing 4 Å molecular sieves and stored under N_2. Methanol (MeOH) was stored over 3 Å molecular sieves for at least one week and degassed using the freeze-pump-thaw method before using. *S*-tritylcysteamine was prepared according to the published procedure.[7,32] All reactions were performed under an inert atmosphere of N_2 using Schlenk line techniques or under an atmosphere of purified N_2 in an MBraun Unilab glovebox.

Physical Methods. Fourier transform infrared (FTIR) spectra were collected on a ThermoNicolet 6700 spectrophotometer running the OMNIC software. All samples were run as

solid samples prepared as pressed KBr pellets. Electronic absorption spectra were collected at 298 K using a Cary-50 spectrophotometer containing a Quantum Northwest TC 125 temperature control unit. The UV-vis samples were prepared in gastight Teflon-lined screw cap quartz cells with an optical pathlength of 1 cm. ^{1}H NMR spectra were recorded in the listed deuterated solvent on a 400 MHz Bruker BZH 400/52 NMR spectrometer or a Varian Unity Inova 500 MHz NMR spectrometer at RT with chemical shifts internally referenced to tetramethylsilane (TMS = $Si(CH_3)_4$), or the residual protio signal of the deuterated solvent.[36] Low-resolution electrospray ionization mass spectrometry (LR ESI-MS) data were collected using a Bruker Esquire 3000 plus ion trap mass spectrometer.

Synthesis of Boc-His(Bzl)-CS-trit (1). To a 3 mL CH_2Cl_2 solution of Boc-His(Bzl)-OH (0.3910, 1.132 mmol) was added 0.1279 g (1.113 mmol) *N*-hydroxysuccinimide in 2 mL CH_2Cl_2 at 0 °C under an N_2 atmosphere. The clear solution was allowed to stir for ~15 min at 0 °C, and to it was added 0.1279 g (1.124 mmol) 1-ethyl-3-(3-dimethylaminopropyl)carbodiimide hydrochloride (EDC·HCl), and the solution stirred for an additional 15 min. To this solution was added 1 equiv *S*-tritylcysteamine (0.3605 g, 1.128 mmol), and the solution stirred for 1 h at 0 °C under N_2. After 24 h stirring at RT, the solution was diluted with CH_2Cl_2 to 100 mL, washed with $NaHCO_3$ satd., NaCl satd., dried over $MgSO_4$, and filtered. The solvent was removed in vacuo to yield 0.6233 g of a white foam, which was purified on silica (THF:DCM, 1:1, R_f = 1.0) to yield 0.5035 g (0.7784 mmol, 69%) of a white solid. ^{1}H NMR (500 MHz, $CDCl_3$ containing 0.05% v/v TMS, δ from solvent): 7.19-7.37 (m, 5H, integrates high due to residual protio solvent), 7.07 (m, 2H), 6.83 (s, 1H), 6.65 (s, 1H), 6.27 (s, 1H), 4.89 (s, 2H, benzyl-CH_2), 4.33 (t, 1H, J = 10 Hz), 3.08 (m, 1H), 2.94 (m, 2H), 2.82 (dd, 1H, J = 10 Hz), 2.27 (t, 2H, J = 10 Hz), 1.39 (s, 9H, Boc). ^{13}C NMR (125 MHz, $CDCl_3$ containing 0.05% v/v TMS, δ from solvent),

171.56 (C=O), 155.67 (C=O), 144.57, 138.44, 136.74, 135.95, 129.62-126.64, 117.27, 68.86, 64.44, 50.78, 38.14, 31.79, 30.50, 28.35, 25.37. FTIR (KBr pellet) ν_{max} (cm^{-1}) 3304 (m), 3056 (m), 2973 (m), 2927 (m), 1780 (m), 1710 (vs, ν_{CO}), 1666 (vs, ν_{CO} peptide), 1491 (s), 1433 (m), 1384 (s), 1246 (m), 1165 (s), 1025 (m), 855 (w), 744 (s), 700 (vs), 620 (m). LR ESI-MS (MeOH) *m/z* $[M+H]^+$ calcd for $C_{39}H_{43}N_4O_3S$, 647.3 (100.0), 648.3 (43.7), 648.3 (12.9); found, 647.4 (100.0), 648.4 (42.2), 648.4 (8.7).

Synthesis of His(Bzyl)-CSH (2). To a 7 mL CH_2Cl_2 solution of **1** (0.4353 g, 0.6730 mmol) was added 4 mL TFA which resulted in a bright yellow solution. To it was added Et_3SiH (0.35 mL, 2.1 mmol) and the color bleached. The solution stirred for 1.5 h under N_2, and the CH_2Cl_2 was removed by vacuum distillation. Insoluble Ph_3CH was filtered off, and the remaining TFA was removed by vacuum distillation from the filtrate. The beige oil was dissolved in ~8 mL MeCN and stirred in K_2CO_3 for 1.5 h to remove excess TFA. The Na_2CO_3 was removed by filtration, and the MeCN was removed in vacuo to yield an oily solid. The solid was triturated with Et_2O to remove any Ph_3CH and dried to yield **2** in quantitative yield. ^1H NMR (400 MHz, $CDCl_3$ containing 0.05% v/v TMS, δ from solvent) 8.40 (s, 1H), 8.15 (s, 1H) 7.46 (d, 3H, J = 4 Hz), 7.30 (m, 6H, integrates high due to residual protio solvent), 7.10 (s, 1H), 5.21 (t, 2H, benzyl-CH_2, J = 4 Hz), 4.56 (s, 1H), 3.49-3.30 (m, 4H), 2.57 (t, 2H, J = 4 Hz), 1.41 (t, 1H, S*H*, J = 4 Hz). ^{13}C NMR (125 MHz, CD_3CN, RT, δ from solvent). 169.11 (C=O), 136.13, 135.14, 130.42, 130.02, 130.00, 129.83, 129.81, 129.27, 53.47, 43.60, 27.98, 23.99. FTIR (KBr pellet) ν_{max} (cm^{-1}) 3108 (w), 2937 (w), 1681 (s, ν_{CO}), 1505 (w), 1442 (m), 1209 (vs), 1136 (vs), 844 (vs), 803 (vs), 725 (vs), 518 (m). LR ESI-MS (MeOH) *m/z* $[M+H]^+$ calcd for $C_{15}H_{21}N_4OS$, 305.1 (100), 306.1 (17.7), 307.1 (5.3); found 305.2 (100), 306.2 (21.4), 307.2 (5.2).

General procedure for the metalation of 2 (see Table 5.1). The conditions, Ni(II) salt, and base (if applicable) used in selected metalation reactions are listed in Table 5.1. To a solution of **2** was added base equivalents and the beige solution stirred for 15 min with no visible changes. To the solution was added one equiv Ni(II) salt in approximately 2 mL of additional solvent. A red-brown color appeared within 5 min of addition, and the mixture was allowed to stir for 1-18 h. The solvent was removed in vacuo to yield a red-brown residue. Sodium or potassium salts, if present, were removed by filtering MeCN solutions of the red-brown material.

Synthesis of H_2N-His(Bzl)-CS-trit (3). To a 5 mL CH_2Cl_2 solution of **1** (0.3962 g, 0.6125 mmol) was added 3 mL of TFA to deprotect the acid-sensitive Boc group. The orange solution stirred for ~ 0.5 h, and the solvent was removed by vacuum distillation. The resulting orange oil was dissolved in 100 mL of CH_2Cl_2, and to it was added 100 mL of deionized H_2O and K_2CO_3 until the organic layer was basic and effervescence stopped. The organic water was separated, washed with $NaHCO_3$ satd., NaCL satd., dried over $MgSO_4$ anhydrous, and filtered. The solvent was removed in vacuo to yield 0.2952 g (0.5399 mmol) of **3** (88%). ^{1}H NMR (500 MHz, $CDCl_3$ containing 0.05% v/v TMS, δ from solvent) 7.49 (t, 1H, J = 5 Hz), 7.39-7.16 (m, 30H, integrates high due to residual protio solvent), 7.08 (d, 2H, J = 10 Hz), 4.95 (s, 2H, benzyl-CH_2), 3.51 (t, 1H, J = 5 Hz), 3.05-2.93 (m, 4H), 2.76 (m, 1H), 2.31 (m, 2H), 1.98 (br, 2H, NH_2). FTIR (KBr pellet) ν_{max} (cm^{-1}) 3396 (w), 2963 (w), 2922 (w), 1770 (w), 1653 (m, ν_{CO}), 1558 (w), 1489 (w) 1443 (w), 1262 (s), 1095 (vs), 1023 (vs), 801 (vs), 742 (w), 698 (m). LR ESI-MS (CH_2Cl_2) *m/z* $[M+H]^+$ calcd for $C_{34}H_{35}N_4OS$, 547.2 (100), 548.2 (39.1), 549.2 (12.3); found 547.3 (100), 548.3 (38.1), 549.3 (10.7).

Synthesis of ($(CH_3)_2$CN)-His(Bzl)-CS-trit (4). To a 6 mL solution acetone/MeOH (2:1) was added **3** (0.3115 g, 0.5698 mmol) and $CaSO_4$ under an N_2 atmosphere. The mixture stirred

for 18 h under N_2, and the $CaSO_4$ was removed by filtration. The solvent was removed in vacuo to yield a white foam, which was then dissolved in 25 mL CH_2Cl_2, washed with $NaHCO_3$ satd., brine, and dried over anhydrous $MgSO_4$. The solvent was removed to yield 0.1522 g (0.2596 mmol) of **4** (46%). ^{1}H NMR (400 MHz, $CDCl_3$ containing 0.05% v/v TMS, δ from solvent) 7.39-7.17 (m, 7H, integrates high due to residual protio solvent), 7.03 (d, 1H, J = 4 Hz), 6.67 (s, 1H), 4.86 (s, 2H, benzyl-CH_2), 3.60 (t, 1H, J = 4 Hz), 2.98-2.89 (m, 4H), 2.62 (m, 1H), 2.42 (m, 1H) 2.28 (m, 2H), 0.95 (s, 3H, imine-CH_3), 0.89 (s, 3H, imine-CH_3). LR ESI-MS (CH_2Cl_2) *m/z* $[M+H]^+$ calcd for $C_{37}H_{39}N_4OS$, 587.3 (100.0), 588.3 (42.8), 589.3 (13.6); found 587.3 (100.0), 588.3 (43.2), 589.3 (13.9).

Synthesis of ($(CH_3)_2$CN)-His(Bzl)-CSH (5). To a 4 mL CH_2Cl_2 solution of **4** (0.1522 g, 0.2596 mmol) was added 2 mL TFA and 3 equiv Et_3SiH (0.125 mL, 0.778 mmol). The pale beige solution stirred for 1.5 h, and the solvent was removed by vacuum filtration. The beige oil was triturated with hexane to remove Ph_3CH and then dissolved in 3 mL MeCN and stirred with excess $NaHCO_3$ for 2 h to neutralize the TFA. The remaining $NaHCO_3$ was removed by filtration and the MeCN filtrate was taken to dryness. Additional triturations with Et_2O removed the remaning Ph_3CH. The product still has impurities present, and further purification is necessary. ^{1}H NMR and LR ESI-MS (*m/z* 345.2) indicate the presence of **5**. ^{1}H NMR (400 MHz, CD_3CN, δ from solvent) 8.09 (m), 7.37-7.11 (m), 6.95 (t), 5.10 (m), 4.26 (m), 3.75 (m), 3.30 (m), 3.08 (m), 2.98 (m), 2.65 (d, 1H, J = 4 Hz), 2.44 (s, 1H), 1.91 (s, 3H), 1.84 (s, 3H), 1.51 (t, J = 8 Hz), 0.090 (t, J = 8 Hz). LR ESI-MS (CH_2Cl_2) *m/z* $[M+H]^+$ calcd for $C_{18}H_{25}N_4OS$, 345.2 (100), 346.2 (21.0), 347.2 (6.3); found 345.2 (100.0), 346.2 (12.0), 347.2 (20.5).

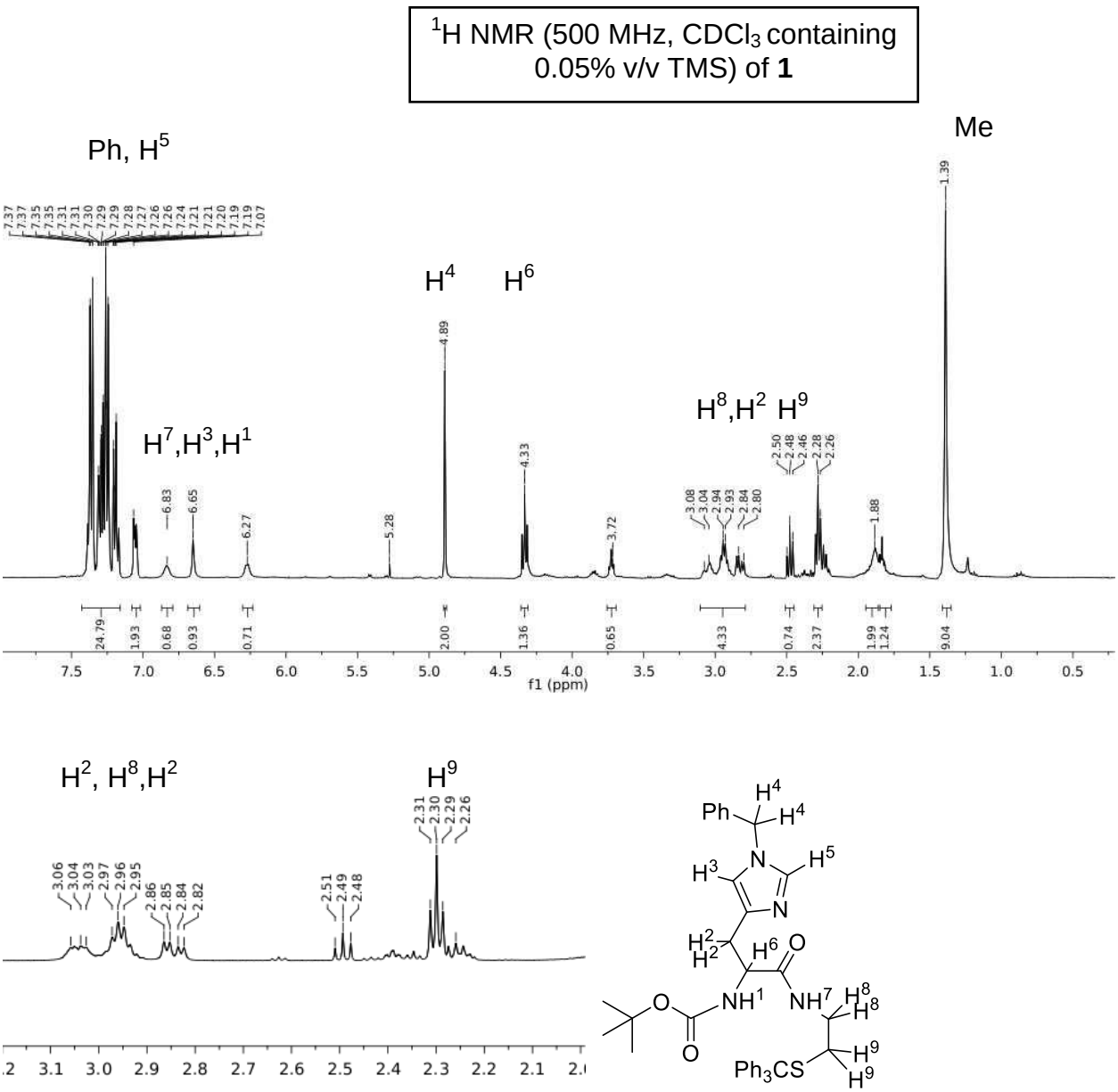

Figure AS.1. *Top:* ^{1}H NMR of **1** in $CDCl_3$ containing 0.05% v/v TMS at RT (δ vs residual protio solvent signal). Residual protio solvent (7.26 ppm), CH_2Cl_2, H_2O and THF from workup are also present (5.28, 1.88, 1.85, and 3.72). *Bottom*: expansion of the aliphatic region.

^{13}C NMR (125 MHz, $CDCl_3$ containing 0.05% v/v TMS) of **1**

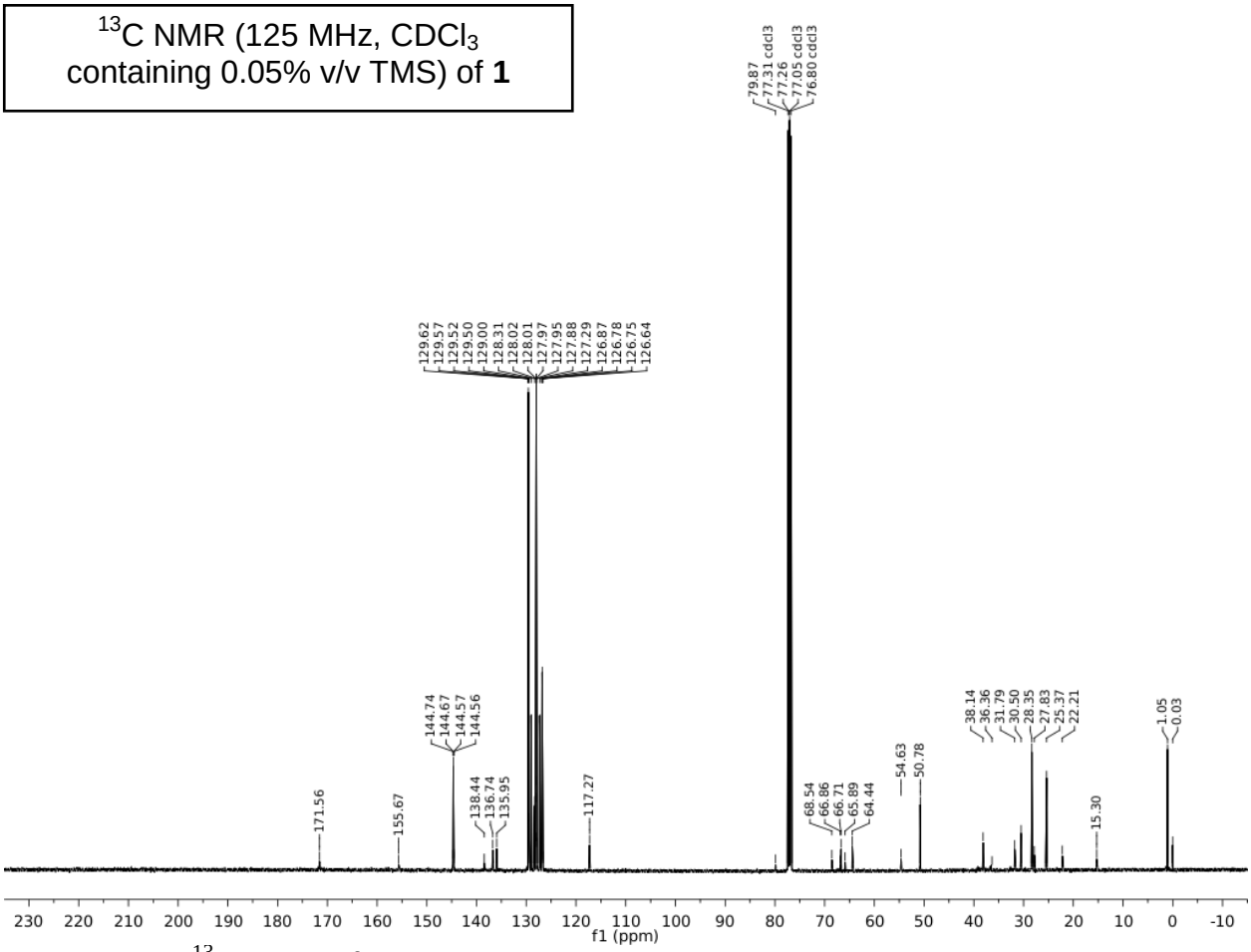

Figure AS.2. ^{13}C NMR of **1** in $CDCl_3$ containing 0.05% v/v TMS at RT. Residual $CDCl_3$ is present (77.26 ppm). Residual Et_2O (65.89, 15.30 ppm) and CH_2Cl_2 from workup are also present (54.63 ppm)

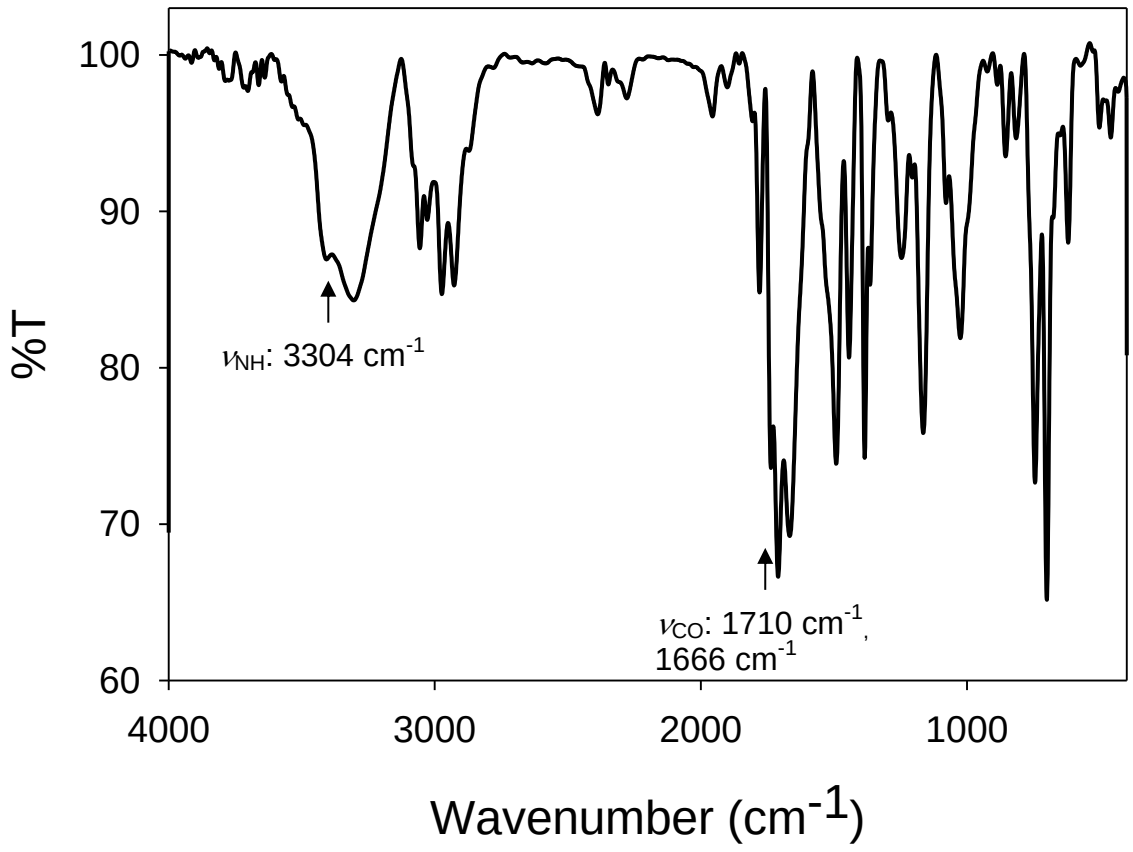

Figure AS.3. Solid-state FTIR (KBr pellet, RT) of **1**.

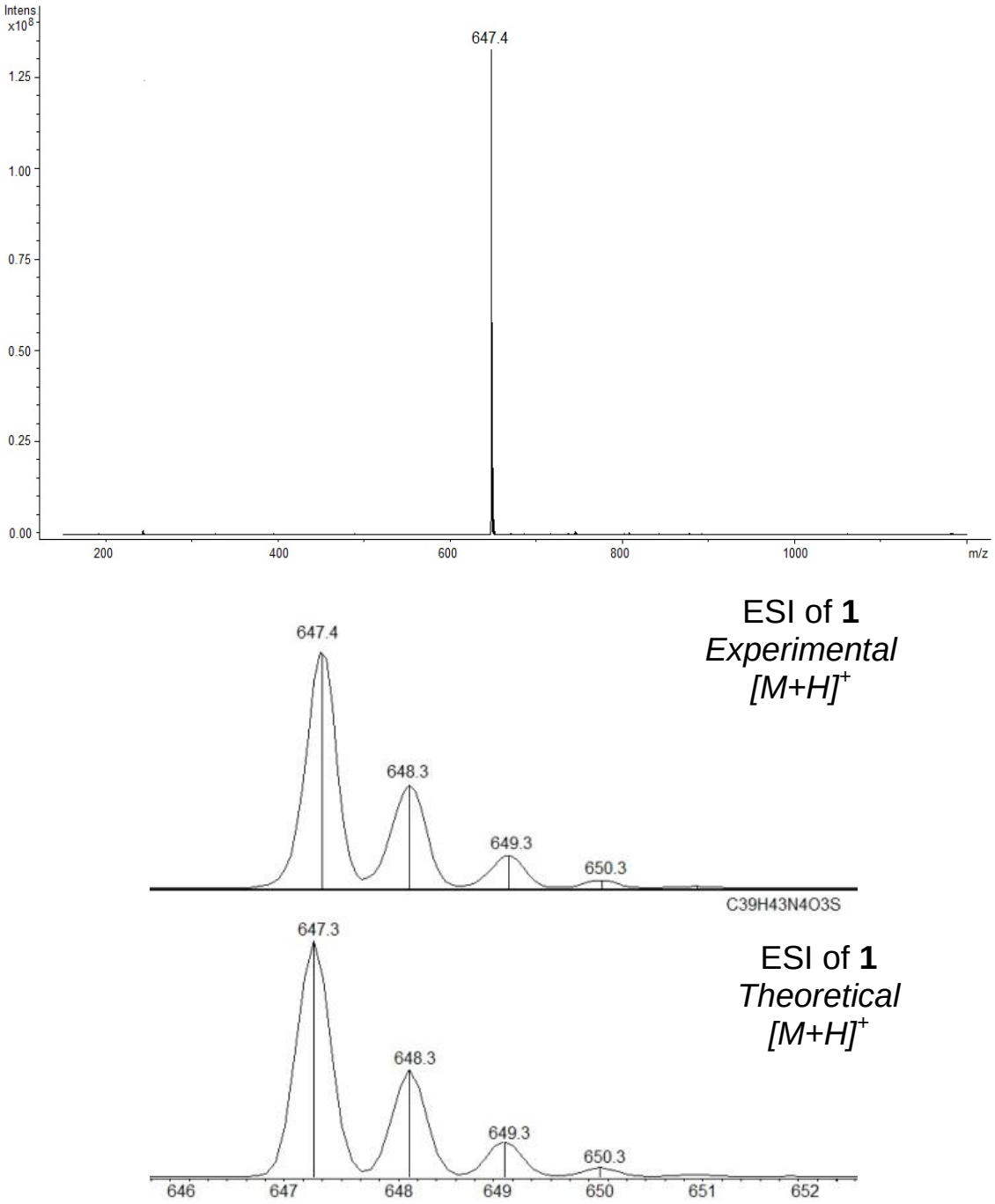

Figure AS.4. Low resolution ESI-MS (positive mode) of **1** (top). Middle and bottom represent a zoom-in of the *m/z* 647.4 peak. Theoretical fit on the bottom.

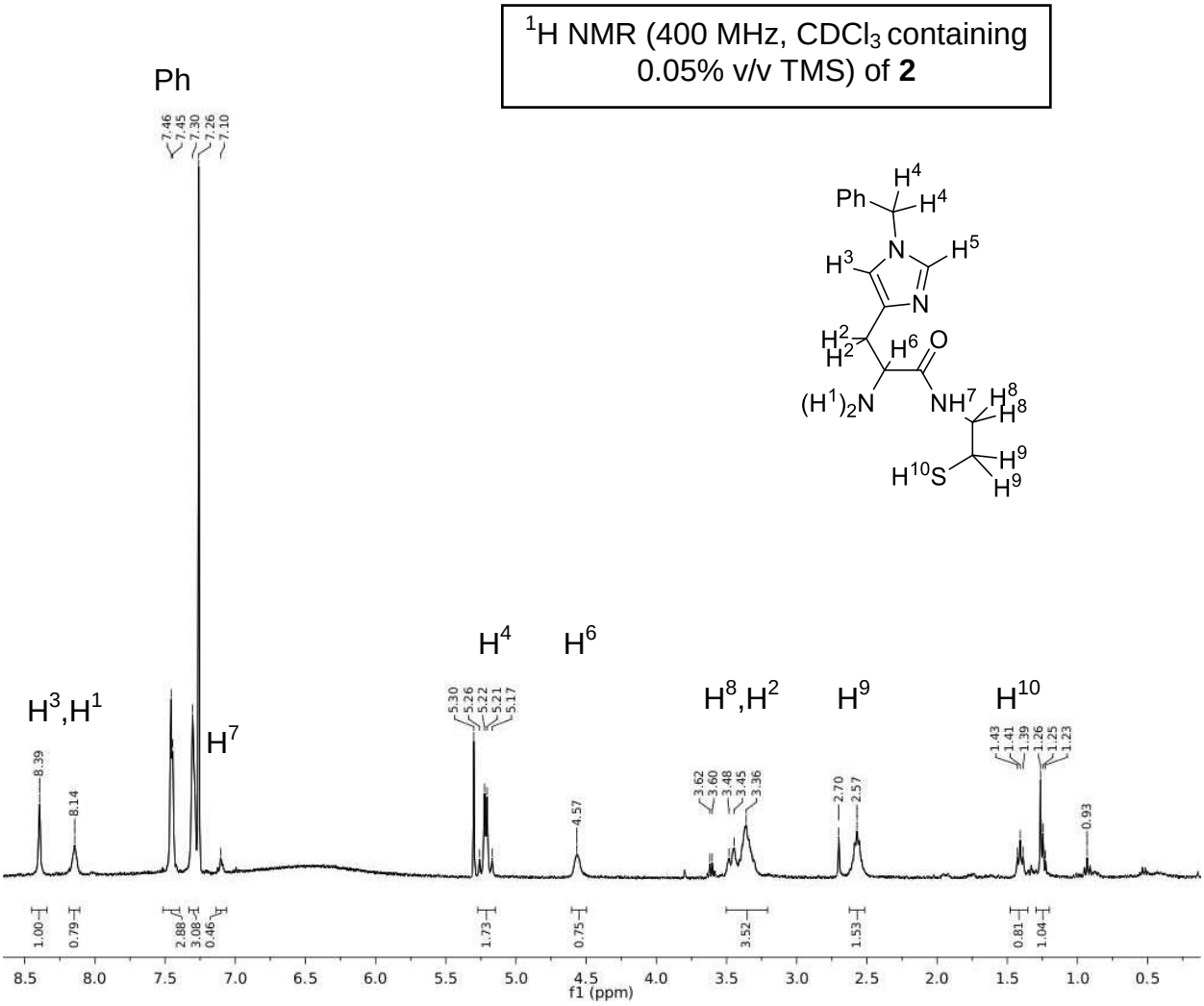

Figure AS.5. ^{1}H NMR of **2** in $CDCl_3$ containing 0.05% v/v TMS at RT (δ vs residual protio solvent signal). TFA is present, as indicated by the broadness at ~6.5 ppm, the imidazole-H at ~8.4 ppm, and the benzyl-CH_2 appearing as a triplet at 5.2 ppm. Residual protio solvent (7.26 ppm), CH_2Cl_2, and Et_2O from workup are also present (5.3, 3.50, 1.25 ppm).

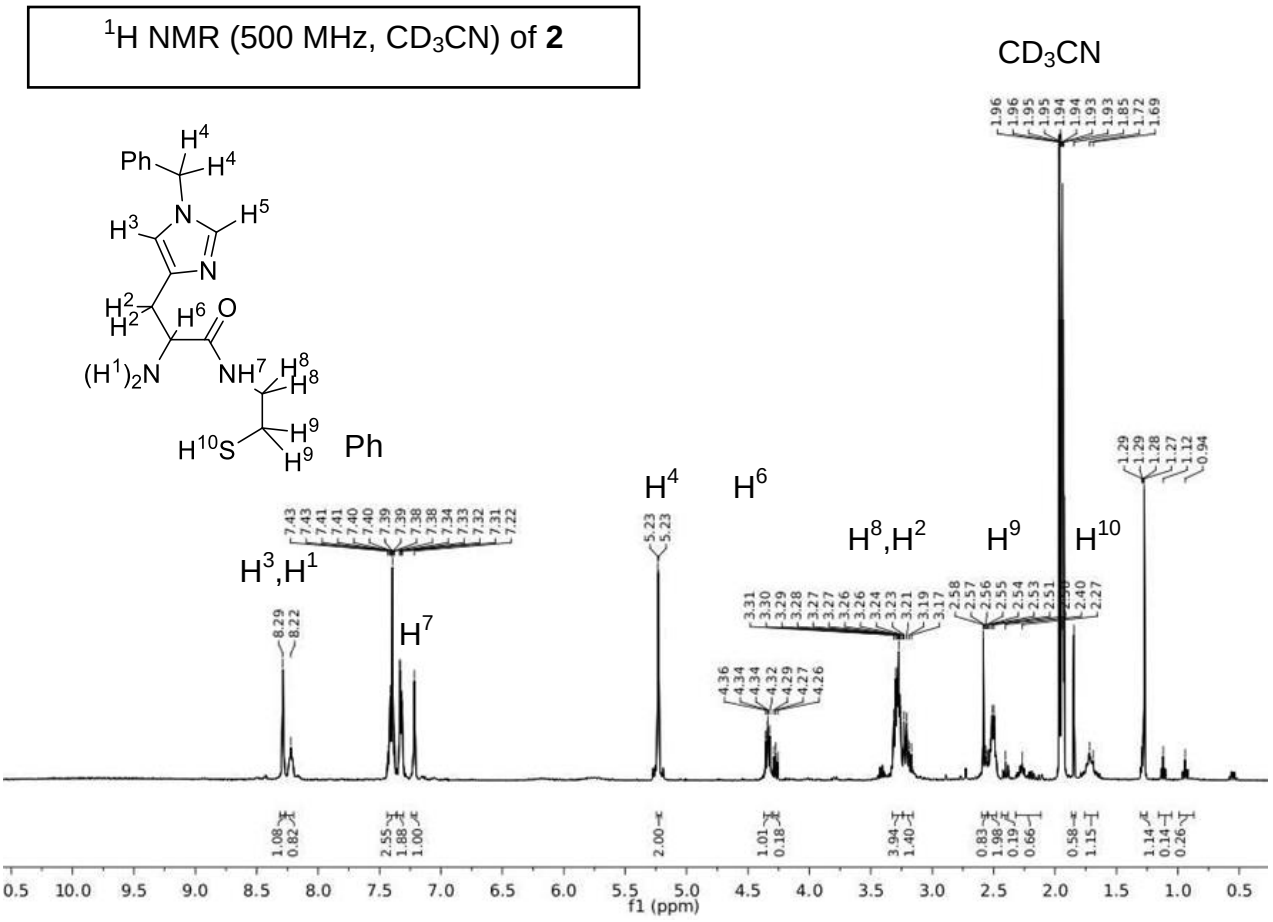

Figure AS.6. ^{1}H NMR of **2** in CD_3CN at RT (δ vs residual protio solvent signal), after stirring a second time in Na_2CO_3 to remove TFA, as indicated by the absence of the broad feature. Residual protio solvent (1.94 ppm) and other residual solvents are present (1.84, 2.27, and 4.26 ppm). Unidentified impurities are also present.

^{13}C NMR (125 MHz, CD_3CN)
of **2**

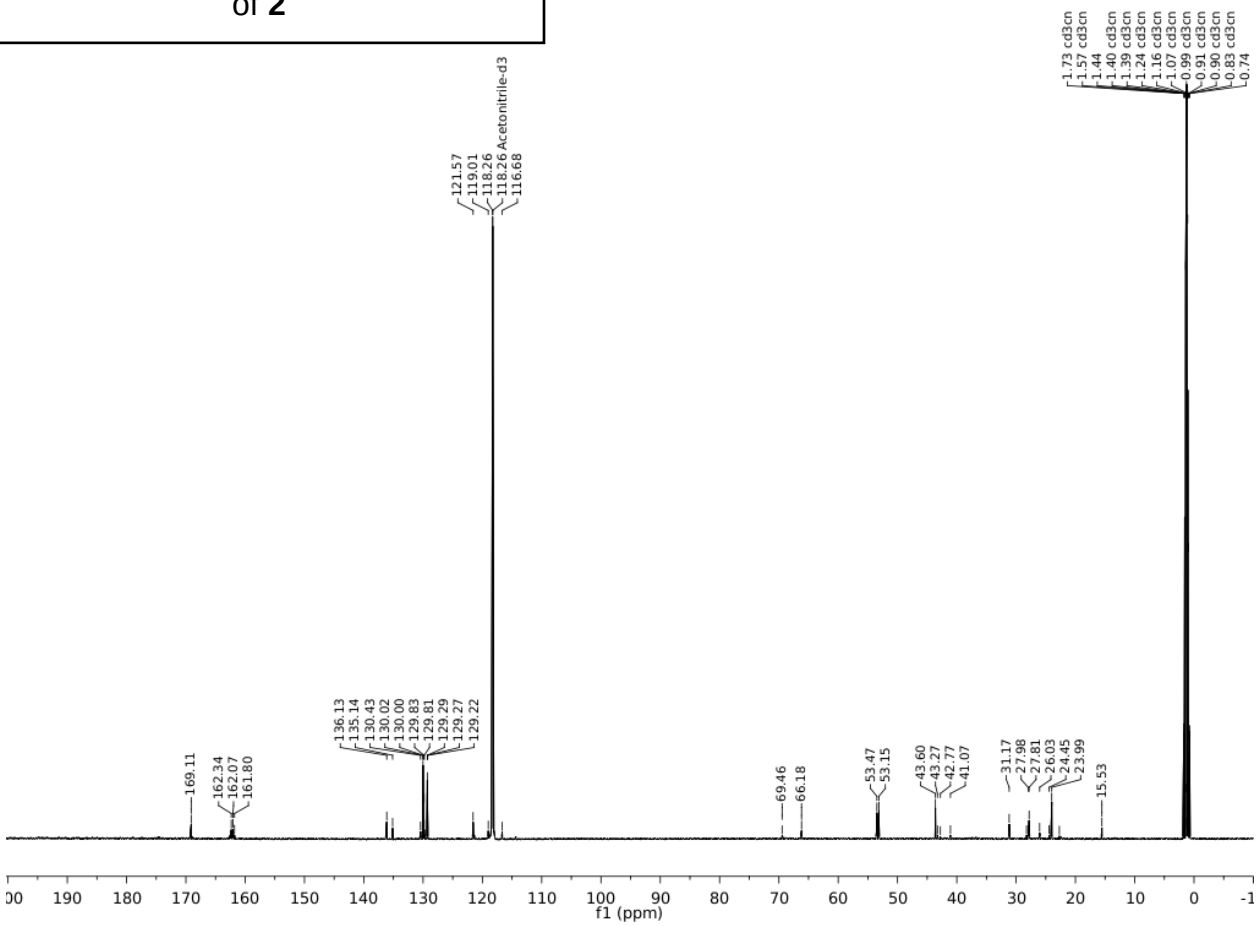

Figure AS.7. ^{13}C NMR (CD_3CN, RT, 125 MHz) of **2** provides definitive evidence for a TFA adduct with a quartet at 162 ppm (J = 20 Hz, through-bond ^{13}C to ^{19}F coupling) and a quartet at 118.1 ppm (J = 291 Hz, ^{13}C to ^{19}F coupling). Residual CD_3CN is present (118.3, 1.07 ppm); Et_2O, THF, and hexane are also present (66.2, 15.5, 69.5, 26.0, 31.6, 22.7 ppm)

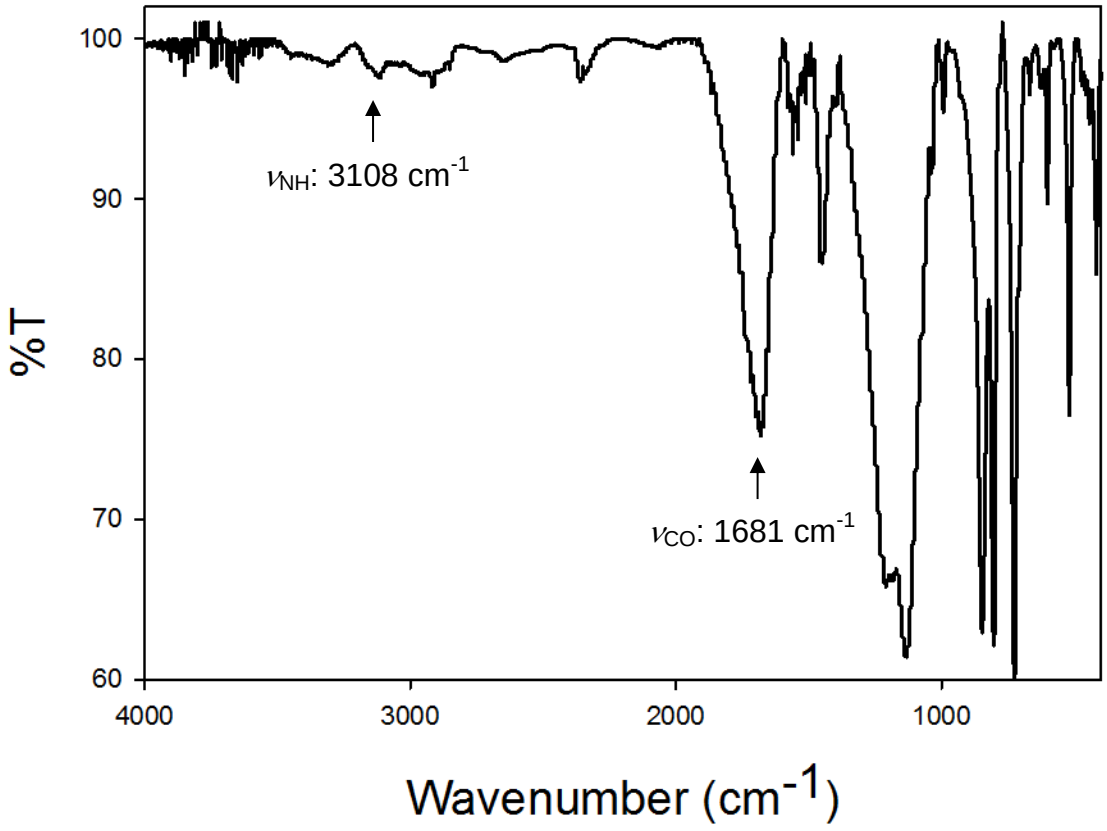

Figure AS.8. Solid-state FTIR (KBr pellet, RT) of **2**.

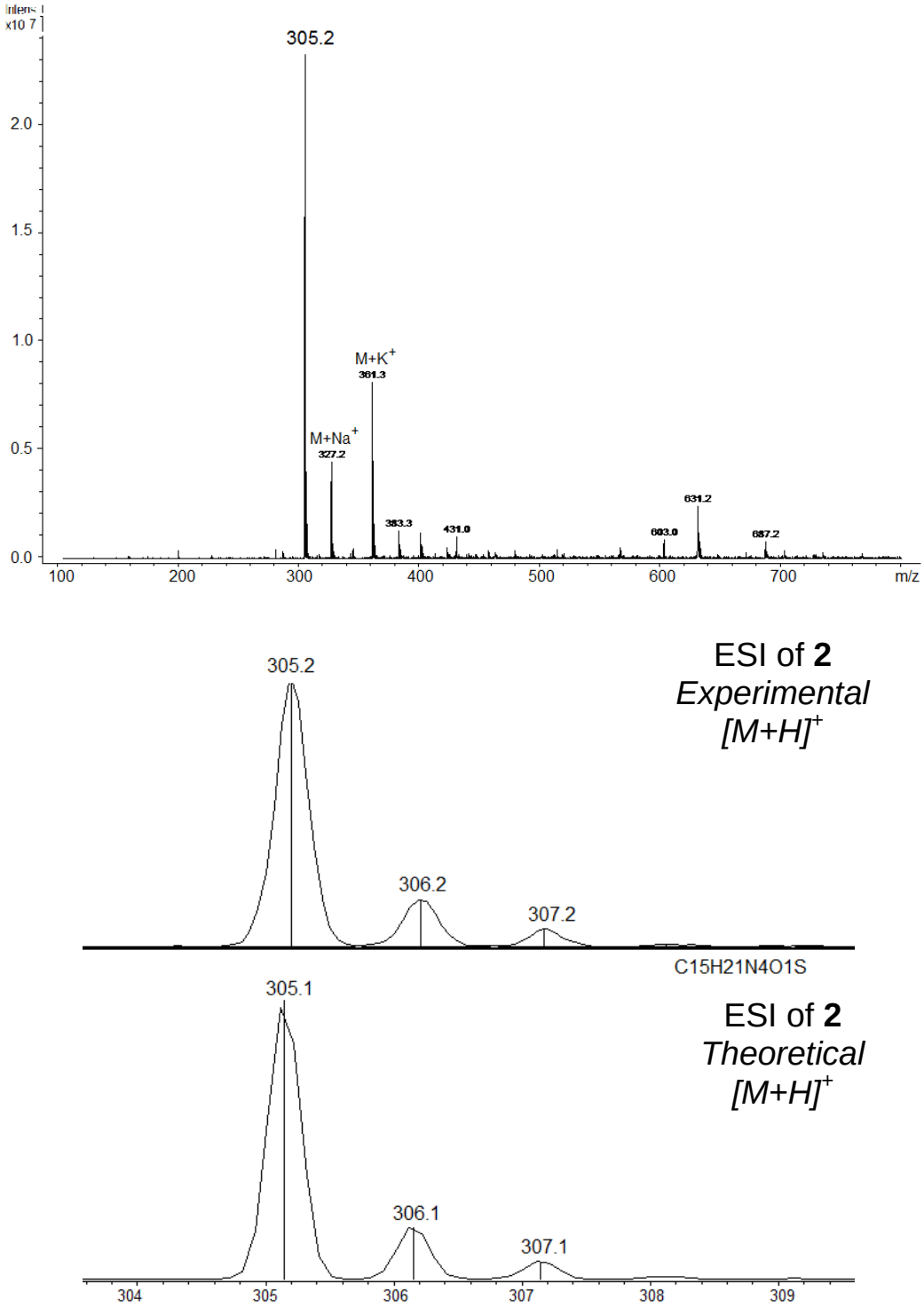

Figure AS.9. Low resolution ESI-MS (positive mode) of **2** (top). Middle and bottom represent a zoom-in of the *m/z* 305.2 peak. Theoretical fit on the bottom.

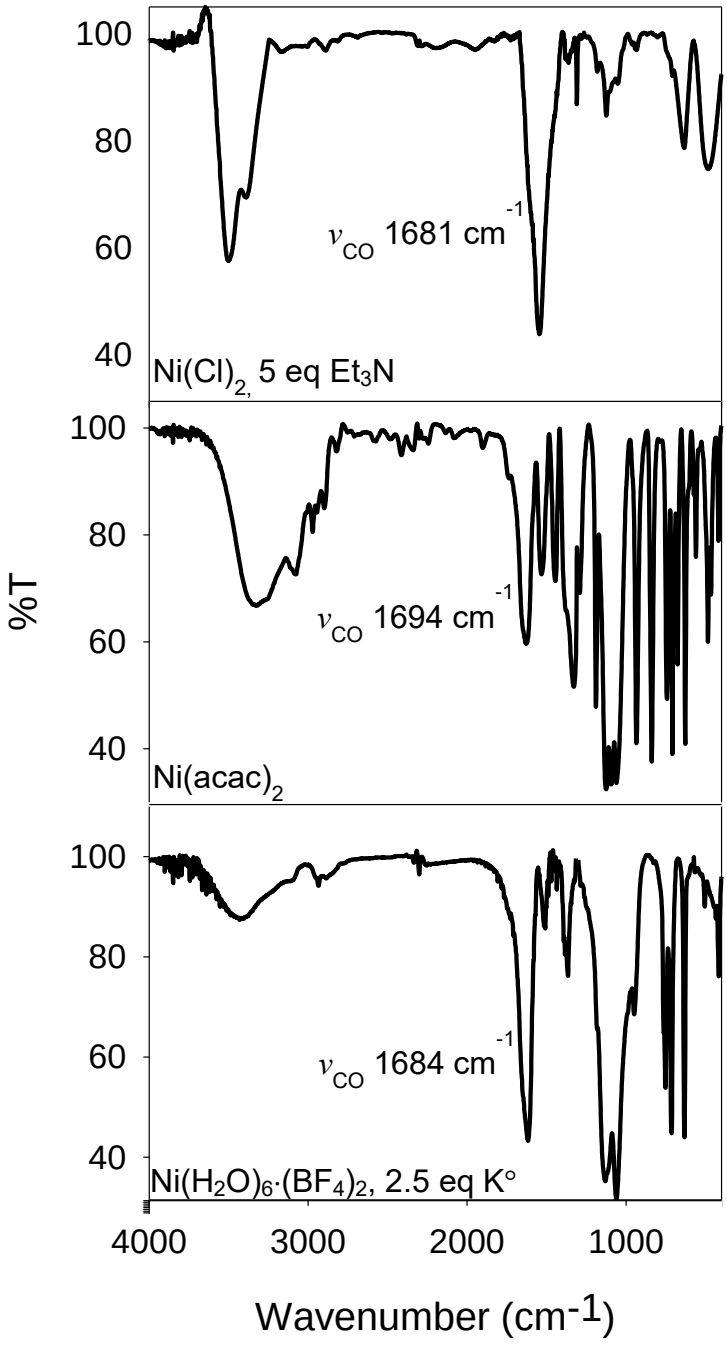

Figure AS.10. Solid-state FTIR spectrum (KBr pellet, RT) of the reaction of **2** and Ni(II) salts. The expected ~50 cm^{-1} ν_{CO} red-shift for carboxamide-N coordination was absent in all conditions (see Table 5.1).

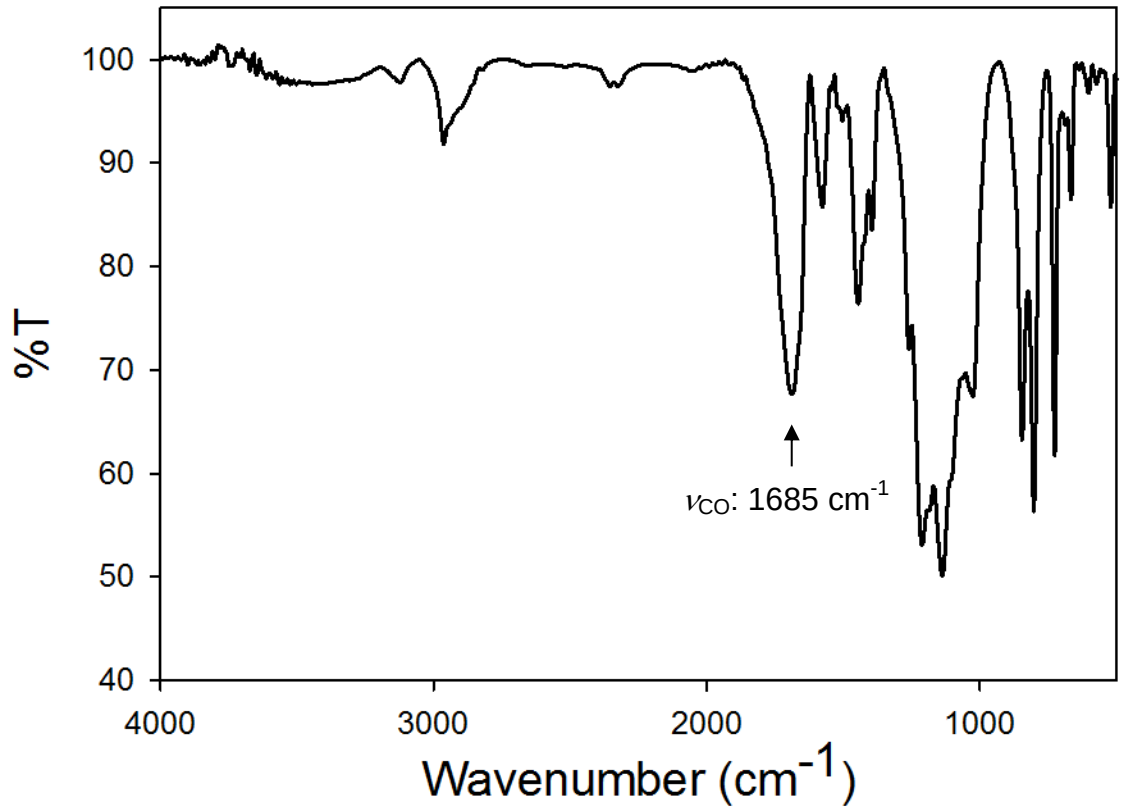

Figure AS.11. Solid-state FTIR spectrum (KBr pellet, RT) of the reaction of **2**, 2.25 equiv KH, and $[Ni(H_2O)_6](BF_4)_2$ in DMF. The expected ~50 cm^{-1} ν_{CO} red-shift for carboxamide-N coordination is absent.

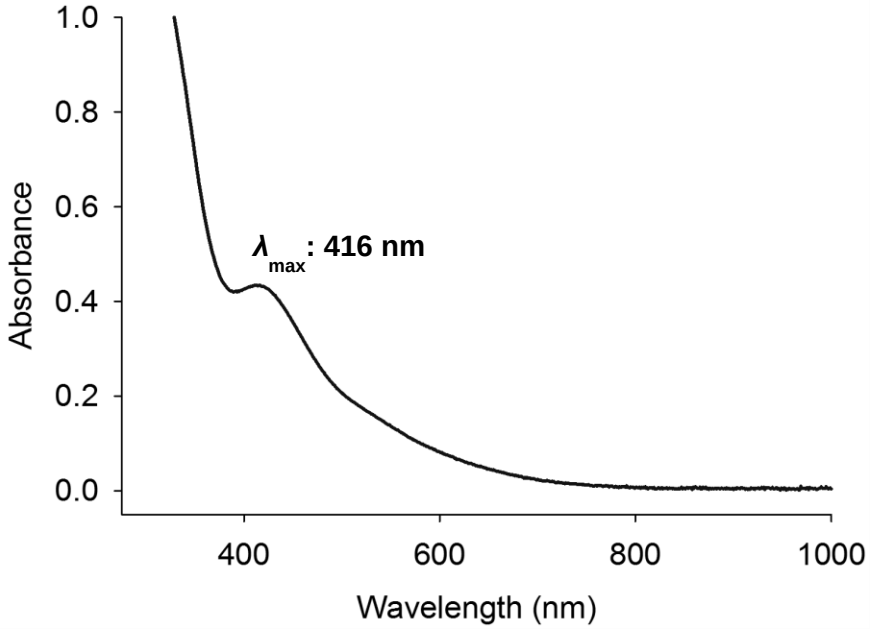

Figure AS.12. UV-vis spectrum of the complex resulting from the reaction of **2** with 2.25 NaH and $[Ni(H_2O)_6](BF_4)_2$ in DMF, RT.

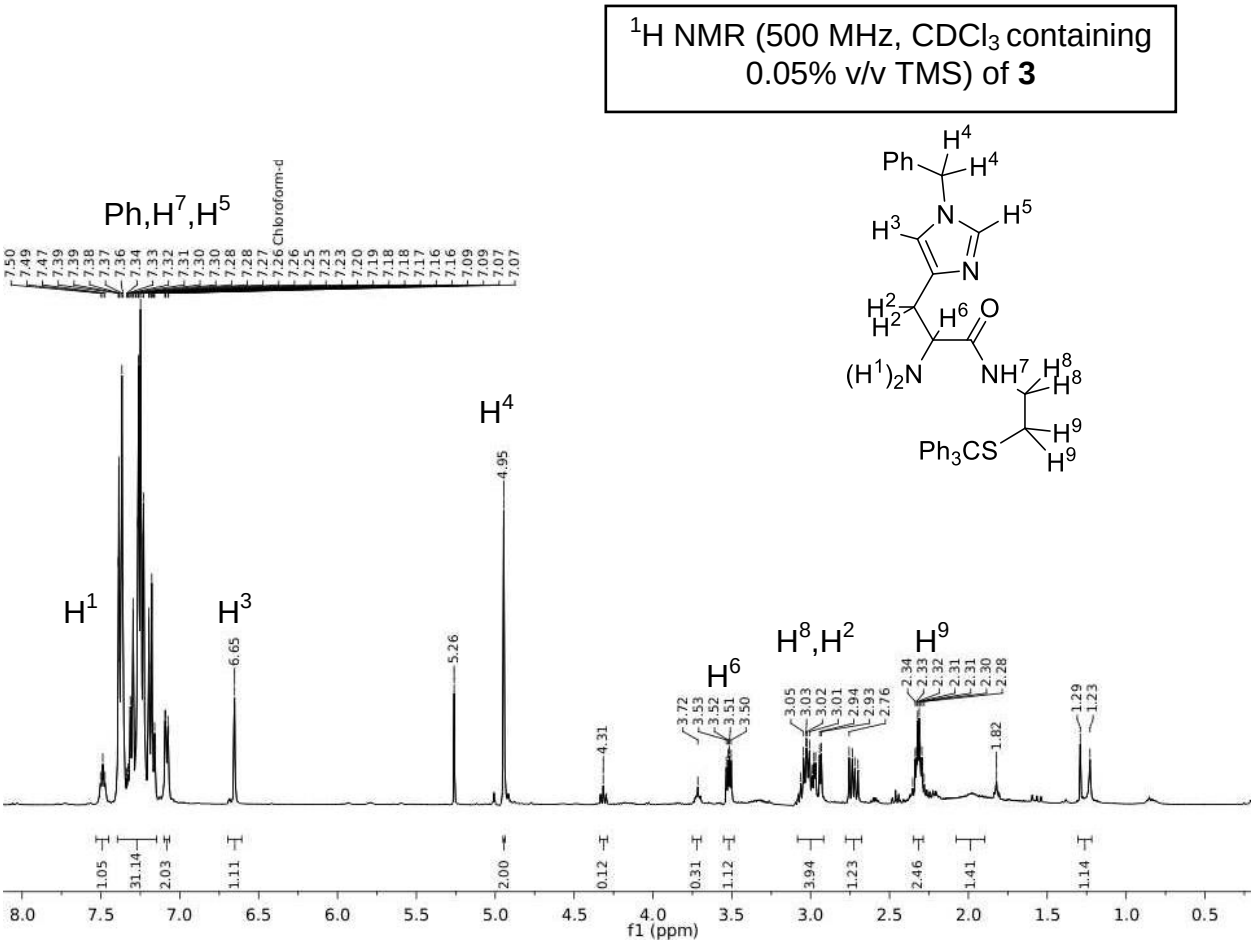

Figure AS.13. ^{1}H NMR of **3** in $CDCl_3$ containing 0.05% v/v TMS at RT (δ vs residual protio solvent signal). Residual protio solvent (7.26 ppm) and other solvents from workup are also present (1.82, 3.53, and 5.26 ppm). *t*-BuOH is present at 1.23 ppm

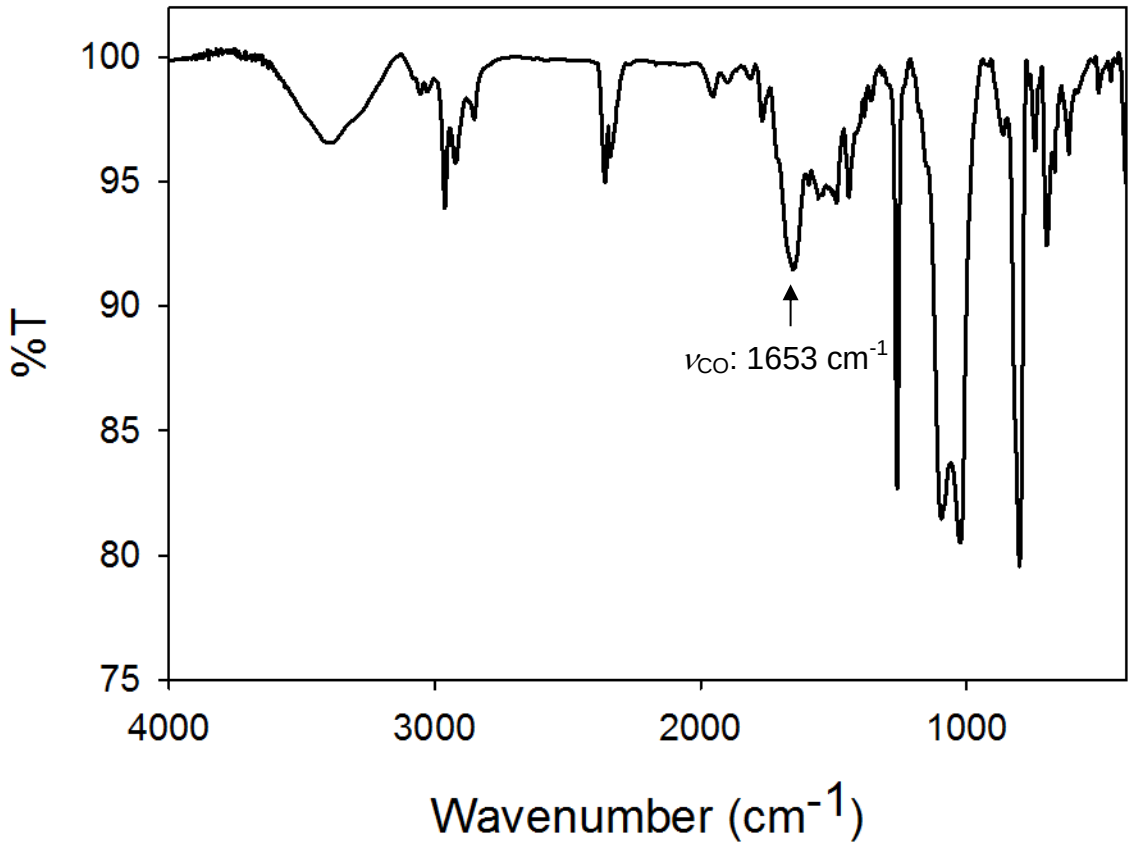

Figure AS.14. FTIR (KBr pellet, RT) of **3**.

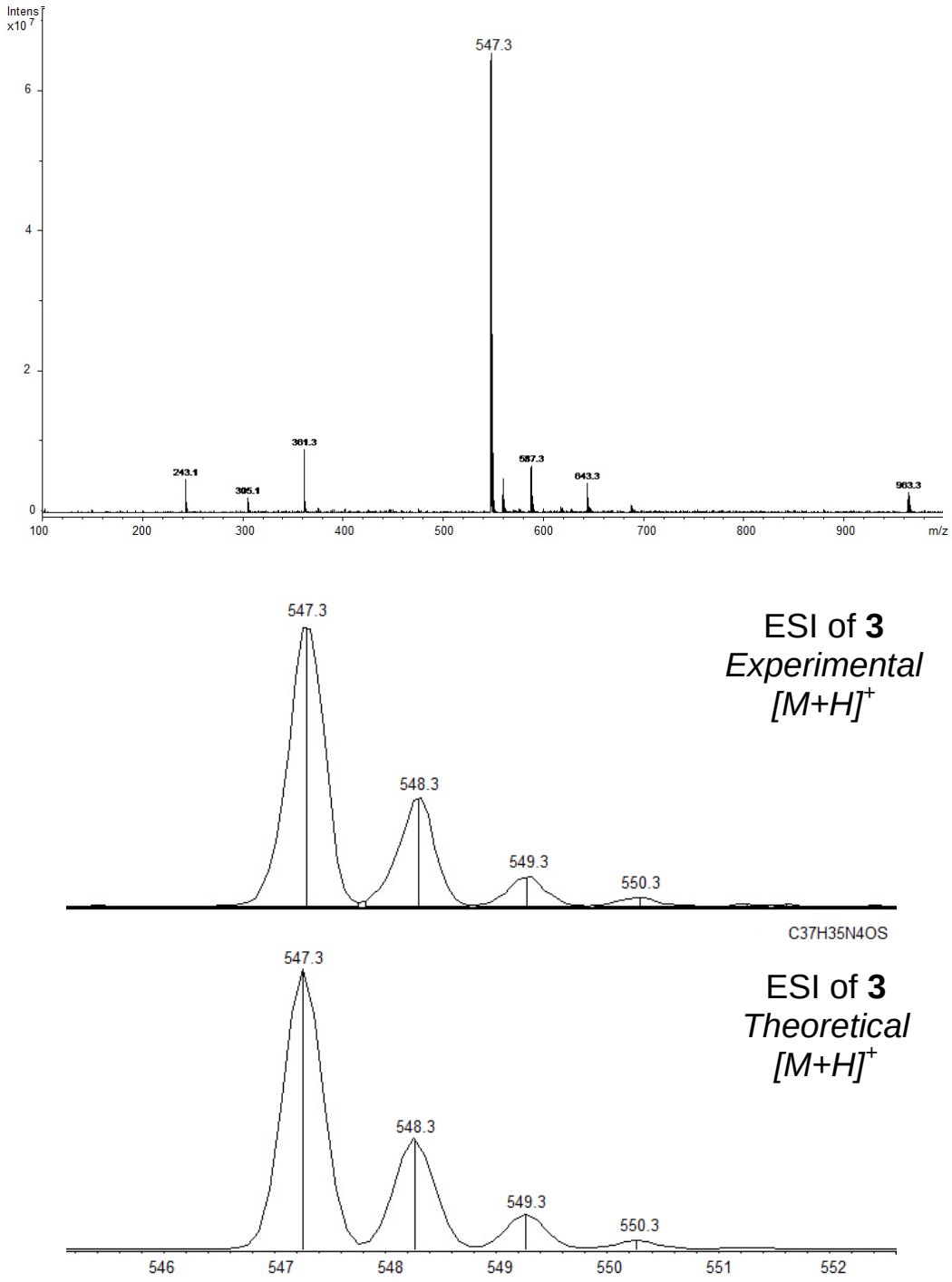

Figure AS.15. Low resolution ESI-MS (positive mode) of **3** (top). Middle and bottom represent a zoom-in of the *m/z* 547.3 peak. Theoretical fit on the bottom.

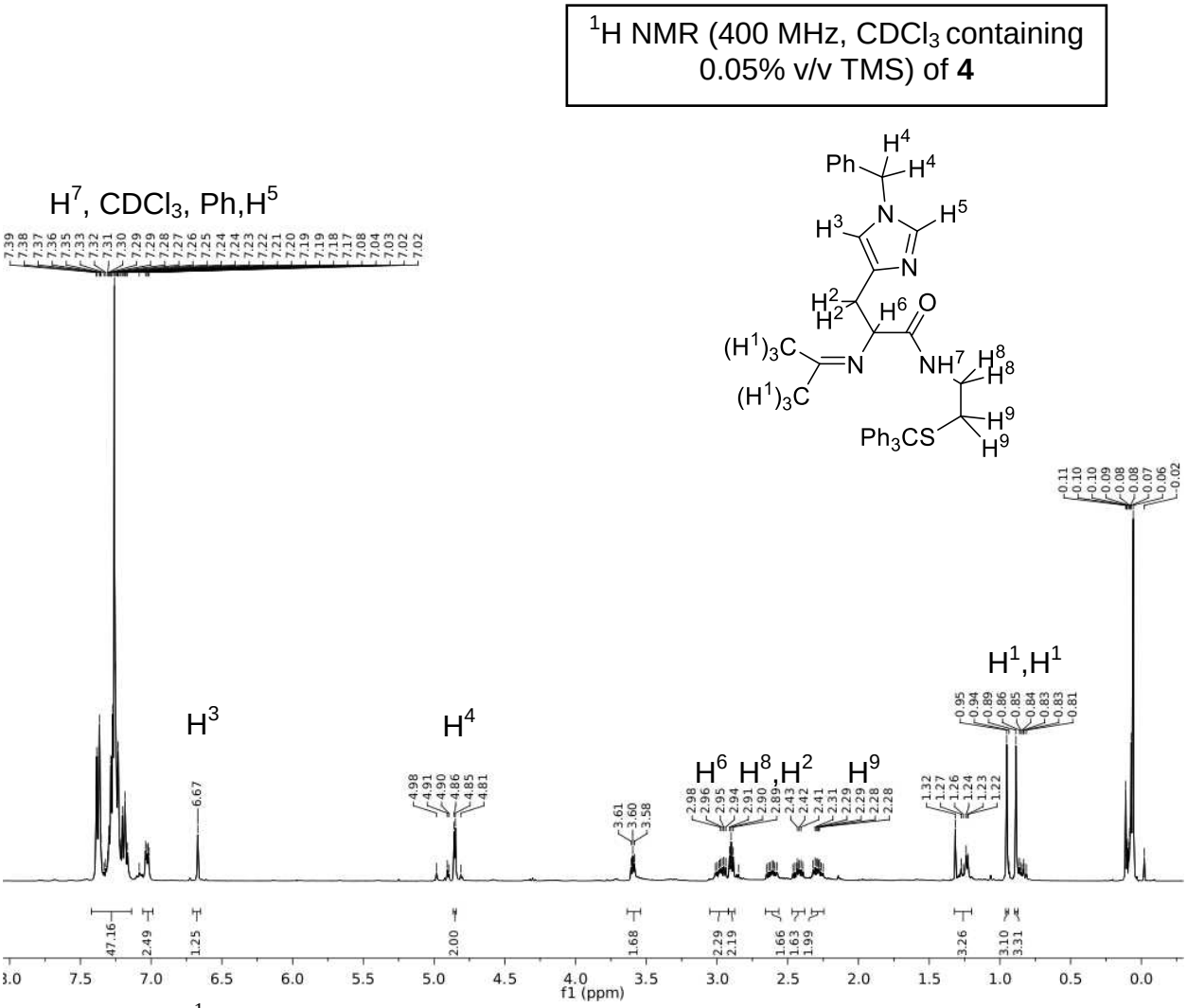

Figure AS.16. ^{1}H NMR of **4** in $CDCl_3$ containing 0.05% v/v TMS at RT (δ vs residual protio solvent signal). Residual protio solvent (7.26 ppm) is present.

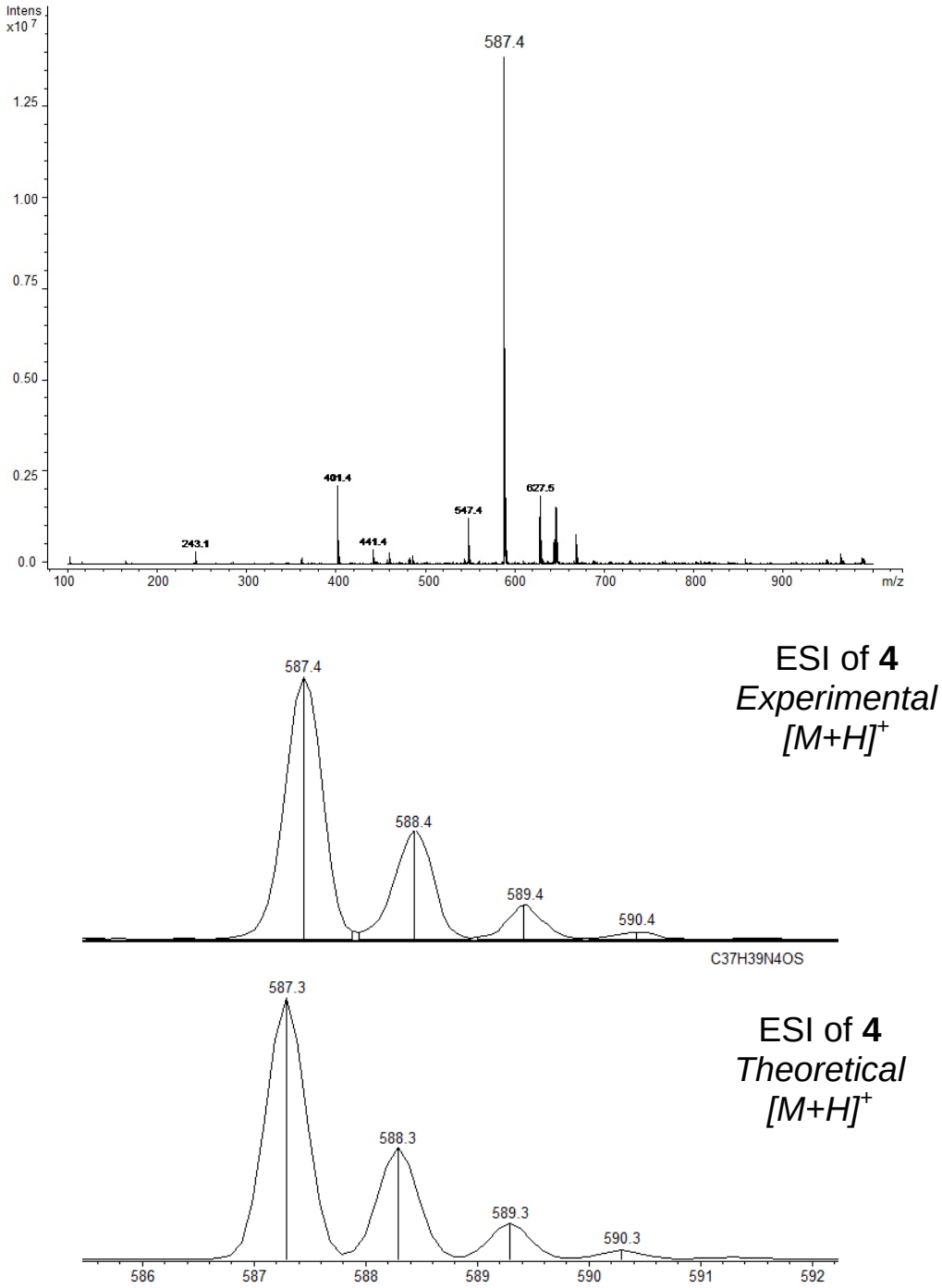

Figure AS.17. Low resolution ESI-MS (positive mode) of **4** (top). Middle and bottom represent a zoom-in of the *m/z* 587.4 peak. Theoretical fit on the bottom.

^{1}H NMR (400 MHz, CD_3CN) of **5**

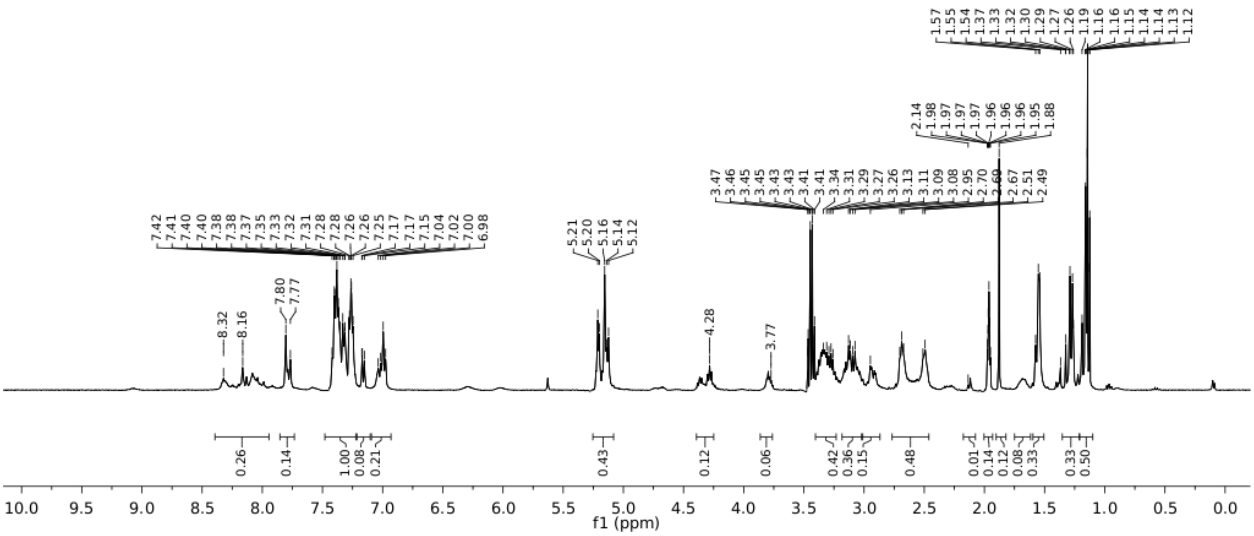

Figure AS.18. ^{1}H NMR of **5** in CD_3CN at RT (δ vs residual protio solvent signal). Residual protio solvent (1.92 ppm) is present, as well as unidentified impurities.

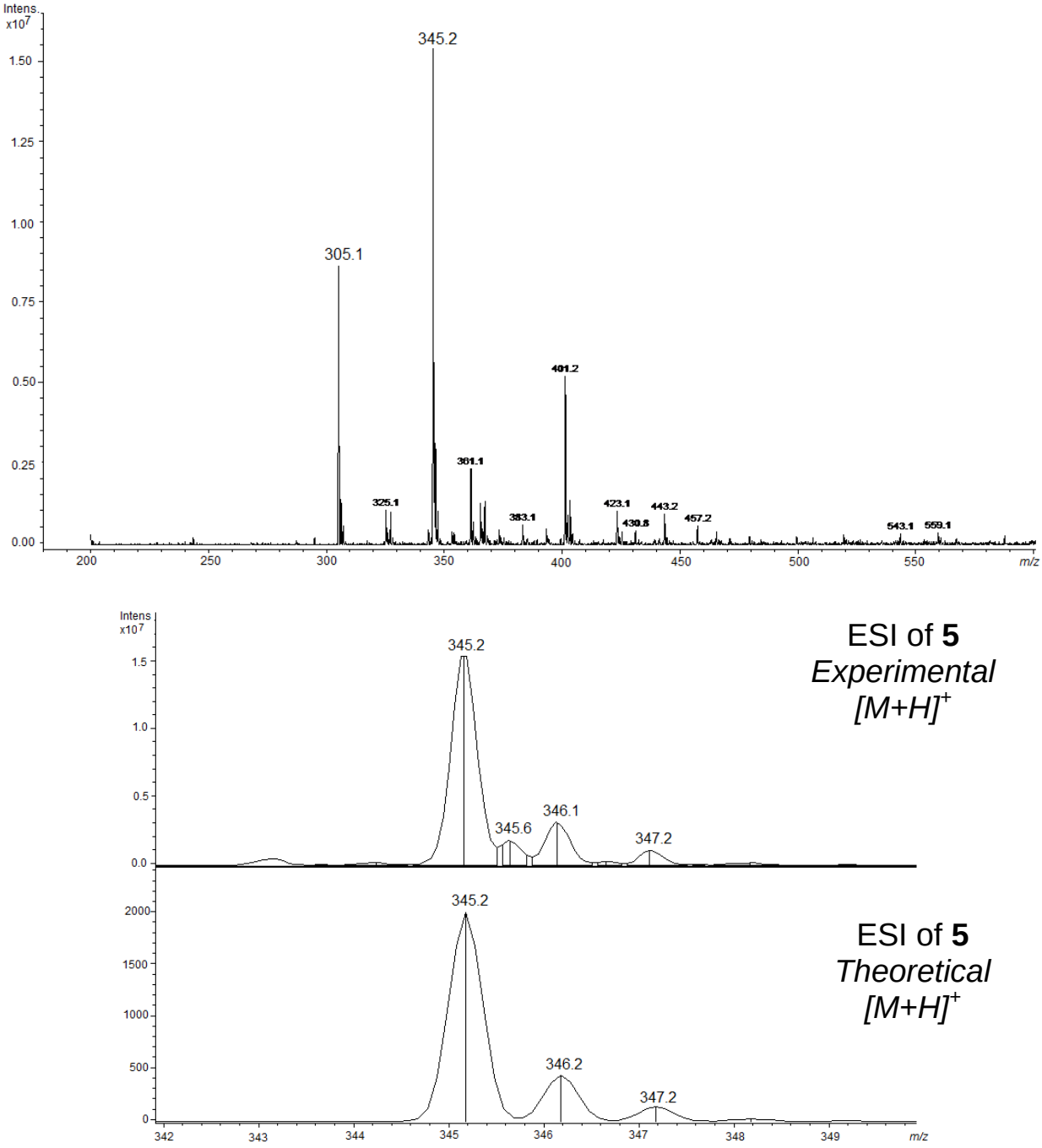

Figure AS.19. Low resolution ESI-MS (positive mode) of **5** (top). Middle and bottom represent a zoom-in of the *m/z* 345.2 peak, with some percentage of a doubly-charged ion present at *m/z* 345.6. Theoretical fit on the bottom.

A.5. References

(1) Youn, H.-D.; Youn, H.; Lee, J.-W.; Yim, Y.-I.; Lee, J. K.; Hah, Y. C.; Kang, S.-O. Unique Isozymes of Superoxide Dismutase in *Streptomyces griseus*. *Arch. Biochem. Biophys.* **1996**, *334*, 341-348.

(2) Barondeau, D. P.; Kassmann, C. J.; Bruns, C. K.; Tainer, J. A.; Getzoff, E. D. Nickel Superoxide Dismutase Structure and Mechanism. *Biochemistry* **2004**, *43*, 8038-8047.

(3) Wuerges, J.; Lee, J.-W.; Yim, Y.-I.; Yim, H.-S.; Kang, S.-O.; Carugo, K. D. Crystal Structure of Nickel-Containing Superoxide Dismutase Reveals Another Type of Active Site. *Proc. Natl. Acad. Sci. U.S.A.* **2004**, *101*, 8569-8574.

(4) Fiedler, A. T.; Bryngelson, P. A.; Maroney, M. J.; Brunold, T. C. Spectroscopic and Computational Studies of Ni Superoxide Dismutase: Electronic Structure Contributions to Enzymatic Function. *J. Am. Chem. Soc.* **2005**, *127*, 5449-5462.

(5) Szilagyi, R. K.; Bryngelson, P. A.; Maroney, M. J.; Hedman, B.; Hodgson, K. O.; Solomon, E. I. S K-Edge X-ray Absorption Spectroscopic Investigation of the Ni-Containing Superoxide Dismutase Active Site: New Structural Insight into the Mechanism. *J. Am. Chem. Soc.* **2004**, *126*, 3018-3019.

(6) Ryan, K. C.; Guce, A. I.; Johnson, O. E.; Brunold, T. C.; Cabelli, D. E.; Garman, S. C.; Maroney, M. J. Nickel Superoxide Dismutase: Structural and Functional Roles of His1 and Its H-Bonding Network. *Biochemistry* **2015**, *54*, 1016-1027.

(7) Gale, E. M.; Patra, A. K.; Harrop, T. C. Versatile Methodology Toward NiN_2S_2 Complexes as Nickel Superoxide Dismutase Models: Structure and Proton Affinity. *Inorg. Chem.* **2009**, *48*, 5620-5622.

(8) Gale, E. M.; Narendrapurapu, B. S.; Simmonett, A. C.; Schaefer, H. F., III; Harrop, T. C. Exploring the Effects of H-Bonding in Synthetic Analogues of Nickel Superoxide Dismutase (Ni-SOD): Experimental and Theoretical Implications for Protection of the Ni−SCys Bond. *Inorg. Chem.* **2010**, *49*, 7080–7096.

(9) Broering, E. P.; Dillon, S.; Gale, E. M.; Steiner, R. A.; Telser, J.; Brunold, T. C.; Harrop, T. C. Accessing Ni(III)-Thiolate versus Ni(II)-Thiyl Bonding in a Family of Ni-N_2S_2 Synthetic Models of NiSOD. *Inorg. Chem.* **2015**, *54*, 3815–3828.

(10) Lee, W.-Z.; Chiang, C.-W.; Lin, T.-H.; Kuo, T.-S. A Discrete Five-Coordinate Ni^{III} Complex Resembling the Active Site of the Oxidized Form of Nickel Superoxide Dismutase. *Chem.-Eur. J.* **2012**, *18*, 50-53.

(11) Chiang, C.-W.; Chu, Y.-L.; Chen, H.-L.; Kuo, T.-S.; Lee, W.-Z. Synthesis and Characterization of Ni^{III}N3S2 Complexes as Active Site Models for the Oxidized Form of Nickel Superoxide Dismutase. *Chem.-Eur. J.* **2014**, *20*, 6283-6286.

(12) Gale, E. M.; Simmonett, A. C.; Telser, J.; Schaefer, H. F., III; Harrop, T. C. Toward Functional Ni-SOD Biomimetics: Achieving a Structural/Electronic Correlation with Redox Dynamics. *Inorg. Chem.* **2011**, *50*, 9216–9218.

(13) Gennari, M.; Orio, M.; Pécaut, J.; Neese, F.; Collomb, M.-N.; Duboc, C. Reversible Apical Coordination of Imidazole between the Ni(III) and Ni(II) Oxidation States of a Dithiolate Complex: A Process Related to the Ni Superoxide Dismutase. *Inorg. Chem.* **2010**, *49*, 6399-6401.

(14) Nakane, D.; Wasada-Tsutsui, Y.; Funahashi, Y.; Hatanaka, T.; Ozawa, T.; Masuda, H. A Novel Square-Planar Ni(II) Complex with an Amino-Carboxamido-Dithiolato-type Ligand as an Active-Sie model of NiSOD. *Inorg. Chem.* **2014**, *53*, 6512−6523.

(15) Shearer, J.; Peck, K. L.; Schmitt, J. C.; Neupane, K. P. Cysteinate Protonation and Water Hydrogen Bonding at the Active-Site of a Nickel Superoxide Dismutase Metallopeptide-Based Mimic: Implications for the Mechanism of Superoxide Reduction. *J. Am. Chem. Soc.* **2014**, *136*, 16009–16022.

(16) Shearer, J. Insight into the Structure and Mechanism of Nickel-Containing Superoxide Dismutase Derived from Peptide-Based Mimics. *Acc. Chem. Res.* **2014**, *47*, 2332−2341.

(17) Shearer, J. Dioxygen and superoxide stability of metallopeptide based mimics of nickel containing superoxide dismutase: The influence of amine/amidate vs. bis-amidate ligation. *J. Inorg. Biochem.* **2013**, *129*, 145-149.

(18) Shearer, J. Use of a Metallopeptide-Based Mimic Provides Evidence for a Proton-Coupled Electron-Transfer Mechanism for Superoxide Reduction by Nickel-Containing Superoxide Dismutase. *Angew. Chem. Int. Ed.* **2013**, *52*, 2569-2572.

(19) Chatterjee, S. K.; Maji, R. C.; Barman, S. K.; Olmstead, M. M.; Patra, A. K. Hexacoordinate Nickel(II)/(III) Complexes that Mimic the Catalytic Cycle of Nickel Superoxide Dismutase. *Angew. Chem. Int. Ed.* **2014**, *53*, 10184-10189.

(20) Liu, Y.; Wang, Q.; Wei, Y.; Lin, Y.-W.; Li, W.; Su, J.-H.; Wang, Z.; Tian, Y.; Huanga, Z.-X.; Tan, X. Functional conversion of nickel-containing metalloproteins via molecular design: from a truncated acetyl-coenzyme A synthase to a nickel superoxide dismutase. *Chem. Comm.* **2013**, *49*, 1452--1454.

(21) Fiedler, A. T.; Brunold, T. C. Spectroscopic and Computational Studies of Ni^{3+} Complexes with Mixed S/N Ligation: Implications for the Active Site of Nickel Superoxide Dismutase. *Inorg. Chem.* **2007**, *46*, 8511-8523.

(22) Johnson, O. E.; Ryan, K. C.; Maroney, M. J.; Brunold, T. C. Spectroscopic and Computational Investigation of Three Cys-to-Ser Mutants of Nickel Superoxide Dismutase: Insight Into the Roles Played by the Cys2 and Cys6 Active-Site Residues. *J. Biol. Inorg. Chem.* **2010**, *15*, 777-793.

(23) Shearer, J. Use of a Metallopeptide-Based Mimic Provides Evidence for a Proton-Coupled Electron-Transfer Mechanism for Superoxide Reduction by Nickel-Containing Superoxide Dismutase. *Angew. Chem. Int. Ed.* **2013**, *52*, 2569-2572.

(24) Mullins, C. S.; Grapperhaus, C. A.; Kozlowski, P. M. Density Functional Theory Investigations of NiN_2S_2 Reactivity as a Function of Nitrogen Donor Type and N–H···S Hydrogen Bonding Inspired by Nickel-Containing Superoxide Dismutase. *J. Biol. Inorg. Chem.* **2006**, *11*, 617-625.

(25) Mullins, C. S.; Grapperhaus, C. A.; Frye, B. C.; Wood, L. H.; Hay, A. J.; Buchanan, R. M.; Mashuta, M. S. Synthesis and Sulfur Oxygenation of a (N_3S)Ni Complex Related to Nickel-Containing Superoxide Dismutase. *Inorg. Chem.* **2009**, *48*, 9974-9976.

(26) Grapperhaus, C. A.; Darensbourg, M. Y. Oxygen Capture by Sulfur in Nickel Thiolates. *Acc. Chem. Res.* **1998**, *31*, 451-459.

(27) Shearer, J.; Neupane, K. P.; Callan, P. E. Metallopeptide Based Mimics with Substituted Histidines Approximate a Key Hydrogen Bonding Network in the Metalloenzyme Nickel Superoxide Dismutase. *Inorg. Chem.* **2009**, *48*, 10560-10571.

(28) Farmer, P. J.; Reibenspies, J. H.; Lindahl, P. A.; Darensbourg, M. Y. Effects of Sulfur Site Modification on the Redox Potentials of Derivatives of [*N*,*N*'-Bis(2-Mercaptoethyl)-1,5-Diazacyclooctanato]Nickel(II). *J. Am. Chem. Soc.* **1993**, *115*, 4665-4674.

(29) Choudhury, S. B.; Lee, J.-W.; Davidson, G.; Yim, Y.-I.; Bose, K.; Sharma, M. L.; Kang, S.-O.; Cabelli, D. E.; Maroney, M. J. Examination of the Nickel Site Structure and Reaction Mechanism in *Streptomyces seoulensis* Superoxide Dismutase. *Biochemistry* **1999**, *38*, 3744-3752.

(30) Bryngelson, P. A.; Arobo, S. E.; Pinkham, J. L.; Cabelli, D. E.; Maroney, M. J. Expression, Reconstitution, and Mutation of Recombinant *Streptomyces coelicolor* NiSOD. *J. Am. Chem. Soc.* **2004**, *126*, 460-461.

(31) Gale, E. M.; Cowart, D. M.; Scott, R. A.; Harrop, T. C. Dipeptide-Based Models of Nickel Superoxide Dismutase: Solvent Effects Highlight a Critical Role to Ni–S Bonding and Active Site Stabilization. *Inorg. Chem.* **2011**, *50*, 10460-10471.

(32) O'Neil, J. P.; Wilson, S. R.; Katzenellenbogen, J. A. Preparation and Structural Characterization of Monoamine-Monoamide Bis(thiol) Oxo Complexes of Technetium(V) and Rhenium(V). *Inorg. Chem.* **1994**, *33*, 319-323.

(33) Nakajima, N.; Ikada, Y. Mechanism of Amide Formation by Carbodiimide for Bioconjugation in Aqueous Media *Bioconjugate Chem.* **1995**, *6*, 123.

(34) In *Carbodiimide Crosslinker Chemistry: Protein Biology Resource Library: Pierce Protein Methods*; ThermoFisher Scientific Inc.; Vol. 2015.

(35) Broering, E. P.; Truong, P. T.; Gale, E. M.; Harrop, T. C. Synthetic Analogues of Nickel Superoxide Dismutase: A New Role for Nickel in Biology. *Biochemistry* **2013**, *52*, 4-18.

(36) Fulmer, G. R.; Miller, A. J. M.; Sherden, N. H.; Gottlieb, H. E.; Nudelman, A.; Stoltz, B. M.; Bercaw, J. E.; Goldberg, K. I. NMR Chemical Shifts of Trace Impurities: Common Laboratory Solvents, Organics, and Gases in Deuterated Solvents Relevant to the Organometallic Chemist. *Organometallics* **2010**, *29*, 2176–2179.

APPENDIX B

SYNTHESIS AND CHARACTERIZATION OF A METHYL-ESTER APPENDED N_2S_2 CHEMOSENSOR FOR Ni(II)

B.1 Introduction

The design of the N_2S_2-Dns sensor was modified to include a methyl ester (OMe) functional group adjacent to the carboxamide-N to provide the four coordinate (4C) N/S sensor, N_2S_2(OMe)-Dns, where Dns is the dansyl chromophore. This chelate is inspired by the basal plane donors found in NiSOD, as is the first generation sensor (see Ch. 6), to provide binding tuned for Ni(II). The prediction is that the addition of methyl ester to the cysteamine backbone will provide improved aqueous solubility. This property is desired, as the ideal Ni(II) sensor will be compatible with physiological conditions for sensing of the metal in cells. We expect the methyl ester functionality to improve the ease of deprotonation as well; the ester can delocalize electron density over the carbonyl, promoting a more facile loss of the proton from the amide and Ni(II) coordination. As compared to free cysteine, the methyl ester functionality decreases the pK_a of the NH_3 and SH from 10.8 to 8.9 and 8.3 to 6.56, respectively.[1] Utilizing cysteine methyl ester in the synthesis of a sensor will afford a more readily deprotonated carboxamide-N and a strong-field ligand environment poised to bind Ni(II) in a square-planar environment.

The synthesis of the trityl protected N_2S_2(OMe)-Dns (**4**) is analogous to the synthesis of the N_2S_2-Dns-trit sensor (see Ch. 5), except for the conditions for dansyl conjugation to the N/S

chelate: refluxing conditions are too harsh for the methyl ester and are a detriment to the yield (as low as 17%). An improved, yet still modest, yield is obtained by stirring dansyl chloride and the N_2S_2(OMe)-$(Tr)_2$ (**3**) compound at RT for more than 5 days. Future directions include the full characterization of the apo sensor N_2S_2(OMe)-Dns (**5**), metalation of **5**, and evaluation of the sensor's photophysical properties. The sensor **5** will be an advancement over the previous generation, due to easier deprotonation of the carboxamide-N, which will in turn result in improved Ni(II) coordination under physiological conditions.

Scheme B.1. Synthesis of the trityl-protected N_2S_2-OMe-FL sensor (**5**).

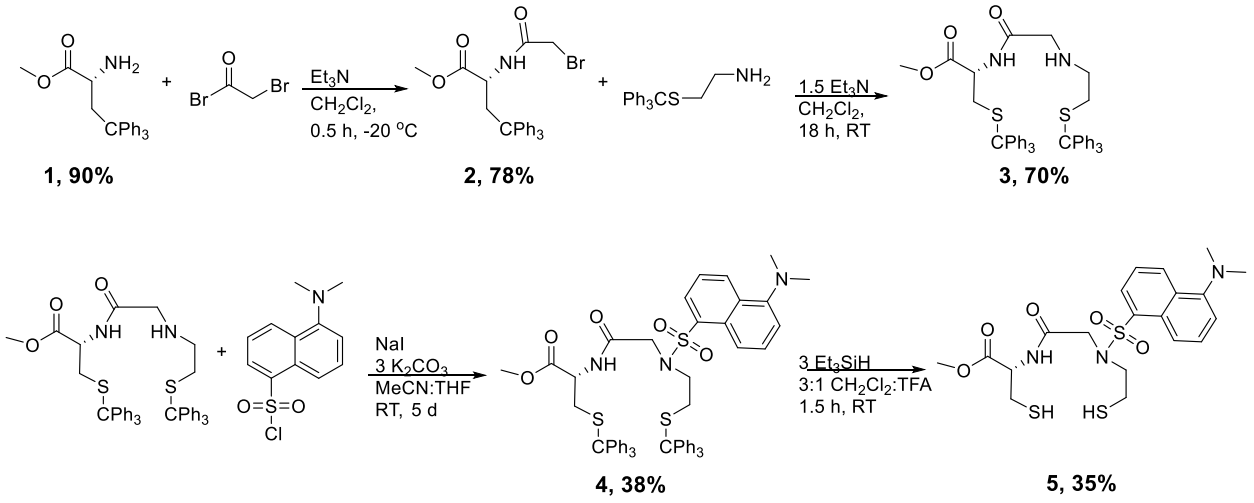

B.2 Experimental

General Information (see Appendix A)

Physical Methods (see Appendix A)

The syntheses of H_2N-L-Cys(STr)-OMe (**1)** and *S*-tritylcysteamine were carried out according to previously published procedures.[2-4]

Synthesis of Bromo-Cys(STrit)-OMe (2). To a solution of **1** (3.7961 g, 10.056 mmol) in 12 mL CH_2Cl_2 was added Et_3N (1.61 mL, 10.1 mmol) and 1 equiv bromoacetyl bromide (0.873 mL, 10.1 mmol) in 2 mL CH_2Cl_2 at 0°C. The purple solution stirred at 0°C for 15 min and was allowed to warm up to RT. The reaction was quenched with 50 mL deionized H_2O, and the organic layer was washed with satd. $NaHCO_3$, satd. NaCl, dried over $MgSO_4$, and filtered. The solvent was removed in vacuo to afford 3.9003 g (7.826 mmol) in 78% yield. The characterization is consistent with previously synthesized **2**.[5]

Synthesis of N_2S_2(OMe)-$(Tr)_2$ (3). To a solution of **2** (3.900 g, 7.825 mmol) in 11 mL CH_2Cl_2 was added 1.5 equiv Et_3N (1.629 mL, 11.72 mmol) and *S*-trityl cysteamine 2.5048 g (7.8407 mmol). The solution stirred for 22 h, and the dark brown mixture was diluted to 50 mL CH_2Cl_2, washed with satd. $NaHCO_3$, satd. NaCl, dried over $MgSO_4$, and filtered. A portion of the resulting brown oil (1.0890 g) was purified over silica with EtOAc/hexane (2:1) (R_f = 0.63) to afford a brown glassy foam (0.7680 g, 1.042 mmol) in 70% yield. ^{1}H NMR (500 MHz, $CDCl_3$ containing 0.05% v/v TMS, δ from TMS): 7.65 (s, 1H), 7.43-7.18 (m, 35H, integrates high due to residual protio solvent), 4.50 (d, 1H, J = 5.0 Hz) 3.63 (s, 3H, Me), 3.06 (d, 2H, J = 5.0 Hz), 2.62 (m, 2H), 2.58 (m, 2H), 2.37 (t, 2H, J = 7.5 Hz). ^{13}C NMR (125 MHz, $CDCl_3$ containing 0.05% v/v TMS, δ from TMS): 171.29 (C=O), 170.79 (C=O), 144.78, 144.33, 129.60, 128.10, 126.76, 66.85, 66.73, 52.55, 51.66, 50.79, 48.15, 33.93, 32.34. FTIR (KBr pellet) ν_{max} (cm^{-1}): 3332 (w, br ν_{NH}), 3055 (w), 2950 (w), 2840 (w), 1744 (vs, ν_{CO}, ester), 1678 (vs, ν_{CO}), 1592 (w), 1495 (s), 1439 (s), 1320 (w), 1254 (w), 1207 (m), 1181 (m), 1121 (w), 1027 (m), 913 (w), 743 (vs), 699 (vs), 618 (w), 498 (w). LR-ESI-MS (*m/z*): $[M+H]^+$ calcd for $C_{46}H_{44}N_2O_3S_2$, 737.3

(100), 738.3 (51.4), 739.3 (21.1), 740.3 (6.4); found: 737.2 100.0), 738.2 (43.7), 739.2 (22.8), 740.2 (7.0).

Synthesis of N_2S_2(OMe)-$(Tr)_2$-Dns (4). To a solution of **3** (1.0516 g, 1.378 mmol) in a 20 mL solution of THF/MeCN (1:1) was added dansyl chloride (0.3711 g, 1.375 mmol) in 8 mL THF/MeCN (1:1). To the resulting orange, homogenous solution was added 1 equiv NaI (0.2122 g, 1.415 mmol) and 3 equiv K_2CO_3 (0.5784 g, 4.185 mmol). The heterogeneous mixture was stirred under N_2(g) in the dark for 5 days to result in a dark orange color. The solvent was removed in vacuo, and the dark orange solid was redissolved in 50 mL CH_2Cl_2, washed with satd. $NaHCO_3$, satd. NaCl, dried over $MgSO_4$, and filtered. The orange oil was purified over silica EtOAc/hexane (2:1) (R_f = 0.58) to afford a bright yellow-green foam (0.5063 g, 0.5218 mmol) in 38% yield. ^{1}H NMR (500 MHz, $CDCl_3$ containing 0.05% v/v TMS, δ from TMS): 8.57 (d, 2H, J = 10.0 Hz), 8.16 (d, 2H, J = 5.0 Hz), 7.53-7.17 (m, 34H, integrates high due to residual protio solvent), 4.24 (m, 1H) 3.63 (t, 5H, J = 5.0 Hz), 3.22 (m, 1H), 3.05 (m, 1H), 2.91 (s, 6H), 2.56-2.39 (m, 4H). ^{13}C NMR (125 MHz, $CDCl_3$ containing 0.05% v/v TMS, δ from TMS): 170.00 (C=O), 167.69 (C=O), 152.07, 144.33, 133.21, 131.19, 130.66, 129.92, 129.55, 128.81, 128.08, 127.98, 126.90, 126.78, 123.21, 118.71, 115.31, 67.21, 66.98, 60.45, 52.55, 51.49, 50.50, 48.58, 45.46, 45.44, 33.32, 29.55, 21.13. FTIR (KBr pellet) ν_{max} (cm^{-1}): 3390 (m, br ν_{NH}), 3056 (w), 3024 (w), 2944 (w), 2832 (w), 2784 (w), 1745 (s, ν_{CO} ester), 1686 (s, ν_{CO}), 1588 (w), 1488 (s), 1442 (s), 1259 (w), 1205 (m), 1141 (vs, ν_{SO}), 1073 (s), 1032 (m), 912 (m), 845 (w), 793 (m), 742 (s), 699.5 (vs), 621 (m), 567 (w), 481 (w). LR-ESI-MS (*m/z*): $[M+K^+]^+$ calcd for $C_{58}H_{55}KN_3O_5S_3$, 1008.3 (100), 1009.3 (65.1), 1010.3 (40.1), 1011.3 (16.1); found: 1008.3 (100), 1009.3 (67.4), 1010.3 (46.3), 1011.3 (20.3).

Synthesis of N_2S_2(OMe)-Dns (5). To a 3 mL CH_2Cl_2 solution of **4** (0.5010 g, 0.5163 mmol) was added 2 mL TFA, which resulted in an orange solution. To it was added Et_3SiH (0.25 mL, 1.6 mmol) and the color bleached. The solution stirred for 1.5 h under N_2, and the solvent was removed vacuum distillation. The beige oil was triturated with hexane (5 mL × 5) to remove Ph_3CH. The beige residue was dissolved in 25 mL CH_2Cl_2, washed with satd. $NaHCO_3$, satd. NaCl, dried over $MgSO_4$, and filtered. The solvent was removed in vacuo to yield **5** as a yellow oil (0.0875 g, 0.1802 mmol) in 35% yield. ^{1}H NMR (500 MHz, $CDCl_3$ containing 0.05% v/v TMS, δ from solvent): 8.64 (d, 1H, J = 10 Hz), 8.34 (d, 1H, J = 10 Hz), 8.29, (d, 1H, J = 5 Hz), 7.66 (t, 1H, J = 10 Hz), 7.60 (t, 1H, J = 10 Hz), 7.35 (d, 1H, J = 5 Hz), 4.82 (d, 1H, J = 10 Hz), 3.99 (dd, 2H), 3.82 (s, 3H, Me), 3.67 (m, 2H), 2.94 (s, 6H, Me), 2.81 (m, 4H), 1.49 (t, 1H, S*H*, J = 7.5 Hz), 1.39 (t, 1H, S*H*, J = 7.5 Hz). ^{13}C NMR (125 MHz, $CDCl_3$ containing 0.05% v/v TMS, δ from solvent): 169.92 (C=O), 152.23 (C=O), 132.90, 131.47, 130.60, 130.18, 129.93, 129.45, 129.02, 128.30, 126.30, 123.27, 118.58, 115.57, 53.85, 53.04, 52.87, 51.82, 45.41, 26.48, 22.91. FTIR (KBr pellet) ν_{max} (cm^{-1}): 3344 (m, br ν_{NH}), 1742 (m, ν_{CO} ester), 1681 (vs, ν_{CO}), 1518 (w), 1475 (w), 1439 (m), 1334 (m), 1207 (vs, ν_{SO}), 1141 (vs, ν_{SO}), 1047 (w), 925 (w), 839 (m), 802 (s), 708 (m), 584 (m), 532 (w). LR ESI-MS (CH_2Cl_2/MeOH) *m/z* $[M+H]^+$ calcd for $C_{20}H_{28}N_3O_5S_3$, 486.1 (100), 487.1 (25.1), 488.1 (16.8); found 486.0 (100), 487.0 (27.1), 488.0 (16.2).

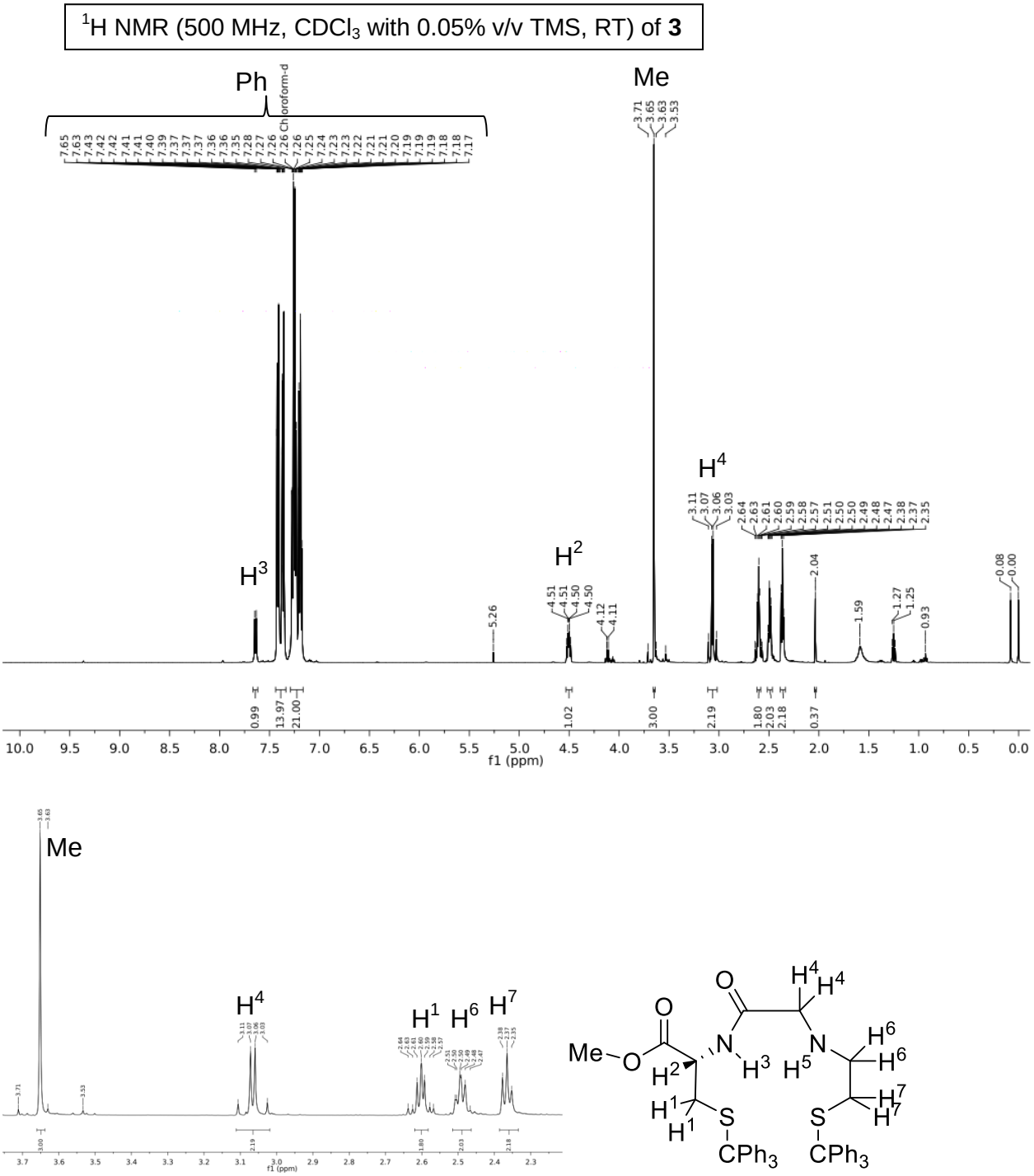

Figure B.1. *Top*: ^{1}H NMR spectrum of N_2S_2(OMe)-(Tr)$_2$ (**3**) in $CDCl_3$ containing 0.05% v/v TMS at RT (δ vs. residual protio solvent signal). The peaks at 7.26, 5.26, 4.12, 2.04, 1.25, and 0.99 ppm are from protio solvent, CH_2Cl_2, EtOAc, and hexane, respectively. *Bottom*: expansion of the aliphatic region.

^{13}C NMR (125 MHz, $CDCl_3$ with 0.05% v/v TMS, RT) of **3**

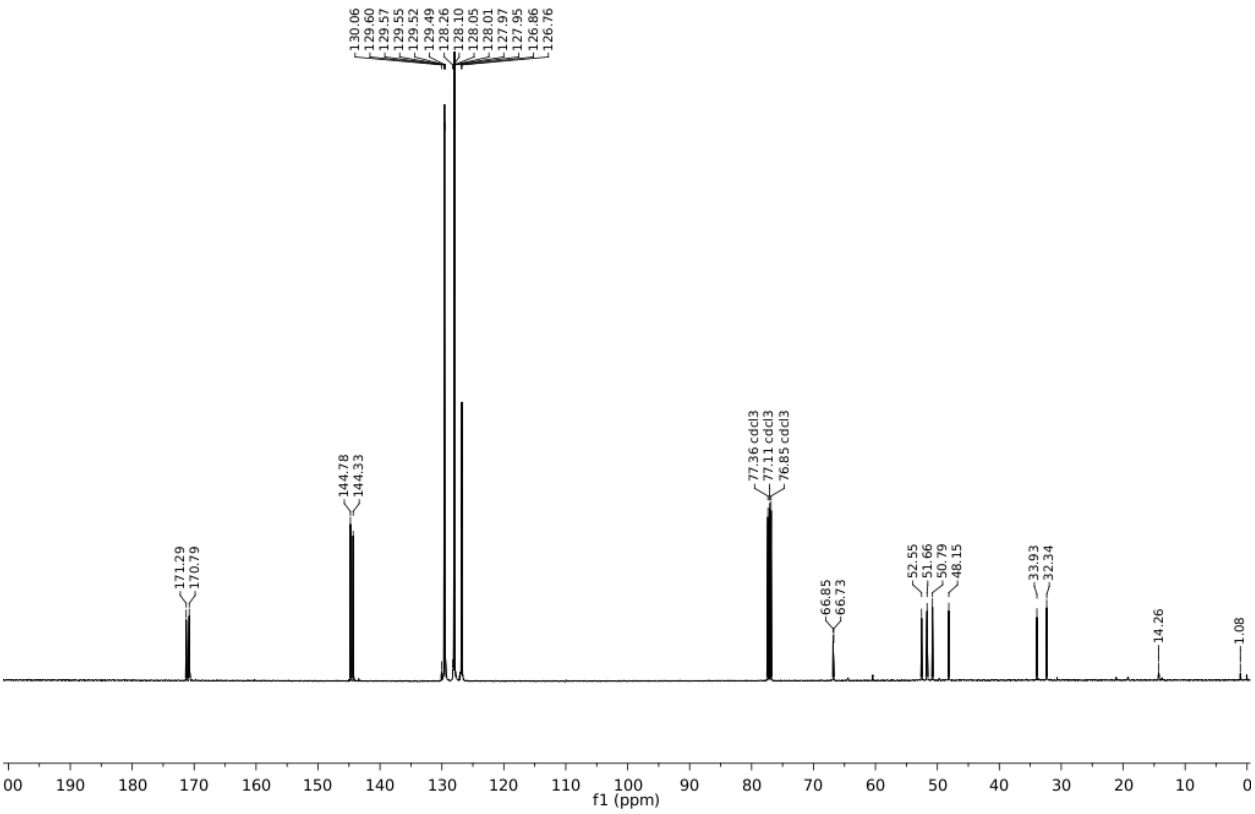

Figure B.2. ^{13}C NMR spectrum of N_2S_2(OMe)-$(Tr)_2$ (**3**) in $CDCl_3$ containing 0.05% v/v TMS at RT (δ vs. residual solvent signal). Solvent signal at 77.16 ppm is indicated. Pentane from workup is present at 14.26 ppm.

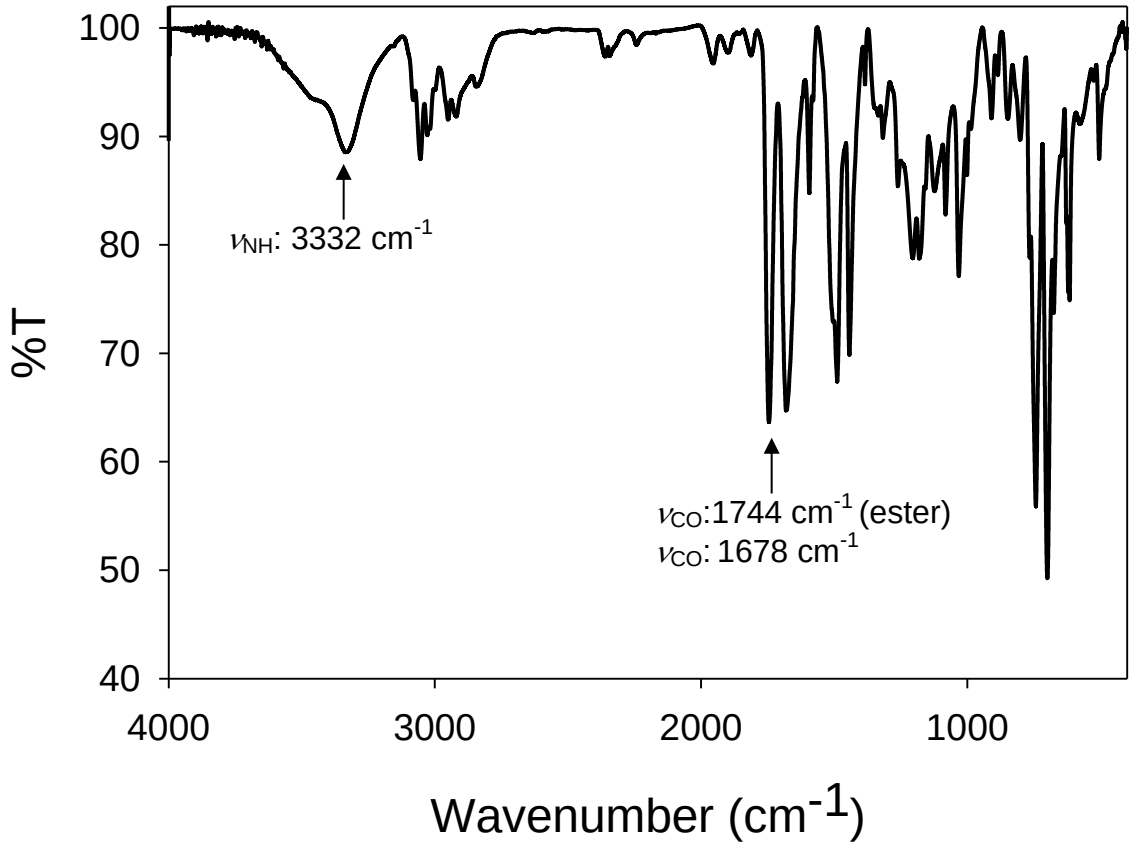

Figure B.3. Solid-state FTIR spectrum of **3** in a KBr matrix at RT.

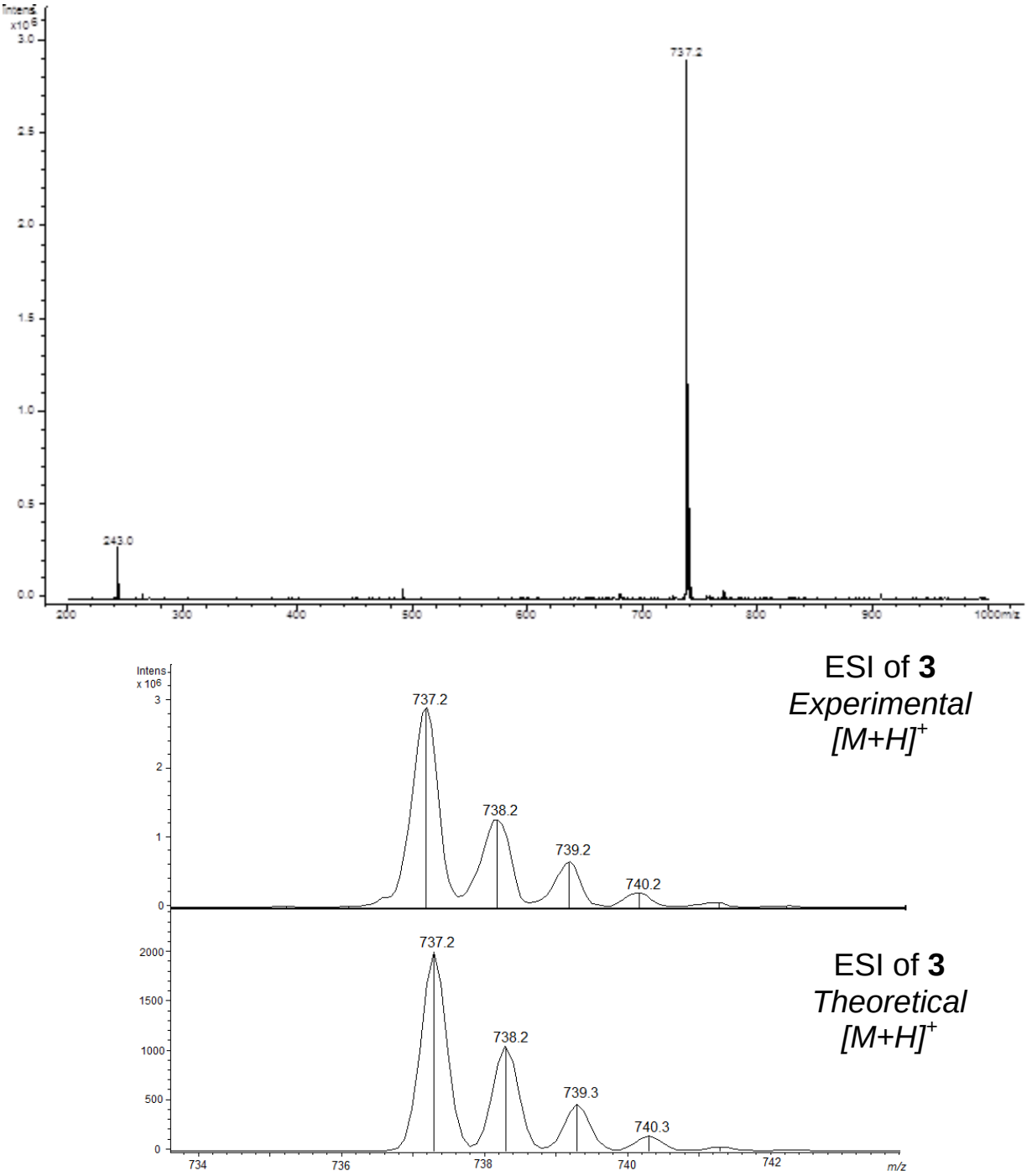

Figure B.4. Low resolution ESI-MS (positive mode) of **3** (top). Middle and bottom represent a zoom-in of the *m/z* 737.2 peak. Theoretical fit on the bottom.

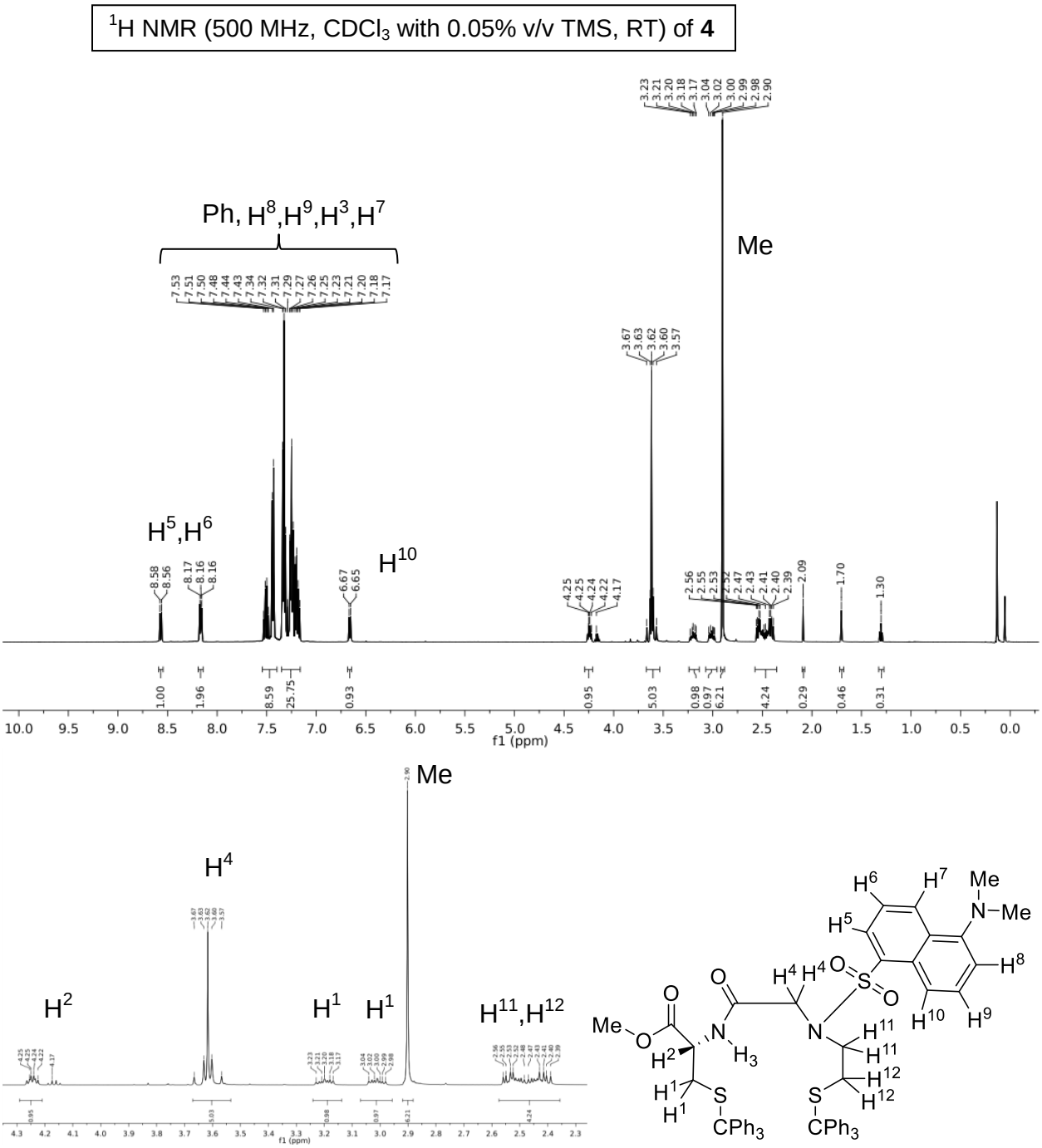

Figure B.5. *Top*: ^{1}H NMR spectrum of N_2S_2(OMe)-$(Tr)_2$-Dns (**4**) in $CDCl_3$ containing 0.05% v/v TMS at RT (δ vs. residual protio solvent signal). The peaks at 7.26, 4.12, 2.04, and 1.25 ppm are from protio solvent and EtOAc, respectively. *Bottom*: expansion of the aliphatic region.

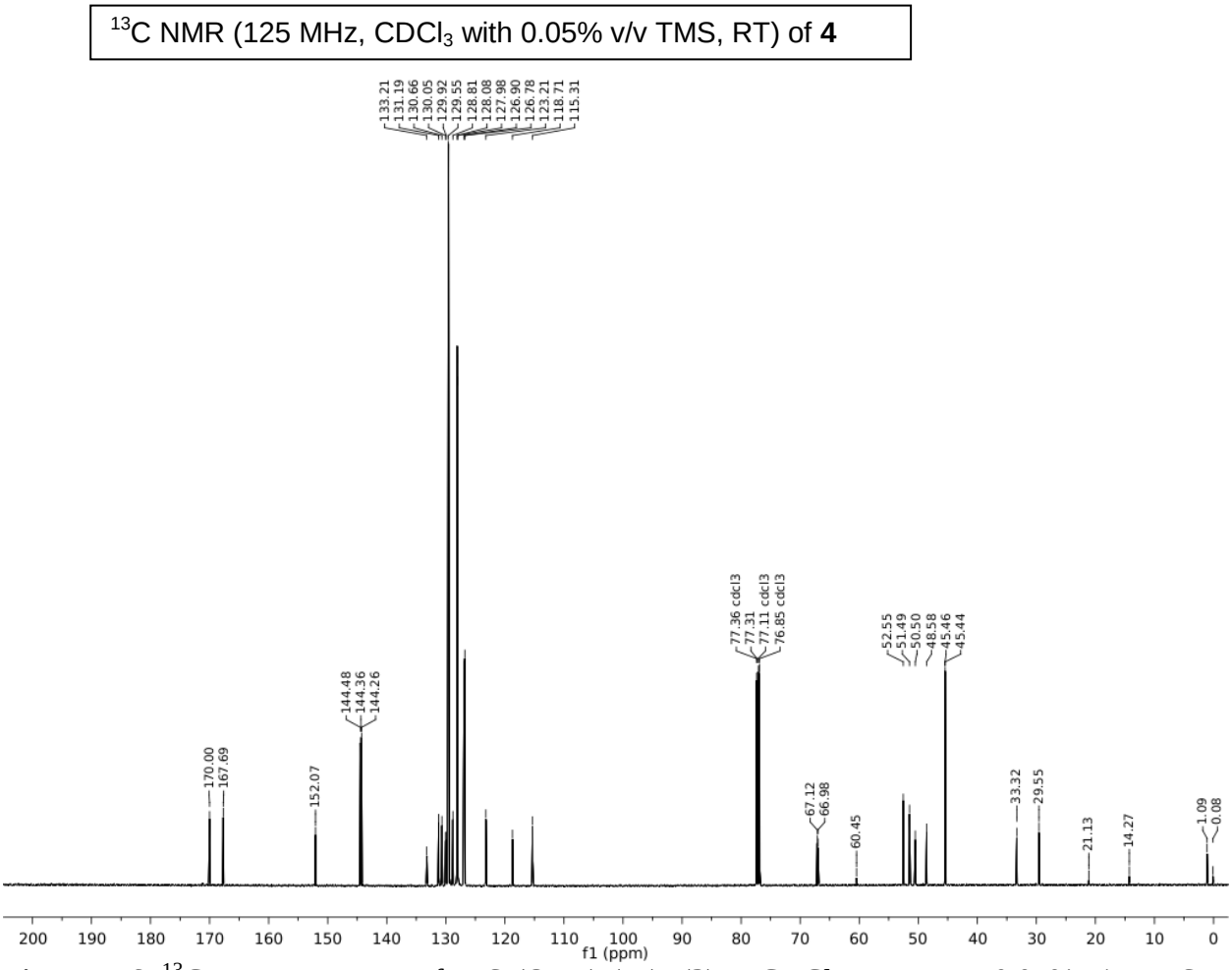

Figure B.6. ^{13}C NMR spectrum of N_2S_2(OMe)-$(Tr)_2$ (**3**) in $CDCl_3$ containing 0.05% v/v TMS at RT (δ vs. residual solvent signal). Solvent signal at 77.16 ppm is indicated. Pentane from workup is present at 14.27 ppm.

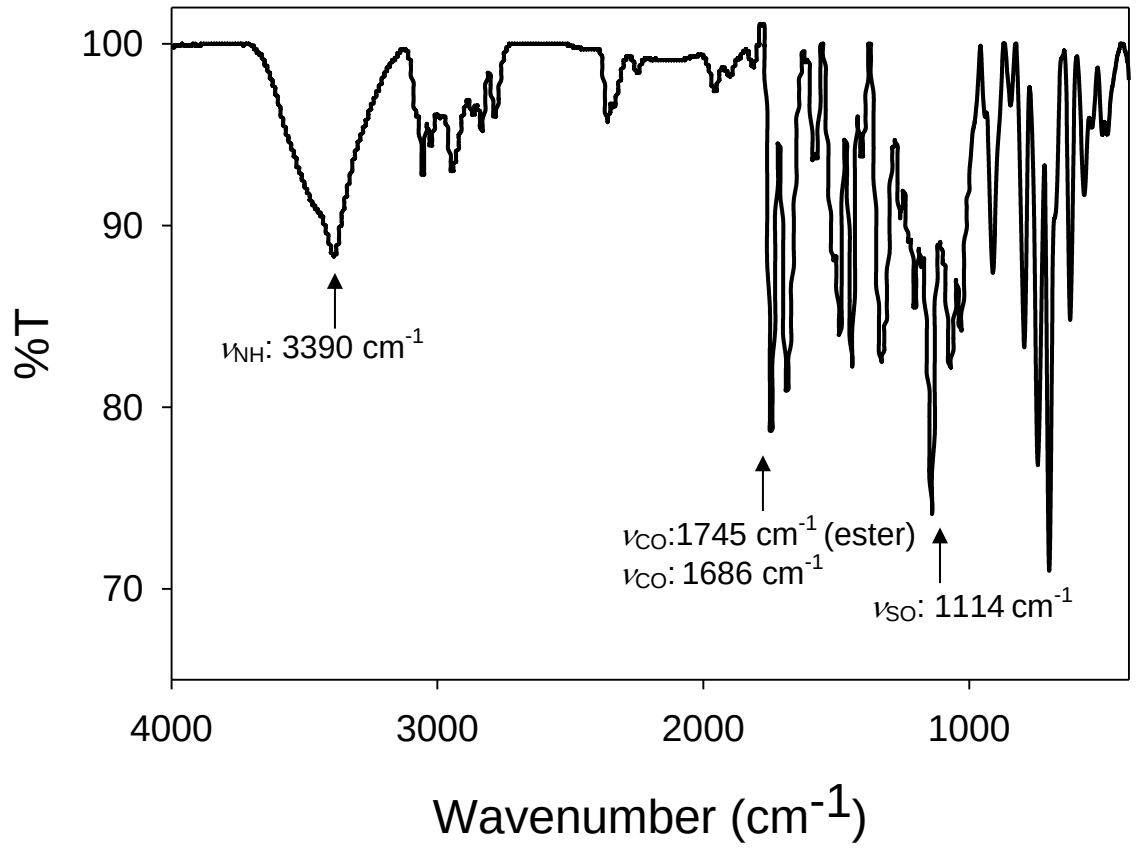

Figure B.7. Solid-state FTIR spectrum of **4** in a KBr matrix at RT.

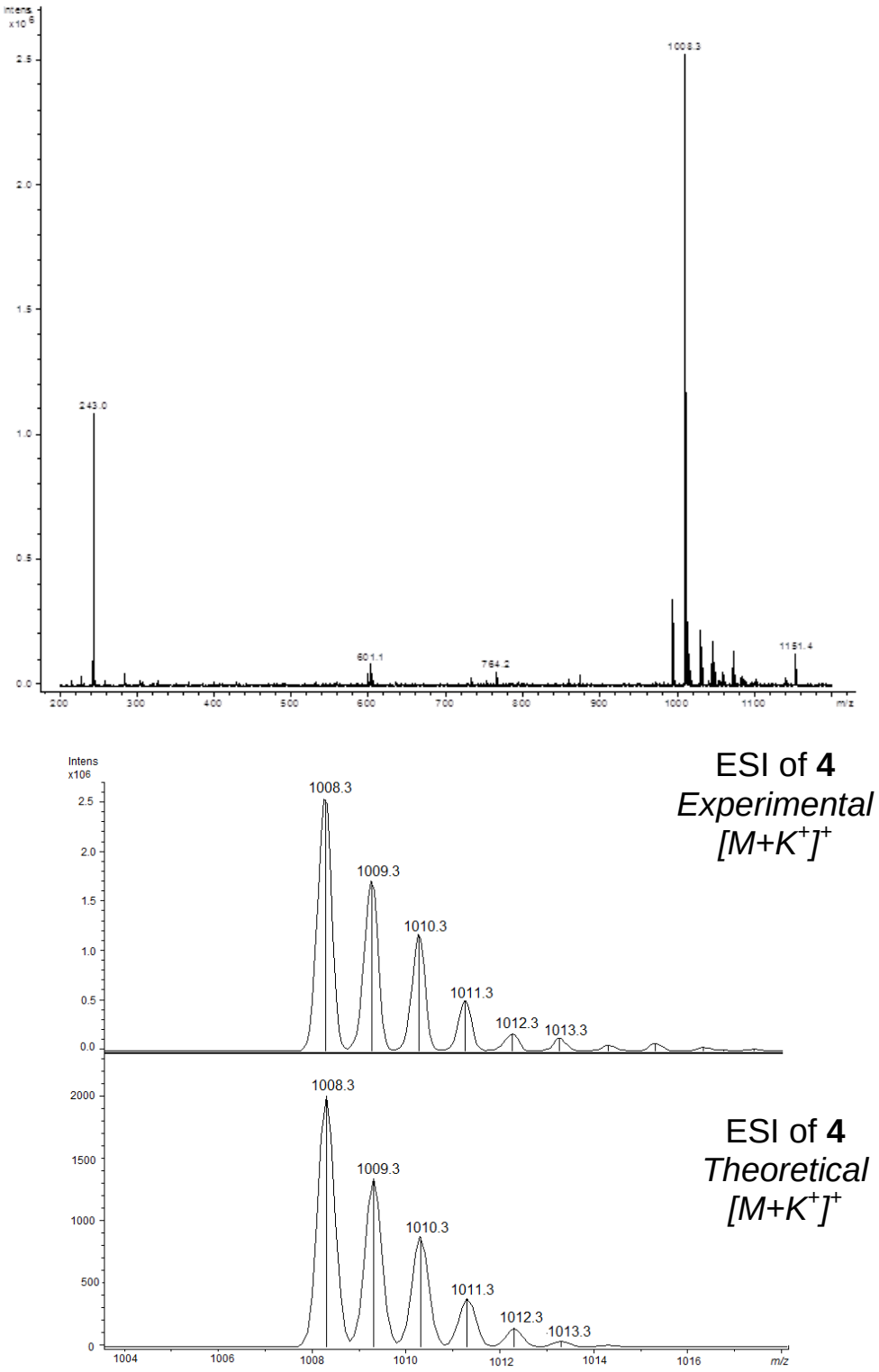

Figure B.8. Low resolution ESI-MS (positive mode) of **4** (top). Middle and bottom represent a zoom-in of the *m/z* 1008.3 peak. Theoretical fit on the bottom.

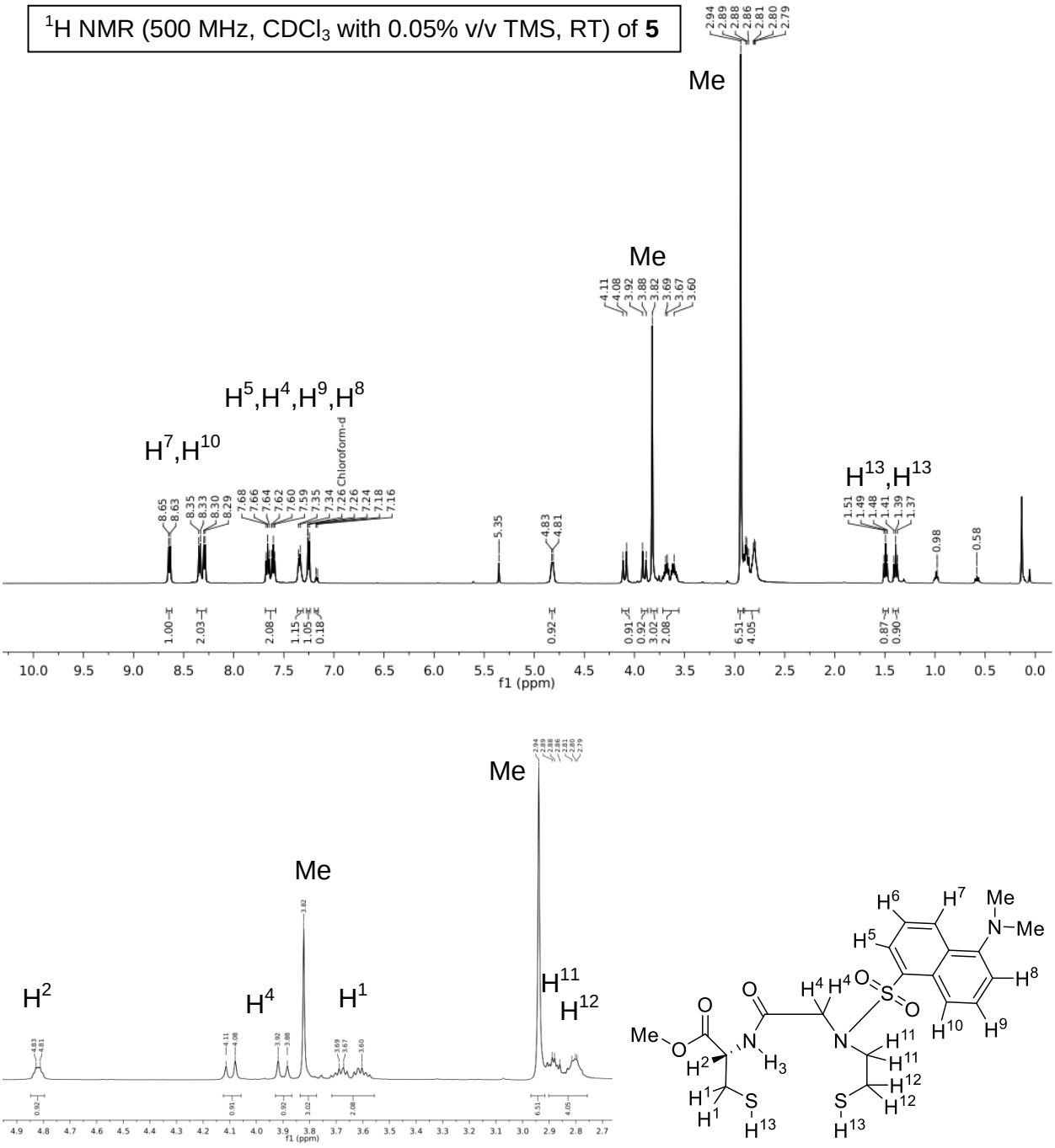

Figure B.9. *Top*: ^{1}H NMR spectrum of N_2S_2(OMe)-Dns (**5**) in $CDCl_3$ containing 0.05% v/v TMS at RT (δ vs. residual protio solvent signal). The peaks at 7.26, 7.16, and 5.35 ppm are from protio solvent and residual Ph_3CH respectively. *Bottom*: expansion of the aliphatic region.

^{13}C NMR (125 MHz, $CDCl_3$ with 0.05% v/v TMS, RT) of **5**

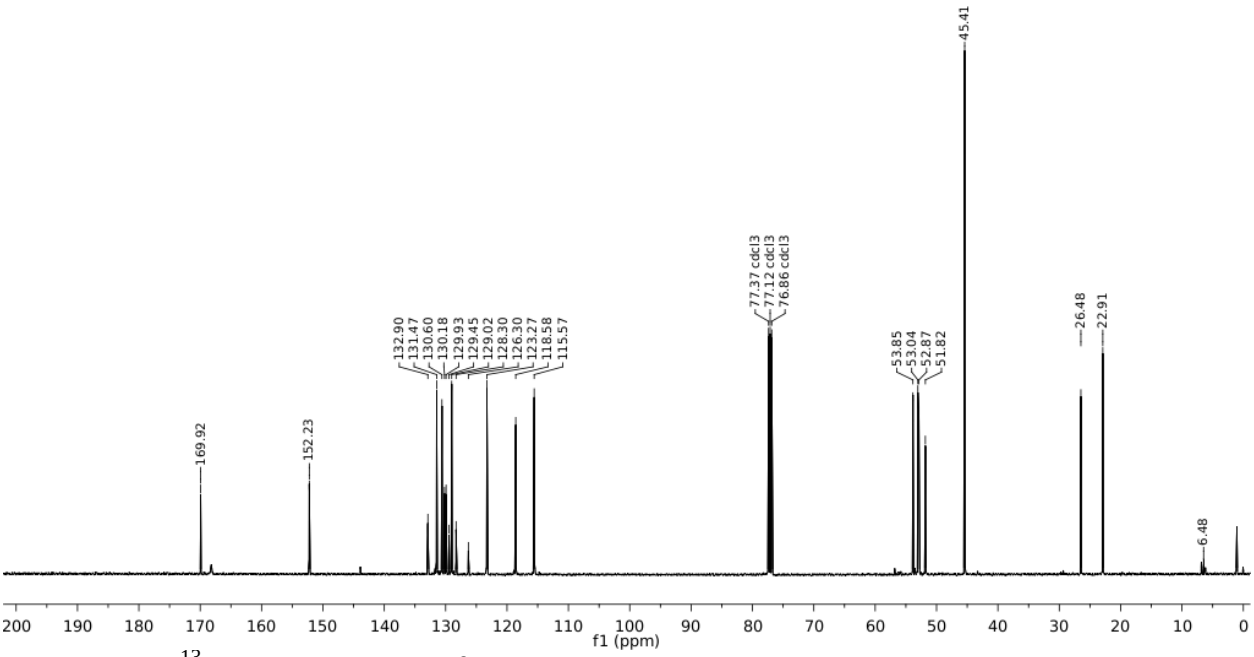

Figure B.10. ^{13}C NMR spectrum of N_2S_2(OMe)-Dns (**5**) in $CDCl_3$ containing 0.05% v/v TMS at RT (δ vs. residual solvent signal). Solvent signal at 77.12 ppm is indicated.

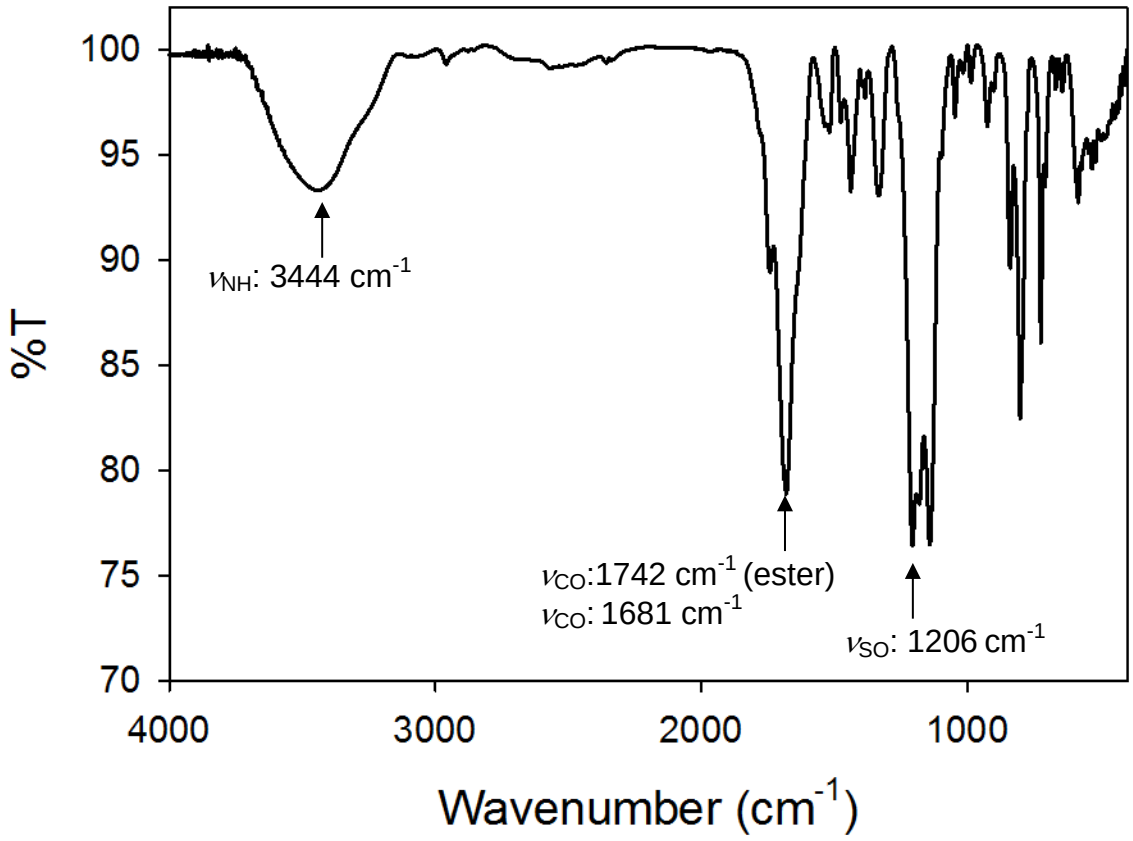

Figure B.11. Solid-state FTIR spectrum of **5** in a KBr matrix at RT.

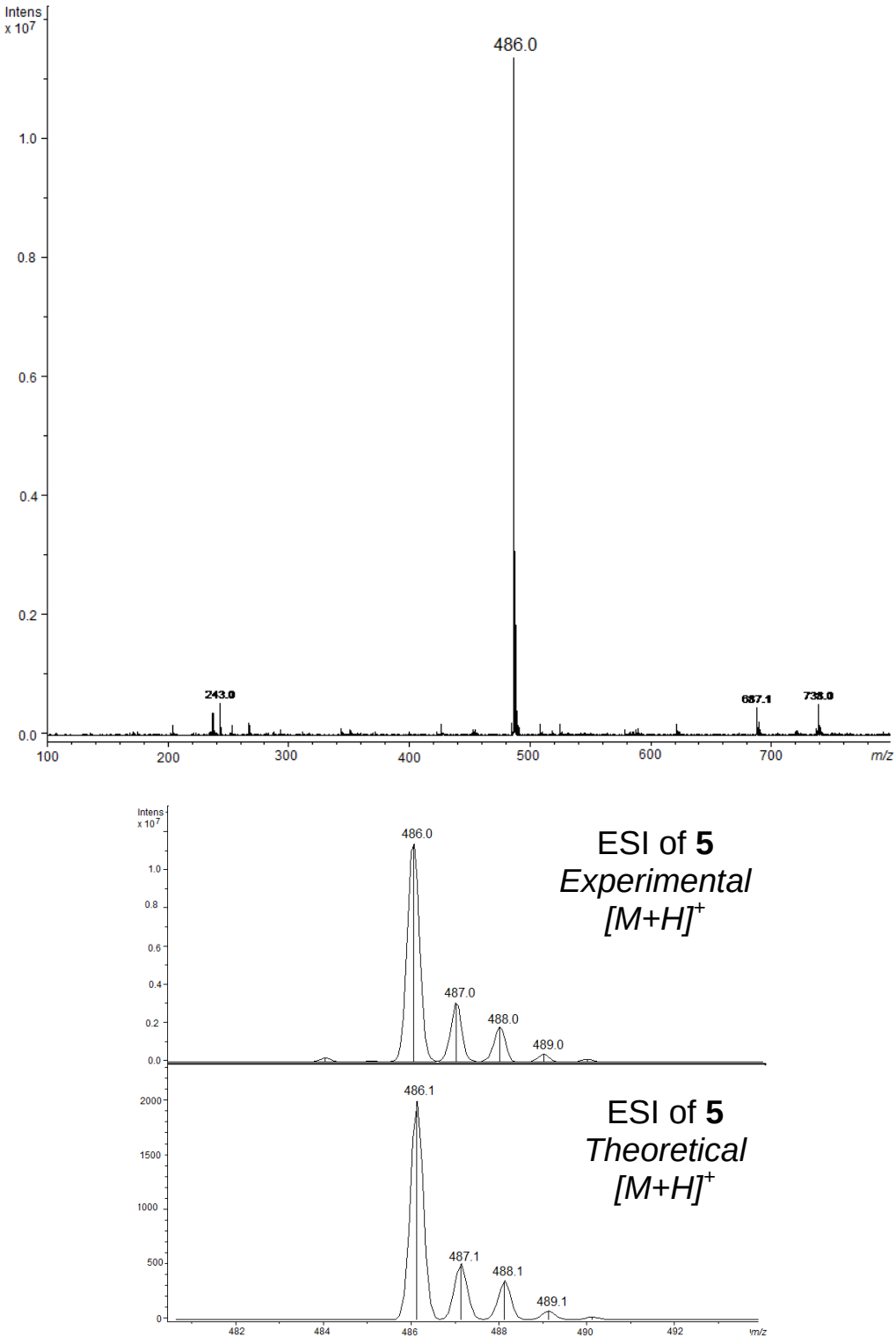

Figure B.12. Low resolution ESI-MS (positive mode) of **5** (top). Middle and bottom represent a zoom-in of the *m/z* 486.0 peak. Theoretical fit on the bottom.

B.3 References

(1) Perrin, D. D. *Dissociation Constants of Organic Bases in Aqueous Solution*; Suppl, 1972 ed.; Butterworths: London, 1972.

(2) Gale, E. M.; Patra, A. K.; Harrop, T. C. Versatile Methodology Toward NiN_2S_2 Complexes as Nickel Superoxide Dismutase Models: Structure and Proton Affinity. *Inorg. Chem.* **2009**, *48*, 5620-5622.

(3) O'Neil, J. P.; Wilson, S. R.; Katzenellenbogen, J. A. Preparation and Structural Characterization of Monoamine-Monoamide Bis(thiol) Oxo Complexes of Technetium(V) and Rhenium(V). *Inorg. Chem.* **1994**, *33*, 319-323.

(4) Gale, E. M.; Cowart, D. M.; Scott, R. A.; Harrop, T. C. Dipeptide-Based Models of Nickel Superoxide Dismutase: Solvent Effects Highlight a Critical Role to Ni–S Bonding and Active Site Stabilization. *Inorg. Chem.* **2011**, *50*, 10460-10471.

(5) Gale, E. M. Coordination Chemistry Inspired by Nickel Superoxide Dismutase: Understand Nickel and Sulfur in the Context of Anti-Oxidant Defense. University of Georgia, Athens, GA. **2012**.